

LIQUID CRYSTALS

Relationship between the Temperature Dependence of the Induced Helical Pitch and the Anisometry of Molecules of Chiral Dopants

N. I. Shkolnikova, L. A. Kutulya, N. S. Pivnenko, R. I. Zubatyuk, and O. V. Shishkin

Institute for Single Crystals, National Academy of Sciences of Ukraine, pr. Lenina 60, Kharkov, 61001 Ukraine

e-mail: nataly@isc.kharkov.com; kutulya@isc.kharkov.com

Received April 17, 2004

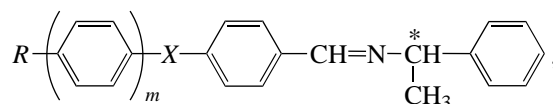
Abstract—The regularities of changes in the temperature dependence of the helical pitch P and the parameter dP/dt are analyzed for induced cholesteric liquid-crystal systems based on nematic 4-pentyl-4'-cyanobiphenyl, including chiral arylidene derivatives of (*S*)-1-phenylethylamine and (*1R*),(*4R*)-isomenthone. In the molecules of these compounds, the length of the π -electron arylidene fragment, the nature of the bridge group between its benzene rings and of the lateral substitution in the cyclohexanone ring, and the length of the terminal alkyl or oxyalkyl substituent are varied. The statistical molecular anisometry of the chiral dopants is calculated using the density functional method and the semiempirical AM1 method. It is shown that the temperature dependence of the induced helical pitch and, correspondingly, its quantitative characteristic dP/dt and the parameter dt/dC , characterizing the effect of a chiral dopant on the thermal stability of the mesophase, are determined by the molecular anisometry of the chiral component. © 2005 Pleiades Publishing, Inc.

INTRODUCTION

The development of display technologies based on nematic liquid crystals (LCs) doped with chiral compounds has increased the urgency of studying the temperature dependence of the induced helical pitch, its changes with a change in the nature of chiral components, and the possibilities of predicting the character of this dependence, which is necessary to implement specific physical effects. Chiral dopants in such systems not only provide a uniform twist structure of LC elements but are also used to control the temperature dependence of threshold voltages, thus ensuring stable device operation. To this end, according to [1, 2], it is preferable to use chiral dopants inducing a helix with a large negative temperature gradient within the helical pitch P ($dP/dt < 0$). In recent years, the design of systems with a temperature-independent helical pitch for the development of data mapping tools with intrinsic memory based on texture transitions in induced cholesteric liquid crystals (CLCs) have become of particular importance [3].

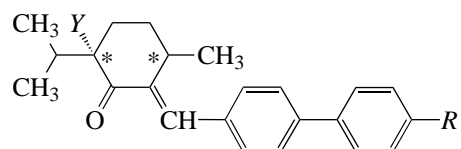
Despite a large amount of data on the effect of chiral components on the macroscopic properties of induced cholesteric mesophases [4, 5], the questions related to the temperature dependence of the induced helical pitch and the influence of the structure of impurity molecules on the degree of order of the mesophase are still to be clarified. The existing theoretical models describe some dependences $P(t)$ quite adequately [6–8]; however, they do not demonstrate convincing predictive possibilities.

The purpose of this study is to reveal the relationship between the molecular structure of chiral components and the macroscopic parameters of LC systems and to develop approaches to intentional preparation of induced CLCs with a specified type and quantitative characteristics of the temperature dependence of the helical pitch. In the systems based on the nematic 4-pentyl-4'-cyanobiphenyl (5CB), we investigated the behavior of chiral arylidene derivatives of (*S*)-1-phenylethylamine (**1–20**) and (*1R*),(*4R*)-isomenthone (**21–31**) with the successively varied molecular structure



where $X = 0$, $m = 0$: $R = \text{OCOCH}_3$ (**1**); $X = \text{COO}$, $m = 1$: $R = \text{H}$ (**2**); CH_3 (**3**); C_2H_5 (**4**); C_3H_7 (**5**); C_4H_9 (**6**); OCH_3 (**7**); OC_2H_5 (**8**); OC_3H_7 (**9**); OC_5H_{11} (**10**); $\text{OC}_{10}\text{H}_{21}$ (**11**); $m = 2$: $R = \text{H}$ (**12**); CH_3 (**13**); C_7H_{15} (**14**); C_8H_{17} (**15**); C_9H_{19} (**16**); $\text{C}_{10}\text{H}_{21}$ (**17**); $X = \text{CH}_2\text{O}$, $m = 1$: $R = \text{CH}_3$ (**18**); C_4H_9 (**19**); and OCH_3 (**20**)

and



where $Y = \text{H}$: $R = \text{H}$ (**21**); OCH_3 (**22**); OC_5H_{11} (**23**); OC_6H_{13} (**24**); $Y = \text{CH}_3$: $R = \text{H}$ (**25**); OCH_3 (**26**); OC_5H_{11}

(**27**); OC₆H₁₃ (**28**); Y = Br; R = H (**29**); OCH₃ (**30**); and OC₅H₁₁ (**31**).

The temperature dependence of the helical pitch in the systems under study was quantitatively characterized by the parameter dP/dt . Taking into account the theoretical prerequisites concerning the temperature dependence of P as a function of the order parameter of LC systems [6, 7], we also studied the regularities of the effect of chiral dopants on the thermal stability and, accordingly, the degree of order in induced CLCs. This effect was characterized quantitatively by the parameter $A_{N^*} = dt_i/dC$, where t_i is the temperature of the phase transition from the induced cholesteric N^* to the isotropic liquid I , and C is the chiral dopant concentration. It is reasonable to analyze experimental changes in the parameters dP/dt and dt_i/dC on the assumption that they are related to the generalized characteristic of the molecular structure of chiral dopants (molecular shape)—anisometry, which was determined on the basis of conformational analysis [9].

EXPERIMENTAL

The synthesis of the chiral dopants under study was described in [10–12]. The measurements of the induced helical pitch P were performed, as in [13], by the Grandjean–Cano method; the concentration of chiral dopants in LC solutions was 0.01–0.02 mol fr. The parameter dP/dt was calculated as the slope of the measured dependences $P(t)$ in a linear approximation (with a correlation coefficient of 0.95–0.99).

The parameter A_{N^*} was determined as the slope of the linear function $t_i(C)$ with a correlation coefficient of 0.98–0.99 in most cases, where t_i is the clearing temperature measured by the capillary method using a device intended for determining melting temperatures accurate to 0.1°C.

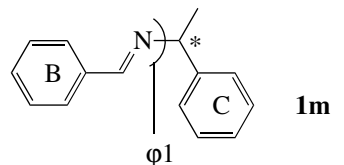
Conformational analysis of the chiral compounds was performed by the semiempirical methods AM1 [14] and PM3 [15] using the MOPAC 6.0 software and by the quantum-chemical method based on the density-functional theory (DFT) using the NWChem software [16]. The hybrid gradient-corrected density functional B3LYP [17] and the atomic basis set cc-pVDZ [18] were used. The relaxed potential-energy surface was scanned within the torsion angles, which determine the molecular conformations. For the minima found on the dependence of the energy on the reaction coordinate, we performed complete optimization of the geometric parameters and calculated the harmonic frequencies of normal vibrations, on the basis of which the thermal corrections to the electronic energy were determined in the rigid-rotator approximation. The positive definiteness of the Hessian matrix in all cases confirms the assignment of the stationary point on the potential-energy surface to minimum.

RESULTS AND DISCUSSION

Specific Features of the Spatial Structure of Chiral Dopants

The behavior of the induced helical pitch is often interpreted on the basis of the possibility of conformational equilibria for chiral dopants [19, 20]. To establish a possible effect of this factor in the 5CB–chiral-dopant systems under consideration, we analyzed the spatial structure of the (*S*)-1-phenylethylamine derivatives. These chiral compounds are *trans*-isomers with respect to the double bond C=N [21]. The compounds **2–17**, containing a phenyl benzoate fragment, are characterized additionally by the *s-cis*-conformation with respect to the partial double bond C–O. (The torsion angle C(Ar)C(=O)OC(Ar), according to the AM1 and PM3 calculations, is close to 180°.) These data are consistent with the DFT data [22] and the X-ray diffraction (XRD) data [23] for the compounds with a phenyl benzoate fragment.

We believe the conformational changes related to the internal rotation with respect to the N–C* bond (the torsion angle ϕ_1) to be the most important. Calculations by the AM1 and PM3 methods revealed significant differences in the description of the relative stability, and, hence, the population of alternative conformers with respect to this bond, which stimulated calculations by the quantum-chemical DFT method. To save computational time, simulation was performed for the simplest compound **1m**—the model structure of all chiral dopants **1–20** under consideration:



The internal rotation in this model molecule around the N–C* bond is characterized by the presence of three energy minima, the deepest of which corresponds to the anticlinal conformation ($-ac$, $\phi_1 = -122.2^\circ$, Fig. 1). The energy of the higher energy synperiplanar form (sp , $\phi_1 = -6.8^\circ$) exceeds the energy of the preferential conformer by 2.4 kcal/mol (ΔG is 2.45 and 2.51 kcal/mol at 0 and 298 K, respectively). The preferential $-ac$ -conformation of the molecule studied is characterized by the eclipsed orientation of the C=N and C*–H bonds at the chiral center (the torsion angle C=NC*H), which is similar to that for the most stable conformation of the ethylene compounds $R_1R_2CH=CHCH_2CH_3$ (with respect to the (=)CH–CH₂) bond [24]. The relative stabilization of this conformation is, apparently, caused by unfavorable steric interactions in alternative conformations. On the one hand, between π electrons of the C=N bond, the unshared electron pair of the N atom, and, on the other hand, the bulk methyl or phenyl groups.

The DFT data are in good agreement with the XRD data for one of the (*S*)-1-phenylethylamine arylidene

derivatives, in crystals of which specifically an *ac* conformation with respect to the N–C* bond is implemented [10]. The dominance of the *ac* conformation in a wide temperature range for the compounds containing the *N*-arylidenephenylethylamine group determines the conformational homogeneity of such compounds with respect to this fragment.

To estimate the characteristics of the molecular shape of chiral dopants (specifically, the molecular anisometry), the geometry of the chiral-dopant molecules **2–17** with an ester group was optimized by the AM1 and PM3 methods with a fixed *–ac* conformation ($\phi_1 = -122.2^\circ$), which was established in the DFT calculation for the model **1m**.

Conformational analysis for the compounds with the bridge group OCH₂ (**18–20**) was performed by the example of compound **18**, also with a fixed value of $\phi_1 = -122.2^\circ$. Both methods give similar results for compound **18** and show the existence of two conformers of the *synclinal* type (the arrangement of benzene rings with respect to the O–C(H₂) bond) (Figs. 2a, 2b) and the antiperiplanar conformation (Fig. 2c, Table 1, ϕ_2). The conformers of the *synclinal* type are almost equiprobable. They dominate significantly over the antiperiplanar form in the entire temperature range. Note that, for all conformers, the –CH=N group and the C–O bond are almost coplanar with the central benzene ring, as in the compounds with an ester bridge group.

The spatial structure of chiral unsaturated ketones (chiral dopants **21–31**), which are isomenthone derivatives, is characterized by the *E*-configuration of substitution at the double bond and the preferential chair conformation of the cyclohexanone ring with *cis*-oriented axial methyl and equatorial isopropyl groups [25–27]. Therefore, these chiral dopants can be considered conformationally homogeneous [4]. When the H atom at C-4 is substituted by a methyl group (chiral dopants **25–28**) or a Br atom (chiral dopants **29–31**), these substituents take the axial orientation preferentially [4] and the conformational homogeneity of molecules of chiral dopants is retained.

Effect of the Nature of Chiral Dopants on the Quantitative Characteristics of the Temperature Dependence of the Induced Helical Pitch

For chiral dopants from the same series ((*S*)-1-phenylethylamines), we observed three possible types of the temperature dependence of the helical pitch: (i) untwisting (P increases with temperature, $dP/dt > 0$), (ii) enhanced twisting ($dP/dt < 0$), and (iii) temperature independence.

In our opinion, when analyzing the effect of the molecular structure of chiral dopants on the behavior of the temperature dependence of the helical pitch and the quantitative parameter dP/dt , one should take into account the following main factors: (i) conformational features of the molecules and the possibility of temper-

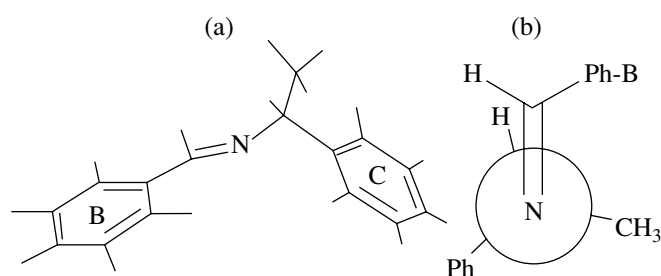


Fig. 1. (a) Preferential *–ac* conformation of *N*-benzylidene-phenylethylamine **1m** and (b) the Newman projection along the N–C*–*sp*³ bond for this conformation.

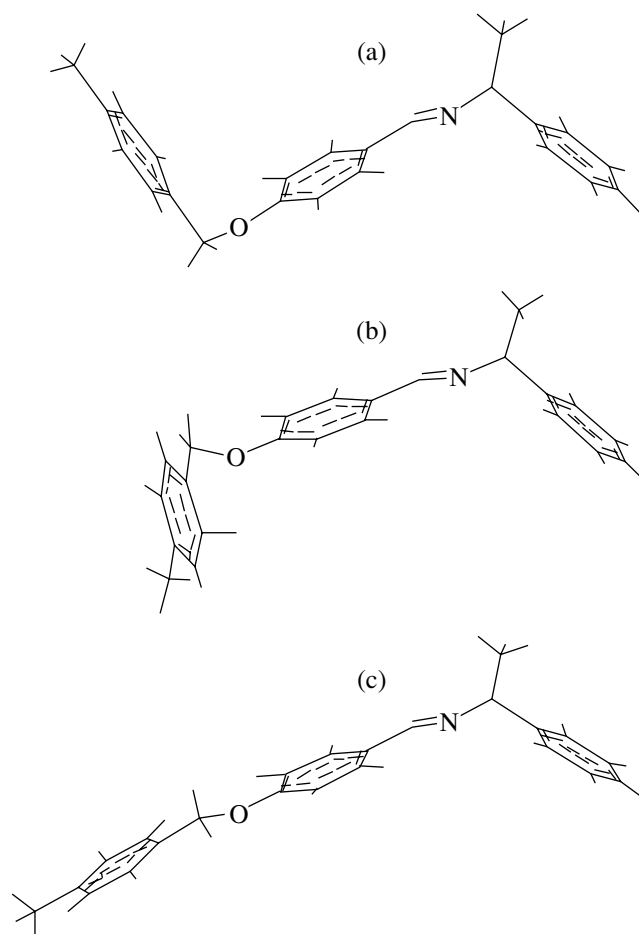
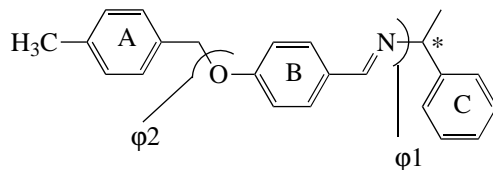


Fig. 2. Alternative *synclinal –sc*- (a) and *+sc*- (b) and *anti-periplanar ap*- (c) conformations of compound **18**.

ature dependence of the concentration ratios of conformers with presumably different helical twisting power; (ii) the geometric parameters of molecules of chiral dopants (molecular anisometry) and, generally changing simabatically (in the systematic series of compounds), polarization characteristics (anisotropy of the molecular polarizability); and (iii) possible influence of chiral dopants on the degree of ordering and elastic

Table 1. Results of the conformational analysis for model compound **18** (the AM1 method, fixed $\varphi_1 = -122.2^\circ$)

Conformer	$\Delta\Delta H$, kcal/mol	φ_2 , deg	Conformer content, mol %			Δ , %	Anisometry, ξ^*
			290 K	313 K	333 K		
a (<i>-sc</i>)	0	-81	45.4	44.9	44.5	-0.9	2.39
b (<i>+sc</i>)	0.016	81	44.2	43.8	43.4	-0.8	2.09
c (<i>ap</i>)	0.857	179	10.4	11.3	12.1	1.7	2.51

* The effective weighted mean molecular anisometry $\xi = 2.27$.

Table 2. Some characteristics of the N^* 5CB–chiral-dopant systems (**1–20**)

Chiral dopant	<i>R</i>	$dP/dt \times 10^4$, $\mu\text{m/K}$	A_{N^*} , K/mol %	Chiral dopant	<i>R</i>	$dP/dt \times 10^4$, $\mu\text{m/K}$	A_{N^*} , K/mol %
1	–	+440 ± 60	–	11	OC ₁₀ H ₂₁	-130 ± 20	-0.71 ± 0.15
2	H	+121 ± 14	-1.88 ± 0.14	12	H	-230 ± 5	-0.16 ± 0.10
3	CH ₃	+18.7 ± 8.6	-1.38 ± 0.03	13	CH ₃	-263 ± 20	+0.48 ± 0.14
4	C ₂ H ₅	+74.0 ± 9.6	-1.42 ± 0.02	14	C ₇ H ₁₅	-354 ± 26	+0.78 ± 0.06
5	C ₃ H ₇	+52.1 ± 11	–	15	C ₈ H ₁₇	-371 ± 45	–
6	C ₄ H ₉	+24.6 ± 2.8	-1.60 ± 0.02	16	C ₉ H ₁₉	-330 ± 27	+0.66 ± 0.09
7	OCH ₃	+28.2 ± 6.8	-1.18 ± 0.04	17	C ₁₀ H ₂₁	-346 ± 34	–
8	OC ₂ H ₅	-47.3 ± 9.4	–	18	CH ₃	+198 ± 31	–
9	OC ₃ H ₇	-34.2 ± 9.4	–	19	C ₄ H ₉	+227 ± 25	-1.91 ± 0.03
10	OC ₅ H ₁₁	-115 ± 12	–	20	OCH ₃	+82 ± 18	-1.42 ± 0.01

properties of the nematic phase (which is related to the differences in the molecular geometry.)

As noted above, the (*S*)-1-phenylethylamine derivatives with a benzoate fragment are almost homogeneous conformationally; therefore, the influence of the conformational effects on the change in the helical pitch with temperature can be excluded.

Experimental data indicate that the effect of the length of the π -electron fragment of molecules of chiral dopants on the parameter dP/dt is the most important. The elongation of this fragment with successive introduction of benzene rings decreases the value of dP/dt significantly and makes it negative (Table 2). In going from the acetyloxy substituted (chiral dopant **1**) to benzoyloxy substituted imine (chiral dopant **2**), dP/dt decreases significantly (by more than a factor of 3). Introduction of the second benzene ring (chiral dopants **12–17**) changes the behavior of the temperature dependence of the helical pitch. With an increase in the number of carbon atoms in the terminal alkyl (or oxyalkyl)

substituent, the parameter dP/dt tends to decrease (Table 2).

Since chiral dopants **1–17** are conformationally homogeneous, the above data suggest that the parameter dP/dt is related to the molecular anisometry of chiral dopants, which depends on the molecular polarizability and, accordingly, on the efficiency of intermolecular interaction in the mesophase. Figure 3a shows the change in the parameter dP/dt with a change in the molecular anisometry ξ of chiral dopants (which was determined from the results of molecular simulation as the ratio of the maximum length a molecule to its maximum width) for the systems containing (*S*)-1-phenylethylamine derivatives with an ester group (**1–17**). It can be seen that dP/dt decreases with an increase in the calculated value of ξ of chiral dopants. Sharp jumps of dP/dt are observed in going from the acetyloxy substituted chiral dopant **1** with one benzene ring in the arylidene fragment to the chiral dopants with two (**2–11**) and three (**12–17**) benzene rings. This phenomenon indicates the significant effect of the polarization factor on the change in twisting, including the temperature

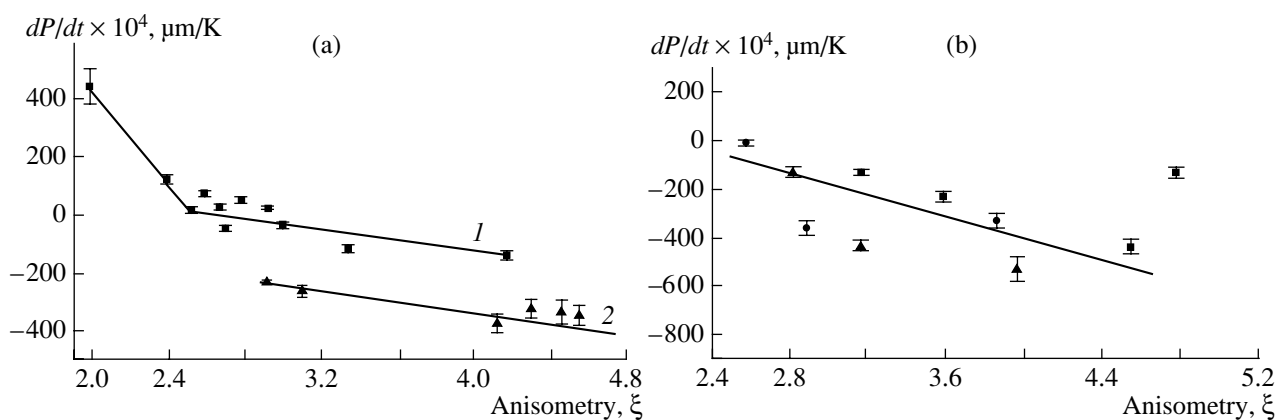


Fig. 3. Dependences of the parameter dP/dt on the molecular anisotropy ξ of chiral dopants for the 5CB-based systems containing derivatives of (a) (*S*)-1-phenylethylamine with chiral dopants (1) 1–11 and (2) 12–17 and (b) isomenthone with chiral dopants (■) 21–24, (●) 25–28, and (▲) 29–31; I is the measurement error.

change. This circumstance, in turn, reflects the dependence of the parameters of helical twisting on the efficiency of intermolecular interaction in the mesophase.

The systems containing chiral dopants with the bridge group CH_2O (18–20) show significantly larger positive values of dP/dt in comparison with chiral dopants 2–17, which contain the bridge group COO with the same terminal substituents (compare chiral dopants 18 and 3, 19 and 6, and 20 and 7 in Table 2). The chiral dopants of this type are conformationally labile; however, the insignificant increase in the fraction of the minor antiperiplanar conformer with an increase in temperature (Table 1) cannot be considered responsible for the temperature behavior of the induced helical pitch.

The established differences in the parameter dP/dt for ether (18–20) and ester (2–17) chiral dopants are in agreement with the estimates of their different molecular anisotropy, which, in the case of conformationally labile compounds 18–20, was evaluated as the effective weighted mean, according to the ratio of conformers with different molecular anisotropies, as shown by the example of compound 18 (Table 1). For chiral dopants 18–20, this value is much smaller in comparison with the similar conformationally homogeneous ester chiral dopants 2–17. The parameter dP/dt increases simultaneously with a decrease in the weighted mean of the molecular anisotropy of these chiral dopants.

For the systems containing isomenthone derivatives (21–31), we can also point to the three above-noted types of the temperature dependence of the helical pitch. The curve $dP/dt(\xi)$ (Fig. 3b) for these systems shows that the parameter dP/dt tends to decrease with an increase in the molecular anisotropy of chiral dopants. This behavior is similar to that of the corresponding dependences for the (*S*)-1-phenylethylamine derivative (Fig. 3a). At the same time, the spread of points in Fig. 3b (the unified plot for all chiral dopants 21–31 with the variable substituent *Y*) may be due to the

fact that the parameter dP/dt actually depends on the anisotropy of molecular polarizability. (The molecular anisotropy is only a qualitative manifestation of its changes in the series of related compounds.) It is likely that different degrees of planarity of the enone fragment in the compounds with different *Y* [4] affects the manifestation of this polarization factor.

In accordance with the theoretical concepts [28, 29] and the experimental data [7], the dependence $P(t)$ is determined generally by the temperature changes in the orientational order parameter $S(t)$ and the related temperature dependences of the elastic constants K_{ii} , primarily, K_{22} . The observed effect of the nature of chiral dopants on the behavior of the dependence $P(t)$ may serve as an argument in favor of the conclusion that doping affects the noted physical properties of a nematic solvent significantly. We suggest two significantly different types of the behavior of a dopant in the nematic mesophase, i.e., two possible mechanisms of the effect on the macroscopic parameters of the systems under study. The molecules of chiral dopants with a relatively low anisotropy (in the limit, quasi-spherical ones, for example, 1 and 2) cannot be ordered effectively orientationally in a nematic medium. These chiral dopants may disturb the local order significantly in the mesophase in the vicinity of an introduced chiral molecule. The ability of a nematic to transfer static distortions of local order at large distances, in turn, leads to a decrease, on the whole, in the long-range orientational order in the mesophase (“the anomalous decrease in S ” in the terminology of [30]) and thus impedes the effective formation of a helical supramolecular structure. The low helical twisting power of such dopants (see, for example, β for chiral dopant 1 [10]) is in agreement with this suggestion. With an increase in temperature, this effect may be stronger than the trivial decrease in the order parameter of a nematic and the decrease in its elastic properties, which facilitates twisting.

The noted effect decreases with an increase in the molecular anisometry of a chiral dopant and, therefore, with an increase in the anisotropy of its polarizability. Another limiting situation occurs in systems containing chiral dopants with a high molecular anisometry (and, accordingly, with enhanced anisotropy of polarizability, for example, chiral dopants **12–17**). Owing to the effective intermolecular interaction with the nematic, such chiral dopants are incorporated optimally into the mesophase without significant disturbance of ordering and change in the physical parameters of the mesophase. In accordance with the temperature behavior of the elastic constant K_{22} of the nematic, these LC compositions are characterized by the negative parameter dP/dt , which changes only weakly with further variation in the terminal alkyl or oxyalkyl substituents. However, this parameter exhibits some trend toward more negative values with the elongation of the substituent. It is not inconceivable that the decrease of the order parameter with an increase in temperature in the systems containing highly anisometric dopants, especially with the elongating terminal alkyl chain, may manifest itself somewhat stronger than for an individual nematic.

Thus, the effect of chiral dopants on the degree of ordering of a doped nematic manifests itself in two ways. At a relatively weak decrease in the order parameter and the corresponding decrease in the elastic constants of a nematic, an increase in temperature leads to enhanced twisting ($dP/dt < 0$). This behavior corresponds to the theoretical concepts, according to which the ability of a nematic to be twisted by chiral dopants increases with a decrease in its elastic constants [5]. The opposite is the situation when a dopant causes a very significant disturbance of local order in the mesophase, especially with an increase in temperature, which hinders the effective formation of a helical supramolecular structure ($dP/dt > 0$). Obviously, between these limiting cases, there are intermediate situations with respect to the change in the order parameter and the elastic constants of a doped nematic (the parameter $dP/dt \approx 0$ or has positive or negative values, small in magnitude).

The investigation of the effect of chiral dopants on the thermal stability of the N^* mesophase, related to the degree of its order, confirms these suggestions somewhat. The parameter $A_{N^*} = dt_i/dC$, which characterizes the change in the thermal stability of the doped mesophase and, accordingly, its degree of ordering, changes regularly with the molecular anisometry of chiral dopants (Table 2). The low-anisometry chiral dopants with a positive parameter dP/dt cause a disordering effect in the mesophase ($A_{N^*} < 0$; see Table 2, chiral dopants **2–4**, **6**, and **7**). In contrast, high-anisometry dopants with $dP/dt < 0$ result in a weaker negative effect on the thermal stability of the mesophase and may even lead to thermal stabilization (Table 2, chiral dopants **11–14** and **16**).

We believe that experimental data on the dual effect of dopants on the degree of ordering in doped nematics can be obtained by studying the small-angle X-ray scattering in the LC compositions containing chiral dopants with significantly different molecular anisometry. Further experiments in this field are being carried out; the results will be published elsewhere.

Thus, the most important characteristics of the behavior of chiral compounds in induced cholesteric systems—the temperature gradient of the helical pitch and the concentration gradient of the cholesteric–isotropic transition temperature—change consistently with a variation in the structure of chiral dopants, especially their molecular anisometry. This experimental phenomenon reflects the dependence of the noted parameters on the energy of intermolecular interaction between the components.

CONCLUSIONS

Chiral *N*-arylidene derivatives of (*S*)-1-phenylethylamine, depending on their molecular structure, induce in the nematic 4-pentyl-4'-cyanobiphenyl a helical supramolecular ordering with three types of temperature changes in the helical pitch: temperature independence ($dP/dt \approx 0$), helix untwisting with an increase in temperature ($dP/dt > 0$), and enhanced helix twisting with an increase in temperature ($dP/dt < 0$).

Two mechanisms of the effect of chiral dopants on the macroscopic parameters of induced cholesteric mesophases have been established. Low-anisometry chiral dopants (statistically quasi-spherical) in the systems based on a cyanophenyl nematic cause a strong disturbance of local order in the mesophase, providing untwisting of the cholesteric helix with an increase in temperature. Highly anisometric chiral molecules are incorporated optimally into an orientationally ordered medium, causing no significant changes in the order parameter and elastic constants of the LC system. The enhancement of twisting with an increase in temperature in such systems is determined mainly by the change in the noted physical parameters of the nematic.

The degree of molecular anisometry determines also the effect of chiral dopants on the thermal stability of the induced cholesteric mesophase. It is found that the parameters dt_i/dC and dP/dt change antipatically in the series of LC systems containing dopants from the same series.

REFERENCES

1. H. Yamamoto, T. Suisyu, Sh. Yano, *et al.*, *J. Phys. Soc. Jpn.* **63** (9), 3326 (1994).
2. N. Emoto, M. Tanaka, S. Saito, *et al.*, *Jpn. J. Appl. Phys.* **28** (1), L121 (1989).
3. A. Kozachenko, S. Valyukh, V. Sorokin, *et al.*, *Funct. Mater.* **7** (4-1), 727 (2000).

4. L. A. Kutulya, in *Functional Materials for Science and Engineering*, Ed. by V. P. Seminozhenko (Inst. for Single Crystals, Kharkov, 2001) [in Russian].
5. G. Gottarelli and G. Spada, *Mol. Cryst. Liq. Cryst.* **123**, 377 (1985).
6. A. Tolmachev and A. Fedoryako, *Ukr. Fiz. Zh.* **36** (2), 231 (1991).
7. A. P. Fedoryako, Candidate's Dissertation in Physics and Mathematics (Inst. for Single Crystals, National Academy of Sciences of Ukraine, Kharkov, 1990).
8. N. I. Shkolnikova, A. P. Fedoryako, L. A. Kutulya, *et al.*, in *Proceedings of the XVI International School-Seminar "Spectroscopy of Molecules and Crystals," Sevastopol, Ukraine, 2003*, p. 278.
9. N. I. Shkolnikova, Candidate's Dissertation in Chemistry (Inst. for Single Crystals, National Academy of Sciences of Ukraine, Kharkov, 2003).
10. G. P. Semenkov, Candidate's Dissertation in Chemistry (Inst. for Single Crystals, National Academy of Sciences of Ukraine, Kharkov, 1995).
11. L. Kutulya, G. Semenkov, and N. Shkolnikova, in *Proceedings of the VIII International Symposium "Advanced Display Technologies," Novy Svit, Ukraine, 1999*, p. 192.
12. V. V. Vashchenko, Candidate's Dissertation in Chemistry (Inst. for Single Crystals, National Academy of Sciences of Ukraine, Kharkov, 1997).
13. L. A. Kutulya, G. P. Semenkov, S. N. Yarmolenko, *et al.*, *Kristallografiya* **38** (1), 183 (1993).
14. M. J. S. Dewar, E. G. Zebisch, E. F. Healy, *et al.*, *J. Am. Chem. Soc.* **107** (15), 3902 (1985).
15. J. J. P. Stewart, *J. Comput. Chem.* **10** (2), 221 (1989).
16. T. P. Straatsma, E. Apra, T. L. Windus, *et al.*, NWChem, A Computational Chemistry Package for Parallel Computers, Version 4.5 (2003).
17. A. D. Becke, *J. Chem. Phys.* **98**, 5648 (1993).
18. D. E. Woon and T. H. Dunning, Jr., *J. Chem. Phys.* **98**, 1358 (1993).
19. A. A. Gerasimov, N. L. Kramarenko, and A. I. Galatina, *Kristallografiya* **34** (3), 772 (1989) [*Sov. Phys. Crystallogr.* **34**, 461 (1989)].
20. G. Heppke, D. Löttsch, and F. Oestreicher, *Z. Naturforsch., A: Phys. Sci.* **42**, 279 (1987).
21. E. Melendez and R. Perez Ossorio, *An. Quim. Real Soc. Esp. Fis. Quim.* **66** (1), 87 (1970).
22. T. Imase, J. Kawauchi, and J. Watanabe, *J. Mol. Struct.* **560**, 275 (2001).
23. J. M. Adams and S. E. Morsi, *Acta Crystallogr. B* **32**, 1345 (1976).
24. E. L. Eliel, S. H. Willen, and L. N. Mander, *Stereochemistry of Organic Compounds* (Wiley, New York, 1994), Chap. 10.2, p. 1267.
25. L. A. Kutulya, N. S. Pivnenko, I. B. Nemchenok, *et al.*, *Zh. Obshch. Khim.* **57** (2), 397 (1987).
26. L. A. Kutulya, T. V. Khandrimailova, V. I. Biba, *et al.*, *Zh. Obshch. Khim.* **58** (8), 1793 (1988).
27. L. A. Kutulya, V. P. Kuznetsov, V. I. Kulishov, *et al.*, *Kristallografiya* **44** (3), 475 (1999) [*Crystallogr. Rep.* **44**, 435 (1999)].
28. A. Wulf, *J. Chem. Phys.* **60** (10), 3994 (1974).
29. B. W. Van der Meer, PhD Thesis (Univ. of Groningen, Groningen, 1979).
30. G. S. Chilaya, *Physical Properties and Application of Liquid Crystals with Induced Helical Structure* (Metsniereba, Tbilisi, 1985) [in Russian].

Translated by Yu. Sin'kov

SURFACE
AND THIN FILMS

Nanoscale Morphological Features in the Structural Evolution of HTSC Films of Organometallic Aerosols

Yu. Ya. Tomashpol'skii and N. V. Sadovskaya

*State Scientific Center of the Russian Federation, Karpov Institute of Physical Chemistry,
ul. Vorontsovo pole 10, Moscow, 105064 Russia
e-mail: tomash@cc.nifhi.ac.ru*

Received October 21, 2004; in final form, April 7, 2005

Abstract—The evolution of the formation of a structure in high-temperature superconducting $\text{Bi}_2\text{Sr}_2\text{CaCu}_2\text{O}_8$ films obtained from organometallic aerosols is investigated by atomic force microscopy and scanning electron microscopy. Nanoscale granular supramolecular structures were found for the first time in the liquid-phase and pyrolytic stages. It is shown that pyrolytic processes occur within individual nanogranules. The minimum sizes of a nanogranule are 30–50 nm in base and 5 nm in height. In the high-order crystallization stage, epitaxial recrystallization occurs, as a result of which platelike crystallites are formed. They are 15–20 nm thick, have growth steps 1–5 nm in height, and are parallel to the substrate. The nonoriented morphological forms are individual three-dimensional crystallites up to 100 nm in size. © 2005 Pleiades Publishing, Inc.

INTRODUCTION

The functional properties of films of high-temperature superconductors (HTSCs) are determined by their structure, which is determined by all stages of its formation. Therefore, the study of the formation of the structure of HTSC films is an important problem that must be solved to optimize film technologies.

Among many methods for fabricating HTSC films, the techniques based on the deposition of solutions on a substrate with subsequent annealing of dried precipitates are spread widely [1]. The advantages of these methods are as follows: simple equipment, requiring no vacuum degassing; high homogeneity of the chemical composition of the film obtained; the possibility of obtaining coatings on substrates of large area and complex shape; and good controllability of the growth processes. Organometallic solutions are promising as starting reagents. They are sufficiently stable and can be purified relatively easily. Alcoholates, acetylacetonates, formates, naphthenates, stearates, and laurates are used to obtain HTSC films [2] under the condition that molecular aggregates formed in the solution do not tend to crystallize upon drying. As a result, pasty precipitates of homogeneous composition are formed from the salts of organic acids. The components of these precipitates are mixed at the molecular level with conservation of local stoichiometry. Solutions of carboxylates have some advantages: they are nontoxic, relatively inexpensive, moisture-resistant, and can be purified easily [3].

The significant drawback of these methods for film preparation is their multistage character: the formation of the crystal structure includes a liquid-phase stage, related to the preparation of initial solutions, evapora-

tion of the solvent, and drying of the precipitates; the pyrolytic stage, in which decomposition of organometallic complexes occurs with the formation of target-phase nuclei as a result of chemical reactions; and the high-order crystallization stage, in which the film structure is formed finally. It is difficult to investigate both the atomic structure and the microstructure of precipitates in all stages, especially in the initial stage, because they have either an amorphous or a nanocrystalline structure. Therefore, the overwhelming majority of the corresponding studies are devoted only to the last stage of the structure formation, whereas there is almost no information about the processes occurring in the initial stage. Hence, the data on the final microstructure of such films can be very contradictory. For example, according to [4, 5], Bi–Sr–Ca–Cu–O films have scaly or needlelike morphology, whereas, according to [6, 7], these films have platelike morphology.

In this study, we investigated in detail the processes of structure formation in HTSC films by the example of the Bi–Sr–Ca–Cu–O system, which, along with the Y–Ba–Cu–O system, is most promising for technical applications. Particular attention has been given to the analysis of nanostructural forms in all stages of the film preparation from organometallic aerosols.

METHODS

Film Preparation

The initial solution for fabrication of $\text{Bi}_2\text{Sr}_2\text{CaCu}_2\text{O}_8$ (2212) HTSC films was prepared from a mixture of bismuth and copper acetates and calcium and strontium carbonates, taken in the amounts required to obtain the stoichiometric cation ratio. Meth-

acrylic acid was added to the mixture obtained, after which the mixture was stirred upon heating until the precipitate was dissolved completely. A working solution with a methacrylate content of 0.5% for deposition onto a substrate was prepared by diluting the initial solution in dimethylacetamide. These processes were described in detail in [8, 9].

Solutions were deposited onto substrates by pneumatic aerosol spraying. The aerosol was formed in a glass setup using air as a carrier gas. The setup provided trapping of the largest (above 100 μm) aerosol particles. The deposition rate of the working solution was 10–15 ml/h, the distance from the outlet to the substrate was about 3 cm, and the substrate temperature was in the range 120–150°C. The deposition of the solution on a substrate included two cycles. In each cycle, 10 ml of the working solution was deposited, and, after drying, the deposition was repeated. To perform pyrolysis of the precipitates from the methacrylate mixture, annealing at 200–500°C for 1–15 h is required. High-temperature annealing was performed at 600–800°C for 3–5 h with a preliminary annealing at 500°C for 1 h.

The above-mentioned annealings were performed in a Nabertherm L31S programmable furnace with an automatic control system, which makes it possible to maintain and change temperature with time by a linear law with an error of ± 1 K. The sample heating rate was 1.6 K/min; the samples were cooled in the furnace.

Preparation of Substrates

LaAlO₃ single-crystal wafers were cut in the (001) plane and polished. Mechanical impurities were removed from the substrate surface with a UZDN-A disperser using ultrasound. A water–alcohol (1 : 1) mixture was used as a dispersion medium. Further purification of the substrates was performed in ether and then in hexane, after which they were washed by distilled water.

Sample Characterization

The preliminary information about the morphology and quality of the sample surface was obtained on an MBS-9 optical stereomicroscope. The microstructure was investigated in a JSM-35 CF scanning electron microscope (SEM) at an accelerating voltage of 20 kV and magnifications from 200 to 10000.

The nanostructure was analyzed in a Solver 47 atomic force microscope (AFM). The resolution for the objects of our study was several nanometers in the *X–Y* plane and several tenths of a nanometer along the vertical *Z* axis. Contact and semicontact scanning techniques were used, applying, respectively, CSG10/10 and NSG10/20 silicon cantilevers (produced by NT-MDT). The scanner was calibrated both in the *X–Y* plane and along the *Z* axis using test objects, shaped as periodic grooves, and the independent SEM data. In the

Z direction, the scanner was calibrated in different height ranges: 500–300 nm, 200–100 nm with an error of 20%, and 50–0 nm with an error of 10%.

The elemental composition of the samples was determined quantitatively with an error of about 5% in the SEM using a LINK attachment, designed for carrying out electron-probe X-ray microanalysis.

The phase composition of the samples was determined by X-ray diffraction analysis on a DRON-4-07 diffractometer (CuK α radiation) at a scan rate of 2 deg/min.

The coating thickness was estimated from the AFM profile of the film/substrate interface and the SEM image of the film cross section.

EXPERIMENTAL

Liquid-Phase Stage

Optical-microscopy analysis showed that the dried precipitates from the mixture of Bi, Sr, Ca, and Cu methacrylates form a homogeneous greenish coating after two cycles of deposition of the working solution. Observation of the precipitate surface at high magnification in SEM and AFM revealed that the precipitates consist of planar aggregates with a round or elliptical base, from several to several tens of micrometers in size. With a further increase in the magnification, inhomogeneities shaped as planar rounded granules with a base 50–100 nm in size and a large volume of the intergranular space are revealed in the precipitates (Fig. 1). The granules look sufficiently loose and do not exhibit a fine structure.

In addition to the main granular morphology of the coating, various three-dimensional (3D) defects are observed: individual rounded particles, dome-shaped aggregates rising above the surface, microcracks, and pores.

Careful observation shows that individual particles are either incorporated into the coating at different depths or lie on the surface. The particles are several tenths of a micrometer in size and their surface exhibits a fine structure: a layer with a thickness of several nanometers with a violated continuity. The particles have a flattened shape with a base-to-height ratio of 8–10. Some particles have excrescences of the same shape in the peripheral region. The cation composition of the particles is identical to the coating composition. The domes are flattened hemispheres with a base of several tenths of a micrometer in size. It can be seen that, in some cases, they are formed owing to the encapsulation of the incorporated particles by the coating; in other cases, domes form a local swelling of the coating with cracks and discontinuities on the surface of the dome.

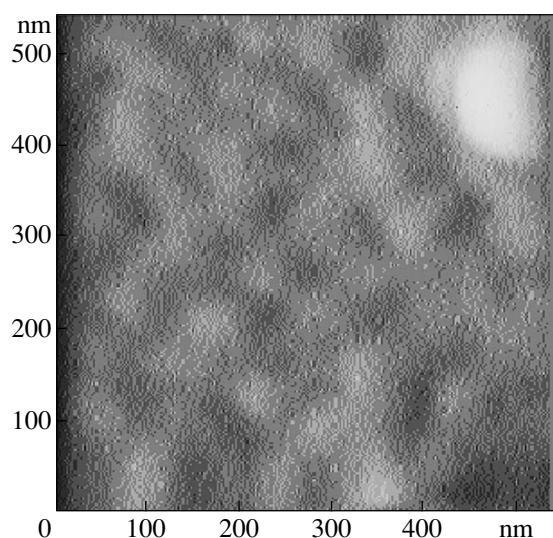


Fig. 1. AFM image of the nanogranular structure in the liquid-phase stage; semicontact scanning.

Some regions of the precipitates contain microcracks and pores of irregular shape with an average depth of about $0.5\ \mu\text{m}$. This value can be used as an additional estimate of the coating thickness.

X-ray diffraction study of the precipitates shows the absence of diffraction maxima. Note that scattering increases monotonically to smaller angles (Fig. 2, curve 1).

Pyrolytic Stage

The subsequent experiments were performed with the precipitates subjected to pyrolytic annealing. After the annealings, the coating thickness decreased approximately by an order of magnitude and was estimated to be several tens of nanometers. However, it was difficult to determine the thickness exactly owing to the complex relief caused by the supramolecular granular micrometric and nanometric morphology found by us. The SEM and, especially, AFM analysis shows structural inhomogeneities of at least two types.

The inhomogeneities of the first type are planar microgranules with a large spread of sizes: from several tenths of a micrometer to several micrometers in base and from several hundreds to several tenths of a micrometer in height (Fig. 3). With an increase in the annealing temperature, microgranules tend to form a chain structure.

The inhomogeneities of the second type are closely packed planar rounded nanogranules forming a scaly surface (Figs. 4a–4d). The bases of the nanogranules are 30–70 nm in size and their height is 5–10 nm. These

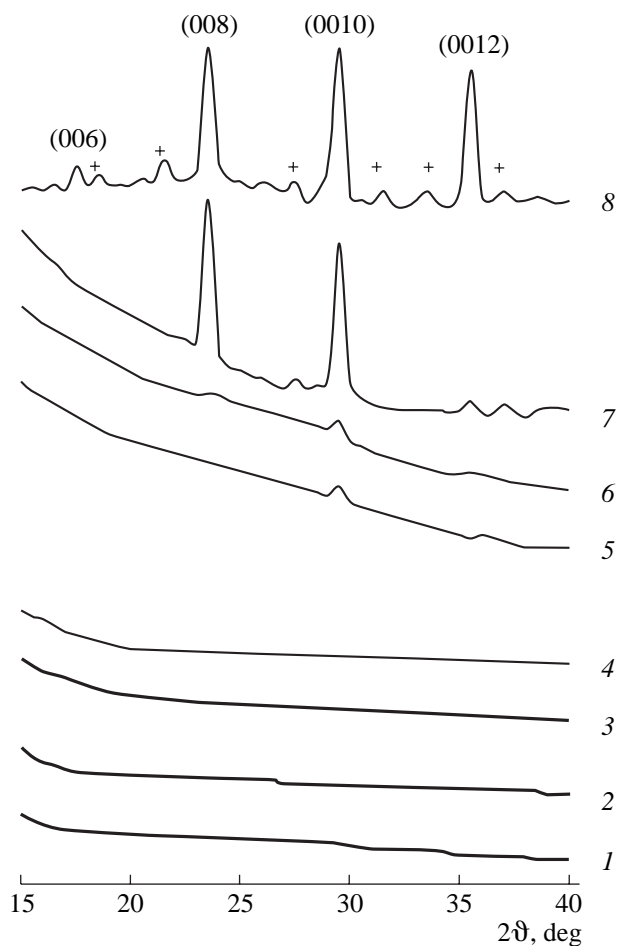


Fig. 2. X-ray diffraction patterns ($\text{CuK}\alpha$ radiation) of the precipitates and films in the (1) liquid-phase, (2–6) pyrolytic, and (7, 8) high-order crystallization stages of the structure formation: annealing (2) at 300°C for 1 h, (3) at 400°C for 1 h, (4) at 500°C for 1 h, (5) at 400°C for 10 h, (6) at 500°C for 10 h, (7) at 700°C for 3 h, and (8) at 800°C for 5 h. The lines of the LaAlO_3 substrate are excluded. The indices of the diffraction peaks correspond to the primary phase HTSC 2212 and the sign + denotes the peaks of the trace phase HTSC 2223.

values almost do not change in the entire range of the pyrolytic annealing.

Morphologically, nanogranules enter the structure of microgranules (Fig. 5). The high-resolution images of the nanogranule structure show that the width of their boundaries is about several nanometers (Fig. 6). All the above-described 3D defects observed in the liquid-phase stage (individual particles, domes, etc.) are present in this stage.

All structural inhomogeneities exhibit no visual high-order crystalline faceted forms. X-ray diffraction analysis revealed no diffraction maxima and the diffraction patterns, as before, have an X-ray amorphous character and demonstrate scattering that increases monotonically to smaller angles (Fig. 2, curves 2–4).

Changes can be observed in the X-ray diffraction patterns after annealing of the precipitates at 400°C for 10 h: a small diffuse peak arises, which cannot be assigned to either simple oxides or known cuprate phases (Fig. 2, curve 5). A similar but more pronounced peak arises after annealing at 500°C for 10 h (Fig. 2, curve 6). Analysis showed that these peaks correspond to the strong maximum (0 0 12) of the 2212 phase.

High-Order Crystallization Stage

After annealings at 600–700°C, isotropic and chain microgranules composed of nanogranules are observed in this stage, as well as in the pyrolytic stage. The characteristic morphological features arising after these annealings are ribbonlike structures with a width of about several nm present in some regions of the films at the crystallite boundaries (Fig. 7). In addition, the stability of the nanogranule boundaries is violated: nanogranules increase in size, transforming into faceted crystallites; the latter are unoriented with respect to the substrate (Fig. 8). The number of these crystallites increases with increasing annealing time. At the same time, there is still some amount of rounded nanogranules 50–100 nm in size, which are distributed randomly among faceted forms. Along with the isotropic forms and the forms with a slightly extended base, needle-shaped forms with a cross section from several tens of to several hundred nanometers and a length up to 5 μm are also observed in small amounts in some regions. We failed to reveal any differences in the cation composition of these forms with respect to the main coating. The diffraction patterns of the films in the beginning of the high-order crystallization stage are similar to those obtained in the previous stages and are characteristic of the amorphous or nanocrystalline states. Then, sharp peaks, related to the HTSC 2212 phase ((0 0 8), (0 0 10), and (0 0 12) maxima) arise against the continuous scattering background (Fig. 2, curve 7). In addition, small peaks, related to the HTSC 2223 phase, can be observed. No other phases were revealed by X-ray diffraction analysis.

A radical change in the film morphology is observed after annealing at 800°C (Fig. 9), which leads to the formation of well-oriented platelike rectangular crystals, growing in layers parallel to the substrate. Separate platelets are inclined with respect to the substrate. The lateral sizes of the platelets reach several micrometers, their thickness is 15–20 nm, and the height of the growth terraces is 1–5 nm. In addition to the dominant platelike form, there are also faceted particles up to 100 nm in size, located on terraces. The diffraction patterns of these films show the presence of high-order oriented structure with a texture of the [0 0 1] type (Fig. 2, curve 8). X-ray phase analysis showed that the films

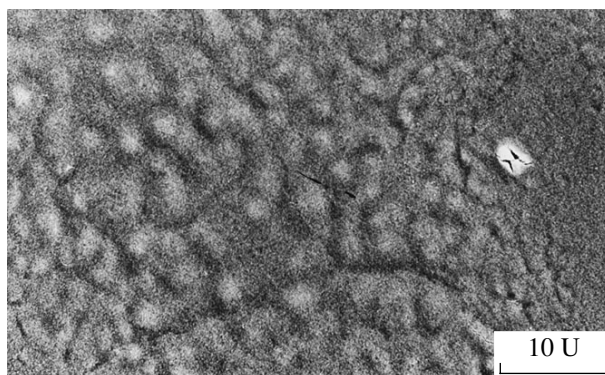


Fig. 3. SEM image of the microgranular structure in the pyrolytic stage; the accelerating voltage is 20 kV.

contain the target HTSC 2212 phase and a small amount of another HTSC phase (2223). The HTSC transition begins at $T \sim 108$ K, and zero resistance is observed at $T = 75$ K.

RESULTS AND DISCUSSION

Classification of the data obtained and analysis of the structural evolution make it possible to suggest a mechanism of the formation of the structure of HTSC films prepared from organometallic aerosols.

The microgranular structure is formed in the liquid-phase stage as a result of the deposition and drying of aerosol drops, whose sizes and dispersion distribution depend on the type of the aerosol generator, the concentration and viscosity of the working solution, and the flow velocity. For example, the pneumatic and ultrasound methods of aerosol generation give significantly different dispersion distributions [10]. Morphologically, the precipitate consists of overlapping planar microgranules. The size of the microgranules depends on the drop size, while their shape is determined by a number of factors: the drying conditions, the physical and chemical properties of the substrate, and the distribution and type of the substrate defects. In the case under consideration, in the liquid-phase stage, we have flattened forms with a round or oval base, which are typical of drops drying on a substrate. In the pyrolytic stage, because of the local inhomogeneity of the pyrolytic process, the boundaries of some microgranules may diffuse. In this case, chain microgranules are formed with a chain width corresponding to the isotropic form, characteristic of the beginning of the pyrolytic stage. The shape of microgranule ensembles becomes complicated as a result of their mutual overlapping and the effect of the substrate microinhomogeneities: polishing bands, 3D defects, etc. All other factors being equal, small aerosol drops can form structures differing from those produced by large drops. For example, individual rounded particles with a size of several tenths of a micrometer are formed from drops several tens of micrometers in size as a result of the sub-

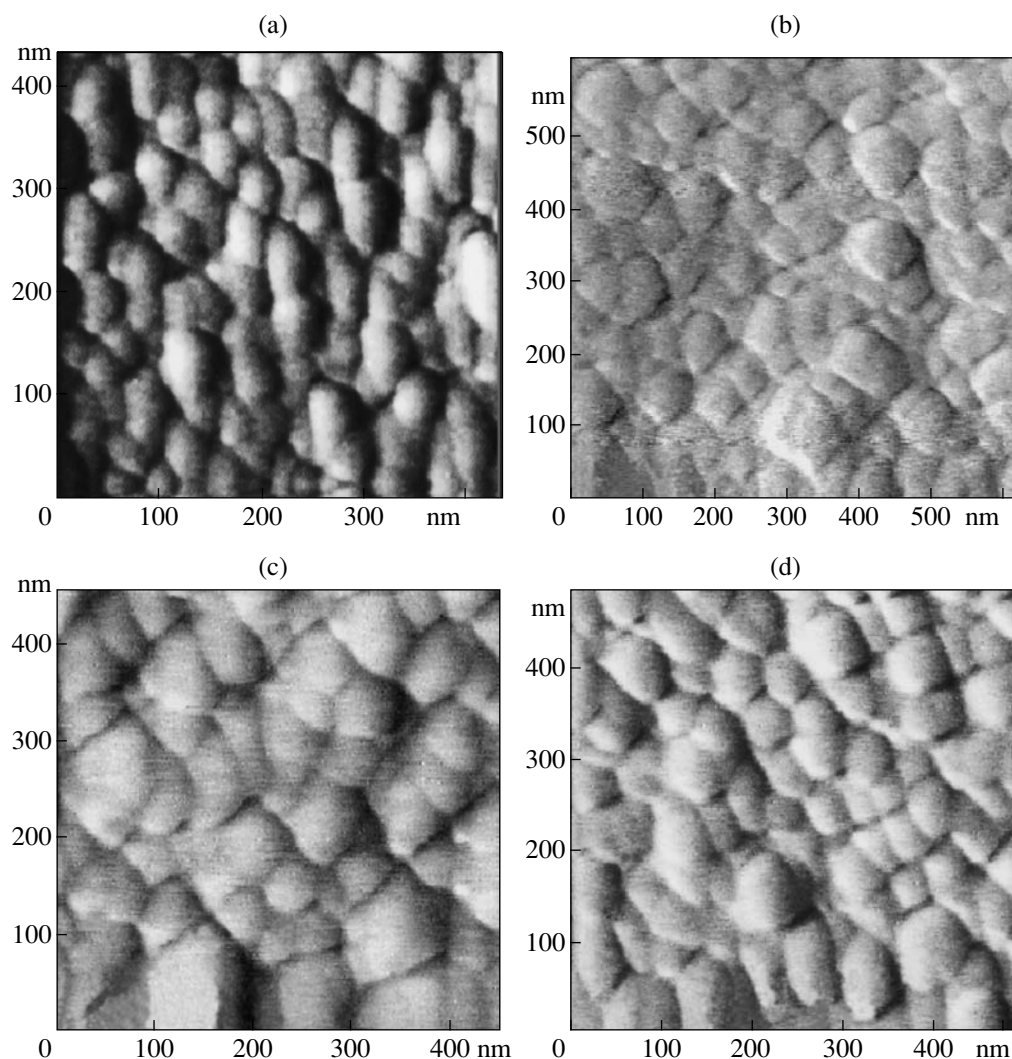


Fig. 4. AFM image of the nanogranular structure in the pyrolytic stage after annealing (a) at 300°C for 15 h, (b) at 400°C for 10 h, (c) at 500°C for 5 h, and (d) at 500°C for 15 h: (a) semicontact and (b–d) contact scanning.

strate heating. In this case, a drop loses a large part of the solvent when it approaches the substrate, whereas the main part of the aerosol dries only after the drop arrives at the substrate. During the pyrolysis, some particles on the substrate exhibit a thin surface layer, which indicates the thickness inhomogeneity of the particle composition. The reason for this phenomenon is that the pyrolytic decomposition occurs nonsimultaneously over depth.

The flattened shape of all structures (including individual particles) arising upon drying of the solution on the substrate confirms their liquid-phase nature. The excrescences on the particle surface can be explained by the residual viscosity, which manifests itself during final drying on an oblique substrate.

There are different mechanisms of the dome formation. The presence of a particle incorporated into the precipitate causes the dome formation due to the layer covering this particle. Another mechanism is related to

the local pressure of solvent-vapor bubbles from inside on the surface of the solidifying matrix. In this case, the vapor goes out either through open pores or as a result of a partial dome fracture [11]. It should be noted that the role of 3D defects (individual particles, domes, and pores) in thin coatings is much less important than in thick coatings, where their concentration may be high [11].

We believe that nanogranules, as the main supramolecular element of the coating morphology in the liquid-phase and pyrolytic stages, nucleate even in the solution, where the mobility of large methacrylate molecules is, naturally, higher than in the subsequent solid-phase coatings. A nanogranule seems to be formed from a molecular cluster, similar to that described for organometallic solutions [12]. After drying, the precipitate consists of nanogranules entering the microgranule composition. The space between nanogranules contains solvent residues and interboundary methacrylate

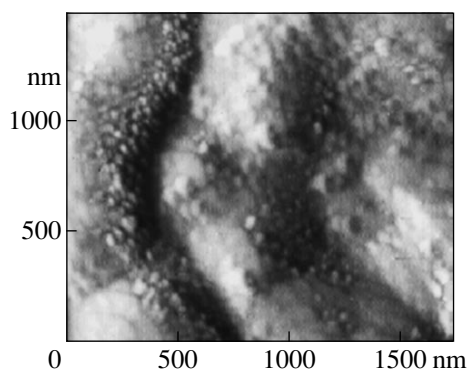


Fig. 5. AFM image showing the morphological relationship between nano- and microgranules in the pyrolytic stage (annealing at 400°C); semicontact scanning.

molecules that did not enter the clusters. Pyrolytic annealing removes solvent residues from the intergranular space, as a result of which the nanogranule packing becomes dense and the coating becomes scaly. Thus, the main difference between the configurations of nanogranules in the liquid-phase and pyrolytic stages is in the character of boundaries.

The size of a nanogranule is determined by the binding energy; the structure of methacrylate molecules; and, probably, the solvent nature. The relative stability of the shape and sizes of nanogranules (30–70 nm in the base) indicates that pyrolysis occurs in each nanogranule. Concerning the shape of nanogranules, it should be approximately isotropic, as well as the shape of a cluster in the solution. However, nanogranules decrease in size owing to the substrate effect in the liquid-phase stage (for example, through the value of wetting). Thus, the nanogranules are flattened, as well as other supramolecular morphological forms. This situation is retained until the bulk recrystallization starts.

Despite the pronounced boundaries; the similarity to crystalline grains in shape; and the sizes, which in some case exceed the size of the X-ray coherent-scattering region (about 50 nm), nanogranules, according to the diffraction patterns, have an amorphous structure at the molecular level up to the decomposition of methacrylates and a nanocrystalline structure after the dissociation of methacrylate molecules and the beginning of synthesis reactions. The amorphous structure is related to the coordination features of the structure of complex methacrylate molecules, whose ordering in the solid phase is impeded significantly. At the same time, the amorphous structure of the precipitates does not decrease the chemical activity since the internal energy of this state is high [13]. The difference in the dissociation temperatures of metal–oxygen bonds in methacrylates (according to the scheme $\text{Cu-O} > \text{Bi-O} > \text{Sr-O} > \text{Ca-O}$ [11]) leads to the conservation of the nanogranule framework as a result of the existence of stronger bonds. In addition, the formation of oxides caused by the decomposition of methacrylate molecules increases

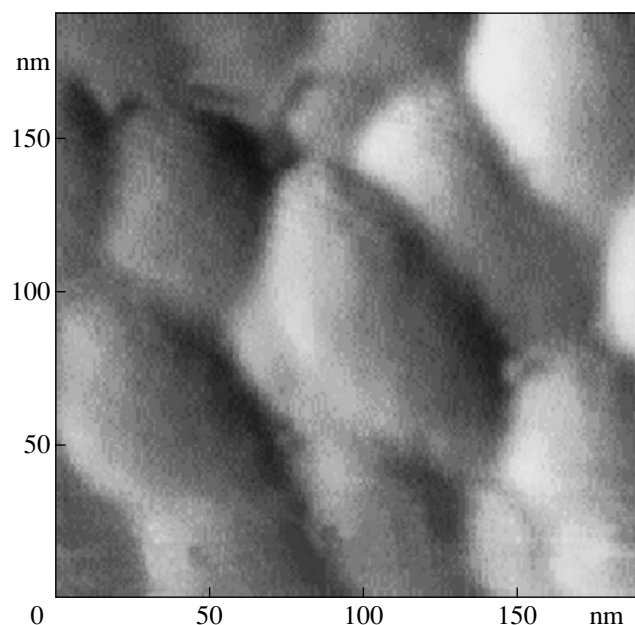


Fig. 6. High-resolution AFM image of the nanogranule boundaries in the pyrolytic stage (annealing at 300°C for 15 h); semicontact scanning.

the diffusion mobility of the components. This circumstance facilitates the solid-phase reactions and allows the crystalline ordering and the formation of nuclei of high-order crystalline phases, including the target phase. The growth of nuclei and the formation of nanocrystallites lead to a gradual change in the mor-

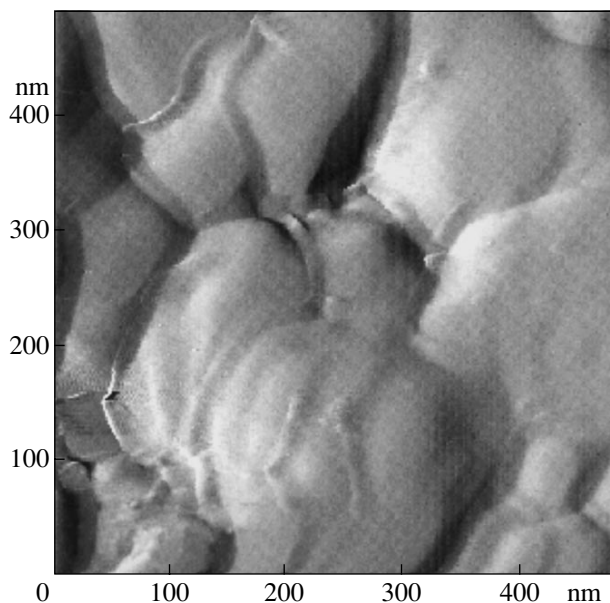


Fig. 7. AFM image of boundary ribbon forms revealed in the high-order crystallization stage in some regions of the nanocrystalline structure (annealing at 500°C for 1 h + 600°C for 5 h); semicontact scanning.

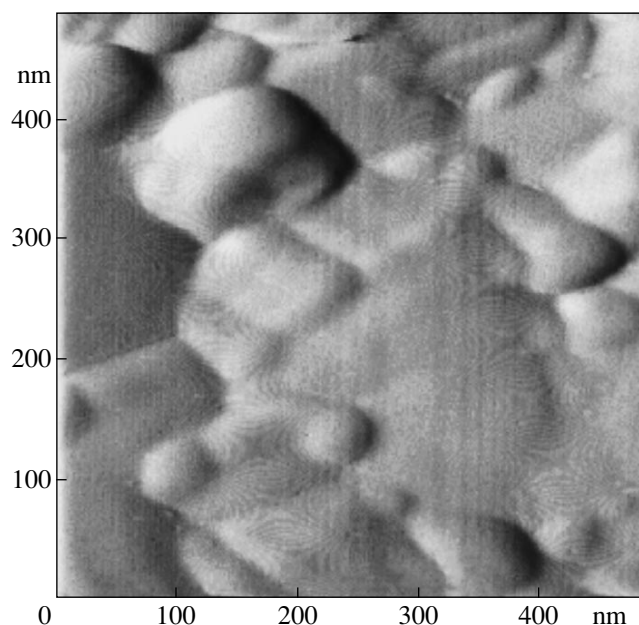


Fig. 8. AFM image of the structure after the primary crystallization in the high-order crystallization stage (annealing at 500°C for 1 h + 700°C for 5 h); semicontact scanning.

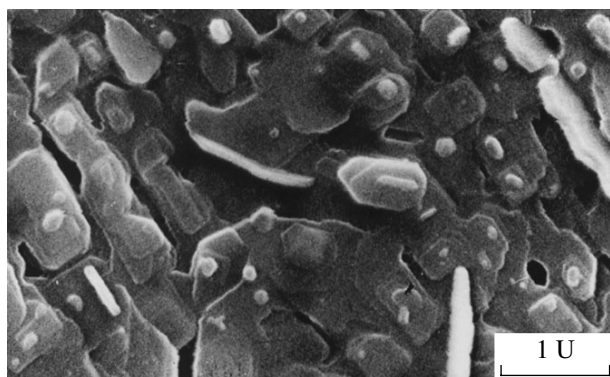


Fig. 9. SEM image of the structure after the epitaxial recrystallization in the high-order crystallization stage; the accelerating voltage is 20 kV.

phology, which evolves from dense scaly packing of nanogranules to close-packed crystalline nanoparticles, exceeding amorphous nanogranules in size. With a further increase in the annealing temperature, epitaxial recrystallization occurs with active participation of the substrate, which orients the growing crystallites with a platelike habit parallel to the substrate plane. In this case, the additional phases, such as the HTSC 2223 phase in the form of ribbonlike structures, are pushed out first into the intergranular space (in the end of the pyrolytic stage); then, into the intercrystallite space (in the beginning of the high-order crystallization stage); and, finally, to the periphery of the oriented plates. This

behavior is consistent with the data on the grain morphology in 2212 ceramics, where grains of the primary phase 2212 are surrounded by thin shells of the impurity HTSC 2223 phase [14].

Thus, scaly crystallites arise in the beginning of the high-order crystallization stage. With an increase in the annealing temperature, they are transformed into oriented platelike forms. The degree of epitaxial orientation (the [001] texture) is determined by the ratio of the number of crystallographically ordered platelike forms to the number of 3D structural forms remaining unoriented.

The 3D defects (domes and pores) are healed actively during the recrystallization in the high-order crystallization stage. Individual particles of the dried aerosol, after the solid-phase synthesis and crystallization reactions, may be involved in the recrystallization processes and produce high-order crystalline forms, including isolated nanocrystallites.

CONCLUSIONS

Nanoscale granular forms of supramolecular structure with stable boundaries, arising in the liquid-phase and pyrolytic stages during the formation of the structure of HTSC films prepared from organometallic aerosols, are established for the first time.

The minimum sizes of the nanogranules are 30–50 nm in base and 5 nm in height. The width of the boundaries between nanogranules is about 1 nm. In the case of the formation of additional phases, the boundary width may increase up to several tens of nanometers. The pyrolytic processes occur within individual nanogranules.

In the high-order crystallization stage, as a result of the oriented helical growth, platelike crystallites are formed, which are predominantly parallel to the substrate and have a thickness of 15–20 nm and a height of growth steps of 1–5 nm. Unoriented morphological forms remain as isolated 3D crystallites up to 100 nm in size.

REFERENCES

1. T. N. Adrianova, L. A. Zakharov, and A. N. Khol'kin, *Elektron. Prom-st.*, No. 2, 45 (1996).
2. M. E. Gross *et al.*, *Appl. Phys. Lett.* **52**, 160 (1988).
3. A. N. Khol'kin *et al.*, *Dokl. Akad. Nauk SSSR* **312** (3), 663 (1990).
4. A. V. Suvorov, *Sverkhprovodimost: Fiz., Khim., Tekh.* **7** (2), 344 (1994).
5. H. Raffy, *Solid State Commun.* **68** (2), 344 (1988).
6. A. L. Shmaev, *Sverkhprovodimost: Fiz., Khim., Tekh.* **7** (6), 975 (1994).

7. M. Lelental, *Physica C (Amsterdam)* **167** (5–6), 614 (1990).
8. S. A. Men'shikh, L. A. Geras'kina, S. G. Prutchenko, *et al.*, *Neorg. Mater.* **35** (5), 621 (1999).
9. Yu. Ya. Tomashpolsky, S. A. Menshikh, L. A. Geraskina, *et al.*, *Integr. Ferroelectr.* **29**, 179 (2000).
10. M. Jergel, *Supercond. Sci. Technol.* **8**, 67 (1995).
11. Yu. Ya. Tomashpol'skiĭ, N. V. Sadvovskaya, M. V. Varshavskii, *et al.*, *Neorg. Mater.* **40** (9), 1098 (2004) [*Inorg. Mater.* **40**, 960 (2004)].
12. A. D. Pomogaĭlo and V. S. Savost'yanov, *Metal-Containing Monomers and Derived Polymers* (Khimiya, Moscow, 1988) [in Russian].
13. B. G. Gribov, G. A. Domrachev, B. V. Zhuk, *et al.*, *Deposition of Films and Coatings by Decomposition of Organometallics* (Nauka, Moscow, 1981) [in Russian].
14. Yu. Ya. Tomashpol'skiĭ, A. K. Kochetov, N. V. Sadvovskaya, *et al.*, *Sverkhprovodimost: Fiz., Khim., Tekh.* **3** (4), 669 (1990).

Translated by Yu. Sin'kov

SURFACE
AND THIN FILMS

Thermally Stimulated Relaxation of Misfit Strains in $\text{Si}_{1-x}\text{Ge}_x/\text{Si}(100)$ Heterostructures with Different Buffer Layers

T. G. Yugova*, M. G. Mil'vidskii*, M. M. Rzaev**, and F. Schäffler***

* State Institute of Rare Metals, Bol'shoi Tolmachevskii per. 5, Moscow, 119017 Russia

e-mail: icpm@mail.girmet.ru

** Lebedev Physical Institute, Russian Academy of Sciences,
Leninskii pr. 53, Moscow, 119991 Russia

*** Institut für Halbleiter- und Festkörperphysik, Johannes Kepler Universität,
Altenbergerstrasse 69, A-4040 Linz, Austria

Received April 18, 2005

Abstract—The regularities of the defect formation in $\text{Si}_{1-x}\text{Ge}_x/\text{Si}$ heterostructures ($x = 0.15$ and 0.30), consisting of a low-temperature Si buffer layer and a SiGe solid solution, during their growth and subsequent annealings at temperatures 550 – 650°C are investigated by the methods of optical and transmission electron microscopy and X-ray diffraction. It is shown that the misfit-strain relaxation by plastic deformation under the conditions studied occurs most intensively in heterostructures with low-temperature SiGe buffer layers. The maximum degree of misfit-strain relaxation (no higher than 45%) is observed in the heterostructures with $x = 0.30$ after annealing at 650°C . The results obtained are explained by the effect of the nature and concentration of dislocation-nucleation centers, existing in low-temperature buffer layers, on the characteristics of the formation of a dislocation structure in the heterostructures under consideration. © 2005 Pleiades Publishing, Inc.

INTRODUCTION

The problem of fabrication of effectively relaxing SiGe epitaxial heterostructures with a low dislocation density to be used as substrates for subsequent growth of high-quality strained silicon layers has recently attracted considerable attention from researchers. The fundamental difficulties occurring in this case are caused primarily by the large lattice mismatch between Si and Ge ($\sim 4.2\%$). During the growth of SiGe structures on silicon substrates, even at small thicknesses of the solid-solution layers, a dense network of misfit dislocations is formed at the SiGe/Si interface. Threading dislocations, arising during this process, grow through the buffer layer into the active region of the device structure. The high density of threading dislocations in strained silicon layers leads to a significant deterioration of their electrical characteristics and makes it impossible to use such structures in practice (to design high-quality high-frequency transistors and integrated circuits on their basis) [1, 2]. To decrease the dislocation density in active strained Si layers, different procedures are used: formation of a depth concentration gradient in the SiGe buffer layer [3], growth on compliant substrates [4], low-temperature growth of Si and SiGe buffer layers [5, 6], etc.

It was shown in [5, 6] that the growth of low-temperature (LT) Si buffer layers decreases the density of threading dislocations in SiGe heterostructures. It was suggested that the introduction of an LT Si buffer layer,

owing to the supersaturation of intrinsic point defects, not only provides the formation of low-energy dislocation-nucleation sources and decreases their mobility but also decreases the level of stresses in heterostructures since this layer is tensile-strained [7]. Postgrowth annealing of heterostructures with LT buffer layers leads to the effective misfit-strain relaxation [8].

Several models were proposed to explain the nature of the phenomena responsible for the defect formation in heterostructures with LT buffer layers [9–13]. Unfortunately, none of these models can describe the complex process of defect formation completely, which is related to the nucleation, propagation, multiplication, and annihilation of dislocations during the misfit-strains relaxation [14–16]. It is suggested that the nonequilibrium point defects present in LT buffer layers are actively involved in the formation of dislocation nucleation centers and affect their kinetic characteristics significantly, while leading to the occurrence of specific features in the generation of misfit-dislocation networks as compared to the conventional high-temperature (HT) heterostructures. It was suggested in [16] that the nonequilibrium point defects formed during the LT growth of buffer layers cause dislocation climb. This process leads to a decrease in the activation energy of misfit-strain relaxation and the annihilation of threading dislocations with opposite Burgers vectors [15, 16].

Table 1. Characteristics of the $\text{Si}_{1-x}\text{Ge}_x/\text{Si}(001)$ heterostructures

LT Si heterostructures		LT SiGe heterostructures		HT SiGe heterostructures	
Si cap, 5 nm, 500°C		Si cap, 5 nm, 500°C		Si cap, 5 nm, 500°C	
HT SiGe layer, $x = 0.15$ 200 nm, 500°C	HT SiGe layer, $x = 0.30$ 80 nm, 500°C	HT SiGe layer, $x = 0.15$ 200 nm, 500°C	HT SiGe layer, $x = 0.30$ 80 nm, 500°C	HT SiGe layer $x = 0.15$ 200 nm, 500°C	HT SiGe layer, $x = 0.30$ 80 nm, 500°C
LT Si buffer, 50 nm, 400°C		LT SiGe buffer, 50 nm, 250°C			
HT Si buffer, 100 nm, 750°C		HT Si buffer, 100 nm, 750°C		HT Si buffer, 100 nm, 750°C	
Si(001) substrate		Si(001) substrate		Si(001) substrate	

The purpose of this study is to obtain additional data for clarification of the nature of the defect formation in SiGe/Si heterostructures with LT buffer layers. In this context, we investigated the effect of the buffer layer type (LT Si and LT SiGe layers of different composition) on the kinetics of the thermally stimulated misfit-strain relaxation in such systems.

EXPERIMENTAL TECHNIQUE

$\text{Si}_{1-x}\text{Ge}_x/\text{Si}(100)$ heterostructures were grown by molecular-beam epitaxy on a Riber Siva 45 system using solid sources. Before the epitaxial growth, substrates were treated chemically using a conventional RCA procedure and annealed in the growth chamber at 1035°C for 15 min to remove the oxide layer from the surface. Then, an undoped Si buffer layer 100-nm-thick was grown at a temperature of 750°C, after which either an LT Si buffer layer was epitaxially grown at 400°C or an LT SiGe buffer layer with a Ge content $x = 0.15$ or 0.30 was grown at 250°C. In all cases, the thickness of the LT layers was 50 nm. At this buffer-layer thickness, according to the data of [17], only partial misfit-strain relaxation occurs during the growth of multilayer heterostructures. Then, an HT SiGe active layer with a Ge content $x = 0.15$ or 0.30 and a thickness of 200 or 80 nm, respectively, was grown at 500°C. The thicknesses of the HT SiGe layers were chosen such that they, significantly exceeding the critical depth h_{cr} of generation of misfit dislocations at the growth temperature (calculated on the basis of the approach suggested in [18]), would also exceed the critical depth at which the misfit-dislocation multiplication by the modified Frank–Read mechanism begins ($h_{FR} \approx 10h_{cr}$) [19]. In the final stage of the epitaxial growth, a 5-nm-thick Si cap was grown at a temperature of 500°C. For comparison, reference heterostructures of the same composition but without LT buffer layers were grown. The characteristics of the heterostructures under study are listed in Table 1.

Postgrowth annealing was carried out in hydrogen at 550, 600, and 650°C for 3–10 min.

The layer composition and the degree of misfit-strain relaxation were determined on a double-crystal diffractometer with a Si(004) monochromator in sym-

metric (400) and asymmetric (115) reflections using $\text{CuK}\alpha_1$ radiation.

The structural features of the heterostructures were investigated by transmission electron microscopy and optical microscopy using patterns of selective chemical etching of angle laps, thus allowing monitoring of the distribution of defects over the total heterostructure depth and revealment of dislocations in the near-interface substrate region. The selective-etch patterns were investigated on an interference optical microscope with Nomarsky contrast. Analysis of dark-field images of the etch patterns was also performed. Since the thicknesses of the HT SiGe layers under study were sufficiently small, the etching time was about 1 s. The dislocation etch pits formed during this time were so small that they could be observed only in dark field.

We analyzed the regularities of changes in the linear density of etch lines related to the misfit dislocations at the layer/substrate interface (N_L), the threading-dislocation density in the layer (N_{TD}), and the dislocation density in the near-interface substrate regions (substrate dislocations) (N_{SD}), depending on the temperature and time of heterostructure annealing.

The dislocation density in the layers and substrates were determined by calculating the density of dislocation etch pits revealed using a CrO_3 -based etchant. Since the linear density of etch lines ranged from 0 to $2 \times 10^4 \text{ cm}^{-1}$, the measurements were performed at different magnifications. By analogy with [16], at a density of etch lines lower than 50 cm^{-1} , the total line length per unit area was measured at a magnification of $\times 200$. At high densities of etch lines, the average distance between lines (number of lines per unit length) was measured in two orthogonal directions at a magnification of $\times 2000$. It should be noted that the density of etch lines is always lower by a factor of 3–5 than the actual density of misfit dislocations.

Hereinafter, the structures under consideration, depending on the buffer layer type, will be denoted as LT Si, LT SiGe, and HT SiGe (without an LT buffer layer).

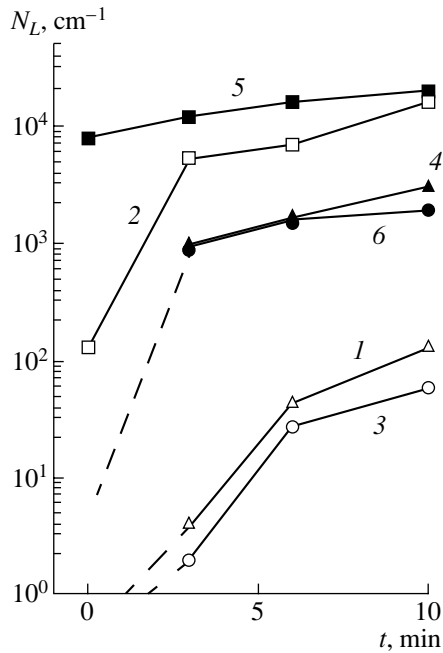


Fig. 1. Dependences of the density of etch lines on the surface of the $\text{Si}_{1-x}\text{Ge}_x/\text{Si}(100)$ heterostructures with different buffer layers on the time of annealing at 550°C : $x = (1-3)$ 0.15 and $(4-6)$ 0.30; (1, 4) LT Si buffer layer, (2, 5) LT SiGe buffer layer, and (3, 6) no LT buffer layer.

EXPERIMENTAL RESULTS

The results of the electron microscopy study of the heterostructures were described in detail in our previous studies [20, 21]. In this study, we focused on the optical microscopy and X-ray diffraction data.

Surface Morphology

The growth surface of the as-grown LT SiGe heterostructures exhibits either separate characteristic morphological lines or a characteristic morphological network (in the structures with $x = 0.15$ or 0.30 , respectively). During annealing, a morphological network is also formed in the LT SiGe heterostructure with $x = 0.15$, the density of lines in which increases with an increase in time and temperature. In the heterostructure with $x = 0.30$, the density of morphological-network lines also increases with an increase in the annealing time and temperature.

In the as-grown LT Si and HT SiGe heterostructures, morphological defects are absent on the layer surface. However, during subsequent annealing, separate cross-shaped morphological defects arise first on the layer surface and then a morphological network of orthogonal lines is formed. The density of the network lines increases with an increase in the annealing time and temperature.

Density of Etch Lines

The changes in the density of etch lines (N_L) during isothermal annealing at 550°C are shown in Fig. 1. The line density first increases sharply and then approaches a constant value slowly. In this case, the maximum density of etch lines depends not only on the composition but also on the type of the buffer layer. A weak dependence of N_L on the annealing time is observed only for the LT SiGe heterostructures with $x = 0.30$ (curve 5), in which a high density of lines is observed even in the as-grown state (the point $t = 0$).

It should be noted that the line density in the layers with $x = 0.30$ is always higher than in the layers with $x = 0.15$. In addition, the highest line density is observed in the LT SiGe heterostructures. The HT SiGe heterostructures show the lowest line density.

Isochronous annealing was carried out at 550 , 600 , and 650°C for 6 min. The obtained dependences of the density of etch lines on the annealing temperature are shown in Fig. 2. The curves for all heterostructures demonstrate a kink near 600°C . This kink is most pronounced for the LT Si and HT SiGe heterostructures with $x = 0.15$.

Density of Threading Dislocations in the HT SiGe Layer

The data on the density of threading dislocations in the HT SiGe layers of the heterostructures under study, annealed at 550°C , are listed in Table 2. For the LT Si and HT SiGe heterostructures with $x = 0.15$, we failed to calculate the dislocation densities reliably because of the low density of dislocation etch pits, which, in addition, were distributed nonuniformly. For all other heterostructures, the dislocation density increases somewhat with an increase in the annealing time but does not exceed $2.5 \times 10^5 \text{ cm}^{-2}$. Comparison of these data with the results shown in Figs. 1 and 2 indicates their fairly good agreement: the higher the density of etch lines, the higher the density of threading dislocations in the HT SiGe layer.

The results of the investigation of the dependence of N_{TD} in the HT SiGe layers on annealing temperature are listed in Table 3. These data show that threading dislocations are observed in all the heterostructures under study at sufficiently high annealing temperatures. The maximum value of N_{TD} in the HT SiGe layers is observed after annealing at 600°C . The heterostructures annealed at a temperature of 650°C are characterized by the absence of clear correlation between the densities of threading dislocations and etch lines.

Dislocation Density in the Near-Interface Substrate Region

It was shown previously [22, 23] that dislocations arise in the near-interface substrate region only when multiplication of misfit dislocations by the modified

Frank–Read mechanism occurs. The obtained dependences of the substrate-dislocation density N_{SD} on annealing time at 550°C are shown in Fig. 3. The multiplication of misfit dislocations is observed only in the LT SiGe heterostructures of both compositions and the HT SiGe heterostructure with $x = 0.30$. This process is more intense in the LT SiGe heterostructures.

The dependences of N_{SD} on annealing temperature are shown in Fig. 4. In the LT SiGe heterostructures of both compositions and the HT SiGe heterostructure with $x = 0.30$, the temperature dependence of N_{SD} is close to linear in the entire range of annealing temperatures under consideration. In the three other heterostructures, dislocations arise in the substrate only after annealing at 600 and 650°C. It is noteworthy that the dislocation multiplication is more intense in the LT Si and HT SiGe heterostructures with $x = 0.15$ than in the corresponding heterostructures with $x = 0.30$. The multiplication of misfit dislocations is most intense in the LT SiGe heterostructures.

X-ray Diffraction Data

X-ray diffraction investigations showed that, in the as-grown state, only the LT SiGe heterostructure with $x = 0.30$ shows more or less significant (~30%) misfit-strain relaxation. Signs of weak relaxation are observed also in the LT Si heterostructure with $x = 0.15$. All other heterostructures are strained completely elastically. Figure 5 shows as an example the rocking curves for the LT Si and LT SiGe heterostructures with $x = 0.30$. It can be seen clearly that, for the LT Si heterostructure (Fig. 5, curve 1), the peak from the SiGe layer is pronounced with a thickness oscillation around it, which is indicative of a high structural quality of this layer. For the LT SiGe heterostructure, the peak from the SiGe layer is wider and shifted to larger angles; the thickness oscillations are absent. This structure of the rocking curve indicates partial misfit-strain relaxation in this heterostructure. This is confirmed by the optical-microscopy data: the density of misfit dislocations in this heterostructure was found to be $\sim 10^4 \text{ cm}^{-1}$.

The degree of relaxation R was determined from the expression $R = (a_{\parallel} - a_s)/(a_l - a_s) \times 100\%$, where a_{\parallel} is the lattice parameter of the layer in the interface plane and a_l and a_s are, respectively, the lattice parameters of the

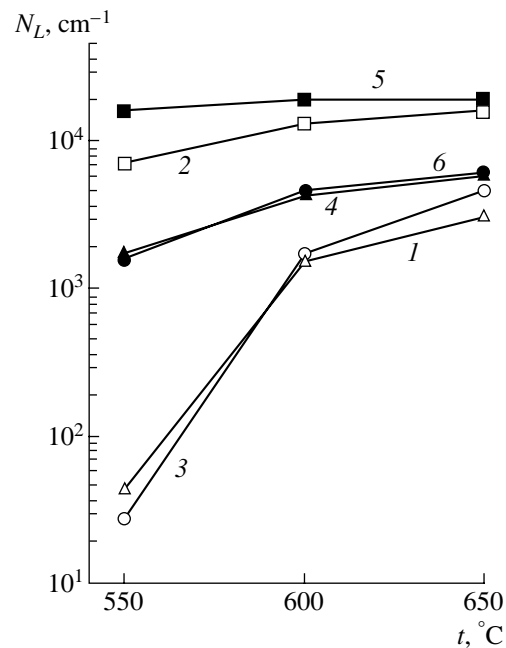


Fig. 2. Dependences of the density of etch lines on the surface of the $\text{Si}_{1-x}\text{Ge}_x/\text{Si}(100)$ heterostructures on the temperature of isochronous annealing. Designations are the same as in Fig. 1.

unstrained layer and substrate. In Fig. 5, arrows indicate the calculated position of the reflection peak from the SiGe layer for the cases of pseudomorphic ($R = 0$) and completely plastically relaxed ($R = 100\%$) layers.

During the annealing, partial misfit-strain relaxation is observed in all heterostructures. However, the degree of relaxation is different for structures of different types. The highest degree of relaxation (~45%) is observed in the LT SiGe heterostructure with $x = 0.30$ after the annealing at 650°C for 6 min. In the LT Si heterostructure with $x = 0.30$, the degree of misfit-strain relaxation after annealing under the same conditions does not exceed 15%. The relaxation is minimum in the heterostructures without an LT buffer layer.

DISCUSSION

The experimental data indicate convincingly that the degree of misfit-strain relaxation in the heterostruc-

Table 2. Threading-dislocation density in the HT SiGe layers of the heterostructures annealed at 550°C

Annealing time, min	Threading-dislocation density, cm^{-2}					
	$x = 0.15$			$x = 0.30$		
	LT Si	LT SiGe	HT SiGe	LT Si	LT SiGe	HT SiGe
3		1.4×10^5		7×10^4	1.6×10^5	5×10^4
6		1.3×10^5		9×10^4	2.2×10^5	8×10^4
10		2.0×10^5		1.2×10^5	2.3×10^5	1×10^5

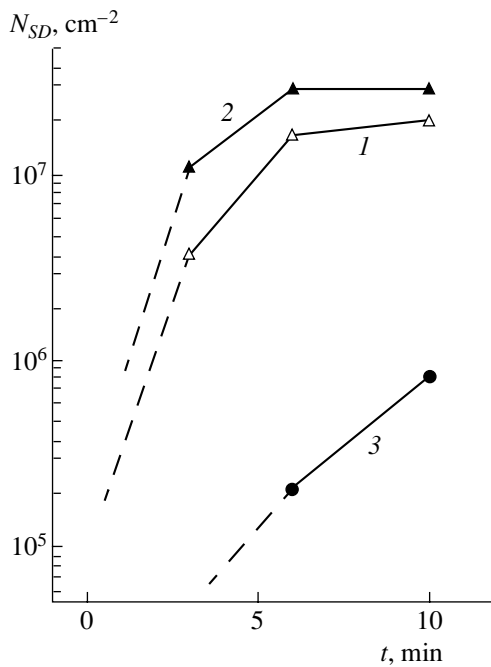


Fig. 3. Dependences of the dislocation density in the near-interface substrate region on the time of annealing at 550°C for the LT SiGe heterostructures with $x = (1)$ 0.15 and (2) 0.30 and (3) the HT SiGe heterostructure with $x = 0.30$.

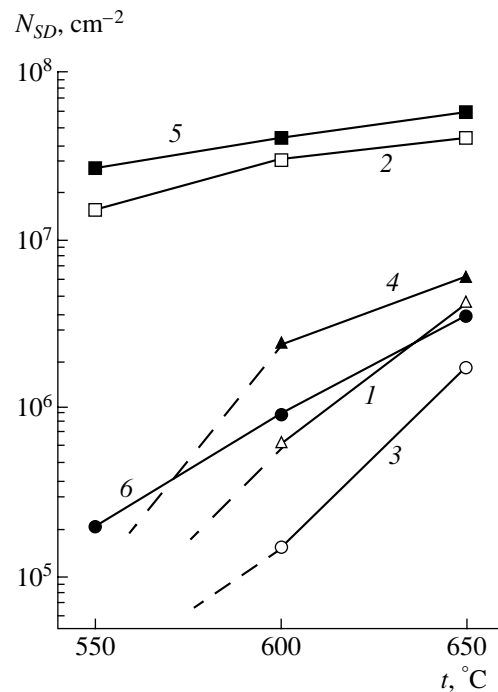


Fig. 4. Dependences of the dislocation density in the near-interface substrate region of the heterostructures on the temperature of annealing at 6 min. Designations are the same as in Fig. 1.

tures under study depends directly on the presence and composition of an LT buffer layer. The relaxation by plastic deformation is most intense in the heterostructures containing an LT SiGe buffer layer. In these heterostructures, partial misfit-strain relaxation is observed even in the growth stage and is accompanied by the formation of a regular planar misfit-dislocation network at the interface [20]. The surface of such heterostructures contains characteristic morphological defects (linear or network profile). Selective etching of an LT SiGe layer reveals characteristic etch lines and threading dislocations. The relaxation continues during subsequent annealings: the misfit-dislocation density at the interface increases and the planar dislocation networks formed in the initial stages of plastic relaxation are transformed gradually into three-dimensional networks. This process is accompanied by intense generation of dislocation half-loops in the near-interface

region of the silicon substrate. Such a transformation indicates that, in this stage of stress relaxation, multiplication of the misfit dislocations (forming a planar network) by the modified Frank–Read mechanism occurs in the heterostructures [22, 23]. In the annealed heterostructures, a gradual increase in the densities of etch lines and threading dislocations is observed in the LT SiGe layer with an increase in the annealing temperature and time. However, for the annealing temperatures and times considered here, the maximum degree of misfit-strain relaxation in the heterostructures with an LT SiGe buffer layer does not exceed 45%.

In the heterostructures with an LT Si buffer layer, the misfit-strain relaxation is much less intense; it is observed only after subsequent annealings of as-grown structures. As a result, the above-described processes of defect formation, accompanying the plastic misfit-strain relaxation, occur in these heterostructures at a

Table 3. Threading-dislocation density in the HT SiGe layers of the heterostructures annealed at different temperatures for 6 min

Annealing temperature, °C	Threading-dislocation density, cm^{-2}					
	$x = 0.15$			$x = 0.30$		
	LT Si	LT SiGe	HT SiGe	LT Si	LT SiGe	HT SiGe
500		1.3×10^5		9×10^4	2.2×10^5	8×10^4
600	2.4×10^5	2.2×10^5	2.7×10^5	1.9×10^5	2.4×10^5	1.9×10^5
650	1.3×10^5	1.9×10^5	1.3×10^5	1.3×10^5	1.3×10^5	1.5×10^5

much lower rate. This phenomenon manifests itself in the smaller values of the misfit-dislocation density at the interface and the densities of etch lines and threading dislocations in the HT SiGe layer. The maximum degree of misfit-strain relaxation in such heterostructures (for the annealing conditions we used) does not exceed 15%. The misfit-strain relaxation rate is the lowest in the heterostructures without an LT buffer layer.

All other factors being equal, the misfit-strain relaxation rate in all three types of heterostructures under study increases with an increase in the Ge content in the solid solution: in the structures with $x = 0.30$, the dislocation density is always higher than in the structures with $x = 0.15$. The most likely reason for this effect is that both the nucleation rate of dislocations and their velocity increase with an increase in the misfit strain caused by the increase in the Ge content in the solid solution [18].

It is noteworthy that, despite the significantly different degrees of misfit-strain relaxation in the heterostructures under study, the threading-dislocation densities in the HT SiGe layer in the heterostructures of all three types are comparable with each other and do not exceed $2.5 \times 10^5 \text{ cm}^{-2}$. This circumstance suggests that the plastic misfit-strain relaxation in such heterostructures occurs most likely through a mechanism different from the conventional mechanism of nucleation of dislocation half-loops on the free heterostructure surface. Apparently, it is pertinent to speak in this case about the presence of internal dislocation-nucleation sources in the heterostructures. Such internal sources in LT Si buffer layers are associates of nonequilibrium intrinsic point defects (vacancies and self-interstitials) [24, 25]. In the layers grown at fairly low temperatures, the concentration of nonequilibrium intrinsic point defects can reach the values sufficient for formation, along with clusters of corresponding defects, of dislocation microloops in the volume of the corresponding supersaturated solid solutions during their decomposition. Under the action of misfit strain, these dislocation loops expand, move, and interact with each other to form a dislocation structure.

In LT SiGe buffer layers, along with associates of nonequilibrium intrinsic point defects, composition microinhomogeneities and microprecipitates that formed as a result of spinodal decomposition of SiGe can also play the role of internal sources of dislocation-loop nucleation [26, 27]. In this case, the presence of nonequilibrium intrinsic point defects in high concentrations in the LT buffer layer of the solid solution is a high-power catalyst of its spinodal decomposition. In this context, it is expected that, all other factors being equal, the concentration of dislocation-nucleation centers in the LT SiGe buffer layer should be much higher than in the LT Si buffer layers and the SiGe layers of the same composition grown at higher temperatures.

According to the well-justified model of defect formation, proposed in [26], the misfit-strain relaxation by

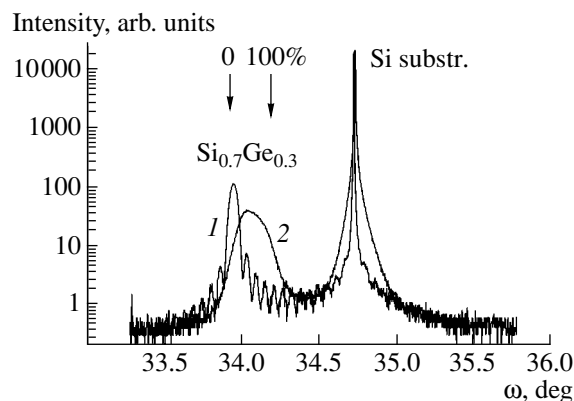


Fig. 5. X-ray rocking curves in the (004) reflection ($\text{CuK}\alpha_1$ radiation) for the as-grown (1) LT Si and (2) LT SiGe heterostructures with $x = 0.30$.

plastic deformation occurs in three stages. In the first stage, the degree of relaxation in an elastically strained film is controlled by the dislocation nucleation in the film. Sufficiently high velocities of dislocation motion in the initial stage of relaxation [28, 29] make it possible to exclude this kinetic factor from consideration as a limiting factor. In this stage, the degree of misfit-strain relaxation is determined by the concentration and nature of the dislocation-nucleation centers present in the heterostructure. With an increase in the misfit-dislocation density in a relaxing heterostructure, the importance of the interaction between dislocations increases. This interaction decreases the velocity of dislocation motion, which thus becomes a determining factor gradually. During the defect formation, the misfit-dislocation density in a heterostructure continues to increase in this relaxation stage, a result which is caused by the dislocation multiplication by the modified Frank–Read mechanism. Since the multiplication of misfit dislocations by this mechanism begins only at a certain value of their density, the nature and the concentration of dislocation-nucleation centers continues to affect (although to a smaller extent in comparison with the first stage) the relaxation rate. In the final relaxation stage, the misfit-dislocation density in a heterostructure becomes so high that the interaction between dislocations almost stops the plastic deformation.

The experimental data obtained here indicate that the misfit-strain relaxation in the heterostructures under consideration stops either in the first stage or at the beginning of the second stage. The maximum degree of relaxation does not exceed 45% and is much below this value in most heterostructures. Under these conditions, the main factors determining the relaxation rate are the concentration and nature of dislocation-nucleation centers. Apparently, the concentration of active dislocation-nucleation centers is much higher in LT SiGe buffer layers than in LT Si buffer layers. This seems to be the main reason for the higher degree of relaxation

in the heterostructures containing an LT SiGe buffer layer.

CONCLUSIONS

The regularities of the defect formation in $\text{Si}_{1-x}\text{Ge}_x/\text{Si}$ heterostructures ($x = 0.15$ or 0.30) containing low-temperature Si and SiGe buffer layers during their growth and subsequent annealings at $550\text{--}650^\circ\text{C}$ are investigated by the methods of optical and transmission electron microscopy and X-ray diffraction. It is shown that, under such conditions, the misfit-strain relaxation by plastic deformation is most intense in the heterostructures with an LT SiGe buffer layer. The maximum degree of relaxation (no higher than 45%) is observed in the heterostructures with $x = 0.30$ after annealing at 650°C .

It is suggested and substantiated that the nature and concentration of internal dislocation-nucleation sources in LT buffer layers determine the specific features of the dislocation-structure formation in the heterostructures under consideration. In LT Si layers, such centers are associates of nonequilibrium intrinsic point defects (including dislocation microloops), which formed as a result of the decomposition of solid solutions supersaturated with these defects. In LT SiGe buffer layers, along with the associates of nonequilibrium intrinsic point defects, composition microinhomogeneities and microprecipitates that formed as a result of the spinodal decomposition of SiGe also serve as internal dislocation-nucleation sources. In this case, nonequilibrium intrinsic point defects present in these layers are catalysts of the spinodal decomposition.

Apparently, in LT SiGe buffer layers, the concentration of active dislocation-nucleation centers is much higher than in LT Si buffer layers. This seems to be the main reason for the higher degree of relaxation in the heterostructures with an LT SiGe buffer layer.

ACKNOWLEDGMENTS

We are grateful to V.I. Vdovin for carrying out the electron microscopy study, N.N. Loiko for performing the annealing, M. Mühlberger for his help in growing the samples, and V.F. Pavlov for carrying out the additional X-ray diffraction measurements.

This study was supported by the Russian Foundation for Basic Research, project nos. 03-02-20007 Bureau for Scientific and Technical Cooperation and 02-02-16692; the program "Leading Scientific Schools," grant no. NSh 1923.2003.2; and INTAS, grant nos. 01-0194 and 03-51-5015.

REFERENCES

1. R. Hull, J. C. Bean, and C. Buescher, *J. Appl. Phys.* **66**, 5837 (1989).
2. L. B. Freund, *J. Appl. Phys.* **66**, 2073 (1990).
3. L. Liu, C. D. Moore, G. D. U'Ren, *et al.*, *Appl. Phys. Lett.* **75**, 1586 (1999).
4. Y. H. Luo, J. L. Lin, G. Jin, *et al.*, *J. Electron. Mater.* **29**, 950 (2000).
5. H. Chen, L. W. Guo, O. Cui, *et al.*, *J. Appl. Phys.* **79**, 1167 (1996).
6. P. M. Mooney, J. L. Jorddan-Sweet, K. Jsmail, *et al.*, *Appl. Phys. Lett.* **67**, 2373 (1995).
7. Y. H. Luo, J. Wan, R. L. Forest, *et al.*, *Appl. Phys. Lett.* **78**, 454 (2001).
8. E. A. Fitzgerald, *Mater. Sci. Rep.* **7**, 87 (1991).
9. B. W. Dodson and J. Y. Tsao, *Appl. Phys. Lett.* **51**, 1325 (1987).
10. B. W. Dodson and J. Y. Tsao, *Appl. Phys. Lett.* **52**, 852 (1988).
11. J. W. Matthews and A. E. Blaclee, *J. Cryst. Growth* **27**, 118 (1974).
12. J. W. Matthews, *J. Vac. Sci. Technol.* **12**, 126 (1975).
13. B. W. Dodson and J. Y. Tsao, *Appl. Phys. Lett.* **53**, 2498 (1988).
14. F. K. LeGouse, B. S. Meyerson, J. F. Morar, and P. D. Kircher, *J. Appl. Phys.* **71**, 4230 (1992).
15. E. Kasper, K. Ljutovich, M. Baner, and M. Ochine, *Thin Solid Films* **336**, 319 (1998).
16. M. R. Re, S. Scalese, S. Mirabella, *et al.*, *J. Cryst. Growth* **227–228**, 749 (2001).
17. M. Bauer, K. Lyutovich, M. Oehme, *et al.*, *Thin Solid Films* **369**, 152 (2000).
18. D. C. Houghton, *J. Appl. Phys.* **70**, 2136 (1991).
19. R. Beanland, *J. Appl. Phys.* **72**, 4031 (1992).
20. V. I. Vdovin, T. G. Yugova, M. M. Rzaev, *et al.*, *Phys. Status Solidi C* **2** (6), 1938 (2005).
21. T. G. Yugova, V. I. Vdovin, M. G. Mil'vidski, *et al.*, *Thin Solid Films* **336**, 112 (1998).
22. M. Rzaev, V. Vdovin, and T. Yugova, *Mater. Sci. Semicond. Process.* **8**, 137 (2005).
23. T. G. Yugova, M. G. Mil'vidskii, and V. I. Vdovin, *Fiz. Tverd. Tela (St. Petersburg)* **46**, 1476 (2004) [*Phys. Solid State* **46**, 1520 (2004)].
24. Cs. Szeles, P. Asoka-Kumar, K. G. Lynn, *et al.*, *Appl. Phys. Lett.* **66**, 2855 (1995).
25. T. Ueno, T. Irisawa, Y. Shiraki, *et al.*, *Thin Solid Films* **369**, 320 (2000).
26. D. D. Perovic and D. C. Houghton, *Inst. Phys. Conf. Ser.* **146**, 117 (1995).
27. V. I. Vdovin, M. G. Mil'vidskii, and T. G. Yugova, *Kristallografiya* **50** (5), 915 (2005) [*Crystallogr. Rep.* **50**, 849 (2005)].
28. R. Hull, J. C. Bean, L. J. Peticolas, *et al.*, *Appl. Phys. Lett.* **65**, 327 (1994).
29. R. Hull and J. C. Bean, *Appl. Phys. Lett.* **54**, 925 (1989).

Translated by Yu. Sin'kov

CRYSTAL GROWTH

The Influence of Crystalline Anisotropy on the Evolution of the Crystallization Front during Directional Solidification

O. P. Fedorov, A. P. Shpak, E. L. Zhivolub, and O. V. Shuleshova

Kurdyumov Institute of Metal Physics, National Academy of Sciences of Ukraine,
bul'v. Akademika Vernadskogo 36, Kiev, 03680 Ukraine

e-mail: shulya@imp.kiev.ua

Received December 14, 2004

Abstract—The evolution of the crystallization front of transparent crystals of succinonitrile and pivalic acid in the course of directional solidification in the field of a temperature gradient (Bridgman method) is investigated experimentally. The influence of crystalline anisotropy is examined using single crystals of different orientations. Bulk (cylindrical) and planar single crystals of the materials under investigation are studied and compared for the first time. It is established that the crystallographic direction of growth plays an important role and determines the structure of the crystallization front at different stages of its evolution. New manifestations of the dynamic effects responsible for the development of the nonstationary periodic structure are revealed. © 2005 Pleiades Publishing, Inc.

INTRODUCTION

When crystals grow from melt through a conventional mechanism, the anisotropy of both the surface energy and the kinetic coefficient (hereafter, for brevity, it will be referred to as crystalline anisotropy) is insignificant. This can be judged from the rounded shape of the crystals growing in a melt and from the weak dependence of the growth rate on the orientation. Moreover, the weak anisotropy is responsible for the direction of growth of a dendrite trunk and for the stability of the parabolic shape of the dendrite tip. It is known that the orientation affects the morphology of the crystallization front during crystal growth in the field of a temperature gradient. Morris and Winegard [1] studied Pb–Sb single crystals and revealed the formation of elongated cells for the $\langle 110 \rangle$ orientation and equiaxial cells for $\langle 100 \rangle$ orientation. The mechanism of this process is illustrated by the scheme depicted in Fig. 1 [1]. A hill arising on a flat surface differently grows in different directions. For a cubic lattice structure and the $\langle 100 \rangle$

direction of the growth, hills on the surface have four symmetrically arranged growth planes with the $\{111\}$ orientation. The growth rate of these closest packed planes is minimum; hence, the perturbation is equiaxial in shape. For the $\langle 110 \rangle$ direction of the growth, the hill on the surface has two (rather than four) slowly growing planes. In this case, an elongated perturbation (an elongated cell) arises. It should be noted that there are experimental data inconsistent with the above scheme. For example, Chernov [2] considered elongated cells as a stage in the development of an unstable structure of the crystallization front (nodes, elongated cells, equiaxial cells), irrespective of the growth direction. Kauerauf *et al.* [3] believed that elongated cells in succinonitrile crystals are associated with the disturbing effect of the grain boundaries.

Investigations of transparent crystals in planar samples have demonstrated that the growth direction affects the structure of the crystallization front [4]. At specific growth orientations, the growth of crystals with an

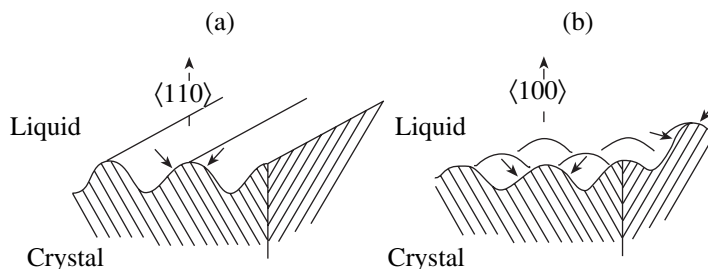


Fig. 1. Schematic drawings of the developing hills for two growth orientations: (a) elongated cells formed for the $\langle 110 \rangle$ direction of the growth and (b) a nodular (equiaxial) structure formed for the $\langle 100 \rangle$ direction of the growth (short arrows indicate the $\{111\}$ planes in the hills).

anisotropic columnar structure gives way to the growth of crystals with a continuously branching isotropic structure due to the weak anisotropy in the $\langle 110 \rangle$ and $\langle 111 \rangle$ crystallographic directions [5]. This means that the orientation is an important factor governing the structure. Furthermore, according to [6], the anisotropy is not a sole factor responsible for the formation of a tilted structure and for splitting of the cells. Similar effects have been observed for isotropic phase boundaries in “liquid–gas” and “liquid crystal–gas” systems.

A comparison of the results obtained by different researchers gives no grounds to believe that particular data are accurate, whereas other data are erroneous. The aforementioned differences can be associated with the growth conditions (a variable pulling rate, a nonuniform distribution of impurities ahead of the crystallization front, varying thermal conditions). These circumstances should be taken into account in the elucidation of the role played by both the instability of external conditions (instrumental factors) and the dynamic effects caused by the processes occurring at the growth front (nucleation and splitting of cells, variations in the cell parameters during growth).

The above factors provided the basis for the experimental approach proposed in the present paper. The purpose of this study was to elucidate how the weak crystalline anisotropy (characteristic of the conventional mechanism of crystal growth) affects the evolution of the morphology of the crystallization front. We used single-crystal seeds of different crystallographic orientations and also materials differing in anisotropy of the surface parameters. Long-term observations of the crystallization fronts were performed under controlled steady-state conditions.

EXPERIMENTAL TECHNIQUE AND RESULTS

The experiments were performed with transparent substances, namely, succinonitrile and pivalic acid, which are characterized by a conventional mechanism of crystal growth from melt and different crystalline anisotropies [7, 8]. The initial compounds (Aldrich) were additionally purified through vacuum distillation. The degree of purification was determined by measuring the liquidus temperatures of the references samples. The content of uncontrollable impurities did not exceed 0.15% (predominantly, in the form of water) in succinonitrile and 0.1% in pivalic acid.

The experiments with planar samples were carried out in a standard apparatus [9], which provided growth of crystals at rates in the range 0.5–2.0 $\mu\text{m/s}$ with an accuracy of 5% and at a constant temperature gradient of 20 K/cm. A technique was developed for preparing single crystals in planar samples. The orientation of the single crystals was determined from the symmetry of branches of the dendrites grown at a high rate.

The crystallization in cylindrical samples was investigated using an apparatus described in detail in [10]. The crystals were grown by the Bridgman method, according to which the sample was moved with respect to the fixed heater and the fixed refrigerator. The working rates varied in the range from 1 to 30 $\mu\text{m/s}$, the temperature gradient was equal to 20 K/cm, and the sample diameter was 12 mm. The design of the apparatus ensured (i) continuous videorecording of the growth process through a layer of the molten material and (ii) automatic adjustment of the image of the crystallization front for sharpness in the course of the front displacement. The technique for preparing single-crystal samples was based on the use of a shaped adapter unit that made it possible to grow a single crystal deviated from the initial direction by a specified angle.

The front images obtained in the digital form were used for subsequent processing. The intercellular spacing λ was calculated by averaging the spacings between the geometric centers of the cells at a chosen instant of time. The degree of order in the arrangement of structural elements (nodes, cells) was determined by the minimal spanning tree (MST) method proposed in [11].

The sequential images of unstable structures formed at different growth rates of the $\langle 100 \rangle$ succinonitrile crystal are displayed in Fig. 2. It can be seen from this figure that perturbations of the flat front manifest themselves in the formation of nodes, i.e., shallow hollows enriched with impurities at the front. This can be judged from the melting (the process inverse to growth) during which the regions adjacent to nodes are melted first. An increase in the growth rate leads to the appearance of ridges, which, for the most part, are initiated by the nodes. However, we clearly observed the formation of ridges not related to the nodes. With the passage of time, the ridges form an almost regular cellular structure, which is characteristic of equiaxial cells (Fig. 2c). At the next stage, dendrites are formed from these cells. Note that, in our experiments, nodes clearly manifest themselves in the bulk and planar succinonitrile single crystals (Fig. 2d).

Figure 3 presents the time τ of appearance of nodes and cells as a function of the growth rate V for the $\langle 100 \rangle$ succinonitrile single crystal. The appearance time τ was determined as the time interval between the beginning of pulling at a given rate and the instant of time at which the specified number of structural units was recorded at the surface of the crystallization front. As can be seen from Fig. 3, the appearance times and their dependences on the growth rate for nodes and cells differ significantly over a rather wide range of growth rates. The dependence of the appearance time on the growth rate has the form $\tau = V^{-2.4 \pm 0.2}$ for nodes and $\tau = V^{-3.9 \pm 0.2}$ for cells. These dependences almost coincide with each other in the range of growth rates (2 $\mu\text{m/s}$ and higher) at which the dendritic growth occurs at the final stage. Note that there is a considerable spread of the experi-

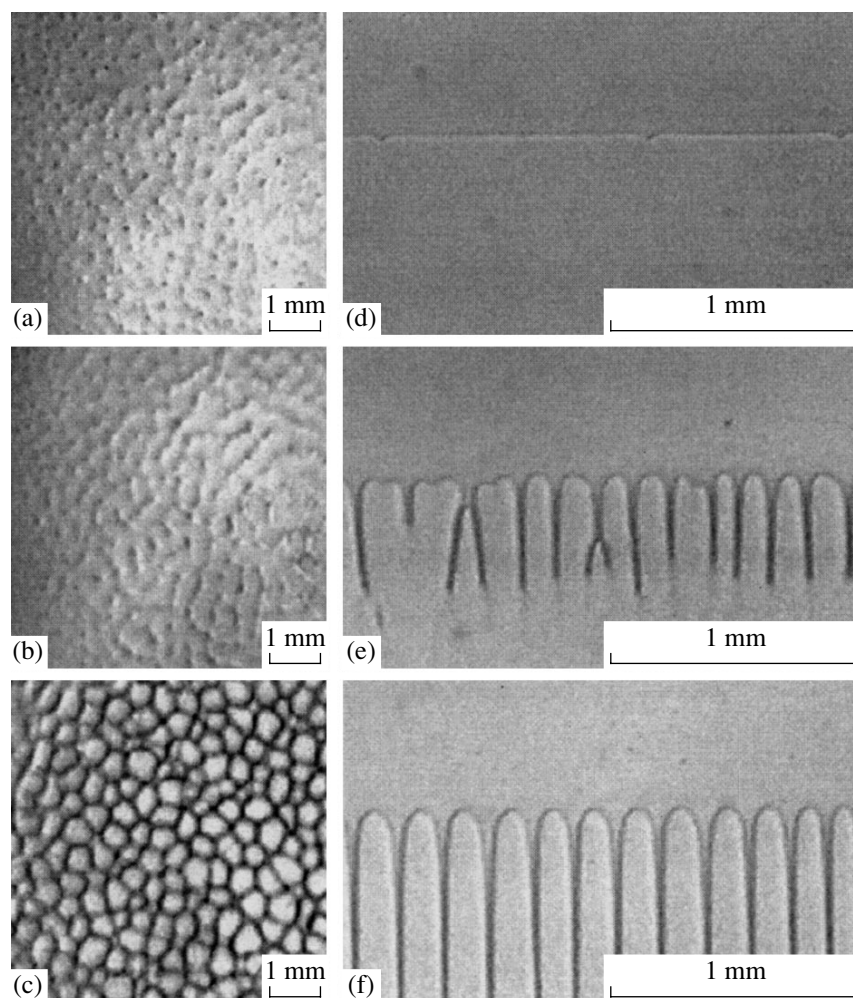


Fig. 2. Sequential images of the unstable structures in (a–c) bulk ($V = 1.1 \mu\text{m/s}$) and (d–f) planar ($V = 0.68 \mu\text{m/s}$) succinonitrile samples (100).

mental values obtained for the same sample under similar experimental conditions.

The characteristic time dependences of the intercellular spacing λ are plotted in Fig. 4. It can be seen from this figure that the times of appearance of the cellular structure under identical growth conditions can differ significantly. Moreover, the time dependences of the intercellular spacing λ exhibited oscillations in all the experiments performed. This effect is caused by the two competing periodic processes observed in planar and bulk samples: the suppression of cells by neighbors and the splitting of growing cells. The maximum in curve 1 (Fig. 4) corresponds to an increase in the total number of cells at the growth front by 10% with respect to the average value. The analysis of the obtained curves did not reveal regularities of the time variations in the amplitude and frequency of oscillations of the intercellular spacing λ . Note also that there is a tendency toward an increase in the average intercellular spacing λ in particular curves in the range of long times (Fig. 4, curves 2, 3).

The dependences shown in Fig. 4 indirectly indicate a change in the impurity concentration ahead of the crystallization front in the course of the growth. Indeed, at the steady-state stage, the impurity concentration ahead of the flat front is characterized by an exponential time-independent profile [12]:

$$C(z) = C_0 \left[1 + \frac{1-k}{k} \exp(-(V/D)z) \right], \quad (1)$$

where C is the impurity concentration in the liquid phase, C_0 is the initial impurity concentration in the alloy, V is the velocity of movement of the interface, z is the distance from the interface, k is the equilibrium distribution coefficient, and D is the diffusion coefficient of the solute in the liquid phase.

During growth, the concentration distribution described by relationship (1) is attained after a transient period. When the concentration profile is a function of the time $C = C(z, \tau)$, the position of the isotherm corresponding to the equilibrium melting temperature

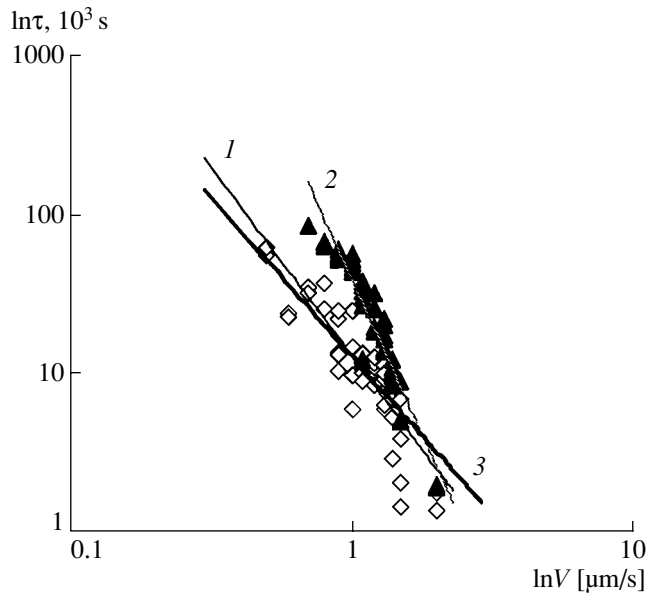


Fig. 3. Dependences of the appearance time of (1) nodes (rhombuses) ($\tau = V^{-2.4}$) and (2) cells (triangles) ($\tau = V^{-3.9}$) on the growth rate V for the bulk succinonitrile sample with the $\langle 100 \rangle$ orientation. (3) Calculated dependence of the appearance time of perturbations arising through the diffusion mechanism [18] ($\tau = V^{-2}$).

should change with time. In this case, the drift velocity of the front $z_0(\tau)$ should be determined by the slope of the liquidus line of the system under investigation and the growth rate [13]. This assumption was verified by direct measurements of the location of the crystallization front $z_0(\tau)$ in planar succinonitrile samples in the

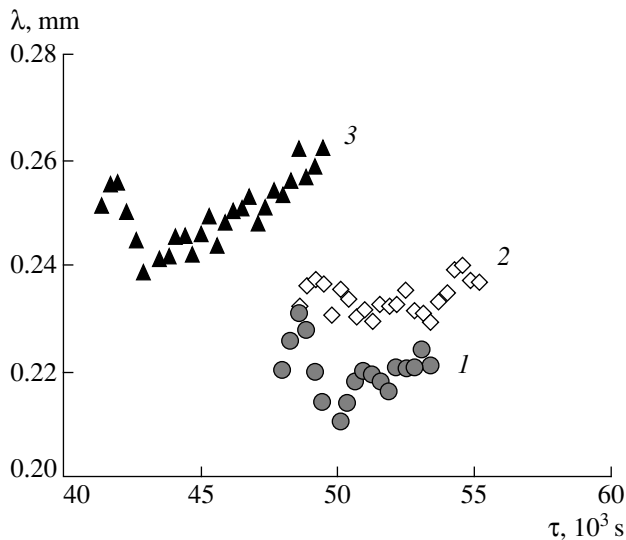


Fig. 4. (1–3) Dependences of the intercellular spacing λ on the time τ for the bulk succinonitrile sample with the $\langle 100 \rangle$ orientation. $V = 1.0 \mu\text{m/s}$. Numerals near the symbols indicate the run number.

fixed system of coordinates. In a series of test experiments, we did not reveal any effect of the instability of the temperature in the operating unit on the location of the crystallization front $z_0(\tau)$.

Figure 5 presents the data for the characteristic growth rates corresponding to the flat, cellular, and dendritic fronts. For the flat front, the front location $z_0(\tau)$ drifts at a constant velocity. It is worth noting that the higher the growth rate, the higher the drift velocity. In the case of dendritic growth, the drift is absent. The cellular front is characterized by a pronounced (even if weak) effect. It should be noted that the data for the planar sample are in qualitative agreement with similar observations for bulk samples [14].

The evolution of the microstructure of the crystallization front in the $\langle 100 \rangle$ direction for succinonitrile (Fig. 3) is qualitatively similar to that for pivalic acid (Fig. 6a). However, in the case of pivalic acid, indication of nodes is absent at the initial stage of stability loss. Subsequently, ridges are formed at the front in both cases. The initial arrangement of ridges seems chaotic. Then, the structure of ridges becomes ordered, but regular hexagons are observed rarely. Indications of elongated cells were found in none of the experiments with the $\langle 100 \rangle$ single crystals. It should be noted that the subboundaries (and grain boundaries in polycrystals) observed in a number of cases initiate the formation of ridges extended along the subboundaries. These cell boundaries can be mistaken for elongated cells. However, similar effects are not observed in perfect single crystals.

A quite different situation occurs during formation of the cellular structure of the $\langle 110 \rangle$ single crystals:

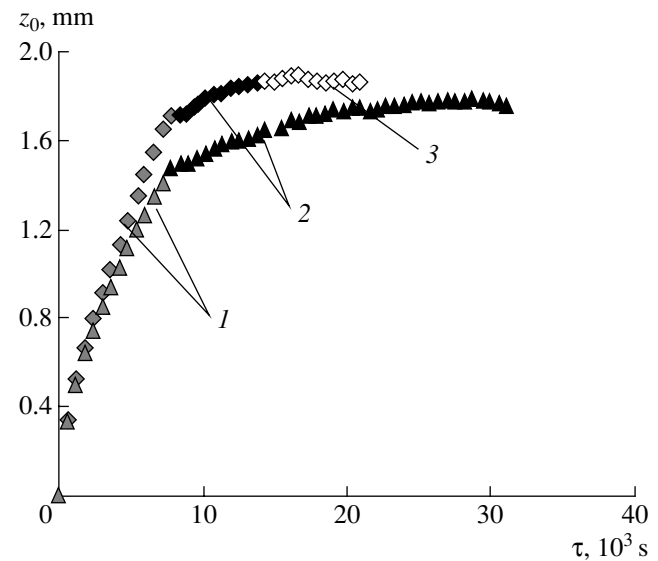


Fig. 5. (1–3) Dependences of the displacement z_0 of the location of different crystallization fronts on the time τ for the planar succinonitrile sample with the $\langle 100 \rangle$ orientation at growth rates $V = 0.9$ (triangles) and 1.1 (rhombuses) $\mu\text{m/s}$. Front type: (1) flat, (2) cellular, and (3) dendritic.

ridges arises and, with time, form boundaries of elongated cells (Fig. 6b). Furthermore, the elongated cells are not completely ordered or geometrically regular for both succinonitrile and pivalic acid. The boundaries between the cells are represented by sinuous lines, and their extension along one direction for pivalic acid is substantially more pronounced. Under identical growth conditions, the elongated cells transform into equiaxial cells to form the front with a structure that differs only slightly from the corresponding structure of the front for the $\langle 100 \rangle$ direction. During long-term growth, inside the elongated cells, there arise necks that separate these cells into sections and then become indistinguishable from the cell boundaries. Therefore, the formation of elongated cells can be treated as a stage of the development of the unstable front structure at specific growth rates. In this case, the higher the growth rate, the shorter this stage. Elongated cells are not observed altogether at growth rates higher than $1.3 \mu\text{m/s}$ for succinonitrile and at rates higher than $0.7 \mu\text{m/s}$ for pivalic acid.

The sequence of morphological transformations for the $\langle 111 \rangle$ succinonitrile single crystals and the single crystals with orientations that deviate from the $\langle 111 \rangle$ orientation by angles up to 10° is identical to the sequence of morphological transformations observed for the $\langle 110 \rangle$ single crystals. The difference lies in the degree of manifestation of elongated cells, which, in the case of high-index directions, appear as a geometric motif rather than as clear-cut structural elements.

The results of analyzing the degree of order in the arrangement of nodes and cells for the $\langle 100 \rangle$ crystallographic orientation are presented in the MST diagram (Fig. 7). The initially formed nodes become somewhat more ordered with time (the corresponding points in the diagram shift toward smaller values of σ), and the symmetry of their arrangement becomes identical to the symmetry of the centers of the growing cells. This implies that the nodes and cells are ordered in different manners. In turn, the arrangement of the cells does not change with time and remains similar in symmetry to regular hexagons. No effect of the crystallographic orientation on the symmetry of the node arrangement is observed.

DISCUSSION

Let us consider the initial stages of stability loss. The formation of nodes at the flat surface of the crystallization front was noted by different authors who were studying metal alloys and bulk succinonitrile samples. It follows from the above data that nodes appear as the first stage of stability loss of the flat front in the succinonitrile single crystals for all the orientations under investigation ($\langle 100 \rangle$, $\langle 110 \rangle$, $\langle 111 \rangle$). Moreover, shallow chaotic hollows that initiate the subsequent development of sinusoidal perturbations at the front are observed in the planar succinonitrile sample. Similar results were obtained by other authors [15]. However, in those works, the onset of the stability loss of the flat

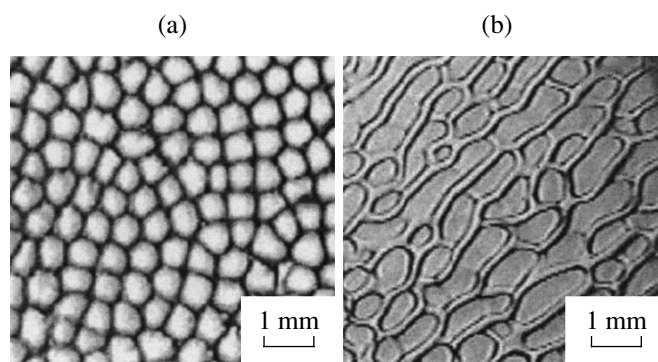


Fig. 6. Images of (a) equiaxial cells for the $\langle 100 \rangle$ orientation and (b) elongated cells for the $\langle 110 \rangle$ orientation of the pivalic acid sample.

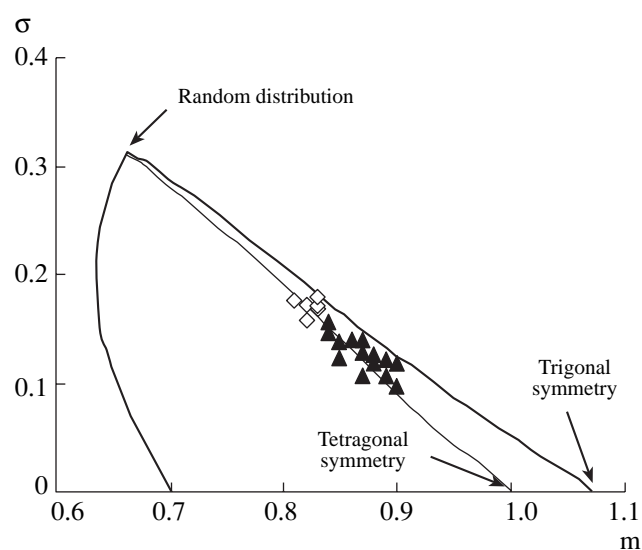


Fig. 7. MST diagrams illustrating the degree of ordering of the nodes (rhombuses) and centers of cells (triangles) for the bulk succinonitrile sample with the $\langle 100 \rangle$ orientation (in the case of trigonal symmetry of the centers, the cells are hexagonal in shape).

front was assigned to the appearance of sinusoidal perturbations. A comparison of the results obtained allows us to propose the following interpretation of the initial stage of the stability loss.

As can be seen from Fig. 7, the arrangement of nodes is very similar to that of the centers of the equiaxial cells (Fig. 1); i.e., nodes are sinusoidal perturbations with an amplitude close to zero. Symmetry of the arrangement cannot be revealed in the planar sample (this is evident from Fig. 2a in which a planar plate can be cut mentally). Furthermore, shallow chaotic hollows are also formed by grain boundaries of polycrystals (which have been predominantly investigated up to now). Therefore, when studying planar samples, the stability loss was determined from the appearance of a wavelike perturbation at the front. Taking into account

this circumstance, we believe that it is justified to treat the node stage as the first stage of stability loss. It should be noted that, in the framework of the Mullins–Sekerka theory [16], perturbations with an infinitesimal amplitude are considered the initial stage of the instability development. The calculated rates of stability loss of the flat front (i.e., a wavelike perturbation) are severalfold less than the experimental rates. It is significant that the appearance of sinusoidal perturbations with a small amplitude depends on the surface properties of the phase boundary (this stage exists for succinonitrile and does not exist for pivalic acid). This result is important for the subsequent analysis of the bifurcation diagrams for different materials.

The crystallographic orientation of the single crystals characterized by the conventional mechanism of growth from melts has a strong effect on the microstructure of the crystallization front. Qualitatively, the front morphology can be correctly described within the scheme proposed by Morris and Winegard [1] (Fig. 1); i.e., equiaxial and elongated cells are formed in the case of the $\langle 100 \rangle$ and $\langle 110 \rangle$ orientations, respectively. However, the dynamic effects change this scheme substantially. First, elongated cells arise at specific growth parameters and then give way to equiaxial cells identical to cells at the front of the $\langle 100 \rangle$ single crystal. Second, elongated cells are irregular in shape due to the periodic events of splitting and suppression.

In their study of succinonitrile, Kauerauf *et al.* [3] made the inference that, in $\langle 100 \rangle$ single crystals, elongated cells can be formed through the mechanism associated with the grain boundaries. Indeed, cells initiated by defects, i.e., boundaries and subboundaries, are formed in polycrystals and single crystals containing subgrains. These cells arise for any growth direction and have a random orientation. Elongated cells in the $[110]$ single crystals are aligned parallel to the $[\bar{1}10]$ direction and are not related to the grain structure of the seed crystal. The “true” and “random” elongated cells differ not only in the formation mechanism and crystallographic features. It is important that specific types of true cells can find practical applications. In our earlier work [17], we studied Al-based single crystals and demonstrated that elongated cells interact with defects in crystals and substantially affect their structural perfection. In particular, we observed the displacement of defects by cell boundaries in the course of growth. By choosing the growth direction (and, thus, by changing the direction of the development of the elongated cells with respect to the crystallization front), it is possible to remove large-sized defects completely from the crystals. Therefore, random cells are irregular perturbations of the front due to the defect structure of the seed crystal. The true elongated cells are front perturbations that are independent of the defect structure and can serve to modify the structure and the degree of structural perfection of the single crystals.

Since the elongated cells are observed in a limited time interval and at a constant rate, there are experimental conditions under which these cells are not observed at all. Moreover, when studying the polycrystals, random elongated cells can be observed for different grains. In this respect, contradictory sequences of morphological transformations of the crystallization front can be found in the literature [18].

The known dynamic effects (the splitting and suppression of cells, the formation of tilted and doublet structures) can be supplemented by the results made in the present study. These are the oscillations observed in the time dependences of the intercellular spacing λ and variations in the appearance time of the perturbations (Figs. 3, 4). It seems to be established that many effects can be explained in terms of the nonstationary accumulation of impurities under steady-state external conditions. Note that this effect is associated with the low content of uncontrollable impurities that are always contained in organic materials.

The morphological data obtained in this study indicate that different types of perturbations can arise as a result of the stability loss of the flat front. Specifically, nodes are small-amplitude long-wavelength perturbations whose evolution with time is controlled by the diffusion (Fig. 3) and whose shape and amplitude do not depend on the crystallographic orientation. The wavelength of cells is comparable to their amplitude, the cell shape depends on the crystallographic orientation, and the evolution of the cells with time differs significantly from the diffusion law. These perturbations develop concurrently and interact with each other. Note that one type of perturbations, namely, nodes, is absent altogether (for pivalic acid) at particular parameters of the crystallization front.

REFERENCES

1. L. R. Morris and W. C. Winegard, *J. Cryst. Growth* **5**, 361 (1969).
2. A. A. Chernov, in *Modern Crystallography*, Vol. 3: *Crystal Growth*, Ed. by B. K. Vainshtein, A. A. Chernov, and L. A. Shuvalov (Nauka, Moscow, 1980; Springer, Berlin, 1984), p. 7.
3. B. Kauerauf, G. Zimmermann, L. Murmann, *et al.*, *J. Cryst. Growth* **193**, 701 (1998).
4. O. P. Fedorov, *J. Cryst. Growth* **156**, 473 (1995).
5. A. G. Borisov, O. P. Fedorov, and V. V. Maslov, *J. Cryst. Growth* **112**, 463 (1991).
6. S. de Cheveigné and C. Guthmann, *J. Phys. I* **2**, 193 (1992).
7. E. R. Rubinstein and M. E. Glicksman, *J. Cryst. Growth* **112**, 84 (1991).
8. M. E. Glicksman and N. B. Singh, *J. Cryst. Growth* **98**, 277 (1989).
9. A. G. Borisov, O. P. Fedorov, and V. V. Maslov, *Kristallografiya* **36** (5), 1267 (1991) [*Sov. Phys. Crystallogr.* **36** (5), 716 (1991)].

10. A. P. Shpak, O. P. Fedorov, E. L. Zhivolub, *et al.*, *Metallofiz. Novejšie Tekhnol.* **26** (3), 419 (2004).
11. C. Dussert, G. Rasigni, M. Rasigni, *et al.*, *Phys. Rev. B: Condens. Matter* **34** (5), 3528 (1986).
12. M. Flemings, *Solidification Processing* (McGraw-Hill, New York, 1974; Mir, Moscow, 1977).
13. W. Losert, B. Q. Shi, and H. Z. Cummins, *Proc. Natl. Acad. Sci. USA* **95**, 431 (1998).
14. H. Jamgotchian, N. Bergeon, and D. Benielli, *Microscopy* **203**, 1 (2001).
15. N. Noel, H. Jamgotchian, and B. Billia, *J. Cryst. Growth* **181**, 117 (1997).
16. W. Mullins and R. Sekerka, in *Proceedings of the International Conference on Crystal Growth, Boston, USA, 1966*, Ed. by H. S. Peiser (Pergamon, Oxford, 1967; Mir, Moscow, 1968).
17. E. L. Zhivolub and O. P. Fedorov, *Kristallografiya* **43** (5), 931 (1998) [*Crystallogr. Rep.* **43** (5), 877 (1998)].
18. W. A. Tiller, K. A. Jackson, J. W. Rutter, *et al.*, *Acta Metall.* **1**, 428 (1953).

Translated by O. Borovik-Romanova

CRYSTAL
GROWTH

Mathematical Model and Numerical Simulation of Faceted Crystal Growth

M. P. Marchenko* and I. V. Fryazinov

*Institute of Mathematical Modeling, Russian Academy of Sciences,
Miusskaya pl. 4a, Moscow, 125047 Russia*

*e-mail: marchenko@imamod.ru

Received March 3, 2004

Abstract—A new mathematical macroscopic model is proposed to describe the nonstationary process of faceted crystal growth by the methods of directional crystallization with a slow change in external thermal conditions and low pulling rate of a cell through the growth system. The facet-growth rate is determined by the Stefan condition, integral over the face. Two boundary conditions are set for temperature: the continuity condition and the relation between the heat-flux jump and the supercooling at the facet points. The supercooling is determined by solving the entire heat problem. A facet is selected as a planar part of the phase boundary. The kinetic coefficient at the facet may depend on the supercooling. The energy conservation law is valid within the model developed. Examples of calculations of some model problems are presented. © 2005 Pleiades Publishing, Inc.

INTRODUCTION

In this study, we consider the crystal-growth processes both in the case of normal growth and under the formation of a planar crystal surface: a face. The mathematical model of faceted growth, proposed here, is based on determining the face-growth rate using the integral Stefan condition (or an equivalent one) and setting two conditions at the phase boundary: the temperature continuity condition and the relation between the heat-flux jump and the supercooling at the surface point under consideration. The supercooling at phase boundary points is determined by solving the entire heat problem. The same model is also obtained on the basis of the mechanism of layer-by-layer faceted crystal growth. The model of faceted growth reported here was previously described briefly in [1].

The calculations were performed for the simplest case of the crystal growth of Ge in the crystallographic direction [001] in a cylindrical ampoule under the conditions of cylindrical symmetry. It was assumed that a facet is a circle centered on the ampoule axis and orthogonal to the crystal axis. A facet can be formed on the part of the phase surface convex to the melt and sufficiently planar. Such a geometry is determined by the external boundary conditions.

The process of faceted growth is considered below for the conditions of axial heat processing (AHP) [2, 3]. This method was described in more detail in [4]. The algorithm of calculation of the processes of faceted growth (see below) was introduced into the KARMA1 software package [5].

In the absence of a facet on the crystal surface, we will consider three conditions: the Stefan condition, the temperature continuity condition, and the condition

determining the normal crystal-growth rate v_n as a function of supercooling $\Delta T = T_* - T$. Here, T_* is the crystallization temperature and T is the temperature at the points of phase boundary. The function $v_n(\Delta T)$ can be linear: $v_n = \beta(T_* - T)$, where β is the proportionality factor referred to as the kinetic coefficient. Beyond the face, this coefficient ($\beta = \beta_0$) is much larger than at the face. The value of the step of an arbitrary function Q (for example, temperature or temperature gradient) at the phase boundary will be denoted as $[Q]_S^L = Q(L) - Q(S)$, where $Q(L)$ and $Q(S)$ are the limiting values of the function Q at the phase boundary from the sides of the liquid (L) and solid (S) phases.

Thus, in the absence of a face, we have at the phase boundary

$$\begin{aligned} [-\kappa \partial T / \partial n]_S^L &= \gamma \rho_S v_n, \quad v_n = \beta_0 (T_* - T), \\ [T]_S^L &= 0. \end{aligned} \quad (1)$$

Hereinafter, κ , c_p , and ρ are the thermal-conductivity coefficient, specific heat, and density, respectively; ρ_S is the density in the solid phase; and γ is the latent heat of the phase transition. References on the normal and faceted crystal growth can be found in [6–9].

During the crystal growth, faces are formed at that part of the phase boundary whose normal is close to the normal of a crystallographic close-packing plane. The coefficient β depends on the angle between these normals. When this angle at a crystal facet is small, β depends on supercooling and, for semiconductors, turns out to be 2 to 3 orders of magnitude smaller than at the other part of the phase boundary—the region of normal crystal growth. If the crystallization rate along

the facet is determined by the advance of steps, whose density on the facet is independent of supercooling, $v_n = \bar{\beta} (T_* - T)^m$. In this case, we assume that $\beta = \beta_*$. Actually, it is generally the process of generation of steps that limits the face-growth rate; hence, the coefficient β depends on temperature: $\beta = \beta_*(T)$. In this case, we will write $v_N = \bar{\beta}(T_* - T)^n$ or $v_n = \beta(T_* - T)$, where $\beta = \bar{\beta} (T_* - T)^{m-1}$. If steps are generated by screw dislocations, m is assumed equal to 2. These dependences were reported in [8–18].

Numerical simulation of the growth of Ge crystals by the AHP method was performed using the power law with $m = 1.65$ and $\bar{\beta} = 0.0274 \text{ cm}/(\text{s K}^{1.65})$ [14] and the linear law with $n = 1$ and $\bar{\beta} = 0.001389 \text{ cm}/(\text{s K})$ (private communication with Golyshev).

The macroscopic model of faceted growth considered below is based on two conditions. One of these is obtained by excluding the rate v_n from the first two conditions in (1). The second condition is the temperature continuity at the phase boundary. These two conditions are used at the phase boundary in the problem for temperature for the case of normal growth. We will use the same conditions in the region of faceted growth.

A facet is determined as a planar part of the phase-boundary surface. Faceted crystal growth occurs with a time-dependent rate v_n , constant over the face. During the crystallization, the facet moves parallel to itself with a possible variation in size, depending on changes in the external conditions.

The crystal growth rate at a facet is determined from the heat-balance equation for the entire face, i.e., from the integral Stefan (or equivalent) condition. The problem is to find the shape of the crystal-growth surface and the evolution of the growth-surface shape with time, with allowance for the growth rate depending on supercooling and for different velocities of motion of the crucible with melt and the crystal through the region with a temperature gradient (which can also change with time). This problem will be solved in both the presence and the absence of convection.

There are other approaches to the solution of this problem [11, 12]. In these approaches, the facet diameter b is determined by the formula $b = \sqrt{8\Delta T_{kin} R/G}$, where R is the radius of curvature of a convex isotherm; G is the averaged local temperature gradient; and ΔT_{kin} is the maximum supercooling at the face, which is the input parameter, as well as the kinetic coefficient [6, 8, 9]. The approach [11, 12] is applied to quasi-stationary problems, in which the crystallization rate is assumed equal to the pulling rate or the cooling rate of the system. The value of ΔT_{kin} is determined by these parameters. To determine the crystallization isotherm, the

quasi-stationary classical Stefan problem should be solved beforehand.

NORMAL CRYSTAL GROWTH

Since the crystal growth rates are determined by the supercooling at the phase boundary, we will find the temperature distribution first of all. Let us exclude v_n from the first two conditions in (1) and add the third condition in (1) to the condition obtained. At the phase boundary, we impose the following two conditions on temperature:

$$[-\kappa \partial T / \partial n]_S^L = \gamma \rho_s \beta (T_* - T), \quad [T]_S^L = 0. \quad (2)$$

At other boundaries of the melt and the crystal with the ampoule, we impose the natural conditions of the temperature and heat flux continuity. At the external boundary of the ampoule, the boundary conditions are determined by the crystal growth technique. These are often the conditions of radiative heat exchange. In the AHP method, the temperature at the external surface of the ampoule is set equal to the value determined by linear interpolation between the points of location of thermocouples measuring temperature during the experiment. For solid phases, the heat-conduction equation is considered. For the liquid phase, convective heat-conduction and diffusion equations, as well as the Navier–Stokes equations in the Boussinesq approximation with the natural conditions at boundaries, are solved [4, 5].

It is sufficient to set conditions (2) to determine the temperature in the entire region at a specified position of the phase boundary. The quantity $\gamma \rho_s \beta (T_* - T)$ sets the amount of heat released per surface unit. The first condition in (2) can be taken into account as a heat source in the equation for temperature

$$c_p \rho (\partial T / \partial t + (\mathbf{v}, \nabla) T) = \text{div}(\kappa \text{grad } T) + \gamma \rho_s \beta (T_* - T) \delta(z - z_f) / \cos \theta. \quad (3)$$

Here, $z = z_f(r, t)$ is the desired function, determining the position of the phase boundary; δ is the Dirac delta function; θ is the angle between normal to the phase boundary and the z axis; and $\cos \theta > 0$. The parameter \mathbf{v} in (3) is the velocity of the melt motion. For the solid phase, the second term on the left-hand side of (3) should be omitted.

Let us clarify the method for solving the problem. We introduce a time grid $t_j = j \Delta t, j = 0, 1, \dots$, where Δt is a sufficiently small time step. Let $T^j = T(r, z, t_j)$, β^j , and \mathbf{v}^j be the temperature, kinetic coefficient, and velocity at the instant of time t_j . Replacing only derivatives with respect to time by difference relations, we obtain the expression

$$c_p \rho ((T^{j+1} - T^j) / \Delta t + (\mathbf{v}^j, \nabla) T^{j+1}) = \text{div}(\kappa \text{grad } T^{j+1}).$$

For the solid phase, the second term on the left-hand side of this equality, as well as in equality (3), is absent. Let us add the boundary conditions to this equation. At the phase boundary z_f^j ,

$$[-\kappa\partial T^{j+1}/\partial n]_S^L = \gamma\rho_s\beta^j(T_* - T^{j+1}), \quad [T^{j+1}]_S^L = 0.$$

At the other part of the phase boundary, we set the necessary boundary or matching conditions. At a known value of T^j , the value of T^{j+1} is found. Furthermore, in the absence of faceted growth, we determine the velocity

$$v_n^{j+1} = \beta^j(T_* - T^{j+1}) \quad (4)$$

and the new position of the phase-transition boundary

$$z_f^{j+1} = z_f^j + \Delta t\beta^j(T_* - T^{j+1})/\cos\theta^j. \quad (5)$$

Thus, finding the temperature distribution, the velocity of the motion of the phase boundary, and its new position, we pass to a new time layer.

This problem was solved by the method of finite differences.

FACETED CRYSTAL GROWTH

It is unknown beforehand whether a facet is formed at the time $t_{j+1} = t_j + \Delta t$; if it did not exist at the moment t_j ; or, vice versa, whether the facet existing at the instant t_j remains at the instant t_{j+1} . We will assume that supercooling occurs at the phase boundary; hence, in any case, the function $z_f^{j+1}(r)$ can be determined from (5) at the instant t_{j+1} . If we find that faceted crystal growth occurs, the obtained values of z_f^{j+1} should be changed in the facet region.

Let us calculate the derivative $\partial z_f^{j+1}/\partial r$ at $t = t_{j+1}$. The requirement for the existence of a planar part of the phase surface is reduced to the validity of the condition $|dz_f^{j+1}/dr| < \varepsilon$ at $0 < r < r_0$, where ε is a sufficiently small number. If, in addition, $dz_f^{j+1}/dr < 0$, the region $0 < r < r_0$ can be considered to be a face. At small values of ε , the surface cannot be strongly concave.

For stable calculation of the faceted-growth problem, the value of ε should be chosen neither too small nor too large. A series of calculations of this problem we performed at different values of ε showed that the calculation is stable at ε about 0.015–0.02 ($\theta \sim 1^\circ$) [1]. An example of the influence of the value of ε on the facet size will be given below.

Let us now find the crystal-growth rate at the facet at $0 < r < r_0$ and change condition (5) at the face. At the phase boundary points, the heat balance is written as $[-\kappa\partial T/\partial n]_S^L = v_n\rho_s[h]_S^L$, where h is the enthalpy. Let us

perform facet averaging of the latter equality. We assume that the velocity v_n is constant at the facet and the average enthalpy at the facet is equal to the latent amount of the phase transition. In this case, the total amount of heat is independent of the character of the crystal growth and the presence or absence of a face.

As a result, we obtain the integral Stefan condition

$$\int_0^{r_0} [-\kappa\partial T/\partial n]_S^L r dr = \gamma\rho_s v_n r_0^2/2. \quad (6)$$

Integrating the first condition in (2) over the facet region and comparing the result with (6), we find the condition for determining the rate v_n , which is equivalent to (6):

$$v_n = \frac{2}{r_0^2} \int_0^{r_0} \beta(T_* - T) r dr. \quad (7)$$

Let us write the approximate heat-balance equation for the entire face:

$$z_f^{j+1} = \bar{z}_f^j + \Delta t \frac{2}{(r_0^{j+1})^2} \int_0^{r_0^{j+1}} \beta^j \frac{T_* - T^{j+1}}{\cos\theta^j} r dr, \quad (8)$$

$$0 < r < r_0^{j+1}.$$

Here, \bar{z}_f^j is the facet-average (in the interval $0 < r < r_0^{j+1}$) value of z_f^j :

$$\bar{z}_f^j = \frac{2}{(r_0^{j+1})^2} \int_0^{r_0^{j+1}} z_f^j r dr.$$

The value of z_f^{j+1} in (8) is independent of r . If the facet existed at the instant t_j , the values of z_f^{j+1} determined by formulas (5) and (8) are close to each other both over the entire facet and at the point r_0^{j+1} .

Thus, the phase surface at $t = t_{j+1}$ has been found. It is determined by the function z_f^{j+1} according to formulas (5) and (8). A region, referred to as a prefacet, can be introduced into consideration. Analyzing the curve $z_f^{j+1}(r)$, we can find on it the point r_1^{j+1} at which the above-introduced angle $\theta = \theta_0$. Let us choose θ_0 to be equal to 2° and assume the region $r_0^{j+1} < r < r_1^{j+1}$ to be a preface. Then, we determine the kinetic coefficient at the instant t_{j+1} , assuming that $\beta^{j+1} = \beta_*^{j+1}$ at $0 \leq r \leq r_0^{j+1}$, $\beta^{j+1} = \beta_0$ at $r_1^{j+1} < r < R$ (R is the radius of the

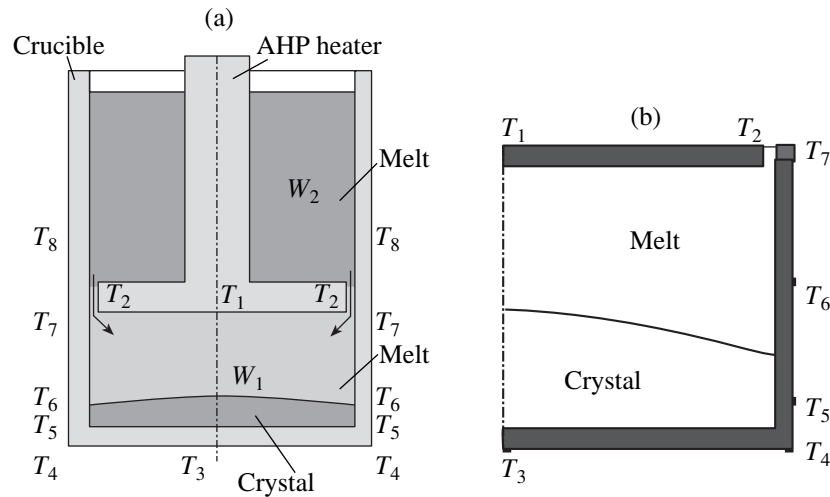


Fig. 1. (a) Schematic of the AHP method; W_1 and W_2 are the regions in the melt below and above the AHP heater, respectively; (b) the calculation region.

crystal), and $\beta^{j+1} = \beta_*^{j+1} + (\beta_0 - \beta_*^{j+1}) \tan \theta^{j+1} / \tan \theta_0$ at $r_0^{j+1} \leq r \leq r_1^{j+1}$.

Thus, we changed from $T^j, z_f^j(r), r_0^j, r_1^j, \beta^j(r)$ at $t = t_j$ to $T^{j+1}, z_f^{j+1}(r), r_0^{j+1}, r_1^{j+1}, \beta^{j+1}(r)$ at $t_{j+1} = t_j + \Delta t$. At $n = 1$ (nucleation growth), the kinetic coefficient $\beta_*^{j+1} = \beta_*$ is constant.

To determine the crystallization rate, we used formulas (4) and (7). The kinetic coefficient in the prefacet region $r_0^{j+1} < r < r_1^{j+1}$ was determined by interpolation between the values of β_* and β_0 . In the prefacet region, the kinetic coefficient can be found by interpolating the crystallization rate between its values at the facet and beyond the preface. For example, the following interpolation formula can be used:

$$v_n^{j+1} = ((\tan \theta^{j+1} - \tan \theta^{j+1}(r_0^{j+1}))v_n^{j+1}(r_1^{j+1}) + v_n^{j+1}(r_0^{j+1})(\tan \theta_0 - \tan \theta^{j+1})) / (\tan \theta_0 - \tan \theta^{j+1}(r_0^{j+1})).$$

The values of $v_n^{j+1}(r_0^{j+1})$ and $v_n^{j+1}(r_1^{j+1})$ are determined by formulas (7) and (4), respectively. The kinetic coefficient at the prefacet is $\beta^{j+1} = v_n^{j+1} / (T_* - T^{j+1})$. In this case, the continuity of the crystallization rate along the phase boundary is guaranteed. However, both these approaches gave almost identical results. All above considerations were implemented in the KARMA1 software package.

The model considered here can be modified in different ways. The above-described approach is generalized to the general case of faceted crystal growth. In

formulas (7) and (8), $r_0^2/2$ should be replaced by $|S_f|$ (the facet surface area), rdr should be replaced by dS_f (element of the facet surface), and the integration should be carried out over the total facet surface. Dissipative thermal terms should be written in the general form, with a tensor instead of the thermal-conductivity coefficient. The facet is to be determined as a part of the phase surface with close directions of normals at all points.

RESULTS OF NUMERICAL SIMULATION

Boundary Conditions in the AHP Method

Numerical simulation of faceted growth will be performed for the problem of AHP crystal growth. The schematic diagram of the AHP method and the calculation region are shown in Figs. 1a and 1b, respectively. An AHP heater is submerged into a cylindrical crucible. The melt is below and above the heater (bottom and top zones, respectively). A seed is located on the internal crucible bottom. As crucible moves downward to the cold zone, crystal growth occurs on the seed. The melt is fed into the bottom zone from the top zone through the gap between the AHP heater and the lateral crucible wall.

Thermocouples are located on the external crucible wall at the points T_1 – T_7 (Fig. 1). We will use the same designations for the values of temperature at these points. The thermocouples T_1 and T_2 were located in the AHP heater at $r = 0$ and 15.8 mm. The thickness of the heater wall is 2.5 mm. The thermocouples T_3 and T_4 were located on the external crucible bottom at $r = 0$ and $r = R = 19.05$ mm. The thermocouples T_5 – T_7 were located on the external surface of the lateral crucible wall. The thermocouple T_7 was at the same level as the thermocouples T_1 and T_2 , the thermocouple T_6 was

12.5 mm below the thermocouple T_7 , and the thermocouple T_5 was 10 mm below the thermocouple T_6 . The relative position of the thermocouples T_1 , T_2 , and T_5 – T_7 was not changed with time. This situation is typical of the AHP method, as well as the setting of corresponding temperatures. We assumed that $T_6 = T_*$, $T_1 = T_2 = T_7 = T_6 + Hg_L$. The temperature gradient $g_L = 10$ K/cm and $H = 10$ mm. The temperature gradient along the lateral crucible wall below the thermocouple T_6 was $g_S = 2.294g_L = 22.94$ K/cm. At such a choice of g_S and g_L , the heat fluxes at the internal crucible wall in the melt and in the crystal are equal to each other. The temperature $T_3 = T_4$ was calculated using the value of the gradient g_S . The crucible wall thickness was 6.6 mm and the initial height of the liquid zone was $H = 10$ mm. The temperature at the external crucible wall between the points of location of the thermocouples was determined by linear interpolation in g_S and g_L .

The pulling rates (velocities of the crucible motion) were $V = 1$ and 5 mm/h. The Sb impurity concentration in the liquid zone W_1 at the initial instant and in the melt arriving from the top zone W_2 (Fig. 1a) was 1.5×10^{19} atoms/cm³. In the seed, the Sb concentration was 4.5×10^{16} atoms/cm³. At the chosen boundary conditions and a constant pulling rate, the solution to this problem was steady-state: the crystallization rate at all points of the phase boundary was equal to the pulling rate, including the vicinity of the point r_0 ; the size of the liquid zone, the melt flow, and the temperature field in the melt did not change. The chosen values of the gradients g_S and g_L were previously used in actual experiments.

Calculation Grid

The faceted growth problems were calculated by the method [5] using fine grids. Two grids were chosen: with 30 and 46 radial points. In the facet region, the grids always turned out to be uniform. In both cases, 54 points along the z axis were chosen; 30 of them fell in the liquid zone. The grids thickened when approaching the boundaries. Near the axis, the grid size was either 0.01 or 0.005. In the gap and at the crucible walls, there were three intervals with different grid sizes. The results of the calculation using the grids with 30 and 46 points in radius turned out to be close to each other.

Choice of the Value of ε

The value of ε was chosen for the pure heat problem using the nonlinear law $\beta = \bar{\beta}(T_* - T)^{0.65}$ at $\bar{\beta} = 0.0274$ cm/(s K^{1.65}) and the pulling rate $V = 1$ mm/h. The radius of the facet formed was about 3.5 mm at the beginning of the process and then became equal to approximately 2.7 mm. The change in the facet size is related to the dynamics of reaching the steady-state

solution. In the initial stage of the process, the crystallization rate in the central part is lower than at the periphery, the phase boundary is slightly concave to the crystal, and the facet is absent. Then the phase boundary becomes convex to the melt. A facet arises in the calculation. At a larger value of ε , the facet size is somewhat larger.

At $\varepsilon = 0.005$, the facet formation is unstable. The facet appears and disappears randomly. Temporal instability occurs also at $\varepsilon = 0.01$ but only at the beginning of the crystallization process. With an increase in ε to 0.02, the facet becomes stable in the calculation (Fig. 2a). The facet radius $r_0 = 3.5$ mm. Figure 2 shows the change in the facet size r_0 (Fig. 2a), the face-averaged supercooling (Fig. 2b, curve 1), and the supercooling at the axis ($r = 0$) (Fig. 2b, curve 2).

An increase in ε leads to an increase in the number of points on the face. In the problem under consideration, the phase boundary is sufficiently planar and a further increase in ε to 0.05 leads to the facet expansion and occurrence of a new instability: the points in the range $4.2 < r < 6$ mm are included in the facet region and excluded from it alternately. At $\varepsilon = 0.06$, the facet includes almost the entire region of the phase boundary, except for the region near the lateral surface, where the phase boundary sharply rises in view of the specified boundary conditions. Such large values of ε should be excluded from consideration. For $\varepsilon = 0.01$ and 0.02, supercooling at the axis is the same as the face-averaged supercooling; the values of r_0 differ only slightly.

Linear and Power Laws

Let us now consider the results of calculation of the same problem using a linear law with $\beta_* = 0.001389$ cm/(s K) (private communication with Golyshv), also for the pure heat problem at $\varepsilon = 0.01$. The value of r_0 is the same for both linear and power laws. Figure 3a shows the time dependences of the supercooling at the axis (curve 2) and the face-averaged supercooling (curve 1) for the linear law. The difference between the linear and power laws (Figs. 3a and 2b, respectively) can be clearly seen. Figure 3b shows the radial distributions of the difference $\bar{T} - T_*$. The top and bottom curves correspond to the power and linear laws, respectively.

Dependence of the Faceted Growth on the Pulling Rate

We solved the problem for the pulling rate $V = 5$ mm/h and $\varepsilon = 0.02$ numerically using the power law in the absence of convection. First, the facet radius was 6.4 mm; then it decreased to 4 mm (Fig. 4a). The supercooling at the facet (Fig. 4b) was almost two times

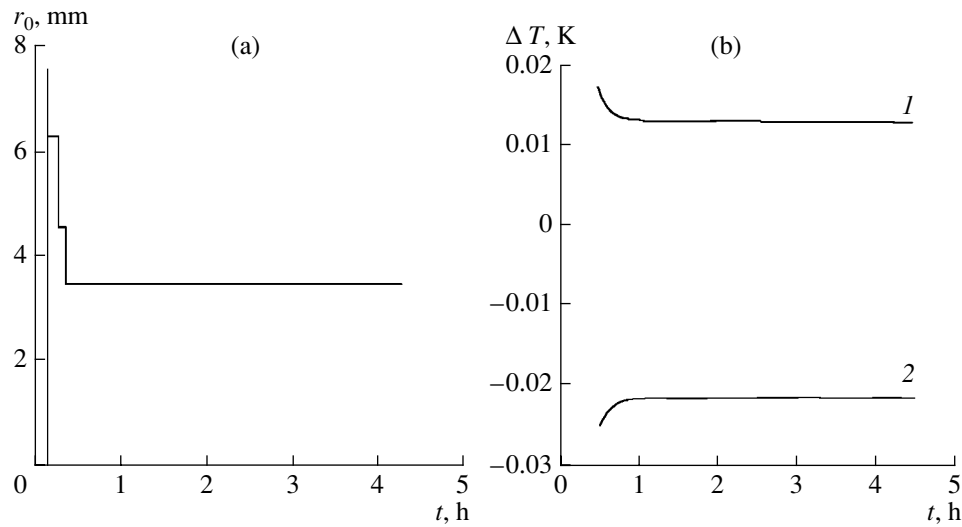


Fig. 2. Time dependences of (a) the facet size and (b) the quantity $\frac{2}{r_0} \int_0^{r_0^2} (T_* - T) r dr$ (1) and the supercooling $T - T_*$ at the facet center (2); $\varepsilon = 0.02$.

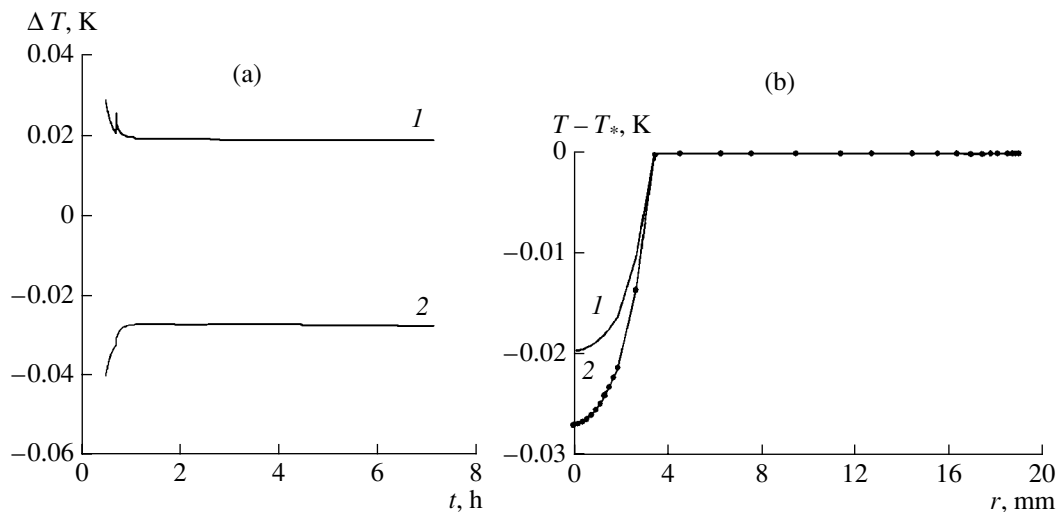


Fig. 3. (a) Time dependences of (1) the quantity $\frac{2}{r_0} \int_0^{r_0^2} (T_* - T) r dr$ and (2) the supercooling $T - T_*$ at the facet center. (b) The change in the supercooling over the crystallization front for (1) nonlinear and (2) linear laws; $\varepsilon = 0.02$.

higher in comparison with the case for $V = 1$ mm/h (Fig. 2b).

Effect of Convection on the Faceted Growth

Let us now consider the results of the calculations of the faceted growth with allowance for the convection in the melt at $\varepsilon = 0.02$, the power dependence of v_n on $T_* - T$, and the pulling rate $V = 1$ mm/h.

The allowance for the convection did not change the facet size in the problem under consideration. The supercooling at $r = 0$ and the face-averaged supercooling also remained the same. However, convection may radically change the situation: at the pulling rate $V = 5$ mm/h, the facet disappears.

Figure 5a shows the facet positions (curves 1, 2) and the crystallization isotherms (curves 3, 4) calculated with and without allowance for the thermal convection.

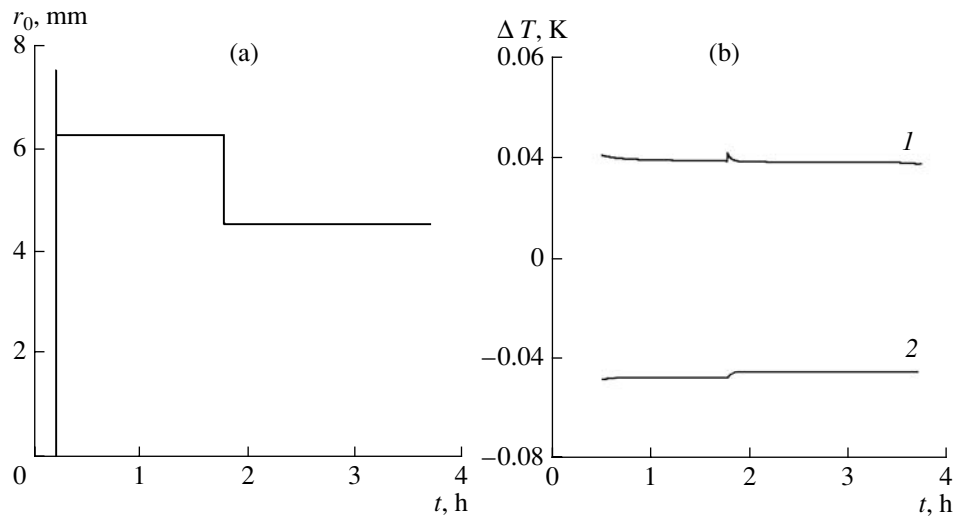


Fig. 4. Time dependences of (a) the facet size and (b) the quantity $\frac{2}{r_0} \int_0^{r_0} (T_* - T) r dr$ (1) and the supercooling $T - T_*$ at the facet center (2); $\varepsilon = 0.02$.

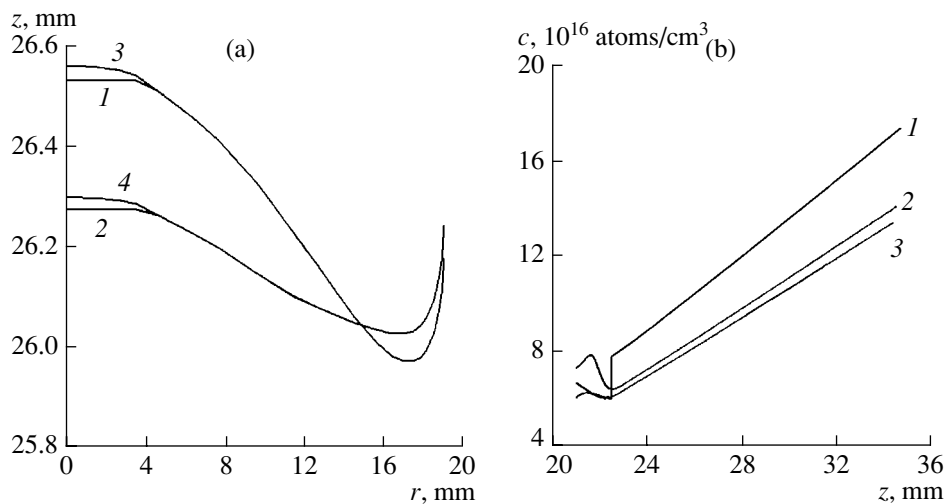


Fig. 5. (a) Crystallization fronts with a facet (1, 2) and the crystallization isotherms (3, 4) for the calculation without (1, 3) and with (2, 4) allowance for the convective motion of the melt. (b) The change in the Sb concentration over the crystal length for three radial cross sections: $r =$ (1) 0, (2) 17.33, and (3) 18.55 mm.

The isotherm beyond the facet region almost coincides with the phase-transition boundary. Allowance for the convection made both the phase boundary and the isotherm flatter.

Figure 5b shows the dependences of the impurity concentration on z in a grown crystal at different r . The concentration is maximum at the axis. The reason for this phenomenon is that the segregation coefficient in the facet region was taken as 30% larger than that in the case of simple supercooling.

The results of the calculation of the classical Stefan problem and the faceted-growth problem (the power

law) under the same boundary conditions are presented in Fig. 6. Figure 6a shows the crystallization isotherm (curve 1) and the phase boundary with a facet (curve 3), obtained with allowance for the faceted growth, and the phase boundary, which is the crystallization isotherm for the classical Stefan problem (curve 2). It can be seen that the crystallization isotherm in the faceted problem is close to the crystallization isotherm (phase-transition boundary) for the classical Stefan problem. The solution to the classical Stefan problem beyond the facet region can be replaced by the solution to the supercooling problem at a small value of V/β_0 . The motion of the

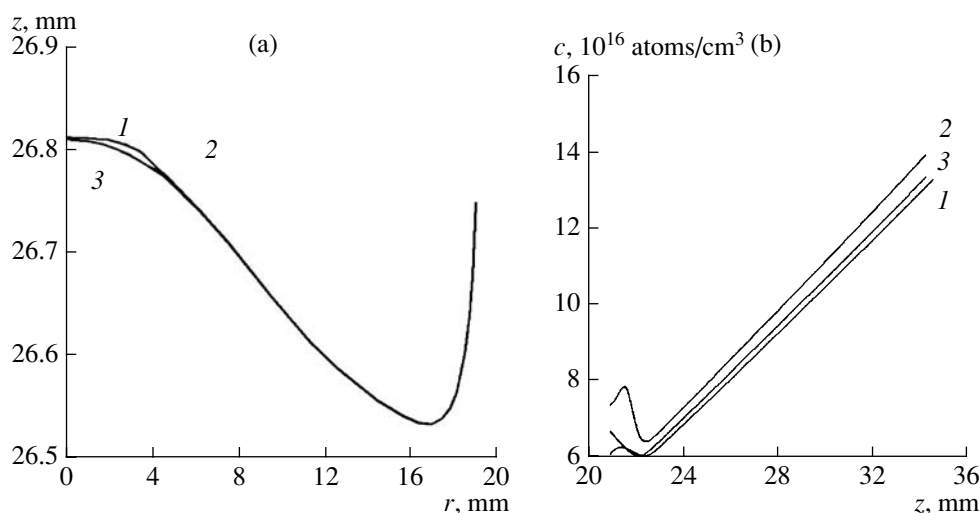


Fig. 6. (a) Crystallization isotherm (1) and the phase boundary with a facet (3), obtained taking into account the faceted growth, and the crystallization isotherm for the classical Stefan problem (2). (b) The change in the Sb concentration over the crystal length for three radial cross sections: $r = (1) 0$, $(2) 17.33$, and $(3) 18.55$ mm.

melt is the same in both cases. The melt flows from the axis to the lateral surface of the crucible along the phase surface and in the opposite direction along the AHP heater. There is a small oppositely directed vortex at the lateral wall of the ampoule and the phase boundary. The concentrations shown in Fig. 6b for the solution to the classical Stefan problem change monotonically with a change in r . Comparison of Figs. 5b and 6b shows a strong effect of a facet on the concentration distribution in the crystal.

In summary, we should make some remarks. A change in the size of a facet (at small ε) during its formation does not affect the melt flow. Only in the case of very weak flows in the stagnation zones do the formation of a facet and temperature drops at the facet lead to enhanced convection. The presence of a facet affects only the change in the radial distribution of the impurity concentration significantly as a result of the change in the impurity segregation coefficient of the crystal. In this study, the melt supercooling turned out to be low because the process of germanium crystallization was considered. For other materials, for example, semi-transparent oxides (such as bismuth orthogermanate), supercooling is higher (above 1°).

Determination of the character of the crystal growth is a complex crystallographic problem. The determination of the facet size by the algorithm proposed here with the use of the parameter ε makes it possible to select a planar part of the phase boundary even for crystallization isotherms weakly convex to the melt. When the radius of curvature is very large, it is quite difficult to use the criterion of [6].

ACKNOWLEDGMENTS

We are grateful to A.A. Chernov for his participation in the discussion of the results and valuable remarks and to R. Abbaschian (University of Florida, Gainesville, FL, USA) and V.D. Golyshev (Center for Thermophysical Research "Termo," Aleksandrov) for the data on the kinetic coefficients.

This study was supported by the Russian Foundation for Basic Research, project no. 02-01-00105.

REFERENCES

1. I. V. Friazinov and M. P. Marchenko, in *Proceedings of the Fifth International Conference on Single Crystal Growth and Heat and Mass Transfer, Obninsk, 2003*, p. 19.
2. A. G. Ostrogorsky, US Patent No. 397741 (1989).
3. V. D. Golyshev and M. A. Gonik, RF Patent No. 1800854 (1990).
4. V. D. Golyshev, I. V. Friazinov, and M. P. Marchenko, in *Proceedings of the Fourth International Conference on Single Crystal Growth and Heat and Mass Transfer, Obninsk, 2001*, p. 715.
5. M. P. Marchenko and I. V. Fryazinov, *Zh. Vychisl. Mat. Mat. Fiz.* **37** (8), 988 (1997).
6. V. V. Voronkov, *Kristallografiya* **17** (5), 909 (1972) [*Sov. Phys. Crystallogr.* **17**, 807 (1972)].
7. É. Kh. Lokharu and V. S. Yuferev, *Izv. Akad. Nauk SSSR* **47** (2), 267 (1983).
8. A. A. Chernov, E. I. Givargizov, Kh. S. Bagdasarov, *et al.*, in *Modern Crystallography* (Akad. Nauk SSSR, Moscow, 1980), Vol. 3, p. 18 [in Russian].
9. A. A. Chernov, *Kristallografiya* **16** (4), 842 (1971) [*Sov. Phys. Crystallogr.* **16**, 734 (1971)].

10. A. A. Chernov and A. A. Belyaev, *Kristallografiya* **7** (5), 658 (1962).
11. Y. Liu, A. Virozub, and S. Brandon, *J. Cryst. Growth* **205**, 333 (1999).
12. C. Lan and C. Tu, *J. Cryst. Growth* **233**, 523 (2001).
13. S. D. Peteves and R. Abbaschian, *Theor. Metallurg. Trans. A* **22**, 1271 (1991).
14. R. Abbaschian, A. B. Gokhale, and D. B. Allen, in *Solidification Science and Processing*, Ed. by I. Ohnako and D. M. Stefanescu (TMS Publication, Warrendale, 1996), p. 73.
15. R. Abbaschian, E. Balikci, A. Deal, *et al.*, in *Proceedings of the Fifth International Conference on Single Crystal Growth and Heat and Mass Transfer, Obninsk, 2003*, p. 545.
16. V. V. Voronkov, *Izv. Akad. Nauk SSSR* **47** (2), 210 (1983).
17. É. Kh. Lokharu and V. S. Yuferev, *Zh. Tekh. Fiz.* **54** (9), 1685 (1984) [*Sov. Phys. Tech. Phys.* **29**, 985 (1984)].
18. É. N. Kolesnikov and V. S. Yuferev, *Zh. Tekh. Fiz.* **51** (12), 2576 (1981) [*Sov. Phys. Tech. Phys.* **26**, 1524 (1981)].

Translated by Yu. Sin'kov

Modeling of the Self-Organizing Processes in Crystal-Forming Systems: Structural Mechanism of Assembly of the $\text{K}_2\text{Ba}[\text{Ge}^{[6]}\text{Ge}_3^{[4]}\text{O}_9]_2$, $\text{K}_2\text{Ge}^{[6]}\text{Ge}_3^{[4]}\text{O}_9$, and $\text{BaGe}^{[6]}\text{Ge}_3^{[4]}\text{O}_9$ Germanates from Subpolyhedral Clusters

G. D. Ilyushin

Shubnikov Institute of Crystallography, Russian Academy of Sciences,
Leninskii pr. 59, Moscow, 119333 Russia

e-mail: ilyushin@ns.crys.ras.ru

Received January 15, 2003; in final form, March 17, 2004

Abstract—The self-assembly of the crystal structures of the $\text{K}_2\text{Ba}[\text{Ge}^{[6]}\text{Ge}_3^{[4]}\text{O}_9]_2$, $\text{K}_2\text{Ge}^{[6]}\text{Ge}_3^{[4]}\text{O}_9$, and $\text{BaGe}^{[6]}\text{Ge}_3^{[4]}\text{O}_9$ germanates formed in the K–Ba–Ge–O system is modeled on a subpolyhedral level. In three topologically different three-dimensional *MT* frameworks (the *M* octahedra GeO_6 and the *T* tetrahedra GeO_4), the equivalent two-dimensional net $6464 + 664$ (*M* : *2T*) is separated, and its two-color decomposition into primary *MT* contours (characterizing the structure of the cluster precursor) and secondary contours (reflecting the bonds between the clusters) is performed. The structural invariant of the *MT* frameworks is determined in the form of an M_2T_4 cyclic hexapolyhedral cluster. It is demonstrated that these stable cyclic precursors of compositions $\text{K}_2M_2T_4$ and BaM_2T_4 control all processes of the subsequent evolution of the *MT* crystal-forming complex and provide the formation of substructural units of a higher level with the participation of additional tetrahedra GeO_4 . © 2005 Pleiades Publishing, Inc.

1. INTRODUCTION

Crystallization is a complex physicochemical phenomenon that occurs as a result of the spontaneous development of self-organizing processes in a chemical system [1–7]. In this case, there arises a long-range order in the arrangement of structural units of arbitrary nature (molecules, clusters) that initially exist in the form of a chaotic mixture [4–8].

Modeling of self-organizing processes in nonequilibrium systems and, eventually, the elucidation of the mechanisms of these processes on the microscopic cluster level within the model of complementary highly selective assembly of crystal structures from micromatrices (precursors) is an important problem in the physics of condensed matter [4–8].

The *identification* of the type of substructural unit (SSU) precursors and the elucidation of the *mechanism of their structural evolution* are the most important problems in geometric–topological modeling of self-organizing processes [5–11] in complex multicomponent silicate and germanate systems.

The determination of the atomic structure of a crystal by diffraction methods makes it possible, in principle, to *read* the symmetric–topological code of the processes of the structure assembly and to draw an inference regarding the nature and properties of the crystal-forming cluster precursors.

The currently available methods for analyzing complex structures (local crystal-structure intersection of symmetry groups [5–8], two-color decomposition of structural graphs into primary and secondary contours [6–8], determination of equivalent coordination sequences [8–11]) provide a means for identifying the geometric–topological code of substructural unit precursors. The algorithm (used in this study) for self-assembling a three-dimensional structure through the universal mechanism of maximum bonding of substructural unit precursors when changing over to a higher level of the structural self-organization of the system was considered in detail in [5–8].

There exists a large crystal-chemical family of alkali $[A(1+)]$ and alkaline-earth $[B(2+)]$ germanates [12] with structures typical of germanates alone. Examples of such structures are provided by six $\text{Li}_2\text{Ge}^{[6]}$ germanates. The topological analysis and modeling of the self-assembly of the crystal structures of the germanates from SSU precursors containing the *M* octahedra GeO_6 and the *T* tetrahedra GeO_4 were carried out in [13, 14]. Other examples are provided by the $\text{K}_2\text{Ba}[\text{Ge}^{[6]}\text{Ge}_3^{[4]}\text{O}_9]_2$ compound that crystallizes in the K–Ba–Ge–O quaternary system [15], as well as by the $\text{K}_2\text{Ge}^{[6]}\text{Ge}_3^{[4]}\text{O}_9$ [16] and $\text{BaGe}^{[6]}\text{Ge}_3^{[4]}\text{O}_9$ [17] compounds formed in the corresponding ternary sub-

systems. All three structural types are represented in a large number of systems, such as A - B - Ge - O [15], A - Ge - O [16], and B - Ge - O [17, 18]. Their topologically different frameworks have the same composition ($MT_3\text{O}_9$), as is the case with a number of structures of the A,Zr and B,Zr silicates and their analogs, which were thoroughly considered in [10].

In this work, the topological analysis and modeling of self-assembly on a subpolyhedral level was carried out for the $\text{K}_2\text{Ba}[\text{Ge}^{[6]}\text{Ge}_3^{[4]}\text{O}_9]_2$, $\text{K}_2\text{Ge}^{[6]}\text{Ge}_3^{[4]}\text{O}_9$, and $\text{BaGe}^{[6]}\text{Ge}_3^{[4]}\text{O}_9$ compounds, which are typical representatives of the aforementioned three structural types. It is assumed that SSU precursors of types identified in the K and Ba germanates with a simpler chemical composition remain unchanged in mixed K,Ba germanates. In this case, it becomes possible to determine the level of structural self-organization of the system at which there arise bifurcations of the evolution paths of the SSU precursors (i.e., points of structural branching) upon the formation of topologically different MT structures.

This study is a continuation of the investigations into the geometric and topological features of the crystal structures and modeling of the self-organizing processes on a subpolyhedral level in silicate and germanate systems [5–11, 13, 14].

2. BASIC NOTIONS AND DESIGNATIONS USED IN THIS INVESTIGATION

The *structural (primary) unit of an MT framework* is an M octahedron or a T tetrahedron.

The *substructural unit precursor* is one of the eight types of cluster precursors having topological symmetry [5] and can be identified as an invariant fragment of topologically different MT frameworks.

The *subpolyhedral structural unit* is a high-level cluster that contains complementary-bonded substructural unit precursors in the integrated form.

The *connectivity index* (in a forming microensemble) is the number of shared vertices of structural units on the complementary surfaces of a substructural unit of a lower level upon the formation of a substructural unit of a higher level.

The *stereon* is the fundamental (independent) region of space group G in a unit cell [19].

The *MTO net* is the topological representation of an MT framework in the form of nets (graphs) composed of vertices (nodes—atoms M , T , O) and edges (bonds) between them [7, 8, 10].

The *coordination sequence* is the set of numbers $\{N_k\}$, where N_k is the number of nodes of the MTO net in the k th coordination sphere of the atom chosen as the central atom [20–22].

3. TOPOLOGICAL ANALYSIS OF THE GERMANATE STRUCTURES

The stereons of the unit cells in the crystal structures under investigation involve a large number of atoms: 10 positions in the K and Ba germanates [16, 17] and 18 positions in the K,Ba germanate [15].

Since the crystallographic structure of the germanates is very complex, the geometric–topological analysis is performed using the method of coordination sequences [21–23]. This method enables one to reveal the highest possible topological symmetry and the functional equivalence of the M $\text{Ge}^{[6]}$, T $\text{Ge}^{[4]}$, or O atoms in the MT frameworks represented in the form of nets (graphs) [10].

As in [10, 11], the algorithm used for analyzing the germanate structures with the TOPOS.3.2 program package [23, 24] includes the following stages:

- (1) the creation of the database for the $A_2M\text{Ge}_3\text{O}_9$ and $BM\text{Ge}_3\text{O}_9$ compounds whose structures are completely determined (ICSD-2002 [18]) (Table 1),
- (2) the calculation of the adjacency matrix for nodes (atoms) (the AutoCN program), and
- (3) the calculation of the coordination sequences $\{N_k\}$ for all topological representations of the structures (the IsoTest program).

In order to determine the individual topological characteristics of the nodes in the MT frameworks in calculations of the sequences $\{N_k\}$, the K and (or) Ba atoms are removed from the structure and the calculation is performed only for the M , T , and O atoms of the framework. The topology of the bonds in the K and (or) Ba sublattices is calculated after all the M , T , and O atoms of the framework are removed [10, 23].

The coordination sequences for the M , T , and O framework-forming atoms in the $\text{K}_2\text{Ge}^{[6]}\text{Ge}_3^{[4]}\text{O}_9$, $\text{BaGe}^{[6]}\text{Ge}_3^{[4]}\text{O}_9$, and $\text{K}_2\text{Ba}[\text{Ge}^{[6]}\text{Ge}_3^{[4]}\text{O}_9]_2$ germanates are presented in Tables 2–4. It should be noted that the composition of the coordination spheres with the sequentially alternating atoms Ge and O is differentiated.

The hierarchical ordering of the MT frameworks of the germanates according to the coordination sequences for the T atoms is illustrated by the data presented in Table 5. The differences in the values of $\{N_k\}$ manifest themselves only beginning with the seventh coordination sphere. As follows from the results obtained (Table 5), the MT framework of the K,Ba germanate with $N = 73$ is a superposition of local substructures of the MT frameworks of the K and Ba germanates with $N = 72$ and 74 , respectively.

The symmetries of the M and T positions occupied by germanium atoms (whose atomic numbering corresponds to the structural data obtained in [15–17]) are given in Table 6.

Table 1. Crystallographic data for germanate structures

Germanate	Space group	Unit cell parameters <i>a</i> and <i>c</i> , Å	<i>V</i> , Å ³	CC code in ICSD- 2002 [18]
			<i>A–(M)–Ge–O</i>	
Na ₂ Ge ^[6] Ge ₃ ^[4] O ₉	<i>P</i> $\bar{3}$ <i>c</i> 1	11.323, 9.681	1075.1	51106
K ₂ Ge ^[6] Ge ₃ ^[4] O ₉	<i>P</i> $\bar{3}$ <i>c</i> 1	11.840, 9.800	1189.8	31969
K ₂ Ti ^[6] Ge ₃ ^[4] O ₉	<i>P</i> $\bar{3}$ <i>c</i> 1	11.916, 10.018	1231.9	19032
Rb ₂ Ge ^[6] Ge ₃ ^[4] O ₉	<i>P</i> $\bar{3}$ <i>c</i> 1	12.080, 9.860	1246.1	91
K ₂ Sn ^[6] Ge ₃ ^[4] O ₉	<i>P</i> $\bar{3}$ <i>c</i> 1	12.082, 10.181	1287.1	19034
Rb ₂ Ti ^[6] Ge ₃ ^[4] O ₉	<i>P</i> $\bar{3}$ <i>c</i> 1	12.195, 10.148	1307.0	19033
Rb ₂ Sn ^[6] Ge ₃ ^[4] O ₉	<i>P</i> $\bar{3}$ <i>c</i> 1	12.305, 10.205	1338.2	19035
Tl ₂ Sn ^[6] Ge ₃ ^[4] O ₉	<i>P</i> $\bar{3}$ <i>c</i> 1	12.351, 10.134	1338.8	19036
			<i>B–Ge–O</i>	
Sr Ge ^[6] Ge ₃ ^[4] O ₉	<i>P</i> 321	11.344, 4.750	529.4	82393
Pb Ge ^[6] Ge ₃ ^[4] O ₉	<i>P</i> 321	11.420, 4.753	536.8	64910
Ba Ge ^[6] Ge ₃ ^[4] O ₉	<i>P</i> 321	11.608, 4.768	556.4	83734
			<i>A–B–Ge–O</i>	
K ₂ Ba[Ge ^[6] Ge ₃ ^[4] O ₉] ₂	<i>P</i> $\bar{3}$ <i>c</i> 1	11.729, 19.278	2296.8	100439

Table 2. Coordination sequences for the framework-forming atoms in the structure of the K₂Ge^[6]Ge₃^[4]O₉ germanate

Framework-forming atoms	Coordination sequence N_k ($k = 1-11$)										
	1	2	3	4	5	6	7	8	9	10	11
O(1), O(3)	2	6	5	22	18	52	34	82	50	180	99
O(2), O(4), O(5)	2	8	8	23	18	55	36	113	68	159	92
Ge(1), Ge(2)	6	6	18	14	36	24	102	62	132	78	198
Ge(3), Ge(4)	4	4	15	12	42	30	72	44	142	80	217

Table 3. Coordination sequences for the framework-forming atoms in the structure of the BaGe^[6]Ge₃^[4]O₉ germanate

Framework-forming atoms	Coordination sequence N_k ($k = 1-11$)										
	1	2	3	4	5	6	7	8	9	10	11
O(1), O(4)	2	6	5	22	18	52	36	90	54	178	93
O(2), O(3), O(5)	2	8	8	23	18	55	36	115	70	161	90
Ge(1), Ge(2)	6	6	18	14	36	24	102	62	132	78	198
Ge(3), Ge(4)	4	4	15	12	42	30	74	50	150	76	207

Table 4. Coordination sequences for the framework-forming atoms in the structure of the $\text{K}_2\text{Ba}[\text{Ge}^{[6]}\text{Ge}_3^{[4]}\text{O}_9]_2$ germanate

Framework-forming atoms	Coordination sequence N_k ($k = 1-11$)										
	1	2	3	4	5	6	7	8	9	10	11
O(1)–O(6)	2	8	8	23	18	55	36	114	69	160	91
O(7)–O(9)	2	6	5	22	18	52	35	86	52	179	96
Ge(1)–Ge(4)	6	6	18	14	36	24	102	62	132	78	198
Ge(5)–Ge(7)	4	4	15	12	42	30	73	47	146	78	212

Table 5. Hierarchical ordering of *MT* frameworks according to the coordination sequences N_k ($k = 7$) for the *T* atoms

Germanate	Coordination sequence N_k ($k = 1-11$)										
	1	2	3	4	5	6	7	8	9	10	11
$\text{K}_2\text{Ge}^{[6]}\text{Ge}_3^{[4]}\text{O}_9$	4	4	15	12	42	30	72	44	142	80	217
$\text{K}_2\text{Ba}[\text{Ge}^{[6]}\text{Ge}_3^{[4]}\text{O}_9]_2$	4	4	15	12	42	30	73	47	146	78	212
$\text{BaGe}^{[6]}\text{Ge}_3^{[4]}\text{O}_9$	4	4	15	12	42	30	74	50	150	76	207

Table 6. Crystallographic symmetry of the *M* and *T* atoms in the germanate structures

$\text{K}_2\text{Ba}[\text{GeGe}_3\text{O}_9]_2$			$\text{K}_2\text{GeGe}_3\text{O}_9$			$\text{BaGeGe}_3\text{O}_9$		
atom	symmetry of position	position code	atom	symmetry of position	position code	atom	symmetry of position	position code
Ge(1)	$\bar{3}$	2 <i>b</i>	Ge(1)	$\bar{3}$	2 <i>b</i>	–	–	–
Ge(2)	32	2 <i>a</i>	–	–	–	Ge(1)	32	1 <i>a</i>
Ge(3)	3	4 <i>d</i>	Ge(2)	3	4 <i>d</i>	Ge(2)	3	2 <i>d</i>
Ge(4)	3	4 <i>d</i>	–	–	–	–	–	–
Ge(5)	1	12 <i>g</i>	Ge(3)	2	6 <i>f</i>	Ge(3)	2	3 <i>f</i>
Ge(6)	1	12 <i>g</i>	Ge(4)	1	12 <i>g</i>	Ge(4)	1	6 <i>g</i>
Ge(7)	1	12 <i>g</i>	–	–	–	–	–	–
K	1	12 <i>g</i>	K	1	12 <i>g</i>	–	–	–
Ba	2	6 <i>f</i>	–	–	–	Ba	2	3 <i>e</i>

The results that should be taken into account when performing the geometric–topological modeling of the assembly of germanate crystal structures from subpolyhedral clusters can be summarized as follows [15–17].

According to the equivalent sets of the calculated coordination sequences, the Ge and O framework-forming atoms in all structures have topological symmetry.

All the Ge and O atoms in the MT_3O_9 structures can be separated into four types of topologically different nodes in three-dimensional nets, namely, the *M* $\text{Ge}^{[6]}$ atoms, the *T* $\text{Ge}^{[4]}$ atoms, the O atoms in the *T*–O–*T* bridges, and the O atoms in the *T*–O–*M* bridges. The numbers of atoms in these four groups in the structures are different. The largest number of equivalent atoms

(four *M* $\text{Ge}^{[6]}$, three *T* $\text{Ge}^{[4]}$) are revealed in the K,Ba germanate. Two equivalent $\text{Ge}^{[6]}$ atoms and two equivalent $\text{Ge}^{[4]}$ atoms are found in the K and Ba germanates.

The results obtained indicate that the crystallographic symmetry of the germanates is substantially lower than the topologically possible symmetry. In the germanates, the atomic bonds both in the polyhedra and in the *M* and *T* polyhedra in three-dimensional *MT* frameworks are characterized by different degrees of asymmetry. According to the data presented in Table 6, the Ge atoms with the equivalent sequences $\{N_k\}$ (Table 5) in the framework of the K,Ba germanate are crystallographically different: the $\text{Ge}^{[6]}$ atoms occupy the positions 32, 3, and $\bar{3}$, whereas the $\text{Ge}^{[4]}$ atoms occupy the positions 2 and 1 (Table 6).

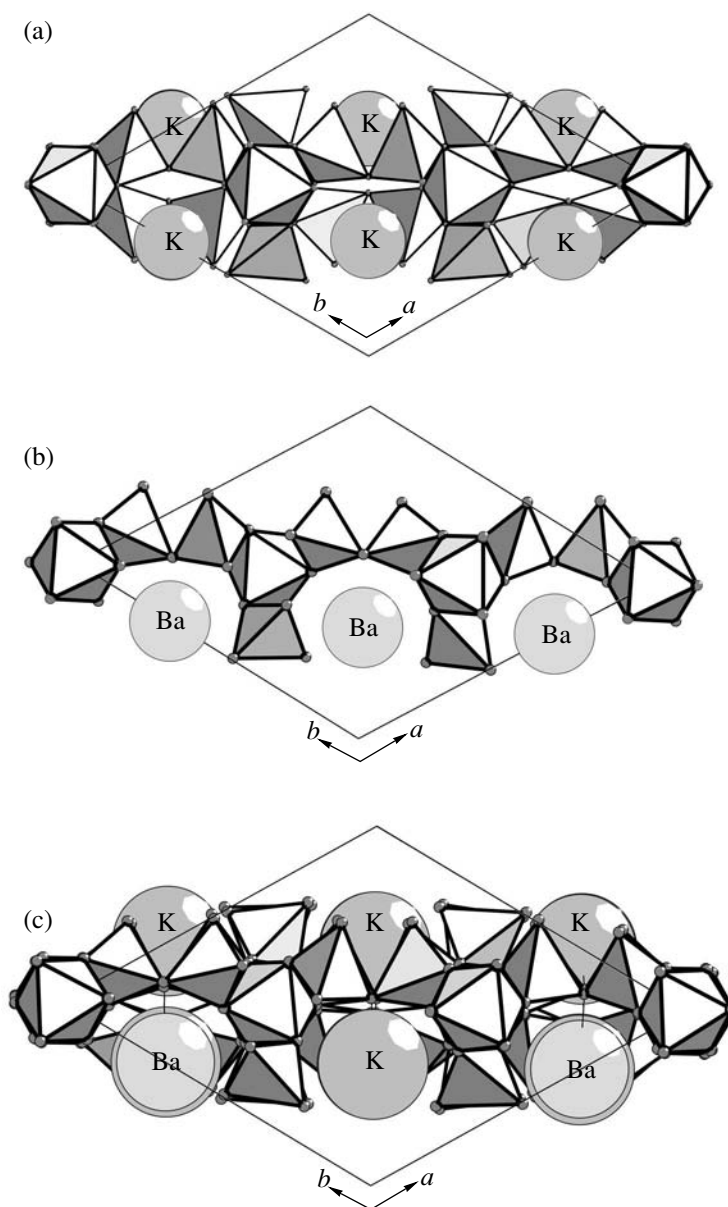


Fig. 1. Two-dimensional *MT* layers separated in the crystal structures of (a) $K_2Ge^{[6]}Ge_3^{[4]}O_9$, (b) $BaGe^{[6]}Ge_3^{[4]}O_9$, and (c) $K_2Ba[Ge^{[6]}Ge_3^{[4]}O_9]_2$ germanates.

Thus, the subsequently separated topologically equivalent SSU precursors contain Ge polyhedra with a different degree of asymmetry.

4. SELF-ASSEMBLY OF GERMANATE CRYSTAL STRUCTURES FROM SUBPOLYHEDRAL CLUSTERS

4.1. Self-Assembly of the $K_2Ge^{[6]}Ge_3^{[4]}O_9$ Structure

4.1.1. General features of the structure. The framework of the structure of the K germanate ($a = b = 11.840 \text{ \AA}$, $c = 9.800 \text{ \AA}$, space group $P\bar{3}2/c1$ [16]) is

formed by the *M* octahedra linked by three-membered rings composed of the *T* tetrahedra. The K sublattice is a three-dimensional network of bound K atoms with a structure of the lonsdaleite type (the bilayer polytype of the C diamond lattice). The formation of the *MT* layer passing through the vector *c* and the diagonal of the unit cell (Fig. 1a) is a characteristic feature of the structure of the K germanate.

4.1.2. Cluster substructure (identification of sub-structural units). In order to determine the topological type of SSU precursor [5], it is necessary to elucidate

the mechanism (type) of bonding of two M octahedra to the T tetrahedra in local regions of the MT framework.

The cluster substructure of the two-dimensional MT layer was determined using the two-color decomposition of nets into elementary cycles [6, 8].

In the framework of this method, the planar nets consisting of nodes (structural units of any nature) are considered packings of equivalent N -membered cyclic substructural units (clusters), where N is the number of structural units. The planar net can be represented as a packing of cyclic clusters if any of its nodes belongs to one and only one substructural unit.

If the net (chemical graph) is completely decomposed into equivalent elementary cycles, these painted cycles can be represented by isolated islands (the main contours or net generators). The combinatorially possible variants (a total of 16) for two-color decomposition of eleven simple (uninodal) Shubnikov nets with equivalent (symmetrically related) nodes were examined in [6–8]. It was revealed that five semiregular nets each have two variants of an elementary cyclic monomer (subgraph). They are characterized by different models of assembly (types of net generators and connectivity indices).

In order to simplify the primary structural analysis of the MT layer of the germanate, the O atoms located in the lines connecting the Ge atoms are removed with retention of these lines. As a result, the layer transforms into a planar Ge net (Fig. 2a).

The use of the two-color decomposition made it possible to reveal the following structural features of the planar two-dimensional MT net.

The planar two-dimensional net composed of bound Ge nodes contains only two types of topologically different nodes; therefore, it is a binodal net.

As in the three-dimensional net (see the calculated coordination sequences $\{N_k\}$ in Table 2), in the two-dimensional net, the crystallographically different atoms [$M = \text{Ge}(1), \text{Ge}(2)$; $T = \text{Ge}(3), \text{Ge}(4)$] are topologically equivalent.

The two-dimensional net is characterized by the Schläfli symbols 6464 for the M nodes and +664 for the T nodes, the node ratio $M : T = 1 : 2$, and the stoichiometric composition MT_2 .

The two-dimensional net 6464 + 664 (1 : 2) contains two different cyclic clusters in the form of tetragons and hexagons. The above notation of the net nodes means that there exist four and three polygons forming the M and T net nodes.

Only one of the three or four polygons, which formed the T node 664 or the M node 6464 in the net, can act as the main polygon (the net generator). All the other polygons of the net are secondary [6–8]. It is found that the type of the two-dimensional net can be reproduced in the course of assembly only from clusters in the form of hexagons. Therefore, hexagons are generators of the net 6464 + 664 (1 : 2). The two K

atoms each are located above and below the centers of these clusters (Fig. 2a).

The topology of the node links in the *secondary contours* of a net characterizes the mechanism of packing of primary contours in a layer. These contours in the form of squares and hexagons (Fig. 2) reflect the specific features of the short-range (pair) and long-range intercluster interactions responsible for the net formation. The local environment of each $K_2M_2T_4$ cluster involves four equivalent $K_2M_2T_4$ clusters; i.e., the cluster coordination number in the layer is 4. The layer separated in the crystal structure has the composition K_2MT_2 .

Therefore, the cluster substructure, namely, the cycle composed of the Ge nodes $M-T-T-M-T-T$, is separated in the MT net (Fig. 2a). Of special note is the uniqueness of the separation of the SSU cluster: cyclic contours in the form of squares cannot be separated as primary contours in the net.

The revealed type of the net 6464 + 664 (1 : 2) of the composition MT_2 is reproduced in the framework structure of the $\text{Li}_2\text{Ge}^{[6]}\text{Ge}_2^{[4]}\text{O}_6(\text{OH})_2$ germanate [25], which has the same polyhedral composition MT_2 . This type of the net (Fig. 2b) was found by modeling the assembly of a layer from $\text{Li}_2M_2T_4$ cyclic clusters [13].

4.1.3. Polyhedral structure of substructural units. After the reconstruction of the O polyhedra (i.e., the GeO_6 octahedra and the GeO_4 tetrahedra) in the net of the M and T nodes (atoms), the hexatomic cycle transforms into a cluster consisting of six polyhedra shared by their vertices. In the cluster, two GeO_6 octahedra are linked together through the Ge_2O_7 diortho groups. According to the topological classification [5], the identified precursor with the diortho group corresponds to the D type. The K atoms in the SSU precursor are located above and below the plane of the six-membered cycle.

In the unit cell of the germanate, the centers of the SSU precursors occupy symmetrically different crystallographic positions with the coordinates (1/2, 1/2, 1/2) (the $6e$ position with local symmetry $\bar{1}$) and (–0.16, 0.83, –0.01) (the $12g$ general position) (Fig. 3).

The stable cyclic clusters of the composition $K_2M_2T_4$ control all processes of the subsequent evolution of the MT crystal-forming complex and provide the formation of substructural units of a higher level with the participation of the additional T tetrahedra, which play the role of tetrahedra linking free vertices of the polyhedra [5, 13] during formation of the primary MT chain and the MT layer.

4.1.4. Structural mechanism of self-assembly. The three-dimensional topology of the structure is reconstructed from the local structural region according to the universal mechanism of maximum bonding of substructural units when changing over to a higher level of structural self-organization of the system.

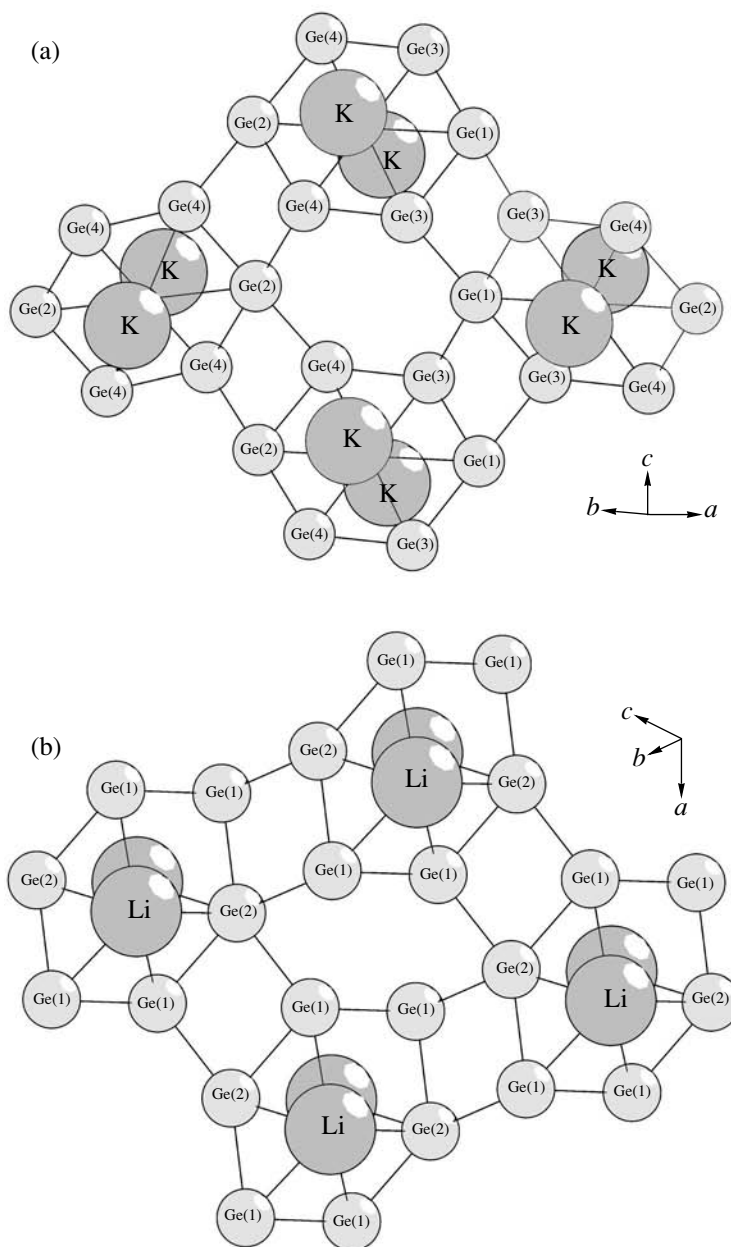


Fig. 2. Planar binodal nets in the crystal structures of (a) $\text{K}_2\text{Ge}^{[6]}\text{Ge}_3^{[4]}\text{O}_9$ and (b) $\text{Li}_2\text{Ge}^{[6]}\text{Ge}_2^{[4]}\text{O}_6(\text{OH})_2$ germanates. Two potassium or two lithium atoms are located above the centers of the M_2T_4 cyclic cluster precursors.

4.1.4.1. The primary MT chain. The one-dimensional periodic structures (*MT* chains) are assembled by bonding the SSU precursors through two shared vertices along the diagonal lying in the $(1\bar{1}0)$ plane (Fig. 3). The index of the complementary bonding of substructural units is equal to 2.

Free vertices of the tetrahedra (in different substructural units) are located close to each other (Fig. 3). This leads to their additional polymerization through the GeO_4 tetrahedron links, and the connectivity index of

substructural units in the primary chain increases to 4 (the maximum possible index).

4.1.4.2. Assembly of the MT layer. The condensation of short *MT* chains (consisting of two substructural units) results in the formation of the *MT* layer (Fig. 3). The connectivity index of chains is equal to 4. Two sterically accessible (to condensation) vertices of the *T* polyhedra in different *MT* chains are additionally polymerized through the tetrahedron links [the Ge(3) and Ge(4) central atoms in the GeO_4 tetrahedra in Fig. 3].

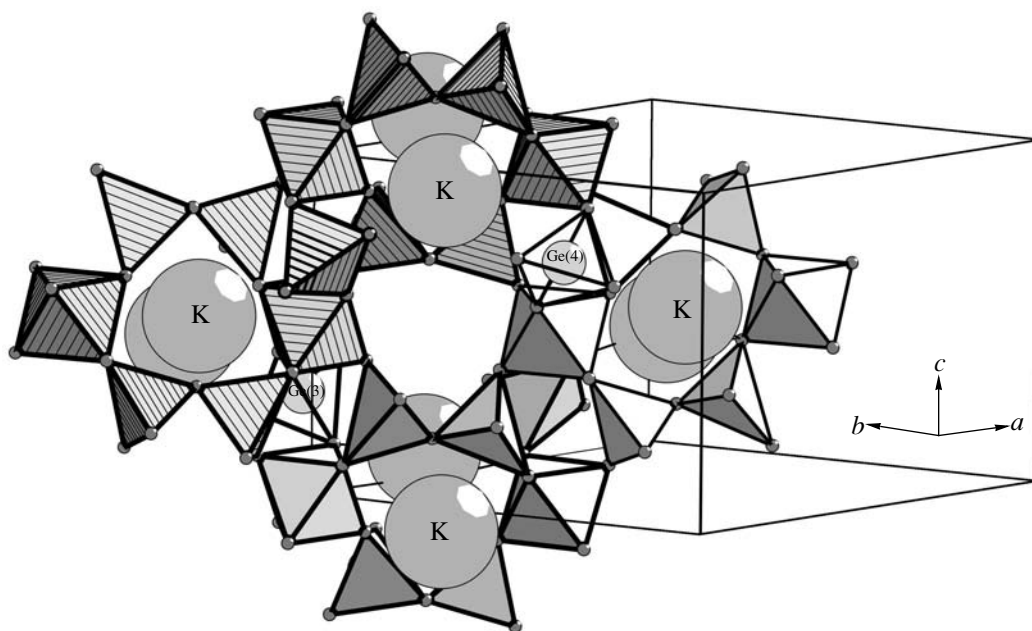


Fig. 3. Structure of the $K_2Ge^{[6]}Ge_3^{[4]}O_9$ germanate: assembly of the layer from two short chains.

The connectivity index of chains in the layer increases to 8 (the maximum possible index).

The layer involves Ge radicals of two types, namely, Ge_2O_7 diortho groups and GeO_4 tetrahedron links (above and below the plane). This mechanism of polymerization of the MT layer leads to a change in the layer composition from MT_2 to MT_3 , which corresponds to the MT composition of the K germanate framework. The projection of the MT_3 layer is depicted in Fig. 1a.

The distance between the centers of the SSU precursors in the parallel MT chains corresponds to the translation $c = 9.800 \text{ \AA}$ (Fig. 3).

4.1.4.3. Assembly of the MT framework. The condensation of germanate layers (Fig. 3) leads to the formation of the three-dimensional MT framework. In this case, the GeO_4 tetrahedra and the Ge_2O_7 diortho groups from different layers are joined together with the formation of Ge_3O_9 rings.

All the MT layers (Fig. 1a) in the germanate structure are translationally equivalent. The germanate structure is represented by the $1L$ -type structure, where the designation $1L$ indicates that the simple translational multiplication of one layer completely determines the topological structure of the three-dimensional MT framework [9]. The distance between the centers of the geometrically equivalent SSU precursors of different MT layers corresponds to the translation $a = 11.840 \text{ \AA}$.

4.2. Self-Assembly of the $BaGe^{[6]}Ge_3^{[4]}O_9$ Structure

4.2.1. General features of the structure. The framework of the structure of the Ba germanate ($a = b = 11.61 \text{ \AA}$, $c = 4.74 \text{ \AA}$, space group $P321$ [17]) is formed by the M octahedra linked together by three-membered rings composed of the T tetrahedra. The Ba sublattice consists of chains formed by translationally related atoms along the c axis (Fig. 1b).

4.2.2. Cluster substructure (identification of substructural units). The cluster substructure of the two-dimensional MT layers (passing through the vector \mathbf{c} and the diagonal of the unit cell, Fig. 1b) was determined using the two-color decomposition into elementary cycles. It was revealed that the Ba germanate, like the K germanate, is characterized by the planar net $6464 + 664$ (1 : 2) and the cyclic substructural unit of the composition BaM_2T_4 .

4.2.3. Polyhedral structure of substructural units. After the reconstruction of the O polyhedra in the net of the M and T nodes (atoms), the hexatomic cycle transforms into a cluster consisting of six linked polyhedra. In the cluster, two GeO_6 octahedra are linked together through the Ge_2O_7 groups. The Ba atoms are arranged in a polar manner and located only below the plane of the six-membered polyhedral ring. In the unit cell, the centers of the SSU precursors are located at symmetrically different crystallographic positions with the coordinates (0.55, 0.55, 1.00) (the $3e$ position with local symmetry 2) and (0.22, 0.88, -0.04) (the $6g$ general position) (Fig. 4).

4.2.4. Structural mechanism of self-assembly.
4.2.4.1. The primary MT chain. The one-dimensional

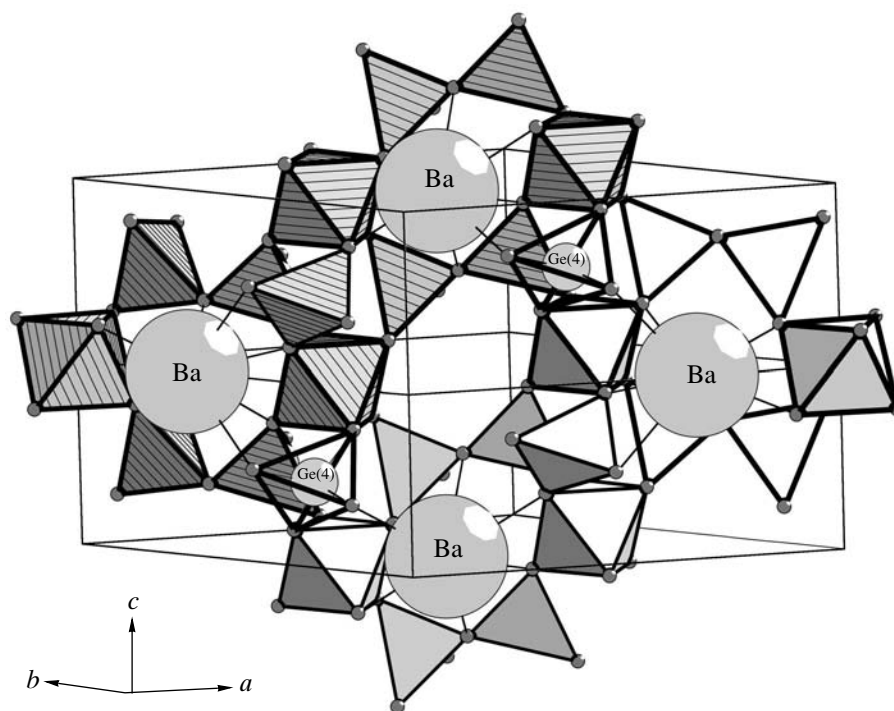


Fig. 4. Structure of the $\text{BaGe}^{[6]}\text{Ge}_3^{[4]}\text{O}_9$ germanate: assembly of the layer from two short chains.

periodic structures (chains) are assembled by bonding the substructural units through common vertices. The connectivity index of the substructural units is equal to 2.

The tetrahedron links [Ge(4) atoms] are located only above the plane of the *MT* chain (in the local environment of the Ba atoms) in contrast to the alternating arrangement of the tetrahedra above and below the plane of the *MT* chain in the K germanate. After the additional polymerization of the chain through tetrahedra, the connectivity index of the substructural units in the primary chain increases to 4 (Fig. 4).

4.2.4.2. *Assembly of the MT layer.* The condensation of parallel *MT* chains results in the formation of the layer. The index of complementary bonding of the chains composed of substructural units is equal to 4. After the additional polymerization through tetrahedra, the connectivity index of the chains increases to 8 (Fig. 4). The polymerization of the layer leads to a change in the layer composition from MT_2 to MT_3 , which corresponds to the *MT* composition of the Ba germanate framework.

The two-dimensional *MT* layer contains Ge radicals of two types, namely, the Ge_2O_7 groups and the GeO_4 tetrahedra. The difference in the topology of the bonds between the tetrahedra in the *MT* layers of the K and Ba germanates lies in the different arrangements of the *T* links, which are located above and below the layer plane in the former case and only above the layer plane

in the latter case. The cluster coordination number in the layer is 4.

4.2.4.3. *Assembly of the MT framework.* The condensation of layers leads to the formation of a three-dimensional framework. In this case, as in the K germanate, the GeO_4 tetrahedra and the Ge_2O_7 groups are joined together with the formation of Ge_3O_9 rings.

All the *MT* layers in the germanate structure are translationally equivalent. The germanate structure is represented by the *1L*-type structure. The distance between the centers of the SSU precursors of different *MT* layers corresponds to the translation $a = 11.608 \text{ \AA}$ (Fig. 1b) in the direction of layer packing.

4.3. Self-Assembly of the $\text{K}_2\text{Ba}[\text{Ge}^{[6]}\text{Ge}_3^{[4]}\text{O}_9]_2$ Structure

4.3.1. **General features of the structure.** The structure of the K,Ba germanate is characterized by the following specific features. The K,Ba germanate, like the K germanate, crystallizes in the space group $P\bar{3}2/c$ [15]. The unit cell parameter $c = 19.278 \text{ \AA}$ for the K,Ba germanate is twice as large as that for the K germanate ($c = 9.80 \text{ \AA}$). The unit cell parameter $a = 11.729 \text{ \AA}$ for the K,Ba germanate is close to the unit cell parameter $a = 11.8400 \text{ \AA}$ for the K germanate.

The framework of the structure is formed by the *M* octahedra linked together by three-membered rings

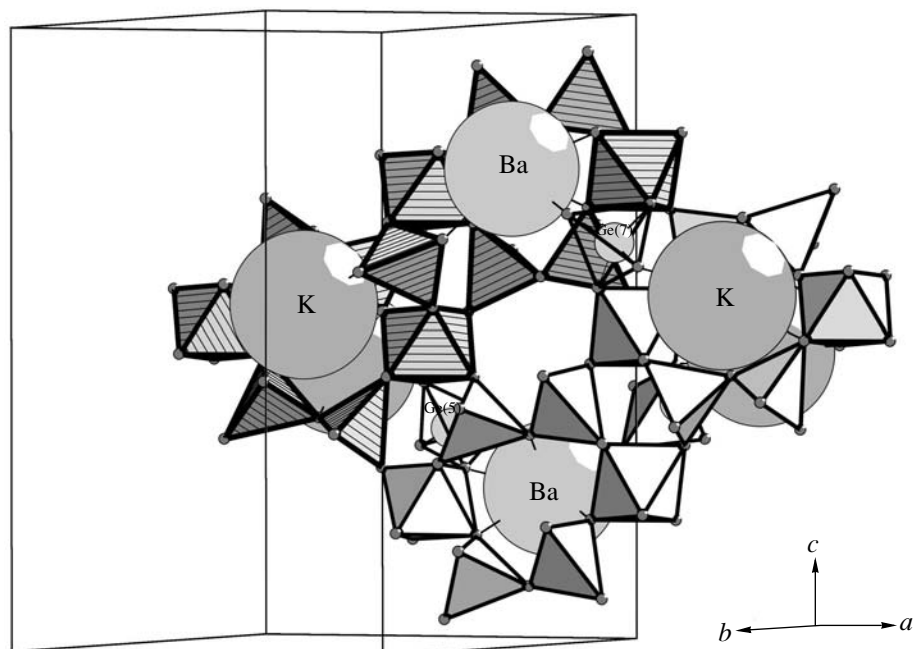


Fig. 5. Structure of the $\text{K}_2\text{Ba}[\text{Ge}^{[6]}\text{Ge}_3^{[4]}\text{O}_9]_2$ germanate: assembly of the layer from two short chains.

composed of the T tetrahedra. The MT holes are occupied by K and Ba atoms in an ordered manner (Fig. 1c).

4.3.2. Cluster substructure (identification of substructural units). It was revealed that the K,Ba germanate, like the K and Ba germanates, is characterized by the planar net $6464 + 664$ (1 : 2) of the Ge nodes (atoms). The equivalent cluster substructure was identified. Two K atoms (in K substructural units) are located above and below the centers of the cyclic SSU precursors (clusters). The Ba atoms (in the Ba substructural units) are located in a polar manner with respect to the centers of the cyclic SSU precursors (clusters).

4.3.3. Polyhedral structure of substructural units. As in the K germanate (Fig. 3), the K substructural units in the structure of the K,Ba germanate (Fig. 5) occupy the centers of the unit cells, i.e., the $6c$ centrosymmetric positions (1/2, 1/2, 1/2). The structures of both germanates also involve asymmetric K-containing SSU precursors. In the K,Ba germanate, the centers of the K substructural units are located at the positions with the coordinates (0.15, 0.82, 0.01) (Fig. 5). Upon the formation of the MT chain and the MT layer, all the K substructural units remain isolated from each other. The environment of each K precursor involves four Ba precursors; i.e., the cluster coordination number in the layer is 4.

The Ba substructural units are located on the 2 axes. The centers of the clusters are located at the positions with the coordinates (0.45, 0.45, 1/4) (Fig. 5). In the cluster, two GeO_6 octahedra are linked together through

the Ge_2O_7 diortho groups. The Ba atoms are located above (or below) the plane of the MT ring.

4.3.4. Structural mechanism of self-assembly.

4.3.4.1. The primary MT chain. The one-dimensional periodic structures (chains) are assembled by bonding the K and Ba substructural units through common vertices (Fig. 5). The connectivity index of the substructural units is equal to 2. The differences between the topological structures of the MT chains in the K germanate, the Ba germanate, and the K,Ba germanate lie in the positions of the T tetrahedra linking the SSU precursors. In the structure of the Ba germanate, all the T tetrahedra are located above the plane of the MT chain (Fig. 4). In the structure of the K germanate, the corresponding tetrahedra are arranged above and below the plane of the MT chain (Fig. 3). In the structure of the K,Ba germanate, two T tetrahedra (in the local environment of the Ba atom) are arranged both above and below the plane of the MT chain (Fig. 5). This leads to the doubling of the translation along the chain and to the aforementioned increase in the unit cell parameter c . After the additional polymerization of the chain through tetrahedra, the connectivity index of substructural units in the primary chain increases to 4 (Fig. 5).

Therefore, among the two possible variants of the formation of primary chains, i.e., when either (as in the K and Ba structures) the chains are formed by identical substructural units (and these K,Ge and Ba,Ge chains are linked into a layer) or the chains are formed by the K and Ba substructural units, the primary chains in the

structure of the mixed K,Ba germanate are formed according to the second variant.

4.3.4.2. Assembly of the MT layer. The condensation of modified MT chains results in the formation of the layer shown in Fig. 1c. The connectivity index of the chains composed of substructural units is equal to 4. After the additional polymerization through the tetrahedra, the connectivity index of the chains increases to 8 (Fig. 5). The polymerization of the layer leads to a change in the layer composition from MT_2 to MT_3 , which corresponds to the MT composition of the K,Ba germanate framework.

The two-dimensional MT layer in the structure of the K,Ba germanate, as in the structures of the K and Ba germanates, contains Ge radicals, namely, the GeO_4 ortho tetrahedron links and Ge_2O_7 groups.

4.3.4.3. Assembly of the MT framework. In the K,Ba germanate, the condensation of the layers leads to the formation of a three-dimensional framework. In this case, as in the K and Ba germanates, the GeO_4 tetrahedra and the Ge_2O_7 groups form radicals, i.e., the three-membered rings $GeO_4 + Ge_2O_7 = Ge_3O_9$.

The layers in the three-dimensional structure of the germanate are translationally equivalent. The structure of the germanate is represented by the $1L$ -type structure and has the translation $a = 11.729 \text{ \AA}$ in the direction of layer packing.

5. CONCLUSIONS

Thus, the SSU precursors in the form of M_2T_4 cyclic hexapolyhedral clusters were revealed for the MT frameworks of the $K_2Ba[Ge^{[6]}Ge_3^{[4]}O_9]_2$, $K_2Ge^{[6]}Ge_3^{[4]}O_9$, and $BaGe^{[6]}Ge_3^{[4]}O_9$ germanates. In the structures of the K and Ba germanates, the primary MT chains are formed by the $K_2M_2T_4$ and BaM_2T_4 clusters joined together by tetrahedron links. The structure of the K,Ba germanate is assembled so that the $K_2M_2T_4$ and BaM_2T_4 substructural units, which are also joined together by tetrahedron links, alternate in primary MT chains. In the MT layer, each of the $K_2M_2T_4$ substructural units is bonded to four BaM_2T_4 substructural units.

It was established that the mechanisms of assembly of the germanate structures from substructural units are different at the initial stage of the evolution of the system when the primary MT chain is assembled so that the tetrahedron links alternate with respect to the chain plane in each structure of the $K_2Ba[Ge^{[6]}Ge_3^{[4]}O_9]_2$, $K_2Ge^{[6]}Ge_3^{[4]}O_9$, and $BaGe^{[6]}Ge_3^{[4]}O_9$ germanates. This made it possible to determine the level of structural self-organization of the system at which there arise bifurcations of the evolution paths of the SSU precursors upon the formation of topologically different MT structures.

In all the stages of assembly, the crystal structures of the three germanates are characterized by the topologically equivalent algorithms because the indices of complementary bonding of the $K_2M_2T_4$ and BaM_2T_4 precursors into clusters of higher levels appear to be identical.

The revealed type of the binodal net MT_2 with the Schläfli symbols 6464 (for the M nodes) and +664 (for the T nodes) accounts for the universality of the topological mechanism of self-assembly through the mechanism of doubly bonded interactions of the SSU precursors. The $Li_2Ge^{[6]}Ge_2^{[4]}O_6(OH)_2$ germanate has the simplest algorithm for assembling chains and layers from $Li_2M_2T_4$ precursors (without participation of tetrahedron links), and the three-dimensional structure of the germanate is formed according to the mechanism of direct condensation of MT layers. The structures of the $A_2MT_3O_9$ family are formed by the $A_2M_2T_4$ cyclic clusters containing atoms $A = Na, K, \text{ or } Rb$ (for the $A, Ge^{[6]}$ germanates) and $A = K, Rb, \text{ or } Tl$ (for germanates with atoms $M = Ti, Sn$). The structures of the BMT_3O_9 family are formed on the basis of the BM_2T_4 clusters ($B = Sr, Ba, Pb$). In the case of both families, the increase in the connectivity index of the $A_2M_2T_4$ and BM_2T_4 clusters is provided by the additional participation of tetrahedron links in the assembly.

Thus, the modeling of the self-assembly of crystal structures of germanates with a complex chemical structure (as in the case of silicates [7]) made it possible to establish that their structure is governed by a particular spatial organization of specific components of two types.

Basic structural components. At this level of self-organization of a chemical system, the Ge polyhedra, together with alkali and alkaline-earth metal atoms, form the stable cyclic SSU precursors $A_2M_2T_4$ and BM_2T_4 , which are the building block for assembly of the three-dimensional suprapolyhedral architecture of the individual compound as a whole.

Additional structural components. The following two situations are possible in the case of SSU precursors whose evolution is accompanied by the formation of substructural units of a higher level:

(1) Substructural unit precursors can be directly incorporated (integrated) into a cluster of a higher level. In this case, the evolution of SSU precursors with the formation of superprecursors [7] of the $Li_2Ge^{[6]}Ge_2^{[4]}O_6(OH)_2$ compound proceeds at the highest rate.

(2) Substructural unit precursors can be bound into high-level clusters through additional polyhedral particle links. This situation is typical of the $K_2Ba[Ge^{[6]}Ge_3^{[4]}O_9]_2$, $K_2Ge^{[6]}Ge_3^{[4]}O_9$, and $BaGe^{[6]}Ge_3^{[4]}O_9$ germanates under consideration and all four representatives of the homological series based on the $Li_2Ge^{[6]}Ge_2^{[4]}O_6(OH)_2$ compound.

The modification through additional structural components corresponds to complementary (bonded) interactions of polyhedral particles with basic structural components, i.e., SSU precursors. According to [7], these interactions always complicate the algorithm of self-assembly and the sequence of correlation events becomes longer. Additional structural components bring about a local modification of an SSU precursor and (or) additionally join SSU precursors (into chains, layers, framework). The assembly of superprecursors of a three-dimensional structure is provided by the sequential performance of elementary operations with the participation of individual complementary components.

ACKNOWLEDGMENTS

The author would like to thank V.A. Blatov for supplying the TOPOS 3.2. program package used in the calculations.

This work was supported by the Russian Foundation for Basic Research, project no. 02-02-16861.

REFERENCES

1. M. Eigen, *Self-Organization of Matter and the Evolution of Biological Macromolecules* (Springer, Heidelberg, 1971; Mir, Moscow, 1973).
2. G. Nicolis and I. Prigogine, *Self-Organization in Non-Equilibrium Systems* (Wiley, New York, 1977; Mir, Moscow, 1979).
3. J. S. Nicolis, *Dynamics of Hierarchical Systems: An Evolutionary Approach* (Springer, Berlin, 1986; Mir, Moscow, 1989).
4. J.-M. Lehn, *Supramolecular Chemistry: Concepts and Perspectives* (VCH, Weinheim, 1995; Nauka, Novosibirsk, 1998).
5. G. D. Ilyushin and L. N. Dem'yanets, *Germanates of Tetravalent Metals* (VINITI, Moscow, 1989) [in Russian].
6. G. D. Ilyushin and L. N. Dem'yanets, in *Physics of Crystallization* (Nauka, Moscow, 2002), p. 82 [in Russian].
7. G. D. Ilyushin, *Modeling of Self-Organizing Processes in Crystal-Forming Systems* (URSS, Moscow, 2003) [in Russian].
8. G. D. Ilyushin and V. A. Blatov, *Kristallografiya* **49** (3), 391 (2004) [*Crystallogr. Rep.* **49** (3), 327 (2004)].
9. G. D. Ilyushin and L. N. Dem'yanets, *Zh. Neorg. Khim.* **47** (8), 1480 (2002) [*Inorg. Chem.* **47** (9), 1353 (2002)].
10. G. D. Ilyushin and B. A. Blatov, *Acta Crystallogr., Sect. B: Struct. Sci.* **58** (2), 198 (2002).
11. G. D. Ilyushin, B. A. Blatov, and Yu. A. Zakutkin, *Acta Crystallogr., Sect. B: Struct. Sci.* **58** (6), 948 (2002).
12. D. Yu. Pushcharovskii, *Structural Mineralogy of Silicates and Their Synthetic Analogues* (Nedra, Moscow, 1986) [in Russian].
13. G. D. Ilyushin and L. N. Dem'yanets, *Kristallografiya* **46** (5), 654 (2001) [*Crystallogr. Rep.* **46** (5), 801 (2001)].
14. G. D. Ilyushin and L. N. Dem'yanets, *Zh. Neorg. Khim.* **47** (10), 1699 (2002) [*Inorg. Chem.* **47** (10), 1559 (2002)].
15. O. Baumgartner and H. Voellenkle, *Monatsch. Chem.* **109**, 1145 (1978).
16. H. Voellenkle and A. Wittmann, *Monatsch. Chem.* **102**, 1245 (1971).
17. Yu. I. Smolin, *Dokl. Akad. Nauk SSSR* **181**, 595 (1968) [*Sov. Phys. Dokl.* **13** (7), 641 (1968)].
18. *Inorganic Crystal Structure Database (ICSD)* (Gmelin-Inst. fur Anorganische Chemie and FIC, Karlsruhe, 2002).
19. B. K. Vaïnshteïn, *Modern Crystallography* (Nauka, Moscow, 1978; Springer, Berlin, 1981), Vol. 1.
20. A. F. Wells, *Three-Dimensional Nets and Polyhedra* (Interscience, New York, 1977).
21. G. O. Brunner and F. Laves, *Tech. Univ. Dresden* **20**, 387 (1971).
22. W. M. Meier and H. J. Moeck, *J. Solid State Chem.* **27**, 349 (1979).
23. V. A. Blatov, *Acta Crystallogr., Sect. A: Found. Crystallogr.* **56** (2), 178 (2000).
24. V. A. Blatov, A. P. Shevchenko, and V. N. Serezhkin, *J. Appl. Crystallogr.* **32** (2), 377 (1999).
25. N. N. Nevskii, L. N. Ivanova, V. V. Ilyukhin, and N. V. Belov, *Dokl. Akad. Nauk SSSR* **242**, 1330 (1978) [*Sov. Phys. Dokl.* **23** (10), 705 (1978)].

Translated by O. Borovik-Romanova

CRYSTAL
GROWTH

A Model of the Separation of Intrinsic Charge Carriers—Protons and Orientational Defects—at the Crystallization Front of Water

A. V. Shavlov

*Institute of the Earth's Cryosphere, Siberian Division, Russian Academy of Sciences,
Tyumen, 625000 Russia*

e-mail: shavlov@ikz.ru

Received April 26, 2004

Abstract—A mechanism and the corresponding mathematical model of the formation of the crystallization potential of water, based on protons and orientational defects, are considered. On the basis of the comparison with the known model based on impurity ions, it is shown that it is orientational defects that are responsible for the formation of the crystallization potential of diluted solutions at a crystallization rate of 10^{-5} m/s. © 2005 Pleiades Publishing, Inc.

INTRODUCTION

The effect of separation of electric charges at the crystallization front of water has been known for more than 50 years. This phenomenon is often referred to when the nature of atmospheric and lightning electricity is explained [1, 2]. The mechanism of charge separation was also used successfully for experimental diagnostics of nucleation and growth of ice [3, 4].

The following experimental facts have been established in numerous studies: (i) ice is positively charged during the growth from pure water or weak solutions [5]; (ii) ice is negatively charged during the crystallization of concentrated solutions of some materials [6]; (iii) the difference between the electrical potentials of ice and water (the crystallization potential) is maximum (up to 400 V [7]) in pure water and weak solutions; (iv) the crystallization potential depends on the linear growth rate of ice and, in pure water and weak solutions, reaches a maximum at a growth rate of about 10^{-5} m/s [5]; and (v) the permittivity of the medium at the crystallization front is hundreds of times higher than the equilibrium value of permittivity for water and ice [8].

The most widely spread model used to explain the phenomenon of charge separation is the ionic model [9–11], which relates this effect to the difference in the diffusivities and the distribution coefficients of anions and cations of the solution. This model has a number of drawbacks [9]. For example, positively charged ammonium ions and negatively charged chlorine ions have relatively high trapping coefficients. Depending on which of these ions are present in the solution, the growing ice should acquire either a positive or negative charge. Experiment does not give this dependence. During freezing of weak solutions, ice has a positive

charge. However, the charge exchange in ice, in going from weak to concentrated solutions, is due likely to the ionic mechanism.

We believe intrinsic charge carriers, whose content is equilibrium in water and ice (for example, protons and hydroxyl ions), to be responsible for the charge separation during crystallization in pure water and weak solutions. A model based on these carriers was proposed by Kachurin [12]. In accordance with this model, for example, protons arrive from water to the crystal, penetrate the crystal freely, and remain in it. As a result, the proton concentration decreases sharply before the crystallization front and, hence, an electrical potential arises in water. Estimation gave the values of the potential in the range 10–100 V. A drawback of this model is the assumption of free penetration of protons from water into crystal, excluding their return to water. Such behavior would be possible if the potential energy of protons in ice was lower than in water. This picture contradicts the fact that the actual proton concentration in ice is a thousand times lower than in water [13].

Protons and hydroxyl ions are not the only intrinsic charge carriers in aqueous systems. Far more numerous are orientational defects. Their concentration in ice is higher than the proton concentration by a factor of 10^4 [13]. This difference is even larger in water. Until now, the role of orientational defects in the occurrence of electrical phenomena at the crystallization front has remained unclear.

Note that the concept of orientational defects is not conventional for water (it was first applied to ice). However, this concept is applicable to water since it does not require the material structure to be crystalline. There are two types of orientational defects: *L* and *D* [14]. They arise, move, and annihilate during rotations of

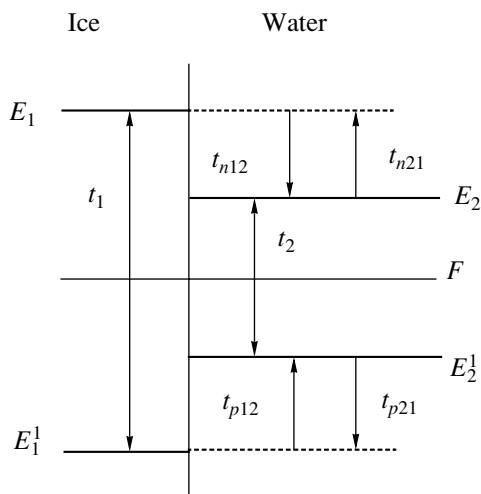


Fig. 1. Energy-level diagram for protons and hydroxyl ions. E_1 and E_2 are the energies of hydroxyl ions in ice and water, respectively; E_1^1 and E_2^1 are the energies of protons in ice and water, respectively; F is the chemical potential of carriers; t_{n12} , t_{n21} , t_{p12} , and t_{p21} are the times of relaxation and thermal excitation of hydroxyl ions and protons, respectively; and t_1 and t_2 are the recombination times of carriers in ice and water, respectively.

water molecules. The D defect (positively charged) corresponds to such an orientation of molecules at which two protons are located on the line connecting the two nearest oxygen atoms. The L defect (negatively charged) corresponds to the case when there are no protons on this line. One proton on the line corresponds to the defect-free state. The existence of orientational defects in water has been confirmed indirectly in experiments. For example, the high value (~ 80) of the low-frequency permittivity of water can be explained by the presence of orientational defects in it by analogy with the interpretation of the high (~ 100) low-frequency permittivity of ice [14].

PROTON-BASED MODEL

To formulate the charge-separation problem based on protons and hydroxyl ions, let us construct the energy diagram of these particles. To this end, we will use the data on the low-frequency conductivities of pure water ($\sigma_2 \sim 10^{-4} \Omega^{-1} \text{ m}^{-1}$) and ice ($\sigma_1 \sim 10^{-8} \Omega^{-1} \text{ m}^{-1}$) [14]. (The conductivity of water and ice, according to [14], is provided equally by orientational defects and protons (hydroxyl ions).) For the proton mobility in ice, $b_{p1} = 8 \times 10^{-7} \text{ m}^2 \text{ V}^{-1} \text{ s}^{-1}$ [13], and approximately the same value of the proton mobility in water, $b_{p2} = 8 \times 10^{-7} \text{ m}^2 \text{ V}^{-1} \text{ s}^{-1}$, we obtain the equilibrium proton concentrations in ice and water $n_1 = \sigma_1/(eb_{p1}) = 10^{17} \text{ m}^{-3}$ and $n_2 = \sigma_2/(eb_{p2}) = 10^{21} \text{ m}^{-3}$, respectively. The difference in these concentrations is related to the fact that the energy of formation of a proton–hydroxyl pair in ice

($E_1 - E_1^1$) is higher than that in water ($E_2 - E_2^1$) (Fig. 1) [15, 16]. Thus, to transfer a proton (hydroxyl ion) from water into ice, some energy should be spent to overcome the potential barrier $\Delta W = kT \ln(n_2/n_1) = 0.21 \text{ eV}$. The reverse transfer is accompanied by the release of energy. At such a profile of the potential energy, protons (hydroxyl ions) are rejected by the phase front during the crystallization. The rejection occurs as follows. At the instant of crystallization, the potential energy of, for example, hydroxyl ions increases owing to the change in the crystal field and they occupy the level E_1 in ice. Some carriers, remaining at the E_1 level, diffuse backward into water and then relax to the ground state with the energy E_2 . The carriers cannot return from water to ice via the diffusion mechanism since the diffusion is hindered by the potential barrier. Protons are rejected in a similar way.

Let us write a system of equations for protons and hydroxyl ions. For water ($x > 0$), in the steady state, we have

$$D_{n2} \frac{d^2 n}{dx^2} + \frac{d}{dx} [(v + b_{n2} E)(n + n_2)] - \frac{n + p + \frac{np}{n_2}}{t_2} = 0, \quad (1)$$

$$D_{p2} \frac{d^2 p}{dx^2} + \frac{d}{dx} [(v - b_{p2} E)(p + n_2)] - \frac{n + p + \frac{np}{n_2}}{t_2} = 0, \quad (2)$$

$$\frac{dE}{dx} = -\frac{e}{\epsilon \epsilon_0} (n - p), \quad (3)$$

where n and p are the nonequilibrium concentrations of hydroxyl ions and protons, respectively; n_2 is their equilibrium concentration; D_{n2} and D_{p2} , and b_{n2} and b_{p2} are their diffusivities and mobilities, respectively; E is the electric-field strength; ϵ is the permittivity; ϵ_0 is the dielectric constant; and v is the crystallization rate. The last terms in (1) and (2) describe the carrier recombination [17]. In these terms, $t_2 = (sv_T n_2)^{-1}$ is the recombination time, s is the recombination cross section, and v_T is the thermal velocity.

For ice ($x < 0$), similar equations are valid with subscript 1 instead of 2.

The boundary conditions have the form:

$$D_{n1} \frac{dn}{dx} \Big|_{x=-0} + b_{n1} E \Big|_{x=-0} (n \Big|_{x=-0} + n_1) + n \Big|_{x=-0} \left(v - \frac{1}{t_{n12} \gamma_{n2}} \right) - n \Big|_{x=+0} \left(v - \frac{1}{t_{n21} \gamma_{n2}} \right) = v n_2, \quad (4)$$

$$D_{p1} \frac{dp}{dx} \Big|_{x=-0} - b_{p1} E|_{x=-0} (p|_{x=-0} + n_1) + p|_{x=-0} \left(v - \frac{1}{t_{p12} y_{p2}} \right) - p|_{x=+0} \left(v - \frac{1}{t_{p21} y_{p2}} \right) = v n_2, \quad (5)$$

$$D_{n2} \frac{dn}{dx} \Big|_{x=+0} + b_{n2} E|_{x=+0} (n|_{x=+0} + n_2) = 0, \quad (6)$$

$$E|_{x=-0} = E|_{x=+0}, \quad (7)$$

$$n|_{x \rightarrow \pm\infty} = p|_{x \rightarrow \pm\infty} = E|_{x \rightarrow \pm\infty} = 0, \quad (8)$$

where y_{n2} and y_{p2} are the roots of the characteristic equations for hydroxyl ions at the E_1 level and for protons at the E_1 level, both in water (see clarifications below).

Boundary condition (4) is derived from the condition of equality of the flux of hydroxyl ions on the left of the crystallization front $j_n|_{x=-0}$ to the sum of four fluxes: (i) the trapping flux $-v(n|_{x=+0} + n_2)$ from the E_2 level in water to the E_1 level in ice; (ii) the trapping flux $-v(i|_{x=+0} + n_1)$ from the E_1 level in water to an excited level (for simplicity, to the E_1 level) in ice, where $(i|_{x=+0} + n_1)$ is the total (nonequilibrium and equilibrium) concentration at the E_1 level in water; (iii) diffusion flux $-D_{n2}(di/dx)$ at the E_1 level in water; and (iv) electric-drift flux $-(i|_{x=+0} + n_1)b_{n2}E|_{x=+0}$:

$$j_n|_{x=-0} = -v(n|_{x=+0} + n_2) - v(i|_{x=+0} + n_1) - D_{n2} \frac{di}{dx} \Big|_{x=+0} - b_{n2} E|_{x=+0} (i|_{x=+0} + n_1), \quad (9)$$

where $j_n|_{x=-0} = -D_{n1} \frac{dn}{dx} \Big|_{x=-0} - (v + b_{n1} E|_{x=-0})(n|_{x=-0} + n_1)$.

The three last terms in Eq. (9) constitute the total flux $j_i|_{x=+0}$ at the E_1 level in water; i.e.,

$$j_i|_{x=+0} = -D_{n2} \frac{di}{dx} \Big|_{x=+0} - (v + b_{n2} E|_{x=+0})(i|_{x=+0} + n_1).$$

The continuity equation at the E_1 level in water has the form

$$\frac{di}{dt} = -\frac{d}{dx} j_i - \frac{i}{t_{n12}} + \frac{n}{t_{n21}} = 0. \quad (10)$$

The two last terms in (10) describe, respectively, the decrease and increase in the carrier concentration at the E_1 level owing to the processes of relaxation to the E_2 level and reverse thermal excitation from the E_2 level.

Integrating (10) over the interval $[0, \infty)$, we obtain

$$j_i|_{x=+0} = -\frac{i|_{x=+0}}{t_{n12} y_{n2}} + \frac{n|_{x=+0}}{t_{n21} y_{n2}} - v n_1, \quad (11)$$

where $i|_{x=+0} = n|_{x=-0}$ owing to the free diffusion through the boundary at the E_1 level.

The quantity $y_{n2} = -\frac{v}{2D_{n2}} - \sqrt{\frac{v^2}{4D_{n2}^2} + \frac{1}{D_{n2} t_{n12}}}$ is the

root of the characteristic equation $D_{2n}(y_{n2})^2 + v y_{n2} - 1/t_{n12} = 0$, obtained from (10) under the assumption (natural for this problem) that the relaxation at the E_1 level in water dominates over the thermal excitation from the E_2 level, i.e., $i/t_{n12} \gg n/t_{n21}$, and the solution for the concentration has the form $i \sim \exp(y_{n2} x)$. The term describing the carrier drift in the electric field (equal in order of magnitude to i/θ_{n2} , $\theta_{n2} = \epsilon \epsilon_0 / (e b_{n2} n_2)$) was neglected in comparison with i/t_{n12} since $\theta_{n2} \gg t_{n12}$.

Substituting (11) into (9), we obtain (4). Boundary condition (5) is obtained similarly. In (5), y_{p2} is the root of the characteristic equation for protons at the E_1 level in water: $D_{p2}(y_{p2})^2 + v y_{p2} - 1/t_{p12} = 0$.

Condition (6) follows from the assumption that the flux of hydroxyl ions in water at the E_2 level is equal to the trapping flux of these ions to the E_1 level in ice; i.e.,

$$D_{n2} \frac{dn}{dx} \Big|_{x=+0} + (v + b_{n2} E|_{x=+0})(n|_{x=+0} + n_2) = v(n|_{x=+0} + n_2).$$

Equation (7) is the electroneutrality condition and equality (8) is the boundedness condition for solutions at infinity.

For numerical calculation of the crystallization potential, we used the following values of the parameters: $n_1 = 10^{17} \text{ m}^{-3}$, $n_2 = 10^{21} \text{ m}^{-3}$, $b_{p1} = b_{p2} = 8 \times 10^{-7} \text{ m}^2 \text{ V}^{-1} \text{ s}^{-1}$, $D_{p1} = D_{p2} = 1.8 \times 10^{-8} \text{ m}^2/\text{s}$, $b_{n1} = b_{n2} = b_{p1}/10 = 8 \times 10^{-8} \text{ m}^2 \text{ V}^{-1} \text{ s}^{-1}$, $D_{n1} = D_{n2} = D_{p1}/10 = 1.8 \times 10^{-9} \text{ m}^2/\text{s}$ [13], $t_{p12} = 1/(s v_T N) = 10^{-13} \text{ s}$ (at $s = 10^{-19} \text{ m}^2$, the thermal velocity of protons $v_T = 2 \times 10^3 \text{ m/s}$ and the concentration of water molecules $N = 3 \times 10^{28} \text{ m}^{-3}$), $t_{n12} = 1/(s v_T N) = 2 \times 10^{-12} \text{ s}$ (at $s = 10^{-19} \text{ m}^2$ and the thermal velocity of hydroxyl ions $v_T = 10^2 \text{ m/s}$ (the difference in the thermal velocities of carriers of opposite sign was chosen according to the difference in their mobilities)), $t_{p21} = t_{p12}(n_2/n_1) = 10^{-9} \text{ s}$, and $t_{n21} = t_{n12}(n_2/n_1) = 2 \times 10^{-8} \text{ s}$. The recombination time $t_1 = 10^{-3} \text{ s}$ was calculated using the known value of the recombination constant for ice, $K_d = 3 \times 10^{-9} \text{ s}^{-1}$, in the formula $t_1 = 1/(K_r n_1) = n_1/(K_d N)$, where $K_r = K_d N / (n_1)^2$ is the recombination-rate constant and N is the concentration of water molecules [14]. The recombination time in water is $t_2 = t_1(n_1/n_2) = 10^{-7} \text{ s}$.

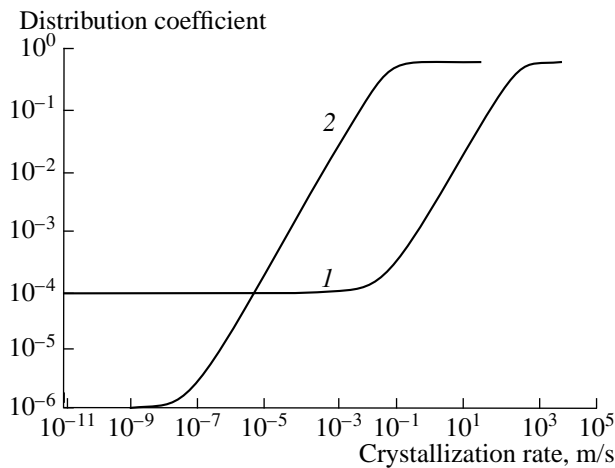


Fig. 2. Dependences of the distribution coefficients of (1) protons and (2) orientational L defects on the crystallization rate.

Figure 2 (curve 1) shows the dependence of the distribution coefficient of protons on the crystallization rate. The distribution coefficient is minimum at low rates, $k_p = n_1/n_2$, and increases to unity at high rates when the diffusion lags behind the crystallization front and the mechanism of rejection of protons does not work.

Figure 3 (curve 1) demonstrates the results of calculation of the crystallization potential for the linearized problem. The problem is linearized by neglecting the term containing the products nE , pE , and np in the system of equations (1)–(8). This procedure is equivalent to the weak-field approximation and small concentration perturbation: $|E| \ll v/b_{n_1, n_2; p_1, p_2}$, $|n|$, $|p| \ll n_{1, 2}$. Though solutions to the linear problem are less exact, they, in the case under consideration, can be obtained technically many times faster than solutions to the nonlinear problem. (The solution of the nonlinear problem will be considered below also.)

The potential (Fig. 3, curve 1) reaches a maximum value of 100 V at crystallization rates in the range 0.01–0.1 m/s. At a rate of 10^{-5} m/s, the potential is 10^{-6} V. Ice is charged negatively in this case. Thus, the protonic mechanism can explain neither the positive sign of the ice charge nor the high potential observed experimentally at a crystallization rate of 10^{-5} m/s.

It can be seen from Fig. 3 that, at a high crystallization rate (more than 10 m/s), the sign of the potential in the model becomes opposite. The change in the sign of the potential is related, on the one hand, to the decrease in the charge separation at the phase boundary since the efficiency of the rejection of carriers by the crystallization front decreases sharply with an increase in its velocity and, on the other hand, to the increase in the contribution of the charge separation in ice to the

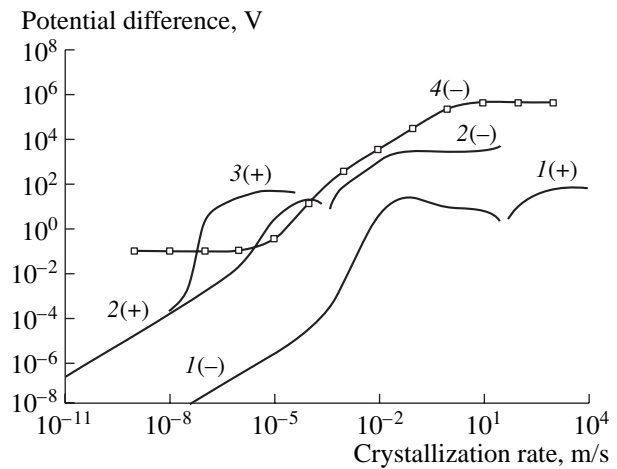


Fig. 3. Crystallization potentials for (1) the protonic mechanism, (2) the mechanism based on orientational defects, (3) the mechanism based on orientational defects in the nonlinear case, and (4) the ionic mechanism in the nonlinear case. The sign of the ice potential with respect to water is indicated in parentheses.

potential. Charge separation in ice occurs for the following reason: owing to their high mobility, nonequilibrium protons faster than hydroxyl ions move away from the crystallization front into the bulk of the solid phase; therefore, deep ice layers become charged positively with respect to the layers adjacent to the front.

MODEL BASED ON ORIENTATIONAL DEFECTS

Let us construct the energy diagram of orientational defects in the vicinity of the crystallization front. To this end, we will compare the concentrations of orientational defects in ice and in water. In ice, the concentration of these defects is $n_1 = 10^{22} \text{ m}^{-3}$ [13]. Their concentration in water, n_2 , will be estimated from the values of the dielectric relaxation time: 2×10^{-5} s in ice and 2×10^{-11} s in water [14]. Let us identify these times with the recombination times of orientational defects t_1 and t_2 : $t_1 = 1/(sv_T n_1) = 2 \times 10^{-5}$ s and $t_2 = 1/(sv_T n_2) = 2 \times 10^{-11}$ s. Dividing t_1 by t_2 , we find that $n_2 = n_1(t_1/t_2) = 10^{28} \text{ m}^{-3}$. The high concentration of orientational defects in water (in comparison with ice) corresponds to the low potential energy of carriers in water, whereas this parameter is higher in ice. Thus, the energy diagram, similar to that for protons and hydroxyl ions (Fig. 1), is quite appropriate for orientational defects, with all the consequences. Similar to protons and hydroxyl ions, orientational defects are rejected by the phase front during the crystallization.

The process of charge separation based on orientational defects can be described by the system of equations (1)–(3) with boundary conditions (4)–(8). To carry out numerical calculations, we will refine the val-

ues of mobilities, diffusivities, and relaxation times of orientational defects. Let us assume, according to the conclusions drawn in [14], that the mobility of L defects exceeds that of D defects by a factor of 3. The mobility b_{n1} of L defects in ice will be estimated on the basis of the known features of the motion of orientational defects [14]. Passing along a chain of water molecules, an L defect reorients them in such a way that the next L defect cannot pass the same path until it is passed by a hydroxyl ion or (in the reverse direction) a proton, as a result of which the chain molecules returns to the initial state. Thus, the conductivities of protons and L defects are equal to each other: $eb_{c1} = eb_{n1}n_1$, where $b_c = 8 \times 10^{-7} \text{ m}^2 \text{ V}^{-1} \text{ s}^{-1}$ and $c_1 = 10^{17} \text{ m}^{-3}$ are, respectively, the mobility and the concentration of protons in ice [13]. Hence, we have $b_{n1} = b_{c1}/n_1 = 8 \times 10^{-12} \text{ m}^2 \text{ V}^{-1} \text{ s}^{-1}$ and $D_{n1} = b_{n1}kT/e = 1.6 \times 10^{-13} \text{ m}^2/\text{s}$. The value of b_{n1} can be estimated in another way: using the experimental values of the high- and low-frequency conductivities of ice. The high-frequency conduction is implemented by the motion of orientational defects, which is not hindered by the proton subsystem (defects execute reciprocating motion with a small amplitude and the motion paths are not in contact), whereas the low-frequency conduction, as noted above, is related closely to the proton subsystem. Therefore, the value of b_{n1} can be determined using the relation $b_{n1}(\text{lf})/b_{n1}(\text{hf}) = \sigma(\text{lf})/\sigma(\text{hf})$. We find that $b_{n1}(\text{lf}) = b_{n1}(\text{hf})\sigma(\text{lf})/\sigma(\text{hf})$, where $\sigma(\text{lf}) = 2 \times 10^{-8} \Omega^{-1} \text{ m}^{-1}$ and $\sigma(\text{hf}) = 2 \times 10^{-5} \Omega^{-1} \text{ m}^{-1}$ are the low- and high-frequency conductivities of ice, respectively, and $b_{n1}(\text{hf}) = 2 \times 10^{-8} \text{ m}^2 \text{ V}^{-1} \text{ s}^{-1}$ is the high-frequency mobility of L defects [13]. The formula gives the value $b_{n1}(\text{lf}) = 2 \times 10^{-11} \text{ m}^2 \text{ V}^{-1} \text{ s}^{-1}$, which is close to the above estimation.

In water, the mobility of L defects is $b_{n2} = b_{c2}(c_2/n_2) = 8 \times 10^{-14} \text{ m}^2 \text{ V}^{-1} \text{ s}^{-1}$ according to the following values of the parameters: the concentration of orientational defects $n_2 = 10^{28} \text{ m}^{-3}$, the proton concentration $c_2 = 10^{21} \text{ m}^{-3}$, and the proton mobility $b_{c2} = 8 \times 10^{-7} \text{ m}^2 \text{ V}^{-1} \text{ s}^{-1}$. $D_{n2} = (kT/e)b_{n2} = 1.6 \times 10^{-15} \text{ m}^2/\text{s}$. The relaxation time of L defects $t_{n12} = 1/(sv_T N) = 6 \times 10^{-13} \text{ s}$ (at $s = 10^{-19} \text{ m}^2$ and $v_T = 500 \text{ m/s}$) and $t_{n21} = t_{n12}(n_2/n_1) = 6 \times 10^{-7} \text{ s}$. Similarly, for D defects, we have $b_{p2} = b_{n2}/3 = 2.7 \times 10^{-14} \text{ m}^2 \text{ V}^{-1} \text{ s}^{-1}$, $D_{n2} = 0.5 \times 10^{-15} \text{ m}^2/\text{s}$, $t_{p12} = 2 \times 10^{-12} \text{ s}$ (at $s = 10^{-19} \text{ m}^2$ and $v_T = 170 \text{ m/s}$ (the ratio of the thermal velocities of L and D defects in the same as the ratio of their diffusivities)), and $t_{p21} = 2 \times 10^{-6} \text{ s}$.

Figure 2 (curve 2) shows the results of calculation of the distribution coefficient of orientational defects and Fig. 3 (curve 2) demonstrates the calculated crystallization potential for the linearized problem. According to the calculation, ice is charged positively with respect to water at low crystallization rates. This result corresponds to the sign of the ice charge observed experi-

mentally. The potential difference reaches a maximum value of about 100 V at crystallization rates in the range 10^{-5} – 10^{-4} m/s , which is also in agreement with experimental results. At crystallization rates exceeding $3 \times 10^{-4} \text{ m/s}$, the potential difference becomes opposite, as in the proton model, owing to the decrease in the charge separation between the phases and the increase in the charge separation in ice.

Furthermore, we will solve the nonlinear problem of charge separation involving orientational defects. This approach makes it possible to describe more exactly, in comparison with the linear problem, the electrokinetic processes in real aqueous systems. We will use the system of equations (1)–(8). The result of calculation of the potential difference by the Runge–Kutta method is shown in Fig. 3 (curve 3).

It can be seen from Fig. 3 that the crystallization potential in the nonlinear problem is much higher than in the linear one in the range of crystallization rates 10^{-8} – 10^{-4} m/s . A potential of about 100 V is obtained in the nonlinear case at lower crystallization rates (specifically, at 10^{-6} – 10^{-5} m/s). This difference is related to the phenomenon of charge-carrier exclusion in ice (extraction of carriers by an electrical field), which can be revealed only by solving the nonlinear problem. The exclusion is illustrated by the concentration distribution near the crystallization front (Fig. 4). It can be seen that, at a low rate (10^{-8} m/s), the total concentration of the most mobile charge carriers in ice— L defects—almost does not differ from the equilibrium concentration (exclusion is absent still). At a rate of 10^{-7} m/s , the total concentration at a distance of 0.1 μm from the front becomes lower than the equilibrium concentration by a factor of almost 100 (exclusion occurs). With a further increase in the growth rate, exclusion decreases gradually. The increase in the potential difference U under exclusion is caused, according to the relation $U = EL_s$, by the increase in the length L_s of screening of the electric field E by charge carriers due to the decrease in their concentration.

As the concentration of more mobile charge carriers in ice (L defects) decreases under exclusion, the concentration of less mobile carriers (D defects) increases. For example, at a rate of 10^{-7} m/s , the total concentration of D defects at a distance of 0.1 μm from the crystallization front exceeds the equilibrium concentration by a factor of almost 100 (Fig. 4). This circumstance should lead to high values of the ice permittivity behind the crystallization front because, according to [14], it is D defects that are responsible for the ice permittivity. Recall that the experimental values of the permittivity in the vicinity of the crystallization front are tens and even hundreds times larger than the equilibrium value [8].

Figure 3 (curve 4) shows for comparison the crystallization potential calculated by us for the nonlinear model based on impurity anions and cations. In this

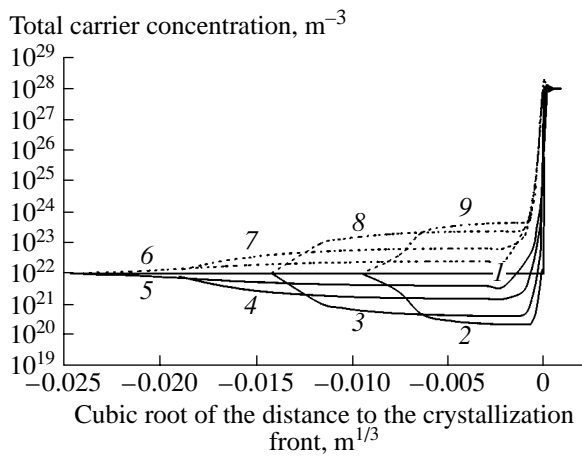


Fig. 4. Spatial distributions of the total concentrations of L and D defects (solid and dotted lines, respectively) at crystallization rates $v = (1) 10^{-8}$, $(2, 9) 10^{-7}$, $(3, 8) 10^{-6}$, $(4, 7) 10^{-5}$, and $(5, 6) 4 \times 10^{-5}$ m/s.

model, in contrast to that considered in [10, 11], the electric field in ice is screened by orientational L defects rather than protons and hydroxyl ions. The following values of the parameters were chosen: the concentration of the initial solution 10^{22} m^{-3} [5], the anion diffusivity $10^{-9} \text{ m}^2/\text{s}$, the cation diffusivity $2 \times 10^{-9} \text{ m}^2/\text{s}$, the distribution coefficient of anions 10^{-3} , and the distribution coefficient of cations 10^{-4} [10, 11]. The concentration of L defects in ice is 10^{22} m^{-3} [13] and their diffusivity is $1.6 \times 10^{-13} \text{ m}^2/\text{s}$.

Comparison of the curves in Fig. 3 shows that the mechanism of charge separation at the crystallization front in water, involving orientational defects, is the most appropriate to describe experimental data at a crystallization rate of about 10^{-5} m/s as compared to the mechanisms based on other charge carriers. The ionic model is valid for concentrated solutions.

ACKNOWLEDGMENTS

I am grateful to V.P. Mel'nikov for his support of this study and D. Bezus for his help with some calculations.

REFERENCES

1. E. G. Workman and S. E. Reynolds, *Phys. Rev.* **78**, 254 (1950).
2. L. G. Kachurin and V. I. Bekryaev, *Dokl. Akad. Nauk SSSR* **130** (1), 57 (1960) [*Sov. Phys. Dokl.* **5**, 137 (1960)].
3. A. A. Shibkov, Yu. I. Golovin, M. A. Zheltov, *et al.*, *J. Cryst. Growth* **236**, 434 (2002).
4. Yu. I. Golovin, A. A. Shibkov, M. A. Zheltov, *et al.*, *Kondens. Sredy Mezsfaz. Granitsy* **1** (4), 304 (1999).
5. L. G. Kachurin, V. I. Bekryaev, and V. F. Psalomshchikov, *Dokl. Akad. Nauk SSSR* **174** (5), 1122 (1967).
6. A. A. Mel'nikova, *Kristallografiya* **14** (3), 548 (1969) [*Sov. Phys. Crystallogr.* **14**, 464 (1969)].
7. B. L. Berri, I. O. Grigorov, L. G. Kachurin, *et al.*, *Problems of Engineering Glaciology* (Nauka, Novosibirsk, 1986), p. 24 [in Russian].
8. L. G. Kachurin and N. O. Grigorov, *Zh. Fiz. Khim.* **51** (7), 2864 (1977).
9. O. M. Rozental' and F. E. Chetin, *Multilayer Structural Ordering in Heterogeneous Processes of Ice Formation* (Izd. Gos. Ped. Inst., Sverdlovsk, 1974) [in Russian].
10. A. A. Chernov and A. M. Mel'nikova, *Kristallografiya* **16** (3), 477 (1971) [*Sov. Phys. Crystallogr.* **16**, 404 (1971)].
11. A. A. Chernov and A. M. Mel'nikova, *Kristallografiya* **16** (3), 488 (1971) [*Sov. Phys. Crystallogr.* **16**, 413 (1971)].
12. L. G. Kachurin, *Elektrokhimiya* **6** (9), 1294 (1970).
13. N. Maeno, *The Science of Ice* (Hokkaido Univ. Press, Sapporo, 1984; Mir, Moscow, 1988).
14. P. V. Hobbs, *Ice Physics* (Clarendon, Oxford, 1974).
15. A. V. Shavlov, *Ice under Structural Transformations* (Nauka, Novosibirsk, 1996) [in Russian].
16. A. V. Shavlov, *Kriosfera Zemli* **2** (2), 58 (1998).
17. S. M. Ryvkin, *Photoelectric Effects in Semiconductors* (Fizmatlit, Moscow, 1963; Consultants Bureau, New York, 1964).

Translated by Yu. Sin'kov

CRYSTAL GROWTH

Periodic Formation of Cracks in Isomorphously Mixed Crystals with a Continuously Varying Composition during Their Growth

M. A. Kuz'mina* and O. M. Boldyreva**

* Research Institute of the Earth Crust, St. Petersburg State University,
Universitetskaya nab. 7/9, St. Petersburg, 199034 Russia
e-mail: dido@ak2244.spb.edu

** NPP Bourestnik, Malookhtinskiĭ pr. 68, St. Petersburg, 195112 Russia

Received November 19, 2004

Abstract—Original data on the periodic formation of crack systems in growing crystals are obtained in experiments on growing isomorphously mixed potassium–rubidium biphthalate crystals with a continuously varying impurity concentration during crystal growth. The origin and conditions of the periodic formation of growth cracks in crystals are explained using the previously developed computer model for calculating heterometry-induced internal stresses in isomorphously mixed crystals during their growth. © 2005 Pleiades Publishing, Inc.

INTRODUCTION

In our earlier work [1], we developed an original growth technique and performed experiments on growing large-sized potassium–rubidium biphthalate crystals with the required properties for the purpose of preparing crystals with continuously varying lattice parameters, i.e., the so-called delta crystals, which are of great interest for solving applied problems of X-ray diffractometry. It was established that, in the majority of growing crystals with a continuously varying composition, crack systems developed predominantly either along the (001) plane in the second cleavage system [2, 3] or along arbitrary directions in all growth sectors. Continuous monitoring of the crystal growth revealed specific features of the crack formation in these crystals. It was found that, for the majority of the growing crystals, the crack formation proceeded in several (two or, more rarely, three) stages (Fig. 1). At the first stage, i.e., within 4.0–4.5 h after the onset of the crystal growth, individual cracks developed in different growth sectors of the crystal over a short period of time. Then, the crystal continued to grow and, after a certain time (2–3 h), there occurred the second stage of the crystal growth, during which a considerably larger amount of cracks grew and propagated throughout the crystal (Fig. 1). In the course of further growth of the crystal, some of the propagating cracks reached growing faces and broke the uniformity of their structure, thus initiating the splitting of the crystal during its growth [4]. As a result, the growing individual ceased to be monocrystalline: small subindividuals began to grow on the faces, which resulted in a transition to the polycrystalline growth. At this stage, the growth of large-sized crystals, as a rule, stopped [1].

RESULTS AND DISCUSSION

The computer model, which we previously developed for calculating heterometry-induced internal stresses (arising both at the growth front and at an arbitrary point inside the growth sector of the face) in crystals with a continuously varying composition during their growth [5], makes it possible (in the elastic approximation) to elucidate how the changes in the composition of the growing faces, for example, in crystal 3, affect the stresses in the course of the crystal growth (Fig. 1). As can be seen from Fig. 2, the magnitudes of the maximum normal stresses σ_n (which are

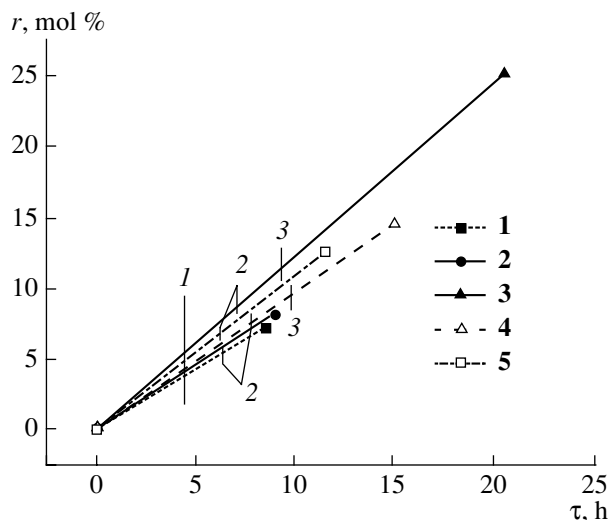


Fig. 1. Changes in the rubidium impurity content r (mol %) with time τ (h) in each of the five potassium–rubidium biphthalate crystals 1–5 during their growth and the (1) first, (2) second, and (3) third stages of crack formation.

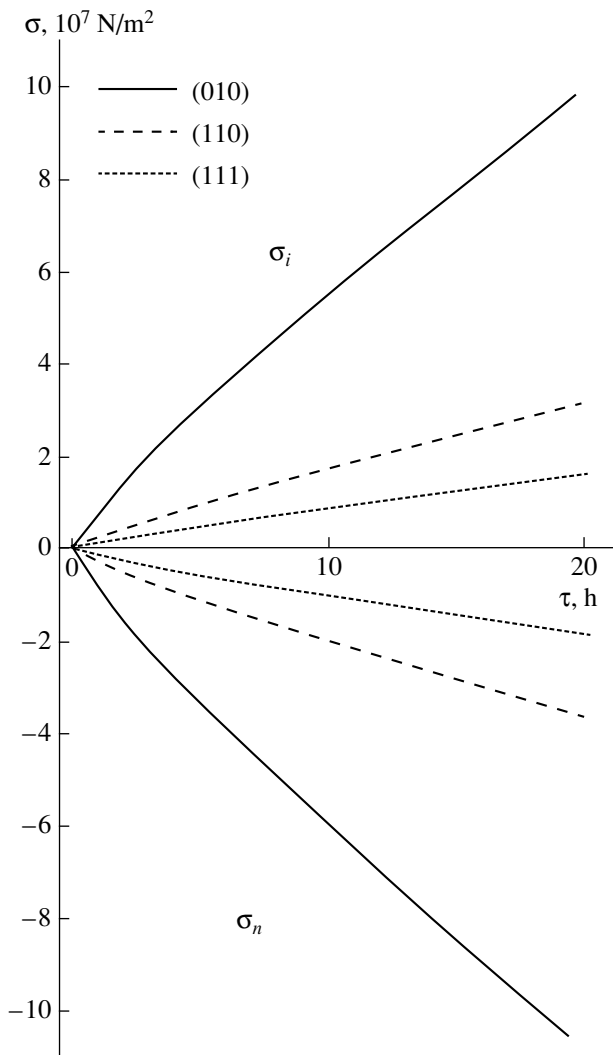


Fig. 2. Calculated (within the model of elastic stresses) changes in the principal normal stress σ_n and in the stress intensity σ_i at the growth front of the faces in all simple forms of potassium-rubidium biphthalate crystal 3 (Fig. 1) during its growth.

responsible for the brittle strains in the crystal [6, 7]) and the stress intensities σ_i (which are responsible for the plastic strains in the crystals [6, 7]) at the growth front of the faces in all simple forms of isomorphously mixed potassium-rubidium biphthalate crystal 3 progressively increase. For the crystal under consideration, the maximum (in magnitude (modulus)) stresses are the compressive normal stresses at the pinacoidal face, which have negative values down to $-1.0 \times 10^8 \text{ N/m}^2$. When analyzing the processes of brittle deformation, it is expedient to use the magnitude of normal stresses arising in the crystal [6, 7] (unlike the magnitude of the stress intensity, which is proportional to the cleavage stress); in this case, the dominant role in the crack formation is played by the tensile normal stresses [7, 8]. The specific feature of the heterometry-induced internal stresses in the crystals grown by us under conditions

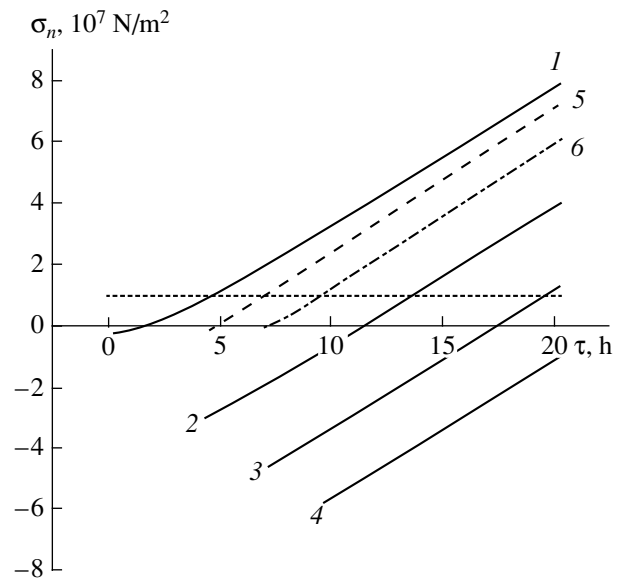


Fig. 3. Changes in the principal normal stress σ_n (within the model of elastic stresses) in (1-4) four different growth layers inside the growth sector of the (010) pinacoidal face of mixed potassium-rubidium biphthalate crystal 3 during growth of this face and the hypothetical changes in the normal internal stresses after the (5) first and (6) second stages of crack formation in the crystal (the horizontal dotted line indicates the level of the actual ultimate stress of the potassium biphthalate crystal under tensile stresses).

of progressive increase in the rubidium impurity concentration [1] resides in the fact that, initially, compressive stresses arise at the growth front of the crystal faces and, then, when the growth layers become internal for the sector of the growing face, gradually decrease, go to zero, and become tensile [5]. Figure 3 illustrates the changes in the principal normal stresses arising in different domains of the growth sector of the (010) pinacoidal face of crystal 3 during the growth of this face (layers of the (010) pinacoidal face sequentially grow in a direction parallel to the seed plate). Curves 1-4 in Fig. 3 correspond to four growth layers formed in different times inside the growth sector of the pinacoidal face of crystal 3 as this face grows. More precisely, curve 1 corresponds to the stresses in the layer formed near the seed plate (at a distance of 0.04 mm from the seed), curve 2 indicates the stresses in the layer formed within 4.4 h after the onset of the growth of the pinacoidal face (at a distance of 0.61 mm from the seed), curve 3 refers to the stresses in the layer formed within 7 h after the onset of the growth of the face (at a distance of 1.02 mm from the seed), and curve 4 shows the stresses in the layer formed within 9.5 h after the onset of the growth of the face (at a distance of 1.35 mm from the seed). All these curves emerge from the points corresponding to the normal stresses at the growth front of the pinacoidal face at the instant when the given layer of the growing face is formed (Fig. 2). The normal stresses at these points of the crystal change with time, as is shown by curves 1-4 in Fig. 3. (According to the

estimates made by the researchers who grew crystals of different compounds [9], the actual ultimate stress of the crystals is found to be $(1-5) \times 10^{-4} E$, which differs from the theoretical ultimate stress estimated at $1.0 \times 10^{-1} E$ [8], where E is the Young's modulus for a given crystal. Therefore, the actual ultimate stress of potassium biphthalate crystals does not exceed $1.0 \times 10^{-3} E$ and is approximately equal to $1.0 \times 10^7 \text{ N/m}^2$ [2].) The heterometry-induced internal stresses arising in the crystal near the seed plate (curve 1) transform rather rapidly from compressive stresses into tensile stresses and reach the actual ultimate stress within 4.5 h after the onset of the growth of the crystal under consideration (Fig. 3). It is in this time interval that the first stage of the crack formation is observed in crystals with a continuously varying composition (Fig. 1). At this stage of the crack formation, all the cracks develop in the vicinity of the seed plate in the inner domains of the growing crystals. If the cracks do not reach growing faces, the growth of the crystal is not upset but is even accelerated (according to the measurements of the growth rates of the crystals faces [1]) as a result of the decrease in the total level of stresses in the crystal.

Then, it was assumed that, after the first stage of the crack formation in the crystal under consideration, the total level of stresses at the growth front of the pinacoidal face decreases to zero. Under this assumption, we introduced the corresponding parameters into the model used for calculating the stresses. The results of these calculations demonstrated that the changes in the stresses in this domain of crystal **3** during its further growth should correspond to curve 5 in Fig. 3. Subsequently, the stresses in this domain of crystal **3** changed and reached the actual ultimate stress in approximately 2.5 h (curve 5 in Fig. 3). (Note that the total time of crystal growth was equal to 7 h.) This time corresponds to the onset of the second stage of the crack formation in crystal **3** (Fig. 1). (In the case of incomplete weakening of stresses at the growth front of the pinacoidal face due to the formation of cracks, the onset of the next stage of their formation should be observed at a later time as compared to that obtained in the calculation.) Similarly, we assumed once more that the total level of stresses at the growth front of the pinacoidal face decreases to zero after the second stage of the crack formation and, under this assumption, calculated the changes in the stresses in this domain (formed in the course of 7.0- to 7.5-h growth of the pinacoidal face) of the crystal during its further growth (curve 6 in Fig. 3). It turned out that these stresses change in the same manner as in the preceding case and, after 2.5–3.0 h, reach the actual ultimate stress. (The total time of crystal growth was equal to 9–10 h.) It is at this instant of time that the onset of the third stage of the crack formation is observed in crystal **3** (Fig. 1). It was revealed that, at this stage of the crack formation in crystal **3**, a large crack developed in the seed plate along the (010) plane in the first cleavage system [2] in such a way that it vir-

tually separated the crystal into two independent halves. Since the configuration of the seed plate and the layer grown changed, the use of the model proposed in [5] for calculating the stresses became impossible. However, the experimentally observed appreciable acceleration of the growth of the pinacoidal face [1] indicates that the stresses at the growth front of this face decrease significantly.

CONCLUSIONS

Thus, the observed periodic formation of intracrystalline cracks in growing isomorphously mixed potassium–rubidium biphthalate single crystals with a continuously varying composition during the crystal growth can be explained almost completely in terms of the behavior of the heterometry-induced internal stresses. These stresses initially arise at the growth front of crystal faces and then gradually transform from compressive stresses into tensile stresses inside the crystal in the course of its growth. After the stresses have reached the actual ultimate stress of the given crystal, individual cracks or their systems are formed in it. Since the crystals with a continuously varying composition during their growth are characterized by regular changes in the stresses both at the growth front and inside the crystal, the tensile stresses in the inner domains of the growing crystal reach the actual ultimate stress at regular intervals, which results in the periodic formation of cracks or their systems.

REFERENCES

1. S. V. Moshkin, O. M. Boldyreva, T. I. Ivanova, *et al.*, *J. Cryst. Growth* **172**, 226 (1997).
2. V. R. Regel', V. I. Vladimirov, N. L. Sizova, *et al.*, *Kristallografiya* **34** (6), 1490 (1989) [*Sov. Phys. Crystallogr.* **34** (6), 892 (1989)].
3. V. R. Regel', N. L. Sizova, and T. N. Turskaya, *Kristallografiya* **41** (5), 918 (1996) [*Crystallogr. Rep.* **41** (5), 875 (1996)].
4. M. A. Kuz'mina and S. V. Moshkin, in *Proceedings of the International Conference on Crystallogenesi and Mineralogy, St. Petersburg, Russia, 2001* (St. Petersburg, 2001), p. 219.
5. M. A. Kuz'mina, S. V. Moshkin, and I. P. Shakhverdova, *Kristallografiya* **46** (6), 1098 (2001) [*Crystallogr. Rep.* **46** (6), 1014 (2001)].
6. N. I. Bezukhov, *Foundations of the Theory of Elasticity, Plasticity, and Creep* (Vysshaya Shkola, Moscow, 1968) [in Russian].
7. N. M. Belyaev, *Problems in the Strength of Materials* (Fizmatgiz, Moscow, 1959; Pergamon, Oxford, 1966).
8. A. A. Urusovskaya, in *Modern Crystallography* (Nauka, Moscow, 1981), Vol. 4, p. 47 [in Russian].
9. E. I. Givargizov, Kh. S. Bagdasarov, V. A. Kuznetsov, *et al.*, in *Modern Crystallography* (Nauka, Moscow, 1980), Vol. 3, p. 233 [in Russian].

Translated by O. Borovik-Romanova

Specific Features of the Growth of Barium Chromate Crystals from Different Precursors

A. V. Zubets, L. L. Klimovich, and N. D. Zhigadlo

*Institute of Solid State and Semiconductor Physics, Belarussian Academy of Sciences,
ul. Brovki 17, Minsk, 220072 Belarus*

e-mail: klim@ifttp.bas-net.by

Received December 22, 2003; in final form, March 31, 2005

Abstract—The influence of precursors on the single-crystal growth of BaCrO_4 in the controlled reactions of BaCl_2 with $\text{K}_2\text{Cr}_2\text{O}_7$, $(\text{NH}_4)_2\text{Cr}_2\text{O}_7$, and K_2CrO_4 in aqueous solutions is studied. The conditions of the reaction of BaCl_2 with $\text{K}_2\text{Cr}_2\text{O}_7$ are found to be most favorable for single-crystal growth. A growth texture is observed in the (011) and (100) planes in the samples prepared by the reactions with $\text{K}_2\text{Cr}_2\text{O}_7$ and K_2CrO_4 , respectively. A more complex type of growth preference was observed in the reaction with $(\text{NH}_4)_2\text{Cr}_2\text{O}_7$. © 2005 Pleiades Publishing, Inc.

INTRODUCTION

The ions with the $3d^2$ configuration (Cr^{4+} , Mn^{5+} , and Fe^{6+}) act as active luminescence centers in various crystals [1]. In particular, FeO_4^{2-} -containing systems have properties of infrared laser materials [2]. Crystals of chromates (CrO_4^{2-}) are suitable for doping with FeO_4^{2-} ions because they are isostructural with the corresponding ferrates [2]. One of the problems related to application of these materials is the growth of large FeO_4^{2-} -doped crystals of good optical quality.

The growth of BaCrO_4 crystals by chemical reactions in aqueous solutions was investigated in [3–6]. In these studies, the influence of various factors on the growth and structure of BaCrO_4 crystals was examined. For example, the effect of pH [4] and the influence of organic admixtures modifying the crystal shape [3, 6] were considered.

In this study we examined the specific features of the growth of BaCrO_4 crystals using different starting components.

EXPERIMENTAL

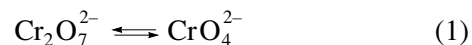
Samples of BaCrO_4 were prepared by spontaneous crystallization in the chemical reactions of BaCl_2 with $\text{K}_2\text{Cr}_2\text{O}_7$ (A), $(\text{NH}_4)_2\text{Cr}_2\text{O}_7$ (B), and K_2CrO_4 (C) in an aqueous solution. The reactions were carried out by the consecutive portionwise addition of the reagents to the reaction volume [7]. The concentrations of the corresponding components of reagent-grade purity (0.003–0.0067 g/l for $\text{BaCl}_2 \cdot 2\text{H}_2\text{O}$ and 0.4 g/l for $\text{K}_2\text{Cr}_2\text{O}_7$, $(\text{NH}_4)_2\text{Cr}_2\text{O}_7$, and K_2CrO_4) and the volume of the BaCl_2 solution (0.05 ml), which was added at 30–300-s

intervals, were the same in all three reactions. The starting solutions had pH values of 4.2, 3.6, and 7.5 for $\text{K}_2\text{Cr}_2\text{O}_7$, $(\text{NH}_4)_2\text{Cr}_2\text{O}_7$, and K_2CrO_4 , respectively.

The crystals grown were ground in an agate mortar and their X-ray diffraction analysis was carried out on a Siemens D5000 powder diffractometer using $\text{CuK}\alpha$ radiation. The quality of the crystals was estimated from their morphological features. This method allowed us to visualize the process of the crystal growth.

RESULTS AND DISCUSSION

It is known that the chromate form of soluble CrO_4^{2-} compounds is transformed into the $\text{Cr}_2\text{O}_7^{2-}$ bichromate form in an acidic medium, and, vice versa, the $\text{Cr}_2\text{O}_7^{2-}$ bichromate form is transformed into the CrO_4^{2-} chromate form in an alkaline medium. Solutions of chromates and bichromates always contain certain amounts of ions of another form. The solubility of BaCrO_4 is much lower than that of BaCr_2O_7 . Hence, BaCrO_4 precipitates in the reactions of Ba^{2+} with both chromate and bichromate. The precipitation of BaCrO_4 from $\text{Cr}_2\text{O}_7^{2-}$ -containing solutions leads to a shift of the equilibrium



to the right, i.e., to the formation of CrO_4^{2-} ions.

The results of the pH measurements suggest that the concentration of CrO_4^{2-} ions increases in the following series of precursors: $(\text{NH}_4)_2\text{Cr}_2\text{O}_7 \rightarrow \text{K}_2\text{Cr}_2\text{O}_7 \rightarrow$

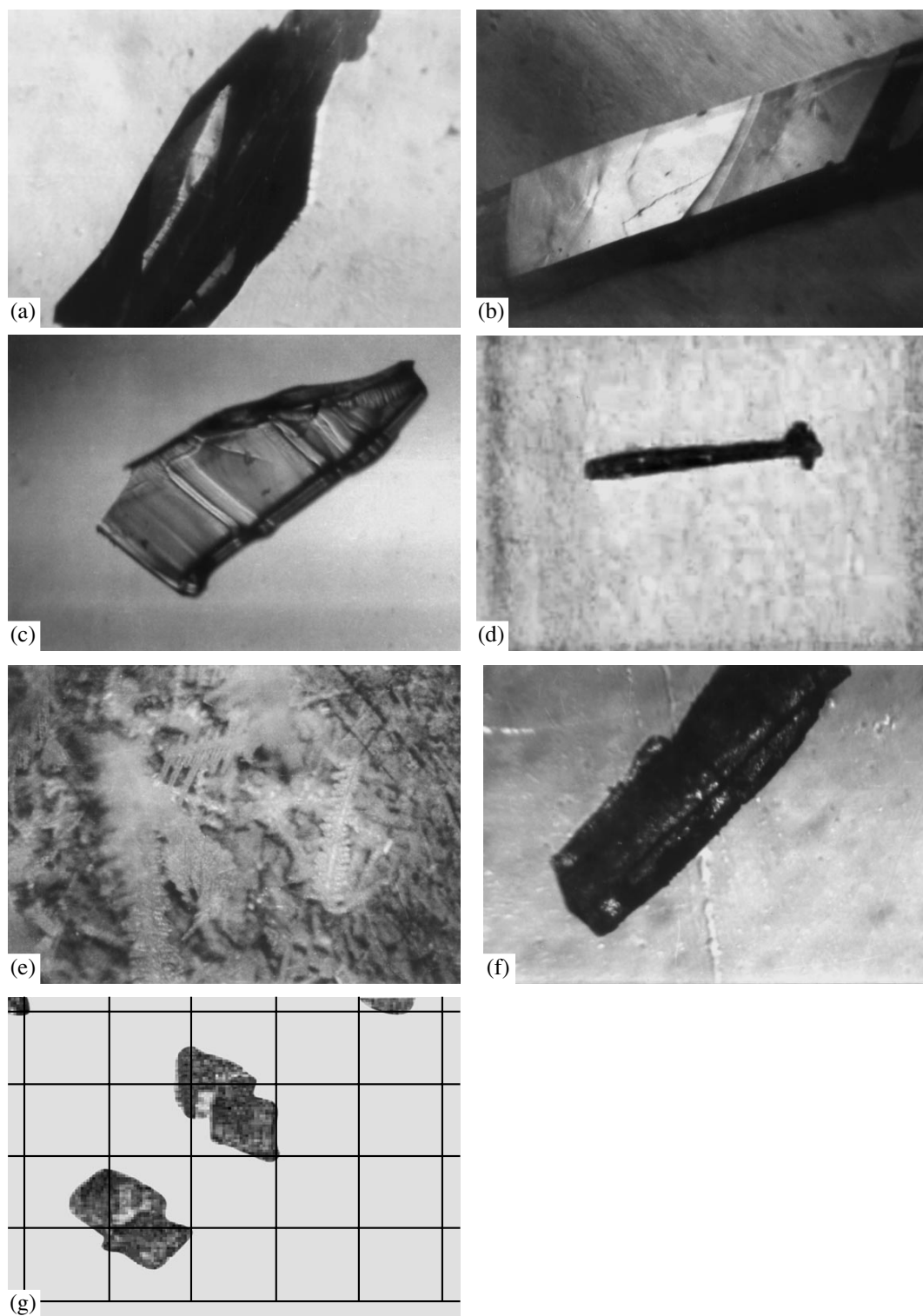


Fig. 1. Crystals of BaCrO_4 grown by chemical reactions from aqueous solutions at room temperature using various precursors: (a) $(\text{NH}_4)_2\text{Cr}_2\text{O}_7$, (b, c, d) $\text{K}_2\text{Cr}_2\text{O}_7$, and (e, f) K_2CrO_4 . The latter gave (e) dendrites and (f) bulk crystals. (g) BaCrO_4 crystals grown by the gel method [4].

K_2CrO_4 . In turn, the rate of reaction (1) with potassium bichromate may differ from the rate of the reaction with ammonium bichromate. Therefore, the rate of the for-

mation of the CrO_4^{2-} chromate ion can be considered as one of the limiting factors of the BaCrO_4 crystallization.

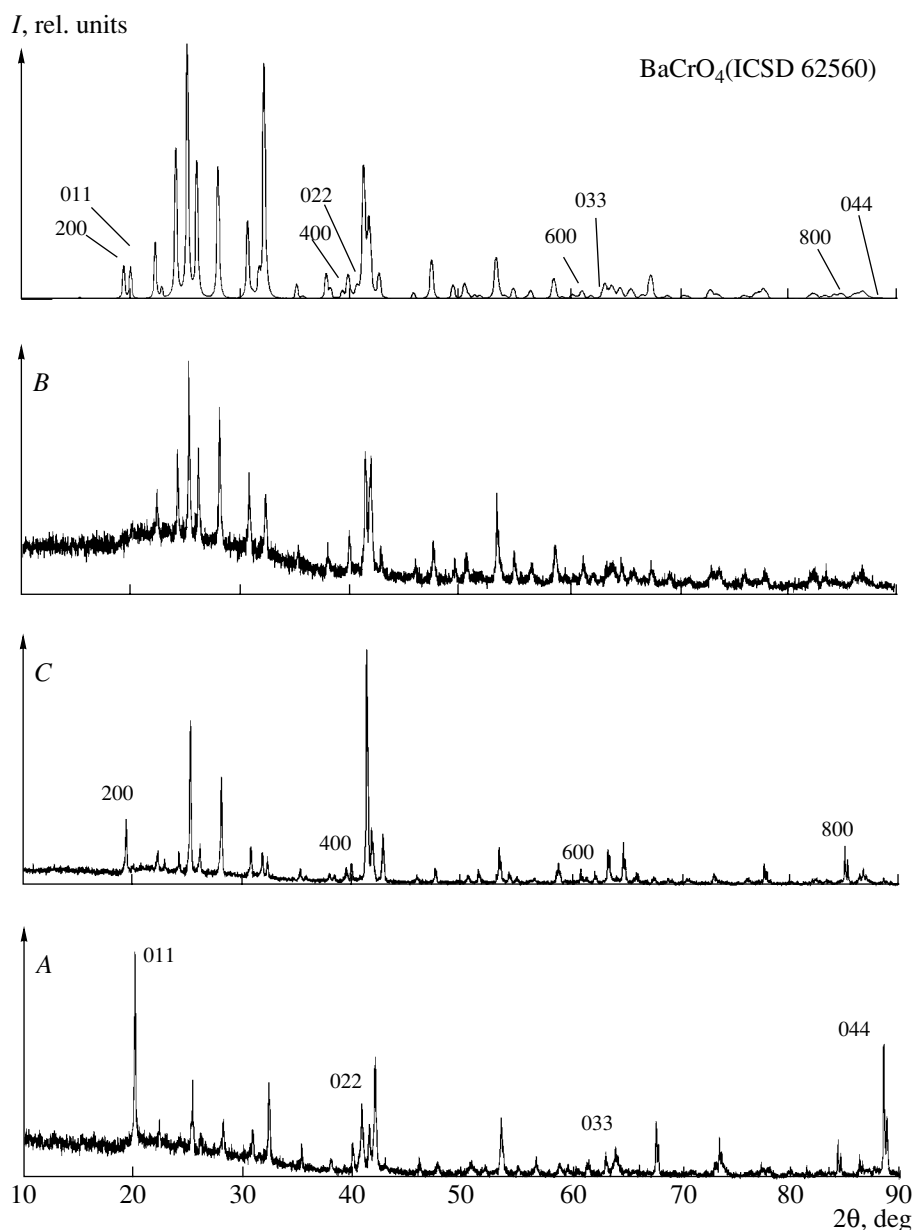


Fig. 2. X-ray diffraction patterns of crystalline BaCrO_4 precipitates obtained in the reactions of aqueous solutions of BaCl_2 with $\text{K}_2\text{Cr}_2\text{O}_7$ (A), $(\text{NH}_4)_2\text{Cr}_2\text{O}_7$ (B), and K_2CrO_4 (C).

The crystal growth occurs differently depending on the reagents used. The reaction of BaCl_2 with the reagent $(\text{NH}_4)_2\text{Cr}_2\text{O}_7$, having the highest acidity, afforded predominantly a precipitate of druses of small single crystals. When BaCl_2 was added at a rate of 3.4×10^{-7} g/min or slower, only a few millimeter-size crystals grew (Fig. 1a), even at long-term growth (more than 10 days).

The reaction of BaCl_2 with $\text{K}_2\text{Cr}_2\text{O}_7$ under the same conditions yielded crystals after three to five days, and, after ten days, the linear sizes of the crystals were as large as several millimeters. These crystals were better faceted and had well-developed prismatic planar faces

(Figs. 1b–1d). Precipitation of BaCrO_4 crystals occurred most rapidly (within one–two days) in the reaction of BaCl_2 with K_2CrO_4 , but the precipitate contained predominantly dendrites, which often formed quasi-two-dimensional symmetric particles. Generally, no further crystal growth occurred (Fig. 1e) and only individual crystallites were observed (Fig. 1f). The highest growth rate of BaCrO_4 crystals in K_2CrO_4 solutions and the specific morphology of these crystals can be related to the highest concentration of chromate ions in K_2CrO_4 solutions and, hence, the highest supersaturation. This suggestion is also supported by the observed fact that the growth of dendritic crystallites

was accompanied by the extensive spontaneous formation of new crystal seeds (nucleation).

The crystalline precipitates formed from different precursors differ in color (greenish yellow, brownish yellow, and golden yellow precipitates were obtained from the precursors *A*, *B*, and *C*, respectively), which is likely to be associated with the dimensions of single-crystal precipitates and the presence of a growth texture. The single crystals obtained were semitransparent.

The X-ray diffraction spectra of the precipitates correspond to the BaCrO₄ compound (ICSD 62560) (Fig. 2). At the same time, there are some differences in the sample growth. The samples prepared from the precursors *A* and *C* are characterized by the presence of a growth texture in the (011) and (100) planes, respectively, whereas the sample prepared from the precursor *B* is characterized by a more complex growth texture.

It should also be noted that the shape of these crystals (Fig. 1d) differs from that of the crystals prepared by the gel method [4, 5], where the same reagents were used, whereas the CrO₄²⁻ to Cr₂O₇²⁻ ratio in solution was varied by changing the pH (Fig. 1g). In addition, it was established [4] that the crystal formation in the reactions of BaCl₂ with K₂Cr₂O₇ and (NH₄)₂Cr₂O₇ at pH 3 occurred in the same way. Prismatic nanocrystals were obtained by using organic modifying agents [3, 6].

CONCLUSIONS

The conditions for the growth of BaCrO₄ single crystals by chemical reactions in aqueous solutions of

the K₂Cr₂O₇, (NH₄)₂Cr₂O₇, and K₂CrO₄ salts were established.

In the studied ranges of reagent concentrations and rates at which these reagents were added to each other, K₂Cr₂O₇ was found to be the most favourable precursor for the crystal growth. (BaCl₂ was added at a rate of 3.4×10^{-7} g/min.) BaCrO₄ crystals grew also in a (NH₄)₂Cr₂O₇ solution at a slower addition of BaCl₂, but they did not grow in K₂CrO₄ solutions under the conditions examined in this study.

ACKNOWLEDGMENTS

We thank V.A. Kuznetsov for his helpful advice in writing the paper.

REFERENCES

1. D. Reinen, W. Rauw, U. Kesper, *et al.*, *J. Alloys Compd.* **246**, 193 (1997).
2. T. C. Brunold, H. U. Gudel, S. Kuck, and G. Huber, *J. Lumin.* **65**, 293 (1996).
3. M. Li, H. Schnablegger, and S. Mann, *Nature* **402**, 393 (1999).
4. A. Lentz, W. Büchele, and H. Suchöllhorn, *Cryst. Res. Technol.* **21** (7), 827 (1986).
5. A. Fernández-González, R. Martín-Díaz, and M. Prieto, *J. Cryst. Growth* **200**, 227 (1999).
6. Sh.-H. Yu, H. Cölfen, and M. Antonietti, *Chem. Eur. J.* **8** (13), 2937 (2002).
7. L. G. Berg, *Priroda*, No. 7, 95 (1957).

Translated by T. Safonova

CRYSTALLOGRAPHIC
SOFTWARE

Structural Analysis by Reduced Data: VI. A New Method for Refining the Parameters of the Model Describing the Absorption of Radiation by a Single-Crystal Specimen

A. P. Dudka

*Shubnikov Institute of Crystallography, Russian Academy of Sciences,
Leninskii pr. 59, Moscow, 119333 Russia*

e-mail: dudka@ns.crys.ras.ru

Received March 23, 2005

Abstract—An approach to the refinement of crystal structures by reduced experimental data is developed. The anisotropic method of intermeasurement minimization is used to refine the parameters determining the absorption of radiation in the cases when some factors are not known with sufficient accuracy: the specimen sizes, the orientation of ellipsoidal specimens, the degree of perfection of spherical specimens, the elemental composition of the unit cell, etc. Spherical and ellipsoidal crystals and crystals in the form of convex polyhedra are considered. © 2005 Pleiades Publishing, Inc.

INTRODUCTION

As is well known, most methods for refining the crystal structure are based on the kinematic diffraction model. Various corrections are introduced to reduce the measurement data to the corresponding scale. In this study, we consider the problem of introduction of a correction for the absorption of radiation by a single-crystal specimen bathing in the primary beam during a diffractometric measurement.

In this approximation, the process of absorption can be mathematically described quite exactly.¹ The value of the correction depends on the following factors: the shape and orientation of a specimen and the value of the linear absorption coefficient (atomic cross sections and the unit-cell chemical composition).

The methods for taking into account the specimen shape can be divided arbitrarily into two groups: calculations and empirical methods. Calculation methods are based on the use of a priori known geometric characteristics of a specimen, while empirical methods use the measured values of integrated intensities. The empirical methods in which the shape of a crystal is described by a model whose parameters are refined by minimization of some functional should be selected into a separate group. The calculation methods are divided into numerical and analytical ones. In this study, elements of both calculation and empirical methods are used.

Calculation methods are proposed for specimens having shapes of a cylinder, sphere, ellipsoid, or convex polyhedron, with known exact external sizes.

For cylindrical and spherical specimens, the techniques proposed in [1–4] are used. The corresponding reference information can be found in the International Tables for Crystallography [5]. It was proposed in [6] to use Gaussian integration to calculate corrections for polyhedral specimens. The use of the Gauss method for ellipsoidal specimens was considered in [7] and this method was developed in [8, 9]. Analytical methods based on the partition of the crystal volume into elementary polyhedra (Howells polyhedra [10, 11]) were applied in [12–17]. The most exact calculation algorithm for the analytical method was found in [18, 19].

In empirical methods, the transmission surfaces are constructed on the basis of different expressions, which relate the integrated intensities and their average values. The azimuthal-scan data can be used in diffractometers of different types: equinclination (proposed by Furnas [20, 21]), Weissenberg [22], and equatorial [23, 24]. Equivalent reflections were taken into account in [25].

The method proposed in [26] describes the model of the specimen shape by Fourier series. In this method, the corresponding coefficients are refined to decrease differences between the integrated intensities of symmetrically related reflections. However, for mathematical convenience, it was proposed in [27] to replace Fourier series by surface harmonics. To this end, normalized spherical harmonics were used in [28]. The harmonic coefficients are refined as parameters in minimization of differences between equivalent reflections, obtained, in particular, by azimuthal scan.

If the shape parameters are refined in minimization of differences between the symmetrically related

¹ The complete literary review and references are accessible from the author.

reflections, the reduction to the absolute scale is performed by introduction of an "equivalent" spherical crystal. This is an evident drawback of minimization methods since it is difficult to determine exactly the radius of such a "crystal" (especially for polyhedral specimens).

Another difficulty is that any method should be stable to correlations between the parameters of all anisotropic effects occurring during the experiment. For example, effects of anisotropic extinction, thermal diffuse scattering (TDS), or simultaneous reflections may compete with the effect of absorption on the reflection intensities. Since the kinematic approximation is considered, the parameters determining all the above-mentioned effects also may undergo correlation distortions. Note that this drawback is most characteristic of purely empirical methods.

The first difficulty can be overcome easily if the shape parameters are optimized in the conventional refinement of a structural model. Such a method, based on the use of Fourier series, was proposed in [29]. This approach was implemented in the DIFABS program [30, 31]. The AREN software also includes the corresponding problem [32]. Unfortunately, in this calculation scheme, along with the extinction parameters, some other parameters (primarily, the scale factor and the thermal parameters) may be involved in the process of correlation distortion. To reduce this negative effect, a particular refinement procedure was proposed however, the efficiency of this procedure has not been established.

The second difficulty, related to the correlations between the parameters of all anisotropic effects, is likely to have no solution (at least, when series are used to describe the specimen shape and one data set).

Generally, the linear absorption coefficient, which is necessary for calculations by any of the above-mentioned methods, is derived from the absorption cross sections of the atoms entering the crystal unit cell. The tables of theoretical cross sections can be found in [5, p. 189]. It was noted in [5] that the differences between the tabular data and the corresponding experimental values are very large. The average value of these differences can be estimated as 2–5%; some deviations may exceed 30%. Therefore, the statement of the problem of refining the values of the cross sections on the basis of the diffraction data seems to be quite justified.

One of the ways to decrease errors in correction of the absorption effect is the method for refining the anisotropic linear absorption coefficient by the experimental azimuthal-rotation data [33]. However, in the kinematic approximation, it is difficult to give a physical interpretation of the anisotropic absorption coefficient.

In some cases, some crystallographic positions are characterized by mixed occupancies. The absorption correction is generally introduced before the exact elemental composition becomes known. Therefore, it is

necessary to perform several processing cycles to fit the absorption coefficient to the refined elemental composition. It would be useful to automate the calculations in this scheme.

The use of different methods for taking into account the radiation absorption showed that the most appropriate structural results can be obtained when the specimen is a sphere or convex polyhedron. In this case, the geometric characteristics of the specimen should be known. The accuracy of empirical methods is insufficient for precise investigations. The methods based on the construction of a multiparameter model of the transmission surface using analytic functions may lead to systematic errors. Thus, the existing methods for taking into account the absorption in a wide range of experimental situations have certain limitations.

It is noteworthy that, when an absorption correction is introduced, it is necessary either to take into account the effect of other anisotropic effects or to establish the absence of the corresponding correlation distortions of the shape parameters of the specimens [34]. The possibility of such an analysis must be provided for the investigation technique itself.

METHOD

The principle of intermeasurement minimization [35] makes it possible to consider the question from more general methodical positions. If some effect (absorption in our case) leads to a difference in the intensities of equivalent reflections, the parameters of the model describing the effect anisotropy should be sought for by minimizing the differences between equivalent reflections. When the model must be reduced to the absolute (kinematic) scale, one has to minimize the conventional model–experiment functional. If some parameters (for example, the specimen sizes, extinction, and the scale factor) reveal a correlation exceeding the allowable level, these parameters must be refined using different experimental data sets. In this case, both the experiment and its processing should be planned so as to provide different data sets. Fortunately, this condition is generally satisfied even in routine investigations. To this end, it is sufficient to carry out measurements in several symmetrically related regions of the reciprocal space. The exception is the crystals with the sp. gr. *P1*.

In this study, we undertook additional measures aimed at decreasing the negative effect of the correlation between parameters in minimization. This concerns both the choice of a model for describing the specimen shape and the choice of the calculation technique. The calculation method based on Gaussian integration [6, 9] is used. On the one hand, this approach makes it possible to process specimens of all three basic forms (sphere, ellipsoid, and polyhedron) in the same way. On the other hand, the models using simple functions (linear or quadratic) to describe the specimen

shape are less flexible than the models using Fourier series or spherical harmonics. This circumstance makes the chosen models inertial and impedes correlations with the parameters of other anisotropic effects. In addition, there arises a unique possibility of visual control of the occurrence of correlation distortions of the shape parameters.

The method is designed to refine the parameters determining the radiation absorption in spherical and ellipsoidal specimens and in specimens shaped as convex polyhedra, when it is desirable to refine some factors determining the radiation absorption: the specimen sizes, the orientation of ellipsoidal specimens, the degree of perfection of spherical specimens, the chemical composition of the unit cell, etc. The software is based on the autonomous version of the program [9], which was introduced into the ASTRA package [36].

As is known [5], the transmission factor A and the inverse quantity—absorption factor A^* —can be written as

$$A = \frac{1}{A^*} = \frac{1}{V} \iiint_V \exp[-\mu T] dV$$

$$= \frac{1}{V(s)} \int \int \exp[-\mu(\sigma, q)T(s, o)] dV.$$

Integration is performed over the specimen volume V , which depends on the shape parameters s . The linear absorption coefficient μ depends on the atomic scattering cross sections σ and the chemical composition of the cell. In other words, only the occupancies q of the atoms in mixed positions can be varied. The sum of the paths of the incident and diffracted rays T before entering and after passing an elementary scattering volume, respectively, depends on the shape parameters s of the specimen and the specimen orientation o . Separation of the parameters describing the specimen orientation into an individual group gives certain advantages in refining the absorption parameters for specimens shaped as ellipsoids or rectangular parallelepipeds. One can fix the sizes of such specimens and refine only their orientation (see APPENDIX).

Let the unaveraged data set (the index nAv) contain N_n reflections ($n = 1, \dots, N_n$), the averaged data set (the index Ave) contain N_a reflections ($a = 1, \dots, N_a$), and the number of equivalent reflections in group a be M_a . We assume that Lorentz and polarization corrections, TDS corrections, and multiple diffraction corrections were introduced into the integrated intensities I . Then, the expression relating the partially corrected measured values $I_{n\text{obs}}$ and the calculated kinematic structure factors F_n has the form

$$I_{n\text{obs}} = A_n(s, o, \sigma, q) k_{nAv} y_n(s, o, \sigma, q) \times |F_n(q, Model)|^2 + \varepsilon_n,$$

where A is the transmission correction; k is the isotropic scale factor; y is the extinction correction, which

depends on all parameters determining the absorption; and ε are errors. The values of $|F_n|^2$ depend on the occupancies q of the atomic positions. All other parameters of the kinematic model are denoted as $Model$.

Thus, in the problem under consideration, we can determine three functionals, which will make it possible to separate the above parameters and avoid very large correlations between them (anisotropic MMM [37]):

$$\Phi_\alpha(s, o, \sigma) = \alpha \sum_{n=1}^{N_n} w_n \left(\frac{A_n^*(s, o, \sigma) I_{n\text{obs}}^{nAv}}{k_{nAv}} - |F_n^{nAv}|^2 \right)^2,$$

$$k_{nAv} = k_{Ave} = \text{const}; \quad q, Model = \text{const},$$

$$\Phi_\delta(s, o, \sigma) = \delta \sum_{n=1}^{N_n} w_{na} (A_n^*(s, o, \sigma) I_{n\text{obs}}^{nAv} - I_{n\text{obs}}^{Ave})^2,$$

$$k_{nAv} \equiv 1; \quad q, Model = \text{const},$$

$$\Phi_{\text{cross}}(Model, k_{Ave}, q)$$

$$= \gamma \sum_{a=1}^{N_a} w_a \left(\frac{I_{a\text{obs}}^{Ave}}{k_{Ave} y_a(q)} - |F_{a\text{calcd}}^{Ave}(q, Model)|^2 \right)^2,$$

$$s, o = \text{const},$$

where I_{obs} are the observed (measured) values; F_{calcd} are the corresponding calculated values; w are the weights of unaveraged reflections; w_a are the weights of averaged reflections; w_{na} are the weights taking into account errors both in the averaged and unaveraged data; and α , γ , and δ are the Lagrange multipliers. The averaged integrated intensity is calculated from the data reduced to absorption:

$$I_{n\text{obs}}^{Ave} = \frac{1}{M_a} \sum_{k=1}^{M_a} A_k^* I_{k\text{obs}}^{nAv}.$$

The number of independent values of $I_{a\text{obs}}^{Ave}$ is equal to N_a ; however, the δ functional contains N_n such values since any unaveraged integrated intensity has a corresponding averaged value. The weights of averaged reflections can be calculated by both the conventional technique used in averaging equivalent reflections and taking into account the Abrahams–Keve test [38]. The functionals Φ_α and Φ_{cross} are classical functionals for the unaveraged and averaged data and Φ_δ is a δ functional. The functionals Φ_α and Φ_δ depend on the same set of parameters and experimental data. Therefore, these functionals can be combined during the refinement.

Calculation of the extinction from Φ_{cross} is performed at fixed shape parameters of the specimen, i.e., at fixed values of its weighted mean absorption lengths, but during variation of the linear absorption coefficient $\mu(\sigma, q)$. If one has to determine if the extinction effect

or the scale factor are anisotropic [34], their parameters should be refined from the δ functional. In the latter case, minimization of Φ_{cross} will be performed at $k_{\text{Ave}} = 1$ and $y_a = 1$ since the extinction contribution from the data will be reduced and the data will be reduced to the absolute scale.

The simplest way is to perform the classical full-matrix refinement of all parameters using an unaveraged data set. As was noted in the Introduction, we are not guaranteed in this case against the negative effect of correlations in the chain shape–extinction–scale–thermal vibrations. The advantages of using the averaged data are also lost. (The relative accuracy of the results is deteriorated.)

The number of calculation schemes arising in the anisotropic intermeasurement minimization is very large even when one data set is used. In this study, we used the following *MMM* scheme. The sum of the functionals $\Phi_\alpha + \Phi_\delta$ of dimension $2N_n$ was used to refine the shape parameters at fixed parameters of the kinematic model. The data reduced to absorption were averaged and only the kinematic model was refined by Φ_{cross} . Then, the procedure was repeated automatically to reach convergence (2–5 cycles). The δ functional Φ_δ is most sensitive to the presence of anisotropy in the integrated intensities of the unaveraged data set. The functional Φ_{cross} provides the highest relative accuracy owing to the averaging of measurements over the ignored factors.

To determine the specimen shape by this method, it is sufficient to have a preliminary structural model and repeat calculations if the model composition changes.

CONCLUSIONS

The method proposed can be used to refine the parameters of any anisotropic effects using a symmetry-averaged data set. The results of the experimental verification will be published in the second part of [34], where, along with the absorption effect, the interdependent effect of anisotropic extinction will be considered briefly.

APPENDIX

REFINEMENT OF THE ORIENTATION OF ELLIPSOIDAL SPECIMENS

The detailed description of the mathematical aspects of the consideration of absorption was given in [9]. There may be a difficulty with determining the matrix of the specimen orientation. Let the specimen be ellipsoidal because the anisotropy of his mechanical properties impedes its shaping into an ideal sphere. In most cases, the ellipsoid axes will be close to the axes of the orthogonal coordinate system of the reciprocal unit cell, determined in [39]. Then, the basic specimen-orientation matrix will coincide with the inverse cell-orientation matrix U^{-1} [40]. Otherwise, the additional rota-

tion should be taken into account. It is proposed to refine the angles of rotation of the ellipsoid axes with respect to the axes of the reciprocal cell, α_x , α_y , and α_z , as parameters since the basic rotation of the cell with respect to the laboratory coordinate system is known exactly. If matrices of separate rotations are set in the form

$$M_x = \begin{pmatrix} 1 & 0 & 0 \\ 0 & \cos \alpha_x & -\sin \alpha_x \\ 0 & \sin \alpha_x & \cos \alpha_x \end{pmatrix},$$

$$M_y = \begin{pmatrix} \cos \alpha_y & 0 & -\sin \alpha_y \\ 0 & 1 & 0 \\ \sin \alpha_y & 0 & \cos \alpha_y \end{pmatrix},$$

$$M_z = \begin{pmatrix} \cos \alpha_z & -\sin \alpha_z & 0 \\ \sin \alpha_z & \cos \alpha_z & 0 \\ 0 & 0 & 1 \end{pmatrix},$$

the general rotation of the specimen shape with respect to the reciprocal cell will be $M = M_z M_y M_x$. The rotation of the ellipsoid with respect to the laboratory coordinate system will be expressed in terms of the matrix $M_{\text{ell}} = MU^{-1}$.

The direction cosines of the primary (S_{pri}) and diffracted (S_{dfr}) beams in the laboratory coordinate system can be calculated before the beginning of the minimization. Then, the desired cosines of the beams in the specimen coordinate system will be

$$S'_{\text{pri}} = M_{\text{ell}} S_{\text{pri}}, \quad S'_{\text{dfr}} = M_{\text{ell}} S_{\text{dfr}}.$$

Thus, the initial data can be set in the form $\alpha_x = \alpha_y = \alpha_z = 0$ with subsequent refinement of the angles α_x , α_y , and α_z .

ACKNOWLEDGMENTS

I am grateful to N.B. Bolotina for supplying the program texts and the help.

REFERENCES

1. C. W. Dwiggin, *Acta Crystallogr. A* **28**, 219 (1972).
2. C. W. Dwiggin, *Acta Crystallogr. A* **31**, 146 (1975).
3. C. W. Dwiggin, *Acta Crystallogr. A* **31**, 395 (1975).
4. H. D. Flack and M. G. Vincent, *Acta Crystallogr. A* **34**, 489 (1978).
5. *International Tables for Crystallography*, Vol. C. (Kluwer, Dordrecht, 1992).
6. W. R. Bussing and H. A. Levy, *Acta Crystallogr.* **10**, 180 (1957).
7. B. J. Wuensch and C. T. Prewitt, *Z. Kristallogr.* **122**, 24 (1965).

8. I. P. Kondratyuk, L. A. Muradyan, and V. I. Simonov, *Kristallografiya* **33**, 318 (1988) [*Sov. Phys. Crystallogr.* **33**, 185 (1988)].
9. N. B. Bolotina and M. I. Sirota, *Kristallografiya* **43**, 557 (1998) [*Crystallogr. Rep.* **43**, 514 (1998)].
10. O. P. Hendershot, *Rev. Sci. Instrum.* **8**, 324 (1937).
11. R. G. Howells, *Acta Crystallogr.* **3**, 366 (1950).
12. M. Wells, *Acta Crystallogr.* **13**, 722 (1960).
13. A. Ferrari, A. Braibanti, and A. Tiripicchio, *Acta Crystallogr.* **18**, 45 (1965).
14. J. De. Meulenaer and H. Tompa, *Acta Crystallogr.* **19**, 1014 (1965).
15. N. W. Alcock, *Acta Crystallogr. A* **25**, 518 (1969).
16. N. W. Alcock, *Acta Crystallogr. A* **26**, 437 (1970).
17. N. W. Alcock, *Acta Crystallogr. A* **30**, 332 (1974).
18. R. C. Clark, *Acta Crystallogr. A* **49**, 692 (1993).
19. R. C. Clark, *Acta Crystallogr. A* **51**, 887 (1995).
20. N. C. Furnas, *Single Crystal Orienter Instruction Manual* (Gen. El. Comp., Milwaukee, 1957).
21. A. C. T. North, D. C. Phillips, and F. S. Mathews, *Acta Crystallogr. A* **24**, 351 (1968).
22. A. Santoro and A. Wlodawer, *Acta Crystallogr. A* **36**, 442 (1980).
23. G. Kopfmann and R. Huber, *Acta Crystallogr. A* **24**, 348 (1968).
24. R. Huber and G. Kopfmann, *Acta Crystallogr. A* **25**, 143 (1969).
25. H. D. Flack, *Acta Crystallogr. A* **30**, 569 (1974).
26. C. Katayama, N. Sakabe, and K. Sakabe, *Acta Crystallogr. A* **28**, 293 (1972).
27. C. Katayama, *Acta Crystallogr. A* **42**, 19 (1986).
28. R. H. Blessing, *Acta Crystallogr. A* **51**, 33 (1995).
29. C. Katayama, N. Sakabe, and K. Sakabe, *Acta Crystallogr. A* **28**, 207 (1972).
30. D. Stuart and N. Walker, *Acta Crystallogr. A* **35**, 925 (1979).
31. N. Walker and D. Stuart, *Acta Crystallogr. A* **39**, 158 (1983).
32. V. I. Andrianov, *Kristallografiya* **32**, 228 (1987) [*Sov. Phys. Crystallogr.* **32**, 130 (1987)].
33. P. J. Rigolt, A. Tomas, and C. Guidi-Morosini, *Acta Crystallogr. A* **35**, 587 (1979).
34. A. P. Dudka, *Kristallografiya* **51** (1) (2006) (to be published).
35. A. P. Dudka, *Kristallografiya* **47**, 156 (2002) [*Crystallogr. Rep.* **47**, 145 (2002)].
36. A. P. Dudka, *Kristallografiya* **47**, 163 (2002) [*Crystallogr. Rep.* **47**, 152 (2002)].
37. A. P. Dudka, *Kristallografiya* **48**, 571 (2003) [*Crystallogr. Rep.* **48**, 524 (2003)].
38. S. C. Abrahams and E. T. Keve, *Acta Crystallogr. A* **27**, 157 (1971).
39. D. M. Kheĭker, *X-ray Diffractometry of Single Crystals* (Mashinostroenie, Leningrad, 1973) [in Russian].
40. W. R. Busing and H. A. Levy, *Acta Crystallogr. A* **22**, 457 (1967).

Translated by Yu. Sin'kov

CRYSTALLOGRAPHIC SYMMETRY

Crystallography of Mendeleev's Periodic Table

R. V. Galiulin* and K. B. Imangazieva**

* Shubnikov Institute of Crystallography, Russian Academy of Sciences,
Leninskiĭ pr. 59, Moscow, 119333 Russia

e-mail: galiulin@ns.crys.ras.ru

** Issyk Kul State University, Karakol, 720044 Kyrgyzstan

Received March 3, 2005

Abstract—Electrons in each atomic orbital (s , p , d , f , and so on) form regular systems on a sphere, which can be easily revealed when constructing Mendeleev's periodic table. Electrons in orbitals (including hybrid orbitals) can be located only at the vertices of isogons: Platonic bodies; Archimedean bodies; and two infinite series of prisms and antiprisms and their affine transforms, which retain the vertex transitivity. Electrons in crystal structures are distributed over isogonal three-dimensional regular systems that are vertices of partitions composed of isogons. © 2005 Pleiades Publishing, Inc.

WHAT DID MENDELEEV DO?

The series of 118 chemical elements with their atomic numbers written in ascending order can be unambiguously divided into seven periods of four different lengths (2, 8, 8, 18, 18, 32, and 32), each of which ends with an inert gas and begins (except for the first period) with an alkali metal. Writing the two last periods one under another, we can see that this double series can be divided into four subperiods with lengths of 2, 14, 10, and 6 elements. In each such subperiod, the elements with related chemical properties will be one under another. These sets of elements are referred to as s , f , d , and p elements, respectively.

The other five periods, on the basis of the chemical relationship with the elements of the last two periods, can be written unambiguously above them and the thus obtained table turns out to be composed of rectangular blocks: s (7 rows, 2 columns), f (2 rows, 14 columns), d (4 rows, 10 columns), and p (6 rows, 6 columns). Apparently, this is all we can say strictly about the periodic table of elements presented on March 1, 1869, by Dmitriĭ Ivanovich Mendeleev (1834–1907), a young professor of chemistry at St. Petersburg University. At that time, only 64 atoms were known, the relationship between atomic numbers and atomic weights had to be violated twice (in the cases of Co, Ni and Te, I), and some numbers (21, 31, 32) had to be omitted. In addition, inert gases and isotopes were unknown then. Indeed, the periodic table of chemical elements could only be seen in a dream at that time. However, the fundamental principle was found: seven periods divided into four blocks with widths of 2, 6, 10, and (later) 14 elements (see table).

These data are quite sufficient to determine the symmetry of an atom. Free atoms in each of these blocks at the lowest energy level are represented, respectively, by

a circle, heptagonal antiprism, pentagonal antiprism, and octahedron. The symmetries of the second and third polyhedra are inconsistent with the symmetries of Euclidean crystals and, in order to enter a crystal, polyhedra should either break the valence electron shells or be crystallized with a non-Euclidean metric. The latter case leads to the formation of nanocrystals.

SHOULD THE TABLE BE DIVIDED INTO GROUPS (8, 18, 32)?

Thus, Mendeleev's periodic table began with the version that is now referred to as superlong. Then, its complication began, which some researchers (for example, [1]) believe not to be justified always. Therefore, in 1989, the International Union of Pure and Applied Chemistry excluded the short form of the periodic table from the educational literature, replacing it by the long form, in which the f block is excluded from the table framework, whereas the table is divided into 18 groups (in the literature published in Russia, the periodic table is still divided into 8 groups). Indeed, many problems related to the periodic table do not require such detailed division of the elements (into 8, 18, and, all the more, 32 groups) at the first stages of working with the table. It is much more important and simpler to divide the table into four blocks (s , p , d , and f), which is generally done by coloring the table in four colors.

In addition, the atomic weight of an element can be replaced by a number of neutrons in the most widespread stable isotope of this element [2], which, in the overwhelming majority of cases, simplifies calculation significantly and makes it absolutely exact for the 22 elements that have only one stable isotope: Be, Al, P, Na, Sc, Ti, Mn, Co, As, Nb, Rh, I, Cs, La, Pr, Tb, Ho,

Crystallographic version of Mendeleev's periodic table

I	1 H $1s^1$ 0	2 He $1s^2$ 2	Elements with spherical symmetry																									
	3 Li $2s^1$ 4	4 Be $2s^2$ 5	<div style="border: 1px dashed black; padding: 10px; width: fit-content; margin: auto;"> <table style="border-collapse: collapse;"> <tr> <td style="border: 1px solid black; padding: 5px; text-align: center;">25</td> <td style="padding: 5px;">→</td> <td style="padding: 5px;">number of protons</td> </tr> <tr> <td style="border: 1px solid black; padding: 5px; text-align: center;">Mn</td> <td style="padding: 5px;">→</td> <td style="padding: 5px;">symbol of chemical element</td> </tr> <tr> <td style="border: 1px solid black; padding: 5px; text-align: center;">$3d^54s^2$</td> <td style="padding: 5px;">→</td> <td style="padding: 5px;">electronic formula</td> </tr> <tr> <td style="border: 1px solid black; padding: 5px; text-align: center;">30</td> <td style="padding: 5px;">→</td> <td style="padding: 5px;">number of neutrons in the most wide-spread natural isotope</td> </tr> </table> </div>														25	→	number of protons	Mn	→	symbol of chemical element	$3d^54s^2$	→	electronic formula	30	→	number of neutrons in the most wide-spread natural isotope
	25	→	number of protons																									
	Mn	→	symbol of chemical element																									
	$3d^54s^2$	→	electronic formula																									
30	→	number of neutrons in the most wide-spread natural isotope																										
11 Na $3s^1$ 12	12 Mg $3s^2$ 12																											
19 K $4s^1$ 20	20 Ca $4s^2$ 20																											
37 Rb $5s^1$ 49	38 Sr $5s^2$ 50	Elements with sevenfold symmetry																										
VI	55 Cs $6s^1$ 78	56 Ba $6s^2$ 82	57 La $5d^16s^2$ 82	58 Ce $4f^15d^16s^2$ 82	59 Pr $4f^36s^2$ 82	60 Nd $4f^46s^2$ 82	61 Pm $4f^56s^2$	62 Sm $4f^66s^2$ 90	63 Eu $4f^76s^2$ 90	64 Gd $4f^75d^16s^2$ 94	65 Tb $4f^96s^2$ 94	66 Dy $4f^{10}6s^2$ 98	67 Ho $4f^{11}6s^2$ 98	68 Er $4f^{12}6s^2$ 98	69 Tm $4f^{13}6s^2$ 100	70 Yb $4f^{14}6s^2$ 104												
VII	87 Fr $7s^1$	88 Ra $7s^2$	89 Ac $6d^17s^2$	90 Th $6d^27s^2$	91 Pa $5f^26d^17s^2$	92 U $5f^36d^17s^2$	93 Np $5f^46d^17s^2$	94 Pu $5f^67s^2$	95 Am $5f^76s^2$	96 Cm $5f^76d^17s^2$	97 Bk $5f^86d^17s^2$	98 Cf $5f^{10}7s^2$	99 Es $5f^{11}7s^2$	100 Fm $5f^{12}7s^2$	101 Md $5f^{13}7s^2$	102 No $5f^{14}7s^2$												

Table (Contd.)

Elements with fivefold symmetry										Elements with threefold symmetry					
										5	6	7	8	9	10
										B $2s^2 2p^1$ 6	C $2s^2 2p^2$ 6	N $2s^2 2p^3$ 7	O $2s^2 2p^4$ 8	F $2s^2 2p^5$ 10	Ne $2s^2 2p^6$ 10
										13	14	15	16	17	18
										Al $3s^2 3p^1$ 14	Si $3s^2 3p^2$ 14	P $3s^2 3p^3$ 16	S $3s^2 3p^4$ 16	Cl $3s^2 3p^5$ 18	Ar $3s^2 3p^6$ 22
21 Sc $3d^1 4s^2$ 24	22 Ti $3d^2 4s^2$ 26	23 V $3d^3 4s^2$ 28	24 Cr $3d^5 4s^1$ 28	25 Mn $3d^5 4s^2$ 30	26 Fe $3d^6 4s^2$ 30	27 Co $3d^7 4s^2$ 32	28 Ni $3d^8 4s^2$ 32	29 Cu $3d^{10} 4s^1$ 34	30 Zn $3d^{10} 4s^2$ 34	31 Ga $4s^2 4p^1$ 38	32 Ge $4s^2 4p^2$ 42	33 As $4s^2 4p^3$ 42	34 Se $4s^2 4p^4$ 46	35 Br $4s^2 4p^5$ 46	36 Kr $4s^2 4p^6$ 48
39 Y $4d^1 5s^2$ 50	40 Zr $4d^2 5s^2$ 50	41 Nb $4d^4 5s^1$ 52	42 Mo $4d^5 5s^1$ 56	43 Tc $4d^5 5s^2$	44 Ru $4d^7 5s^1$ 58	45 Rh $4d^8 5s^1$ 58	46 Pd $4d^{10} 5s^0$ 60	47 Ag $4d^{10} 5s^1$ 60	48 Cd $4d^{10} 5s^2$ 66	49 In $5s^2 5p^1$	50 Sn $5s^2 5p^2$ 70	51 Sb $5s^2 5p^3$ 70	52 Te $5s^2 5p^4$ 74	53 I $5s^2 5p^5$ 74	54 Xe $5s^2 5p^6$ 78
71 Lu $4f^{14} 5d^1 6s^2$ 104	72 Hf $5d^2 6s^2$ 104	73 Ta $5d^3 6s^2$ 108	74 W $5d^4 6s^2$ 110	75 Re $5d^5 6s^2$ 110	76 Os $5d^6 6s^2$ 112	77 Ir $5d^7 6s^2$ 116	78 Pt $5d^9 6s^1$ 116	79 Au $5d^{10} 6s^1$ 118	80 Hg $5d^{10} 6s^2$ 122	81 Tl $6s^2 6p^1$ 124	82 Pb $6s^2 6p^2$ 126	83 Bi $6s^2 6p^3$ 126	84 Po $6s^2 6p^4$	85 At $6s^2 6p^5$	86 Rn $6s^2 6p^6$
103 Lr $5f^{14} 6d^1 7s^2$	104 Rf $6d^2 7s^2$	105 Db $6d^3 7s^2$	106 Sg $6d^4 7s^2$	107 Bh $6d^5 7s^2$	108 Hs $6d^6 7s^2$	109 Mt $6d^7 7s^2$	110	111	112	113	114 Fl	115	116	117	118

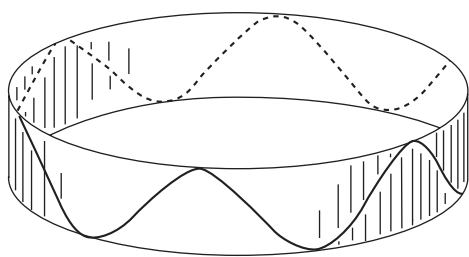


Fig. 1. Relationship between a de Broglie wave and an antiprism.

Tm, Lu, Ta, Au, and Bi. Some problems can now be solved at the level of integers (the mass number of an element as the sum of protons and neutrons of its nucleus) and, what is more, at the more/less level (the rank formula of the composition [3]). The order of filling of orbitals by electrons is completely set by their electronic formula, which is also given for each element of the table. This approach removes the ambiguity that arises in determining the position of lanthanum (*d* or *f*) [4, 5]. However, the main essence of this replacement is that Mendeleev's periodic table, owing to the indication of the number of neutrons in the stable isotope, becomes more attractive for studying the crystallography of the atomic nucleus [6]. This is a direct way to the investigation of atomic nuclei. For this reason, in the table proposed, the atomic masses of elements are replaced by the numbers of neutrons in the corresponding isotopes that are the most widespread in nature.

The division of Mendeleev's periodic table into four blocks, which was carried out at the very beginning of spectroscopic investigations [7], reveals a very deep physical concept related to the representation of an electron as a particle and the relationship between this representation and the wave approach. An electron in an atom forms a standing wave, which can be modeled by the edge grid of an antiprism (Fig. 1) with equal edges and an oddfold axis: (1, 3, 5, 7, ...) [8]. For *s*, *p*, *d*, and *f* electrons, this model will be, respectively, a segment (Fig. 2a), an octahedron (Fig. 2b), a pentagonal antiprism (Fig. 2c), and a heptagonal antiprism

(Fig. 2d). Such representation of orbitals leads to Fedorov isogons.

FEDOROV'S SUGGESTION

In 1880, the manuscript by Evgraf Stepanovich Fedorov, a prominent crystallographer and geometer, under the title "An Attempt to Describe Atomic Weights by a General Law" was given to Mendeleev. (History is silent about this event.) Seventy five years later, this manuscript was found by Shchukarev and Dobrotin in Mendeleev's archives and published in the collected works devoted to the 100th anniversary of the birth of Academician Fedorov (1853–1919) [9]. Commenting on this paper, Shchukarev and Dobrotin are inclined to believe that Fedorov's concept about the existence of close packing of particles in an atom is related to atomic nuclei rather than atoms themselves [10], having focused their attention on the idea of closest packings, which was developed in detail by the prominent crystallographer Belov (1891–1982) [11]. However, Fedorov's paper begins with the words "mankind seeks regularity always and everywhere," which could be a leading idea for all his creative activity [12]. The well-known Fedorov groups (not "so-called" [13] but discrete groups of motions of the Euclidean space with a finite independent region) are the brightest example of regularity which nature obeyed by arranging atoms in crystal structures according to the laws of these groups. Fedorov groups became a strict criterion for distinguishing crystal structures from all other atomic aggregates.

However, regular closest packings are a particular case of the manifestation of regularity. Let us cite some passages from Fedorov's work, which show that his understanding of regularity was wider and included the regularity of individual atoms [9]:

"Atoms, in turn, consist of particles even more elementary (and, at the same time, identical) ..., the surface of an atom is the most important chemical agent, determining the proceeding of a chemical reaction ..., small bodies forming an atom are spaced, like planets, at rather large distances rather than close to each other ..."

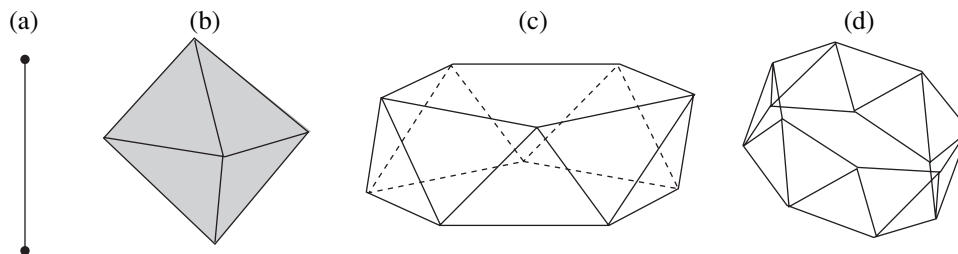


Fig. 2. Figures representing the *s*, *p*, *d*, and *f* orbitals: (a) segment, (b) octahedron, (c) pentagonal antiprism, and (d) heptagonal antiprism.

a system can be sufficiently stable not at any number of such small bodies”

Hence, the discovery of an electron could be attributed to Fedorov, actually, in accordance with his claim [14].

Adding Fedorov's supreme understanding of regularity to the above-said, it can be concluded easily that electrons should be arranged regularly. If it is asked whether it is possible to derive the regularity of electron arrangement from Mendeleev's periodic table, we should say yes. The above-noted isogons are specifically regular representations of atomic orbitals.

ELECTRON ORBITALS—REGULAR SYSTEMS OF POINTS ON A SPHERE

The main specific feature of atoms in each of four blocks is that their electron shells contain the same number of vacancies: 2, 6, 10, and 14 (in the *s*, *p*, *d*, and *f* orbitals, respectively). The vacancies are identical in each of these orbitals. Therefore, they form regular systems on a sphere. Each such regular system is a set of the vertices of an isogon—polyhedron, all vertices of which are equivalent in the group of its symmetry. Such polyhedra are Platonic bodies; Archimedean bodies; two infinite series of prisms and antiprisms; and their affine transforms, retaining transitivity of the vertices. Figure 3 contains all combinatorially different isogons, which are presented by their most symmetric representatives. Electrons on a sphere can reach a stable state being located only at the vertices of these polyhedra [15] (in contrast to [16]). Generally, a system of identical particles will be stable only when these particles form a regular system of points (on a sphere, in Euclidean space, and in Lobachevsky space, i.e., in all spaces of constant curvature). All vertices of these isogons are occupied equiprobably by electrons, independent of their number in this orbital. The configuration of these orbitals can be repeated in molecules.

An individual atom or an aggregate of atoms is most stable when all its orbitals are filled (filled orbitals are closed into compact locally Euclidean varieties, which are self-sufficient and, in the ideal case, do not affect other orbitals) and the *p* orbital is the last one. Such properties are typical of inert gases. Hybridization (aggregation) of orbitals and their decay are also shown in Fig. 3. For example, association of an *s* orbital with a *d* orbital gives rise to an icosahedral orbital, while a *d* orbital may decay into a *p* orbital (a regular octahedron) and a regular tetrahedron [17].

At the atomic level, this model can be justified physically by the words of the prominent physicist Richard Feynman (1918–1988): “if the arrangement of atoms in some place corresponds to the lowest energy, this arrangement will be repeated by atoms in some other

place” [18]. However, the existence of groups cannot be derived directly from this consideration. To implement them physically, these finite arrangements must have the property of the so-called unambiguous reconstruction [19].

The orbitals of Rydberg atoms (i.e., atoms with excited electron shells [20]) of large periods can only be prisms and antiprisms with a large number of vertices (Fig. 4).

NONCRYSTALLOGRAPHIC ORBITALS

Note that the polyhedra modeling *d* and *f* orbitals have noncrystallographic symmetry. Therefore, atoms with unfilled *d* and *f* orbitals cannot directly enter a crystal. For this reason, the corresponding chemical elements are rare and trace. To enter a crystal growing in Euclidean space, such atoms must reconstruct or destroy the electron shells with noncrystallographic symmetry. (There may be even two such shells, for example, in the uranium atom.) At the same time, other spaces of constant curvature (spherical and hyperbolic) allow for the existence of crystals with such atomic symmetry. A striking example is fullerene C₆₀—a spherical crystal shaped as a truncated icosahedron (see Fig. 3). However, fullerene is a slightly deformed Archimedean body since it has bonds of two types: single and double. All three geometries of the spaces of constant curvature are Euclidean in small scale. Therefore, nanocrystals can have any geometry. For example, carbon can form not only regular hexagonal nets (graphite) but also heptagonal ones [21]. The latter regularly divide the Lobachevsky plane, which cannot be inserted into a 3D Euclidean space [22]. Therefore, when such a net becomes sufficiently large in size, it is divided into nanocrystals. For example, dolomite powder arises [23].

In this year, we celebrate the 100th anniversary of the theory of relativity. The essence of this theory is that as a result of some physical phenomena space acquires negative curvature (becomes a hyperbolic space, which was discovered in 1826 by N.I. Lobachevsky (1792–1856)). The growth of crystals from *f* atoms can be considered a possible reason for the occurrence of negative curvature. “During the growth, crystals change the curvature of space,” was noted by the discoverer of long-range order in plasma, A.A. Vlasov (1908–1975) [24].

THE FUNDAMENTAL THEOREM OF DISCRETE PLANE GEOMETRY

To derive all different isogons (regular graphs on a sphere), as well as regular graphs and regular tilings on a plane, the generalized Euler's formula is used. Let a graph be located on a plane or on a sphere. We will define the face formed by the graph on the plane (sphere) as follows: a set of all points of the plane (sphere) that can be reached from a particular point of this plane (sphere), which does not coincide with any

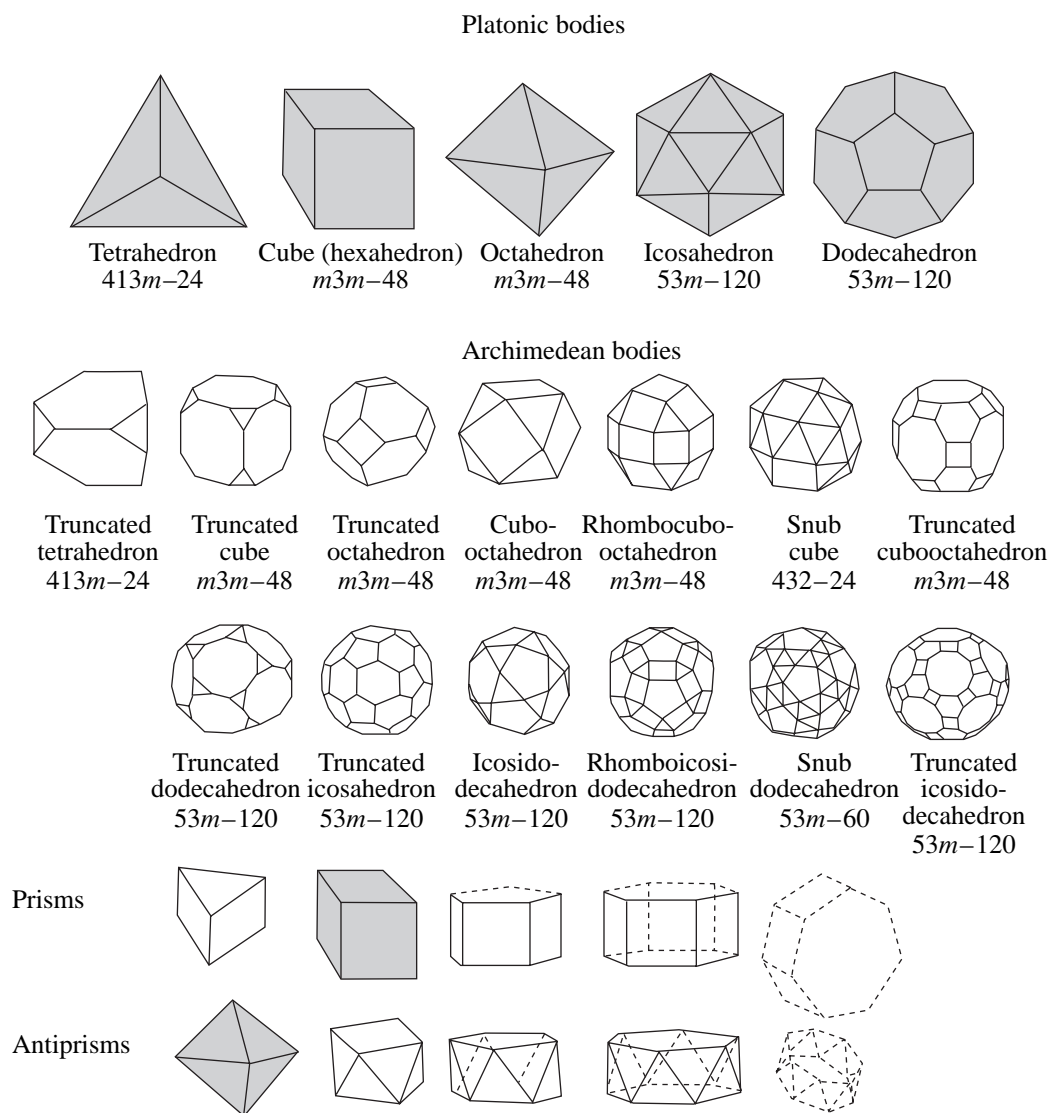


Fig. 3. Isogons representing all allowable orbitals and all their hybridizations.

graph vertex and does not lie on any graph edge, by the path lying in the plane (on the sphere) and passing through neither vertex and intersecting neither edge.

*Formulation of the Fundamental Theorem
of Discrete Plane Geometry*

If a graph has F faces, V vertices, E edges and C components, the following relation holds true: $V - E + F = C + 1$ [25].

Proof. Let us remove edges of the graph one by one, leaving vertices at its ends. The formula is retained. In the end, we have only vertices (components) and one face; i.e., the entire plane excluding these vertices. Therefore, $V + 1 = C + 1$, which is true because $V = C$.

Restoring all edges in reverse order one by one, we find that the initial parts are also equal to each other.

If we project a convex polyhedron on a sphere with a center lying in the polyhedron, the set of its vertices and edges will yield a graph on the sphere, composed of one component; i.e., $V - E + F = 2$. For isohedra, Euler's formula can be written as

$$F - F \cdot k / 2 + F(1/\alpha_1 + 1/\alpha_2 + \dots + 1/\alpha_k) = 2,$$

where k is the number of edges in a face (each edge belongs to two faces); $\alpha_1, \alpha_2, \dots, \alpha_k$ are the numbers of edges convergent in each vertex; and $1 - k/2 + 1/\alpha_1 + 1/\alpha_2 + \dots + 1/\alpha_k = 2/F$, $2 < k < 6$.

All solutions to Euler's formula for isogons

$$V - V \cdot k / 2 + V(1/\alpha_1 + 1/\alpha_2 + \dots + 1/\alpha_k) = 2,$$

where k is the number of edges corresponding to a vertex; $\alpha_1, \alpha_2, \dots, \alpha_k$ are the numbers of vertices in each of the k faces convergent in one vertex; and $3 \leq k \leq 6$, are represented in the form of polyhedra (see Fig. 3).

Euler's formula for regular tilings on a Euclidean plane can be written as

$$1/\alpha_1 + 1/\alpha_2 + \dots + 1/\alpha_k = k/2 - 1,$$

where k is the number of sides of a polygon; $\alpha_1, \alpha_2, \dots, \alpha_k$ are the numbers of polygons convergent in each of k vertices of a polygon (tile); and $3 \leq k \leq 6$.

Euler's formula for regular isogonal nets has the form

$$(1/\alpha_1 + 1/\alpha_2 + \dots + 1/\alpha_k) = k/2 - 1,$$

where k is the number of edges convergent in one vertex; $\alpha_1, \alpha_2, \dots, \alpha_k$ are the numbers of edges in each of k polygons convergent in one vertex; and $3 \leq k \leq 6$. There are 11 such combinatorially different nets [Fig. 1 in 12]. They were introduced for the first time by the founder of the Institute of Crystallography, A.V. Shubnikov (1887–1970), for simulation of crystal growth. Euler's formula for a hyperbolic plane has the form $V - E + F < 0$. It can be easily seen from this formula that the number of Fuchsian groups is infinitely large since a hyperbolic plane can be partitioned regularly by any regular polygon, even by an infinite number of different ways. The generalized Euler's formula for spheres with holes is $V - E + F \geq 2$.

Three-dimensional (although incomplete) analogs of Shubnikov nets are Andreini partitions [26, table]. Atoms arranged in a regular Andreini system can be considered an infinite orbital for electrons (band). A filled band is a plasma crystal composed of electrons [27]. The rules for filling such bands were reported in [28]. The fundamental importance of Mendeleev's diagonal rows in studying isomorphism was also shown in [28]. The probabilistic methods for studying isomorphism were described in [29].

NANOCRYSTALS

Matching of equivalent points at the boundaries of independent regions of Fedorov groups leads to compact locally Euclidean varieties (torus, Klein bottle, Mobius band, etc.). This matching has not only mathematical [30, 31] but also physical meaning [32]. The above-considered atomic orbitals have such a nature. Hence, each atom can be represented by compact locally Euclidean varieties of those Fedorov groups in which it can be crystallized. When an object is closed into a compact locally Euclidean variety, it is no more related to the entire surrounding world, becomes self-sufficient, and has no surface; i.e., in some sense, it disappears. Filled atomic orbitals do not interact with each other. Such orbitals exist in nanocrystals [33], and the

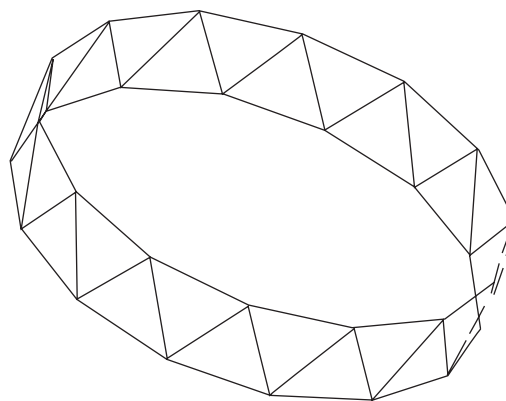


Fig. 4. Rydberg atoms.

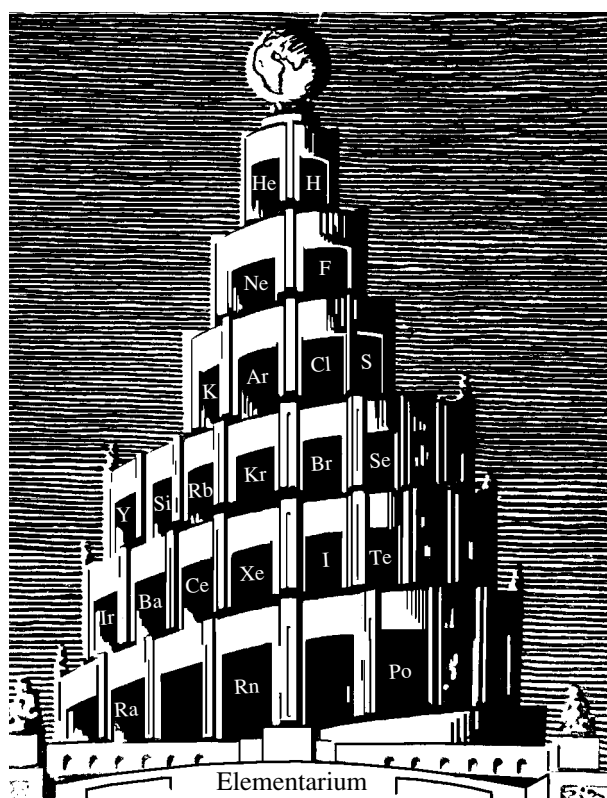


Fig. 5. Spiral Mendeleev's periodic table.

absence of interaction is the reason for their superfluidity. Note that, if the groups generated by reflections, are excluded an independent region of a group can be chosen by many different ways. However, the variety is recovered unambiguously from the independent region, no matter how it was chosen.

The formation of nanocrystals satisfies the tendency of atoms to be regular and form finite sets. Linear atomic chains (one-dimensional (1D) linear crystals) always tend to decay into rings (1D spherical crystals).

For example, soot is formed from carbines in such a way. Nanocrystals obey both the Shubnikov topological theorem [34] and the Shubnikov crystallochemical law [35, 36].

THE HEURISTIC ROLE OF CRYSTALLOGRAPHY IN MODERN SCIENCE

The model of the universe in the form of a crystallographic variety was proposed by Poincaré [37]. It is possible that this idea, as well as some others (Fuchsian groups, Lorentz groups, etc.) came to Poincaré owing to the comprehensive crystallographic education he received at the Mining Institute [38]. The prominent geometer B.N. Delone (1890–1980) also studied a complete course of crystallography (including laboratory practice and expeditions) in the Mining Institute, while he was a professor of mathematics at Leningrad University. His pupil D.K. Faddeev (1908–1989), a well-known expert in algebra, gave a special course of mathematical crystallography for many years at the same institute. Faddeev's tables of representations of Fedorov groups [39] are most appropriate for the problems related to the prediction of structures of crystals from given electron formulas of the atoms entering these crystals. Note that the spiral form of Mendeleev's periodic table [40] (Fig. 5) was proposed by the professor of mechanics N.B. Delone, father of B.N. Delone.

Contemporaries of the great scientist Louis Pasteur (1822–1895) believed crystallography to be science of all sciences. Therefore, the relationship between crystallography and Mendeleev's periodic table is not accidental. B.N. Delone in his paper "Fedorov as a Geometer" [41] noted that the greatest representatives of exact natural sciences in Russia were Lobachevsky, Mendeleev, and Fedorov. Mendeleev's periodic table is a kind of synthesis of prominent achievements of not only these researchers but all mankind.

REFERENCES

1. R. S. Saifullin and A. R. Saifullin, *Khimiya i Zhizn'*, No. 13, 14 (2003).
2. I. P. Selinov, *Structure and Systematics of Atomic Nuclei* (Nauka, Moscow, 1990) [in Russian].
3. T. G. Petrov, *Zap. Vses. Mineral. O-va* **114** (4), 489 (1985).
4. E. I. Semenov, *Dokl. Akad. Nauk SSSR* **231** (2) (1976).
5. A. A. Marakushev, N. M. Gavrilov, and S. A. Marakushev, *Dokl. Akad. Nauk* **397** (5), 664 (2004).
6. M. M. Protod'yakonov and I. L. Gerlovin, *Electronic Structure and Physical Properties of Crystals* (Nauka, Moscow, 1975) [in Russian].
7. J. B. Marion, *Physics and Physical Universe* (Mir, Moscow, 1975) [in Russian].
8. *Physics*, Ed. by A. S. Akhmatov (Nauka, Moscow, 1965), p. 805 [in Russian].
9. E. S. Fedorov, *Kristallografiya* (Leningr. Gorn. Inst., Leningrad, 1955), No. 3, p. 85 [in Russian].
10. S. A. Shchukarev and R. B. Dobrotin, *Kristallografiya* (Leningr. Gorn. Inst., Leningrad, 1955), No. 3, p. 81 [in Russian].
11. N. V. Belov, *Structure of Ionic Crystals and Metal Phases* (Akad. Nauk SSSR, Moscow, 1947) [in Russian].
12. R. V. Galiulin, *Kristallografiya* **48** (6), 965 (2003) [*Crystallogr. Rep.* **48**, 899 (2003)].
13. A. A. Boyarchuk and L. V. Keldysh, *Usp. Fiz. Nauk* **169** (12), 1289 (1999) [*Phys. Usp.* **42**, 1183 (1999)].
14. E. S. Fedorov, *Scientific Heritage* (Nauka, Moscow, 1991), Vol. 16, p. 168 [in Russian].
15. R. V. Galiulin, *Usp. Fiz. Nauk* **172** (2), 229 (2002) [*Phys. Usp.* **45**, 221 (2002)].
16. A. M. Lifshits and Yu. G. Lozovik, *Kristallografiya* **47** (2), 214 (2002) [*Crystallogr. Rep.* **47**, 179 (2002)].
17. T. F. Veremeichik and R. V. Galiulin, *Kristallografiya* **49** (5), 935 (2004) [*Crystallogr. Rep.* **49**, 847 (2004)].
18. R. P. Feynman, R. B. Leighton, and M. Sands, *The Feynman Lectures on Physics* (Addison-Wesley, Reading, Mass., 1966; Mir, Moscow, 1977), Vol. 7.
19. R. V. Galiulin, *Zh. Vychisl. Mat. Mat. Fiz.* **43** (6), 791 (2003).
20. N. B. Delone, *Soros Educational Journal*, No. 4, 64 (1998).
21. R. V. Galiulin, *Materialovedenie*, No. 6, 2 (1999).
22. É. G. Pozdnyak and A. G. Popov, *Sinus-Gordon Equation: Geometry and Physics* (Znanie, Moscow, 1991) [in Russian].
23. M. S. Pichugin, Yu. A. Kharitonov, and N. V. Belov, *Zap. Vses. Mineral. O-va* **498**, 55 (1969).
24. L. S. Kuz'menkov, in *Processes of Real Crystal Formation*, Ed. by N. V. Belov (Nauka, Moscow, 1977) [in Russian].
25. R. V. Galiulin, *Crystallographic Geometry* (Nauka, Moscow, 1984) [in Russian].
26. R. V. Galiulin, *Kristallografiya* **43** (2), 366 (1998) [*Crystallogr. Rep.* **43**, 332 (1998)].
27. V. E. Fortov, A. G. Khrapak, S. A. Khrapak, *et al.*, *Usp. Fiz. Nauk* **174** (5), 495 (2004).
28. N. V. Belov, *Essays on Structural Mineralogy* (Nedra, Moscow, 1976) [in Russian].
29. E. V. Kolonichenko, *Atlas of Probable Isomorphic Substitutions of Basic Elements* (Ukhta, 2000).
30. V. V. Nikulin and I. R. Shafarevich, *Geometries and Groups* (Nauka, Moscow, 1983) [in Russian].
31. A. T. Fomenko, *Visual Geometry and Topology* (Mosk. Gos. Univ., Moscow, 1998) [in Russian].
32. *Crystalline Mobius Sheet*, *Usp. Fiz. Nauk* **172** (7) (2002) (Internet News).

33. R. V. Galiulin, in *Proceedings of the XI All-Russia Conference on Crystal Growth, Moscow, December, 2004* (Inst. of Crystallography, Moscow, 2004).
34. A. V. Shubnikov, *Izv. Ros. Akad. Nauk, Ser. 6* **16** (1-18), 515 (1922).
35. A. V. Shubnikov, *Izv. Imp. Akad. Nauk, Ser. 6* **10** (9), 755 (1916).
36. R. V. Galiulin and V. R. Khachaturov, in *Mathematical Modeling of Compositional Objects* (Vychisl. Tsentr RAN, Moscow, 1994), p. 31 [in Russian].
37. G. Collins, *World of Science*, No. 10, 52 (2004).
38. A. Tyapkin and A. Shibanov, *Puankare* (Molodaya Gvardiya, Moscow, 1979).
39. D. K. Faddeev, *Tables of the Principal Unitary Representations of the Fedorov Groups* (Akad. Nauk SSSR, Moscow, 1961; Pergamon, New York, 1964).
40. A. E. Fersman, *Geochemistry Can Be Fun* (Prosveshchenie, Moscow, 1948) [in Russian].
41. B. N. Delone, *Tr. Inst. Istor. Estestvozn. Tekh. Akad. Nauk SSSR* **10**, 5 (1953).

Translated by Yu. Sin'kov

STRUCTURE OF INORGANIC COMPOUNDS

Crystal Structure of Celadonite from the Electron Diffraction Data

A. P. Zhukhlistov

Institute of Geology of Ore Deposits, Petrography, Mineralogy, and Geochemistry, Russian Academy of Sciences,
Staromonetnyĭ per. 35, Moscow, 119017 Russia

e-mail: anzhu@igem.ru

Received March 14, 2005

Abstract—The crystal structure of the dioctahedral celadonite mica *1M* (space group $C2/m$; R , 2.98%; 184 unique reflections) is refined from the oblique-texture electron diffraction patterns obtained with the use of imaging plates. The maximum characterizing the location and potential of the hydrogen atom of the hydroxyl group oriented into the unoccupied *trans* octahedron at an angle of 4.4° with respect to the *ab* plane is revealed from the difference Fourier-potential syntheses. The O–H interatomic distance is equal to 0.98 Å. The superstructure reflections observed in the selected-area electron diffraction patterns for a number of particles arise from the superposition of two cells, namely, the main cell with a broken base-centered symmetry and the base-centered supercell with the triple parameter *a*. These reflections are caused by the ordered distribution of the trivalent and divalent cations Fe and Mg over the octahedral *cis* positions. © 2005 Pleiades Publishing, Inc.

INTRODUCTION

Celadonites belong to dioctahedral potassium micas in which the octahedral positions 2 : 1 in layers are almost equally occupied by trivalent and divalent cations with a predominance of the Fe^{3+} cations among the octahedral cations. Celadonite has the ideal crystal chemical formula $K(Fe^{3+}, Al)(Mg, Fe^{2+})Si_4O_{10}(OH)_2$. Upon limited replacements of Si by Al in the tetrahedra, the layer charge is determined by the content of divalent cations in the octahedra.

Structural investigations of celadonite have been carried out only by electron diffraction methods because of the finely dispersed form of the celadonite samples. Zvyagin [1] was the first to perform an electron diffraction study of celadonite of the polytypic modification *1M* (Pobuzh'e, Ukraine). More accurate structural data were obtained for the celadonite *1M* from the Krivorozhskii iron-ore basin (Ukraine) [2]. The parameters of the base-centered monoclinic cell of celadonite with the crystal chemical formula $(K_{0.83}Na_{0.01}Ca_{0.04})(Fe_{1.15}^{3+}Fe_{0.36}^{2+}Mg_{0.41}Al_{0.05})Ti_{0.01} \cdot (Si_{3.94}Al_{0.06})O_{10}(OH)_2$ are as follows: $a = 5.23$ Å, $b = 9.05_5$ Å, $c = 10.15$ Å, and $\beta = 100^\circ 35'$. According to the ratio $Mg/(Mg + Fe^{2+}) = 0.53$, the sample studied is similar to ferroceldonite [3]. The use of the oblique-texture electron diffraction patterns recorded with a high-voltage electron diffraction camera, as well as the visual evaluation of the intensities in micrographs with multiple exposures, made it possible to determine the statistical distribution of the octahedral cations over the *cis* positions in the celadonite structure (space group $C2/m$, $R = 10.8\%$); the average interatomic distances

$M-O = 2.04_5$ Å, $T-O = 1.63_5$ Å, and $K-O = 3.07_5$ Å; and the angles of ditrigonal rotation of the octahedron bases $\varphi = 2.3^\circ$ and tetrahedron bases $\psi = 1.3^\circ$ [2].

Using the electrometric recording of the intensities of reflections in the oblique-texture electron diffraction patterns, Tsipurskiĭ and Drits [4] refined the structure of the celadonite *1M* from Zaval'e (Pobuzh'e, Ukraine). It was found that this celadonite has a structure with the parameters of the base-centered monoclinic cell $a = 5.223$ Å, $b = 9.047$ Å, $c = 10.197$ Å, and $\beta = 100.43^\circ$ and the crystal chemical formula $(K_{0.89}Ca_{0.10})(Fe_{0.90}^{3+}Fe_{0.32}^{2+}Mg_{0.73}Al_{0.05})(Si_{3.94}Al_{0.06})O_{10}(OH)_2$ ($R = 5.1\%$). The revealed lowering of the symmetry to $C2$ was explained by the predominant location of Fe^{3+} cations in one of the two nonequivalent *cis* octahedra. The average interatomic distances are as follows: $M-O = 2.027$ and 2.060 Å, $T-O = 1.616$ and 1.618 Å, and $K-O = 3.103$ Å. The angle of ditrigonal rotation of the octahedron bases is equal to 0.54° , and the angles of ditrigonal rotation of the tetrahedron bases are 3.9° and 1.3° . The hydrogen atom inside the empty *trans* octahedron (the angle between the O–H bond and the layer plane is 14°) was located from the difference Fourier-potential syntheses. The O–H interatomic distance is 0.8 Å.

In this respect, it was of special interest to refine the celadonite structure from the oblique-texture electron diffraction patterns obtained with imaging plates. Experience on the application of digital imaging plates (DITABIS, Germany) in the study of layered minerals has opened up strong possibilities for their use in electron diffraction investigations. Owing to the wide dynamic range and the linearity of signal transmission,

all intensities of the reflections observed in the oblique-texture electron diffraction pattern can be recorded with the use of only one imaging plate [5]. The refinement of the crystal structure of brucite $\text{Mg}(\text{OH})_2$ ($R = 3.4\%$) from the oblique-texture electron diffraction patterns made it possible to reveal fine features in the brucite structure, such as the statistical distribution of hydrogen atoms over three positions located around the threefold axes, and clearly demonstrated the efficiency of using imaging plates in electron diffraction structure analysis, specifically in the study of hydroxyl-containing minerals [5].

EXPERIMENTAL TECHNIQUE

The structure of the previously studied celadonite sample from Krivoř Rog [2] was refined from the digital oblique-texture electron diffraction patterns measured using a high-voltage electron diffraction camera with imaging plates (resolution, 25 μm) and a DITABIS laser scanner. The intensities of diffraction reflections were estimated from the radial intensity distribution profiles obtained with the MICRON program package (DITABIS) [5]. The reflection profiles were approximated according to the Gaussian–Lorentzian Sum (Area) formula after subtracting the background (the PeakFit program). The intensities of the diffraction reflections were determined as the areas under the approximating curves. Partially overlapped or closely spaced reflections were separated using the profile analysis. The intensities of the reflections coinciding in the oblique-texture electron diffraction patterns were determined under the assumption that they are proportional to the corresponding values $IF_{\text{theor}}I^2$. The structure amplitudes were calculated from the intensities according to the following formula for local intensities:

$IF_{hkl}I_{\text{exp}} = \sqrt{I_{hkl\text{exp}}/d_{hkl}d_{hk0}p}$, where the indices hkl refer to the reflections of the same ellipsoid as the reflections with the indices hkl and p is the multiplicity factor [6]. The structural calculations were performed with the AREN-90 program package [7] and the electron atomic scattering factors for neutral atoms. We used 184 unique reflections with the maximum indices $l = 12$ in 12 ellipsoids up to $\sin\theta/\lambda = 0.69 \text{ \AA}^{-1}$. The parameters of the base-centered monoclinic cell [$a = 5.227(2) \text{ \AA}$, $b = 9.053(2) \text{ \AA}$, $c = 10.153(3) \text{ \AA}$, and $\beta = 100.53(3)^\circ$] were calculated from the electron diffraction patterns measured with TICl as an internal standard. The analysis of the intensities demonstrated that scattering for the majority of the reflections occurs according to the kinematic law. The intensities of eight strong reflections were corrected for primary extinction in the Blackman two-wave approximation [8] for the calculated average effective thickness of crystallites $t_{\text{av}} = 490 \text{ \AA}$.

The celadonite structure was refined in the space group $C2/m$ and also in the space group $C2$ in order to reveal the possible ordering of octahedral cations. As the starting models, we used the atomic coordinates

taken from [4] for the celadonite structure refined in the space group $C2$; the atomic coordinates in the space group $C2/m$, which were determined by averaging the coordinates of the atoms related by the m pseudoplane in the space group $C2$ [4]; and the atomic coordinates obtained in [2]. It should be noted that, in the starting models with space group $C2$, we varied the distributions of octahedral cations over two nonequivalent *cis* positions. It turned out that, when refining the models in the space group $C2$, the standard deviations of the coordinates of the atoms located in the vicinity of the m pseudoplane are considerably larger than those of the other atoms. Moreover, the average T – O distances in two tetrahedra also differ from each other. Crystal chemically, this is not justified in terms of the insignificant substitution of Al atoms for Si atoms in tetrahedra of the celadonite structure. For this reason, further refinement of the celadonite structure was carried out in the space group $C2/m$. A similar situation was considered in detail when refining the structure of the muscovite $1M$ [9].

After the least-squares refinement of the non-hydrogen atoms and their thermal parameters in the anisotropic approximation, the maximum associated with the hydrogen atom of the hydroxyl group was revealed from the difference Fourier-potential syntheses (Fig. 1). The final refinement of the celadonite structure was performed in the anisotropic approximations for all the atoms to $R = 2.98\%$. The atomic coordinates and the anisotropic thermal parameters are presented in Table 1. The interatomic distances are given in Table 2. The projection of the structure onto the ab plane is depicted in Fig. 2.

RESULTS AND DISCUSSION

It is established that celadonite from Krivoř Rog is characterized by a statistical distribution of octahedral cations with the average interatomic distance M – $O = 2.042 \text{ \AA}$ and the shortest distance M – $\text{OH} = 2.025 \text{ \AA}$. The octahedra are slightly oblate; the average distances $(O-O)_{\text{base}}$ and $(O-O)_{\text{side}}$ are equal to 2.945 and 2.831 \AA , respectively; and the height of the octahedral sheet is 2.263 \AA . The octahedron bases are rotated through the angle $\varphi = 2.56^\circ$.

The tetrahedra are elongated along the normal to the layers. The average distances $(O-O)_{\text{base}}$ and $(O-O)_{\text{side}}$ are equal to 2.613 and 2.665 \AA , respectively. The tetrahedral cations are displaced to the O_{apex} atom shared by the octahedral and tetrahedral sheets. The T – O_{apex} and $(T-O_{\text{base}})_{\text{av}}$ distances are equal to 1.598 and 1.623 \AA , respectively. The average T – O distance is 1.617 \AA . The surface of the basal tetrahedral oxygen atoms is puckered. The O_{base} atom lying in the m plane is located 0.032 \AA closer to the octahedral sheet as compared to the other O_{base} atom.

For a small angle of ditrigonal rotation of the tetrahedron bases ($\psi = 0.5^\circ$) and a small interlayer displace-

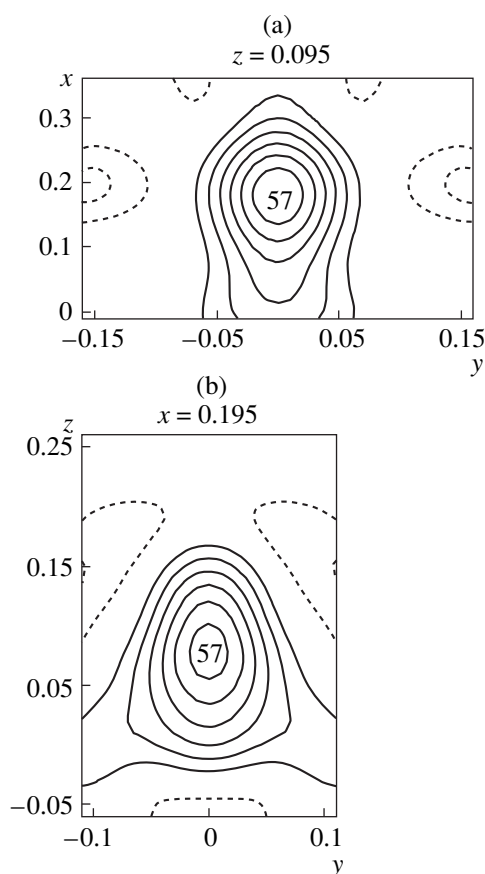


Fig. 1. Difference Fourier synthesis sections passing through the hydrogen atom and parallel to (a) the ab plane and (b) the bc plane of the celadonite structure. The contours are drawn at an interval of 10 V. Numbers indicate the potential at the maximum.

ment ($t = 0.003$), the interlayer cations K are located in a nearly regular hexagonal prism with average $(K-O)_{\text{inner}}$ and $(K-O)_{\text{outer}}$ distances equal to 3.084 and 3.107 Å, respectively [$(K-O)_{\text{av}} = 3.096$ Å]. For a small interlayer displacement t , the value of $-c \cos \beta / a =$

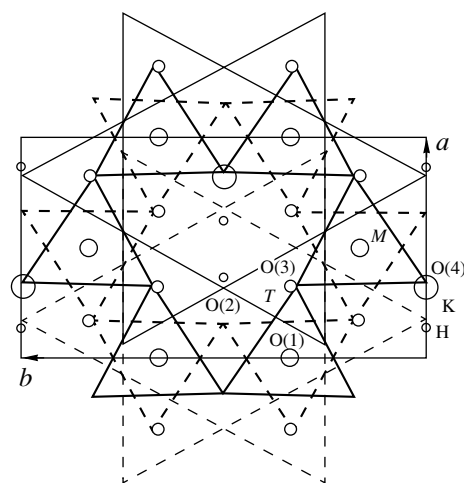


Fig. 2. Schematic drawing of the celadonite structure in the normal projection onto the ab plane. Heavy solid lines indicate the upper bases of the octahedra, heavy dashed lines correspond to the lower bases of the octahedra, thin solid lines represent the upper bases of the tetrahedra, and thin dashed lines show the lower bases of the tetrahedra.

0.355 (the ideal value is $1/3$) is provided by the intralayer displacement $s = 0.321$.

Compared to our earlier work [2], this study of the celadonite structure with modern digital methods used for recording the diffraction patterns made it possible to substantially refine a number of fine features in the celadonite structure. In particular, it should be noted that the data obtained in our present work confirmed neither the increase in the average $T-O$ distance nor the ratio between the $T-O_{\text{apex}}$ and $(T-O)_{\text{base}_{\text{av}}}$ distances, which were found in [2].

The fact that we succeeded in determining the location and specific features of the hydrogen atom of the OH hydroxyl group is of particular importance. As can be seen from the difference Fourier-potential syntheses (Fig. 1), the maximum attributed to the hydrogen atom has an anisotropic shape and is extended in the ac plane. This agrees with the established anisotropy of

Table 1. Atomic coordinates and anisotropic thermal parameters ($\text{Å}^2 \times 10^{-4}$) for the celadonite structure

Atom	x/a	y/b	z/c	B_{11}	B_{22}	B_{33}	B_{12}	B_{13}	B_{23}
K	0.5	0	0.5	48(14)	18(5)	34(5)	0	12(11)	0
M	0.5	0.1663(2)	0	44(7)	16(3)	18(3)	0	8(7)	0
T	0.4139(3)	0.3329(2)	0.2736(1)	53(8)	19(3)	18(3)	4(9)	16(7)	0
O(1)	0.1879(6)	0.2507(3)	0.3348(3)	81(16)	36(6)	24(4)	-18(11)	7(11)	5(6)
O(2)	0.4426(7)	0.5	0.3315(3)	108(19)	20(7)	34(6)	0	11(17)	0
O(3)	0.3684(5)	0.3257(3)	0.1137(3)	115(16)	28(5)	32(4)	22(13)	22(12)	-13(7)
O(4)	0.3954(7)	0	0.1126(4)	56(20)	21(6)	30(6)	0	13(18)	0
H	0.204(6)	0	0.105(3)	579(141)	54(39)	137(46)	0	19(114)	0

Table 2. Interatomic distances (Å) in the celadonite structure

Octahedron					
$M-O(3) \times 2$	2.044(3)	Base edges		Side edges	
$-O(3') \times 2$	2.057(3)	$O(3)-O(3') \times 2$	2.951(4)	$O(3)-O(3')$	2.895(4)
$-O(4) \times 2$	2.025(3)	$O(3')-O(4) \times 2$	2.931(4)	$O(3')-O(4) \times 2$	2.917(4)
Average	2.042	$O(4)-O(3) \times 2$	2.952(3)	$O(4)-O(4)$	2.708(5)
		Average	2.945	$O(3)-O(3') \times 2$	2.774(3)
$O(4)-H$	0.98(2)			Average	2.831
Tetrahedron					
$T-O(1)$	1.613(4)	Base edges		Side edges	
$-O(1')$	1.638(3)	$O(1)-O(1')$	2.163(4)	$O(3)-O(2)$	2.686(4)
$-O(2)$	1.619(2)	$-O(2)$	2.603(3)	$-O(1')$	2.633(4)
$-O(3)$	1.598(3)	$O(2)-O(1')$	2.623(3)	$-O(1)$	2.674(4)
Average	1.617	Average	2.613	Average	2.665
Interlayer spacing					
	$K-O(1') \times 4$				3.077(3)
	$-O(2') \times 2$				2.097(3)
	$-O(1) \times 4$				3.102(3)
	$-O(2) \times 2$				3.118(4)
	Mean				3.096

Note: O and O' are the oxygen atoms related by the symmetry elements.

thermal vibrations of the hydrogen atom and reflects different configurations of the Fe and Mg trivalent and divalent cations distributed statistically over the *cis* positions in the nearest environment of the hydrogen atom. The O–H bond is oriented toward the empty octahedron and forms an angle of 4.4° with the *ab* plane (the hydrogen atom is slightly displaced inside the empty octahedron). The O–H interatomic distance is equal to 0.98(2) Å.

It should be noted that, among the dioctahedral micas, only the celadonite structure is characterized by the displacement of the hydrogen atom of the hydroxyl group inside the empty octahedron. In muscovites, the hydroxyl group is oriented toward the empty octahedron at an acute angle (15°–17°) with respect to the plane of the layer from the octahedral sheet [10]. The orientation of the hydroxyl group into the empty octahedron in the celadonite structure favors the interaction of the interlayer K cation with the oxygen atom of the hydroxyl group (the interatomic distance $K-OH = 3.870$ Å is the shortest among those observed in the mica structures). In the mica structures, this is the only oxygen atom that is located in the octahedral sheet at a sufficiently short distance from the interlayer cation and, moreover, is not shielded by the basal oxygen atoms. For a relatively weak interaction of the K cation with the basal oxygen atoms due to an insignificant

substitution of Al atoms for Si atoms in the tetrahedra, the interaction of the K cation with the oxygen atom of the hydroxyl group is an important factor stabilizing the celadonite structure. This can be judged, in particular, from the small interlayer spacing (3.325 Å as compared to $c \approx 3.40$ Å in muscovites), which is observed when the basal oxygen atoms of the adjacent tetrahedral sheets are superposed in the projection onto the *ab* plane. This superposition is favored by the small negative charge of the O_{base} atoms. In the present work, the angle of deviation of the O–H bond from the plane of the layer into the empty *trans* octahedron is smaller than that obtained in [4]. It seems likely that this deviation is associated both with the high content of trivalent cations in the octahedral sheet and with the deficit of interlayer cations in the structure of the celadonite from Krivoi Rog.

An interesting feature of the celadonite from Krivoi Rog is that the selected-area electron diffraction patterns of a number of band-shaped single-crystal particles extended along the *a* axis exhibit triads of weak additional reflections between strong reflections attributed to the main base-centered cell (Fig. 3). Similar electron diffraction patterns were also observed earlier [11]. The intensity ratio of reflections in triads (Fig. 3) varies both for different particles and within a single particle (the intensity of central reflections can be either

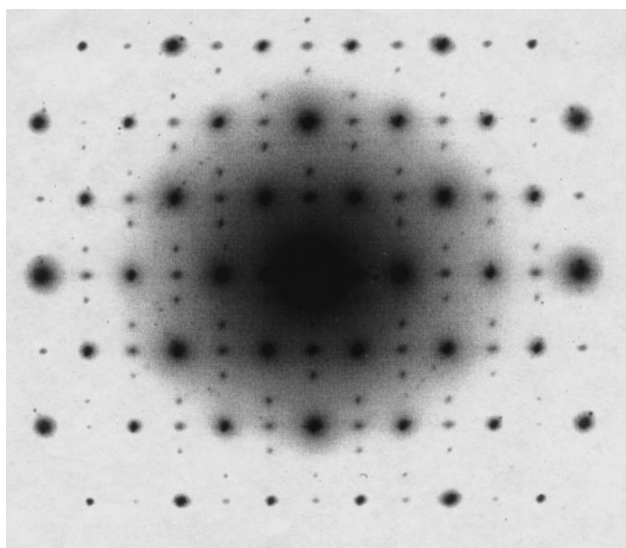


Fig. 3. Selected-area electron diffraction pattern of a single celadonite particle (the ab plane is oriented perpendicular to the incident beam). Triads of weak reflections extended along the a axis are seen. The central reflections in triads are attributed to the main cell with a broken base-centered symmetry. The extreme reflections correspond to the base-centered supercell with $a_s = 3a_0$ and $b_s = b_0$.

higher or lower than that of the extreme reflections, and the former reflection are always more smeared than the latter reflections). This indicates that the appearance of additional reflections is caused by the superposition of two cells. In triads, the extreme reflections correspond to the base-centered supercell with the triple parameter a , whereas the central reflections are attributed to the main cell with a broken base-centered symmetry. This feature of the celadonite apparently can be associated with the ordered distribution of trivalent and divalent cations Fe and Mg over the cis positions. The two models proposed for cation ordering are consistent with the observed intensity distribution. According to these models, when the octahedral cations are in the ratio $Fe^{3+} : Fe^{2+} : Mg = 2 : 1 : 1$, the Fe^{3+} cations occupy one system of octahedral cis positions (related by the C translation in the main cell), whereas the Fe^{2+} , Mg, and (Fe^{2+} , Mg) cations (the base-centered cell with $a_s = 3a_0$ and $b_s = b_0$) or the Fe^{2+} and Mg cations (the main cell with a broken base-centered symmetry) alternate in an ordered manner along the a axis in the other system of cis positions.

CONCLUSIONS

Thus, the above analysis of the selected-area electron diffraction patterns of single crystals confirmed the tendency (revealed from the oblique-texture electron diffraction patterns in [4]) toward ordered distribution of trivalent and divalent octahedral cations in celadonite and demonstrated that the Fe^{2+} and Mg^{2+} divalent cations are also ordered. The superstructure reflections observed only for particular particles most likely indicate that, in the vast majority of the celadonite particles, regions with ordered cations are characterized by incoherent scattering. This leads to an averaged structure with a statistical distribution of octahedral cations, as was established in the refinement of the celadonite structure from the oblique-texture electron diffraction patterns obtained with the use of imaging plates.

ACKNOWLEDGMENTS

This work was supported by the Russian Foundation for Basic Research, project no. 02-05-64952.

REFERENCES

1. B. B. Zvyagin, *Kristallografiya* **2** (3), 393 (1957) [*Sov. Phys. Crystallogr.* **2**, 388 (1957)].
2. A. P. Zhukhlistov, B. B. Zvyagin, E. K. Lazarenko, and V. I. Pavlishin, *Kristallografiya* **22** (3), 498 (1977) [*Sov. Phys. Crystallogr.* **22**, 284 (1977)].
3. V. Rieder, G. Cavazzini, Y. S. Dyakonov, *et al.*, *Clays Clay Miner.* **46** (5), 586 (1998).
4. S. I. Tsipurskiĭ and V. A. Drits, *Mineral. Zh.* **8** (3), 32 (1986).
5. A. P. Zhukhlistov, M. S. Nickolsky, B. B. Zvyagin, *et al.*, *Z. Kristallogr.* **219**, 224 (2004).
6. B. K. Vainshteĭn, *Structural Electronography* (Akad. Nauk SSSR, Moscow, 1956) [in Russian].
7. V. I. Andrianov, *Kristallografiya* **32** (1), 228 (1987) [*Sov. Phys. Crystallogr.* **32**, 130 (1987)].
8. B. K. Vainshtein, B. B. Zvyagin, and A. S. Avilov, *Electron Diffraction Techniques* (Oxford University Press, Oxford, 1992), Vol. 1, p. 216.
9. S. I. Tsipurskiĭ and V. A. Drits, *Izv. Akad. Nauk SSSR* **41** (11), 2363 (1977).
10. R. F. Giese, *Rev. Mineral.* **13**, 105 (1984).
11. B. B. Zvyagin, *Electron Diffraction Analysis of Clay Minerals* (Nauka, Moscow, 1964; Plenum, New York, 1967).

Translated by O. Borovik-Romanova

STRUCTURE OF INORGANIC COMPOUNDS

Refinement of the Crystal Structures of Three Fluorine-Bearing Elbaites

I. V. Rozhdestvenskaya, O. V. Frank-Kamenetskaya, A. A. Zolotarev,
Yu. M. Bronzova, and I. I. Bannova

St. Petersburg State University, Universitetskaya nab. 7/9, St. Petersburg, 199034 Russia

e-mail: ivrozhdestvenska@mail.ru

Received September 24, 2004

Abstract—The crystal structures of three Li–Al natural tourmalines (elbaites) containing 0.88–1.39 wt % F are refined to $R = 0.0294$, 0.0308 , and 0.0417 . It is revealed that the W threefold anion site is split into two sites, namely, the $W1$ threefold site and $W2$ ninefold site ($W1-W2 \sim 0.4$ Å, $Y-W_1 \geq 1.94$ Å, $Y-W_2 \geq 1.75$ Å). The following hypothesis is proposed and justified: the $W1$ and $W2$ sites are partially occupied by OH groups and fluorine anions, respectively. The ratio of the $[YO_4(OH)_2]$ octahedra to the $[YO_4(OH)F]$ octahedra depends on the fluorine content and varies from structure to structure. The fact that the W site is more than 50% occupied by fluorine in the structures of two tourmalines under investigation allows the conclusion that fluor-elbaite with the ideal formula $Na(Li_{1.5}Al_{1.5})Al_6(Si_6O_{18})(BO_3)_3(OH)_3F$ is a new mineral species and that elbaite can be considered a superspecies. © 2005 Pleiades Publishing, Inc.

INTRODUCTION

Natural borosilicates of complex composition, namely, minerals of the tourmaline group, are stable over a wide range of thermodynamic conditions and, consequently, have been widely used by geologists in prospecting and evaluation [1–3]. Tourmalines are characterized by a great variety of compositions due to their specific crystal structure [4–6]. Owing to their unique crystal physical properties, including pyroelectric and piezoelectric effects, and also the presence of boron, tourmalines can be used for the design of measuring devices that operate over a wide range of temperatures and pressures (including corrosive media) and for manufacturing of structural materials providing biological protection against neutron radiation. Transparent brightly colored tourmaline species have found applications in jewelry.

Taking into account the results of numerous structural investigations [7–10], Hawthorne and Henry [11] proposed to represent the crystal chemical formula of tourmaline (space group $R3m$) in the form $X^{IX}Y_3^VI Z_6^VI [T_6^{IV}O_{18}][B^{III}O_3]_3V_3W$. The sites in the tourmaline structure can be occupied by the following elements: $X = Ca^{2+}$, Na^+ , K^+ , and \square (vacancy); $Y = Li^+$, Mg^{2+} , Fe^{2+} , Mn^{2+} , Al^{3+} , Cr^{3+} , V^{3+} , Fe^{3+} , and, possibly, Ti^{4+} ; $Z = Mg^{2+}$, Al^{3+} , Fe^{3+} , V^{3+} , and Cr^{3+} ; $T = Si^{4+}$, Al^{3+} , and B^{3+} ; $B = B^{3+}$ and, possibly, \square ; and V [O(3) site] and W [O(1) site] = OH^- , F^- , and O^{2-} . The distribution of OH^- , F^- , and O^{2-} anions over the V and W sites remains questionable. First and foremost, this is associated with the fact that such a distribution is difficult to determine directly from X-ray structure refinement of mixed

occupancies of crystallographic sites because of the closer scattering powers of oxygen and fluorine atoms (having eight and nine electrons, respectively).

In this study, we succeeded in deriving new information on the distribution of univalent anions in the structures of three Li–Al tourmalines (elbaites) with the ideal formula $Na(Li_{1.5}Al_{1.5})Al_6(Si_6O_{18})(BO_3)_3(OH,F)_4$.

CHEMICAL COMPOSITION OF TOURMALINE UNDER INVESTIGATION

For our investigations, we chose three jewelry tourmalines (described in detail in [12]) from miarolitic pegmatites (Eastern Pamirs) with different fluorine contents: rose rubellite (sample $T-17$), blue indicolite (sample $T-14$), and green verdelite (sample $T-7$).

The chemical composition of tourmalines (Table 1) was determined by electron microprobe analysis on a JEOL SXA-8600S microanalyzer (analysts A.N. Zaitsev and R. Wilson, University of Lester, UK). Moreover, the Li_2O and B_2O_3 contents in samples $T-14$ and $T-17$ were also determined by plasma emission spectroscopy and titration (variant 1 in Table 1) (analyst S.V. Zimina, OOO MEKHANOB R INZHINIRING ANALIT). The B_2O_3 content was additionally measured by potentiometric titration (variant 2 in Table 1) (analyst M.P. Semenov, Laboratory of Analytic and Inorganic Chemistry, Grebenshchikov Institute of Silicate Chemistry, Russian Academy of Sciences). In view of the complex isomorphism of tourmalines and possible errors in the chemical analysis, the chemical formulas of the samples were calculated in different ways: per 31 anions ($O + F + OH$); per 29 and 24.5 oxygen atoms;

Table 1. Chemical composition of the studied tourmalines (wt %)

Component	Samples		
	<i>T</i> -17	<i>T</i> -14	<i>T</i> -7
SiO ₂	37.16	35.68	37.11
TiO ₂	0.10	0.04	0.05
Al ₂ O ₃	40.17	36.16	36.81
Cr ₂ O ₃	0.00	0.00	0.03
FeO*	0.02	6.93	3.50
B ₂ O ₃ , variant 1	11.61	14.52	Not determined
B ₂ O ₃ , variant 2	9.43	9.09	Not determined
MnO	0.47	0.07	2.66
MgO	0.00	0.00	0.01
CaO	1.26	0.17	0.11
Na ₂ O	1.65	2.75	2.97
K ₂ O	0.00	0.03	0.02
Li ₂ O	1.63	0.96	Not determined
F	0.88	1.16	1.39
Total	94.95	98.51	84.66
-O=F ₂	0.37	0.49	0.58
Total	94.58	98.02	84.08

* FeO (the total iron content).

per 19, 18, 16, or 15 cations; and per 6 silicon atoms. The data on the B₂O₃ content obtained for the same samples at different laboratories differ substantially. According to the calculations from these data by different methods, the numbers of boron atoms in the formulas of samples *T*-14 and *T*-17 differ significantly from three and, hence, are unjustified structurally. The calcu-

lations of the coefficients in the tourmaline formulas from the experimentally determined Li₂O content (per 15 cations or 24.5 oxygen atoms) require the appearance of vacancies at the *Y* site. As follows from previous structural investigations, this is not typical of tourmalines. Consequently, the obtained experimental data on the boron and lithium contents are not reliable and cannot be used to calculate the formulas for the tourmalines under investigation.

In this respect, the preliminary crystal chemical formulas for the studied solid solutions (Table 2, variant 1) were calculated from the data of the electron microprobe analysis per six silicon atoms under the assumption that the number of boron atoms in the formula is equal to three. The number of lithium atoms was calculated by assuming that the *Y* site is fully occupied. The distribution of cations (including bivalent and trivalent iron cations) over octahedral sites was examined according to the technique proposed by Gorskaya *et al.* [5] with the use of the unit cell parameters (Table 3). The distribution of iron cations in the structure of sample *T*-14 was analyzed by Mössbauer spectroscopy [13]. Anions over the *V* and *W* sites were not separated. The amounts of OH groups and oxygen anions were estimated from the charge balance.

CRYSTAL STRUCTURE REFINEMENT

The intensities of the diffraction reflections were measured in an area equal to one-sixth of the reciprocal space on four-circle single-crystal diffractometers (graphite monochromator, MoK_α radiation, ω scan mode) (Table 3). The measurements at angles up to 2θ = 30° were performed without regard for the *R*-centering (characteristic of tourmalines) for a hexagonal unit cell. Since no distortions of the *R* cell were found at this stage, only diffraction reflections satisfying the

Table 2. Crystal chemical formulas XY₃Z₆(Si₆O₁₈)(BO₃)₃(OH)₃(O,OH,F) of the studied tourmalines (space group *R*3*m*, *Z* = 3)

Sample	Variant	Formula
<i>T</i> -17	1	(Na _{0.52} Ca _{0.22} □ _{0.26})(Al _{1.65} Li _{1.28} Mn _{0.06} ²⁺ Ti _{0.01})Al _{6.00} (Si ₆ O ₁₈)(BO ₃) ₃ (OH _{3.20} F _{0.45} O _{0.35})
	2	(Na _{0.68} Ca _{0.22} □ _{0.10})(Li _{1.56} Al _{1.44})(Al _{5.82} Mn _{0.18} ³⁺)(Si ₆ O ₁₈)(BO ₃) ₃ (OH) ₃ (OH _{0.64} F _{0.36})
<i>T</i> -14	1	(Na _{0.90} Ca _{0.03} K _{0.01} □ _{0.06})(Al _{1.23} Fe _{0.86} ²⁺ Li _{0.85} Fe _{0.05} ³⁺ Mn _{0.01})(Al _{5.94} Fe _{0.06} ²⁺)(Si ₆ O ₁₈)(BO ₃) ₃ (OH _{3.04} F _{0.62} O _{0.34})
	2	(Na _{0.89} Ca _{0.03} K _{0.01} □ _{0.07})(Al _{1.09} Li _{1.05} Fe _{0.82} ²⁺ Fe _{0.04} ³⁺)(Al _{5.94} Fe _{0.06} ²⁺ (Si ₆ O ₁₈)(BO ₃) ₃ (OH) ₃ (F _{0.57} OH _{0.43})
<i>T</i> -7	1	(Na _{0.93} Ca _{0.02} □ _{0.02})(Li _{1.14} Al _{1.02} Mn _{0.36} ²⁺ Fe _{0.33} ²⁺ Fe _{0.14} ³⁺ Ti _{0.01})Al ₆ (Si ₆ O ₁₈)(BO ₃) ₃ (OH _{3.29} F _{0.71})
	2	(Na _{0.97} Ca _{0.03})(Li _{1.14} Al _{1.02} Fe _{0.45} ²⁺ Mn _{0.30} ²⁺ Fe _{0.09} ³⁺)Al ₆ (Si ₆ O ₁₈)(BO ₃) ₃ (OH) ₃ (F _{0.60} OH _{0.40})

Table 3. Characteristics of the samples and X-ray diffraction experiment

Characteristics	Samples		
	<i>T</i> -17	<i>T</i> -14	<i>T</i> -7
Fluorine content, wt %	0.88	1.16	1.39
Diffractometer	Nicolett <i>R3</i>	Nicolett <i>R3</i>	SYNTEX <i>P21</i>
<i>a</i> , Å	15.833(4)	15.902(5)	15.905(6)
	15.826(3)*	15.916(3)*	15.931(2)*
<i>c</i> , Å	7.101(1)	7.127(2)	7.121(2)
	7.098(1)*	7.119(1)*	7.123(1)*
<i>V</i> , Å ³	1542(1)	1561(1)	1560(2)
	1539.7(1)*	1561.8(1)*	1565.6(1)*
ρ_{calcd} , g/cm ³	3.046(2)	3.104(2)	3.096(3)
μ , cm ⁻¹	10.73	15.21	14.57
Weighting scheme	$1/(\sigma_F^2 + 0.001 F_{\text{exp}}^2)$	$1/(\sigma_F^2 + 0.0018 F_{\text{exp}}^2)$	$1/(\sigma_F^2 + 0.002 F_{\text{exp}}^2)$
Number of reflections measured ($I > 2\sigma_I$)	2162	2223	1746
Number of unique reflections ($F > 4\sigma_F$)	1148	1164	986
$R(F)^{**}$	0.0306	0.0335	0.0429
$R(F)_{\text{final}}$	0.0294	0.0308	0.0417
R_w	0.0302	0.0359	0.0405

* Parameters determined by X-ray powder diffraction analysis.

** Before introducing the hydrogen atoms into the structural model and splitting of the site O(1) (*W*).

condition $-h + k + l = 3n$ were measured at the subsequent stages. The intensities were corrected for the Lorentz and polarization factors, fluctuations of the primary beam, and absorption according to the DIFABS program package [7].

The crystal structures were refined by alternating the least-squares procedure (in the anisotropic approximation of thermal atomic vibrations) and the analysis of the difference Fourier syntheses with the CSD software package [14]. The atomic coordinates in the structure of aluminum elbaite [15] served as the initial data. Aluminum atoms were placed at the *Y* and *Z* octahedral sites, and sodium atoms were positioned at the alkali cation site. In order to weaken correlations between the occupancies and other (primarily, thermal) structural parameters, the occupancies at the initial stage were refined using the reflections with $\sin\theta/\lambda < 0.5$. The positions of the hydrogen atoms and the splitting of the O(1) (*W*) site were determined from a detailed analysis of the difference Fourier synthesis maps after the *R* factors reached ~3–4%. The final *R* factors are presented in Table 3. The fractional atomic coordinates, isotropic thermal parameters of atoms, and site occupancies are listed in Table 4. The bond lengths in the main polyhedra of the tourmalines structures are given in Table 6.

RESULTS AND DISCUSSION

The refinement of the occupancies of the crystallographic sites (Table 4) revealed that the Li⁺/Al³⁺ cation

ratio for the *Y* site is close to unity and the site occupancy for these cations is no less than 70%. The mean lengths of the *Y*–O bonds (2.022–2.053 Å) (Table 6) increase with an increase in the Fe and Mn cation contents and are close to those in the structures of previously studied elbaites [9, 15–19]. The occupancies of the *Z* octahedra and the mean lengths of the *Z*–O bonds (1.907–1.909 Å) (Table 6) confirm that these octahedra in all the structures are fully (or almost fully) occupied by aluminum cations. The *X* sites in all the structures are predominantly occupied by sodium cations. The mean length of the *X*–O bonds varies from 2.655 Å in sample *T*-17, to 2.670 Å in sample *T*-14, and to 2.673 Å in sample *T*-7 (Table 6). Therefore, an increase in the size of the *Y* octahedra is accompanied by an increase in the size of the *X* nine-vertex polyhedra. This is well explained by the specific features of chemical deformations of the tourmaline structure [6]. The refinement of the occupancies of the tetrahedral sites confirmed that, in all the cases, these sites are almost fully occupied by Si⁴⁺ cations. The mean tetrahedral distances are equal to 1.618–1.620 Å, and the mean O–Si–O angle is equal to 109.44°.

It is known that protons in the tourmaline structure are located in the symmetry plane near the O(3) (*V*) sites and on the threefold axis near the O(1) (*W*1) sites [16, 20]. The detailed analysis of the difference Fourier syntheses revealed the hydrogen atoms only near the O(3) (*V*) sites in the structures under investigation (Table 4). The parameters of the O(3)–H···O(5) hydro-

Table 4. Fractional atomic coordinates, thermal parameters, and site occupation in the structures of the tourmalines under investigation

Sample	Site	Occupation, au*	<i>x/a</i>	<i>y/b</i>	<i>z/c</i>	$U_{eq/iso}^{**} \times 100, \text{\AA}^{-2}$	
T-17	X	3a	Na _{0.68} Ca _{0.22} □ _{0.10}	0	0	0.2358(4)	1.37(5)
T-14			Na _{0.89} Ca _{0.03} K _{0.01} □ _{0.07}	0	0	0.2344(5)	2.12(8)
T-7			Na _{0.97} Ca _{0.03}	0	0	0.2357(8)	2.40(1)
T-17	Y	9b	Li _{0.52} Al _{0.48}	0.1230(1)	1/2x	0.6362(3)	0.42(4)
T-14			Al _{0.36} Li _{0.35} Fe _{0.29}	0.12417(8)	1/2x	0.6284(2)	1.02(3)
T-7			Li _{0.38} Al _{0.34} (Fe + Mn) _{0.28}	0.1241(1)	1/2x	0.6275(3)	0.69(4)
T-17	Z	18c	Al _{0.97} Mn _{0.03}	0.29677(5)	0.25990(5)	0.6102(1)	0.57(2)
T-14			Al _{0.99} Fe _{0.01}	0.29778(6)	0.26092(6)	0.6114(1)	0.83(2)
T-7			Al _{1.0}	0.29751(8)	0.26082(8)	0.6116(2)	0.46(3)
T-17	B	9b	B	0.1090(1)	2x	0.4546(4)	0.60(7)
T-14			B	0.1097(1)	2x	0.4561(5)	0.98(9)
T-7			B	0.1090(2)	2x	0.4550(8)	0.44(1)
T-17	Si	18c	Si	0.19186(4)	0.18986(4)	0	0.43(2)
T-14			Si	0.19195(5)	0.18998(5)	0	0.75(2)
T-7			Si	0.19191(7)	0.18997(7)	0	0.38(3)
T-17	O(1) (W1)	3a	OH _{0.64} □ _{0.36} ***	0	0	0.772(3)	2.0(3)
T-14			OH _{0.43} □ _{0.57} ***	0	0	0.784(5)	3.9(1)
T-7			OH _{0.40} □ _{0.60} ***	0	0	0.762(1)	2.1(5)
T-17	F(W2)	9b	F _{0.12} □ _{0.88}	0.022(1)	1/2x	0.801(3)	0.5(5)
T-14			F _{0.19} □ _{0.81}	0.028(2)	1/2x	0.787(3)	0.7(2)
T-7			F _{0.20} □ _{0.80}	0.024(1)	1/2x	0.798(2)	0.5(5)
T-17	O(2)	9b	O	0.06012(9)	2x	0.4870(4)	1.43(7)
T-14			O	0.0607(1)	2x	0.4848(5)	1.98(9)
T-7			O	0.0610(2)	2x	0.4850(7)	1.7(1)
T-17	O(3) (V)	9b	OH***	0.2659(2)	1/2x	0.5086(3)	1.22(7)
T-14			OH***	0.2690(2)	1/2x	0.5096(4)	1.19(7)
T-7			OH***	0.2698(2)	1/2x	0.5100(6)	0.9(1)
T-17	O(4)	9b	O	0.09310(9)	2x	0.0744(3)	0.86(6)
T-14			O	0.0929(1)	2x	0.0718(4)	1.09(7)
T-7			O	0.0931(2)	2x	0.0714(5)	0.7(1)
T-17	O(5)	9b	O	0.1860(2)	1/2x	0.0964(3)	0.88(6)
T-14			O	0.1865(2)	1/2x	0.0948(4)	1.05(7)
T-7			O	0.1859(3)	1/2x	0.0932(6)	0.7(1)
T-17	O(6)	18c	O	0.1951(1)	0.1847(1)	0.7751(2)	0.69(5)
T-14			O	0.1970(1)	0.1868(1)	0.7758(3)	0.96(5)
T-7			O	0.1973(2)	0.1867(2)	0.7759(4)	0.58(8)
T-17	O(7)	18c	O	0.2862(1)	0.2857(1)	0.0793(2)	0.59(4)
T-14			O	0.2854(1)	0.2856(1)	0.0809(3)	0.89(5)
T-7			O	0.2857(2)	0.2858(2)	0.0805(4)	0.54(8)
T-17	O(8)	18c	O	0.2096(1)	0.2702(1)	0.4398(2)	0.72(4)
T-14			O	0.2097(1)	0.2703(1)	0.4416(3)	1.00(6)
T-7			O	0.2097(2)	0.2703(2)	0.4412(4)	0.68(8)
T-17	H	9b	H	0.251	1/2x	0.398	5.4(7)
T-14			H	0.274(5)	1/2x	0.386(9)	4.2(9)
T-7			H	0.281	1/2x	0.395	3.5(2)

* The standard error in the determination of the site occupancy for an element is less than or equal to 0.01 au.

** $U_{eq} = 1/3[U^{11}(a^*)^2a^2 + \dots + 2U_{23}b^*c^*bc\cos\alpha]$.

*** The occupation of the sites V and W by univalent anions is confirmed by the analysis of the valence balance (Table 5).

Table 5. Calculated bond valences for anions in the structures of the tourmalines under investigation

Sample	Variant	Anion site									
		O(1)	F	O(1) + F	O(2)	O(3)	O(4)	O(5)	O(6)	O(7)	O(8)
<i>T</i> -17	1	0.657	0.303	0.960	1.851	1.107	2.040	1.911	1.959	2.027	1.995
	2	1.179	0.303	1.482	1.851	1.998	2.040	2.010	1.959	2.027	1.995
<i>T</i> -14	1	0.372	0.560	0.932	1.858	1.101	2.038	1.890	1.953	2.024	1.994
	2	0.704	0.560	1.264	1.858	1.982	2.038	2.008	1.953	2.024	1.994
<i>T</i> -7	1	0.435	0.479	0.914	1.893	1.092	2.043	1.920	1.947	2.005	1.948
	2	0.755	0.479	1.234	1.893	1.994	2.043	2.018	1.947	2.005	1.948

Note: The calculations were performed without (variant 1) and with (variant 2) inclusion of the hydrogen atoms.

gen bonds between the *Y* octahedra and the tetrahedral rings of the neighboring (in height) antigorite fragments (Table 7) are close to those determined in the structures of other elbaïtes. The occurrence of protons in the vicinity of the O(1) (*W*1) sites, which are partially occupied in our structures, is supported by the results of the valence balance analysis performed by Pyatenko [21] with allowance made for the occupancies of the cation and anion sites.

According to the scarce data available in the literature on the crystal structures of Li–Al fluorine-containing tourmalines [17, 18, 22], the *Y*–O(1) bond lengths (1.790–2.126 Å) are smaller than the *Y*–O(3) bond lengths (2.153–2.186 Å). In the structures studied in our work, the *Y*–O(1) bond lengths (1.94–2.04 Å) are also somewhat smaller than the *Y*–O(3) bond lengths (2.16–2.17 Å). Such a ratio between these bond lengths is also typical of hydroxyl-containing tourmalines [16] and results from the presence of two strong bonds between the O(3) anions and cations of two neighboring *Z* octahedra. In the crystal structures of elbaïtes from the Eastern Pamirs, the *W* [O(1)] site is split into two partially occupied sites, namely, the *W*1 threefold site and *W*2 ninefold site (Table 4). Each atom (vacancy) at the *W*1 site (on the threefold axis) is surrounded by three corresponding structural units at the *W*2 sites (Fig. 1). The total occupancy of this grouping is equal to unity. As consequence, the following shortened forbidden distances appear in the structures: *W*1–*W*2 = 0.36(2), 0.38(2), and 0.42(5) Å and *W*2–*W*2 = 0.52(3), 0.66(4), and 0.57(2) Å for samples *T*-17, *T*-14, and *T*-7, respectively. In all the structures, the *Y*–*W*2 bond lengths are approximately equal to 1.8 Å (Table 6). This can suggest that the *W*2 sites are statistically occupied by fluorine anions. The above assumption is confirmed by the fact that the fluorine contents determined by the chemical analysis in samples *T*-17, *T*-14, and *T*-7 (0.45, 0.62, and 0.71 au per formula) are close to those calculated from the occupancies of the *W*2 site (0.36, 0.57, and 0.60 au per formula). The analysis of the valence balance in the elbaïte structures (Table 5) demonstrates that the O(1) (*W*1) and O(3) (*V*) sites are occupied only by univalent anions, i.e., with

Table 6. Bond lengths (Å) in the *Y*, *Z*, and *X* polyhedra of the tourmaline structures under investigation

Sample	Bond, length	Bond, length	Bond, length	
<i>T</i> -17	<i>Y</i> –O(1)	<i>Z</i> –O(6)	<i>X</i> –O(2) × 3	
	1.94(1)	1.862(4)	2.429(4)	
	<i>T</i> -14	2.04(2)	1.855(5)	2.446(5)
<i>T</i> -7		1.96(4)	1.848(6)	2.444(7)
		<i>Y</i> –O(6) × 2	<i>Z</i> –O(8)	<i>X</i> –O(4) × 3
	1.963(4)	1.884(4)	2.799(4)	
<i>T</i> -14	2.020(5)	1.886(5)	2.809(5)	
	<i>T</i> -7	2.026(7)	1.886(6)	2.820(7)
		<i>Y</i> –O(2) × 2	<i>Z</i> –O(7)	<i>X</i> –O(5) × 3
1.976(4)		1.953(4)	2.736(5)	
<i>T</i> -14	1.977(5)	1.959(4)	2.755(5)	
	<i>T</i> -7	1.975(7)	1.954(6)	2.755(8)
		<i>Y</i> –O(3)	<i>Z</i> –O(3)	<i>X</i> –O _{mean}
2.158(6)		1.954(5)	2.655	
<i>T</i> -14	2.167(6)	1.964(5)	2.670	
	<i>T</i> -7	2.171(7)	1.962(6)	2.673
		<i>Y</i> –O _{mean}	<i>Z</i> –O(8)	
2.022		1.903(4)		
<i>T</i> -14	2.033	1.912(5)		
	<i>T</i> -7	2.053	1.912(6)	
		<i>Y</i> –F	<i>Z</i> –O(7)	
1.82(3)		1.886(3)		
<i>T</i> -14	[2.20(3)] × 2			
	1.75(3)	1.878(4)		
	[2.24(2)] × 2			
<i>T</i> -7	1.84(4)	1.882(6)		
	[2.25(4)] × 2			
	<i>Y</i> –F _{mean}	<i>Z</i> –O _{mean}		
<i>T</i> -17	2.07	1.907		
	<i>T</i> -14	2.08	1.909	
		<i>T</i> -7	2.11	1.907

Table 7. Parameters of the O(3)–H...O(5) hydrogen bonds in the elbaite structures

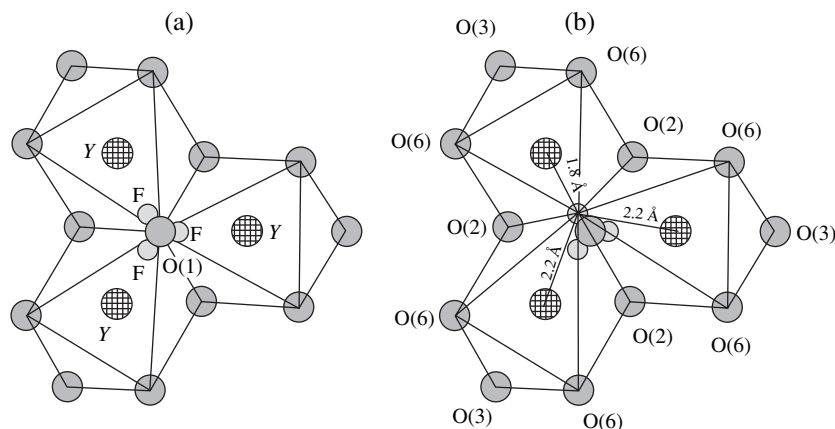
Tourmaline	Distance, Å			Angle, deg
	H–O(3)	H...O(5)	O(3)...O(5)	O(3)–H...O(5)
<i>T</i> -17	0.81	2.32	3.125(4)	172
<i>T</i> -14	0.88	2.40	3.167(5)	145
<i>T</i> -7	0.83	2.51	3.184(6)	138
Al elbaite [15]	0.940(2)	2.070(2)	2.993(5)	170(1)
Fe elbaite [16]	0.820(4)	2.340(3)	3.154(4)	169(3)

due regard for the aforesaid, by OH groups. An ordered distribution of fluorine anions and OH groups leads to a positional disorder and is characteristic, for example, of the crystal structure of hydroxyfluoroapatite [23]. Hence, there are strong grounds to believe that the splitting of the *W* site in the tourmaline structures under investigation is associated with the tendency toward ordering of fluorine anions and OH groups.

The crystal chemical formulas obtained for elbaite from the results of the structural analysis (Table 2, variant 2), on the whole, agree well with those calculated from the data of the electron microprobe analysis (Table 2, variant 1). The main difference consists in refining the occupancies of the *W* and *V* sites. Furthermore, it is found that, in the structure of sample *T*-17, the contribution of vacancies to the occupancy of the *X* sites appears to be smaller than the previously assumed contribution and the manganese cation impurity is located at the *Z* site. The results obtained show that the incorporation of iron and manganese bivalent cations into the *Y* octahedra in elbaite predominantly proceeds according to the scheme $\text{Li}^+ + \text{Al}^{3+} \rightleftharpoons 2(\text{Fe}^{2+}, \text{Mn}^{2+})$ and does not lead to the appearance of additional vacancies at the *X* sites or bivalent anions at the *V* or *W* sites.

The ordered distribution of OH groups and fluorine anions over the *W*1 and *W*2 sites indicates that the tourmaline structures involve octahedra of two types:

$[\text{YO}_4(\text{OH})_2]$ and $[\text{YO}_4(\text{OH})\text{F}]$ (Fig. 1). Their ratio depends on the fluorine content and varies from structure to structure. These ratios in samples *T*-17, *T*-14, and *T*-7 are equal to 1.78, 0.75, and 0.67, respectively. The $[\text{YO}_4(\text{OH})_2]$ octahedra located at the center of $\text{XY}_3\text{T}_6\text{O}_{18}$ antigorite islands are joined together into triads through a common vertex *W*1 lying on the threefold axis (Fig. 1a) and, hence, are equivalent to each other. With rare exceptions [18], similar triads composed of equivalent *Y* octahedra are observed in the majority of tourmaline structures. The fluorine anions are displaced from the threefold axis. Therefore, the $[\text{YO}_4(\text{OH})\text{F}]$ octahedra are linked together into triads that are statistically distributed with respect to this axis (Fig. 1b). In each triad, the *Y*–*F* bond length in one octahedron (1.75–1.84 Å) is considerably smaller than those in the two other octahedra (2.20–2.25 Å). Similar triads consisting of nonequivalent *Y* octahedra were found in the structure of elbaite from Brazil with the crystal chemical formula $(\text{Na}_{0.66}\text{Ca}_{0.30}\square_{0.31})(\text{Al}_{1.53}\text{Li}_{1.03}\text{Mn}_{0.41}\text{Fe}_{0.03})\text{Al}_6(\text{BO}_3)_3 \times (\text{Si}_{5.82}\text{B}_{0.18}\text{O}_{18})(\text{OH})_3(\text{F}_{0.62}\text{OH}_{0.34}\text{O}_{0.04})$ [18]. However, in the structure of this mineral, unlike the structures studied in the present work, no splitting of the *W* site was revealed. The displacement of this site from the threefold axis leads to the formation of the *Y* octahedra in a ratio of 1 : 2 in which the *Y*–*W* bond lengths are

**Fig. 1.** Triads composed of (a) $[\text{YO}_4(\text{OH})_2]$ and (b) $[\text{YO}_4(\text{OH})\text{F}]$ octahedra in the structures of the elbaite under investigation.

equal to 1.790 and 2.126 Å, respectively. We can assume that a substantial anisotropy of the $Y-W$ bond lengths in the crystal structures of tourmalines in which the W sites are displaced from the threefold axis may be due to the symmetry lowering. This lowering is so insignificant that it virtually does not affect the trigonal lattice parameters measured at room temperature. A similar effect in the crystal structure of the $K(Al_{0.95}Cr_{0.05})(SO_4)_2 \cdot 12H_2O$ alum was revealed in our earlier work [24].

CONCLUSIONS

Interrelated isomorphous substitutions at different sites in tourmaline structures suggest a certain convention in the separation of independent mineral species among them [11, 25]. Hawthorne and Henry [11] attempted to revise the nomenclature of minerals in the tourmaline group and proposed to recognize the fluor-, hydroxy-, and oxy-species on the basis of different occupancies of the V and W sites by the corresponding anions. The aforementioned results of the refinement of the crystal structures for three Li–Al natural fluorine-containing tourmalines (elbaite) confirm the validity of this classification.

The revealed splitting of the W threefold anion site into two sites, the refinement of their occupancies, and the analysis of the corresponding bond lengths allowed us to conclude that fluorine anions occupy the W sites in a regular way. There are grounds to believe that such a distribution of fluorine anions is a general feature of Li–Al tourmalines and, hence, can be used for determining their crystal chemical formulas from the chemical analysis data.

In the structures of two tourmalines under investigation (samples $T-14$, $T-7$), fluorine anions make a dominant contribution to the occupancy of the W site. This enables us to make the inference that fluor-elbaite with the ideal formula $Na(Li_{1.5}Al_{1.5})Al_6(Si_6O_{18})(BO_3)_3(OH)_3F$ is a new mineral species. Elbaite in which the W sites are occupied predominantly by OH groups (including sample $T-17$) can be referred to as hydroxy-elbaite with the ideal formula $Na(Li_{1.5}Al_{1.5})Al_6(Si_6O_{18})(BO_3)_3(OH)_3OH$. Therefore, elbaite is a superspecies involving no less than two mineral species.

ACKNOWLEDGMENTS

This work was supported by the Russian Foundation for Basic Research, project no. 04-05-64298.

REFERENCES

1. A. E. Fersman, *Selected Works* (Akad. Nauk SSSR, Moscow, 1960) [in Russian].

2. V. I. Kuz'min, I. V. Dobrovol'skaya, and L. S. Solntseva, *Tourmaline and Its Use in Prospecting and Evaluation* (Nedra, Moscow, 1979) [in Russian].
3. G. G. Afonina, V. M. Makagon, L. A. Bogdanova, and L. D. Zorina, *Tourmaline (X-ray Diffraction and Typomorphism)* (Nauka, Novosibirsk, 1990) [in Russian].
4. I. S. Peretyazhko, *Mineral. Zh.* **11**, 18 (1989).
5. M. G. Gorskaya, O. V. Frank-Kamenetskaya, and V. A. Frank-Kamenetskiĭ, in *Diffraction Methods for Investigating Crystalline Materials* (Nauka, Novosibirsk, 1989), p. 119 [in Russian].
6. O. V. Frank-Kamenetskaya and I. V. Rozhdestvenskaya, *Itogi Nauki Tekh., Ser.: Kristalloghimiya* **33**, 71 (2004).
7. G. E. Hamburger and H. J. Buerger, *Am. Mineral.* **33**, 532 (1948).
8. N. V. Belov and E. N. Belova, *Dokl. Akad. Nauk SSSR* **69**, 185 (1949).
9. T. Ito and R. Sadanaga, *Acta Crystallogr.* **4** (5), 385 (1951).
10. M. J. Buerger, C. W. Burnham, and D. R. Peacor, *Acta Crystallogr.* **15** (4), 583 (1962).
11. F. C. Hawthorne and D. J. Henry, *Eur. J. Mineral.* **11**, 201 (1999).
12. A. A. Zolotarev, *Zap. Vseross. Mineral. O–va* **125** (4), 32 (1996).
13. N. O. Ovchinnikov and A. A. Zolotarev, *Zap. Vseross. Mineral. O–va* **126** (4), 66 (1997).
14. L. G. Akselrud, Yu. N. Grin, P. Yu. Zavaliĭ, *et al.*, in *Proceedings of the XII European Crystal Meeting, Moscow, 1989* (Moscow, 1989), Vol. 3, p. 155.
15. M. G. Gorskaya, O. V. Frank-Kamenetskaya, I. V. Rozhdestvenskaya, and V. A. Frank-Kamenetskiĭ, *Kristallografiya* **27** (1), 107 (1982) [*Sov. Phys. Crystallogr.* **27** (1), 63 (1982)].
16. M. G. Gorskaya, Candidate's Dissertation in Geology and Mineralogy (Leningrad, 1985).
17. G. Donnay and R. Barton, *TMPM Tschermaks Mineral. Petrogr. Mitt.* **18**, 273 (1972).
18. J. D. Grice and T. S. Ercit, *Neues Jahrb. Mineral., Abh.* **165**, 245 (1993).
19. E. L. Belokoneva and V. G. Tsirel'son, *Zh. Neorg. Khim.* **38**, 1351 (1993).
20. A. Tippe and W. C. Hamilton, *Am. Mineral.* **50** (1–2), 101 (1971).
21. Yu. A. Pyatenko, *Kristallografiya* **17** (4), 773 (1972) [*Sov. Phys. Crystallogr.* **17** (4), 677 (1972)].
22. B. Nuber and K. Schmetzer, *Neues Jahrb. Mineral., Abh., No. 5*, 215 (1981).
23. K. Sudarsanan and R. Young, *Acta Crystallogr., Sect. B: Struct. Crystallogr. Cryst. Chem.* **34**, 1401 (1978).
24. I. V. Rozhdestvenskaya, O. V. Frank-Kamenetskaya, A. G. Shtukenberg, and I. I. Bannova, *Zh. Strukt. Khim.* **42** (4), 754 (2001).
25. A. A. Zolotarev and A. G. Bulakh, *Zap. Vseross. Mineral. O–va* **128** (2), 32 (1999).

Translated by O. Borovik-Romanova

STRUCTURE OF INORGANIC COMPOUNDS

Crystal Structure of $\text{CoUO}_2(\text{SO}_4)_2 \cdot 5\text{H}_2\text{O}$ at 293 K

E. V. Alekseev*, E. V. Suleimanov*, E. V. Chuprunov*, and G. K. Fukin**

* Nizhni Novgorod State University, pr. Gagarina 23, Nizhni Novgorod, 603950 Russia

e-mail: alev@uic.nnov.ru

** Institute of Organometallic Chemistry, Russian Academy of Sciences,
ul. Tropinina 49, Nizhni Novgorod, 603950 Russia

Received December 2, 2004; in final form, May 20, 2005

Abstract—Single crystals of cobalt uranyl sulfate are grown. The crystal structure is established by X-ray diffraction: the orthorhombic system, sp. gr. $Pmc2_1$, $a = 6.452(2)$ Å, $b = 8.295(2)$ Å, $c = 11.288(3)$ Å, $R_1 = 0.0303$, $wR_2 = 0.0735$ for reflections with $I > 2\sigma(I)$. The structure of $\text{CoUO}_2(\text{SO}_4)_2 \cdot 5\text{H}_2\text{O}$ consists of infinite two-dimensional uncharged $[\text{CoUO}_2(\text{SO}_4)_2\text{H}_2\text{O}]_{2\infty}$ layers, which are linked to each other by hydrogen bonds. © 2005 Pleiades Publishing, Inc.

INTRODUCTION

Complex studies of metal uranyl sulfates have been carried out over many decades. Interest in these compounds is related to the development of technologies for conversion of uranium ore. Study of the compounds with the general formula $A_{II}\text{UO}_2(\text{SO}_4)_2 \cdot 5\text{H}_2\text{O}$ [1] demonstrated that the replacement of such A_{II} atoms as Mn or Cd with Mg, Fe, Co, Ni, Cu, or Zn results in a morphotropic phase transition. In the former case, compounds crystallize in the monoclinic system with the angle β of about 91° . The structural features of the representatives of this structure type were considered in [2] for manganese compounds. The main difference of uranyl sulfates of the second structure type is that they crystallize in the crystal system of higher symmetry (orthorhombic). It is of interest to investigate the crystal structures of compounds of this class in more detail.

EXPERIMENTAL

Single crystals of cobalt uranyl sulfate pentahydrate $\text{CoUO}_2(\text{SO}_4)_2 \cdot 5\text{H}_2\text{O}$ were grown by isothermal evaporation of an aqueous solution of a 1 : 1 mixture of cobalt sulfate and uranyl sulfate. The resulting ruby-colored crystals were prismatic in shape.

X-ray diffraction data were collected from a crystal $0.28 \times 0.14 \times 0.06$ mm³ in size. (The crystal was not spherically ground because of its fragility.) X-ray diffraction study was carried out on a Smart Apex (Bruker) diffractometer equipped with an area detector. The unit-cell parameters were determined from 900 reflections using the Saint Plus program package. The calculations showed that the monoclinic ($\beta \sim 90.1^\circ$) and orthorhombic crystal systems are possible. The refinement of the unit-cell parameters using all X-ray diffraction data demonstrated that the orthorhombic system is

more likely. The equivalent reflections were merged and the semiempirical absorption correction was applied using the Sadabs program, as a result of which the factor R_{int} reduced from 21 to 4.5%.

Table 1. Details of X-ray diffraction study and crystallographic characteristics of $\text{CoUO}_2(\text{SO}_4)_2 \cdot 5\text{H}_2\text{O}$

Formula	$\text{CoUO}_2(\text{SO}_4)_2 \cdot 5\text{H}_2\text{O}$
M	611.16
T , K	293(2)
Sp. gr., Z	$Pmc2_1$, 2
a , Å	6.452(2)
b , Å	8.295(2)
c , Å	11.288(3)
V , Å ³	604.1(3)
ρ_{calcd} , g/cm ³	3.360
μ , mm ⁻¹	15.185
$F(000)$	562
Diffractometer	Smart Apex (Bruker)
Radiation	$\text{MoK}\alpha$
Crystal dimensions, mm ³	$0.28 \times 0.14 \times 0.06$
Scanning mode	ϕ - ω
Scan range	$-8 < h < 8$; $-11 < k < 11$; $-15 < l < 15$
Number of measured/independent reflections	5722/1695 $R_{\text{int}} = 0.045$
Number of reflections with $I > 2\sigma(I)$	1659
Program for structure calculations	SHELXTL
S on F^2	1.115
R [$I > 2\sigma(I)$]	$R_1 = 0.0303$, $wR_2 = 0.0735$
R (total data set)	$R_1 = 0.0309$, $wR_2 = 0.0738$

Table 2. Atomic coordinates and equivalent thermal parameters in the structure of $\text{CoUO}_2(\text{SO}_4)_2 \cdot 5\text{H}_2\text{O}$

Atom	<i>x/a</i>	<i>y/b</i>	<i>z/c</i>	Occupancy factor	$U_{\text{eq}}, \text{\AA}^2$
U(1)	0.5	-0.38695(2)	-0.88020(8)	1	0.00686(5)
S(1)	0.5	-0.7574(3)	-0.6920(1)	1	0.0097(4)
S(2)	0.5	-0.2611(4)	-0.5732(2)	1	0.056(1)
Co(1)	0	-0.8309(2)	-0.7103(2)	1	0.0318(4)
O(1)	0.243(1)	-0.432(1)	-0.9133(8)	0.5	0.020(2)
O(2)	0.242(2)	-0.341(2)	-0.8456(9)	0.5	0.026(3)
O(3)	0.5	-0.603(1)	-0.751(1)	1	0.053(3)
O(4)	0.321(1)	-0.854(1)	-0.724(1)	1	0.052(2)
O(5)	0.5	-0.723(2)	-0.568(1)	1	0.043(4)
O(6)	0.386(1)	-0.280(1)	-0.6945(6)	0.5	0.045(2)
O(7)	0.292(1)	-0.248(1)	-0.571(1)	0.5	0.053(4)
O(8)	0.355(2)	-0.121(2)	-0.524(1)	0.5	0.032(3)
O(9)	0.385(2)	-0.402(1)	-0.504(1)	0.5	0.022(2)
O(10)	0.420(2)	-0.0932(9)	-0.895(1)	0.5	0.024(3)
O(11)	0	-0.790(1)	-0.888(2)	1	0.053(3)
O(12)	0	-0.859(1)	-0.530(1)	1	0.046(3)
O(13)	0	0.084(1)	0.727(1)	1	0.041(3)
O(14)	0	-0.581(1)	-0.670(1)	1	0.049(3)

Note: The O(1) and O(2) atoms belong to uranyl groups UO_2 , the O(3)–O(5) atoms belong to the S(1) O_4 tetrahedron, the O(6)–O(9) atoms belong to the S(2) O_4 tetrahedron, the O(10) atom belongs to the water molecule in the UO_7 polyhedron, and the O(11)–O(14) atoms belong to the water molecules located between the layers.

Table 3. Selected interatomic distances (\AA) and bond angles (deg) in the structure of $\text{CoUO}_2(\text{SO}_4)_2 \cdot 5\text{H}_2\text{O}$

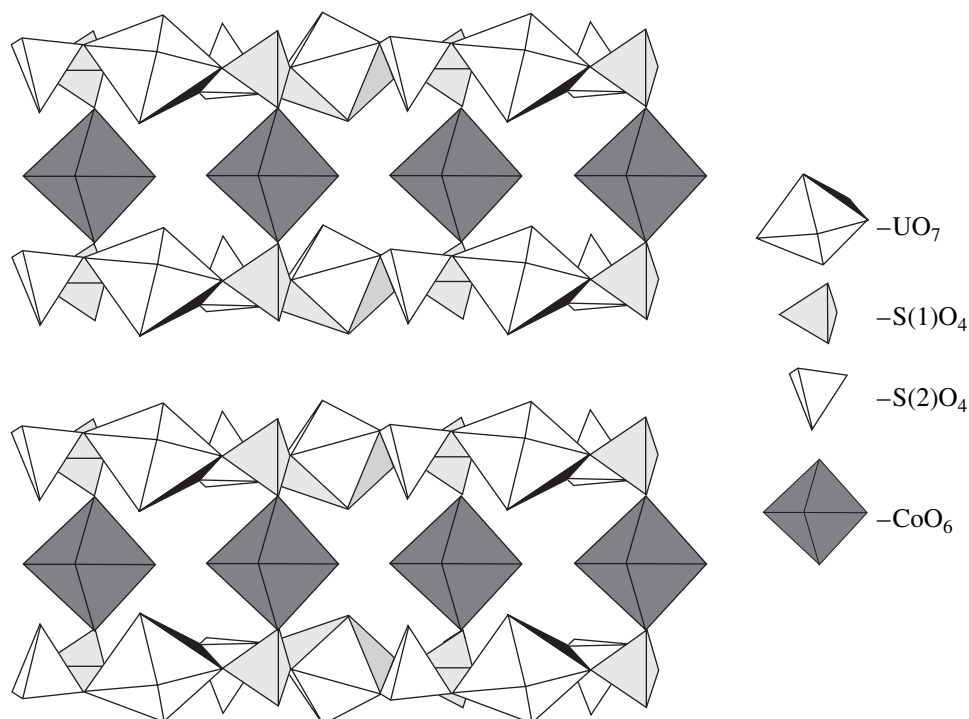
U–O, \AA		S(1)–O, \AA		S(2)–O, \AA		Co–O, \AA	
U–O(1)	1.745(9)	S(1)–O(3)	1.447(9)	S(2)–O(6)	1.563(7)	Co–2 · O(4)	2.087(6)
O(2)	1.75(1)	2 · O(4)	1.450(7)	O(7)	1.349(7)	O(11)	2.03(2)
O(3)	2.307(9)	O(5)	1.42(2)	O(8)	1.59(1)	O(12)	2.05(1)
O(5)	2.31(2)			O(9)	1.59(1)	O(13)	2.11(1)
O(6)	2.393(6)					O(14)	2.123(9)
O(9)	2.35(1)						
O(10)	2.496(8)						
Angle						Angle	
O(1)–U–O(2)	179.5(5)					O(4)–Co–O(4)	166.5(5)

The statistics of the normalized structure-factor amplitudes provided evidence that the most probable space group is noncentrosymmetric. Systematic absences indicated that the most probable space group is $Pmc2_1$. The crystal structure was solved by the direct method using the SHELXTL program package and refined by the least-squares method with anisotropic displacement parameters for all atoms. In the course of structure solution, some oxygen atoms were located in general positions with an occupancy of 0.5. The details

of X-ray diffraction study and crystallographic characteristics are given in Table 1. The atomic coordinates and equivalent thermal parameters are listed in Table 2. The principal interatomic distances and bond angles are given in Table 3.

RESULTS AND DISCUSSION

On the whole, the structure of $\text{CoUO}_2(\text{SO}_4)_2 \cdot 5\text{H}_2\text{O}$ is similar to the structure of $\text{MnUO}_2(\text{SO}_4)_2 \cdot 5\text{H}_2\text{O}$ [2].



Possible conformations of adjacent ribbons in the $[\text{CoUO}_2(\text{SO}_4)_2\text{H}_2\text{O}]_{2\infty}$ layers parallel to the (010) plane.

The crystal structure contains ribbons running along the z axis, which are formed by UO_7 pentagonal bipyramids and SO_4 tetrahedra (figure). The vertices of the pentagonal bipyramid are occupied by the oxygen atoms of the uranyl group (UO_2^{2+}), which is approximately perpendicular to the ribbon plane. The equatorial plane of the bipyramid is formed by one oxygen atom of a water molecule [O(10)] and four oxygen atoms of four sulfate groups [S(1)–O(3), S(1)–O(5), S(2)–O(6), and S(2)–O(9)], two O atoms of each sulfate group being involved in two adjacent bipyramids. Two other oxygen atoms of the sulfate group are coordinated to the Co atoms with the result that the ribbons are linked to each other along the x axis and form electroneutral $[\text{CoUO}_2(\text{SO}_4)_2\text{H}_2\text{O}]_{2\infty}$ layers parallel to the xz plane. As opposed to numerous uranyl compounds, the low-charged cations in the structure under consideration are involved in the layers. The layers are linked to each other by the hydrogen bonds between the O(8) atom of the $\text{S}(2)\text{O}_4$ group and the water molecule involved in the UO_7 polyhedron. The coordination environment of the cobalt ion is formed by two O(4) atoms of SO_4 groups and four molecules of crystallization water [O(11)–O(14)]. The CoO_6 polyhedron is a distorted octahedron (figure).

The difference between the structure of $\text{CoUO}_2(\text{SO}_4)_2 \cdot 5\text{H}_2\text{O}$ and that of $\text{MnUO}_2(\text{SO}_4)_2 \cdot 5\text{H}_2\text{O}$, established previously [2], is that some crystallographic positions in the former structure are randomly occupied

(Table 2). In our opinion, this phenomenon can be explained by two factors: a coherent intergrowth of microdomains rotated with respect to each other by 180° (i.e., microtwinning), which is responsible for the observed X-ray diffraction pattern, or the existence of two possible conformations of uranyl sulfate chains in one layer. As can be seen from Table 2, the positions of $\text{S}(1)\text{O}_4$ tetrahedra, CoO_6 octahedra, and $\text{S}(2)$ atoms (figure) are fixed. Two different arrangements of a particular uranyl group can be specified, which automatically determines the conformation of the ribbon as a whole. However, the UO_2 groups serving as the starting elements for the ribbon construction have arbitrary positions in the adjacent ribbons of the same layer. Taking into account this fact, the figure shows two different structures of two adjacent ribbons within one $[\text{CoUO}_2(\text{SO}_4)_2\text{H}_2\text{O}]_{2\infty}$ layer. It should be noted that $\text{S}(2)\text{O}_4$ tetrahedra can take different positions. This is also evidenced by the rather high thermal parameters of $\text{S}(2)$ atoms, which are indicative of particular random disorder within the crystal structure as a whole.

Two different arrangements of two neighboring ribbons from adjacent layers are theoretically possible. In one configuration, the O(10)–O(7) distance corresponding to the hydrogen bond between the water molecule and the terminal oxygen atom of the sulfate tetrahedron is 2.72(2) Å. In the other configuration, the O(10)–O(7) distance is 2.34(2) Å, which is highly improbable [3]. Hence, when specifying a particular position of the uranyl group in one ribbon, we automat-

ically determine the configurations of all parallel ribbons in the adjacent layers. However, as mentioned above, the adjacent ribbons in the same layer can be arranged arbitrarily.

In our opinion, the above facts suggest that it is the presence of different conformations that is responsible for the higher symmetry of the structure of $\text{CoUO}_2(\text{SO}_4)_2 \cdot 5\text{H}_2\text{O}$ in comparison with that of manganese uranyl sulfate.

CONCLUSIONS

In summary, we demonstrated that ribbons in layers of the structure of cobalt uranyl sulfate can adopt two

conformations with equal statistical probability, as evidenced by the statistics of the occupancies of some oxygen atoms of sulfate tetrahedra.

REFERENCES

1. V. N. Serezhkin and L. B. Serezhkina, *Zh. Neorg. Khim.* **23** (3), 751 (1978).
2. V. V. Tobachenko, V. N. Serezhkin, L. B. Serezhkina, and L. M. Kovba, *Koord. Khim.* **5** (10), 1563 (1979).
3. A. F. Wells, *Structural Inorganic Chemistry* (Clarendon, Oxford, 1984; Mir, Moscow, 1987–1988).

Translated by T. Safonova

STRUCTURE
OF INORGANIC COMPOUNDS

Structure Refinement of Cadmium Cerium(IV)
Phosphate $\text{Cd}_{0.5}\text{Ce}_2(\text{PO}_4)_3$

M. P. Orlova*, D. B. Kitaev*, M. L. Spiridonova*, N. V. Zubkova**,
Yu. K. Kabalov**, and A. I. Orlova*

* Faculty of Chemistry, Nizhni Novgorod State University,
pr. Gagarina 23, Nizhni Novgorod, 603950 Russia
e-mail: ormp@uic.nnov.ru

** Faculty of Geology, Moscow State University, Vorob'evy gory, Moscow, 119992 Russia
Received September 15, 2003; in final form, August 5, 2004

Abstract—Cadmium cerium orthophosphate $\text{Cd}_{0.5}\text{Ce}_2(\text{PO}_4)_3$ is synthesized by precipitation from aqueous solutions. The structure refinement from powder X-ray diffraction data is preceded by the sample preparation and structure solution. The refinement is carried out by the Rietveld method (ADP-2 diffractometer, $\text{Cu}_{K\alpha}$ radiation, Ni filter, $15^\circ < 2\theta < 120^\circ$, 2θ -scan step 0.02° , counting time 10 s per step). All calculations are carried out using the WYRIET program (version 3.3) within the sp. gr. $P2_1/n$. The structure is refined with anisotropic displacement parameters for cations and isotropic displacement parameters for oxygen atoms. © 2005 Pleiades Publishing, Inc.

INTRODUCTION

Among the crystalline materials used to immobilize wastes from nuclear power plants, compounds with a structure of the natural mineral monazite (Ce,La,Y,Ca,Th) PO_4 have attracted attention as promising materials. Cerium(III) phosphate CePO_4 (monoclinic system, sp. gr. $P2_1/n$) [1–3] is a synthetic analog of monazite. The latter occurs as an accessory mineral in many granitoids. Relatively large crystals are commonly found in pegmatites. Monazite is present in black-sand placer deposits as one of the heaviest and most stable components. In some cases it occurs as intergrowths with radioactive black (metamict minerals) formed owing to the presence of natural long-lived alpha-radioactive elements (thorium, uranium, transuranium elements). Monazite-like compounds have high stability under extreme conditions (high temperature, high pressure, radiation, aggressive chemical environment) [4]. In passing from simple to complex compositions, the phase homogeneity of phosphates is retained over wide concentration and temperature ranges [4–9].

Cerium(IV) generally serves as a chemical analog of plutonium in the design of crystalline (ceramic) materials for immobilization of plutonium-containing wastes. The presence of neutron-capture elements (such as Cd, Gd, and other rare earth metals) in cured products, necessary to provide a high safety barrier to radioactivity, must be taken into account.

Previously, we have synthesized cerium(IV) double phosphate of the composition $\text{Cd}_{0.5}\text{Ce}_2(\text{PO}_4)_3$ and characterized it by powder X-ray diffraction and IR spectroscopy [6]. This compound was found to belong to the monazite structure type.

The aim of this study was to synthesize cerium(IV) orthophosphate of the composition $\text{Cd}_{0.5}\text{Ce}_2(\text{PO}_4)_3$, examine the conditions of phase formation, refine the structure, and perform a comparative analysis of the changes in the structural parameters in a series of phosphates of the general formula $B_{0.5}\text{Ce}_2(\text{PO}_4)_3$, where B is an alkaline earth metal or cadmium.

EXPERIMENTAL

Cadmium cerium double orthophosphate was synthesized by precipitation followed by heating of the precipitates. A 1 M H_3PO_4 solution (reagent grade), $(\text{NH}_4)_2\text{Ce}(\text{NO}_3)_6$ (reagent grade), and $\text{Cd}(\text{NO}_3)_2 \cdot 4\text{H}_2\text{O}$ (reagent grade) were used as starting components. A specified amount of H_3PO_4 was added dropwise to stoichiometric mixtures of aqueous solutions of cerium(IV) and cadmium nitrates. Continuous stirring of the suspension was accompanied by the formation of a yellowish precipitate, which was dried at 80°C until the moisture evaporated. The powder was ground in an agate mortar and subjected to isothermal annealing in air and in oxygen in the temperature range $600\text{--}1100^\circ\text{C}$. The time of thermal treatment was 24 h per step.

The reaction product was studied by IR spectroscopy, powder X-ray diffraction, and single-crystal X-ray diffraction. The IR absorption spectra were recorded on a Specord-75 IR spectrophotometer in the frequency range from 1800 to 400 cm^{-1} . A sample was prepared as a fine-grain film on a KBr substrate. The X-ray diffraction spectrum was measured on an ADP-2 diffractometer ($\text{Cu}_{K\alpha}$ radiation, Ni filter) using the

2 θ -scan technique with a step of 0.02°; the counting time was 10 s per step. The structure was refined using the WYRIET program (version 3.3) [10]. The crystal structure of cheralite [7] served as the starting model. The peak profiles were approximated by the Pearson VII function. The asymmetry was refined at 2 $\theta \leq 60^\circ$. Ionic scattering curves were used in the refinement. The crystal structure was refined by successively adding the parameters under refinement and graphically modeling the background until the *R* factors ceased to change.

RESULTS AND DISCUSSION

The samples (several series) were prepared as gray-greenish polycrystalline powders.

The features of the IR spectrum indicate that the compound under study belongs to orthophosphates (Fig. 1). The synthesis was completed at 800°C. The compound was obtained as a powder upon heating to 1000°C. At higher temperatures (up to 1600°C), a dense sintered substance was obtained.

Powder X-ray diffraction analysis demonstrated that the compound synthesized belongs to the monazite structure type.

The results of the Rietveld refinement are shown in Fig. 2 (dotted and solid lines for the calculated and experimental data, respectively) and given in Table 1. The atomic coordinates and displacement parameters are listed in Table 2.

The fragment of the structure (Fig. 3) was constructed on the basis of the refined data. The refined crystal-chemical formula is $\text{Cd}_{0.17}\text{Ce}_{0.68}\square_{0.32}\text{P}_{0.99}\text{O}_4$.

The refinement demonstrated that the phosphate $\text{Cd}_{0.5}\text{Ce}_2(\text{PO}_4)_3$, like its analog CePO_4 , has a framework structure. The structure consists of nine-vertex polyhedra and tetrahedra, which are linked to each other to form a three-dimensional network. Oxygen atoms form bridging bonds with either two or (one-fourth of the oxygen atoms) three metal atoms. Phosphorus atoms occupy the centers of tetrahedra. Cadmium and cerium(IV) atoms occupy the centers of nine-vertex polyhedra. The monazite structure has one type of positions that can be occupied by metal cations. Hence, according to the chosen model, the cadmium and cerium atoms in the structure of the compound under consideration randomly substitute each other. The compound can be considered as a solid solution described by the crystal-chemical formula $\text{Cd}_{1/6}\square_{1/6}\text{Ce}_{2/3}\text{PO}_4$. The crystal-chemical model of cation substitutions in going from the analog $\text{Ce}^{\text{III}}\text{PO}_4$ to cadmium cerium(IV) phosphate is described by the formula $\text{Ce}^{3+} \longleftrightarrow 1/6\text{Cd}^{2+} + 1/6\square + 2/3\text{Ce}^{4+}$.

The occupancies of the metal position by cadmium and cerium are 0.168(2) and 0.684(1), respectively. The total occupancy is 0.852(2). The uncertainty was evaluated according to [11].

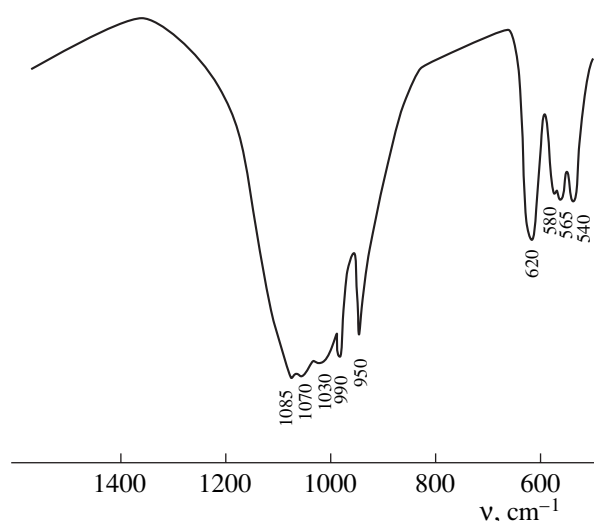


Fig. 1. IR spectrum of phosphate $\text{Cd}_{0.5}\text{Ce}_2(\text{PO}_4)_3$.

The bond distances and bond angles in the polyhedra (tetrahedron and nine-vertex polyhedron) of the phosphate $\text{Cd}_{0.5}\text{Ce}_2(\text{PO}_4)_3$ were compared with the corresponding parameters of magnesium phosphate $\text{Mg}_{0.5}\text{Ce}_2(\text{PO}_4)_3$ and calcium phosphate $\text{Ca}_{0.5}\text{Ce}_2(\text{PO}_4)_3$ [7], which are described by the same general formula, and the phosphate analog CePO_4 [12] (Fig. 4).

In magnesium, calcium, and cadmium phosphates, the average P–O distances in the PO_4 tetrahedron have similar values (1.59, 1.57, and 1.57 Å, respectively), which are slightly larger than the average P–O distance in the phosphate CePO_4 (1.527 Å). The longest dis-

Table 1. Unit-cell parameters and results of the Rietveld refinement of the crystal structure of $\text{Cd}_{0.17}\text{Ce}_{0.68}\square_{0.32}\text{P}_{0.99}\text{O}_4$

<i>a</i> , Å	6.7909(1)
<i>b</i> , Å	7.0163(1)
<i>c</i> , Å	6.4662(1)
β , deg	103.49(1)
<i>V</i> , Å ³	299.60(1)
Sp. gr.	<i>P</i> 2 ₁ / <i>n</i>
2 θ -angle range, deg	15.00–120
Number of reflections ($\alpha_1 + \alpha_2$)	960
Number of parameters in refinement	53
<i>R</i> _{wp}	3.98
<i>R</i> _B	3.37
<i>R</i> _F	3.23
<i>DWD</i> *	1.55
<i>S</i>	1.18

* The Durbin–Watson statistics [10].

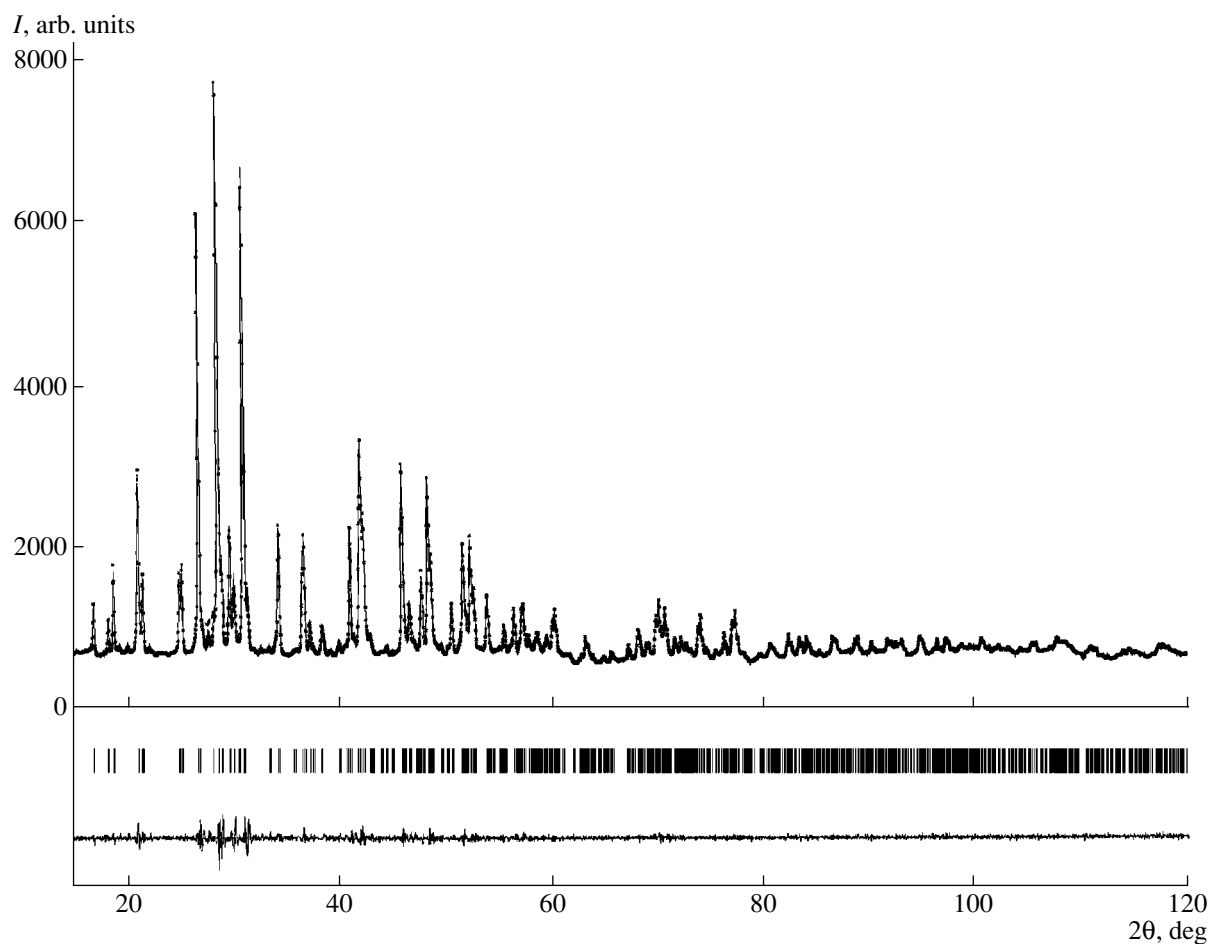


Fig. 2. X-ray diffraction spectrum of phosphate $\text{Cd}_{0.5}\text{Ce}_2(\text{PO}_4)_3$. The theoretical and experimental data are shown by asterisks and a solid line, respectively.

tances in these four compounds are 1.61, 1.60, 1.60, and 1.53 Å, respectively. The maximum differences in the distances in the tetrahedra of these compounds are 0.06, 0.07, 0.07, and 0.014 Å, respectively. The average O–P–O angles vary within a narrow range (109.4°–109.5°), although the maximum difference in the O–P–

O angles (20.2°) is observed in cadmium phosphates. For magnesium and calcium phosphates and CePO_4 , these differences are 14.4°, 12.7°, and 9.3°, respectively. Analysis of the above data demonstrated that the phosphate groups in the phosphate CePO_4 are least distorted. The distortions in the phosphates $B_{0.5}\text{Ce}_2(\text{PO}_4)_3$

Table 2. Atomic coordinates, occupancies of the Q positions, and displacement parameters $B_{\text{aniso}}/B_{\text{iso}}$ in the structure of phosphate $\text{Cd}_{0.168}\text{Ce}_{0.684}\square_{0.316}\text{P}_{0.979}\text{O}_4$

Position	Q	x	y	z	$B_{\text{aniso}}/B_{\text{iso}}$
[Cd/Ce]	0.852(25)	0.2167(5)	0.1577(5)	0.3986(5)	β_{11} 0.0056(6), β_{12} 0.0002(13), β_{13} 0.0011(5), β_{22} 0.0069(6), β_{23} 0.0016(13), β_{33} 0.0079(7)
P	0.979(7)	0.201(1)	0.160(2)	0.889(2)	β_{11} 0.011(3), β_{12} -0.001(5), β_{13} 0.002(2), β_{22} 0.010(2), β_{23} -0.002(5), β_{33} 0.011(3)
O(1)	1	0.249(3)	0.496(3)	0.441(3)	0.9(5)
O(2)	1	0.014(2)	0.133(3)	0.694(2)	2.0(5)
O(3)	1	0.376(2)	0.213(3)	0.787(6)	1.3(5)
O(4)	1	0.121(2)	0.343(3)	-0.008(3)	1.8(4)

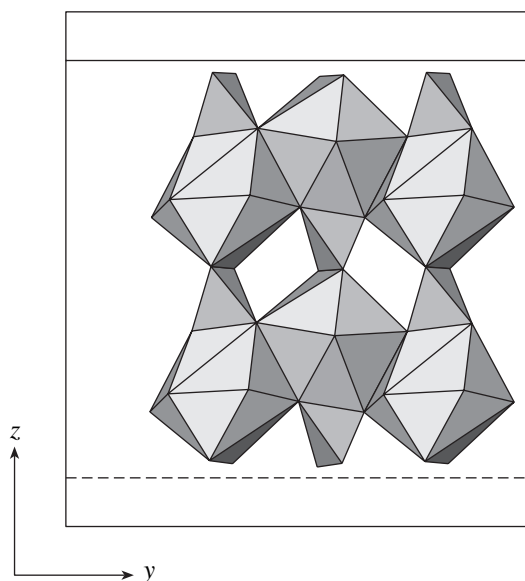


Fig. 3. Fragment of the structure of phosphate $\text{Cd}_{0.5}\text{Ce}_2(\text{PO}_4)_3$ projected onto the yz plane.

depend weakly on the nature of the B cation (Mg, Ca, Cd).

In the nine-vertex polyhedra of all compounds, one bond is longer than others: 2.86 Å (Mg/Ce–O), 2.87 Å (Ca/Ce–O, Cd/Ce–O), and 2.78 Å (Ce^{3+} –O). The average interatomic distances have similar values (2.55–2.56 Å). In phosphates of divalent metals and Ce(IV), the maximum differences in the distances in polyhedra, which characterize the degree of polyhedron distortion, have similar values. The difference between them is even smaller in cerium(III) phosphate. Therefore, the polyhedron in the analog CePO_4 , like the nine-vertex polyhedron in the compound under study, is less distorted. Hence, the replacement of one type of cations (Ce^{3+}) with pairs of cations, which differ in charge and size ($B^{2+} = \text{Mg}, \text{Cd}, \text{or Ca}, \text{and Ce}^{4+}$), leads to distortions in both types of the polyhedra and, consequently, in the $B_{0.5}\text{Ce}_2(\text{PO}_4)_3$ structures on the whole as compared to CePO_4 owing to a more complex chemical composition resulting from the heterovalent replacement of Ce(III) with a divalent metal and Ce(IV).

Nevertheless, it should be noted that distortions in the structure of synthetic monazite CePO_4 caused by the introduction of divalent metals and cerium(IV) into phosphates are insignificant. The changes in the unit-cell volumes are no larger than 1%. This is a prerequisite for the formation of complex monazite-type solid solutions in technogenic processes, in particular, in the processing of radioactive wastes. Moreover, it is known that actinide-containing analogs (i.e., containing uranium, neptunium, plutonium) of the compounds under consideration also crystallize in this structure type. The compounds $\text{Mg}_{0.5}\text{Np}_2(\text{PO}_4)_3$, $\text{Ca}_{0.5}\text{Np}_2(\text{PO}_4)_3$, $\text{Sr}_{0.5}\text{Np}_2(\text{PO}_4)_3$ [13], and $\text{Ca}_{0.5}\text{Pu}_2(\text{PO}_4)_3$ [8] form mon-

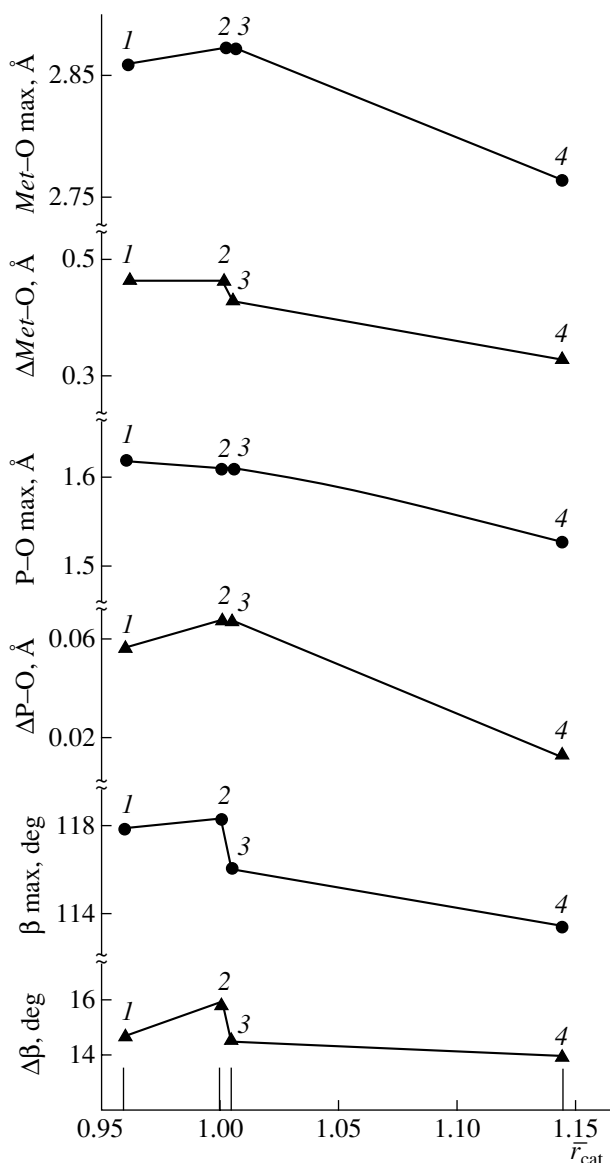


Fig. 4. Dependences of the interatomic distances and bond angles in the polyhedra of phosphates (1) $\text{Mg}_{0.5}\text{Ce}_2(\text{PO}_4)_3$, (2) $\text{Cd}_{0.5}\text{Ce}_2(\text{PO}_4)_3$, (3) $\text{Ca}_{0.5}\text{Ce}_2(\text{PO}_4)_3$, and (4) CePO_4 on the effective average radius of alkaline-earth and cerium cations \bar{r}_{cat} ; $\bar{r}_{\text{cat}} = \sum r_{i\text{cat}}/i$; Δ is the difference between the minimum and maximum values.

azite-type phases at 1000–1200°C, have similar crystallographic parameters, and form (together with cerium phosphates) a large group of isostructural monazite-like phases, which can, under corresponding process conditions crystallize as multicomponent multiphase products.

REFERENCES

1. T. Kato, *Mineral. J. Jpn.* **2**, 224 (1958).

2. C. Keller and K. H. Walter, *J. Inorg. Nucl. Chem.* **27**, 1253 (1965).
3. Y-X. Ni, J. M. Hughes, and A. N. Mariano, *Am. Mineral.* **80**, 21 (1995).
4. D. F. Mullica, E. L. Sappenfield, and L. A. Boatner, *Inorg. Chim. Acta* **244**, 247 (1996).
5. A. I. Orlova, D. B. Kitaev, Yu. F. Volkov, *et al.*, *Radiokhimiya*, No. 3, 202 (2001).
6. A. I. Orlova, D. B. Kitaev, G. N. Kazantsev, *et al.*, *Radiokhimiya* **44** (4), 299 (2002).
7. N. V. Zubkova, Yu. K. Kabalov, A. I. Orlova, *et al.*, *Kristallografiya* **48** (3), 445 (2003) [*Crystallogr. Rep.* **48** (3), 401 (2003)].
8. D. B. Kitaev, Yu. F. Volkov, and A. I. Orlova, *Radiokhimiya* **46** (3), 195 (2004).
9. A. I. Orlova, V. I. Pet'kov, and O. V. Egor'kova, *Radiokhimiya* **38** (1), 15 (1996).
10. J. Schneider, in *International Workshop on the Rietveld Method* (Petten, 1989), p. 71.
11. *Quantitative Description of Uncertainty in Analytical Measurements* (VNIIM im. D.I. Mendeleeva, St. Petersburg, 2002), p. 149 [in Russian].
12. J. J. Finney and N. N. Rao, *Am. Mineral.* **52**, 13 (1967).
13. Yu. F. Volkov, *Radiokhimiya* **41** (2), 161 (1999).

Translated by T. Safonova

STRUCTURE
OF ORGANIC COMPOUNDS

Crystal Structure of the Supramolecular System
of Indole-2,3-dione 1-(2-Oxopropyl)-3-Ethylene Ketal
and Its Thiosemicarbazone

O. M. Radul, S. T. Malinovskii, R. Luboradzki*, and F. Z. Macaev

Institute of Chemistry, Academy of Sciences of Moldova, Academiei 3, Chisinau, MD-20-28 Moldova

e-mail: stanis@dnt.md

* Institute of Physical Chemistry, Polish Academy of Sciences, Kasprzaka 44/52, Warsaw, 01-224 Poland

e-mail: romeek@ichf.edu.pl

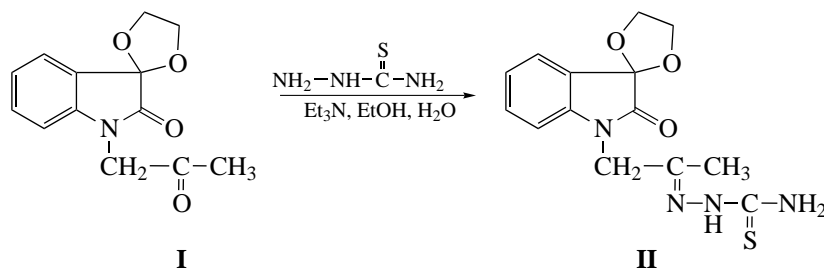
Received September 10, 2004

Abstract—The crystal structure of a supramolecular system consisting of indole-2,3-dione 1-(2-oxopropyl)-3-ethylene ketal (**I**) and indole-2,3-dione 1-(2-oxopropyl)-3-ethylene ketal thiosemicarbazone (**II**) molecules that are linked together by hydrogen bonds is determined using X-ray diffraction. The crystal is monoclinic, and the unit cell parameters are as follows: $a = 12.8360(3) \text{ \AA}$, $b = 10.7330(3) \text{ \AA}$, $c = 19.4610(3) \text{ \AA}$, $\beta = 99.566(1)^\circ$, space group $P2_1/c$, and $Z = 4$ ($C_{27}H_{29}N_5O_7S$). In molecules **I** and **II**, the indole-2,3-dione 3-ethylene ketal fragments have a virtually identical structure. The pyrrole and dioxolane fragments are spiro-linked through the carbon atom with a dihedral angle close to 90° . The adjacent pyrrole and benzene rings are coplanar to within 4.4° . In molecule **II**, the oxygen atom of the dioxolane fragment and the terminal nitrogen atom of the thiosemicarbazide fragment are involved in the $N-H \cdots O$ intramolecular hydrogen bond [$3.294(2) \text{ \AA}$]. The key role in the formation of the crystal structure is played by intermolecular hydrogen bonds of the $N-H \cdots O$, $C-H \cdots O$, $C-H \cdots N$, and $N-H \cdots S$ types. © 2005 Pleiades Publishing, Inc.

INTRODUCTION

The considerable interest expressed in the structure of the products formed upon the interaction of carbonyl compounds with thioacylhydrazines and thiosemicarbazides is associated with their biological activity and

the possible manifestation of ring–chain isomerism [1–3]. It is known that linear thiosemicarbazone molecules can transform into cyclic 1,3,4-thiadiazoles [4, 5]. We investigated the condensation reaction of a previously known compound, namely, *N*-acetylisonatin β -ethylene ketal (**I**) [6], with thiosemicarbazide (see scheme).



Scheme

However, the results of the elemental analysis and ^1H NMR investigation of the compound synthesized disagreed with the predicted structure of thiosemicarbazone **II**. In this respect, we carried out a complete X-ray diffraction analysis of the compound under consideration.

EXPERIMENTAL TECHNIQUE

Synthesis. A mixture of *N*-acetylisonatin β -ethylene ketal (1.23 g, 0.005 mol), thiosemicarbazide (0.45 g, 0.005 mol), and triethylamine (0.5 g, 0.005 mol) was boiled in a water–alcohol solution (1 : 5, 30 ml) for

Table 1. Main crystal data, data collection, and refinement parameters for the structure under investigation

Empirical formula	C ₂₇ H ₂₉ N ₅ O ₇ S
Molecular weight	567.61
Temperature, K	223(2)
Wavelength, Å	0.71073
Crystal system	Monoclinic
Space group, <i>Z</i>	<i>P</i> 2 ₁ / <i>c</i> , 4
<i>a</i> , Å	12.8360(3)
<i>b</i> , Å	10.7330(3)
<i>c</i> , Å	19.4610(3)
β, deg	99.566(1)
<i>V</i> , Å ³	2643.8(1)
ρ _{calcd} , g/cm ³	1.426
<i>F</i> (000)	1192
Crystal shape, mm	0.30 × 0.25 × 0.15
μ, mm ⁻¹	0.179
θ range, deg	2.17–27.47
Index ranges	–16 ≤ <i>h</i> ≤ 16, –10 ≤ <i>k</i> ≤ 13, –25 ≤ <i>l</i> ≤ 24
Number of reflections measured	8584
Number of unique reflections	6035
Number of reflections observed	3274 [<i>R</i> _{int} = 0.0190]
Number of parameters refined	479
<i>S</i> for <i>F</i> ²	1.036
Final <i>R</i> factor [<i>I</i> > 4σ(<i>I</i>)]	<i>R</i> ₁ = 0.0406, <i>wR</i> ₂ = 0.093
<i>R</i> factor (for all reflections measured)	<i>R</i> ₁ = 0.0616, <i>wR</i> ₂ = 0.0985

10 h. The precipitate (0.58 g) was subjected to fractional crystallization from an alcohol solution. The single crystals thus prepared were examined using X-ray diffraction.

X-ray diffraction analysis. The experimental set of intensities of X-ray reflections was collected on a KM4-CCD diffractometer (ω scan mode). The main crystal data and the data-collection and refinement parameters are presented in Table 1. The structure was solved by direct methods and refined with the SHELXS97 and SHELXL97 program packages [7]. The non-hydrogen atoms were refined in the anisotropic approximation. The hydrogen atoms were located from the difference Fourier synthesis and refined in the isotropic approximation. The coordinates of the non-hydrogen atoms are listed in Table 2.

RESULTS AND DISCUSSION

The crystal structure of the supramolecular complex synthesized is shown in Fig. 1. The crystal is built up of indole-2,3-dione 1-(2-oxopropyl)-3-ethylene ketal (**I**) and indole-2,3-dione 1-(2-oxopropyl)-3-ethylene ketal

Table 2. Coordinates of the non-hydrogen atoms (×10⁴) and their equivalent isotropic thermal parameters *U*_{eq} (×10³) for the structure under investigation

Atom	<i>x</i>	<i>y</i>	<i>z</i>	<i>U</i> _{eq}
S(1)	1127(1)	8676(1)	494(1)	17(1)
N(1A)	–2821(1)	4917(1)	–35(1)	16(1)
N(2A)	–957(1)	5979(1)	357(1)	15(1)
N(3A)	–23(1)	6647(1)	525(1)	16(1)
N(4A)	–818(1)	8222(2)	–167(1)	21(1)
O(1A)	–2100(1)	4545(1)	–1027(1)	19(1)
O(2A)	–2901(1)	7148(1)	–1219(1)	18(1)
O(3A)	–4177(1)	5711(1)	–1620(1)	19(1)
C(2A)	–2720(1)	5082(2)	–715(1)	15(1)
C(3A)	–3494(1)	6132(2)	–1019(1)	16(1)
C(4A)	–4866(1)	7252(2)	–373(1)	19(1)
C(5A)	–5270(1)	7293(2)	253(1)	23(1)
C(6A)	–4831(1)	6556(2)	812(1)	23(1)
C(7A)	–3994(1)	5749(2)	777(1)	19(1)
C(8A)	–3613(1)	5710(2)	151(1)	15(1)
C(9A)	–4037(1)	6455(2)	–412(1)	15(1)
C(10A)	–4011(1)	6495(2)	–2194(1)	19(1)
C(11A)	–2910(1)	6981(2)	–1960(1)	21(1)
C(12A)	–2057(1)	4225(2)	452(1)	17(1)
C(13A)	–1033(1)	4933(2)	661(1)	15(1)
C(14A)	–222(1)	4325(2)	1198(1)	20(1)
C(15A)	23(1)	7809(2)	264(1)	15(1)
N(1B)	2554(1)	6977(1)	2567(1)	16(1)
O(1B)	4139(1)	6205(1)	3128(1)	22(1)
O(2B)	2744(1)	5926(1)	4208(1)	23(1)
O(3B)	2594(1)	4308(1)	3433(1)	24(1)
O(4B)	2813(1)	9531(1)	2685(1)	30(1)
C(2B)	3180(1)	6285(2)	3053(1)	16(1)
C(3B)	2455(1)	5606(2)	3496(1)	18(1)
C(4B)	391(1)	5766(2)	3330(1)	22(1)
C(5B)	–495(1)	6293(2)	2922(1)	24(1)
C(6B)	–384(1)	7110(2)	2386(1)	22(1)
C(7B)	611(1)	7414(2)	2231(1)	19(1)
C(8B)	1472(1)	6862(2)	2631(1)	16(1)
C(9B)	1373(1)	6060(2)	3179(1)	17(1)
C(10B)	3196(2)	4845(2)	4566(1)	28(1)
C(11B)	2684(2)	3792(2)	4110(1)	27(1)
C(11K)	3288(13)	3911(12)	4046(6)	27(4)
C(12B)	2964(1)	7673(2)	2037(1)	17(1)
C(13B)	3084(1)	9050(2)	2181(1)	18(1)
C(14B)	3548(2)	9774(2)	1645(1)	27(1)

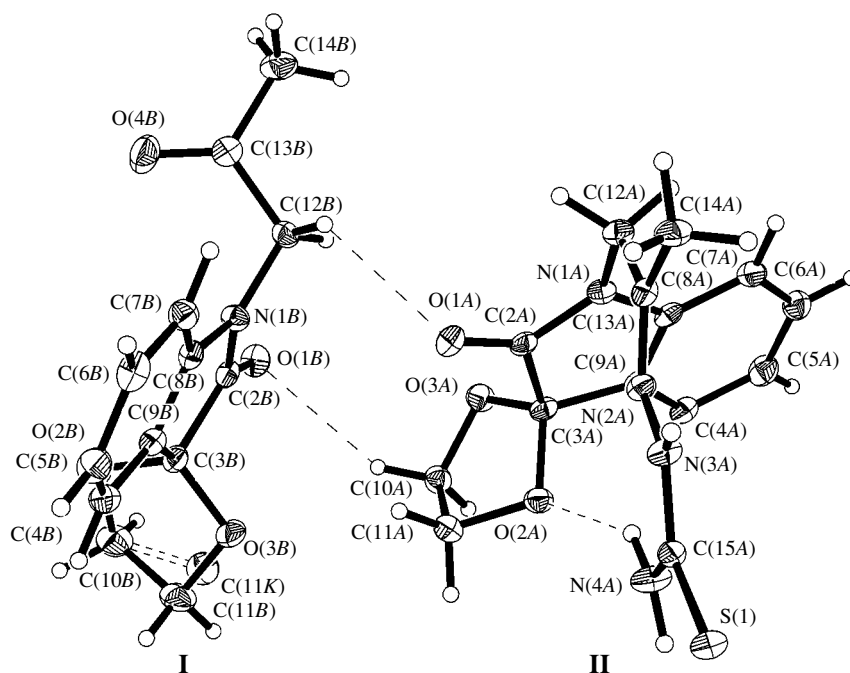


Fig. 1. Structures of molecules **I** and **II**.

thiosemicarbazone (**II**) molecules that are linked together into a noncentrosymmetric dimer through the intermolecular hydrogen bonds $C(12B)\cdots H(12e)\cdots O(1A)$ and $C(10A)\cdots H(10b)\cdots O(1B)$ [the $H\cdots O$ distances are 2.54(2) and 2.53(2) Å], for which the graph set can be written in the form $R_2^2(11)$ [8]. The geometric parameters of the hydrogen bonds are presented in Table 3.

The structures and configurations of the indole fragments of indole-2,3-dione 3-ethylene ketal in molecules **I** and **II** are nearly identical to each other and differ only slightly from those described in [9]. In both cases, the pyrrole and dioxolane rings in the indole

fragment of the structure are spiro-linked through the C(3) carbon atom and form dihedral angles of $84.5(1)^\circ$ and $82.7(1)^\circ$ in molecules **I** and **II**, respectively. The pyrrole and benzene rings lie in virtually the same plane to within $1.8(1)^\circ$ in molecule **I** and $4.4(1)^\circ$ in molecule **II**. The considerable acoplanarity of the indole fragments can be associated with the fact that molecule **II** is stabilized by the intramolecular hydrogen bond $N(4A)\cdots H\cdots O(2A)$ [3.294(2) Å], which is described by the graph set $S(11)$ and formed by the terminal nitrogen atom of the thiosemicarbazide fragment and the oxygen atom of the dioxolane fragment. In molecules **I** and **II**, the dioxolane fragment adopts an envelope conformation, which is characteristic of this class of compounds

Table 3. Geometric parameters of the hydrogen bonds in the structure under investigation

D–H...A	D–H, Å	H...A, Å	D...A, Å	DHA angle, deg
$N(3A)\cdots H(3a)\cdots O(1A)^{\#1}$	0.85(2)	2.20(2)	3.022(2)	161(2)
$N(4A)\cdots H(4a)\cdots S(1)^{\#5}$	0.93(3)	2.49(3)	3.400(2)	168(2)
$N(4A)\cdots H(4b)\cdots O(2A)$	0.88(2)	2.53(2)	3.294(2)	145(2)
$C(4A)\cdots H(4c)\cdots O(1B)^{\#2}$	0.97(2)	2.45(2)	3.413(2)	170(2)
$C(10A)\cdots H(10b)\cdots O(1B)$	0.98(2)	2.53(2)	3.411(2)	148(2)
$C(10A)\cdots H(10a)\cdots O(1B)^{\#2}$	0.97(2)	2.64(2)	3.553(2)	159(1)
$C(11B)\cdots H(11c)\cdots N(4A)^{\#3}$	0.98(3)	2.10(3)	3.035(3)	159(2)
$C(12B)\cdots H(12e)\cdots O(1A)$	0.96(2)	2.54(2)	3.167(2)	123(1)
$C(14A)\cdots H(14c)\cdots O(1A)^{\#1}$	0.94(3)	2.51(3)	3.286(2)	140(2)
$C(14B)\cdots H(14i)\cdots O(1bB)^{\#4}$	0.93(3)	2.48(3)	3.307(2)	147(2)

Note: Symmetry operations: $\#1 -x, -y+1, -z$; $\#2 -x-1, y+0.5, -0.5-z$; $\#3 x, 1.5-y, -0.5-z$; $\#4 -1-x, -0.5+y, -0.5-z$; $\#5 -x, -y+2, -z$.

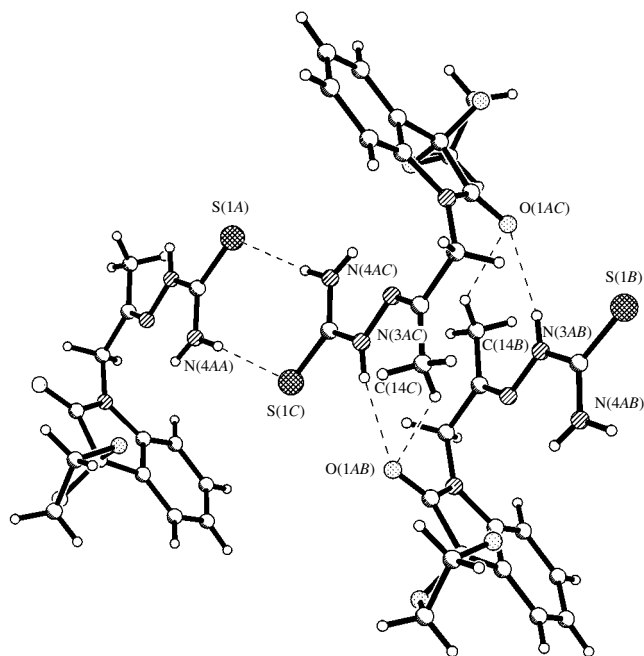


Fig. 2. A fragment of the chain formed by molecules **I**.

[10]. In molecule **II**, the C(11A) atom deviates by $-0.578(2)$ Å from the root-mean-square plane formed by the O(2A), C(3A), O(3A), and C(10A) atoms. The dioxolane fragment in molecule **I** exists in the form of two conformers due to the statistical disordering of the C(11) atoms over two positions, C(11B) and C(11K), with occupancies of 0.834 and 0.166, respectively. The C(11B) and C(11K) atoms deviate by $0.508(4)$ and $-0.31(2)$ Å, respectively, from the root-mean-square plane formed by the O(2B), C(3B), O(3B), and C(10B) atoms. Since the occupancy of the position of the

C(11K) atom is not very high and, consequently, the hydrogen atoms cannot be located at this position, we do not analyze the role played by the C(11K) atom in the formation of the crystal structure.

The structure and configuration of the thiosemicarbazide fragment in molecule **II** differ only slightly both from those observed for the free molecule [11] and from the structure of the thiosemicarbazide fragment attached to the carbon atom through the N=C double bond [12], as in the case under consideration. The N(2A)–C(13A) bond length is equal to $1.280(2)$ Å, and the N(2A)–N(3A)–C(15A)–N(4A) torsion angle is $3.1(2)^\circ$. The S(1)–C(15A) distance [$1.692(2)$ Å] suggests that the thiosemicarbazide fragment of the molecule has the thione form. Molecules **I** and **II** have a substantially nonplanar structure. The dihedral angles between the planar indole fragment and the acetonitrile group in molecule **I** and the thiosemicarbazide fragment in molecule **II** are equal to $79.4(1)^\circ$ and $78.5(1)^\circ$, respectively.

In the crystal, molecules **II** form infinite chains with centrosymmetric motifs through the hydrogen bonds N(3A)–H(3a)···O(1A)^{#1} [$3.022(2)$ Å], C(14A)–H(14c)···O(1A)^{#1} [$3.286(2)$ Å], and N(4A)–H(4a)···S(1)^{#5} [$3.400(2)$ Å] (Table 3). It is worth noting that the first two hydrogen bonds are responsible for the centrosymmetric motif with two different centrosymmetric fragments, namely, $R_2^2(16)$ and $R_2^2(14)$, whereas the third hydrogen bond leads to the formation of the fragment $R_2^2(8)$ (Fig. 2). The criteria for the formation of these bonds were considered in [13–15]. Molecules **I** are joined by the intermolecular hydrogen bonds C(14B)–H(14f)···O(1B)^{#4} [$3.307(2)$ Å] with the graph set $C(7)$ and form zigzag chains parallel to the [010] direction (Fig. 3), as is the case with molecules **II**. In

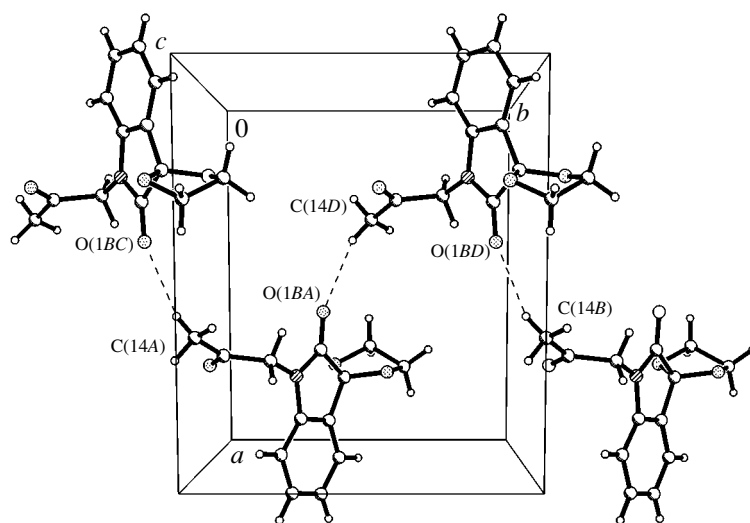


Fig. 3. A fragment of the chain formed by molecules **II**.

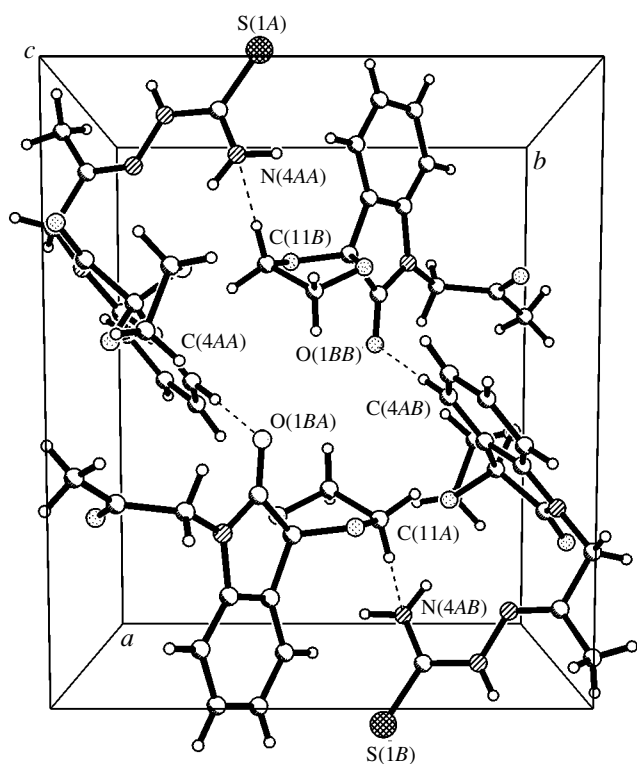


Fig. 4. A centrosymmetric fragment of the crystal structure formed by molecules **I** and **II**.

turn, the formation of the hydrogen bonds $C(4A)\cdots H(4c)\cdots O(1B)^{\#2}$ [3.413(2) Å] and $C(11B)\cdots H(11b)\cdots N(4A)^{\#3}$ [3.035(3) Å] between molecules **I** and **II** is responsible for the centrosymmetric motif with the graph set $R_4^4(34)$ (Fig. 4).

CONCLUSIONS

Thus, the results of the X-ray diffraction analysis performed in this study demonstrated that the reaction

shown in the scheme actually leads to the formation of thiosemicarbazone **II**; however, this compound crystallizes in the form of a complex with the initial ketal **I**. The crystal structure formed by two molecules, **I** and **II**, which have different compositions, can be considered a three-dimensional supramolecular system.

REFERENCES

1. V. A. Khrustalev, K. N. Zelenin, V. P. Sergutina, *et al.*, *Khim. Geterotsikl. Soedin.*, No. 8, 1188 (1980).
2. K. N. Zelenin, V. A. Khrustalev, V. V. Pinson, *et al.*, *Zh. Org. Khim.* **16** (10), 2237 (1980).
3. K. N. Zelenin, V. V. Alekseev, and V. A. Khrustalev, *Zh. Org. Khim.* **20** (1), 169 (1984).
4. V. G. Yusupov, V. M. Toshev, S. O. Saidov, *et al.*, *Zh. Neorg. Khim.* **37** (5), 1039 (1982).
5. M. Uda and S. Kubota, *J. Heterocycl. Chem.* **16**, 1273 (1979).
6. G. Zhungietu, *Roum. Chem. Q. Rev.* **46**, 517 (2001).
7. G. M. Sheldrick, *SHELXS97 and SHELXL97* (University of Göttingen, Göttingen, 1997).
8. J. Bernstein, E. Raymond, E. Davis, *et al.*, *Angew. Chem., Int. Ed. Engl.* **34**, 1555 (1995).
9. M. Oestreich, P. R. Dennison, J. J. Kodanko, *et al.*, *Angew. Chem. Int. Ed. Engl.* **40**, 1439 (2001).
10. A. De, *Acta Crystallogr., Sect. C: Cryst. Struct. Commun.* **48**, 660 (1992).
11. F. Hansen and R. G. Hazell, *Acta Chem. Scand.* **23**, 1359 (1969).
12. A. Morsali, A. Ramarani, F. Jamali, *et al.*, *Z. Kristallogr.-New Cryst. Struct.* **216**, 607 (2001).
13. Jagarlapudi A. R. P. Sarma and G. R. Desiraju, *J. Chem. Soc., Perkin Trans. 2*, 1195 (1987).
14. G. R. Desiraju and T. Steiner, *The Weak Hydrogen Bond* (Oxford University Press, New York, 1999).
15. T. Steiner, *Angew. Chem., Int. Ed. Engl.* **41**, 48 (2002).

Translated by O. Borovik-Romanova

STRUCTURE OF ORGANIC COMPOUNDS

Synthesis, Conductivity, and the Crystal Structure of a New Stable Metal, β'' -(*DOEO*)₂HSeO₄ · H₂O

A. A. Bardin*, A. I. Kotov**, G. V. Shilov**, and L. I. Buravov**

* Institute of Microelectronics Technology,
Russian Academy of Sciences, Chernogolovka, Noginskiĭ raĭon, Moscow oblast, 142432 Russia
e-mail: bardin@ipmt-hpm.ac.ru

** Institute of Problems of Chemical Physics, Russian Academy of Sciences,
Chernogolovka, Noginskiĭ raĭon, Moscow oblast, 142432 Russia

Received June 28, 2005; in final form, July 7, 2005

Abstract—The stable metal β'' -(*DOEO*)₂HSeO₄ · H₂O (**I**) based on a new donor compound, 3,4-(1,4-dioxanediyl-2,3-dithio)-3',4'-ethylenedioxo-2,5,2',5'-tetrathiafulvalene] (*DOEO*), is synthesized and structurally characterized for the first time. The synthesis is performed by the electrocrystallization technique (direct current density $j = 2 \times 10^{-6}$ A/cm²). The crystals are triclinic, and the unit cell parameters are as follows: $a = 5.495(1)$ Å, $b = 9.715(2)$ Å, $c = 16.878(3)$ Å, $\alpha = 83.52(3)^\circ$, $\beta = 82.54(3)^\circ$, $\gamma = 73.51(3)^\circ$, $Z = 1$, and space group $P\bar{1}$. The salt has a layered structure. The *DOEO*^{1/2+} radical cation layers are aligned parallel to the *ab* planes. The HSeO₄⁻ · H₂O solvated anions are located in channels along the *a* axis and are disordered over two positions near the center of symmetry (1/2 0 0) with a probability of 50%. The conductivity of the salt is equal to 300–400 Ω⁻¹ cm⁻¹ at room temperature and increases upon cooling to the boiling point of liquid helium (4.2 K) by a factor of 100–200 depending on the sample. © 2005 Pleiades Publishing, Inc.

INTRODUCTION

Radical cation salts based on a new donor compound, 3,4-(1,4-dioxanediyl-2,3-dithio)-3',4'-ethylenedioxo-2,5,2',5'-tetrathiafulvalene (*DOEO*), are poorly known. At present, there are data on the structure of only one of such salts, namely, (*DOEO*)₂BF₄ [1] (however, these data have not been deposited with the Cambridge Crystallographic Data Center). The data available in the literature on the structure of the *DOEO* salts are very scarce because the preparation of this donor presents considerable difficulties and the anion subsystem of these salts is strongly disordered [2]. Investigation into the crystal structure of β'' -(*DOEO*)₂HSeO₄ · H₂O (**I**) is necessary both for subsequent calculations of the electronic structure of the crystal and for the determination of the structure–property correlations, in particular, with the aim of elucidating the nature of high conduction of this salt.

EXPERIMENTAL TECHNIQUE

Synthesis. Compound **I** was prepared through electrocrystallization under direct current conditions [3]. 3,4-(1,4-Dioxanediyl-2,3-dithio)-3',4'-ethylenedioxo-2,5,2',5'-tetrathiafulvalene (10 mg, 24 μmol), 18-crown-6 (100 mg, 378 μmol), and CsHSeO₄ (50 mg, 180 μmol) were placed in an electrochemical cell and dissolved in chlorobenzene (20 ml) with an additive of

dehydrated ethanol (2 ml). The electrochemical cell was filled with argon. Platinum electrodes with an anode area of ≈0.3 cm² were placed in the cell. Then, the cell was sealed. The electrosynthesis was performed in a thermostat at a temperature of 20°C. At an initial current of 0.1 μA, nucleation was not observed. Then, the current was sequentially increased to 0.2, 0.3, 0.4, 0.5, and 0.6 μA. At the last value of the current, needle-shaped crystals began to grow. In this case, the voltage was varied in the range from 0.5 V (0.1 μA) to 1.2 V (0.6 μA). Single crystals suitable for X-ray diffraction analysis precipitated on the anode for two weeks.

Conductivity measurements. The electrical conductivity of crystals **I** was measured in the *ab* plane by the standard four-point probe method on an automated setup. The electrical conductivity in the *ab* plane at room temperature $\sigma_{||294}$ was equal to 300–400 Ω⁻¹ cm⁻¹. The samples were slowly cooled from room temperature to the boiling point of liquid helium (4.2 K) at a rate of ≈1 K/min. The temperature dependence of the electrical conductivity exhibits a metallic behavior over the entire temperature range. During cooling, the electrical conductivity gradually increases by a factor of 100–200 (at 4.2 K) depending on the sample (Fig. 1).

X-ray diffraction analysis. The crystals C₂₄H₂₃O₁₃S₁₂Se [$M = 983.18(4)$] are triclinic, $a = 5.495(1)$ Å, $b = 9.715(2)$ Å, $c = 16.878(3)$ Å, $\alpha = 83.52(3)^\circ$, $\beta = 82.54(3)^\circ$, $\gamma = 73.51(3)^\circ$, $V = 853.9(3)$ Å³,

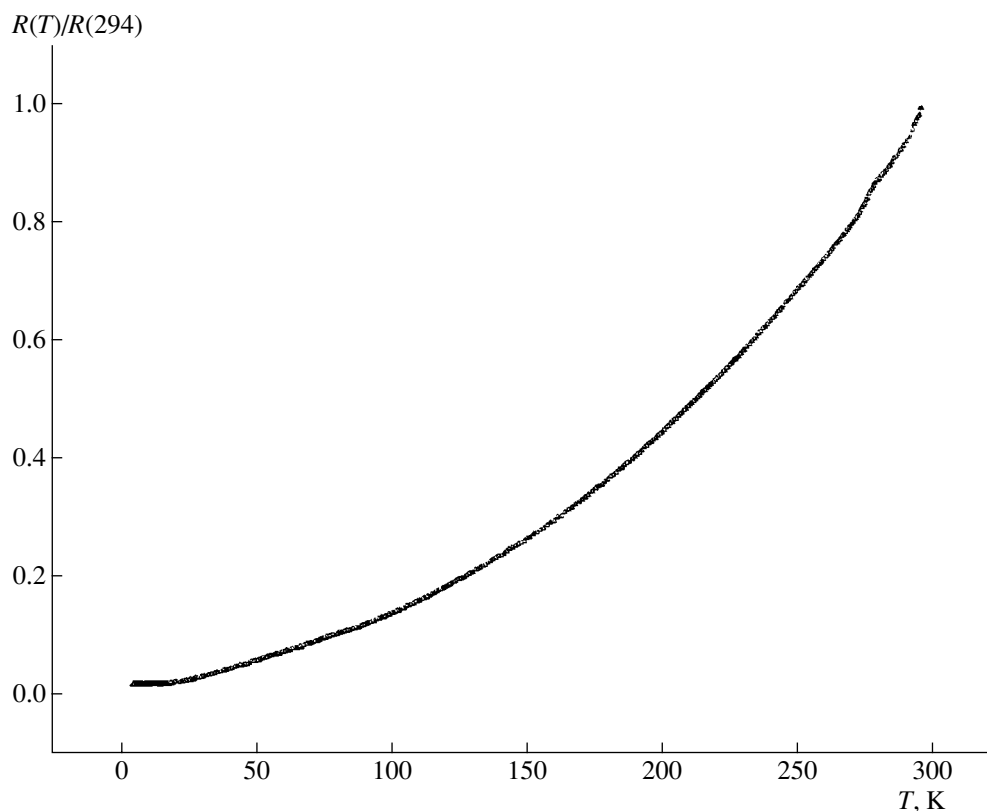


Fig. 1. Temperature dependence of the resistance for crystals of compound I.

$Z = 1$, space group $P\bar{1}$, $\rho_{\text{calcd}} = 1.910 \text{ g/cm}^3$, and $\mu(\text{Mo}) = 1.898 \text{ mm}^{-1}$.

The experimental set of diffraction reflections was collected on a KUMA DIFFRACTION KM-4 automated diffractometer ($\lambda \text{ MoK}\alpha$, $\omega/2\theta$ scan mode, $1.22^\circ < \theta < 25.94^\circ$) for a single crystal $1.00 \times 0.25 \times 0.04 \text{ mm}$ in size. The structure was solved by direct methods with the SHELXS97 program package [4]. The hydrogen atoms of the *DOEO* radical cation were placed in the calculated positions and refined within a riding model. The positions of the hydrogen atoms of the solvated water molecule were located from the difference synthesis and refined with fixed values $U_{\text{iso}} = 0.05 \text{ \AA}^2$. The positions of the non-hydrogen atoms were refined by the least-squares method in the anisotropic approximation with the SHELXL97 program package [5].

The structure was refined to $R_1 = 0.0440$ and $wR_2 = 0.1200$ for 2048 reflections with $I > 4\sigma(I)$, $R_1 = 0.0898$ and $wR_2 = 0.1308$ for all 2959 unique reflections, and $S = 0.979$. The residual electron density lies in the range $0.652 > \Delta\rho > -0.689 \text{ e/\AA}^3$. The calculations and data processing were performed with the WinGX and ORTEP program packages [6, 7]. The crystallographic data for the structure of compound I have been deposited with the Cambridge Crystallographic Data Center (CCDC no. 280707).

RESULTS AND DISCUSSION

In compound I, the asymmetric part of the unit cell involves one *DOEO* radical cation (A) and the $\text{HSeO}_4^- \cdot \text{H}_2\text{O}$ solvated anion disordered over two positions. The occupancy of the anion positions is equal to 0.5. According to the electroneutrality condition, the formal charge of the *DOEO* radical cation is +0.5. The crystal structure of compound I is formed by layers consisting of *DOEO* radical cations (Fig. 2).

The dioxane rings of the *DOEO* radical cations deviate from the radical cation layers and form walls of channels that are aligned parallel to the a axis and in which the $\text{HSeO}_4^- \cdot \text{H}_2\text{O}$ solvated anions are located.

The disordered anions HSeO_4^- have a tetrahedral structure (Fig. 3). Both of the disordered anion positions are arranged in the same cavity in the immediate vicinity of the center of symmetry $(1/2 \ 0 \ 0)$. The distance between the central selenium atoms in the anions occupying two disordered positions is short and equal to $1.415(5) \text{ \AA}$. The Se–O bond lengths are close to those in the structures with ordered solvated anions $\text{HSeO}_4^- \cdot \text{H}_2\text{O}$, for example, in the structure of $(\text{APA})\text{HSeO}_4 \cdot \text{H}_2\text{O}$ [8], where *APA* is 9-azaphenanthrene.

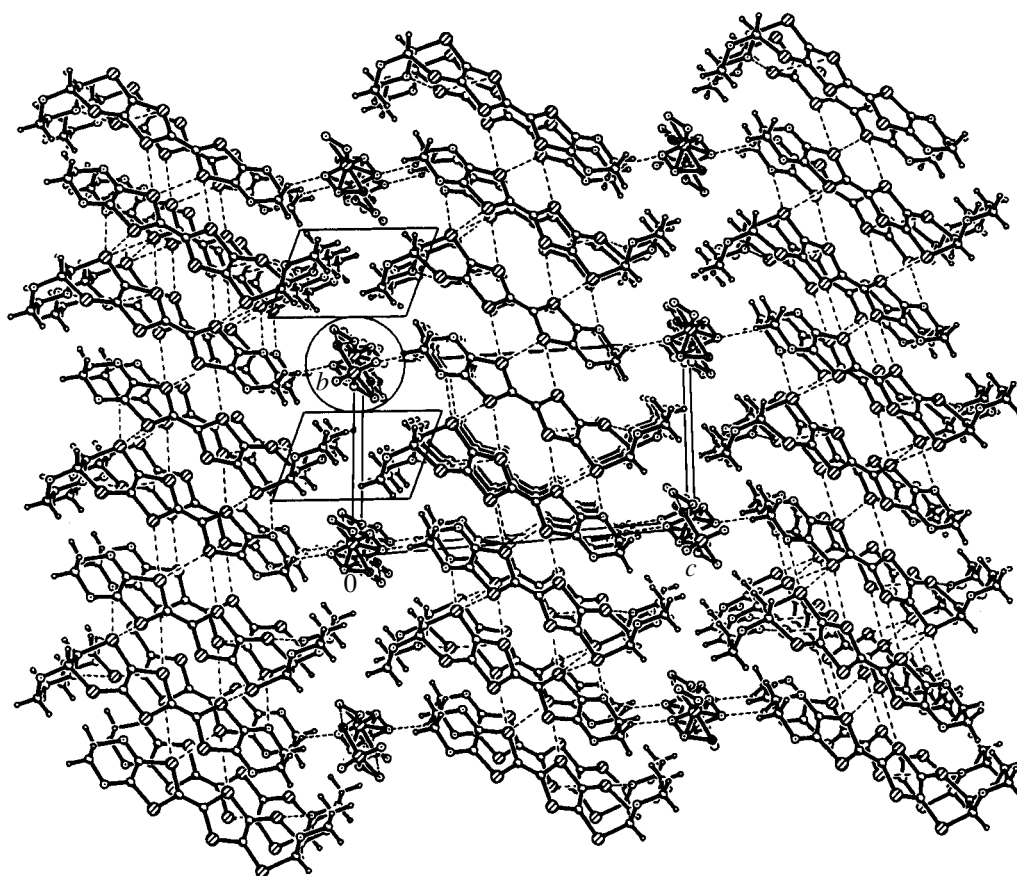


Fig. 2. Crystal structure of compound **I**. Dashed lines represent shortened intermolecular contacts, parallelograms indicate the dioxane rings, and the circle shows the anion channel.

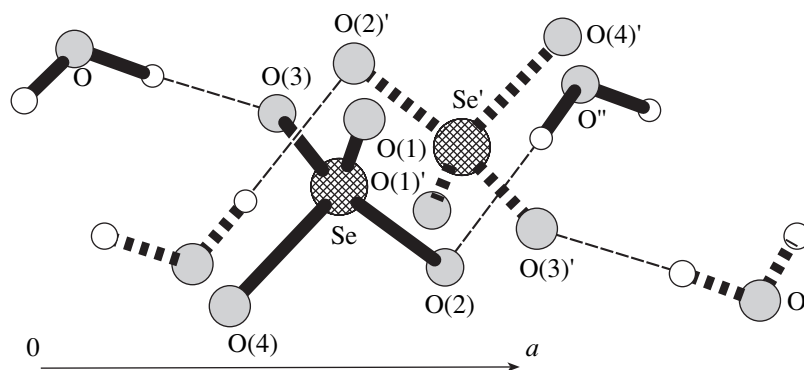


Fig. 3. Two variants for the location of the $\text{HSeO}_4^- \cdot \text{H}_2\text{O}$ solvated anion. Thin and dashed lines indicate hydrogen bonds.

The distances (corresponding to hydrogen bonds) between the oxygen atoms of the anion and those of the solvated water molecule in the anion sublattice of the structure of compound **I** are equal to 2.278 Å [O(2)–O''] and 2.641 Å [O(3)–O]. The anomalously small value of the former distance is most likely associated with the disordering of the anion. In the (APA) $\text{HSeO}_4 \cdot \text{H}_2\text{O}$ compound, the relevant distances are equal to 2.528 and

2.776 Å [8]. In the structure of the DABCOH_2 compound (DABCOH_2 is 1,4-diazabicyclo[2.2.2]octane H_2), which involves disordered anions HSeO_4^- but does not contain water molecules, the distances between the oxygen atoms bonded by hydrogen bonds in the anion are equal to 2.57(1) and 2.60(1) Å [9]. Therefore, in the anion sublattice of the structure of

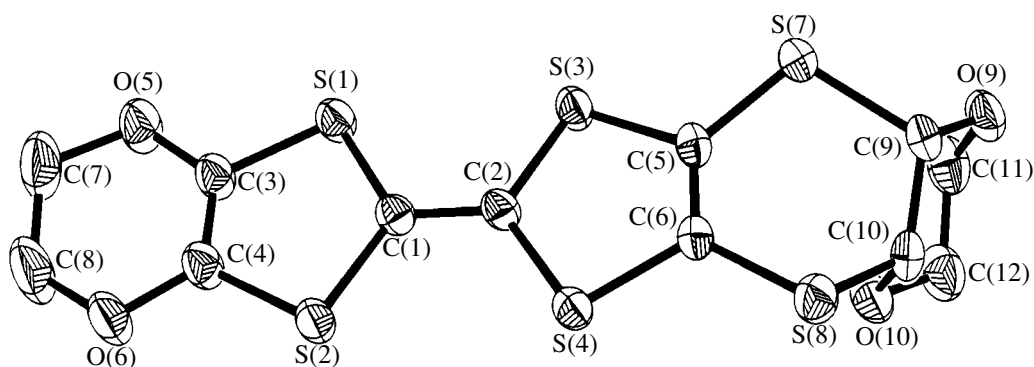


Fig. 4. Atomic numbering in the *DOEO* radical cation.

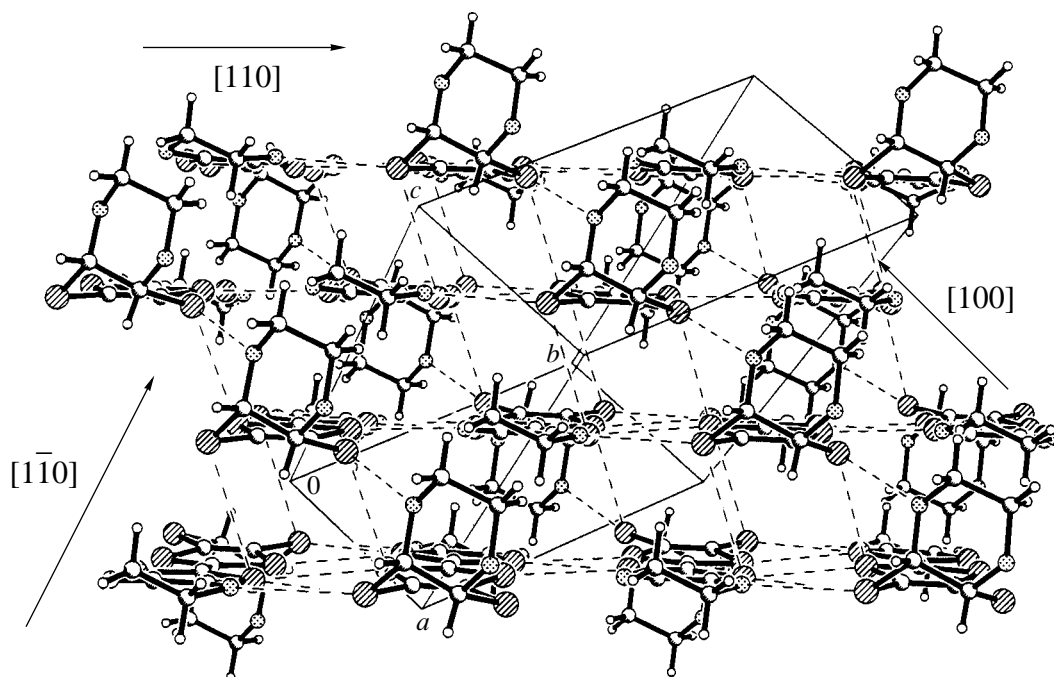


Fig. 5. A fragment of the radical cation layer in the structure of compound I.

compound **I**, there exists a chain of strong hydrogen bonds aligned parallel to the *a* axis (Fig. 3). The fact that the hydrogen atoms of the disordered solvated water molecule are revealed from the difference synthesis (see Experimental Technique) can indicate the formation of hydrogen bonds with the anion.

The intramolecular conjugated system of the *DOEO*^{1/2+} radical cation contains two groups of atoms. One group involves the C(1)–C(4), S(1)–S(4), O(5), and O(6) atoms, and the other group includes the C(5), C(6), S(3), S(4), S(7), and S(8) atoms. The atoms are coplanar accurate to within ± 0.028 Å in the former group and ± 0.015 Å in the latter group. The mean planes of both groups form a small angle. The S(1)S(3)S(4)S(8) torsion angle is equal to 173° . There-

fore, all the above atoms can be considered approximately coplanar (to within ± 0.076 Å) (Fig. 4).

The dioxane ring [the C(9)–C(12), O(9), and O(10) atoms] has a typical chair conformation: the C(9)–C(12) atoms are coplanar to within ± 0.031 Å, and the O(9) and O(10) atoms deviate from the corresponding plane by -0.579 and 0.654 Å, respectively. In the *DOEO*^{1/2+} radical cation, the plane of the conjugated atoms and the plane of the C(9)–C(12) atoms are nearly perpendicular to each other. The angle between these planes is equal to 94.9° .

The ethylene carbon atoms C(7) and C(8) deviate from the mean plane of the *DOEO*^{1/2+} radical cation by $0.530(7)$ and $0.036(8)$ Å, respectively. This means that the C(8) atom lies virtually in the plane. Consequently, the C(3)C(4)O(5)O(6)C(7)C(8) ring adopts a sofa con-

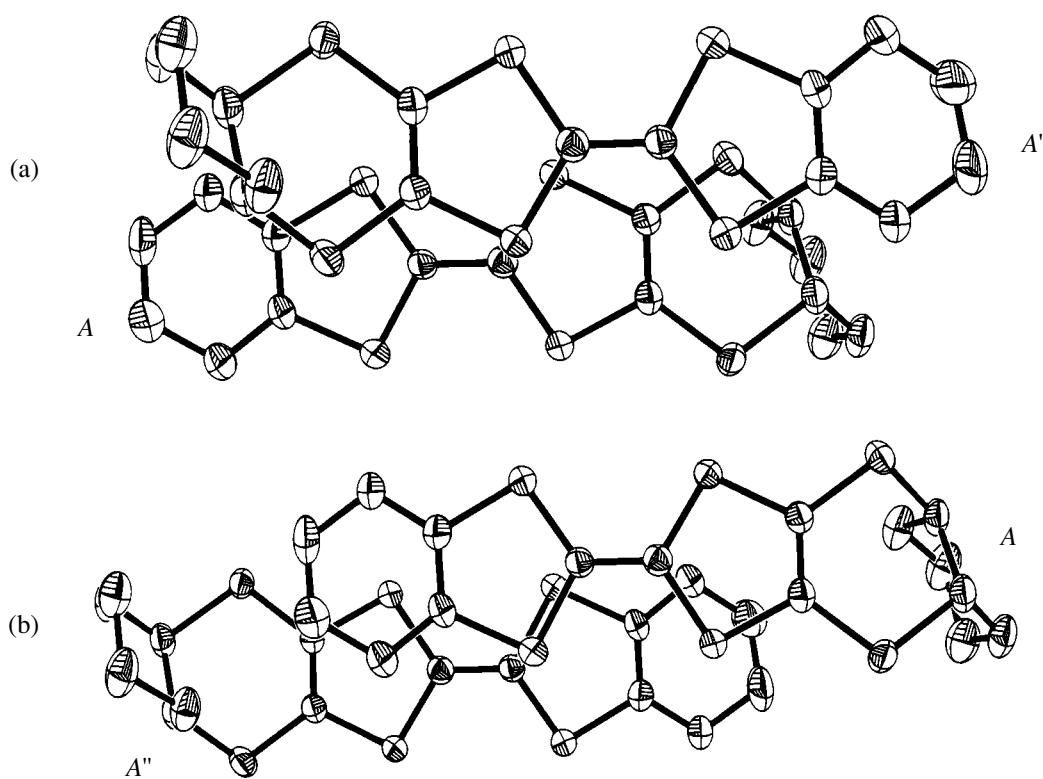


Fig. 6. Types of overlap of the $DOEO^{1/2+}$ radical cations (a) inside the dimer and (b) between the dimers. Symmetry operations for the $DOEO^{1/2+}$ radical cations are as follows: x, y, z (A); $1-x, 1-y, 1-z$ (A'); and $2-x, -y, 1-z$ (A'').

formation. The C(9) and C(10) ethyne atoms deviate from the mean plane of the $DOEO^{1/2+}$ radical cation by $-0.293(4)$ and $-0.890(4)$ Å, respectively. The considerable deviation of the C(10) atom is caused by the steric

Shortened intermolecular contacts in the radical cation layer of compound **I** (the corrections are introduced according to [12])*

Contact	Distance, Å	Direction	Contact type
S(1)⋯S(1) ¹	3.522(2)	[110]	$S_{in} \cdots S_{in}$
S(1)⋯S(3) ¹ , S(3)⋯S(1) ¹	3.437(2)	[110]	$S_{in} \cdots S_{in}$
S(2)⋯S(4) ² , S(4)⋯S(2) ²	3.440(2)	[110]	$S_{in} \cdots S_{in}$
S(2)⋯S(8) ² , S(8)⋯S(2) ²	3.447(2)	[110]	$S_{in} \cdots S_{ex}$
S(2)⋯S(8) ³ , S(8)⋯S(2) ³	3.595(2)	[1 $\bar{1}$ 0]	$S_{in} \cdots S_{ex}$
S(3)⋯O(5) ¹ , O(5)⋯S(3) ¹	3.301(4)	[110]	$S_{in} \cdots O_{ex}$
S(4)⋯S(7) ⁴ , S(7)⋯S(4) ⁴	3.533(2)	[100]	$S_{in} \cdots S_{ex}$
O(5)⋯S(7) ¹ , S(7)⋯O(5) ¹	3.322(4)	[110]	$S_{ex} \cdots O_{ex}$
O(6)⋯S(8) ² , S(8)⋯O(6) ²	3.247(4)	[110]	$S_{ex} \cdots O_{ex}$

* Symmetry operations for the atoms are as follows: ¹ $1-x, -y, 1-z$; ² $2-x, 1-y, 1-z$; ³ $1-x, 1-y, 1-z$; ⁴ $1+x, y, z$; ⁵ $-1+x, y, z$.

effect of the bulky dioxane ring. The ethylene and ethyne groups exhibit an eclipsed mutual conformation.

The $DOEO^{1/2+}$ radical cations form layers aligned parallel to the ab plane. In a layer, the cations form pseudostacks along the $[1\bar{1}0]$ direction (Fig. 5). The difference between the pseudostacks and the stacks lies in the fact that the neighboring radical cations in the pseudostacks are displaced along the short axis of the radical cation. This displacement in the structure of compound **I** is equal to 1.88 Å; i.e., it is approximately half the width of the $DOEO^{1/2+}$ radical cation. In the pseudostacks, the $DOEO^{1/2+}$ radical cations are weakly dimerized. The interplanar distance (the mean plane passes through all the conjugated atoms) inside the $A-A'$ centrosymmetric dimer is equal to 3.429(5) Å, and the $A-A''$ interdimer distance is 3.637(3) Å (Fig. 6). In the dimer, the arrangement of the radical cations corresponds to a head-to-tail configuration.

In the pseudostacks, the $DOEO^{1/2+}$ radical cations are also displaced along their long axis by 2.63 Å, i.e., by approximately 1/5 of the whole length of the $DOEO^{1/2+}$ radical cation. This displacement is caused by the steric effect of the dioxane rings. Although the planar structure of the $DOEO^{1/2+}$ radical cation is considerably distorted by the dioxane rings, their effect is virtually canceled by the specific features of the pack-

ing: the dioxane rings appear to be located outside the radical cation layer, thus forming walls of the anion channels, and the overlap of radical cations in pseudostacks inside the dimers and between them is nearly identical.

Apart from the pseudostacks with a plane-to-plane arrangement of the $DOEO^{1/2+}$ radical cations, the structure of compound **I** involves the radical cation chains lying along the [110] direction, in which the $DOEO^{1/2+}$ radical cations are arranged in a side-to-side manner, and even all the more distorted stacks parallel to the [100] direction. In these distorted stacks, the radical cations are arranged in a manner similar to that observed in the pseudostacks, but the displacement along the short axis of the $DOEO^{1/2+}$ radical cations is equal to the $DOEO^{1/2+}$ radical cation width and the mutual arrangement of the radical cations corresponds to a tail-to-tail configuration (Fig. 5). According to the above features, the packing in the structure of compound **I** can be assigned to the β'' type in the nomenclature proposed in [10].

The structure of compound **I** is characterized by a large number of shortened intermolecular contacts $S\cdots S$ (less than 3.65 Å) and $S\cdots O$ (less than 3.37 Å) (table). It is worth noting that the network of interchalcogenide contacts in the structure of compound **I** has a high density: the total number of contacts per radical cation can be as large as 17.

Unlike the *DOET* salts [where *DOET* is 3,4-(1,4-dioxanediy1-2,3-dithio)-3',4'-ethylenedithio-2,5,2',5'-tetrathiafulvalene] [11], the structure of compound **I** contains not only the $S_{ex}\cdots S_{ex}$ and $S_{in}\cdots S_{ex}$ contacts [where S_{in} are the internal atoms S(1)–S(4), S_{ex} are the external atoms S(7) and S(8), and O_{ex} are the external atoms O(5) and O(6)] but also the $S_{in}\cdots S_{in}$ contacts. This is associated with the replacement of two external sulfur atoms in the donor molecule by two oxygen atoms, which provides an easier access to the internal sulfur atoms. The shortened contacts $S_{in}\cdots O_{ex}$ and $S_{ex}\cdots O_{ex}$ are also revealed in the structure. This suggests a rather close packing of radical cations in the layer. The shortened contacts in the structure of compound **I** are predominantly formed along the chains (the [110] direction), and each radical cation has contacts with all the $DOEO^{1/2+}$ radical cations in the nearest environment (table).

In conclusion, it should be noted that, among the known metal salts $(DOEO)_2Au(CN)_2$, $(DOEO)_2PF_6$,

and $(DOEO)_2BF_4$ [1, 2], the structure was determined only for the last salt. However, the available data on the crystal structure of this salt in [1] are very scarce and the accuracy of the structure determination is unknown.

Thus, compound **I** is the first structurally characterized stable metal based on the new donor *DOEO*. According to its conducting properties, this compound belongs to the best quasi-two-dimensional molecular metals.

The high conductivity of the salt under investigation can be associated with the formation of a dense network of $S\cdots S$ and $S\cdots O$ contacts, among which the $S_{in}\cdots S_{ex}$ contacts are large in number. The low degree of dimerization of radical cations in stacks can be responsible for the stabilization of the metallic state down to low temperatures.

ACKNOWLEDGMENTS

We would like to thank É.B. Yagubskii for his participation in the discussion of the results obtained in this study and for helpful remarks.

REFERENCES

1. K. Kikuchi, S. Ikeda, H. Nishikawa, *et al.*, *Synth. Met.* **120**, 901 (2001).
2. J.-I. Yamada, H. Akutsu, H. Nishikawa, and K. Kikuchi, *Chem. Rev. (Washington, DC, US)* **104**, 5057 (2004).
3. P. Batail, K. Boubekeur, M. Fourmigue, and J.-C. P. Gabriel, *Chem. Mater.* **10**, 3005 (1998).
4. G. M. Sheldrick, *Acta Crystallogr., Sect. A: Found. Crystallogr.* **46**, 467 (1990).
5. G. M. Sheldrick, *SHELXL97: Program for the Refinement of Crystal Structures* (University of Göttingen, Göttingen, Germany, 1997).
6. L. J. Farrugia, *J. Appl. Crystallogr.* **32**, 837 (1999).
7. L. J. Farrugia, *J. Appl. Crystallogr.* **30**, 565 (1997).
8. M. Slouf and I. Cisarova, *Acta Crystallogr., Sect. C: Cryst. Struct. Commun.* **55**, IUC9900003 (1999).
9. M. A. Zakharov, S. I. Troyanov, L. A. Aslanov, and Z. Kemnitz, *Acta Crystallogr., Sect. A: Found. Crystallogr.* **56** (Suppl.), S311 (2000).
10. T. Mori, *Bull. Chem. Soc. Jpn.* **71**, 2509 (1998).
11. O. A. D'yachenko, A. A. Bardin, A. I. Kotov, *et al.*, *Izv. Akad. Nauk, Ser. Khim.*, No. 2, 359 (2003).
12. W. R. Busing and H. A. Levy, *Acta Crystallogr.* **17**, 142 (1964).

Translated by O. Borovik-Romanova

LATTICE DYNAMICS AND PHASE TRANSITIONS

Two Types of Structural Domains in $\text{Pb}_3(\text{PO}_4)_2$

V. A. Nepochatenko

Bila Tserkva State Agrarian University, Sobornaya pl. 8/1, Bila Tserkva, Kiev oblast, 09117 Ukraine

e-mail: aaa@btsau.kiev.ua

Received January 19, 2004; in final form, March 2, 2005

Abstract—The conditions of the formation of suborientation states in multidomain and single-domain $\text{Pb}_3(\text{PO}_4)_2$ crystals are analyzed. It is shown that suborientation states belong to sets of two structurally different types of domains differing in the angle sign and the orientation of the axis of rotation with respect to the coordinate system of the paraelastic phase. These structural differences are proposed to be described by the Gibbs vector. It is concluded that this macroscopic parameter corresponds to cooperative displacement of some groups of atoms with respect to other groups, with the crystal matrix being at rest. It is found that the modulus of the Gibbs vector is proportional to the spontaneous-strain components and depends linearly on the crystallographic parameter c in the ferroelastic phase. © 2005 Pleiades Publishing, Inc.

INTRODUCTION

It is known that, with an increase in spontaneous strain, rotations (in opposite directions) of the crystallographic axes in adjacent domains, separated by a domain wall, are observed in ferroelastics [1, 2] and multiaxial ferroelectrics [3–5]. This phenomenon leads to the formation of similar orientation (suborientation) states in crystals. In this context, the question arises as to whether the difference in the suborientation states is due to only their spatial orientation or if there are certain structural differences between them.

Therefore, it is of interest to perform comprehensive analysis of the conditions of formation and the properties of suborientation states in the most studied ferroelastic: lead orthophosphate.

Lead orthophosphate $\text{Pb}_3(\text{PO}_4)_2$ is a pure improper ferroelastic, in which a first-order phase transition from the rhombohedral β -phase ($R\bar{3}m$) to the monoclinic α -phase ($C2/c$) is observed [6]. In the ferroelastic phase, without allowance for small distinctions ($\sim 2^\circ$), three orientation states (C_1, C_2, C_3) and two types of domain walls (W', W) are possible [7, 8]. At room temperature, domains separated by a W' domain wall have coplanar (100) planes and the angle α between the b axes is 118° . When a W domain wall is formed, the angle γ between the (100) planes is $178.6^\circ \pm 0.1^\circ$ and the angle α is 58° [1]. In this domain geometry, two suborientation states correspond to each C_i .

In the coordinate system with the X_1 and X_2 axes parallel to the c and b axes, respectively, the spontane-

ous-strain tensor has the form [9]

$$S = \begin{pmatrix} e_{11}^s & 0 & e_{13}^s \\ & -e_{11}^s & 0 \\ & & 0 \end{pmatrix}, \quad (1)$$

where $e_{11}^s = \left(\frac{c}{\sqrt{3}} - b\right)/2b$ and $e_{13}^s = \frac{c + 3a \cos \beta}{6a \sin \beta}$.

Hereinafter, we will denote the orthogonal coordinate axes in the β -phase as X_{0i} and in the α -phase as X_{ji} ($j = 1, 2, 3$, according to the number of C_j). The domain walls separating C_i and C_j will be denoted as W_{ij} or W'_{ij} .

FORMATION OF SUBORIENTATION STATES IN A MULTIDOMAIN CRYSTAL

Previously [10, 11], we proposed a model of a ferroelastic domain wall consisting of an induced phase (interlayer). This interlayer matches the crystal lattices of the adjacent domains. There are two possible structures corresponding to the W' and W walls. In the case of the W' wall (P type of twinning), the interlayer has the symmetry of the paraelastic phase. To match the lattices of the α -phase and the interlayer, it is necessary to rotate the crystallographic axes of the α -phase with respect to the coordinate system of the β -phase. The magnitude of the rotation depends on the value of the spontaneous strain. It was shown in [11] that the orientation state, for example, C_1 , which is separated from C_2 and C_3 by W' domain walls (W'_{12}, W'_{13}), is described by the following matrices of coordinate-system trans-

formation from the β - to the α -phase:

$$A_{12} = \begin{pmatrix} a_{11} & a_{12} & a_{13} \\ a_{21} & a_{22} & a_{23} \\ a_{31} & a_{32} & a_{33} \end{pmatrix}, \quad A_{13} = \begin{pmatrix} a_{11} & -a_{12} & a_{13} \\ -a_{21} & a_{22} & -a_{23} \\ a_{31} & -a_{32} & a_{33} \end{pmatrix}, \quad (2)$$

where, for $t = 20^\circ\text{C}$, $a_{11} = 0.99984$, $a_{12} = -0.01756$, $a_{13} = -0.0019$, $a_{21} = 0.01753$, $a_{22} = 0.99976$, $a_{23} = -0.0134$, $a_{31} = 0.00213$, $a_{32} = 0.01338$, and $a_{33} = 0.99991$.

The structure of a W wall (F type of twinning) includes two interlayers in which only the main spontaneous-strain components are zero. This circumstance results in two types of rotations: φ_1 , corresponding to the lattice matching between the ferroelectric phase and the nearest interlayer, and φ_2 , corresponding to the lattice matching between two interlayers. Rotation of the latter type leads to the formation of a relief on the crystal surface. If the orientation state C_1 is separated from C_2 and C_3 by W domain walls (W_{12} , W_{13}), almost similar W' walls correspond to them but the sequence of the transformation matrices is reversed:

$$B_{12} = \begin{pmatrix} b_{11} & -b_{12} & b_{13} \\ -b_{21} & b_{22} & -b_{23} \\ b_{31} & -b_{32} & b_{33} \end{pmatrix}, \quad B_{13} = \begin{pmatrix} b_{11} & b_{12} & b_{13} \\ b_{21} & b_{22} & b_{23} \\ b_{31} & b_{32} & b_{33} \end{pmatrix}, \quad (3)$$

where $b_{11} = 0.99978$, $b_{12} = -0.0186$, $b_{13} = -0.0096$, $b_{21} = 0.01854$, $b_{22} = 0.99981$, $b_{23} = -0.0056$, $b_{31} = 0.00969$, $b_{32} = 0.00548$, and $b_{33} = 0.99994$.

As can be seen, the components of the matrices A_{1i} and B_{1j} almost coincide; insignificant differences seem to be due to the rotation φ_2 . Therefore, without allowance for these small differences, each orientation state in a multidomain lead orthophosphate crystal can have two similar orientations corresponding to the matrices A_{12} and A_{13} . We will denote these orientations as C_1 and C_1' , C_2 and C_2' , and C_3 and C_3' .

FORMATION OF SUBORIENTATION STATES AT A PHASE TRANSITION

A model of a thin phase boundary separating two monoclinic phases was proposed in [12]. The term "thin phase boundary" corresponds to the direct contact between two phases, at which the phase boundary is shared by two different crystal lattices. To match the lattices of two phases separated by a thin phase boundary, the crystallographic axes should also be rotated. It was shown in [12, 13] that two types of thin planar phase boundaries (PB1 and PB2) exist in $\text{Pb}_3(\text{PO}_4)_2$. They form similar orientation states corresponding to the following coordinate-transformation matrices from

the β - to the α -phase:

$$D_{01} = \begin{pmatrix} c_{11} & c_{12} & c_{13} \\ c_{21} & c_{22} & c_{23} \\ c_{31} & c_{32} & c_{33} \end{pmatrix}, \quad D_{02} = \begin{pmatrix} c_{11} & -c_{12} & c_{13} \\ -c_{21} & c_{22} & -c_{23} \\ c_{31} & -c_{32} & c_{33} \end{pmatrix}, \quad (4)$$

where $c_{11} = 0.9999943$, $c_{12} = -0.00335$, $c_{13} = 0.000148$; $c_{21} = 0.00335$, $c_{22} = 0.9999942$; $c_{23} = 0.00056$, $c_{31} = 0.000146$, $c_{32} = -0.0005638$, and $c_{33} = 0.9999998$.

As can be seen, the coordinate-transformation matrices obtained from the model of the thin phase boundary and the model of the ferroelastic domain wall have the same form. Hence, the formation of two suborientation states is also possible at the formation of a single-domain crystal. It should be noted that, if a specific suborientation state was formed in a single-domain crystal at the $\beta \rightarrow \alpha$ phase transition by a definite phase boundary (for example, PB1), the phase boundary of this type is always formed at $\alpha \rightarrow \beta$ transitions. This phenomenon can be explained only by the structural differences of the two possible suborientation states from the paraelastic phase.

ETCH PATTERNS OF THE SURFACE OF A $\text{Pb}_3(\text{PO}_4)_2$ CRYSTAL

In view of the above considerations, it is of interest to establish the mechanism of rotation of crystallographic axes, specifically, to find out if this rotation is due to the rotation of a domain as a whole or results from cooperative displacement of some groups of atoms with respect to other groups, the domain matrix being at rest. To solve this problem, we studied experimentally the etch patterns obtained at room temperature on the top (A) surface of a single-domain (100) sample formed by the phase boundary PB1. Then the etch patterns on the bottom (B) surface were investigated after the second suborientation state was formed by the phase boundary PB2. Analysis of the etch patterns was performed using an optical microscope focused on the top or bottom crystal surfaces. A special acid etchant was used to obtain etch patterns with a pronounced plane of symmetry (Fig. 1). The angle α_1 between the planes of symmetry of the etch patterns on the surfaces A and B is $2.3^\circ \pm 0.5^\circ$ (Fig. 1).

Hence, the difference in the orientations of the C_1 and C_1' states is caused by the rotation of the crystallographic axes with respect to the crystal matrix at rest. As was shown in [14, 15], displacements of Pb(1) and Pb(2) atoms, as well as distortions and rotations of PO_4 tetrahedra, are observed in the ferroelastic phase of lead orthophosphate. Apparently, it is these factors that determine the rotation of the crystallographic axes during a change in spontaneous strain. According to the symmetry of the paraelastic phase, a reversible displacement ($-\Delta_z$) of a Pb(2) atom along the threefold

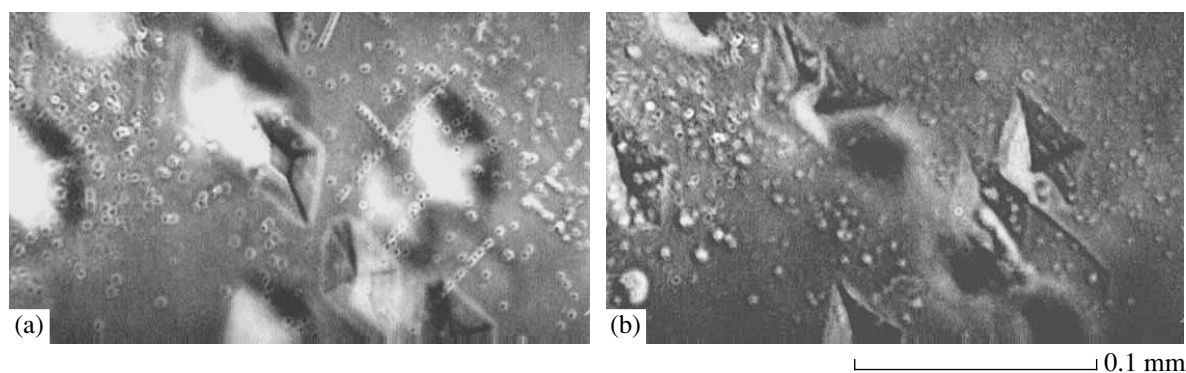


Fig. 1. Etch patterns of the (100) face of a single-domain $\text{Pb}_3(\text{PO}_4)_2$ crystal: (a) the surface A (C_1) and (b) the surface B (C_1').

axis may occur, which leads to changes in the position of all lattice atoms corresponding to the second suborientation state.

RESULTS AND DISCUSSION

The analysis performed showed that two types (classes) of structural domains (C_1, C_2, C_3 and C_1', C_2', C_3') are formed in lead orthophosphate, which differ by the sign of the angle of rotation and the orientation of the axis of rotation of the crystallographic axes of domains with respect to the paraelastic phase. This circumstance determines their different roles in the formation of the domain structure. According to [13], equilibrium domain walls are formed at the intersection of domains of different types; for example, intersection of C_1 and C_1' yields W'_{12} and intersection of C_1' and C_2 yields W_{12} . Nonequilibrium domain walls are formed at intersection of domains of the same type (C_i and C_j or C_i' and C_j'). The difference in the operations of alignment of different pairs of orientation states is also related to this factor.

If two domains belong the same type, their orientation states can be aligned by the operation of F symmetry of the paraelastic phase

$$X_{1i} = B_{ij}X_{2j}, \quad (5)$$

where B_{ij} is the rotation matrix around the X_{03} axis by an angle of $\pm 120^\circ$.

It was shown in [11] that, for domains of different types, the matrix K corresponds to the alignment operation:

$$K = A_{12}^T B A_{13}, \quad (6)$$

where A_{12}^T is the matrix transposed to A_{12} .

The suborientation states C_i and C_i' are aligned by the matrix

$$D = A_{12}^T A_{13}. \quad (7)$$

The components of the K and D matrices are temperature-dependent. This is their significant difference from B .

Thus, we can speak about a number n of possible orientation states in a crystal for a domain of certain type. Within this approach, n is equal to the ratio of the orders of groups of the initial and ferroelastic phases, a result which is consistent with the data of [16].

The value of the angle and the orientation of the axis of rotation of crystallographic axes represent a macroscopic parameter of cooperative displacement of some groups of atoms with respect to other groups in a crystal. It is convenient to describe this parameter by the Gibbs vector

$$\mathbf{G} = g_1\mathbf{e}_1 + g_2\mathbf{e}_2 + g_3\mathbf{e}_3, \quad (8)$$

where $g_1 = c_1 \tan(\delta/2)$, $g_2 = c_2 \tan(\delta/2)$, and $g_3 = c_3 \tan(\delta/2)$. δ is the angle of rotation, and c_i are the direction cosines of the positive rotation axis.

On the basis of the matrix A_{12} (2), we can obtain the parameters of the Gibbs vector \mathbf{G}_1 (corresponding to C_1) by the formulas

$$\begin{aligned} \cos \delta &= 0.5(a_{11} + a_{22} + a_{33} - 1); \\ c_1 &= (a_{32} - a_{23}) / (2 \sin \delta); \end{aligned} \quad (9)$$

$$c_2 = (a_{13} - a_{31}) / (2 \sin \delta); \quad c_3 = (a_{21} - a_{12}) / (2 \sin \delta),$$

$\mathbf{G}_1 = (6.7 \times 10^{-3}; -1.01 \times 10^{-3}; 8.77 \times 10^{-3})$. Similarly, from the matrix A_{13} (2), we determine the parameters of the vector \mathbf{G}_1' corresponding to C_1' : $\mathbf{G}_1' = (-6.7 \times 10^{-3}; -1.01 \times 10^{-3}; -8.77 \times 10^{-3})$. The angle α_3 between the vectors \mathbf{G}_1 and \mathbf{G}_1' is 169.6° . With an increase in temperature, the angle α_3 increases and becomes close to 180° near the phase-transition point.

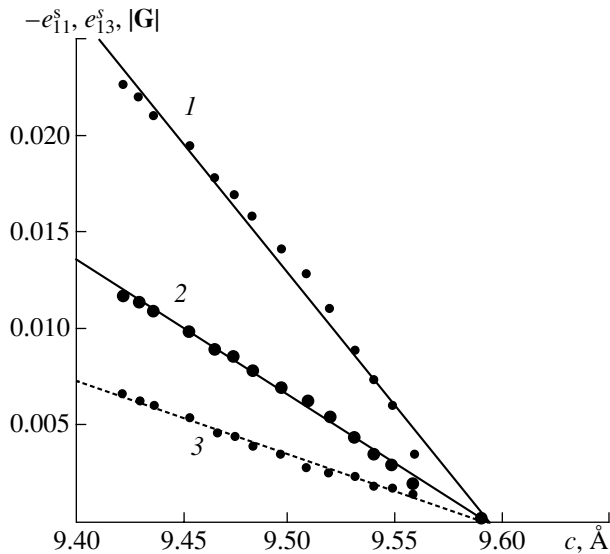


Fig. 2. Dependences of the spontaneous-strain components (1) $-e_{11}^s$ and (3) e_{13}^s and (2) the modulus of the vector \mathbf{G} on the crystallographic parameter c .

The following equations of equilibrium W and W' domain walls in the coordinate system of the ferroelastic phase were obtained in [17]:

$$X_1 \pm \frac{(\sqrt{31} - a - c^2)}{3(1+a)} X_2 - c X_3 = 0, \quad (10)$$

$$X_1 \pm \frac{\sqrt{3}a(c^2 - 1 + a)}{(1+a)(2c^2 + a)} X_2 - \frac{2c(1 - a/2)}{(2c^2 + a)} X_3 = 0, \quad (11)$$

where $a = -e_{11}^s$ and $c = e_{13}^s$ are the components of the spontaneous-strain tensor.

Since the equations of these domain walls in the coordinate system of the paraelastic phase are known [18], we can determine the matrices A_{12} and A_{13} and, therefore, the Gibbs vector in the α -phase at any temperature.

Figure 2 shows the dependence of the modulus of the vector \mathbf{G} and the spontaneous-strain components $-e_{11}^s$ and e_{13}^s on the crystallographic parameter c . Circles correspond to the values of $-e_{11}^s$, e_{13}^s , and $|\mathbf{G}|$ obtained from (1), (8), and (9) using the data on the temperature dependence of the lattice parameters [19]. Straight lines correspond to linear regressions. As can be seen from Fig. 2, $|\mathbf{G}|$ is proportional to spontaneous strain and depends linearly on the parameter c ; i.e., the Gibbs vector accounts for certain structural changes in a crystal. Apparently, suborientation states in lead orthophosphate are electrically neutral analogs of domains with almost antiparallel (179.4° [5]) directions of the spontaneous polarization vector in the tetragonal phase of BaTiO_3 .

CONCLUSIONS

Thus, two types of structurally different domains exist in lead orthophosphate, which are formed by phase boundaries of certain types. According to the symmetry of the paraelastic phase, three allowable orientation states correspond to each type of domains. The rotation of the crystallographic axes of the ferroelastic phase is caused by cooperative displacement of some groups of atoms with respect to other groups, with the crystal matrix being at rest. Suborientation states differ in the direction of the Gibbs vector and belong to different types of domains. The modulus of the Gibbs vector is proportional to spontaneous strain and depends linearly on the crystallographic parameter c . Equilibrium domain walls separate only structurally different domains. Nonequilibrium walls separate domains of the same type. If the alignment matrix of two orientation states is temperature-dependent, domains of different type correspond to these orientation states.

REFERENCES

1. M. Chabin and F. Gilletta, *J. Appl. Crystallogr.* **10**, 247 (1977).
2. L. S. Wainer, R. F. Baggio, and H. L. Dussel, *Ferroelectrics* **31**, 121 (1981).
3. *Modern Crystallography* (Nauka, Moscow, 1981), Vol. 4 [in Russian].
4. N. S. Afonikova, I. M. Shmyt'ko, and V. Sh. Shekhtman, *Izv. Akad. Nauk SSSR* **43** (8), 1611 (1979).
5. L. G. Shabel'nikov, V. Sh. Shekhtman, and O. M. Tsarev, *Fiz. Tverd. Tela (Leningrad)* **18** (6), 1529 (1976) [*Sov. Phys. Solid State* **18**, 889 (1976)].
6. V. Keppler, *Z. Kristallogr.* **132**, 228 (1970).
7. L. H. Brixner, P. E. Bierstedt, W. F. Jaep, and J. R. Barkley, *Mater. Res. Bull.* **8**, 497 (1973).
8. E. F. Dudnik, E. V. Sinyakov, V. V. Gene, and S. V. Vagin, *Fiz. Tverd. Tela (Leningrad)* **17**, 1212 (1975) [*Sov. Phys. Solid State* **17**, 1212 (1975)].
9. J. C. Toledano, L. Pateau, J. Primot, *et al.*, *Mater. Res. Bull.* **10**, 103 (1975).
10. V. A. Nepochatenko, *Kristallografiya* **48** (2), 324 (2003) [*Crystallogr. Rep.* **48**, 290 (2003)].
11. V. A. Nepochatenko and E. F. Dudnik, *Fiz. Tverd. Tela (St. Petersburg)* **45** (10), 1870 (2003) [*Phys. Solid State* **45**, 1966 (2003)].
12. E. F. Dudnik and V. A. Nepochatenko, *Kristallografiya* **25** (6), 984 (1980) [*Sov. Phys. Crystallogr.* **25**, 564 (1980)].
13. V. A. Nepochatenko, *Kristallografiya* **47** (3), 514 (2002) [*Crystallogr. Rep.* **47**, 467 (2002)].
14. H. H. Ng and C. Calvo, *Can. J. Phys.* **53** (1), 42 (1975).
15. D. M. C. Guimaraes, *Acta Crystallogr. A* **35** (1), 108 (1979).
16. L. A. Shuvalov, *Izv. Akad. Nauk SSSR* **43** (8), 1554 (1979).
17. V. A. Nepochatenko and A. Yu. Kudzin, in *Proceedings of the 17th All-Russian Conference on Physics of Ferroelectrics* (Penza, 2005), p. 186.
18. J. Sapriel, *Phys. Rev. B* **12** (11), 5128 (1975).
19. D. M. C. Guimaraes, *Phase Transitions* **1**, 143 (1979).

Translated by Yu. Sin'kov

LATTICE DYNAMICS AND PHASE TRANSITIONS

Calculations of the Percolation Thresholds of a Three-Dimensional (Icosahedral) Penrose Tiling by the Cubic Approximant Method

R. M. Zakalyukin and V. A. Chizhikov

*Shubnikov Institute of Crystallography, Russian Academy of Sciences,
Leninskiĭ pr. 59, Moscow, 119333 Russia*

e-mail: chizhikov@ns.crys.ras.ru

Received February 17, 2005

Abstract—The percolation thresholds of a three-dimensional Penrose tiling with icosahedral symmetry are determined using the cubic approximant method. The percolation thresholds of the three-dimensional Penrose tiling for the site problem and the bond problem are calculated with an accuracy of 0.001. © 2005 Pleiades Publishing, Inc.

INTRODUCTION

The percolation theory is one of the theoretical approaches that have long been in use for predicting a great variety of properties of materials [1, 2]. This theory has found wide application in many fields of research, specifically in the growth phenomena [3] and conduction processes [4], strength of materials, theory of phase transitions, etc. Applications of the percolation theory for solving problems in the physics of partially ordered and disordered media, as well as in the soft-matter physics, are of special interest.

The percolation theory and appropriate numerical methods have been developed continuously: available data on the percolation thresholds for even very simple structures, such as simple cubic, face-centered cubic, body-centered cubic, and other lattices, have been refined and complemented using calculations performed within the percolation theory under different conditions [5]. The percolation theory is an efficient tool for studying disordered structures [6]. In recent years, publications have appeared that are concerned with the percolation in structures of a new type, namely, quasi-periodic tilings. The first numerical experiments for two-dimensional decagonal Penrose tilings were carried out by Ziff and Babalievski [7]. However, there is an appreciable gap in the calculations of the percolation thresholds for three-dimensional quasi-periodic structures, which is associated primarily with the considerable difficulties encountered in performing computer experiments.

The purpose of this study was to calculate the percolation thresholds for the three-dimensional icosahedral Penrose tiling, which is of interest as a model object of investigation for several reasons. The three-dimensional Penrose tiling, like random disordered structures, is locally inhomogeneous but exhibits a long-

range quasi-periodic order. This tiling has an exact mathematical description. In particular, the coordination numbers of all sites and the mean coordination number can be determined exactly. Special interest expressed by researchers in the three-dimensional Penrose tiling is associated with the discovery of icosahedral quasicrystals whose structures have much in common with the tiling structure [8, 9].

ICOSAHEDRAL SYMMETRY AND ICOSAHEDRAL LOCAL ORDER

The point symmetry inherent in periodic crystals imposes specific requirements on the internal structure of the crystal, specifically on the local atomic order. In this case, the local order is considered to be understood as the nearest environment of each atom within one or several coordination spheres. The natural constraint placed on the structure is that, for any local atomic configuration and an arbitrary element of the symmetry point group, it is possible to find another atomic configuration related to the initial configuration by the given symmetry element. Consequently, a set of possible bonds between atoms in the structure can be described by a finite set of vectors whose point symmetry is no lower than the point symmetry of the crystal itself.

Unlike periodic crystals, in quasicrystals, as well as in amorphous materials, each atom has a unique nearest environment. Therefore, a set of possible bonds between the nearest atoms is an infinite set of vectors. This set of vectors in amorphous materials possesses spherical symmetry, whereas the symmetry of the set of interatomic distances in quasicrystals coincides with the point symmetry of the quasicrystal itself. It should be noted that the density of the set of interatomic distances reaches maxima at specific points that can be associated with particular ideal positions of the bonds.

This allows one to construct an idealized model of the quasicrystal in which the set of possible interatomic bonds, as in the crystal, is reduced to a finite set of vectors. It is worth noting that the smaller the number of vectors in the set, the more effective the model. It is obvious that the reduced set of interatomic distances should retain the symmetry of the quasicrystal.

Let us consider an idealized structure of an icosahedral quasicrystal. A set of bonds between the nearest neighbors forms a set of vectors that has icosahedral symmetry. An arbitrary vector related by the elements of the icosahedral symmetry group gives a set consisting of 120 vectors. This set seems too cumbersome. It is much more convenient to use specific vectors aligned parallel to the symmetry axes of the icosahedron. Earlier, it was established that the experimental data obtained for structures of icosahedral quasicrystals are in excellent agreement with the local order at which the nearest neighbor atoms are spaced at r_3 , r_5 , and r_2 intervals along the twofold, fivefold, and twofold axes, respectively [10, 11]. The ratios between these distances are as follows: $r_3 : r_5 : r_2 = \sqrt{3} : \sqrt{\tau + 2} : 2$, where

$\tau = \frac{\sqrt{5} + 1}{2} \approx 1.618$ is the golden mean. In the particular

case, the bonds r_3 are absent. Hence, the local order is referred to as the icosahedral order. Generally speaking, the icosahedral order can be described by introducing only the distances r_5 . In this case, the distances r_2 appear automatically as sums of the vectors r_5 . Examples of the icosahedral local order are provided by structures of an Al_{12}Mn crystal and three-dimensional Penrose tiling [12].

Expressions for the vectors r_5 have the simplest form in the coordinate system in which the Cartesian axes coincide with three mutually perpendicular twofold axes of the icosahedron. These 12 vectors, which are directed from the center to the vertices of the icosahedron, can be written in the form $(\pm 1, \pm\tau, 0)$ to within a scale factor. This formula accounts for the cyclic permutations of the coordinates, and the plus and minus signs can be chosen for each of the coordinates independently. In essence, the icosahedral local order is as follows: by going from neighbor to neighbor and using only the vectors r_5 , any two atoms of the structure can be connected by a chain of steps. If an arbitrary atom is placed at the origin of the coordinates, the coordinates of any other atom can be represented as a linear combination of the vectors r_5 with integral coefficients. However, proper allowance must be made for the fact that the vectors directed to opposite vertices of the icosahedron differ only in sign and, hence, the number of independent vectors is reduced to six (Fig. 1). Therefore, the coordinates of an arbitrary atom in the structure with

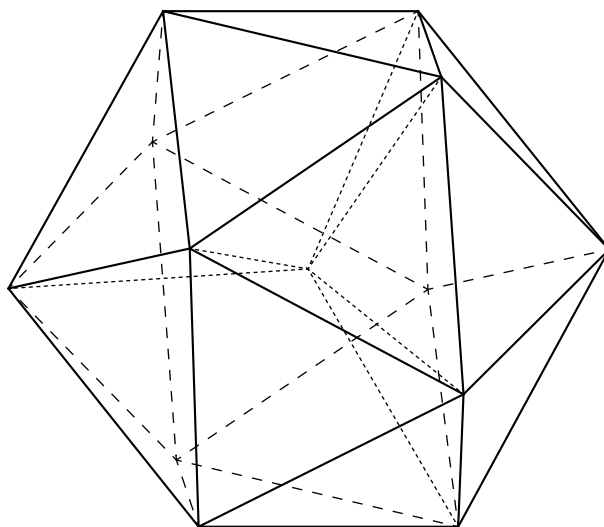


Fig. 1. Six basis vectors (dotted lines) of the structure with an icosahedral local order connect the icosahedron center with its vertices.

icosahedral local order can be written in the form

$$\mathbf{r} = n_1 \begin{pmatrix} 1 \\ \tau \\ 0 \end{pmatrix} + n_2 \begin{pmatrix} 0 \\ 1 \\ \tau \end{pmatrix} + n_3 \begin{pmatrix} \tau \\ 0 \\ 1 \end{pmatrix} + n_4 \begin{pmatrix} 1 \\ -\tau \\ 0 \end{pmatrix} + n_5 \begin{pmatrix} 0 \\ 1 \\ -\tau \end{pmatrix} + n_6 \begin{pmatrix} -\tau \\ 0 \\ 1 \end{pmatrix}. \quad (1)$$

By changing over to the matrix form, relationship (1) can be rewritten as

$$\mathbf{r} = E_{ph} \mathbf{n}, \quad E_{ph} = \begin{pmatrix} 1 & 0 & \tau & 1 & 0 & -\tau \\ \tau & 1 & 0 & -\tau & 1 & 0 \\ 0 & \tau & 1 & 0 & -\tau & 1 \end{pmatrix}, \quad (2)$$

where E_{ph} is the matrix specifying the projection of sites \mathbf{n} of the six-dimensional hypercubic lattice onto the three-dimensional physical space and \mathbf{n} and \mathbf{r} are column vectors. In such a manner, we introduced the multidimensional formalism typical of the theory of quasicrystals [12–14].

In the framework of the multidimensional formalism, the physical space, i.e., the space in which the structure and its physical properties are determined, is treated as a subspace of the space of higher dimension (in our case, it is the six-dimensional space). The three-dimensional subspace complementary to the physical

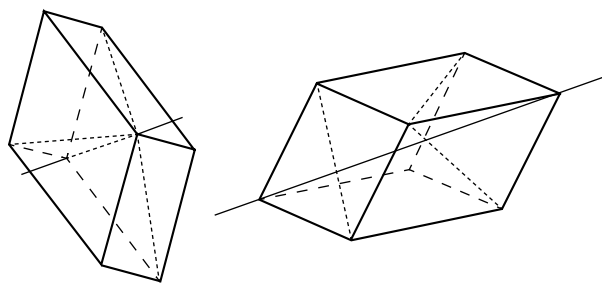


Fig. 2. Oblate (at the left) and prolate (at the right) Ammann rhombohedra. Thin solid lines indicate the threefold symmetry axes. The rhombohedron edges are the vectors r_5 . Dotted lines represent the short diagonals r_2 of the visible faces and the short internal diagonal r_3/τ of the oblate rhombohedron.

subspace is defined by the projection

$$\mathbf{r}_\perp = E_\perp \mathbf{n}, \quad E_\perp = \begin{pmatrix} \tau & 0 & -1 & \tau & 0 & 1 \\ -1 & \tau & 0 & 1 & \tau & 0 \\ 0 & -1 & \tau & 0 & 1 & \tau \end{pmatrix}. \quad (3)$$

This complementary subspace is called the perpendicular space of the icosahedral quasicrystal.

All the sites of the six-dimensional hypercubic lattice projected by the matrix E_{ph} densely occupy the physical space, much as all the sites projected by the matrix E_\perp densely occupy the perpendicular space. In order to simulate structures with physically realistic atomic densities, it is necessary to decrease the number of sites of the six-dimensional lattice projected onto the physical space. A characteristic feature of icosahedral quasicrystals is that their projection onto the perpendicular space is a set with limited linear sizes. It is common practice to consider a bounded domain (or several disconnected domains) in the perpendicular space such that only those sites of the six-dimensional lattice whose projections \mathbf{r}_\perp lie in this bounded domain belong to the structure. This domain is referred to as the acceptance domain. Therefore, the acceptance domain in the perpendicular space completely determines the atomic structure in the physical space. It should be noted that the acceptance domain of the structure with icosahedral symmetry should also have icosahedral symmetry.

THE THREE-DIMENSIONAL PENROSE TILING

A three-dimensional Penrose tiling has icosahedral symmetry. By analogy with the two-dimensional Penrose tiling composed of rhombi of two types (with acute angles of $\frac{2\pi}{5}$ and $\frac{2\pi}{10}$) [15, 16], the three-dimensional Penrose tiling consists of elementary polyhedra of two types, namely, the so-called Ammann rhombohedra [12]. The oblate and prolate Ammann rhombohedra are

parallelepipeds whose faces each are represented by identical rhombi with the acute angle $\alpha = \arccos \frac{1}{\sqrt{5}} \approx$

63.4° (Fig. 2). Each of the Ammann rhombohedra can be represented as a cube that is either oblate or prolate along one of the internal diagonals (with retention of the edge size), which explains their names. The volume of the prolate rhombohedron is larger than that of the oblate rhombohedron by a factor of τ .

Inside the tiling, the edges of the rhombohedra are aligned parallel to the fivefold axes of the icosahedron and, hence, can be related to the vectors r_5 . For example, the parallelepiped constructed by the vectors $(\tau, 0, 1)$, $(1, \tau, 0)$, and $(0, 1, \tau)$ is a prolate Ammann rhombohedron, whereas the parallelepiped constructed by the vectors $(\tau, 0, -1)$, $(-1, \tau, 0)$, and $(0, -1, \tau)$ is an oblate Ammann rhombohedron. Therefore, the three-dimensional Penrose tiling can be treated as a structure with icosahedral local order in which atoms are located at vertices of the rhombohedra.

The three-dimensional Penrose tiling is conveniently described in terms of the aforementioned multi-dimensional formalism. In this case, the acceptance domain has the form of a rhombic triacontahedron, which, in turn, can be represented by the projection of the six-dimensional hypercubic unit cell onto the perpendicular space (Fig. 3). The rhombic triacontahedron possess the required icosahedral symmetry. This polyhedron contains 30 rhombic faces perpendicular to the twofold axes of the icosahedron. If the center of the triacontahedron is placed at the origin of the coordinates, its 32 vertices are specified by vectors of the type $(\pm\tau^2, \pm\tau, 0)$, $(\pm\tau, \pm\tau, \pm\tau)$, and $(\pm\tau^2, 0, \pm 1)$. These relationships take into account the cyclic permutations of the coordinates, and the plus and minus signs can be chosen for each coordinate independently.

Special attention should be focused on the boundary of the acceptance domain. When the projection of a particular site of the six-dimensional lattice onto the perpendicular space lies on one of the faces of the triacontahedron, the projection of another site should also be located at the corresponding position on the opposite face. For example, we consider two opposite rhombic faces of the triacontahedron in the planes $z_\perp = -\tau^2$ and $z_\perp = \tau^2$. (It is assumed that the center of the triacontahedron coincides with the origin of the coordinates.) In this case, the distance between the faces is determined by the vector $(0, 0, 2\tau^2)$ in the perpendicular space to which the vector $\Delta\mathbf{n} = (0, -1, 1, 0, 1, 1)$ corresponds in the six-dimensional space. Consequently, if the projection of the site \mathbf{n}_b lies on the lower rhombus, the site $\mathbf{n}_t = \mathbf{n}_b + \Delta\mathbf{n}$ is projected onto the upper rhombus. The projections of these sites onto the physical space are separated by the distance $\left(0, 0, -\frac{2}{\tau}\right)$, which is not typical of three-dimensional Penrose tilings.

In order to exclude the appearance of surplus sites in the tiling, it is necessary to take into account the portion of the boundary belonging to the acceptance domain. However, there exists another method frequently used for eliminating frustrations: the triacontahedron as a whole can be shifted in such a way that its faces will not contain projections of the sites. In actual fact, although the projections of the sites of the six-dimensional lattice completely occupy the perpendicular space, their coordinates have the special form $i\tau + j$, where i and j are integral numbers. If the center of the acceptance domain is displaced from the origin of the coordinates, for example, to the point $(\pi, e, \sqrt{2})$, it is obvious that none of the sites will be projected onto the triacontahedron boundary.

In the general case, different positions of the triacontahedron center correspond to different tilings. In this respect, it is customary to speak about Penrose tilings in plural. However, without a loss in generality, we can speak about the Penrose tiling as a single structure if we consider that all the possible tilings are locally isomorphic to each other. The meaning of the term "local isomorphism" can be briefly explained as follows [17]. Two infinite structures are said to be locally isomorphic if any finite fragment of one structure can be found in another structure. When we are dealing with Penrose tilings, any fragment containing in one tiling is repeated an infinite number of times in each tiling and the distance from an arbitrary point of the tiling to the nearest repetition of the given fragment does not exceed its several linear sizes.

The local isomorphism plays an important role in the definition of the concept of point symmetry of quasi-periodic structures. Indeed, the lack of translational symmetry, which is characteristic of these structures, can be explained by the fact that their point groups involve elements, in particular, fivefold axes, which are incompatible with the periodicity. Such axes can be encountered in the structure only once for each of the possible directions. For example, the structure with icosahedral point symmetry can be characterized by no more than six fivefold axes aligned parallel to the six different directions. Furthermore, symmetry elements that transform the quasi-periodic structure into itself can be absent altogether. The question arises as to which argument counts in favor of the hypothesis that this structure has a symmetry point group. For mathematical rigor, the point symmetry element can be defined as follows: a structure has a point symmetry element if the related structure is locally isomorphic to the initial structure. It is in this sense that any three-dimensional Penrose tiling has icosahedral point symmetry.

SITES AND BONDS

Investigation into the structural properties within the percolation theory requires knowledge of the topology

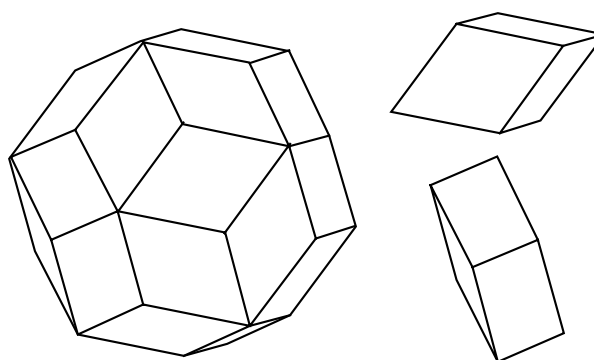


Fig. 3. Acceptance domain in the form of a rhombic triacontahedron for the three-dimensional Penrose tiling in the perpendicular space (at the left). The prolate (at the upper right) and oblate (at the lower right) Ammann rhombohedra are the respective projections of the oblate and prolate Ammann rhombohedra in the physical space onto the perpendicular space.

of the bonds between sites (atoms). In this case, other structural features, such as precise coordinates of sites, symmetry, or curvature of the enclosing space, are immaterial. For the three-dimensional Penrose tiling under consideration, the vertices of Ammann rhombohedra are naturally chosen as sites. Bonds between the sites can be chosen using different variants; however, in any case, the set of all bonds should include the set of all edges of the rhombohedra.

In the first variant, the bonds can be reduced to the edges of the Ammann rhombohedra. Then, the coordination numbers of specific sites vary from 4 to 12 (except for 11). The mean coordination number is 6. This holds true for any structures constructed from parallelepipeds when the edges are chosen as bonds. Actually, for one parallelepiped in the structure, there are one vertex and three edges. (This becomes evident if vertices and edges of the parallelepiped are represented in a "volume" form, i.e., vertices in the form of spheres and edges in the form of cylinders. The sum of internal solid angles at vertices of any parallelepiped is equal to 4π , which corresponds to one full sphere. At the same time, the sum of internal angles between the adjacent faces of the parallelepiped is equal to 6π , which corresponds to three circles in the bases of the cylinders.) Consequently, for one site in the structure, there are three bonds. Taking into account that each bond connects two sites, the desired mean coordination number can be determined as $\langle z \rangle = 6$.

In the initially chosen length units [see relationships (1), (2)], the edges of the Ammann rhombohedra have the length $r_5 = \sqrt{\tau + 2} \approx 1.902$. However, in the three-dimensional Penrose tiling, there are considerably shorter distances between a number of sites. These are vertices located at opposite ends of the short diagonal in the oblate Ammann rhombohedron (Fig. 2). The short internal diagonals of the oblate rhombohedra are parallel to the threefold axes and have the length $r_3/\tau =$

$\frac{\sqrt{3}}{\tau} \approx 1.070$; i.e., they are equal to almost half the edges. Therefore, it is reasonable to include these diagonals in the set of bonds and to consider such a set of sites and bonds as the second variant. In this case, the coordination numbers of specific sites vary from 6 to 12 (except for 11). In order to determine the change in the coordination number, it is necessary to calculate the ratio between the oblate and prolate Ammann rhombohedra.

There exists a general method for determining the frequency of occurrence of a particular fragment in a structure. First, it is necessary to construct the projection of this fragment onto the perpendicular space. In order for this fragment to be involved in the structure, the projection of the fragment should be located in the acceptance domain. The set of all possible displacements in the perpendicular space that form the projection of the fragment in the acceptance domain determines a specific region of finite volume V_{fr} . It is clear that the frequency of occurrence of the given fragment in the structure is proportional to the volume V_{fr} . Consequently, the problem of determining the frequency of occurrence of a particular fragment is reduced to a purely geometric problem.

The projection of the oblate Ammann rhombohedron onto the perpendicular space is a prolate Ammann rhombohedron and vice versa (Fig. 3). By displacing the projections inside the triacontahedron, it is possible to determine the volumes corresponding to the oblate ($V_{fr,o}$) and prolate ($V_{fr,p}$) rhombohedra. The ratio of these volumes is equal to the ratio between the numbers of prolate and oblate rhombohedra in the three-dimensional Penrose tiling $v_p/v_o = V_{fr,p}/V_{fr,o}$. This ratio is given by

$$v_p/v_o = \tau. \quad (4)$$

Therefore, the frequency of occurrence of prolate rhombohedra is higher than that of oblate rhombohedra by a factor of τ . Hence, it follows that the fraction of

oblate rhombohedra is $v_o/(v_o + v_p) = \frac{1}{\tau^2}$. Note that each

of the oblate rhombohedra has only one short diagonal r_3/τ connecting two vertices. As a result, the change in the coordination number of sites is equal to $\frac{2}{\tau^2}$ and,

therefore, we have $\langle z \rangle = \left(6 + \frac{2}{\tau^2}\right) = (10 - 2\tau) \approx 6.764$.

The set of bonds can be complemented by short diagonals of the rhombic faces of the Ammann rhombohedra (the third variant). These diagonals are aligned parallel to the twofold axes and have the length $r_2 = 2$ (Fig. 2); i.e., they are only slightly longer than the edges: $r_2/r_3 \approx 1.051$. For one rhombohedron in the structure, there are three rhombic faces and, hence,

three diagonals r_2 . Consequently, the mean coordination number increases by 6: $\langle z \rangle = (16 - 2\tau) \approx 12.764$. Note that the coordination numbers of specific sites take on values from 11 to 19.

Two oblate Ammann rhombohedra can share a face. In this case, they share a vertex from which two short internal diagonals r_3/τ of these rhombohedra emerge. The distance between the other two ends of these diagonals is also equal to r_2 . The inclusion of these distances in the set of bonds is not justified physically because one more site is located at the midpoint between two sites almost in the same line with them: the angle between the short diagonals of the adjacent oblate Ammann rhombohedra is equal to

$$\arccos\left(-\frac{\sqrt{5}}{3}\right) \approx 138.2^\circ. \text{ In general, among the three}$$

aforementioned sets of bonds, the first variant is of formal mathematical interest, whereas the last variant is most justified physically.

CUBIC APPROXIMANTS

The irrational number τ can be approximated by rational relationships. In this situation, the best approximation can be achieved with natural numbers of the Fibonacci series. This number sequence, which was originally derived as the solution of the rabbit reproduction problem, is determined by the recurrent relation

$$f_{n+1} = f_n + f_{n-1}, \quad (5)$$

where $f_1 = f_2 = 1$. The first terms of this series of natural numbers are as follows:

$$1, 1, 2, 3, 5, 8, 13, 21, 34, 55, \dots$$

The n th Fibonacci number is given by the formula

$$f_n = \frac{1}{\sqrt{5}} \left[\tau^n - \left(-\frac{1}{\tau}\right)^n \right]. \quad (6)$$

This formula immediately leads to the limiting relationship

$$\lim_{n \rightarrow \infty} \frac{f_n}{f_{n-1}} = \tau. \quad (7)$$

The relationship between the Fibonacci numbers and the golden mean

$$\tau^n = f_n \tau + f_{n-1} \quad (8)$$

turned out to be very useful and has often been used to simplify mathematical calculations. Note that, if the Fibonacci series of natural numbers is complemented by the terms $f_0 = 0$ and $f_{-n} = (-1)^{n+1} f_n$, relationship (8) will be valid for all integral exponents of the number τ . It is interesting to note that the new terms of the extended Fibonacci series also satisfy the recurrent relation (5) and expression (6) for the n th term.

Another important property of the Fibonacci numbers is associated with their parity. The greatest common divisor of two sequential Fibonacci numbers is equal to unity. This can be easily demonstrated by *reductio ad absurdum*. Indeed, let us assume that two sequential terms of the series f_n and f_{n-1} have a common divisor $k \geq 2$. Hence, it follows from the recurrent relation (5) that any Fibonacci number can be divided by k , which is obviously not true. In particular, the given property implies that two sequential Fibonacci numbers cannot be even simultaneously. It can be readily seen that even (*e*) and odd (*o*) Fibonacci numbers alternate with a period of 3 (*ooe*). As will be shown below, the parity of the Fibonacci numbers affects the symmetry of cubic approximants.

The noncrystallographic point symmetry of the quasicrystals can be achieved by specially choosing the perpendicular space E_{\perp} . By changing the space E_{\perp} , one can obtain structures with other symmetries, including periodic structures. The main constraint, as before, is that the projection of the structure onto the perpendicular space should have limited linear sizes. Note that the physical space remains the same. This ensures retention of the initial icosahedral local order.

The situation in which a new perpendicular space is obtained from projection (3) through a simple replacement of the number τ by the rational fraction f_n/f_{n-1} is of particular interest. After this replacement, the projection of the sites of the six-dimensional hypercubic lattice onto the new perpendicular space can be defined by the matrix

$$E_{\perp}^n = \frac{1}{f_{n-1}} \begin{pmatrix} f_n & 0 & -f_{n-1} & f_n & 0 & f_{n-1} \\ -f_{n-1} & f_n & 0 & f_{n-1} & f_n & 0 \\ 0 & -f_{n-1} & f_n & 0 & f_{n-1} & f_n \end{pmatrix}. \quad (9)$$

The three-dimensional space E_{\perp}^n determines a cubic periodic structure, the so-called Fibonacci crystal of the n th order. The Fibonacci crystals are often referred to as cubic approximants of icosahedral quasicrystals. Many cubic approximants of low orders have been revealed in alloys similar in composition to quasicrystals. In the largest known approximants, the number of atoms in a unit cell can be as large as several hundreds. The basic symmetry properties of the Fibonacci crystals [18, 19] are given below without proof.

Projection of a Six-Dimensional Lattice onto the Space E_{\perp}^n

In the case of icosahedral symmetry, the projections of the sites of the six-dimensional hypercubic lattice completely occupy the space E_{\perp} . A different situation occurs with Fibonacci crystals. Actually, it follows from matrix (9) that the sites of the six-dimensional lat-

tice are projected onto the space E_{\perp}^n into sites of a simple cubic lattice with spacing $\frac{1}{f_{n-1}}$. However, this does not necessarily mean that all sites of the simple cubic three-dimensional lattice are the projections of the sites of the six-dimensional lattice. In this situation, an important role is played by the parity of the Fibonacci numbers f_n and f_{n-1} corresponding to the n th order of the approximant. If one of the numbers f_n and f_{n-1} is an even number (the cases of *e/o* and *o/e*), the projection of the six-dimensional hypercubic lattice onto the space E_{\perp}^n occupies all the sites of the simple cubic lattice with spacing $\frac{1}{f_{n-1}}$. However, when both f_n and f_{n-1} are odd numbers (the case of *o/o*), the projection of the six-dimensional hypercubic lattice onto the space E_{\perp}^n occupies one face-centered cubic sublattice of the simple cubic lattice or, to put it differently, form a face-centered cubic lattice with spacing $\frac{2}{f_{n-1}}$.

Periodicity

The projection of the six-dimensional hypercubic lattice onto the space E_{\perp}^n is degenerate: to each point of the projection there corresponds an infinite set of the sites of the six-dimensional lattice. The criterion that a particular site belongs to the structure is the location of its projection in the acceptance domain. Therefore, all the sites projected into the same point either belong to the structure or do not belong to it (in principle, it is possible to analyze the exceptions from the formulated rule: this leads to the formation of Fibonacci crystals with double, triple, and similar unit cells). In order for two sites \mathbf{n}_1 and \mathbf{n}_2 of the six-dimensional lattice to be projected into the same point of the space E_{\perp}^n , they should obey the obvious equation

$$E_{\perp}^n \Delta \mathbf{n} = 0. \quad (10)$$

Here, we introduced the designation $\Delta \mathbf{n} = (\mathbf{n}_2 - \mathbf{n}_1)$. In the cases of *e/o* and *o/e*, the solution of Eq. (10) has the form

$$\Delta \mathbf{n} = m_x \mathbf{n}_x + m_y \mathbf{n}_y + m_z \mathbf{n}_z. \quad (11)$$

Here, m_x , m_y , and m_z are integral numbers and \mathbf{n}_x , \mathbf{n}_y , and \mathbf{n}_z are six-dimensional vectors with the following integral coordinates:

$$\begin{aligned} \mathbf{n}_x &= (f_{n-1}, 0, f_n, f_{n-1}, 0, -f_n), \\ \mathbf{n}_y &= (f_n, f_{n-1}, 0, -f_n, f_{n-1}, 0), \\ \mathbf{n}_z &= (0, f_n, f_{n-1}, 0, -f_n, f_{n-1}). \end{aligned} \quad (12)$$

Therefore, the vectors \mathbf{n}_x , \mathbf{n}_y , and \mathbf{n}_z can be treated as spacings of the Fibonacci crystals in the six-dimensional space and their projections onto the physical space $\mathbf{p}_i = E_{ph}\mathbf{n}_i$, where $i \in \{x, y, z\}$, can be treated as spacings of the Fibonacci crystals in the physical space. From relationships (2) and (12) with the use of equality (8), it is easy to find that $\mathbf{p}_x = (2\tau^n, 0, 0)$, $\mathbf{p}_y = (0, 2\tau^n, 0)$, and $\mathbf{p}_z = (0, 0, 2\tau^n)$; i.e., the Fibonacci crystals in the cases e/o and o/e have a primitive cubic structure with spacing $2\tau^n$. In the case of o/o , there arise an additional spacing $\frac{1}{2}(\mathbf{n}_x + \mathbf{n}_y + \mathbf{n}_z)$ in the six-dimensional space and the corresponding spacing (τ^n, τ^n, τ^n) in the physical space; i.e., the Fibonacci crystals have a body-centered cubic structure with the cubic unit cell parameter $2\tau^n$.

Acceptance Domain

In contrast to the case of icosahedral quasicrystals for which the acceptance domain is completely occupied by projection points, the Fibonacci crystals are characterized by the acceptance domain with a finite number of projection points; more precisely, the number of points in the acceptance domain is equal to the number of atoms in the unit cell of the Fibonacci crystal. In principle, this circumstance makes it possible to do without an acceptance domain: in order to determine the structure completely, it is sufficient to specify a particular number of points on a cubic (simple or face-centered) lattice in the space E_{\perp}^n . Nonetheless, the acceptance-domain formalism remains useful for a number of reasons. First, high-order approximants can contain a very large number of atoms in the unit cell whose simple enumeration is always extremely tedious and useful only rarely. Second, the Fibonacci crystals can bear a closer structural resemblance to the icosahedral crystal only in the case where their projection onto the perpendicular space E_{\perp}^n will also resemble the projection of the quasicrystal onto the space E_{\perp} . In this respect, it is desirable to adapt the acceptance domain of the ideal quasicrystal to the Fibonacci crystals. Actually, for cubic approximants of the three-dimensional Penrose tiling, the role of the acceptance domain is played by a distorted rhombic triacontahedron whose 32 vertices are specified by the vectors $\left(\pm\frac{f_{n+1}}{f_{n-1}}, \pm\frac{f_n}{f_{n-1}}, 0\right)$, $\left(\pm\frac{f_n}{f_{n-1}}, \pm\frac{f_n}{f_{n-1}}, \pm\frac{f_n}{f_{n-1}}\right)$, and $\left(\pm\frac{f_{n+1}}{f_{n-1}}, 0, \pm 1\right)$ drawn from the center of the polyhedron. Unlike the coordinates of the vertices of the ideal rhombic triacontahedron, these coordinates are obtained with the replacements $\tau \rightarrow \frac{f_n}{f_{n-1}}$ and $\tau^2 \rightarrow \frac{f_{n+1}}{f_{n-1}}$.

Point Symmetry

The cubic approximants of icosahedral quasicrystals belong to the tetrahedral class T rather than to the cubic class O . In actual fact, unlike the cube, the icosahedron has no fourfold axes. As a result, the tetrahedral group rather than the cubic group is the icosahedral symmetry subgroup. In order for the Fibonacci crystal to possess tetrahedral symmetry, the projection of the crystal onto the perpendicular space E_{\perp}^n should also have tetrahedral symmetry. Since this projection consists of a finite number of points that belong to the simple cubic or face-centered cubic lattice in the perpendicular space E_{\perp}^n , it is clear that the center of the projection and, hence, the center of the acceptance domain can be located only at points of a special type. These points for the simple cubic lattice (cases e/o , o/e) are represented by the origin of the cell $(0, 0, 0)$ and the center of the cell $\left(\frac{1}{2}, \frac{1}{2}, \frac{1}{2}\right)$, whereas the corresponding points for the face-centered lattices (case o/o) have the coordinates $(0, 0, 0)$, $\left(\frac{1}{2}, \frac{1}{2}, \frac{1}{2}\right)$, and $\left(\frac{1}{4}, \frac{1}{4}, \frac{1}{4}\right)$ (here, for convenience, the spacings of the cubic lattices are taken to be equal to unity, as is customary in crystallography). All the other special points are equivalent to the above points; i.e., they are related to them by the symmetry operations of the cubic lattices.

Spatial Symmetry

The symmetry space group of the n th-order Fibonacci crystal depends on the parity of the Fibonacci numbers f_n and f_{n-1} and also on the location of the center of the crystal projection in the perpendicular space. All the possible space groups of the Fibonacci crystals were determined earlier. The groups with the highest symmetry for all the cases under consideration are as follows: $Pm\bar{3}$ [cases e/o , o/e ; the center of the projection is located at the point $(0, 0, 0)$], $Pa\bar{3}$ [cases e/o , o/e ; the center of the projection is located at the point $\left(\frac{1}{2}, \frac{1}{2}, \frac{1}{2}\right)$], $Im\bar{3}$ [case o/o , the center of the projection is located at the point $(0, 0, 0)$ or the point $\left(\frac{1}{2}, \frac{1}{2}, \frac{1}{2}\right)$], and $I2_13$ [case o/o , the center of the projection is located at the point $\left(\frac{1}{4}, \frac{1}{4}, \frac{1}{4}\right)$]. The other possible groups with lower symmetry for the Fibonacci crystals are subgroups of the aforementioned groups.

*Approximation of the Quasicrystal Structure
by Approximants*

In the case where the order n of the cubic approximant increases by unity, the unit cell parameter increases by a factor of τ and the unit cell volume increases by a factor of $\tau^3 \approx 4.236$. Hence, the number of atoms in the unit cell increases by a factor of more 4. Note that, on a scale of the order of one unit cell, the structure of the approximant coincides with the structure of the ideal quasicrystal. As a result, the quasicrystal can be considered the limit of the sequence of cubic approximants at $n \rightarrow \infty$. The approximants, as if, approach the quasicrystal (approximate the quasicrystal) in the structure and physical properties, which explains their names. For example, the diffraction pattern of the approximants with an increase in the order n becomes similar in relative intensities and positions of the Bragg reflections to the diffraction pattern of the quasicrystal. Beginning with a specific value of n , which is associated with the experimental error, the approximants become virtually identical to the quasicrystals [20].

The structural relation to icosahedral quasicrystals, on the one hand, and the periodicity, on the other hand, make the Fibonacci crystals convenient model objects for use in investigating the properties of the quasicrystals themselves. Specifically, the local atomic structure of quasicrystals can be more easily understood and described when the low-order cubic approximants whose atomic structures are determined exactly are known. Moreover, many mathematical statements regarding the ideal quasicrystals can be more readily proved first for approximants and then can be generalized with the use of the limit $n \rightarrow \infty$.

For example, let us prove relationship (4) for the three-dimensional Penrose tiling by using the Fibonacci crystals. The unit cell volume for the n th-order Fibonacci crystal can be written as $V_{cell} = (2\tau^n)^3 = 8\tau^{3n}$. We assume that the Fibonacci crystal is composed of structural units identical to the structural units of the Penrose tiling, i.e., oblate and prolate Ammann rhombohedra. The volume of the prolate Ammann rhombohedron constructed using the vectors $(\tau, 0, 1)$, $(1, \tau, 0)$, and $(0, 1, \tau)$ and the volume of the oblate Ammann rhombohedron constructed using the vectors $(\tau, 0, -1)$, $(-1, \tau, 0)$, and $(0, -1, \tau)$ are as follows:

$$V_p = \begin{vmatrix} \tau & 0 & 1 \\ 1 & \tau & 0 \\ 0 & 1 & \tau \end{vmatrix} = \tau^3 + 1 = 2\tau + 2 = 2\tau^2$$

and

$$V_o = \begin{vmatrix} \tau & 0 & -1 \\ -1 & \tau & 0 \\ 0 & -1 & \tau \end{vmatrix} = \tau^3 - 1 = 2\tau.$$

The volume ratio is equal to the irrational number $V_p/V_o = \tau$. As a result of this incommensurability, the unit cell volume of the Fibonacci crystal can be uniquely determined by the volumes of the oblate and prolate Ammann rhombohedra. Actually, we have

$$\begin{aligned} V_{cell} &= 8\tau^{3n} = 4f_{3n-1} \times 2\tau^2 + 4f_{3n-2} \times 2\tau \\ &= 4f_{3n-1}V_p + 4f_{3n-2}V_o. \end{aligned}$$

By changing over to the three-dimensional Penrose tiling at $n \rightarrow \infty$, we obtain relationship (4); that is,

$$v_p/v_o = \lim_{n \rightarrow \infty} \frac{4f_{3n-1}}{4f_{3n-2}} = \tau.$$

DETAILS OF THE COMPUTER EXPERIMENT

The percolation thresholds of the three-dimensional Penrose tiling were determined using computer simulation of the percolation in unit cells of the cubic approximants of the Penrose tiling. The Fibonacci crystals of the sixth, seventh, ninth, and tenth orders with space group $Pa\bar{3}$ were chosen as the objects of investigation. Table 1 presents the main characteristics of the unit cells in these crystals, such as the total number of sites in the cell, the number of sites on each face, and the numbers of prolate (n_p) and oblate (n_o) Ammann rhombohedra per unit cell. It can be seen from this table that the total number of rhombohedra ($n_p + n_o$) coincides with the number of sites. The ratio n_p/n_o is given for comparison with the ratio $v_p/v_o = \tau$ in order to illustrate the degree of similarity of the structure of the approximant to the ideal structure of the three-dimensional Penrose tiling.

In the percolation theory, there exist two different problems, namely, the site problem and the bond problem. In the site problem, each site either can be occupied (with probability p) or can be empty (with probability $1 - p$). If the site is empty, all bonds of this site are assumed to be dangling. In the bond problem, all sites are considered to be occupied, whereas the bonds either can connect the sites (with probability p) or can be dangling (with probability $1 - p$). A criterion for percolation in an infinite structure is the existence of an infinite cluster consisting of occupied sites that are connected to each other. Computer simulation experiments have been performed with bounded structural regions for which, historically, the natural criterion for percolation is the existence of a connected path between the opposite boundaries of the region under consideration.

In our case, we assumed that the cell of the cubic approximant percolates if there exists a connected path between any occupied site belonging to one of the faces (for example, the upper face) and any occupied site belonging to the opposite (lower) face. The periodic boundary conditions were imposed on the other (four) faces. The site of the cell was considered to belong to

Table 1. Characteristics of the unit cells of the cubic approximants of the three-dimensional Penrose tiling with space group $Pa\bar{3}$

n	f_n/f_{n-1}	Number of sites		Number of Ammann rhombohedra		$(n_p/n_o) - \tau$
		in the cell	on the face	prolate (n_p)	oblate (n_o)	
6	8/5	10336	466	6388	3948	4.6×10^{-7}
7	13/8	43784	1220	27060	16724	-2.6×10^{-8}
9	34/21	785672	8362	485572	300100	-7.9×10^{-11}
10	55/34	3328160	21892	2056916	1271244	4.4×10^{-12}

the face when this site had at least one bond that emerged from the cell and intersected the given face.

Let $P(p)$ be the statistical probability that the structure percolates at a specified occupation number p . It is evident that the statistical probability satisfies the conditions $P(0) = 0$ and $P(1) = 1$. For a bounded structural region, $P(p)$ is a smooth function, which gradually increases when the occupation number p takes on values from 0 to 1. By contrast, for an infinite structure, the function $P(p)$ has a specific feature: the interval $[0, 1]$ can be separated into the two subintervals $[0, p_c)$ and $(p_c, 1]$ in such a way that $P(p \in [0, p_c)) = 0$ and $P(p \in (p_c, 1]) = 1$ and, at the point p_c , which is referred to as the percolation threshold, the value of $P(p)$ changes jumpwise from 0 to 1. For a number of simple two-dimensional structures, the percolation threshold can be determined by analytical methods. However, for the majority of structures, it is necessary to perform numerical experiments by the Monte Carlo method. The experimentally obtained functions $P(p)$ for bounded structural regions depend substantially on the region size. As the linear sizes of the cells under investigation increase, the graph $P(p)$ becomes more and more similar in appearance to a step, thus approaching the dependence $P(p)$ for an infinite structure. A comparison of the dependences $P(p)$ for cells of different sizes makes it possible to reveal the general regularities and to determine the percolation threshold with a required accuracy.

Now, we describe a direct algorithm for calculating the statistical probability P at a specified occupation number p for the site problem. Since any site either can be occupied or can be empty, for an arbitrary cell with N sites, there exist 2^N possible configurations with the probability $p^k(1-p)^{N-k}$, where k is the number of occupied sites. Then, the percolation probability can be calculated from the relationship

$$P(p) = \sum' p^k (1-p)^{N-k}, \quad (13)$$

where the prime on the sum sign denotes that the summation is performed only over the configurations for which the cell percolates.

Direct calculation of sum (13) cannot be accomplished in practice because of the very large number of configurations involved. In rare cases, it has been possible to apply some mathematical tricks to the calcula-

tion of the percolation probability $P(p)$ without direct summation. However, for the vast majority of systems, it is necessary to use the Monte Carlo method and to determine the percolation probability $P(p)$ with a small random sample from the total number of configurations.

Let $p \in (0, 1)$ be a specified value of the occupation number. The configuration is constructed as follows: for each site of the cell, we determine in a random manner (using a random number generator) whether this site is occupied (with probability p) or is empty (with probability $1-p$). This configuration either percolates or does not percolate. Similarly, we construct M configurations, among which m configurations turn out to percolate. At $M \rightarrow \infty$, the ratio m/M tends toward the percolation probability; that is,

$$P(p) = \lim_{M \rightarrow \infty} \frac{m}{M}. \quad (14)$$

Moreover, it is advisable to know the root-mean-square deviation $\Delta P(p)$ of the percolation probability calculated according to relationship (14) from its true value determined from expression (13). The integral number m can take on values from 0 to M ; the probability that the integer m will take on a particular value, apparently, can be found from the formula $C_M^m P^m (1-P)^{M-m}$,

where $C_M^m = \frac{M!}{m!(M-m)!}$ is the number of combinations of M things taken m at a time. Therefore, the mean error of the computer experiment can be determined from the relationship

$$\Delta P(p) = \sqrt{\sum_{m=0}^M C_M^m P^m (1-P)^{M-m} \left(\frac{m}{M} - P\right)^2}$$

or, after simple mathematical transformations, from the expression

$$\Delta P(p) = \sqrt{\frac{P(p)(1-P(p))}{M}}. \quad (15)$$

ANALYSIS OF THE RESULTS
OF THE COMPUTER SIMULATION
AND THE PERCOLATION THRESHOLDS

The computer simulation of the percolation was carried out for six cases: the number of bonds sequentially included the edges of the Ammann rhombohedra (case I), the short internal diagonals of the oblate Ammann rhombohedra (case II), and the short diagonals of the faces of the Ammann rhombohedra (case III); moreover, the site problem and the bond problem were considered separately. In each case, the occupation number p took on specified values in successive steps $\Delta p = 0.001$ and the number of experiments performed at each point was $M = 1000$.

Figure 4 shows the characteristic dependences $P(p)$ obtained from the computer experiments. Four graphs in this figure correspond to Fibonacci crystals of the sixth, seventh, ninth, and tenth orders. It can be seen that, as the order n of the cubic approximant increases, the graph $P(p)$ becomes more and more similar in appearance to a step. It is also worth noting that points of pairwise intersections of all four graphs fall in a narrow range both along the abscissa axis and along the ordinate axis. Visually, it seems that all these graphs "meet" at a point in the vicinity of a particular value of the occupation number p . At $n \rightarrow \infty$, the percolation probability P at the given point remains unchanged, tends toward zero to the left of this point, and tends toward unity to the right of it. Now, it is not difficult to understand that this value of the occupation number is the percolation threshold p_c .

Of course, it is not to be expected that, with an increase in the accuracy of the experiment, all the graphs should actually intersect at the same point. Most likely, the pairwise intersections of the graphs will form a set of points $S(n, m)$ in the graph plane, where n and m are the orders of Fibonacci crystals ($n \neq m$). In this case, the percolation threshold will be determined as the abscissa of the limiting point of this set of points $S(n, m)$ with the quantities n and m tending toward infinity.

Nonetheless, even from these graphs, the percolation threshold can be determined with a certain accuracy dictated by the error of the experiment itself. Indeed, the points of intersections are arranged inside a rectangle whose base has a length close to the experimental step $\Delta p = 0.001$ and whose height is less than $6\Delta P$. Here, $\Delta P \approx 0.0158$ is the root-mean-square deviation of the percolation probability, which was calculated from relationship (15) for $P = 1/2$. (In this case, we can use the closeness of the discrete binominal distribution $C_M^m P^m (1 - P)^{M-m}$ to the continuous normal

distribution $\frac{1}{\sigma\sqrt{2\pi}} \exp\left(-\frac{(m/M - P)^2}{2\sigma^2}\right)$ of the quantity (m/M) with a mean value P and a root-mean-square deviation $\sigma = \Delta P$. For a normal distribution, there exists

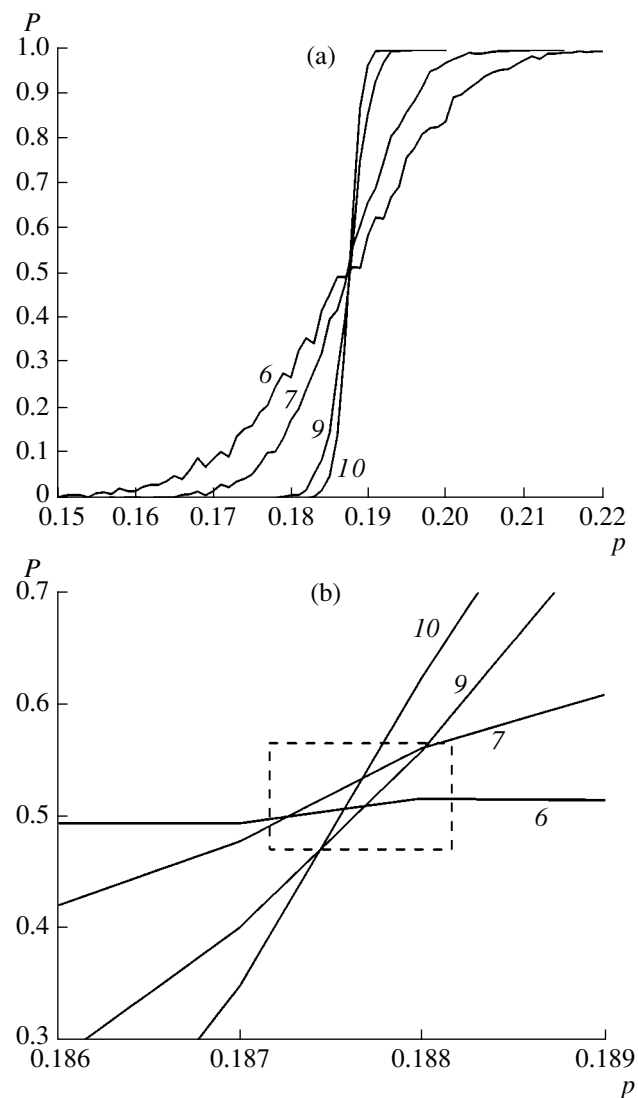


Fig. 4. Dependences of the percolation probability P on the occupation number p according to the computer simulation of the percolation for case III and the site problem (the graphs correspond to Fibonacci crystals of the sixth, seventh, ninth, and tenth orders): (a) the general view of the dependences and (b) the region of intersection of the graphs. The dashed rectangle of size $\Delta p \times 6\Delta P$ corresponds to the experimental error (it can be seen that the scatter of intersection points is of the order of the experimental error).

a nonformal rule, the so-called three-sigma estimate, according to which the great bulk of the distribution is concentrated inside the domain $[P - 3\sigma, P + 3\sigma]$.) Thus, it is evident that the discrepancy between the points $S(n, m)$ does not exceed the experimental error and, hence, the percolation threshold can be considered to be determined accurate to within $\Delta p = 0.001$.

The percolation thresholds determined accurate to within $\Delta p = 0.001$ for the aforementioned six cases under investigation are presented in Table 2. These results are justified logically. It can be seen that an increase in the number of bonds in the structure leads to

Table 2. Percolation thresholds of the three-dimensional Penrose tiling

Included bonds	Mean coordination number	Site problem	Bond problem
Case I: Edges (r_5) of the Ammann rhombohedra	6	0.285	0.225
Case II: Edges of the Ammann rhombohedra and short internal diagonals (r_3/τ) of the oblate Ammann rhombohedra	$6 + \frac{2}{\tau^2} \approx 6.764$	0.271	0.207
Case III: Edges of the Ammann rhombohedra, short internal diagonals (r_3/τ) of the oblate Ammann rhombohedra, and short diagonals (r_2) of the faces of the Ammann rhombohedra	$12 + \frac{2}{\tau^2} \approx 12.764$	0.188	0.111

a decrease in the percolation threshold. On the other hand, the local inhomogeneity in the given case also brings about a decrease in the percolation threshold. In particular, for case I, as well as for a simple cubic lattice, the mean coordination number is 6. However, the percolation thresholds in the three-dimensional Penrose tiling appear to be substantially lower: 0.285 for the site problem (0.312 for the cubic lattice) and 0.225 for the bond problem (0.249 for the cubic lattice). Moreover, the following approximate relationship holds for the bond problem: $\langle z \rangle p_c \approx \text{const}$, where $\langle z \rangle p_c$ is equal to 1.35 for case I, 1.40 for case II and 1.42 for case III.

ACKNOWLEDGMENTS

The authors acknowledge the support of the Russian Science Foundation. This work was supported in part by the Russian Foundation for Basic Research (project nos. 02-02-16275-a and 05-02-16763-a), the Council for Grants of the President of the Russian Federation for Support of Leading Scientific Schools of the Russian Federation (grant no. NSh-1954.2003.2), and the Ministry of Education and Science of the Russian Federation within the program "Development of the Scientific Potential of the Higher School" (project no. III-3-4851).

REFERENCES

1. D. Stauffer and A. Aharony, *Introduction to Percolation Theory* (Taylor and Francis, London, 1992).
2. G. Grimmett, *Percolation and Disordered Systems* (Springer-Verlag, Berlin, 1997).
3. M. Kleman and O. B. Lavrentovich, *Soft Matter Physics: Introduction* (Springer-Verlag, Berlin, 2003).
4. B. I. Shklovskii and A. L. Efros, *Electronic Properties of Doped Semiconductors* (Nauka, Moscow, 1979; Springer-Verlag, New York, 1984).
5. S. P. Friedman and N. A. Seaton, *Transp. Porous Media* **30**, 241 (1998).
6. G. Schliecker and C. Kaiser, *Physica A (Amsterdam)* **269**, 189 (1999).
7. R. M. Ziff and F. Babalievski, *Physica A (Amsterdam)* **269**, 201 (1999).
8. D. Shechtman, I. Blech, D. Gratias, and J. W. Cahn, *Phys. Rev. Lett.* **53**, 1951 (1984).
9. D. Levine and P. J. Steinhardt, *Phys. Rev. Lett.* **53**, 2477 (1984).
10. V. E. Dmitrienko, *Acta Crystallogr., Sect. A: Found. Crystallogr.* **50**, 515 (1994).
11. V. E. Dmitrienko, *Mater. Sci. Forum* **150–151**, 199 (1994).
12. P. Kramer and R. Neri, *Acta Crystallogr., Sect. A: Found. Crystallogr.* **40**, 580 (1984).
13. P. A. Kalugin, A. Yu. Kitaev, and L. S. Levitov, *Pis'ma Zh. Éksp. Teor. Fiz.* **41**, 119 (1985) [*JETP Lett.* **41** (3), 145 (1985)].
14. M. Duneau and A. Katz, *Phys. Rev. Lett.* **54**, 2688 (1985).
15. R. Penrose, *Intelligencer* **2**, 32 (1979).
16. M. Gardner, *Penrose Tiles to Trapdoor Ciphers* (Freeman, New York, 1989; Mir, Moscow, 1993).
17. D. Levine and P. J. Steinhardt, *Phys. Rev. B* **34**, 596 (1986).
18. K. Niizeki, *J. Phys. A: Math. Gen.* **25**, 1843 (1992).
19. V. A. Chizhikov, *Kristallografiya* **44** (6), 814 (1999) [*Crystallogr. Rep.* **44** (6), 1024 (1999)].
20. V. E. Dmitrienko, *J. Phys. (France)* **51**, 2717 (1990).

Translated by O. Borovik-Romanova

PHYSICAL PROPERTIES OF CRYSTALS

Dilatometric and Ultrasound Study of $[\text{NH}_2(\text{CH}_3)_2]\text{MnCl}_3 \cdot 2\text{H}_2\text{O}$ Crystals

A. U. Sheleg*, E. M. Zub*, A. Ya. Yachkovskii*, and L. F. Kirpichnikova**

* *Institute of Solid-State and Semiconductor Physics, Belarussian Academy of Sciences,
ul. Brovki 17, Minsk, 220072 Belarus
e-mail: sheleg@ifftp.bas-net.by*

** *Shubnikov Institute of Crystallography, Russian Academy of Sciences,
Leninskii pr. 59, Moscow, 119333 Russia
e-mail: luba@ns.crys.ras.ru*

Received April 28, 2005

Abstract—The unit-cell parameters of $[\text{NH}_2(\text{CH}_3)_2]\text{MnCl}_3 \cdot 2\text{H}_2\text{O}$ crystals are determined by X-ray diffraction analysis and the velocities of longitudinal ultrasonic waves in these crystals are measured by the echo-pulse method in the temperature range 100–315 K. The coefficients of thermal expansion along the principal crystallographic axes are derived from the temperature dependences of the unit-cell parameters. The temperature dependences of the characteristics studied reveal kink anomalies at temperatures of ~125, 179, 203, 260, and 303 K. These anomalies are indicative of structural transformations in the $[\text{NH}_2(\text{CH}_3)_2]\text{MnCl}_3 \cdot 2\text{H}_2\text{O}$ crystals, which may be related to the dynamics of dimethylammonium cations. © 2005 Pleiades Publishing, Inc.

INTRODUCTION

Crystals of the $[\text{NH}_2(\text{CH}_3)_2]\text{MnCl}_3 \cdot 2\text{H}_2\text{O}$ (DMA · MnCl_3) compound belong to the family of organometallic compounds of transition metals, which have a number of interesting physical properties (in particular, unusual magnetic resonance behavior [1, 2]). In addition, DMA · MnCl_3 crystals are characterized by a significant anisotropy of proton conductivity [3] and belong to the monoclinic system (sp. gr. $C2/c$) with the unit-cell parameters $a = 17.154 \pm 0.006$ Å, $b = 11.992 \pm 0.003$ Å, $c = 9.321 \pm 0.002$ Å, and $\beta = 90.09^\circ$ at room temperature [2]. The structure of this crystal at room temperature was investigated previously [4] and assigned to the orthorhombic system with the unit-cell parameters $a = 17.156 \pm 0.009$ Å, $b = 12.000 \pm 0.006$ Å, and $c = 9.313 \pm 0.004$ Å. This discrepancy may be related to the existence of a phase transition at 302 K (i.e., close to room temperature).

Kapustianik [3] carried out dilatometric study and measurements of the dielectric properties of a DMA · MnCl_3 crystal at low temperatures and showed the existence of a sequence of second-order phase transitions in this crystal at $T_1 = 300$ K, $T_2 = 235$ K, and $T_3 = 180$ K.

The optical properties of $[\text{NH}_2(\text{CH}_3)_2]\text{MnCl}_4 \cdot 3.5\text{H}_2\text{O}$ crystals were investigated in [5] and phase transitions were revealed at $T_1 = 302$ K and $T_2 = 230$ K, i.e., at approximately the same temperatures as in DMA · MnCl_3 crystals [3]. This circumstance indicates a possible identity of the chemical compositions of the crystals studied by different researchers. It is possible that

the crystals of manganese dimethylaminotrichloride, investigated in [5], also had the chemical formula $[\text{NH}_2(\text{CH}_3)_2]\text{MnCl}_3 \cdot 2\text{H}_2\text{O}$.

In this paper, we report the results of studying the temperature changes in the unit-cell parameters and the coefficients of thermal expansion (CTEs) of DMA · MnCl_3 crystals and ultrasonic wave velocities in these crystals in a wide temperature range.

EXPERIMENTAL

$[\text{NH}_2(\text{CH}_3)_2]\text{MnCl}_3 \cdot 2\text{H}_2\text{O}$ crystals were grown by slow evaporation of the solvent from an aqueous solution of chlorides of dimethylamine ($[\text{NH}_2(\text{CH}_3)_2]\text{Cl}$) and manganese (MnCl_2) taken in a stoichiometric ratio. The crystal growth was implemented at room temperature both by spontaneous crystallization and using a seed rotating at a speed of 2 rpm. Growth for 2 to 3 weeks resulted in light pink transparent crystals $30 \times 15 \times 10$ mm³ in size. They showed good optical quality and pronounced faceting. The habit of the crystals obtained was a slightly distorted hexagonal prism. The natural growth faces of the crystal coincided with the crystallographic planes (100), (001), and (110). In addition, the (101) and (111) planes were sometimes observed on the crystal surface.

It should be noted that DMA · MnCl_3 crystals become nontransparent and may fracture in vacuum, as well as upon long-term annealing. Such behavior seems to be related to the presence of crystallization water in the structure of the crystals, which emerges from them upon annealing.

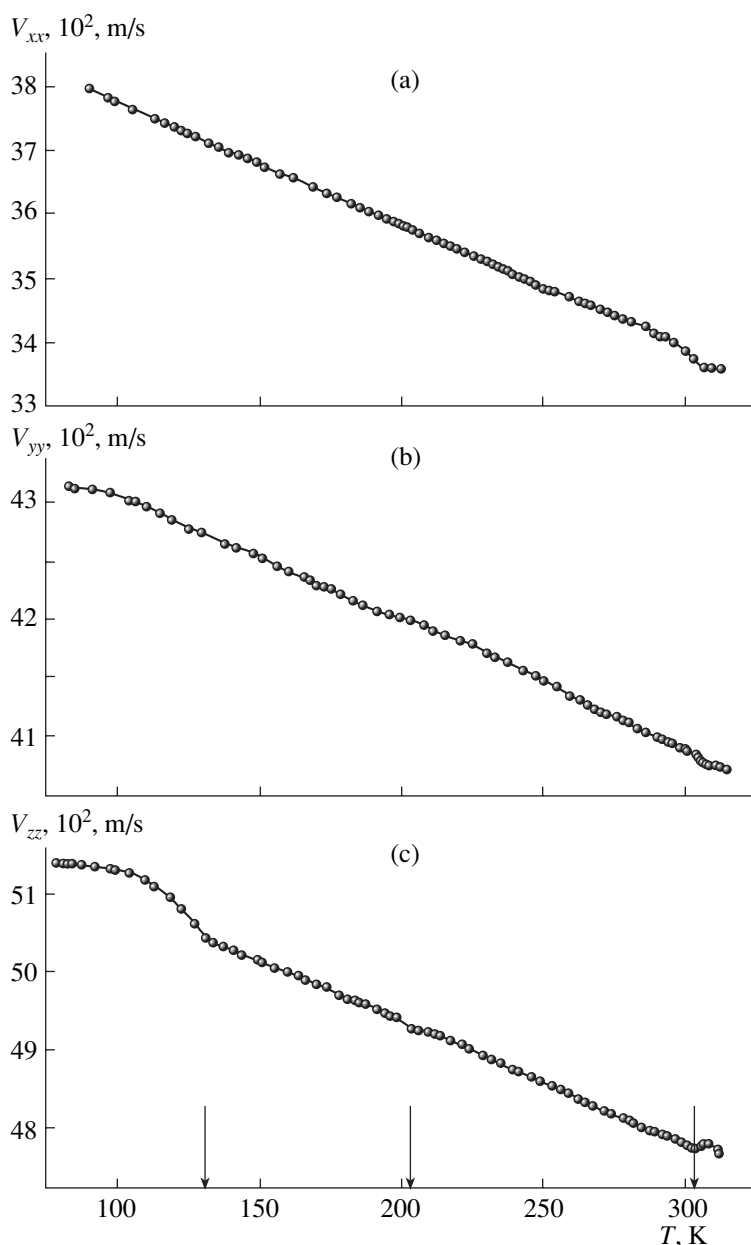


Fig. 1. Temperature dependences of the velocities of longitudinal ultrasonic waves in the $\text{DMA} \cdot \text{MnCl}_3$ crystal in the (a) [100], (b) [010], and (c) [001] crystallographic directions.

The velocities of longitudinal ultrasonic waves were measured by the echo-pulse method on an IS-3 ultrasonic-velocity meter. The time between the reflected signals was determined using calibration marks. Longitudinal ultrasonic waves were excited by a piezoelectric quartz plate cut in the X plane. Polyorganosilicon hydrophobizing liquid of the 136-157 grade was used as an acoustic lubricant. The measurements were performed in the temperature range 100–315 K at a frequency of 11 kHz. The experimental samples were cut in the form of parallelepipeds and were 5–7 mm in size in the directions in which the velocities of ultrasonic waves were determined. The samples were oriented in

such a way that the crystallophysic axis X was parallel to the a axis, the Y axis was oriented accurate to 1° along the twofold symmetry axis b , and the Z axis coincided with the c axis. Temperature was measured by a Chromel–Copel thermocouple, whose junction was in direct contact with the sample located in the measuring line. The temperature dependence of the ultrasonic wave velocity was recorded under the conditions of quasi-stationary heating of samples at a rate of ~ 0.4 K/min. The samples were preliminary cooled in liquid nitrogen vapor. Heating was performed by a heater mounted on a thermostat shield covering the measuring line.

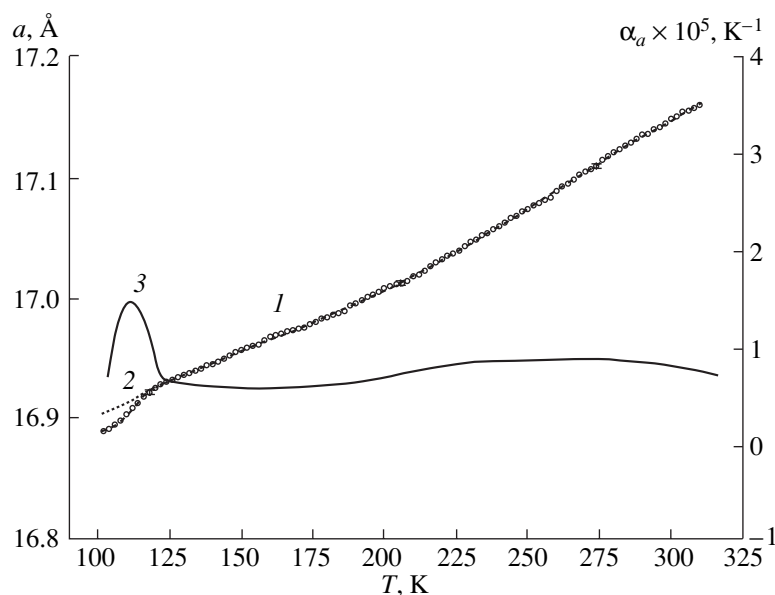


Fig. 2. Temperature dependence of the unit-cell parameter a of the $\text{DMA} \cdot \text{MnCl}_3$ crystal: (1) experiment (circles), (2) approximation (dashed line), and (3) the CTE α_a (solid line).

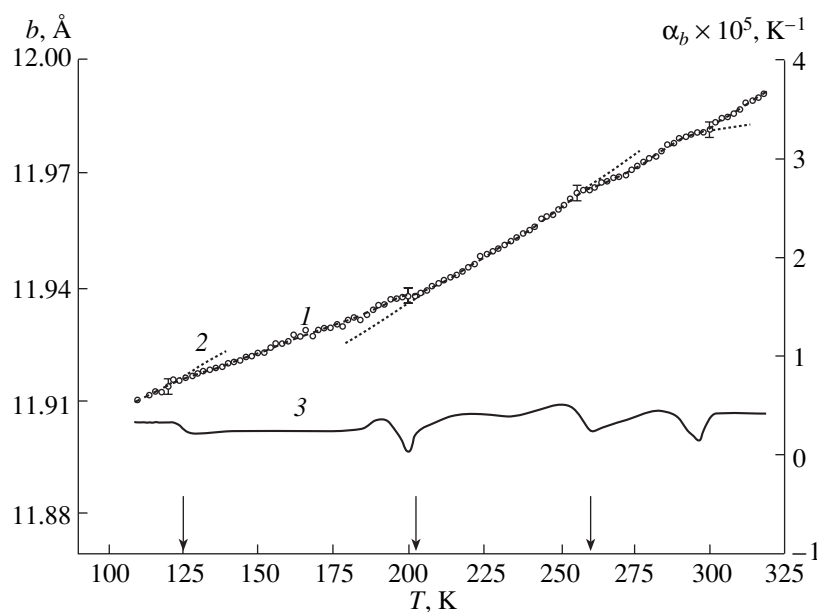


Fig. 3. Temperature dependence of the unit-cell parameter b of the $\text{DMA} \cdot \text{MnCl}_3$ crystal: (1) experiment (circles), (2) approximation (dashed line), and (3) the CTE α_b (solid line).

X-ray diffraction study of the unit-cell parameters was performed on a TUR-M62 diffractometer ($\text{CuK}\alpha$ radiation) in the temperature range 100–315 K, using a low-temperature X-ray camera (Rigaku). The samples were single-crystal $\text{DMA} \cdot \text{MnCl}_3$ plates $\sim 4 \times 4 \times 3 \text{ mm}^3$ in size, cut in such a way that their faces coincided with the (100), (001), and (010) planes. The (100) and (001) planes were the growth planes and the (010) plane was extracted to the surface accurate to $\sim 7'$ by the X-ray diffraction method. Since $\text{DMA} \cdot \text{MnCl}_3$ crystals

break in vacuum, the samples prepared for X-ray analysis were covered by a thin layer of the vacuum compound G9647. Before each measurement, the sample was thermostated at a given temperature for 10–15 min. The reflection intensity profiles were recorded every 2–3 K at a counter rate of $1/4 \text{ K/min}$ in the mode of continuous θ – 2θ scanning. The diffraction angles were determined from the positions of the centroids of the (18.00), (0.12.0), and (00.10) reflection profiles with an error of $0.2'$ – $0.4'$. The experimental values of the inter-

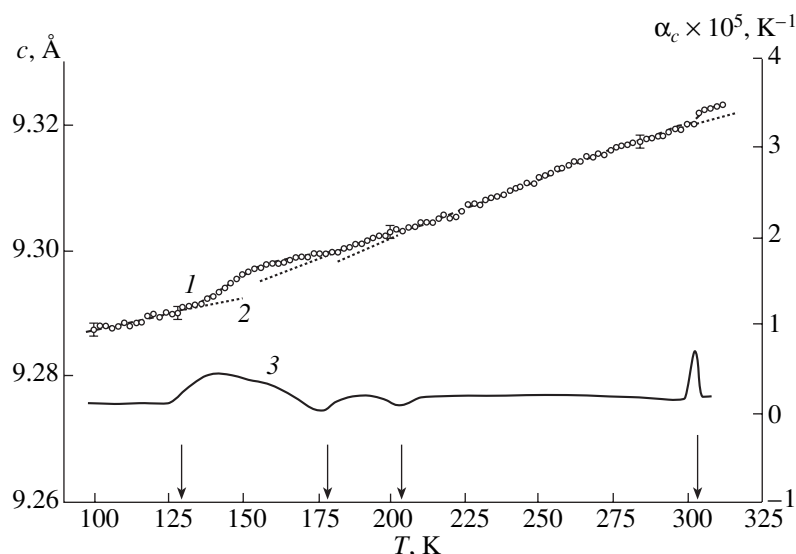


Fig. 4. Temperature dependence of the unit-cell parameter c of the $\text{DMA} \cdot \text{MnCl}_3$ crystal: (1) experiment (circles), (2) approximation (dashed line), and (3) the CTE α_c (solid line).

planar spacings $d_{18.00} = f(T)$, $d_{0.12.0} = f(T)$, and $d_{00.10} = f(T)$ were used to determine the temperature dependences of the parameters $a = f(T)$, $b = f(T)$, and $c = f(T)$. The CTEs were determined by the technique described in [6].

RESULTS AND DISCUSSION

Figure 1 shows the temperature dependences of the velocities v_{xx} , v_{yy} , and v_{zz} of longitudinal ultrasonic waves propagating along the principal crystallographic axes [100], [010], and [001], respectively. As can be seen from Fig. 1, the velocities of the waves propagating along all three principal directions decrease with an increase in temperature. However, it should be noted that all the curves— $v_{xx} = f(T)$, $v_{yy} = f(T)$, and $v_{zz} = f(T)$ —show anomalies in the form of a kink at $T_1 = 303$ K, thus confirming the existence of phase transitions in the crystal at this temperature. Unusual behavior of the temperature dependence of the velocity v_{zz} is observed at low temperatures (in the range 80–130 K), where there is a decrease in the ultrasonic wave velocity with an increase in temperature in nonlinear, while, upon further heating, the dependence $v_{zz} = f(T)$ become linear. As can be seen from Fig. 1c, a kink anomaly is observed at $T = 130$ K on the curve $v_{zz} = f(T)$, which is typical of organic crystals of such type at temperatures close to the phase transition. In addition, an anomaly in the form of small step is observed at $T_2 \sim 203$ K on this dependence.

It should be noted that the elastic properties of the $\text{DMA} \cdot \text{MnCl}_3$ crystal exhibit an anisotropy: $v_{zz} > v_{yy} > v_{xx}$. Such an anisotropy of the elastic wave velocities is related to the specific structural features of this crystal [4]. The unit cell of $\text{DMA} \cdot \text{MnCl}_3$ consist of chains of

inorganic complexes MnCl_3 , aligned along the c axis. The chains are located in the plane perpendicular to the a axis and are bound to each other by hydrogen bonds along the b axis. Between these planes, $[\text{NH}_2(\text{CH}_3)_2]^+$ ions are located. Stronger chemical bonds (similar to covalent) are observed between Mn and Cl atoms along the chains (the c axis) and the weakest (hydrogen) bonds are observed along the b axis and between the planes containing chains, i.e., along the a axis. Such a structure of the crystal determines its mechanical properties: it can be cleaved easily in the {100} planes, it is more difficult to cleave it in the {001} planes, and the crystal almost cannot be cleaved in the {001} planes.

The unit-cell parameters of the $\text{DMA} \cdot \text{MnCl}_3$ crystal, determined by us at room temperature, are $a = 17.132 \pm 0.002$ Å, $b = 11.976 \pm 0.002$ Å, and $c = 9.335 \pm 0.001$ Å. If we take into account that the properties of $\text{DMA} \cdot \text{MnCl}_3$ crystals depend strongly on the presence of impurities, the degree of lattice perfection, and the growth conditions, our data on the unit-cell parameters of this crystal at room temperature are in agreement with the results of [2, 4].

The temperature dependences of the unit-cell parameters a , b , and c of the $\text{DMA} \cdot \text{MnCl}_3$ crystal in the temperature range 100–315 K are shown in Figs. 2–4. As can be seen, all the parameters increase gradually with an increase in temperature.

Small kink anomalies are observed on the curve $b = f(T)$ (Fig. 3) at temperatures $T_1 \sim 125$ K, $T_2 \sim 202$ K, $T_3 \sim 260$ K, and $T_4 \sim 300$ K, which is indicative of the existence of phase transformations in the $\text{DMA} \cdot \text{MnCl}_3$ crystal at these temperatures. Similar anomalies at $T_1 \sim 129$ K, $T_1' \sim 179$ K, $T_2 \sim 203$ K, and $T_4 \sim 303$ K are observed on the curve $c = f(T)$ (Fig. 4). On the temper-

ature dependence of the parameter $a = f(T)$ (Fig. 2), phase transformations manifest themselves only at $T_1 \sim 123$ K. It can be seen from these data that the temperatures at which the anomalies are observed are somewhat different for different crystallographic directions. It is known that the crystals with hydrogen bonds are extremely sensitive to external effects of different types and the presence of inhomogeneities and lattice defects. In addition, the $\text{DMA} \cdot \text{MnCl}_3$ crystals contain crystallization water, which, upon heating and vacuum degassing, easily emerges from the crystals, i.e., makes them unstable. Apparently, this is the reason for some spread in the temperatures at which anomalies are observed on the temperature dependences of the different parameters of the crystals.

The temperature dependences of the CTEs α_a , α_b , and α_c for the crystallographic directions [100], [010], and [001], respectively, are shown in Figs. 2–4 (solid lines). The curves $\alpha_a = f(T)$, $\alpha_b = f(T)$, and $\alpha_c = f(T)$ demonstrate pronounced anomalies at the phase-transition temperatures. It is noteworthy that the CTEs are almost temperature-independent in all three crystallographic directions in the temperature range under study. It should be noted that an CTE anisotropy is observed in the $\text{DMA} \cdot \text{MnCl}_3$ crystal: $\alpha_a > \alpha_b > \alpha_c$, which is in agreement with the data on the elastic properties: $v_{xx} < v_{yy} < v_{zz}$. The ultrasonic wave velocity is higher in the crystallographic directions that are characterized by a larger hardness of chemical bonds and, accordingly, smaller values of CTEs.

Thus, the investigation of the elastic properties and crystallographic characteristics of $\text{DMA} \cdot \text{MnCl}_3$ con-

firmed the existence of phase transitions in this crystal at $T_1' = 179$ K and $T_4 = 303$ K and revealed new transitions at $T_1 \sim 125$ K, $T_2 \sim 203$ K, and $T_3 \sim 260$ K.

The sequence of the phase transitions in the crystals containing dimethylamine ions is determined to a great extent by the change in the dynamics of dimethylammonium ions and their ordering with a change in temperature [7, 8].

REFERENCES

1. A. I. Zvyagin, M. I. Kobets, V. N. Krivoruchko, *et al.*, Zh. Éksp. Teor. Fiz. **89**, 2298 (1985) [Sov. Phys. JETP **62**, 1328 (1985)].
2. A. A. Stepanov, E. N. Khan'ko, M. I. Kobets, *et al.*, Fiz. Nizk. Temp. (Kiev) **20** (6), 540 (1994).
3. V. B. Kapustianik, Phys. Status Solidi A **168**, 109 (1998).
4. R. E. Caputo and R. D. Willet, Acta Crystallogr. B **37**, 1618 (1981).
5. O. G. Vlokh, V. B. Kapustyanyk, I. A. Mikhalyna, *et al.*, Izv. Akad. Nauk SSSR **55** (3), 433 (1991).
6. A. U. Sheleg, E. M. Zub, A. Ya. Yachkovskii, and L. F. Kirpichnikova, Kristallografiya **49** (6), 1142 (2004) [Crystallogr. Rep. **49**, 1028 (2004)].
7. Z. Chapla, S. Dacko, U. Krzewska, and A. Waskowska, Solid State Commun. **71**, 139 (1989).
8. L. F. Kirpichnikova, A. Petrashko, and M. Polomska, Kristallografiya **41**, 722 (1996) [Crystallogr. Rep. **41**, 685 (1996)].

Translated by Yu. Sin'kov

PHYSICAL PROPERTIES
OF CRYSTALS

Circular Dichroism of Some Nd-Doped Crystals
of the Langasite Family

V. I. Burkov*, A. V. Butashin**, E. V. Fedotov*,
A. F. Konstantinova**, and I. A. Gudim***

* Moscow Institute of Physics and Technology, Institutskii per. 9,
Dolgoprudnyi, Moscow oblast, 141700 Russia

** Shubnikov Institute of Crystallography, Russian Academy of Sciences,
Leninskii pr. 59, Moscow, 119333 Russia

e-mail: afkonst@ns.crys.ras.ru

*** Kirensky Institute of Physics, Siberian Division, Russian Academy of Sciences,
Krasnoyarsk, Russia

Received April 29, 2005

Abstract—The absorption and circular-dichroism spectra of neodymium-doped crystals of langasite $\text{La}_3\text{Ga}_5\text{SiO}_{14}$ and the compounds $\text{La}_3\text{Ga}_{5.5}\text{Nb}_{0.5}\text{O}_{14}$ and $\text{Pb}_3\text{Ga}_2\text{Ge}_{3.92}\text{Si}_{0.08}\text{O}_{14}$, isostructural with langasite, are investigated in the wavelength range 320–940 nm. Electronic transitions in Nd atoms, which substitute the main cation of the salts (La or Pb) in the positions with the local symmetry C_2 , are observed in the spectra. All transitions observed in the absorption spectrum are also active in the circular-dichroism spectrum. Detailed analysis is performed for several (well separated) bands: Dipole strengths D_{ok} , rotation strengths R_{ok} , and the anisotropy factors G_{ok} are calculated. Some specific features of the spectra obtained are noted and their possible relationship with the structure of impurity centers of neodymium and effect on the intensity of the Stark components are discussed. © 2005 Pleiades Publishing, Inc.

INTRODUCTION

Synthesis of crystals of the $\text{Ca}_3\text{Ga}_2\text{Ge}_4\text{O}_{14}$ compound—the parent compound of the langasite family—and interpretation of their crystal structure were carried out for the first time 25 years ago [1]. Further complex investigations (see review [2]) made it possible to obtain a number of single crystals with this structure and reveal some piezoelectric, laser, and optical properties of these crystals that are of interest for practical application.

Currently, crystals with langasite structure serve as commercial piezoelectric materials [3]. Therefore, researchers pay attention to the fabrication of these crystals [4], their piezoelectric properties [5], and refinement of their structure [6, 7].

Concerning the optical properties, an interesting feature of these crystals is that they have the axial symmetry 32 ; exist in two enantiomorphic modifications; and, showing significant optical activity, contain no helical elements in the structure. The gyrotropy of crystals with langasite structure was investigated in [8]. (The circular-dichroism method was applied to crystals containing ions of $3d$ metals.) Analysis of the nature of intrinsic and impurity optical centers in these crystals by the circular-dichroism method turned out to be very effective.

In this study, the circular-dichroism method is used to investigate a number of crystals with langasite struc-

ture doped with Nd^{3+} ions: $\text{La}_3\text{Ga}_5\text{SiO}_{14}$ (LGS), $\text{La}_3\text{Ga}_{5.5}\text{Nb}_{0.5}\text{O}_{14}$ (LGN), and $\text{Pb}_3\text{Ga}_2\text{Ge}_{3.92}\text{Si}_{0.08}\text{O}_{14}$ (PGGO). The lattice constants (a , c) are (8.162, 5.087 Å), (8.218, 5.122 Å), and (8.419, 5.015 Å) for the LGS, LGN, and PGGO compounds, respectively. According to the structural data [2, 6, 7], La and Pb atoms occupy equivalent positions at the center of the polyhedron with the coordination number 8 (distorted Thompson cube) and have the point symmetry C_2 . Each unit cell contains three La and three Pb atoms. When La and Pb atoms are substituted by impurity Nd ions, the chiral crystal field of the matrix induces circular dichroism in the electronic transitions in Nd^{3+} ions. This phenomenon is the subject of the present study.

LGS and LGN crystals were grown from melt by the Czochralski method. The PGGO crystal was grown from flux by the Kirpulos method and doped with neodymium and silicon in equal proportions. Introduction of Si^{4+} ions was used to increase the incorporation coefficient of neodymium in the crystals. It is most likely that silicon substitutes germanium isomorphously in this case.

EXPERIMENTAL

The absorption and circular-dichroism spectra of the noted crystals were studied in the range 10638–31250 cm^{-1} (320–940 nm). The Nd concentration in

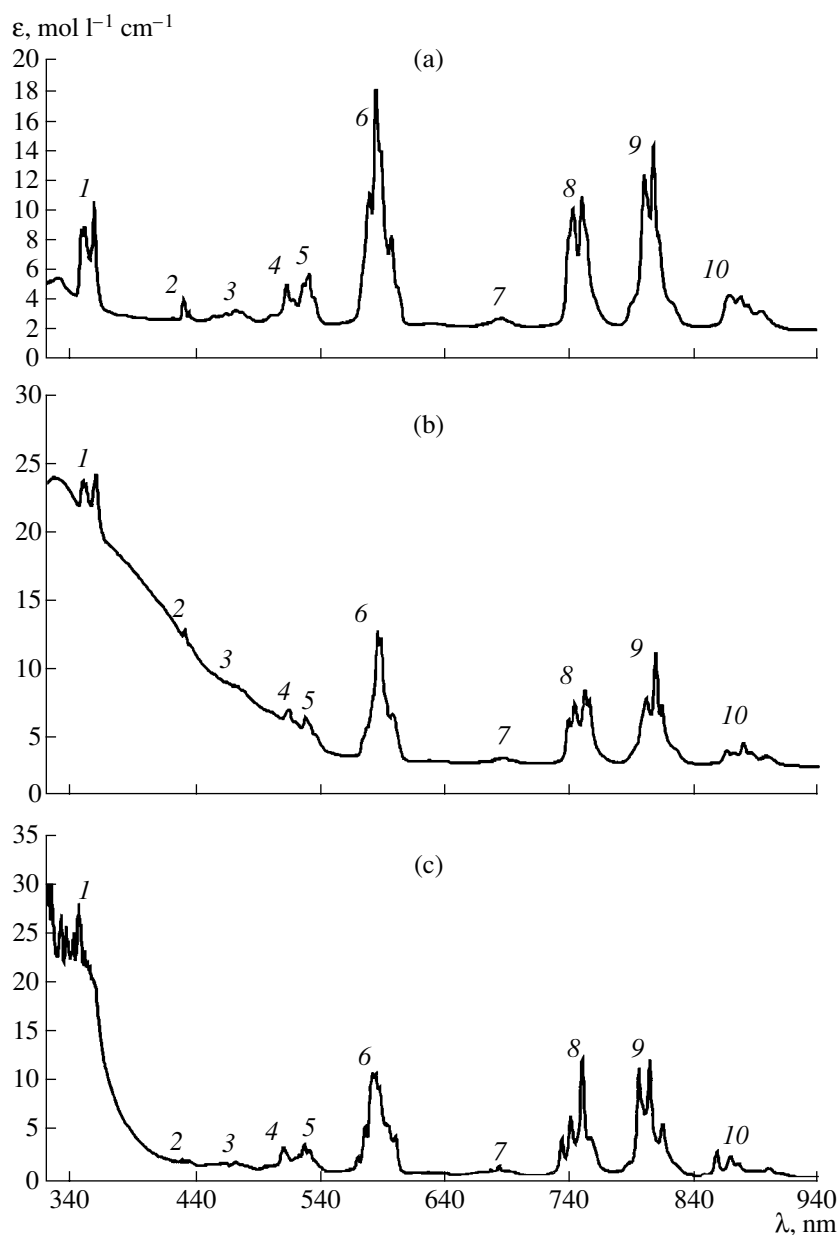


Fig. 1. Entire absorption spectrum of the crystals doped with Nd^{3+} ions: (a) LGN, (b) LGS, and (c) PGGO. The ground state of the Nd^{3+} ion is $^4I_{9/2}$. Numbers denote the excited states to which a transition occurs: (1) $^2I_{11/2}$; (2) $^2D_{5/2}$; (3) $^4G_{11/2}$, $^4G_{9/2}$, and $^2K_{15/2}$; (4) $^2K_{13/2}$; (5) $^4G_{7/2}$; (6) $^4G_{5/2}$ and $^2G_{7/2}$; (7) $^4F_{9/2}$; (8) $^4F_{7/2}$; (9) $^4F_{5/2}$ and $^2H_{9/2}$; and (10) $^4F_{3/2}$.

the LGS, LGN, and PGGO samples, measured by laser mass spectrometry, was 0.168, 0.79, and 0.7 mol/l, respectively. The absorption spectra were recorded on a Specord M40 spectrophotometer and the circular-dichroism spectra were measured on a Mark-3S (Jobin Yvon) dichrograph. The measurements were performed at room temperature.

All transitions in the Nd^{3+} ion are active in the circular-dichroism spectrum and manifest themselves as bands of both positive and negative signs. However, for most transitions, the corresponding spectral lines are

overlapped at room temperature, which hinders their study significantly. In such cases, the spectra were processed and analyzed only for the transitions with clearly separated bands.

RESULTS

Figure 1 shows the absorption spectra of the crystals under study. Figures near the spectral bands are the indices of the excited states to which the corresponding transitions occur. To interpret the spectra, we used the

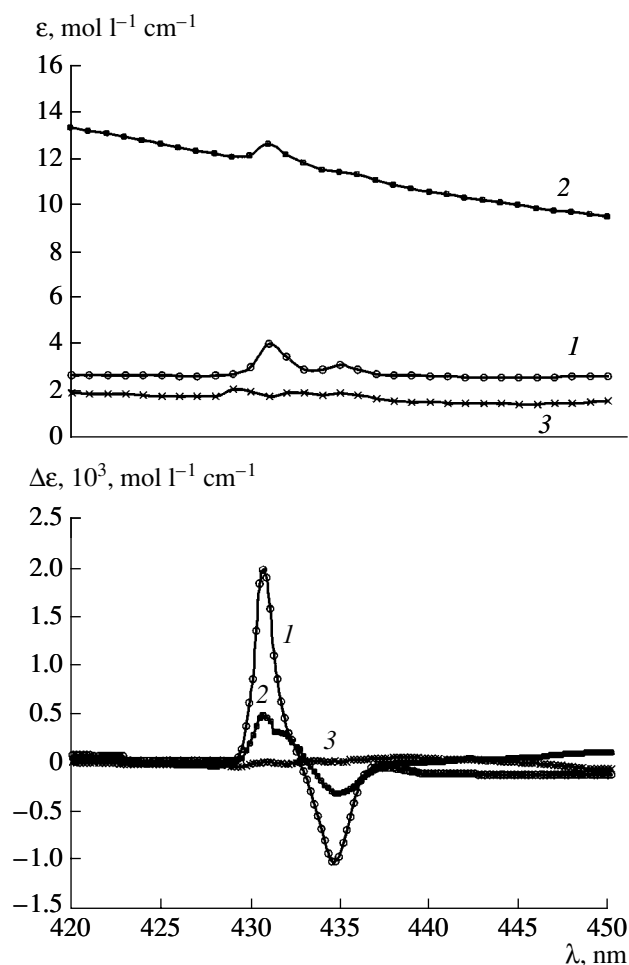


Fig. 2. Absorption spectra $\varepsilon(\lambda)$ and circular-dichroism spectra $\Delta\varepsilon(\lambda)$ in the range 420–450 nm (transition I) of the crystals doped with Nd^{3+} ions: (1) LGN, (2) LGS, and (3) PGGO.

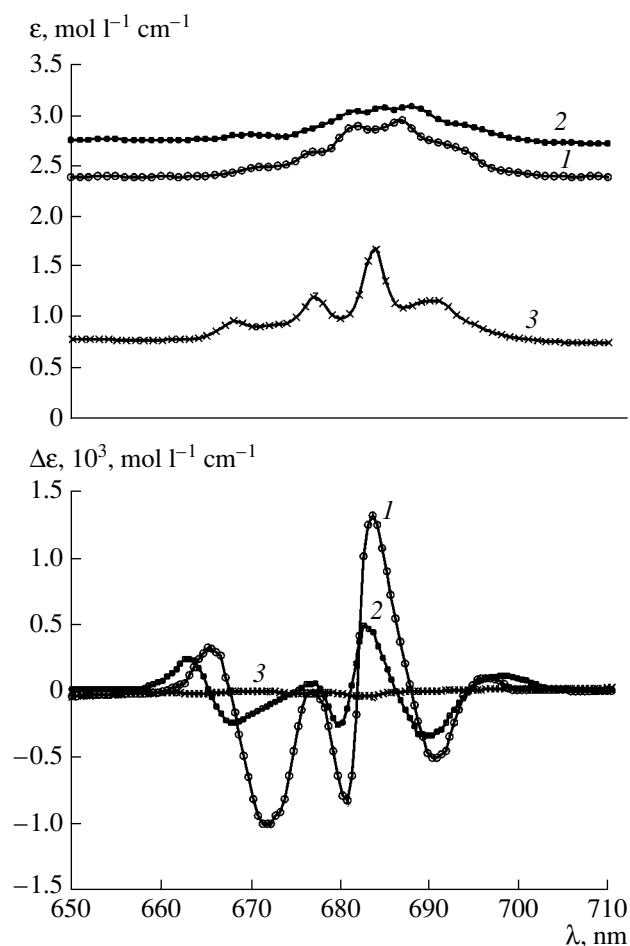


Fig. 3. Absorption spectra $\varepsilon(\lambda)$ and circular-dichroism spectra $\Delta\varepsilon(\lambda)$ in the range 650–710 nm (transition II) of the crystals doped with Nd^{3+} ions: (1) LGN, (2) LGS, and (3) PGGO.

results of the numerical simulation of the spectrum of neodymium [9, 10].

Detailed analysis of the experimental data was performed for four transitions: ${}^4I_{9/2} \rightarrow {}^2D_{5/2}$ (I), ${}^4I_{9/2} \rightarrow {}^4F_{9/2}$ (II), ${}^4I_{9/2} \rightarrow {}^4F_{7/2}$ (III), and ${}^4I_{9/2} \rightarrow {}^4F_{3/2}$ (IV). The corresponding absorption bands are located in the wavelength ranges around 430, 680, 740, and 870 nm.

Figures 2–5 show the absorption and circular-dichroism spectra in these wavelength ranges for all the samples under consideration.

The expressions for the dipole strength (D_{ok}), the rotation strength (R_{ok}), and the anisotropy factor (G_{ok}) of the transitions from a low-lying state of the ground multiplet to the Stark components of excited states have the form [11]

$$\begin{aligned} D_{ok} &= \langle 0|p|k\rangle^2 + \langle 0|m|k\rangle^2, \\ R_{ok} &= \text{Im}[\langle 0|p|k\rangle\langle 0|m|k\rangle], \quad G_{ok} = 4R_{ok}/D_{ok}. \end{aligned} \quad (1)$$

Here, $\langle 0|p|k\rangle$ is the matrix element of the electric dipole moment and $\langle 0|m|k\rangle$ is the matrix element of the magnetic dipole moment, which are related to the $0 \rightarrow k$ transition. These expressions are written without consideration for the quadrupole terms.

The generally accepted relations used to determine D_{ok} and R_{ok} in processing of experimental data have the form [12]

$$\begin{aligned} D_{ok} &= 91.8 \frac{g_1}{N_f} \int \frac{\varepsilon(\nu)}{(\beta^2/n\nu)} d\nu \quad (D^2), \\ R_{ok} &= 22.97 \frac{g_1}{N_f} \int \frac{\Delta\varepsilon}{\beta\nu} d\nu \quad (D \text{ Bohr magneton}). \end{aligned} \quad (2)$$

Here, ε is the decimal molar extinction coefficient, $\Delta\varepsilon$ is the decimal molar dichroism coefficient, n is the refractive index, $\beta = (n^2 + 2)/3$ is the Lorentz factor, g_1 is the degeneracy factor of the ground state, and N_f is

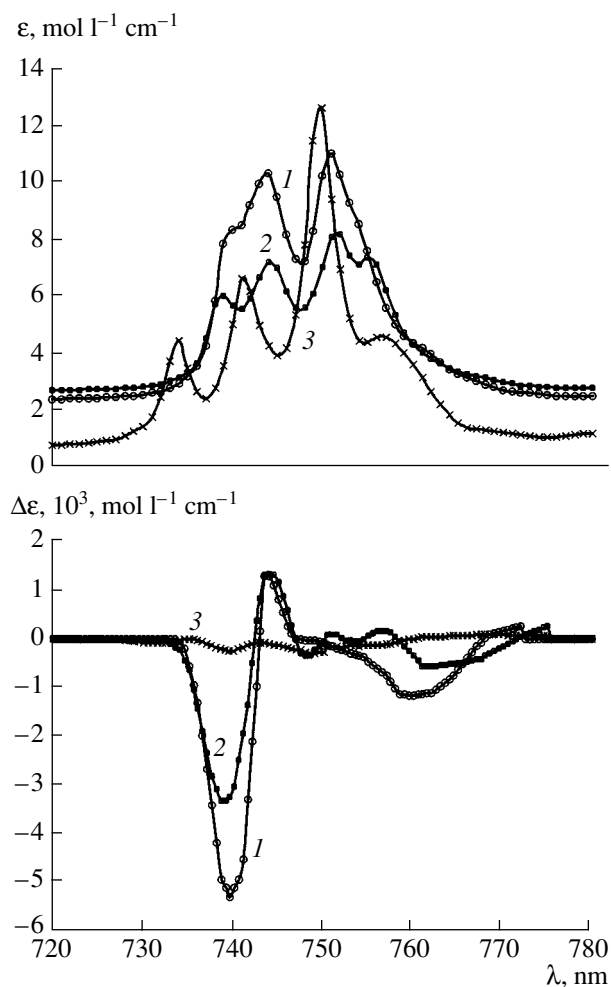


Fig. 4. Absorption spectra $\varepsilon(\lambda)$ and circular-dichroism spectra $\Delta\varepsilon(\lambda)$ in the range 720–780 nm (transition III) of the crystals doped with Nd^{3+} ions: (1) LGN, (2) LGS, and (3) PGGO.

the ground-state population (normalized to unity) at a measurement temperature.

In the crystal field of symmetry C_2 , all Stark components for f elements with a half-integer spin are Kramers doublets and, therefore, their degeneracy factor $g_1 = 2$. Since we have no spectroscopic data on the values of splitting of the ground multiplet in the crystals under consideration, we can use the values of splitting of the excited states derived from the absorption spectra obtained (Figs. 2–5) to estimate the population N_f approximately. Assuming the distribution of electrons over the Stark components to be of the Boltzmann type, we will calculate the estimates for N_f and, using the refractive indices from [2, 13], determine the values of β . The calculated values of the average splitting q , the population of the ground state N_f , the refractive index n , and the Lorentz factor β for all crystals and bands studied here are listed in Table 1.

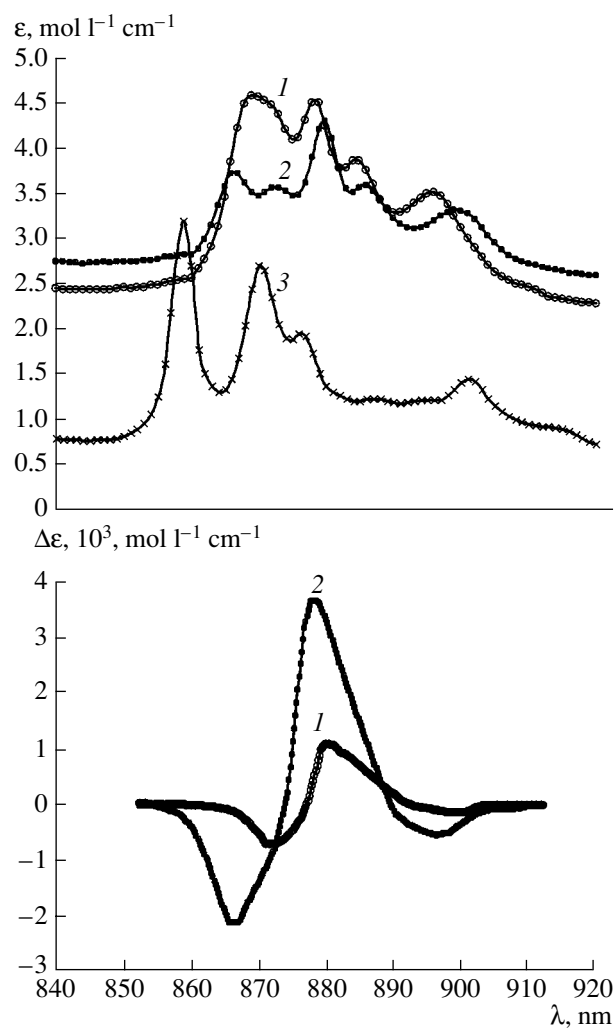


Fig. 5. Absorption spectra $\varepsilon(\lambda)$ and circular-dichroism spectra $\Delta\varepsilon(\lambda)$ in the range 840–920 nm (transition IV) of the crystals doped with Nd^{3+} ions: (1) LGN, (2) LGS, and (3) PGGO.

Taking into account narrow bandwidths in the spectra and applying the mean-value theorem to the integrals, we derive the final formulas for data processing:

$$D_{ok} = \frac{K_D}{v_{\max}} \int \varepsilon(v) dv, \quad R_{ok} = \frac{K_R}{v_{\max}} \int \Delta\varepsilon(v) dv, \quad (3)$$

where v_{\max} is the frequency corresponding to the center (maximum) of a given band. The calculated coefficients K_D and K_R for the LGS, LGN, and PGGO crystals are given in Table 1.

DISCUSSION

The results of the processing of the absorption and circular-dichroism spectra are listed in Table 2. The maximum values of ε and $\Delta\varepsilon$, the wavelengths at which they are observed, the dipole and rotation strengths, and the anisotropy factors are indicated for each band pro-

Table 1. Values of the average splitting q , the ground-state population N_f , the refractive index n , the Lorentz factor β , and the coefficients K_D and K_R in formulas (2, 3) for processing experimental data for the Nd-doped LGS, LGN, and PGGO samples in the vicinity of the transitions investigated

Calculated values	Crystals with langasite structure doped with Nd ³⁺ ions		
	LGS	LGN	PGGO
q, cm^{-1}	140	145	160
N_f	0.48	0.50	0.53
	Transition I, 430 nm		
n	1.94	2.01	2.10
β	1.92	2.01	2.14
$K_D \times 10^{40}$	193	187	158
$K_R \times 10^{40}$	47.8	46.8	40.2
	Transition II, 680 nm		
n	1.9	1.95	2.02
β	1.87	1.93	2.03
$K_D \times 10^{40}$	200	197	168
$K_R \times 10^{40}$	49	49	42
	Transition III, 740 nm		
n	1.90	1.95	2.01
β	1.87	1.93	2.01
$K_D \times 10^{40}$	199	197	171
$K_R \times 10^{40}$	49	49	43
	Transition IV, 870 nm		
n	1.89	1.94	2
β	1.86	1.92	2
$K_D \times 10^{40}$	201	198	172
$K_R \times 10^{40}$	49	49	43

cessed. The calculated values of R_{ok} are in good agreement with the data of [10, 12, 14, 15], whereas the values of D_{ok} and G_{ok} differ significantly.

On the basis of the data obtained, we can draw some conclusions. Primarily, we should note that, when an impurity is incorporated into a crystal nonstructurally, circular dichroism is not observed generally. The point is that the averaging of the contributions of disordered atoms into circular dichroism over the symmetry operations of the point group of the crystal yields zero. In this case, the circular dichroism of all bands is nonzero; therefore, Nd³⁺ should substitute a particular atom in the crystal lattice isomorphously. Obviously, in this case, the only atoms with the appropriate coordination ability are La³⁺ (for LGN and LGS) and Pb²⁺ (for PGGO).

Applying the selection rules for the f - f transitions in the electric-dipole and electric-quadrupole approximations and the magnetic-dipole approximation [16] to

the transitions under consideration, we find that transition I is allowed in the electric-quadrupole approximation and transitions II and III are allowed in the magnetic-dipole approximation, whereas transition IV is forbidden in these approximations. In this case, transition III is the strongest in the absorption spectra, the forbidden transition IV is weaker, and transitions I and II (which are allowed in the electric-quadrupole and magnetic-dipole approximations, respectively) have approximately the same, very low dipole strengths. Therefore, it is obvious that it is the electric dipole moment that makes the main contribution to the intensity of the above-mentioned transitions, whereas the contributions of other components are insignificant.

This statement is also confirmed by the relation between the anisotropy factors of the transitions. The largest value of this factor is observed for transition II, which is allowed in the magnetic-dipole approximation. However, transition III, also allowed in this approximation, has the smallest value of G_{ok} from all values obtained. The anisotropy of transition I, allowed in the electric-quadrupole approximation, is almost the same as that of transition IV, which is forbidden in the magnetic-dipole and electric-quadrupole approximations. Thus, on the average, the anisotropy factor is independent of the contributions of the magnetic-dipole and electric-quadrupole modes.

Hence, the intensity and dichroism of the spectral lines are determined completely by the efficiency of the mechanisms of involvement of both the electric and magnetic dipole moments.

The selection rules with respect to the change in the projection of the angular momentum ΔM_J are determined by the specific symmetry of an object studied. Since the local symmetry of Nd ions in the crystals under consideration is C_2 , all transitions between the first Stark component of the ground state and the Stark components of excited states are allowed in symmetry. Nevertheless, as the results obtained show, the intensity of the transitions to different Stark components within one multiplet change very significantly: by one or two orders of magnitude.

Obviously, in LGN and LGS crystals doped with neodymium, the latter substitutes lanthanum isomorphously. This is confirmed by the strong similarity of the dichroism spectra of these crystals both in shape and the values of the parameters D_{ok} and R_{ok} . In the PGGO compound, trivalent Nd³⁺ substitutes the divalent ion Pb²⁺. In this case, the charge compensation occurs owing to the redistribution of Ge⁴⁺ and Ga³⁺ ions in the second coordination sphere.

A change in the crystal field affects the circular-dichroism spectrum. Indeed, the circular-dichroism spectrum of PGGO differs radically from those of LGN and LGS. Primarily, the rotation strength and the anisotropy factor of PGGO are lower by 1–2 orders of magnitude. In addition, some circular-dichroism bands

Table 2. Values of the energies, intensities, dipole strengths, rotation strengths, and anisotropy factors of the transitions in the Nd³⁺ ion from the first Stark component of the ground state ⁴I_{9/2} to the Stark components of the excited states ⁵D_{5/2}, ⁴F_{9/2}, ⁴F_{7/2}, and ⁴F_{3/2}

No.	λ , nm	ν , cm ⁻¹	ϵ_{\max} , mol l ⁻¹ cm ⁻¹	$\Delta\epsilon_{\max}$, mol l ⁻¹ cm ⁻¹	Dipole strength $D_{ok} \times 10^{44}$, D ²	Rotation strength $R_{ok} \times 10^{44}$, D \times (Bohr magneton)	$G_{ok} = \frac{4R_{ok}}{D_{ok}} \times 10^4$
Transition I, ⁴ I _{9/2} \rightarrow ⁵ D _{5/2} , $\Delta J = 2$							
PGGO							
1	429	23310	0.262	-2.98×10^{-5}	1850	-0.035	-0.76
2	432	23140	0.127	-2.17×10^{-5}	1010	-0.027	-1.07
3	435	22990	0.137	-1.29×10^{-5}	929	-0.018	-0.77
LGN							
1	431	23200	1.219	1.99×10^{-3}	8520	3.15	14.8
2	435	22990	0.274	-9.94×10^{-4}	1800	-2.15	-47.8
LGS							
1	431	23200	0.749	4.96×10^{-4}	7380	1.15	6.25
2	435	22990	0.123	-3.09×10^{-4}	1040	-0.80	-30.9
Transition II, ⁴ I _{9/2} \rightarrow ⁴ F _{9/2} , $\Delta J = 0$							
PGGO							
1	670	14930	0.176	1.31×10^{-5}	2270	0.062	1.10
2	677	14760	0.368	9.92×10^{-6}	4140	0.017	0.16
3	682	14650	0.761	-2.20×10^{-5}	9120	-0.057	-0.25
LGN							
1	665	15040	0.007	3.17×10^{-4}	140	0.764	218
2	670	14930	0.020	-1.01×10^{-3}	860	-3.91	-183
3	680	14700	0.460	-8.36×10^{-4}	5500	-1.46	-10.6
4	683.5	14630	0.540	1.30×10^{-3}	8320	3.15	15.2
5	690	14490	0.339	-5.19×10^{-4}	5550	-1.41	-10.1
LGS							
1	662.5	15090	0.011	2.27×10^{-4}	120	0.628	218
2	668	14970	0.031	-2.57×10^{-4}	410	-1.04	-102
3	679.5	14720	0.297	-3.09×10^{-4}	4710	-0.494	-4.19
4	682.5	14650	0.337	4.78×10^{-4}	2840	0.978	13.8
5	690	14490	0.346	-3.47×10^{-4}	6050	-1.27	-8.38
Transition III, ⁴ I _{9/2} \rightarrow ⁴ F _{7/2} , $\Delta J = 1$							
PGGO							
1	734	13620	3.235	-7.59×10^{-5}	42500	-0.248	-0.233
2	741	13490	5.087	-2.07×10^{-4}	73570	-0.624	-0.340
3	750	13330	10.148	-2.57×10^{-4}	168200	-0.124	-0.030
LGN							
1	739	13530	5.835	-5.32×10^{-3}	74000	-17.0	-9.2
2	744	13440	7.817	1.29×10^{-3}	89600	1.67	0.74
LGS							
1	739	13530	3.326	-3.35×10^{-3}	41400	-11.1	-10.7
2	744	13440	4.523	1.34×10^{-3}	60100	2.64	1.8
Transition IV, ⁴ I _{9/2} \rightarrow ⁴ F _{3/2} , $\Delta J = 3$							
LGN							
1	869	11510	2.09	-6.96×10^{-4}	32200	-2.81	-3.4
2	878	11390	2.011	1.10×10^{-3}	28800	5.03	7.0
LGS							
1	864	11530	1.027	-2.10×10^{-3}	19400	-10.7	-22.0
2	877	11380	1.599	3.67×10^{-3}	22100	17.4	31.6

in multiplets even change their sign. Note that this effect generally never occurs in isostructural crystals. The parameters of circular-dichroism bands are of the same order of magnitude even for different compounds [12, 14, 15, 17].

An unusual circumstance should be noted: all these changes occur almost without any changes in the absorption spectra and the dipole strengths. In our opinion, the most likely explanation is that several different Nd impurity centers may exist in PGGO crystals. When the difference in the energies of the transitions in these centers is small, the values of the circular dichroism of the corresponding bands may differ both in magnitude and in sign. In this case, the populations of the positions are not quite equivalent, which explains the residual circular dichroism observed.

CONCLUSIONS

To conclude, let us formulate some problems arising in the context of the investigation performed here, which can be the subject of further spectral study of Nd-doped langasites.

Primarily, as indicated above, the circular dichroism in the electronic transitions in rare earth impurity ions is related to the existence of an effective mechanism of involvement of the electric and magnetic dipole moments. To determine the mechanism of this involvement (static or dynamic) and its source, it is necessary to perform numerical calculations using the experimental data on the absorption and circular-dichroism spectra in a maximally wide spectral range.

At present, the technique of numerical simulation of absorption spectra has been developed extensively and gives good results. Calculation of circular-dichroism spectra has been developed much less and is restricted mainly to the studies considering a very narrow range of crystals [17]. Further development of such numerical calculations can answer many important questions. From this point of view, the experimental data on the absorption and circular-dichroism spectra of the crystals that were not investigated previously can serve as a basis for further development of the methods of numerical simulation of circular dichroism.

The structure of the Nd impurity center in PGGO is also of interest. However, the structural identification of an impurity center is a difficult problem, the solution of which requires additional investigations by special methods, in particular, measurements of the electron-spin resonance spectrum.

If the above suggestion about the existence of Nd³⁺ impurity centers of different types in lead gallogermanate is valid, it can also hold true for other crystals of this family. Therefore, a possible method to verify it is measurement of the absorption and circular-dichro-

ism spectra for a group of gallogermanates of other divalent elements (currently, the technique of growing large single crystals of calcium and strontium gallogermanates is being developed) with subsequent comparison of the data obtained with the results of this study.

ACKNOWLEDGMENTS

We are grateful to B.V. Mill' for supplying the samples of crystals for measurements.

This study was supported by the Russian Foundation for Basic Research, project no. 03-02-16871.

REFERENCES

1. E. L. Belokoneva, M. A. Simonov, B. V. Mill', *et al.*, Dokl. Akad. Nauk SSSR **255** (5), 1099 (1980) [Sov. Phys. Dokl. **25**, 954 (1980)].
2. A. A. Kaminskiĭ, B. V. Mill', and S. É. Sarkisov, *Physics and Spectroscopy of Laser Crystals* (Nauka, Moscow, 1986), p. 197 [in Russian].
3. Fomos Technology, Moscow, www.fomos-t.ru.
4. S. Q. Wang and S. Uda, *J. Cryst. Growth* **250**, 463 (2003).
5. A. E. Blagov, G. D. Mansfeld, B. V. Mill', *et al.*, *Proc. of the IEEE Intern. Frequency Control Symp., Montreal, Canada* (2004), p. 634.
6. B. A. Maksimov, V. N. Molchanov, B. V. Mill', *et al.*, *Kristallografiya* **50** (5) (2005) [Crystallogr. Rep. **50**, 751 (2005)].
7. E. L. Belokoneva, S. Yu. Stefanovich, Yu. V. Pisarevskii, and A. V. Mosunov, *Zh. Neorg. Khim.* **45** (11), 1786 (2000).
8. K. A. Kaldybaev, A. F. Konstantinova, and Z. B. Perekalina, *Gyrotropy of Uniaxial Absorbing Crystals* (In-t Sotsial'no-ekonomicheskikh i Proizvodstvenno-ekologicheskikh Problem Investirovaniya, Moscow, 2000) [in Russian].
9. V. Gasparik, *Acta Phys. Slov.* **28** (3), 222 (1978).
10. J. R. Quagliano, G. W. Burdick, D. P. Glover-Fisher, and F. S. Richardson, *Chem. Phys.* **201** (2-3), 321 (1995).
11. J. A. Shellman, *Chem. Rev.* **75** (23), 323 (1976).
12. V. I. Burkov, A. V. Egorysheva, A. Ya. Vasil'ev, *et al.*, *Neorg. Mater.* **38** (10), 1228 (2002).
13. A. V. Butashin, L. E. Li, A. F. Konstantinova, and I. A. Gudim, *Kristallografiya* **49** (3), 514 (2004) [Crystallogr. Rep. **49**, 459 (2004)].
14. V. I. Burkov, V. A. Kizel', N. I. Leonyuk, *et al.*, *Kristallografiya* **29** (1), 101 (1984) [Sov. Phys. Crystallogr. **29**, 58 (1984)].
15. V. I. Burkov, V. A. Kizel', N. I. Leonyuk, and N. M. Sitenkov, *Kristallografiya* **27** (1), 196 (1982) [Sov. Phys. Crystallogr. **27**, 121 (1982)].
16. F. S. Richardson, *Inorg. Chem.* **9** (9), 2806 (1980).
17. F. S. Richardson, *J. Less-Common Met.* **149** (1), 161 (1989).

Translated by Yu. Sin'kov

PHYSICAL PROPERTIES OF CRYSTALS

Refractometry of Mechanically Compressed RbKSO₄ Crystals

V. I. Stadnik*, N. A. Romanyuk*, and R. S. Brezvin**

* Lviv State University, ul. Kirilla i Mefodiya 8, Lviv, 79005 Ukraine
e-mail: stavas@mail.ru

** Institute of Physical Optics, Ministry of Education of Ukraine,
ul. Dragomanova 23, Lviv, 79005 Ukraine

Received March 1, 2004

Abstract—The unit-cell parameters and the spatial symmetry of RbKSO₄ crystals are determined. The temperature and spectral dependences of the refractive indices and birefringence of these crystals are measured. Two first-order phase transitions are found to occur at 116 and 820 K, and the occurrence of isotropic points for three crystallophysical directions is established. The effect of uniaxial stresses on the optical properties of the crystal is studied. Both the birefringence and the birefringence-sign inversion points are found to be rather sensitive to the action of uniaxial mechanical stresses. The temperature–spectral and spectral–baric diagrams of the isotropic state of the RbKSO₄ crystal, as well as the baric shifts of the phase-transition temperatures, are determined.
© 2005 Pleiades Publishing, Inc.

INTRODUCTION

The study of the temperature and spectral dependences of the refractive indices n_i and the birefringence Δn_i of crystals of the group $ABSO_4$ ($A, B = \text{Li, Rb, K, NH}_4$) showed that the replacement of atoms in the crystal space lattice has a significant effect on these parameters, as well as on the birefringence-sign inversion (BSI). Furthermore, it was found that, upon such replacement, the optical properties of these crystals exhibit nonstandard behavior near the phase transition.

In K₂SO₄, Rb₂SO₄ and LiKSO₄ crystals, BSI points were found, which occur in wide spectral and temperature ranges. It was found that, the isotropic point of the LiKSO₄ crystal shifts toward the long-wavelength spectral range upon cooling, the temperature dependence of this point changes at a temperature of 255 K, and this point vanishes at a temperature of the first-order phase transition (185 K) [1, 2]. These data differ considerably from the characteristics of the isotropic point of the isomorphous K₂SO₄ crystal [3], for which $d\lambda_0/dT \rightarrow \infty$. A similar behavior of the isotropic point was observed for the X direction of the Rb₂SO₄ crystal [4].

It should be noted that BSI points are observed in most known compounds of the $ABSO_4$ type. Therefore, the search for new isomorphous compounds aimed at detecting isotropic states in them, which can extend the temperature and spectral ranges of occurrence of BSI points, is, in our opinion, of undeniable interest. For this purpose, we chose the crystal RbKSO₄ as an isomorphous compound. The objectives of this study are to determine the spatial symmetry of this crystal and study the spectral and temperature behavior of its refractive indices n_i and birefringence Δn_i in order to reveal the

effect of cation replacement on these characteristics, as well as on BSI points and on their baric dependence.

EXPERIMENTAL

RbKSO₄ crystals were grown by slow evaporation from an aqueous stoichiometric salt solution: $\text{Rb}_2\text{SO}_4 + \text{K}_2\text{SO}_4 \rightarrow 2\text{RbKSO}_4$. The crystals grown consisted of three clearly pronounced pseudoorthorhombic blocks; the axes made an angle of 120°. The setting was performed as in the case of the LiRbSO₄ crystal, whose pseudohexagonal axis was taken as the c axis, while the axes of the crystal block perpendicular to the c axis corresponded to the a and b axes.

To determine the parameters of the crystal structure of this compound (the unit-cell periods, atomic coordinates, thermal parameters, etc.), we used a profile obtained by discrete scanning on an HZG-4a diffractometer ($\text{CuK}\alpha$ radiation). The crystal structure of the sample was determined by the powder method. All the calculations related to the identification and refinement of the structure of the compounds by the powder method were performed using the software package CSD [5]. The atomic coordinates, temperature corrections and occupancies of regular sets of points were refined by the least-squares method in the isotropic and anisotropic approximations.

The reliability of the model chosen was checked by the value of the R factor:

$$R = \frac{\sum I_{\text{obs}} - I_{\text{calcd}}}{\sum I_{\text{obs}}}, \quad (1)$$

where I_{obs} and I_{calcd} are the observed and calculated intensities, respectively.

Table 1. Dispersion and parameters of the Sellmeier formula for RbKSO₄ crystals

Axis	λ_{01} , nm	λ_{02} , nm	B_i , 10 ⁻⁶ nm ⁻²	B'_i , 10 ⁻⁹ nm ⁻²
X	97.118	8225.82	128.91	15.31
Y	94.708	9120.13	134.03	6.96
Z	84.198	11230.4	172.20	3.69
$\lambda = 500$ nm	$\partial n_i / \partial \lambda$, 10 ⁻⁵ nm ⁻¹	α_i , 10 ⁻²⁴ cm ³	R_i , cm ³	
X	-4.5	8.99	21.15	
Y	-5.0	8.93	21.19	
Z	-5.1	8.97	21.09	

The temperature–spectral dependences of the refractive indices of the crystal under study were measured by the Obreimov photographic and immersion methods, while the birefringence was determined by the interference method. The uniaxial mechanical pressure was created using a special attachment providing pressures up to ~200 bar. The change in the birefringence of a crystal under the action of a mechanical field is determined by the expression

$$\Delta n_i(\sigma_m) = k(\sigma_m)\lambda/d_i(\sigma_m), \quad (2)$$

where Δn_i is the birefringence, k is the interference-fringe order, λ is the light wavelength, d_i is the crystal thickness along the light-propagation direction, and i , $m = X, Y, Z$ are the crystallophysical axes. (Different values of i and m indicate that, in these experiments, the pressure was always applied along a direction perpendicular to that of the light propagation in the sample.) Under the simultaneous action of thermal and mechanical fields, the birefringence is determined as

$$\Delta n_i(T, \sigma_m) = k(T, \sigma_m)\lambda/d_i(T, \sigma_m). \quad (3)$$

Changing one of the parameters (T or σ_m) with the other parameter fixed, one can unambiguously determine the temperature or baric dependence of Δn_i from the shift of the order of interference fringes.

RESULTS AND DISCUSSION

A Mechanically Free Crystal

The RbKSO₄ crystal was found to belong to the rhombic crystal system (sp. gr.) *Pnma* and had the following unit-cell parameters: $a = 7.5526(4)$ Å, $b = 5.8048(3)$ Å, and $c = 10.1156(6)$ Å. The distribution of the atoms is as follows: O1 in $8(d)xyz$ ($x = 0.3080$, $y = 0.0430$, $z = 0.1530$); O2 in $4(c)x^{1/4}z$ ($x = 0.0450$, $z = 0.0830$); Rb in $4(c)x^{1/4}z$ ($x = 0.1728$, $z = 0.4100$); S in $4(c)x^{1/4}z$ ($x = 0.2324$, $z = 0.0815$); K in $4(c)x^{1/4}z$ ($x = 0.4895$, $z = 0.7048$); and O3 in $4(c)z^{1/4}z$ ($x = 0.7930$, $z = 0.5580$). The reliability factor is $R = 0.09$.

It was established that, in the spectral range 300–800 nm, the dispersion of the refractive indices $n_i(\lambda)$ ($i = X, Y, Z$) of the RbKSO₄ crystal is normal and can be well described by the two-term Sellmeier formula. The refractive indices n_x and n_z tend to converge in the near UV range, which allows us to assume that a BSI point should exist in this range. Using relation (2), the parameters λ_{01} , λ_{02} , B_i , and B'_i of the two-term Sellmeier formula were determined from the experimental dependences $n_i(\lambda)$ (Table 1). Comparison of the refractive characteristics of the crystals RbKSO₄, K₂SO₄ [6–8], and Rb₂SO₄ showed the following. The replacement Rb⁺ → K⁺ does not lead to substantial changes in n_i (an increase amounts to ~10⁻³), with the centers of gravity of UV oscillators being shifted toward both longer ($\lambda_{0x} \sim 4$ –6 nm) and shorter ($\lambda_{0z} \sim 5$ –6 nm) wavelengths. The shift λ_{0i} is accompanied by different changes in the strength of effective UV oscillators: B_x decreases by 20×10^{-6} nm², while B_z increases by 22×10^{-6} nm².

Upon replacement K⁺ → Rb⁺, the refractive indices n_i decrease by $(4$ – $7) \times 10^{-3}$, λ_{0x} shifts toward longer wavelengths by ~3 nm, and λ_{0z} shifts toward shorter wavelengths by ~4 nm. In accordance with this, the specific refraction decreases by ~1–2 cm³ and the electronic polarizability decreases by $\sim(0.1$ – $0.2) \times 10^{-24}$ cm³.

In turn, comparison of the parameters of the optical indicatrix of the RbNH₄SO₄ and RbKSO₄ crystals showed that their refractive indices differ fairly considerably in magnitude ($\sim(18.7$ – $22.0) \times 10^{-3}$). This is caused by a significant difference between the specific refractions of these compounds (~2 cm³), as well as by the fact that the centers of the UV absorption bands observed along the X axis shift toward longer wavelengths by ~10 nm, while the centers of the bands measured along the Z axis shift toward shorter wavelengths by ~13 nm.

The calculated total refraction of the RbKSO₄ crystal agrees well with the sum of individual refractions,

$$\begin{aligned} R_{\text{RbKSO}_4} &\longrightarrow R_{\text{Rb}^+} + R_{\text{K}^+} + R_{\text{SO}_4^{2-}} \\ &= 5.0 + 3.5 + 14.5 = 23 \text{ cm}^3. \end{aligned}$$

It is seen from this relation that the contributions from the K⁺ and Rb⁺ cations to the total refraction of this crystal amount to 15 and 21%, respectively.

Analysis of the temperature and spectral dependences of the refractive indices and birefringence of the RbKSO₄ crystal suggests the occurrence of isotropic points. Figure 1 shows the temperature–spectral diagram of the isotropic state of the RbKSO₄ crystal for the X and Z directions. It is seen from this figure that, in very large temperature (150–800 K) and spectral (300–

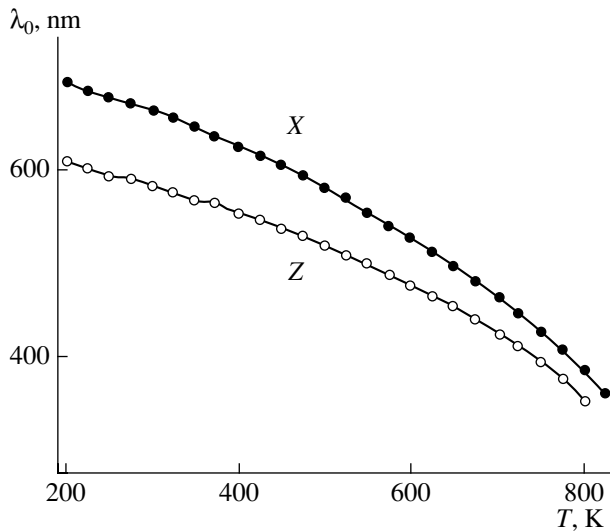


Fig. 1. Temperature and spectral diagram of the isotropic state of a RbKSO₄ crystal.

700 nm) ranges, λ_{0x} and λ_{0z} decrease nonlinearly with temperature.

We found that, in the temperature range 116–820 K, the dependence $\lambda_{0y}(T)$ is virtually linear, with the proportionality coefficient $\partial\lambda_{0y}/\partial T = -0.007 \text{ \AA/K}$ being considerably smaller than that for the LiKSO₄ crystal.

Taking into account that the crystals K₂SO₄, RbKSO₄, and LiKSO₄ exhibit the occurrence of BSI points in wide temperature and spectral ranges, the comparison of the parameters of the optical indicatrix of isomorphous crystals can serve as a basis for the method of search for crystals with BSI points. Since the replacement of cations causes insignificant changes in the parameters of the optical indicatrix, one can expect that, depending on the percentage ratio of the components in a mixture, this replacement will cause the spectral and/or the temperature ranges of occurrence of the isotropic state to either change in size or shift along the corresponding scales.

A Mechanically Compressed Crystal

Our investigation of the effect of uniaxial stress on the birefringence of the RbKSO₄ crystal showed that the action of stresses σ_x , σ_y , and $\sigma_z \sim 200$ bar leads to changes in the birefringence Δn_i , which differ both in sign and in magnitude. Table 2 shows the increments Δn_i induced by mechanical stresses applied along the crystallophysical axes of RbKSO₄ at room temperature.

In Fig. 2, the dispersion Δn_i of this crystal is presented for different directions of application of the stress at room temperature. The uniaxial pressure was found not to affect the character and value of each $\Delta n_i(\lambda)$ significantly. As is seen, the X direction is the

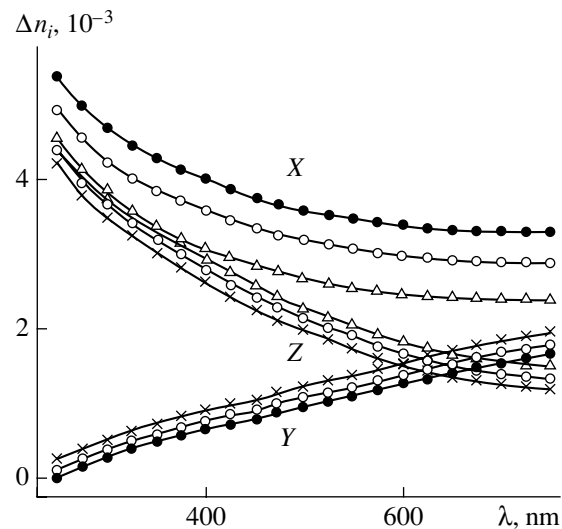


Fig. 2. Birefringence dispersion of a RbKSO₄ crystal at room temperature for different directions of an applied pressure (200 bar): (×) σ_x , (Δ) σ_y , (●) σ_z , and (○) $\sigma = 0$.

most sensitive to the action of uniaxial stresses. It is also seen from this figure that the dispersion Δn_y is anomalous ($d\Delta n/d\lambda > 0$), and that an isotropic point occurs in the crystal at $\lambda_0 \sim 235$ nm. It was found that, under the action of a uniaxial pressure σ_x , this point shifts toward shorter wavelengths, with the rate $d\lambda/d\sigma = 0.09 \text{ nm bar}^{-1}$, and, for $\sigma_x = 200$ bar, it is located at $\lambda_{0y}^x \sim 217$ nm. Conversely, under the action of σ_z , this point shifts toward longer wavelengths, with the rate $d\lambda/d\sigma = 0.04 \text{ nm bar}^{-1}$, and, for $\sigma_z = 200$ bar, it is located at $\lambda_{0y}^z \sim 247$ nm. Since the values of Δn_x and Δn_z are similar, the pressure σ_y leads to their equality near $\lambda = 348$ nm, and, in this case, $\Delta n_x = \Delta n_z = 3.35 \times 10^{-3}$. Since, for the RbKSO₄ crystal, $n_y > n_x > n_z$, this equality will take place provided that $n_x = n_z$, which corresponds to a BSI point. That is, the uniaxial mechanical stress not only shifts existing BSI points along the temperature and wavelength scales but also creates new such points.

As for most crystals, uniaxial pressures were found not to affect the character of the curves $\Delta n_x(T)$ significantly: in the temperature range 120–800 K, the deriv-

Table 2. Birefringence increments $\delta\Delta n_i \times 10^{-4}$ for RbKSO₄ crystals subjected to uniaxial stresses $\sigma_m \sim 200$ bar

Pressure	Light		
	X	Y	Z
X		-5.1	4.2
Y	1.5		-1.2
Z	-1.6	3.1	

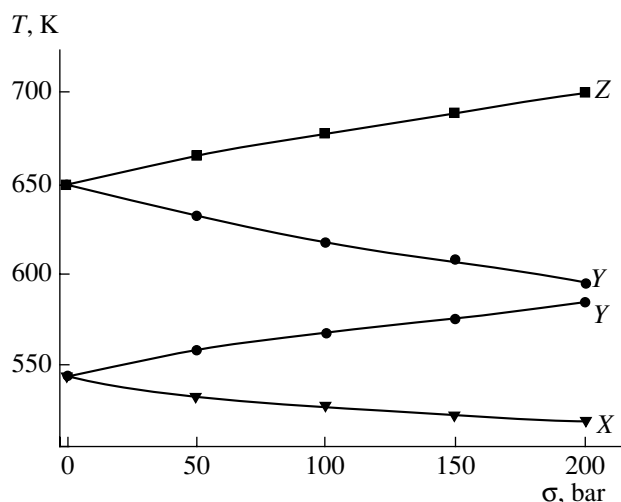


Fig. 3. Temperature–baric diagram of the isotropic state of a RbKSO₄ crystal at $\lambda = 500$ nm for different directions of a uniaxial pressure.

ative $d\Delta n_x/dT$ varies from 9.1×10^{-6} to 9.5×10^{-6} for the mechanically free and compressed crystals, respectively. By drawing the straight line $\Delta n_x = 0$, one can estimate the value and the sign of the baric shift of the BSI point λ_{0x} : the uniaxial pressures σ_x and σ_y shift this point toward lower temperatures, whereas the pressure σ_z shifts it toward higher temperatures.

Figure 3 presents the effect of a uniaxial stress on the isotropic points of the RbKSO₄ crystal. The following coefficients of the baric shift of the BSI point are determined: $\partial T_0/\partial \sigma_z = 0.245$ and $\partial T_0/\partial \sigma_y = -0.251$ K/bar (for the X direction) and $\partial T_0/\partial \sigma_x = -0.115$ and $\partial T_0/\partial \sigma_y = 0.135$ K/bar (for the Z direction). Comparison of Figs. 1 and 3 shows that the isotropic points of this crystal cover favorable and fairly large spectral and temperature intervals; therefore, RbKSO₄ can be added to the list of already-known isomorphous crystals for crystal optical temperature transducers.

Figure 4 shows the temperature behavior of Δn_z in the vicinity of the phase transition at 116 K for different directions of the uniaxial stress $\sigma_m = 200$ bar. As is seen from this figure, the uniaxial stresses along the X and Y directions shift the phase-transition point toward lower temperatures. (Under these stresses, the phase transition occurs at $T^Y = 114$ K and at $T^X = 113$ K, respectively.) Analysis of the baric dependence of Δn_z showed that the stress σ_z shifts the phase-transition point toward higher temperatures ($T^Z = 119.5$ K). The baric coefficients of the shift of the phase transition point are determined to be $dT_i/d\sigma_m = -0.015$, -0.01 , and 0.0175 K/bar. The sum coefficient of the baric shift (an analogue of the hydrostatic pressure) of the phase-transition point amounts to $\sum_{im}^3 dT_i/d\sigma_m = dT_i/d\sigma_x + dT_i/d\sigma_y + dT_i/d\sigma_z = -0.0085$ K/bar.

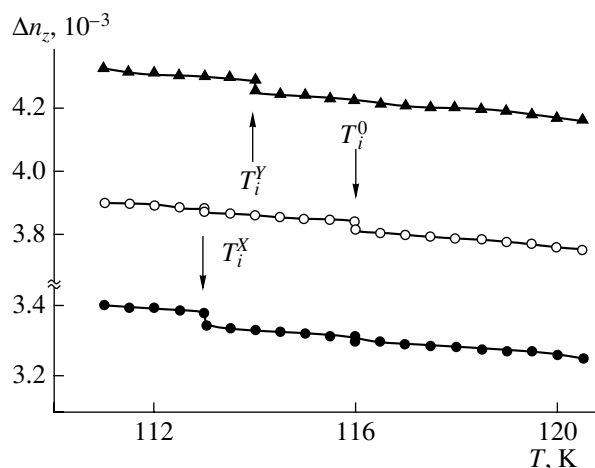


Fig. 4. Temperature dependences of the birefringence Δn_z of RbKSO₄ crystal in the phase-transition vicinity for different directions of an applied pressure.

On the basis of our experimental results and by analogy with the known data on the crystals LiKSO₄, LiRbSO₄, and (NH₄)₂BeF₄ [9–11], we can conclude that the phase transition in the RbKSO₄ crystal is associated with rotation of tetrahedral groups SO₄²⁻. Indeed, since the stresses σ_x and σ_y shift the phase-transition point toward lower temperatures, they hinder the rotation of tetrahedra that should rotate around the X and Y axes. The pressure σ_z increases T_C , i.e., facilitates the rotation of tetrahedral groups. Different numerical values of the coefficients $\partial T_C/\partial \sigma$ can point to different orientations of the axes of rotation of the SO₄²⁻ tetrahedra around the crystallophysical axes.

CONCLUSIONS

We determined the spatial symmetry of the crystal RbKSO₄, which was synthesized for the first time. The temperature and spectral dependences of the refractive indices and birefringence, as well as the baric dependences of the principal values of Δn_i , are measured. Two first-order phase transitions were detected at $T_1 = 116$ K and $T_2 = 820$ K, and three BSI points, which cover wide temperature (200–820 K) and spectral (300–700 nm) ranges, were observed. It is found that the birefringence of this crystal is rather sensitive to the action of uniaxial pressures applied along the principal crystallophysical directions. These experiments confirmed a regular feature that was previously observed for crystals isomorphous with RbKSO₄ and that consists in the fact that the uniaxial mechanical pressures $\sigma_{k,j}$ applied along the principal crystallophysical axes lead to changes in Δn_i ($i, j, k = 1, 2, 3$) different both in value and in sign. It is found that the action of uniaxial

stresses extends the temperature and spectral ranges of occurrence of BSI points and induces a new BSI point. The point of the low-temperature phase transition was found to exhibit a baric shift toward higher or lower temperatures depending on the direction of compression of the sample. This gives grounds to assume that this phase transition is caused by the rotation of tetrahedral groups around the crystallophysical axes. In this case, the sign of the baric shift of the phase-transition point depends on whether the signs of the temperature and baric deformations of the crystal structure are the same or opposite.

REFERENCES

1. V. Y. Stadnyk, M. O. Romanjuk, and V. F. Vachulovych, *Acta Pol. Phys.* **83**, 469 (1993).
2. V. I. Stadnik, M. O. Romanyuk, and V. F. Vakhulovich, *Ukr. Fiz. Zh.* **37**, 1334 (1992).
3. N. A. Romanyuk, V. M. Gaba, Z. M. Ursul, and V. I. Stadnik, *Opt. Spektrosk.* **62**, 94 (1987) [*Opt. Spectrosc.* **62**, 58 (1987)].
4. Z. M. Ursul, N. A. Romanyuk, and V. M. Gaba, *Opt. Spektrosk.* **63**, 109 (1988).
5. L. G. Akselrud, Yu. N. Grin, P. Yu. Zavalii, *et al.*, in *Collected Abstracts of 12th European Crystallographic Meeting, Moscow, August 20–29, 1989* (Nauka, Moscow, 1989), Vol. 3.
6. M. O. Romanjuk and V. Y. Stadnyk, *Ferroelectrics* **192**, 235 (1997).
7. M. O. Romanyuk, V. I. Stadnik, R. S. Brezvin, and V. I. Kardash, *Kristallografiya* **41**, 882 (1996) [*Crystallogr. Rep.* **41**, 840 (1996)].
8. M. O. Romanjuk, V. Y. Stadnyk, and R. S. Brezvin, *Ferroelectrics* **192**, 203 (1997).
9. W. Steurer, H. Wittmann, and H. Jagodzinski, *Acta Crystallogr., Sect. B: Struct. Sci.* **42**, 11 (1986).
10. A. Kunishige and H. Mashiyama, *J. Phys. Soc. Jpn.* **56**, 3189 (1987).
11. M. O. Romanyuk and V. Y. Stadnyk, *Condensed Matter Physics* **2**, 711 (1999).

Translated by V. Rogovoi

PHYSICAL PROPERTIES OF CRYSTALS

Dielectric Properties of $Y_3Fe_5O_{12}$ Garnet Crystals in the IR Range

I. D. Lomako*, S. N. Shashkov**, and I. I. Makoed***

* Institute of Solid-State and Semiconductor Physics, Belarussian Academy of Sciences,
ul. Brovki 17, Minsk, 220072 Belarus

e-mail: lomako@iftt.bas-net.by

** Belarussian State University, ul. Leninskaya 14, Minsk, Belarus

*** Brest State University, bul'v. Kosmonavtov 21, Brest, 224016 Belarus

Received June 9, 2004; in final form, March 17, 2005

Abstract—The dielectric properties of a series of yttrium–iron garnet single crystals of different structural and optical quality are investigated in the IR range ($400\text{--}1000\text{ cm}^{-1}$). Some regularities of the dependence of the permittivity ϵ_∞ of the garnet samples on the charge-carrier fraction (the parameter k/nk) are revealed. The maximum values of ϵ_∞ are found for the samples containing magnetoactive Sm and Mn ions as dominant impurities, which increase the concentration of conduction electrons and, therefore, provide large values of k/nk . A correlation between ϵ_∞ of the $Y_3Fe_5O_{12}$ samples and the concentration of oxygen ions is established. © 2005 Pleiades Publishing, Inc.

INTRODUCTION

The crystal structure of yttrium–iron garnet $Y_3Fe_5O_{12}$ (YIG) is unique from the point of view of possibilities for different ions to be incorporated into three nonequivalent cationic sublattices. As the investigations of the structural and kinetic characteristics of YIGs show, the growth of YIG crystals is inevitably accompanied by the formation of defects and deviation from stoichiometry. These effects are caused by the growth and morphological anisotropies [1, 2].

The effect of the deviation from stoichiometry and the competing character of the interaction of impurities (Ba, Mn, and Sm ions) on the structural properties and the IR absorption were studied in [1].

The purpose of this study is to reveal regularities of the dielectric properties of real YIG crystals caused by the incorporation of ions of dominant impurities and structural defects. To this end, a unified approach is used.

EXPERIMENTAL

The objects of study were YIG single crystals grown by the flux technique based on the $PbO\text{--}PbF_2\text{--}B_2O_3$ solvents. The samples studied were plates $6 \times 7 \times (1.5\text{--}2.6)\text{ mm}^3$ in size, cut parallel to the crystallographic planes (110), (111), and (100). To reveal regularities of the physical properties on the basis of a unified mechanism, we chose YIG samples of different optical quality: high (the IR absorption coefficient $\alpha < 3\text{ cm}^{-1}$), intermediate ($3 < \alpha < 7.5\text{ cm}^{-1}$), and poor ($\alpha > 7.5\text{ cm}^{-1}$) [3]. The samples with (110) orientation can be divided into two groups. Group I contains samples of high (nos. 7 and 41) and partially intermediate (nos. 43–3

and 52) quality. Samples of group II (oriented samples 50", 51, and 50 and an unoriented sample 32-UO) are plates with $\alpha > 7\text{ cm}^{-1}$. The samples with (111) orientation have different optical quality: $\alpha = 1.1$ and 6.16 cm^{-1} for samples 44 and 34, respectively. For sample 3 (100), $\alpha = 2.3\text{ cm}^{-1}$.

The optical reflection spectra were recorded from a sample surface area of about 40 mm^2 at room temperature on SPECORD 75IR and SPECORD 61NIR spectrophotometers using unpolarized light. When reconstructing the magnitudes of the energy reflection coefficient R , an Al mirror with $R = 97\%$ and a single-crystal Si plate were used as references. The incident light beam made an angle of 20° with the reflecting surface. To reconstruct the real and imaginary components of the permittivity (ϵ_1 and ϵ_2 , respectively) from the R spectra near the lattice resonance, a program based on the subtractive Kramers–Kronig method [4] was used. The frequencies of longitudinal (ν_{LO}) and transverse (ν_{TO}) optical phonons for the three resonance modes ν_1 , ν_2 , and ν_3 and the electronic contribution ϵ_∞ to the permittivity at $\nu = 1000\text{ cm}^{-1}$ ($\lambda = 10\text{ }\mu\text{m}$) were calculated for 11 YIG samples. The values of the dielectric constant ϵ_0 for all three modes ν_i were determined from the Lyddane–Sachs–Teller relation, which links the frequencies of the longitudinal and transverse optical modes, taking into account the value of ϵ_∞ for a particular sample.

The quantitative content of impurities in the YIG samples under study was determined by X-ray radio-metric analysis [3]. The same method was used to find the ratio of the intensities of coherent and incoherent X-ray scattering (k/nk) [5]. The value of k/nk characterizes the fraction of charge carriers for each YIG sample

with consideration for an individual ensemble of impurity ions of different valence (Ba, Mn, Sm, Pt, and V), the oxygen vacancies, and other structural defects. The scattering of conduction electrons, caused by the ionic disorder in a crystal, is one of the factors determining the kinetic properties of the crystal. Along with doping, defects and impurities scatter charge carriers and phonons, while significantly affecting the conductivity [6]. The lattice distortion caused by the presence of impurity centers, which demonstrate competing character of interaction, is determined by the specificity of their nature.

In [7], where the lattice reflection spectra of single crystals of $Y_3Fe_{5-x}Ga_xO_{12}$ solid solutions were investigated, the peaks of bands were compared with the values of the unit-cell volume at variation in from 0 to 5.

In this paper, we report the results of studying of $Y_3Fe_5O_{12}$ crystals, whose growth is accompanied by the incorporation of both inevitable process impurities (Ba ions from the solvent) and Mn and V ions (Fe_2O_3 impurity in very small amounts) and Sm ions (Y_2O_3 impurity in very small amounts), with different concentrations and in unpredictable combinations due to the competing character of their interaction in real samples. Therefore, the value of the lattice parameter, which ranges from 12.370 to 12.377 Å, cannot be used to estimate the quality of the YIG samples. (This point of view was discussed in detail in [1].) The series of YIG samples (11 in total) was investigated by different techniques [1, 2, 4, 5]. Neutron activation analysis made it possible to reveal a quality criterion: the ratio of the total concentration of Y and Fe cations to the concentration of O anions, $(Y + Fe)/O$ (wt %). The parameters characterizing the quality of the YIG samples under study change in wide ranges: $0.4 < \alpha < 13.2 \text{ cm}^{-1}$ and $k/nk = 0.038\text{--}0.053$.

In this study, we propose to interpret the changes in the dielectric properties of the YIG samples by comparing these properties with the parameter k/nk and the concentration of oxygen ions (O) in real crystals by taking into account their crystallographic orientation.

DIELECTRIC PROPERTIES OF YIG CRYSTALS

The dielectric properties of YIG single crystals in the IR range are similar to the properties of ionic compounds, which are characterized by high resistivity. The group-theoretical analysis of the garnet structure predicts 17 frequencies of the same symmetry, active in the IR spectra [8]. In the frequency range from 400 to 1000 cm^{-1} (25–10 μm), the reflection spectra $R(\nu)$ of the YIG samples contain high-energy bands in the range 550–650 cm^{-1} . Within these bands, three peaks can be distinguished for each sample. The experimental data on the lattice vibrations in similar compounds [9–11] make it possible to attribute the modes observed in the spectra with displacements of Fe cations located

in tetrahedral complexes formed by oxygen ions. The low-energy bands, due to the cations in octahedral and dodecahedral positions, were not investigated because of the limited operating frequency range (400–1000 cm^{-1}) of the 75IR spectrophotometer.

Figure 1 shows the spectra of the real component of the permittivity of the YIG samples, ϵ_1 , near the lattice resonance. The spectra $\epsilon_1 = f(\nu)$ of samples 7, 41, and 52 (110) are characterized by small values of α ($< 5.2 \text{ cm}^{-1}$) (Fig. 1a). Sample 7, having the best transparency ($\alpha = 0.4 \text{ cm}^{-1}$), takes the place of the “golden mean” in the spectrum, whereas sample 52, with the maximum content of Sm ions in the dodecahedral sublattice, demonstrates the largest values of ϵ_1 for the mode ν_1 . The latter circumstance is most likely to be related to the incorporation of V ions of different valence into the tetrahedral sublattice of sample 52 [1]. Sample 41, containing many Ba ions and Sm and Mn ions in very small amounts, has the largest values of ϵ_1 for the modes ν_2 and ν_3 . It is known that Ba ions in the garnet structure are the inevitable process impurity, which substitutes yttrium in the dodecahedral sublattice [1]. Barium ions have a stable valence of +2 and serve as acceptors in YIG crystals.

Some samples of the series under study (50, 32-UO, 52, 50", 41, 34, and 44) contain a large number of Ba ions ($Ba/Y \geq 1 \text{ wt } \%$). The electrical neutrality of YIG crystals containing divalent ions can be retained by the formation of tetravalent Sm, Mn, and Fe ions. Partial compensation of charges may be caused by the presence of impurity V ions (samples 32-UO and 52). Note that V^{3+} ions ($r = 0.7 \text{ Å}$) are located in the octahedral sublattice and V^{5+} ions ($r = 0.35 \text{ Å}$) occupy the tetrahedral sublattice. When V ions are substituted in the tetrahedral position, their number should be smaller by a factor of 2 than the number of Ba ions in the dodecahedral lattice. In sample 50, incomplete compensation of Ba^{2+} ions may be caused by the presence of Pt^{4+} ions.

When YIG samples contain a high concentration of Ba^{2+} ions and no (or very few) ions of variable valence (Sm, Mn, V), electrical neutrality is provided by the formation of Fe^{4+} ions in the tetrahedral position and/or oxygen anion vacancies.

The ϵ_1 spectra of sample 50" (110) (intermediate optical quality; $\alpha = 6.91 \text{ cm}^{-1}$) and sample 51 (poor optical quality; $\alpha = 12 \text{ cm}^{-1}$) are shown in Fig. 1b. These samples are characterized by a small value of k/nk (0.038 and 0.042 for 50" and 51, respectively). The resonance peaks corresponding to the mode ν_2 in the spectra of these samples have large amplitudes, comparable with the corresponding amplitude for sample 41, which has the minimum value of k/nk (0.0427) among the samples represented in Fig. 1a.

Figure 1c shows the spectra of ϵ_1 for the samples with different orientations: 3 (100), 44 (111), and 32-UO. The ϵ_1 spectrum for sample 32-UO has a more

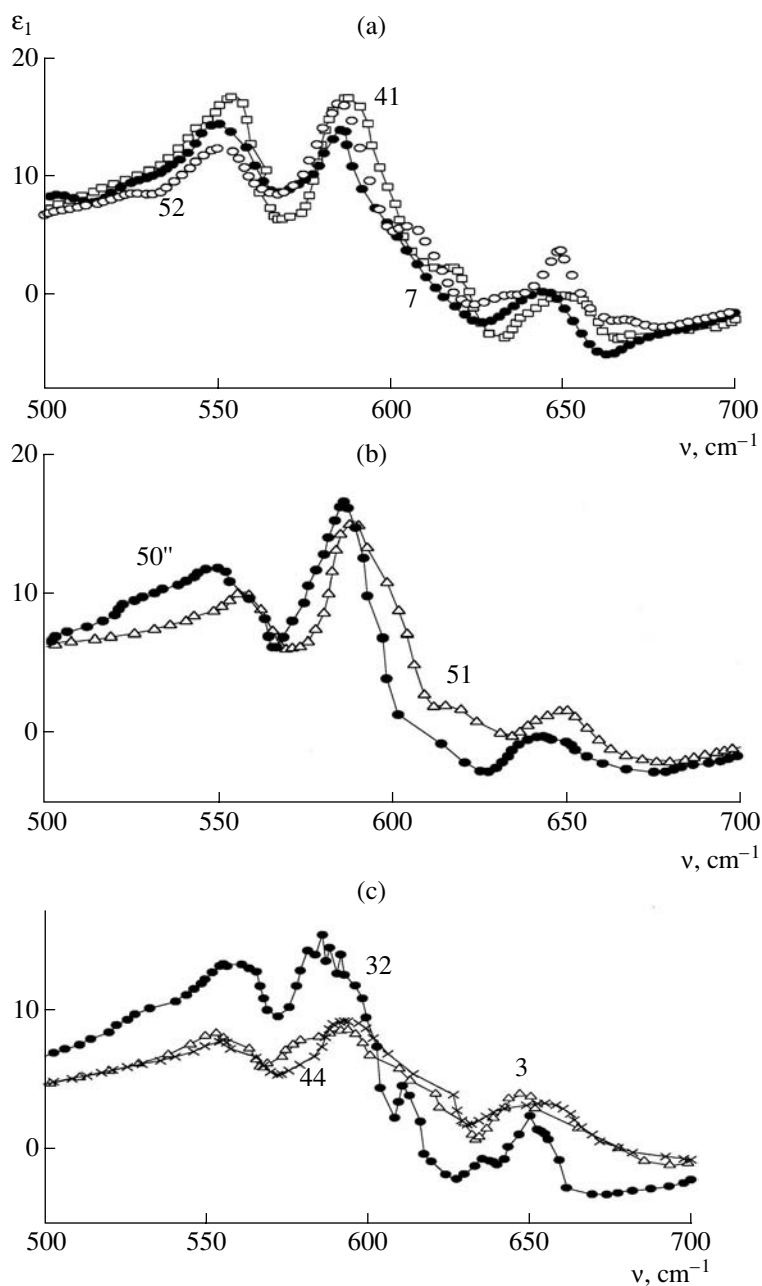


Fig. 1. Spectra of the real component ϵ_1 of the permittivity of the YIG samples near the lattice resonance (500–700 cm^{-1}): (a) samples 7, 41, and 52, orientation (110); (b) samples 50'' and 51, orientation (110); and (c) ϵ_1 spectra of samples 3 (100), 44 (111), and 32-UO.

complex structure and contains seven local peaks. Such a shape of the ϵ_1 spectrum of sample 32-UO is related to the absence of a pronounced crystallographic orientation.

Note that negative values of ϵ_1 are observed in the vicinity of the peak at $\nu_1 \approx 650 \text{ cm}^{-1}$ for all YIG samples. When the illumination frequency is in the range between the frequencies of the longitudinal (ν_{LO}) and transverse (ν_{TO}) optical phonons, the real component ϵ_1 takes negative values [9], which indicates that an inci-

dent electromagnetic wave with such a frequency undergoes reflection and thus cannot propagate in the crystal.

The frequencies of the longitudinal (ν_{LO}) and transverse (ν_{TO}) phonons for the three peaks and the value of the electronic contribution to the permittivity, ϵ_∞ , for the YIG samples under study are listed in the table. As can be seen, the values of the optical permittivity ϵ_∞ range from 3.70 to 4.40.

Frequencies of the longitudinal and transverse optical phonons in the YIG crystals and the values of the electronic permittivity ϵ_∞ and the imaginary part of the permittivity ϵ_2 (in parenthesis) at $\lambda = 10 \mu\text{m}$

	ν_1, cm^{-1}		ν_2, cm^{-1}		ν_3, cm^{-1}		$\epsilon_\infty(\epsilon_2)$ at 1000cm^{-1}
	ν_{TO}	ν_{LO}	ν_{TO}	ν_{LO}	ν_{TO}	ν_{LO}	
43-3	655.58	723.47	595.28	645.65	564.48	573.64	3.80 (2.65)
34 (111)	652.92	722.90	600.33	675.34	570.94	593.84	4.40 (2.97)
41	664.33	714.36	596.2	645.20	556.69	564.97	4.20 (2.56)
3 (100)	664.74	714.42	609.30	631.69	562.92	571.94	4.12 (2.11)
32-HO	654.40	719.93	602.39	643.44	566.21	568.46	3.90 (2.45)
44 (111)	663.44	718.23	605.78	634.26	565.08	571.86	3.85 (2.20)
50 (first side)	652.14	721.02	618.22	630.55	560.23	564.47	3.89 (2.50)
50 (second side)	648.49	686.54	598.48	627.09	549.29	558.69	3.94 (2.15)
50 (average)	650.31	703.78	607.16	628.82	554.76	561.58	3.915 (2.32)
51	652.17	711.29	605.91	635.36	565.17	569.12	4.02 (2.49)
52	650.29	714.58	593.98	635.36	557.78	564.12	4.14 (2.29)
50"	652.29	714.24	592.33	640.17	562.92	568.18	3.70 (2.62)
7	650.44	715.34	595.60	641.65	558.29	587.34	4.22 (2.48)

In Fig. 2, the values of ϵ_∞ are compared with the value of k/nk for the samples with different orientation, including sample 32-UO. Curve 1 shows the data for the (110) and (111) YIG samples, which generally have small values of α and the highest values of the permittivity ϵ_∞ . All three curves exhibit a general trend: the values of ϵ_∞ increase with an increase in the parameter k/nk . This result is quite justified from the physical point of view: with an increase in the number of charge carriers in a specific sample, the electronic permittivity also increases. Note that the maximum values of ϵ_∞ are observed in samples 34, 52, and 3 (curves 1, 2, and 3, respectively), which contain Sm ions as a dominant impurity. We believe that sample 34 has the maximum value of ϵ_∞ (4.40) not only as a result of the incorporation of Sm ions but also because its crystallographic orientation is (111).

In the previous studies considering the mechanism of charge transfer in YIG samples, it was concluded that the charge transfer along the crystallographic [111] axis occurs through the bond chains with the highest concentration of defects, along which the easy-magnetization axis, dislocations, and domain boundaries are oriented [2, 3]. Sample 7, whose permittivity is $\epsilon_\infty = 4.22$ (curve 1), contains microinclusions of Mn ions (the dominant impurity in this sample).

The magnetic ordering of spins occurs in YIGs through the superexchange interaction of iron cations in tetrahedral and octahedral complexes, which are the main magneto-optical active centers. This interaction is indirect; it is implemented through ligands: oxygen ions O^{2-} . As a result of this interaction, O^{2-} ions become polarized, and the electromagnetically induced electric dipole moment, corresponding to the vibrations of ions

along the ligand–central-cation bond of the complexes, will be higher than for other mode vibrations. This effect should increase the intensity of the corresponding peaks both in the reflectance spectra and in the spectra of the permittivity components.

In view of the strong effect of oxygen ions on the dielectric properties of the YIG samples, we will con-

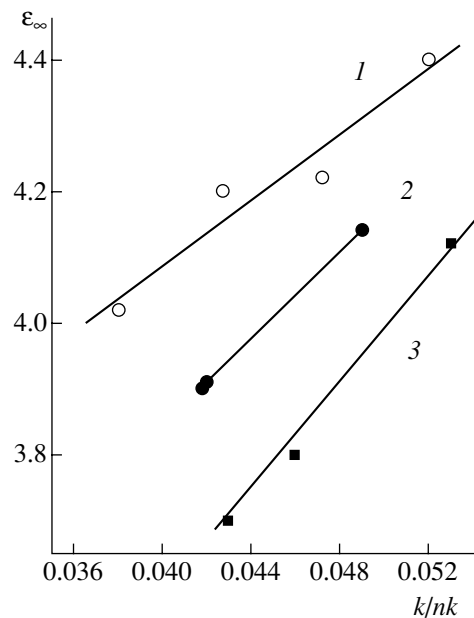


Fig. 2. Correlation between the electronic permittivity ϵ_∞ of the YIG samples and the parameter k/nk : (1) samples 51, 41 and 7 (110) and sample 34 (111) (in ascending order of the permittivity ϵ_∞); (2) samples 32-UO, 50 (110), and 52 (110); and (3) samples 50", 43-3 (110), and 3 (100).

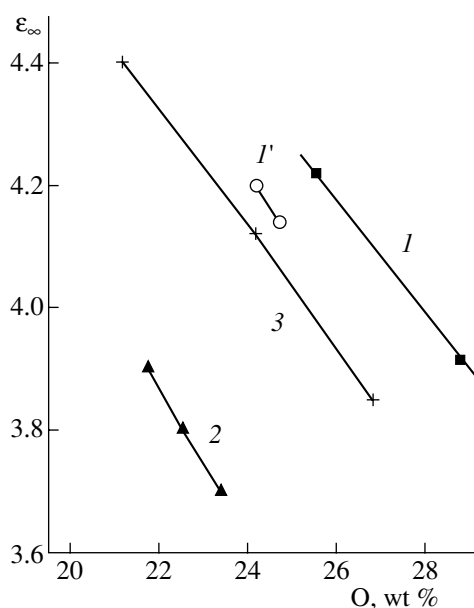


Fig. 3. Correlation between the electronic permittivity ϵ_{∞} of the YIG samples and the concentration O of oxygen ions (wt %) in the samples: (*I*) samples 7 and 50 (110); (*I'*) samples 41 and 52 (110) (in descending order of the permittivity); (*2*) samples 32-UO, 43 (110), and 50" (110); and (*3*) samples 34 and 44 (111) and sample 3 (100).

sider the dependence of ϵ_{∞} on the oxygen content (Fig. 3). The oxygen content in the samples was calculated as a difference between the sample weight and the total weight of Y and Fe cations. These data were obtained by neutron activation analysis. Table 1 in [5] contains the results of the calculation for the main YIG components: Y and Fe ions (in wt %). Curves *I*, *I'*, and *2* show the data for the samples with (110) orientation: curves *I* and *I'* are for the samples of group I and curve *2* is for the samples of group II. Curves *I* and *I'*, representing the data for the samples containing Sm, Mn, and Pt ions as dominant impurities, make an angle of $\approx 123^{\circ}$ with the abscissa axis. Curve *2* is for the samples with minimum values of ϵ_{∞} . In these samples, the dominant impurities are passive Ba and V (32-UO, 50") ions or Ba ions with a low concentration (sample 43-3). Curve *3* makes an angle of 118° with the abscissa axis. Curve *3* represents the data for the samples with (111) orientation, 34 (with the highest permittivity ϵ_{∞}) and 44, and for sample 3 (100). The top of Fig. 3 shows the data for the YIG samples with the largest values of ϵ_{∞} , which are related to the incorporation of Sm ions with variable valence into these samples. Curve *3* makes an angle of $\approx 122^{\circ}$ with the abscissa axis. A general regularity can be seen in Fig. 3: the lower the concentration of oxygen ions in a given YIG sample (the data for which lie in one of the four curves), the higher the permittivity ϵ_{∞} of this sample. Comparing Figs. 2 and 3, we can conclude that the maximum values of ϵ_{∞} are observed in the YIG samples characterized by the larg-

est values of k/nk (samples 34 (111), 7, 52 (110), and 3 (100)) or the lowest concentration of oxygen ions.

Analyzing the data in Figs. 2 and 3, one should take into account the following. Samples 7 and 41 with (110) orientation, having small values of α (0.4 and 1.27 cm^{-1} , respectively), contain inclusions of Mn, Ba, and Sm in very small amounts. Sample 52 has the value of $\alpha = 5.15 \text{ cm}^{-1}$ (the intermediate transparency) and contains Sm ions as a dominant impurity, which are distributed very nonuniformly over the sample thickness [2]. Sample 50 (100) contains Pt^{4+} ions as the dominant impurity. This impurity, in view of its small ionic radius, is located in tetrahedral positions. Its influence on the spectra of the imaginary component of the permittivity, ϵ_2 , is demonstrated in Fig. 4, which shows the reflection and ϵ_2 spectra recorded from both sides of sample 50. The differences between these spectra are large, a phenomenon which is caused by both the large gradient of the distribution of Pt ions over the sample thickness and their incorporation specifically into tetrahedral sites, which is revealed in the IR spectral range under study. The amplitudes of the peaks in the ϵ_2 spectrum for both sides of sample 50 change by more than a factor of 2 in the vicinity of the mode ν_2 .

According to the data of [8], the presence of magnetic interactions in the system of imperfect impurity YIG crystals leads to some broadening of the reflection bands. In the spectrum of sample 34 (111), the reflection band is narrower (81.98 cm^{-1}) as compared to samples 43-3 and 41 (91.1 and 91.64 cm^{-1} , respectively).

The value of splitting ($\nu_{LO} - \nu_{TO}$) = $\Delta\nu_1$ in sample 34 (111) (69.98 cm^{-1} for the mode ν_1) exceeds the corresponding values for samples 43-3 (67.89 cm^{-1}) and 41 (50.03 cm^{-1}). The values obtained are close to the data reported in [8], which were reconstructed by the Kramers–Kronig method from the reflection spectra of a polished unoriented single-crystal sample (32-UO). The minimum values of $\Delta\nu_1$ are observed for samples 44 (111) (about 55 cm^{-1}) and 3 (110) (49.68 cm^{-1}).

Figure 5 shows the dependences of $\Delta\nu_2$ on the parameter k/nk for a set of YIG samples. For the YIG(110) samples (curves *I* and *I'*), the value of $\Delta\nu_2$ linearly decreases with an increase in the argument k/nk . Curves *I* and *I'* correspond to the YIG samples with $\alpha < 7 \text{ cm}^{-1}$ and have approximately the same slope, whereas the slope of curve *2* is significantly different. For samples 44 and 34 with the (111) orientation, $\Delta\nu_2$ increases with an increase in k/nk (curve *3*). The anomalous behavior of the YIG(111) samples was revealed previously during study of their electrical properties [2, 3]. The YIG(111) samples have the lowest resistivity because the charge transfer occurs in them through the periodic chains with the highest content of defects (including Fe ions located in the octahedral sublattice, O anions, and Y ions in dodecahedral

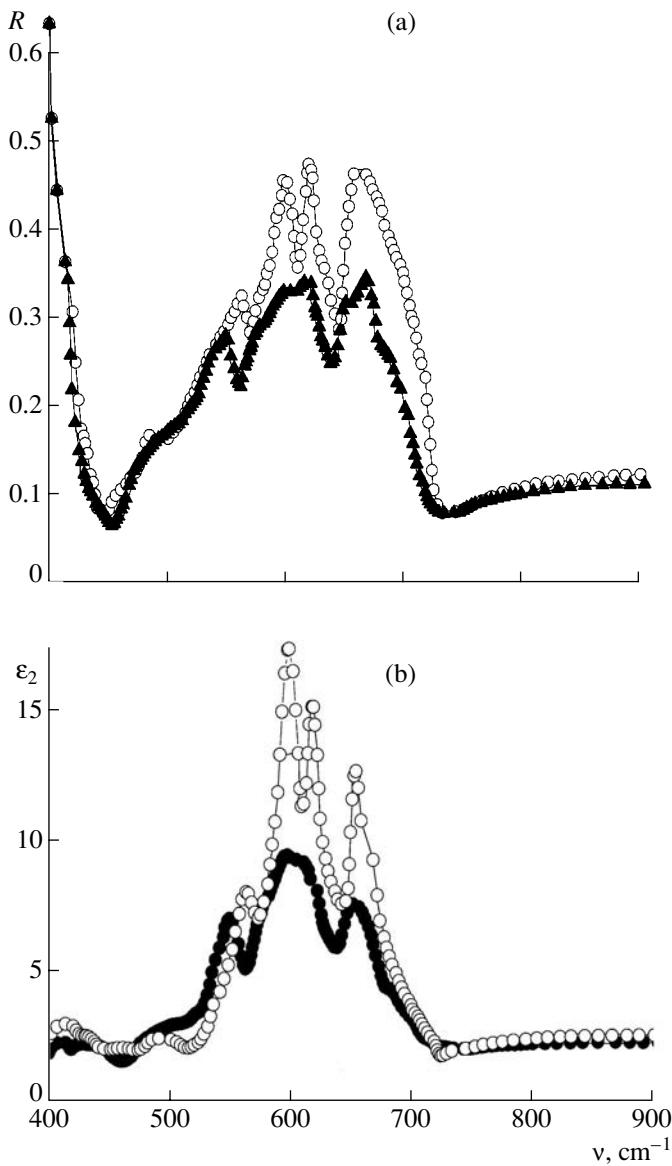


Fig. 4. Reflection spectra R (a) and the spectra of the imaginary component of the permittivity, ϵ_2 , (b) for the two sides of sample 50 (110) near the lattice resonances (400–900 cm^{-1}). The open circles in the R and ϵ_2 spectra correspond to the side of sample 50 with a higher concentration of Pt^{4+} ions.

sites), which are aligned along the easy-magnetization axis.

The value of splitting $\Delta\nu_2$ for the YIG samples is shown in Fig. 6 as a function of the ratio of the electronic permittivity ϵ_∞ to $\epsilon_0(\nu_2)$. The dependences shown are not only linear but almost parallel. The larger the electronic contribution ϵ_∞ to the dielectric constant ϵ_0 for the YIG samples, the smaller the splitting they exhibit. This regularity is observed for all samples under consideration. Samples 3 (110), 50, and 51 (110) have the smallest values of $\Delta\nu_2$: 22–29 cm^{-1} . In this

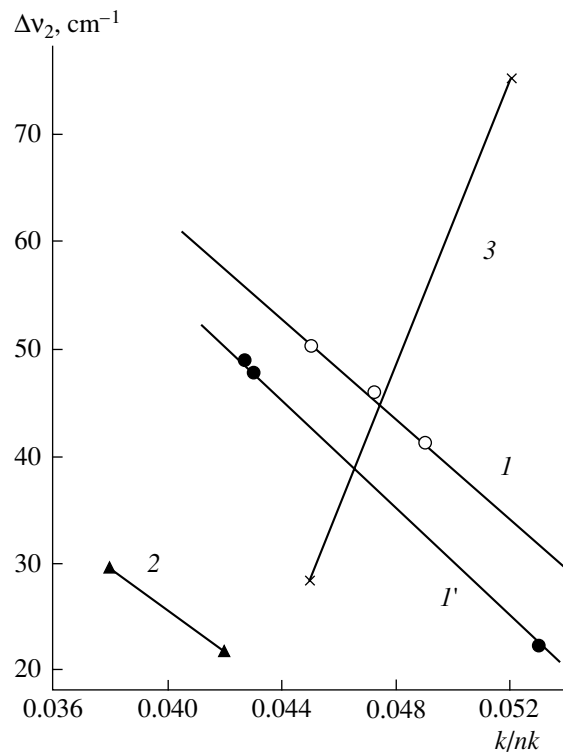


Fig. 5. Dependence of the splitting $\Delta\nu_2$ (cm^{-1}) on the parameter k/nk : (1) samples of group I (43, 7, and 52 (110)), (1') samples 41 and 50" (110) and sample 3 (100) (in descending order of the splitting $\Delta\nu_2$), (2) samples of group II (51 and 50 (110)), and (3) samples 34 and 44 (111).

case, the ratio $\epsilon_\infty/\epsilon_0$ ranges from 90.5 to 93%. The maximum values of $\Delta\nu_2$ ($\approx 52.5 \text{ cm}^{-1}$) are observed for samples 43, 41, and 50 with (110) orientation. The ratio $\epsilon_\infty/\epsilon_0$ for these samples is 85–86%. The data for samples 34 and 44 with (111) orientation, as well as samples 51 (110) and 3 (100), are represented by curve 2.

For the mode ν_1 , the dependences $\Delta\nu_1 = f(\epsilon_\infty/\epsilon_0)$ are similar. The value of $\Delta\nu_1$ ranges from 50 to 70 cm^{-1} (samples 3 and 34, respectively), while the argument monotonically decreases from 87 to 81.5%. The data for the nine samples of three orientations lie in the same straight line in the following sequence: 34, 43, 7, 52, 50", 51, 44, 50, and 3. The data corresponding to samples 41 (110) and 32-UO are beyond this line.

For the mode ν_3 , the values of splitting $\Delta\nu_3$ are small (29–2.25 cm^{-1}) and the ratio $\epsilon_\infty/\epsilon_0$ is in the range 90–99%. The maximum values of splitting $\Delta\nu_3$ are observed for samples 7 and 34 (29 and 22 cm^{-1} , respectively); for other samples, $\Delta\nu_3 < 7 \text{ cm}^{-1}$. Note that it is only the mode ν_3 for which the maximum value of $\Delta\nu_3$ corresponds to sample 7 (110) containing Mn^{2+} ions as the dominant impurity. Incorporation of magnetoactive Mn^{2+} ions into the dodecahedral sublattice is accompanied by the competing interaction with neutral Ba ions

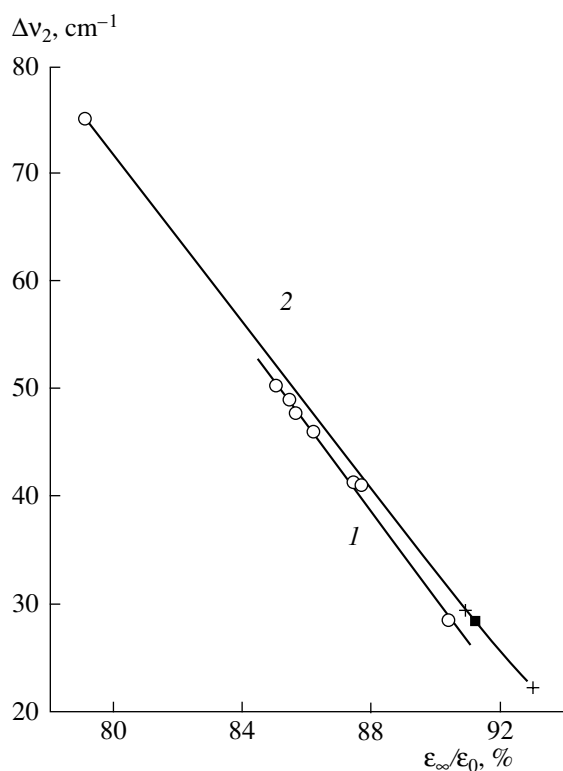


Fig. 6. Dependence of the splitting Δv_2 (cm^{-1}) on the ratio $\epsilon_\infty/\epsilon_0$: (1) samples 43, 41, 50", 7, 52 (110), 32-UO and 50 (in descending order of the splitting Δv_2) and (2) samples 34, 51, 44, and 3 (100).

[1, 3]. The following correlation was revealed: sample 7 with the maximum Mn concentration ($\text{Mn}/\text{Fe} = 0.21$ wt %) has the lowest content of Ba ions ($\text{Y}/\text{Ba} = 0.023$ wt %) (see [5], Tables 1 and 2). The (110) face, characterized by a low growth rate, has a significant advantage in the uniform filling of tetrahedral positions alternating with dodecahedral ones. We assume the electrical neutrality of sample 7 to be caused by the incorporation of Fe^{4+} ions into the tetrahedral sublattice and the formation of oxygen anion vacancies.

It is of interest to compare the values of the dielectric constant ϵ_0 of the YIG samples for the three modes with the concentration of oxygen ions corresponding to an actual sample. Figure 7 shows the dependence $\epsilon_0(v_3) = f(\text{O, wt \%})$ for the samples under study. Curve 1 represents the data for samples 3 (100), 7, and 50 (110); curve 2 corresponds to the samples with (110) orientation of group II: 51, 43, and 50". Since these two curves correspond to the samples of group II (except for samples 3 (100) and 7), they are linear and make angles of 115° and 117° with the abscissa axis, respectively. Curve 3 represents the data for the four samples of two orientations: 44 and 34 (111) and 41 and 52 (110). Samples 34, 3, and 52 have a fairly high concentration of Sm ions. An analogy between Fig. 7 and Fig. 3 can be

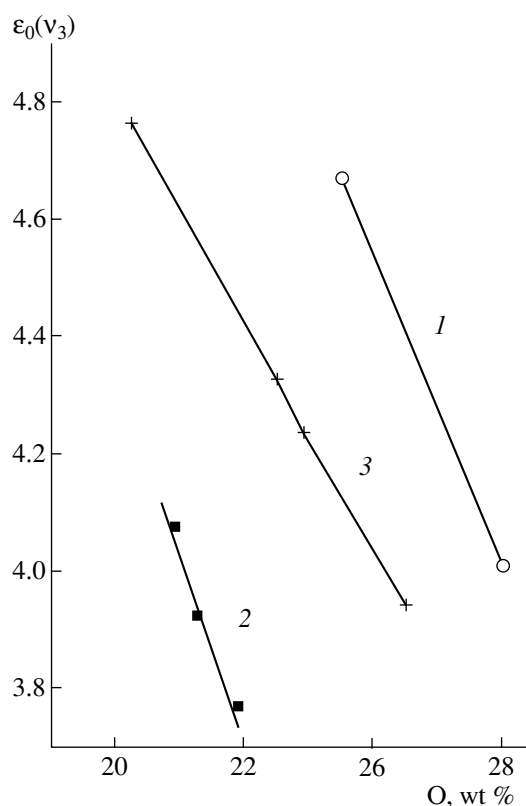


Fig. 7. Dependences of the dielectric constant $\epsilon_0(v_3)$ for the mode v_3 in the YIG samples on the concentration of oxygen ions: (1) samples 3 (100), 7 (110), and 50 (110); (2) samples 51, 43-3, and 50" (110) (in descending order of ϵ_0); and (3) samples of group I (34 (111) (with the maximum value of ϵ_0), 44 (111), 41 (110), and 52 (110)).

seen since these figures represent dependences of the same parameter: the concentration of oxygen ions, including anion vacancies. The data for curve 1' (samples 41 and 52) in Fig. 3 are absent in Fig. 7, where they are obscured by curve 3. A general regularity manifests itself in all curves: the lower the concentration of oxygen ions in a sample, the larger the value of $\epsilon_0(v_3)$ of this sample.

CONCLUSIONS

We investigated the dielectric properties of YIG single crystals with different degrees of structural and optical perfection as functions of the character of the incorporated dominant impurities (Sm, Mn, Ba, and V) and the crystallographic orientation of the sample. On the basis of the previously obtained data on the elemental composition, the finding of the dominant impurities in the samples, and the use of the parameter k/nk , a new approach is suggested to determine the regularities in the dielectric properties.

In this study, we restricted our consideration to the relationship between the main dielectric properties (optical permittivity ϵ_∞ , the dielectric constant ϵ_0 , and

the splitting Δv_1) and the parameter k/nk , the concentration of oxygen ions in the YIG samples, and the ratio $\epsilon_\infty/\epsilon_0$.

For the YIG crystals with different crystallographic orientation, regularities in the dependences of components ϵ_1 , ϵ_∞ , and ϵ_0 of the permittivity on the fraction of the charge carriers k/nk and the concentration of oxygen ions are revealed. The optical permittivity ϵ_∞ of the samples under study ranges from 3.70 (sample 50") to 4.40 (sample 34 (111)). In samples 34, 3, and 52, the dominant impurities are Sm ions, which have a magnetic moment and a variable valence, and Mn ions, which are incorporated inhomogeneously into sample 7 with a maximum concentration. The YIG samples that contain no (sample 51) or very few (sample 43-3) Ba ions are characterized by small values of ϵ_∞ . The minimum values of ϵ_∞ are typical of the samples containing many passive Ba and V ions (samples 50" and 32-UO) or Pt^{4+} ions (sample 50). We believe that, in the case of high concentrations of Ba^{2+} ions in the YIG samples containing no (or very few) Sm, Mn, and V ions with a variable valence, the charge can be compensated owing to the incorporation of Fe^{4+} ions into the tetrahedral sublattice or the formation of oxygen anion vacancies.

In the YIG samples oriented parallel to the (111) plane, which is perpendicular to the easy-magnetization axis, the band in the reflection spectrum related to the interaction of radiation with tetrahedral complexes is 1.2–1.8% wider than for the (110) samples. The YIG(111) samples demonstrate anomalous dependence of the splitting Δv_2 (as well as the splitting Δv_1) on the parameter k/nk : with an increase in the argument, the values of Δv_2 increase sharply. For other YIG samples (with (110) and (100) orientations), the splitting Δv_2 decreases monotonically with an increase in the charge-carrier concentration.

The linear character of the splitting Δv_2 differently manifests itself in the YIG samples, depending on the ratio of the electronic permittivity ϵ_∞ to $\epsilon_0(v_2)$. This dependence is represented for all YIG samples by two almost parallel straight lines. The following regularity is revealed for the YIG samples: the larger the ratio $\epsilon_\infty/\epsilon_0(v_i)$, the smaller value of the splitting Δv_i is observed in this sample. This holds true for all three modes: v_1 , v_2 , and v_3 . For the mode v_1 , the exception is two samples: 41 (110) and 32-UO, which disobey this regularity.

A change in the shape and intensity of the lattice-reflection spectra and the spectra of the imaginary part of the permittivity ϵ_2 is found experimentally. The effect of the concentration gradient of dominant impurities (Pt^{4+}) on the character of the spectra recorded from two sides of sample 50 is revealed. The differences in the spectra are due to both the nonuniform distribution of Pt ions over the sample thickness and their incorporation into tetrahedral sites, which is observed in the IR spectral range under study. The amplitudes of the peaks in the spectra of the imaginary part of permittivity ϵ_2 recorded from the two sides of sample 50 change by more than a factor of 2 in the vicinity of v_2 .

ACKNOWLEDGMENTS

This study was supported by the Foundation for Basic Research, project no. F05BR-003.

REFERENCES

1. I. D. Lomako and A. G. Dutov, *Kristallografiya* **47** (1), 128 (2002) [*Crystallogr. Rep.* **47**, 120 (2002)].
2. I. D. Lomako, V. I. Pavlov, and N. Ya. Shishkin, *Kristallografiya* **48** (1), 121 (2003) [*Crystallogr. Rep.* **48**, 116 (2003)].
3. N. N. Dorozhkin and A. V. Leont'ev, *Application of the Kramers–Kronig Relation in the Solid-State Physics and Its Implementation*, Available from VINITI, No. 189-86 (December 12, 1985).
4. I. D. Lomako, A. G. Dutov, and A. N. Igumentsev, *Zh. Prikl. Spektrosk.* **67** (2), 217 (2000).
5. I. D. Lomako, *Kristallografiya* **47** (4), 724 (2002) [*Crystallogr. Rep.* **47**, 666 (2002)].
6. J. S. Blakemore, *Semiconductor Statistics* (Macmillan, New York, 1962; Mir, Moscow, 1964).
7. V. F. Zhovanik, V. A. Odarich, V. A. Ruban, and S. N. Rud'ko, *Ukr. Fiz. Zh.*, No. 3, 464 (1982).
8. J. P. Hurrell, S. P. S. Porto, I. E. Chang, *et al.*, *Phys. Rev.* **173** (3), 851 (1968).
9. A. M. Hofmeister and K. R. Campbell, *J. Appl. Phys.* **72** (2), 638 (1992).
10. Yu. K. Voron'ko, L. M. Ershova, N. A. Es'kov, *et al.*, *Fiz. Tverd. Tela (Leningrad)* **30** (2), 512 (1988) [*Sov. Phys. Solid State* **30**, 291 (1988)].
11. H. D. Lutz, G. Waschenbach, G. Kleiche, and H. Haueuseler, *J. Solid State Chem.* **48**, 196 (1983).

Translated by Yu. Sin'kov

PHYSICAL PROPERTIES
OF CRYSTALS

The ESR Spectra of Mn^{2+} Ions and the Low-Temperature NQR Spectra of ^{175}Lu in $LuNbO_4$ Crystals

A. G. Beda¹, A. A. Bush², A. F. Volkov², and V. F. Meshcheryakov^{2,3}

¹ State Scientific Center of the Russian Federation, Alikhanov Institute for Theoretical and Experimental Physics, Bol'shaya Cheremushkinskaya ul. 25, Moscow, 117218 Russia

e-mail: afvolkov@mirea.ru

² Moscow State Institute of Radio Engineering, Electronics, and Automation (Technical University), pr. Vernadskogo 78, Moscow, 119454 Russia

³ Shubnikov Institute of Crystallography, Russian Academy of Sciences, Leninskii pr. 59, Moscow, 119333 Russia

Received September 3, 2004

Abstract—The electron-spin resonance spectra of Mn^{2+} ions and nuclear-quadrupole resonance spectra of ^{175}Lu are investigated to find out the possibility of implementing the technique of dynamic alignment of nuclei using $LuNbO_4$ single crystals doped with Mn^{2+} . An estimate for the electron-spin resonance frequency of Mn^{2+} ions is obtained, and the temperature dependences of the quadrupole coupling constant eQq and the anisotropy parameter that characterizes the asymmetry of the electric field gradient at ^{175}Lu nuclei are studied. It is demonstrated that $LuNbO_4$ single crystals doped with Mn^{2+} ions can be used as working media in experiments on dynamic alignment of nuclei. © 2005 Pleiades Publishing, Inc.

Targets with oriented nuclei are widely used in nuclear and high-energy physics. Both polarized and aligned nuclear targets are applied. In the former case, the dynamic polarization of nuclei is usually implemented. This technique is based on introduction of a paramagnetic impurity into a system of nuclei (a working medium). The impurity ions have a free unpaired electron at one of their outer shells. Since the magnetic moment of an electron exceeds that of a nucleus by about three orders of magnitude, a system of electron spins should have a degree of polarization close to 100% at 0.5 K in a magnetic field of about 2.5 T. Then, this high degree of polarization attained by the system of electron spins is transferred to nuclear spins using microwave radiation, thus increasing their polarization up to about 100%. In this study, we consider the possibility of implementing the technique of dynamic alignment of nuclei, proposed in [1]. In this technique, paramagnetic impurities are also introduced into a working medium. The ground state of paramagnetic ions with the electron spin $S > 1/2$ is split by the crystal field, thereby allowing us to observe electron-spin resonance (ESR) in a zero magnetic field. At sufficiently high ESR frequencies (exceeding 30 GHz) and at temperatures T of about 0.5 K, the system of electron spins of paramagnetic impurities is characterized by nearly 100% alignment. Then, this high degree of alignment attained by the system of electron spins is transferred to nuclear spins using microwave radiation, thus increasing the alignment of nuclear spins up to about 100%.

This study is a continuation of [2, 3], where lutetium niobate was proposed as a model substance for a work-

ing medium in such nuclear-quadrupole resonance (NQR) experiments. Working media should meet the following requirements: the nuclei resonating in the single crystal should have NQR frequencies of several tens of MHz, whereas the paramagnetic impurity centers in the working crystal should exhibit (as mentioned above) a sufficiently high degree of splitting of ESR levels in the absence of an external magnetic field.

In this paper, we report the ESR data obtained on a single crystal of manganese-doped lutetium niobate grown by crucibleless zone melting using a stoichiometric mixture of lutetium and niobium oxides with the addition of 0.5 mol % Mn_2O_3 . The single-crystal sample for the ESR measurements was $0.1 \times 0.1 \times 0.5$ mm³ in size. X-ray phase analysis performed on a DRON-4 diffractometer showed that the crystals grown belong to the $LuNbO_4$ phase.

The ESR spectra consisted of separate groups, determined by the position of the paramagnetic center in the crystal structure of lutetium niobate. The splitting of spectral lines within a group allowed us to estimate the values of ESR frequencies in a zero magnetic field, which turned out to be about 10 GHz, i.e., of the same order of magnitude as the frequencies observed for a Cr impurity in lutetium niobate single crystals [2].

For the experiments with dynamic alignment of nuclei, we need to know the NQR spectra at temperatures of several Kelvin. The entire NQR spectrum of ^{175}Lu was first measured on ceramic samples of lutetium niobate in liquid nitrogen temperature range [4]. The spectrum consists of three NQR lines correspond-

¹⁷⁵Lu NQR data for LuNbO₄ at different temperatures

T, K	NQR frequencies (linewidths), MHz			η	eQq , MHz
	Transition ($ m\rangle \longleftrightarrow m + \Delta m\rangle$)				
	1/2 \longleftrightarrow 3/2*	3/2 \longleftrightarrow 5/2	5/2 \longleftrightarrow 7/2		
12**, 20***	80.4	69.7 (1.3)**	108.8(1.1)***	0.715 ± 0.014	536.8 ± 5.0
30	80.4	69.7 (1.2)	108.7 (1.0)	0.715 ± 0.014	536.4 ± 5.0
50	80.2	69.5 (1.0)	108.5 (1.0)	0.715 ± 0.014	535.3 ± 5.0
77	80.6	69.5 (1.2)	108.3 (1.3)	0.720 ± 0.014	535.4 ± 5.0
160	–	68.5 (1.0)	–	–	–

* The data in this column are calculated from the middle and upper frequencies.

** The middle resonance frequency in the first row was measured at 12 K.

*** The upper resonance frequency in the first row was measured at 20 K.

ing to the single crystallographically inequivalent position of lutetium in the niobate structure. The ¹⁷⁵Lu nucleus has the nuclear spin $I = 7/2$. Hence, any crystallographically nonequivalent position of the ¹⁷⁵Lu nucleus in the crystal structure gives rise to three resonance lines corresponding to the changes in the absolute value of the magnetic quantum number $|m\rangle \longleftrightarrow |m + \Delta m\rangle$, where $\Delta m = 1$ for the allowed transitions.

In this paper, we report for the first time the data on the ¹⁷⁵Lu NQR spectra of a lutetium niobate single crystal recorded at temperatures different from those in the liquid nitrogen temperature range (see table). This single crystal with a volume of about 1 cm³ was grown by us previously and was already used in the ESR experiments reported in [2]. The low-temperature experimental NQR data were obtained for the middle and upper NQR lines corresponding to the 3/2 \longleftrightarrow 5/2 and 5/2 \longleftrightarrow 7/2 transitions, respectively. Using the experimental data for these lines, we calculated the lower frequency corresponding to the 1/2 \longleftrightarrow 3/2 transition, the quadrupole coupling constant eQq , and the anisotropy parameter characterizing the asymmetry of the electric-field gradient in the crystal, $\eta = (q_{xx} - q_{yy})/q_{zz}$. All these results are listed in the table. The NQR data obtained demonstrate that the NQR frequencies remain nearly constant below 50 K. This result indicates the absence of any significant anharmonicity at low temperatures and instabilities of the crystal structure with respect to phase transformations.

Thus, sufficiently high (>10 GHz) ESR frequencies in a zero magnetic field and high (about 100 MHz) and

nearly temperature-independent NQR frequencies for ¹⁷⁵Lu demonstrate the possibility of using LuNbO₄ crystals doped with Mn²⁺ ions as a working medium in experiments with dynamic alignment of nuclei.

ACKNOWLEDGMENTS

We are grateful to A.A. Gippius and E.N. Morozova (Faculty of Physics, Moscow State University) for measuring the ¹⁷⁵Lu NQR spectra of the lutetium niobate single crystal at low temperatures.

This work was supported by the Russian Foundation for Basic Research, project no. 03-02-16050.

REFERENCES

1. V. A. Atzarkin, A. L. Barabanov, A. G. Beda, and V. V. Novitsky, Nucl. Instrum. Methods Phys. Res., Sect. A (in press).
2. A. G. Beda, A. A. Bush, A. F. Volkov, and V. F. Meshcheryakov, Kristallografiya **47** (2), 357 (2002) [Crystallogr. Rep. **47**, 320 (2002)].
3. A. L. Barabanov, A. G. Beda, and A. F. Volkov, in *Proceedings of the X International Seminar on Interaction of Neutrons with Nuclei, Dubna, May, 2002* (JINR, Dubna, 2003), p. 26 [in Russian].
4. A. F. Volkov, L. A. Ivanova, Yu. N. Venevtsev, and L. L. Rappoport, Zh. Fiz. Khim. **56**, 1002 (1982).

Translated by K. Kugel

PHYSICAL PROPERTIES OF CRYSTALS

Electrostatic Model of the α -LiIO₃ Pyroelectric

A. V. Yatsenko

Taurida National University, Yaltinskaya ul. 4, Simferopol, 95007 Ukraine

e-mail: lab2@crimea.edu

Received January 26, 2005

Abstract—The range of possible combinations of the components of the electronic-polarizability tensors of oxygen and iodine ions and the effective charges of these ions is established on the basis of the experimental study of the parameters of the electric-field gradient tensor at ⁷Li nuclei in an α -LiIO₃ crystal and the calculation of the electric-field gradient from the classical electrostatic model. The I–O bonds in α -LiIO₃ are shown to be mixed ionic-covalent bonds with low ionicity. Spontaneous polarization of the crystal is estimated. © 2005 Pleiades Publishing, Inc.

INTRODUCTION

The hexagonal modification of lithium iodate (α -LiIO₃) shows a specific set of electrical, thermal, and optical properties, which makes it possible to use α -LiIO₃ crystals in acoustoelectronic and nonlinear optical devices [1]. A peculiarity of this crystal is the high ionic conductivity along the polar axis at $T = 293$ K, which results in a fast internal screening of the spontaneous polarization and makes it impossible to measure this characteristic exactly [2]. It has been found that high ionic conductivity greatly affects not only electrical but also some optical properties of lithium iodate [3]. In view of these circumstances, α -LiIO₃ is an interesting object for the computer simulation of its physical properties and the specific features of its structure.

Computer simulation of the structure and specific features of various compounds, based on either quantum-mechanical [4] or electrostatic [5] approaches, has become widespread in recent years. The simulation based on the electrostatic approach requires complete information about the electrical characteristics of the ions entering into the composition of the crystal under study and the parameters of the ion–ion repulsion potential. In the case of α -LiIO₃, this information is contradictory and incomplete [6].

The objective of this study is to establish the range of possible effective charges of ions in α -LiIO₃ crystals and their dipole electronic polarizabilities with consideration of the anisotropy of the electronic polarizability of iodine ions. The criteria for testing the results were (i) agreement between the experimental (found by the NMR method) and calculated principal components of the electric-field gradient (EFG) tensor V_{zz} , at the ⁷Li nuclei [7] and (ii) analysis of the stability of Li⁺ ions.

CALCULATION OF THE ELECTRONIC POLARIZABILITY OF IONS IN α -LiIO₃

To calculate the electronic polarizabilities of ions in an α -LiIO₃ crystal, we used the method based on the analysis of the refractive indices of optically uniaxial crystals, which makes it possible to take into account the anisotropy of the electronic polarizability of ions [8]. This method applies the modified Lorentz–Lorenz equation

$$\frac{n_k^2 - 1}{n_k^2 + 2} = \frac{1}{3\epsilon_0} \sum_{i=1}^S N_i (\alpha_{\text{eff}})_{ik},$$

where n_k is the refractive index of the crystal for the light wave with the electric field oriented in the k direction, $(\alpha_{\text{eff}})_{ik}$ is the effective electronic polarizability of an ion of type i , and S is the number of structurally non-equivalent ions in the unit cell of the crystal. When the vector \mathbf{E} is parallel to the x axis of the crystal, the expression for $(\alpha_{\text{eff}})_{ix}$ has the form

$$\begin{aligned} (\alpha_{\text{eff}})_{ix} &= \sum_{l=1}^3 (\alpha_{ll})_i \cos^2 \theta_{lxi} \left[1 + \sum_{j=1}^S (T_{ijx})_x \right] \\ &+ \sum_{l=1}^3 (\alpha_{ll})_i \cos \theta_{lxi} \cos \theta_{lyi} \sum_{j=1}^S (T_{ijx})_y \\ &+ \sum_{l=1}^3 (\alpha_{ll})_i \cos \theta_{lxi} \cos \theta_{lzi} \sum_{j=1}^S (T_{ijx})_z, \end{aligned} \quad (1)$$

where $(\alpha_{ll})_i$ are the components of the electronic-polarizability tensor of an ion of type i in the system of eigenaxes and θ_{ljj} are the angles between the l th principal axis of the electronic-polarizability tensor and the direction f , where $f = x, y, z$. The structural sums $(T_{ijx})_x$,

$(T_{ijx})_y$, and $(T_{ijx})_z$ are defined as

$$(T_{ijx})_g = \frac{1}{4\pi\epsilon_0} \left[\sum_{l=3}^3 \sum_f (\alpha_{ll})_j \cos\theta_{lxj} \cos\theta_{lfx} \right. \\ \left. \times \sum_{m=1}^{M_j} \frac{3G_{ijm}F_{ijm} - \delta_{gf}R_{ijm}^2}{R_{ijm}^5} \right], \quad (2)$$

where $g = x, y, z$; R_{ijm} is the distance between a selected i -type ion and the m th j -type ion; G_{ijm} and F_{ijm} are the projections of the \mathbf{R}_{ijm} vector on the g and f directions; and δ_{gf} is the Kronecker delta. A similar expression for $(\alpha_{\text{eff}})_{iz}$ is obtained from (1) by the index permutation ($x \leftrightarrow z$).

As for LiNbO_3 , the electronic polarizability was calculated within the approximation of independent ion polarizability and within the bond-polarizability approximation [8]. In the first case, the induced dipole electric moments of the ions are considered to be independent, which is correct for purely ionic bonding. When the bond-polarizability approximation is used, the electronic polarizability of short bonds (I–O) is considered. This polarizability is the sum of the independently determined electronic polarizabilities of I and O ions. During calculation of the structural sums (2), the dipole interaction of ions in the short bonds I–O is neglected.

In the calculations, we used the data on the α - LiIO_3 structure obtained in [9] and the following values of the ordinary (n_o) and extraordinary (n_e) refractive indices of the crystal: $n_o = 1.860$ and $n_e = 1.719$ ($\lambda = 1060$ nm) [10]. The electronic polarizability of Li^+ ions (α_{Li}) was taken to be $0.032 \times 10^{-24} \text{ cm}^3$.

The first attempt to determine the range of possible values of effective charges of the ions and their electronic polarizabilities in lithium iodate, performed under the assumption of isotropic electronic polarizability of I ions [6], was unsuccessful. Calculation of the EFG at ^7Li nuclei using the results [6] showed that, for all sets of the electrical characteristics of the ions, the value of the principal component of the EFG tensor V_{zz} is several times larger than the experimental value. A possible reason for this difference is the ionic-covalent character of the bond between oxygen and iodine ions, which leads to the anisotropy of the electronic polarizability of iodine ions owing to the developed electron shell of the I ion.

On the basis of the symmetry of the IO_3^- group (Fig. 1), one can assume that the principal axis “3” of the EP tensor of O^{2-} ions is directed along the I–O bond, while the principal axis of the EP tensor of I ions is directed along the polar axis c of the crystal. The corresponding EP tensors were assumed to be axially symmetric. The sets of possible combinations of the principal components of the EP tensors calculated in the

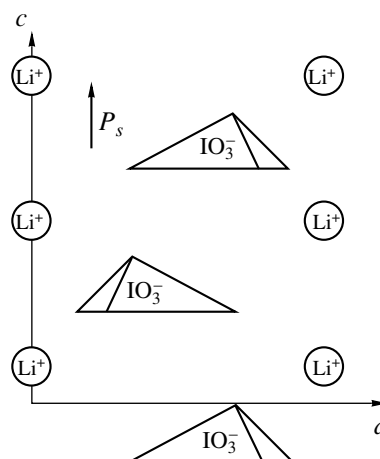


Fig. 1. Orientation of IO_3^- groups in the α - LiIO_3 structure (projection on the (101) plane).

bond-polarizability approximation for oxygen and iodine ions are listed in the table. Further analysis showed that the electronic polarizabilities of ions calculated in the independent-ion polarizability approximation do not satisfy simultaneously the conditions for the stability of Li^+ ions and the agreement between the calculated and experimental values of the EFG tensor at ^7Li nuclei.

EXPERIMENTAL STUDY OF THE ELECTRIC-FIELD GRADIENT AT ^7Li NUCLEI IN α - LiIO_3

Experimental NMR study of ^7Li (with spin $I = 3/2$) in a nominally pure α - LiIO_3 single crystal was performed on a continuous NMR spectrometer with an autodyne detector. It is known that the NMR spectrum of ^7Li in α - LiIO_3 has a complex structure [11]. Therefore, the emphasis was on the study of the orientation dependence of the quadrupole splitting of the NMR spectrum, which generally yields unambiguous information about the EFG tensor at the nuclei under study. The ^7Li NMR spectrum at $\theta = 0^\circ$ (θ is the angle between the crystallographic axis c and an external magnetic field B_0) is shown in Fig. 2.

The fine structure of the spectrum may result from the existence of several local minima of the potential energy of the Li^+ ion in the LiO_6 octahedron, which are related to the symmetry axis c of the crystal or located along this axis. These minima are occupied by Li^+ ions with different probabilities. If the potential barrier is not high, the disordering of Li^+ ions will be dynamical [12] and the NMR spectrum will correspond to the axial symmetry of the EFG tensor. As a result, the NMR spectrum will be a superposition of several quadrupole triplets with different splittings, obeying the $(3\cos^2\theta - 1)$ law. This is precisely what is observed experimentally.

Relationship between the principal components of the electronic-polarizability tensors of O^{2-} ions, α_{11} and α_{33} , and I ions, $\alpha_{xt}(I)$ and $\alpha_{zz}(I)$. The data are given in 10^{-24} cm^3

$\alpha_{11}(I)$	$\alpha_{33}(I)$								
	0.125	0.187	0.25	0.375	0.5	0.75	1.00	1.25	1.5
0.125	2.100	2.063	2.025	1.955	1.888				
	2.500	2.528	2.568	2.642	2.712				
0.187	2.110	2.073	2.035	1.963	1.895				
	2.441	2.481	2.521	2.599	2.670				
0.250	2.123	2.084	2.045	1.972	1.903				
	2.388	2.430	2.472	2.551	2.624				
0.375	2.149	2.108	2.068	1.991	1.918	1.783	1.657		
	2.280	2.327	2.371	2.455	2.536	2.683	2.819		
0.50	2.180	2.136	2.094	2.013	1.937	1.797	1.667	1.546	1.434
	2.163	2.215	2.263	2.352	2.440	2.596	2.741	2.873	2.996
0.75	2.261	2.210	2.160	2.068	1.984	1.830	1.691	1.563	1.451
	1.895	1.957	2.019	2.128	2.227	2.409	2.570	2.716	2.827
1.00	2.395	2.324	2.260	2.148	2.048	1.874	1.722	1.587	1.461
	1.537	1.628	1.712	1.852	1.978	2.196	2.383	2.547	2.697
1.25					2.145	1.935	1.764	1.615	1.482
					1.669	1.947	2.168	2.360	2.528
1.5						2.028	1.822	1.655	1.509
						1.633	1.917	2.145	2.340
1.75						2.222	1.913	1.711	1.546
						1.133	1.595	1.894	2.125
2.00							2.097	1.798	1.600
							1.100	1.569	1.873

* Top and bottom values in the table cells correspond to α_{11} and α_{33} , respectively.

If this model is taken as a basis, one can determine the principal value of the EFG tensor V_{zz} at ${}^7\text{Li}$ nuclei from the maximum splitting $\Delta\nu((51 \pm 1) \text{ kHz})$ of the quadrupole satellites at $\theta = 0^\circ$:

$$|V_{zz}| = (\Delta\nu h)(eQ)^{-1}(1 - \gamma_\infty)^{-1},$$

where h is Planck's constant, eQ is the quadrupole moment of ${}^7\text{Li}$ nuclei, $(1 - \gamma_\infty)$ is the antiscreening factor, and the z axis coincides with the c axis of the crystal. Using the values $eQ = 0.036|e| \times 10^{-24} \text{ cm}^2$ [13] and $(1 - \gamma_\infty) = 0.740$ [14], we find that $|V_{zz}| = (0.784 \pm 0.016) \times 10^{20} \text{ V/m}^2$.

CALCULATION OF THE ELECTRIC-FIELD GRADIENT AT ${}^7\text{Li}$ NUCLEI AND ANALYSIS OF THE STABILITY OF Li^+ IONS IN $\alpha\text{-LiIO}_3$

In the case of the mixed ionic-covalent character of the I-O bond, the effective charges of iodine and oxygen ions differ from their formal values. The effective charge of Li^+ ions was taken to be $0.98|e|$ ($|e|$ is the absolute value of the electron charge), while that of the iodine ion (q_I) was varied in the range $(1.0-4.0)|e|$ provided that the electroneutrality of the unit cell is maintained. The ionic contribution to the local electric field and the electric-field gradient at the ions of the $\alpha\text{-LiIO}_3$ crystal lattice were calculated by the transient-region

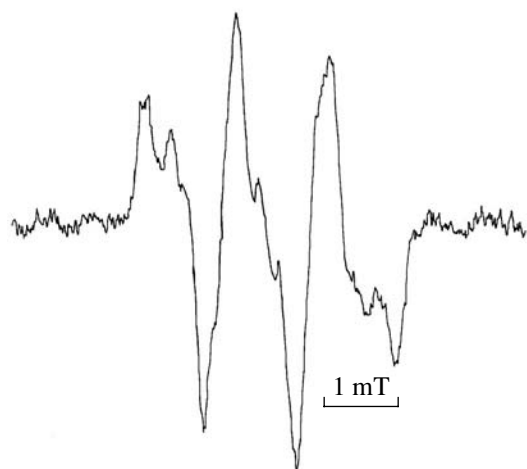


Fig. 2. NMR spectrum of ^7Li in an undoped $\alpha\text{-LiIO}_3$ crystal at $\theta = 0^\circ$.

method [15]; the dipole contribution, by the standard iterative procedure.

It was found that, at $q_1 > 1.6|e|$, the calculated values of V_{zz} are much higher than the experimental ones (at reasonable values of the electronic polarizability of iodine ions). Therefore, further analysis was carried out for $1.00|e| \leq q_1 \leq 1.60|e|$. The calculated values of EFG at ^7Li nuclei for one of the sets of effective charges are shown in Fig. 3.

Using these results, one can select the sets of the electronic polarizabilities of iodine and oxygen ions for which the calculated and experimental values of the EFG at ^7Li nuclei are equal. The data obtained can be represented as the dependence of one component of the EP tensor of iodine ions (α_{xx}) on q_1 at fixed values of α_{zz} . These dependences are shown in Fig. 4.

For further analysis of these results, it is necessary to take into consideration some fundamental features of the anisotropy of the electronic polarizability of the ions forming mixed ionic-covalent bonds. On the basis of the configuration of the $(\text{IO}_3)^-$ complex, we may conclude that, by analogy with the LiNbO_3 crystal [8], the relation $\alpha_{33} > \alpha_{11}$ for the components of the EP tensor of oxygen ions must hold true. Taking into account the deformation of the outer electron shells of iodine ions, which is caused by their overlap with the outer electron shells of oxygen ions, we may suggest that the condition $\alpha_{zz} \geq \alpha_{xx}$ for the principal components of the EP tensor of iodine ions must be satisfied. The region in which this condition is met is located in Fig. 4 below the dotted line. Note that, in the same region (see table), the condition $\alpha_{33} \geq \alpha_{11}$ is also satisfied.

As can be seen from Fig. 4, the region of the combinations of the effective charges of the ions and the sets of the electric polarizabilities of oxygen and iodine ions, in which the calculated and experimentally found

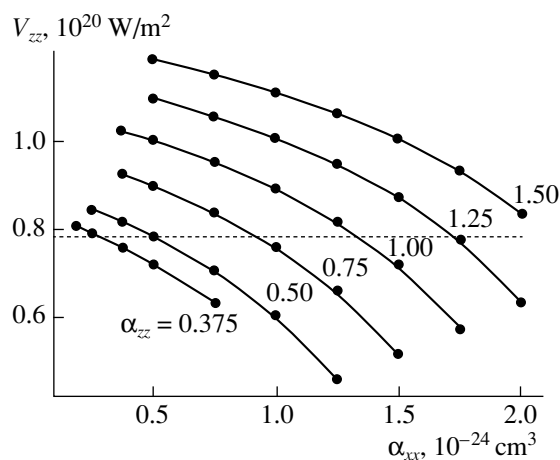


Fig. 3. Dependences of the principal component of the tensor of EFG at ^7Li nuclei in an $\alpha\text{-LiIO}_3$ crystal on α_{xx} at $q_1 = 1.15|e|$ for some values of α_{zz} (shown in the figure). The dotted line shows the experimental value of V_{zz} .

values of V_{zz} at ^7Li nuclei are in agreement, corresponds to a low (lower than $1.25|e|$) effective charge of the iodine ions. This is consistent with the essentially covalent character of the I–O bond and was initially assumed in the model used.

The results obtained were additionally verified by considering the stability of the Li^+ ion in the LiO_6 octahedron. The balance equation for the forces acting on the Li^+ ion has the form

$$q_{\text{Li}}E_z(\text{Li}) + p_z(\text{Li})V_{zz}(\text{Li}) + F_z(\text{Li}) = 0, \quad (3)$$

where $E_z(\text{Li})$ is the z component of the field E_{loc} at the Li^+ ion, $p_z(\text{Li})$ is the z component of its dipole moment, and $F_z(\text{Li})$ is the resultant repulsive force determined by the distortion and overlap of the electron shells of the

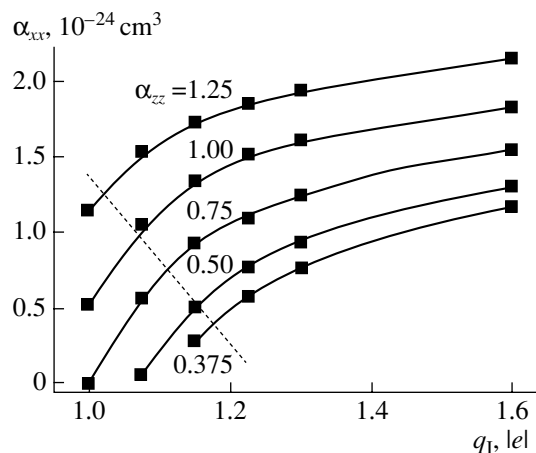


Fig. 4. Dependences of α_{xx} on q_1 for some values of α_{zz} , provided that the experimental and calculated values of V_{zz} at ^7Li nuclei are equivalent. The dotted line connects the points with $\alpha_{xx} = \alpha_{zz}$.

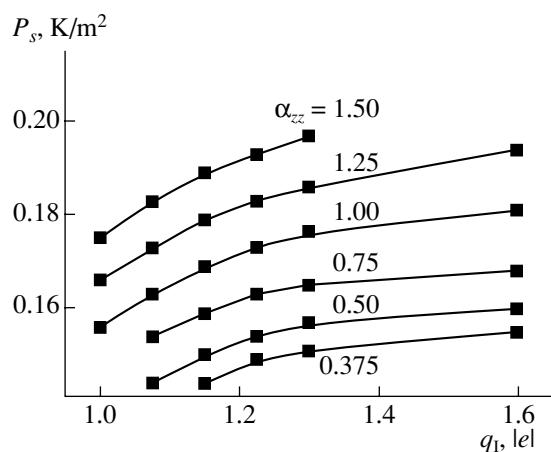


Fig. 5. Dependences of the spontaneous polarization of an α -LiIO₃ crystal on the effective charge of I ions for different sets of the components of the electronic-polarizability tensors of oxygen and iodine ions.

ions in the LiO₆ octahedron. The repulsive force F_r between the Li⁺ and O²⁻ ions was assumed to have the Born-Mayer form:

$$F_r = -A\rho^{-1}\exp(-r\rho^{-1}), \quad (4)$$

where A and ρ are the parameters of the repulsive potential and r is the distance between the centers of the outer electron shells of the ions. For evaluation, we used the following parameters of the repulsive potential: $A = 816$ eV and $\rho = 26.0$ pm, which are characteristic of the Li⁺-O²⁻ interaction in the LiNbO₃ crystal [16]. It was found that, for the set of the electrical parameters of the ions satisfying the equivalence of the parameters of the EFG tensor at ⁷Li nuclei, condition (3) is satisfied with an error no larger than 15% of the maximal term.

ESTIMATION OF THE SPONTANEOUS POLARIZATION OF α -LiIO₃ CRYSTALS

To determine the relationship between the possible combinations of the sets of effective charges and electronic polarizabilities of ions in an α -LiIO₃ crystal, we only used three experimentally determined parameters: the ordinary and extraordinary refractive indices and the EFG at ⁷Li nuclei. If the spontaneous polarization P_s of this crystal were known, one would be able to narrow the set of possible combinations of effective charges and electric polarizabilities of the ions additionally [7]. Discussion on the value of P_s for α -LiIO₃ crystals has been underway for a long time already. Various estimates of P_s are in the range (0.17–1.2) C/m² [17, 18, 19]. Using the data obtained in this study, it is easy to estimate the range of the values of P_s corresponding to the sets of electronic polarizabilities and q_{eff} of the ions shown in Fig. 4. The calculation was performed by the

standard formula [20]

$$P_s = \frac{1}{V} \left[\sum_i^N (q_i d_i + p_i) \right],$$

where V is the unit-cell volume, N is the number of ions in the unit cell, q_i is the effective charge of the i th ion, d_i is the displacement of the i th ion along the polar axis with respect to the nonpolar position, and p_i is the projection of the induced dipole moment of the i th ion on the polar axis.

The calculation results are shown in Fig. 5. It is worth noting that the ionic and dipole contributions to P_s have opposite signs, the dipole contribution being dominant. As can be seen from Fig. 5, the calculated values of P_s are in the range 0.14–0.20 C/m². However, with regard to the analysis of possible relations between α_{xx} and α_{zz} (see above), this range must be narrowed to 0.14–0.17 C/m².

CONCLUSIONS

One of the main results of this study is the calculation of the sets of the components of the tensors of dipole electronic polarizability of oxygen ions (α_{11} and α_{33}) and iodine ions (α_{zz} and α_{xx}) that are responsible for the optical properties of α -LiIO₃ crystals. On the basis of the experimental NMR study of ⁷Li in an undoped α -LiIO₃ single crystal, we refined the value of the principal component of the EFG tensor at ⁷Li nuclei and calculated the EFG from the structural data using the sets of the components of the EP tensors of oxygen and iodine ions. Comparison of the calculated and experimental data revealed that the effective charge of iodine ions is low (lower than 1.25 |e|) and, thus, the I–O bond is essentially covalent.

The results obtained can be used, in particular, in computer simulation of the crystal potential relief and analysis of the dynamics of ⁷Li ions, as well as in study of some optical properties of α -LiIO₃ single crystals.

ACKNOWLEDGMENTS

I am grateful to A.I. Barabash and D.F. Bais (Institute of Physics, National Academy of Sciences of Ukraine) for supplying the sample for NMR analysis and to A.V. Fomin for his help in the calculations.

REFERENCES

1. A. A. Blistanov, *Crystals in Quantum and Nonlinear Optics* (Izd. MISIS, Moscow, 2000) [in Russian].
2. K. I. Avdienko, S. V. Bogdanov, S. M. Arkhipov, *et al.*, *Lithium Iodate. Growth of Single Crystals, Their Properties and Applications* (Nauka, Novosibirsk, 1980) [in Russian].

3. Q. Sun, R. A. Rupp, M. Fally, *et al.*, *Opt. Commun.* **189**, 151 (2001).
4. J. Liu, C. Duan, Ossowski, *et al.*, *Phys. Chem. Miner.* **28**, 586 (2001).
5. S. V. Evdokimov and A. V. Yatsenko, *Kristallografiya* **48** (4), 594 (2003) [*Crystallogr. Rep.* **48**, 542 (2003)].
6. S. N. Khrykina and A. V. Yatsenko, *Funct. Mater.* **9** (1), 86 (2002).
7. A. V. Yatsenko, *Kristallografiya* **48** (3), 545 (2003) [*Crystallogr. Rep.* **48**, 500 (2003)].
8. A. V. Yatsenko, *Physica B (Amsterdam)* **305**, 287 (2001).
9. C. Svensson, J. Albertsson, R. Liminga, *et al.*, *J. Chem. Phys.* **78**, 7343 (1983).
10. A. A. Blistanov, V. S. Bondarenko, N. V. Perelomova, F. N. Strizhevskaya, V. V. Chkalova, and M. N. Shaskol'skaya, *Acoustic Crystals* (Nauka, Moscow, 1982) [in Russian].
11. D. F. Baïsa, D. L. Lifar, V. V. Safronov, and I. S. Rez, *Ukr. Fiz. Zh.* **18** (4), 583 (1973).
12. A. V. Yatsenko, H. M. Ivanova, and N. A. Sergeev, *Physica A (Amsterdam)* **240**, 254 (1997).
13. I. W. Hannel and J. Klinovski, *Fundamentals of Nuclear Magnetic Resonance* (Longman Scientific and Technical, Harlow, 1993).
14. K. D. Sen, A. Weiss, and P. C. Schmidt, *Hyperfine Interact.* **30**, 253 (1986).
15. A. V. Yatsenko, *Kristallografiya* **46** (2), 411 (2001) [*Crystallogr. Rep.* **46**, 361 (2001)].
16. H. Donnerberg, S. M. Tomlinson, C. R. A. Catlow, and O. F. Shirmer, *Phys. Rev. B: Solid State* **40** (17), 11909 (1989).
17. R. Liminga and S. C. Abrahams, *J. Appl. Crystallogr.* **9** (1), 42 (1976).
18. Yu. V. Shaldin, *Fiz. Tverd. Tela (Leningrad)* **19** (6), 1580 (1977) [*Sov. Phys. Solid State* **19**, 922 (1977)].
19. R. Poprawski, J. Shaldin, and S. Matyjasik, *Phys. Status Solidi A* **90**, 167 (1985).
20. S. C. Abrahams, *Acta Crystallogr. A* **50**, 658 (1994).

Translated by A. Zolot'ko

PHYSICAL PROPERTIES
OF CRYSTALS

Slip and Cleavage Systems in the New Crystal $\text{Li}_6\text{YB}_3\text{O}_9$

E. F. Dolzhenkova, V. N. Baumer, and A. V. Tolmachev

Institute for Single Crystals, National Academy of Sciences of Ukraine, pr. Lenina 60, Kharkov, 61001 Ukraine

e-mail: dol@isc.kharkov.ua

Received October 27, 2004

Abstract—The structure of single crystals of the double lithium–yttrium borate $\text{Li}_6\text{YB}_3\text{O}_9$ is investigated. It is shown that the cleavage planes are parallel to the layers that are located at the largest distance from each other and characterized by the weakest electrostatic interaction. Thus, cleavage of a crystal occurs through the longest Li–O bonds in the lithium five-vertex polyhedra and the bridge Y–O bonds. It is ascertained that slip in $\text{Li}_6\text{YB}_3\text{O}_9$ occurs in the planes that are most close packed with respect to oxygen ions, while the reason for the absence of plastic deformation at room temperature is that $(10\bar{2})$ B triangles impede the motion of $(\bar{3}01)$ B triangles. © 2005 Pleiades Publishing, Inc.

Crystals of complex borates of alkali and rare earth metals, which are promising scintillation materials for detection of thermal neutrons, have been described previously [1]. However, these crystals are characterized by high sensitivity to gamma radiation. Since neutron diffraction investigations are performed near a reactor under the conditions of intense background gamma radiation, the quality of neutron diffraction images is deteriorated. Single crystals of the double alkali–rare-earth borate, $\text{Li}_6\text{YB}_3\text{O}_9$ (LYBO), were successfully grown in [2]. These crystals are free of the above-mentioned drawback since they have a lower density and an almost twice lower atomic weight in comparison with the known alkali–rare-earth borates and are characterized by a lower sensitivity to gamma radiation. The optical and scintillation parameters of this crystal have been studied in detail [1–3]. However, the existing data on its crystallographic characteristics and real structure are insufficient.

In this study, we investigated the internal structure of a LYBO single crystal grown by the Czochralski method and considered the relationship between its crystallographic features with such characteristics as cleavage and slip.

Crystals of lithium–yttrium borate are isostructural to the crystals of the double alkali–rare-earth borates that are being studied at present: lithium–ytterbium ($\text{Li}_6\text{YbB}_3\text{O}_9$), lithium–holmium ($\text{Li}_6\text{HoB}_3\text{O}_9$), and lithium–gadolinium ($\text{Li}_6\text{GdB}_3\text{O}_9$) borates [4–7].

X-ray diffraction study of the LYBO crystal was performed on a Siemens D500 powder diffractometer (CuK_α radiation, Ni filter, $\lambda = 1.540629 \text{ \AA}$, $2\theta/\theta$ scan in the range $3^\circ < 2\theta < 120^\circ$). The basic crystallographic data for $\text{Li}_6\text{YB}_3\text{O}_9$ are $M_r = 306.98$, $T = 290(2) \text{ K}$, monoclinic system, sp. gr. $P 2_1/c$, $a = 7.1819(4) \text{ \AA}$, $b = 16.4247(10) \text{ \AA}$, $c = 6.6419(3) \text{ \AA}$, $\beta = 105.286(4)^\circ$, $V = 757.77(7) \text{ \AA}^3$, $Z = 4$, $F(000) = 576$, $d_{\text{calcd}} = 2.698 \text{ g/cm}^3$,

and $\mu(\text{CuK}_\alpha) = 11.218 \text{ mm}^{-1}$. Rietveld refinement of the unit-cell parameters was performed by the FullProf program [8–10] using the model structure proposed in [11]. Structural analysis was carried out using the PLATON program [12]. The illustrations were made in the Ball&Stick program [13, 14].

The specificity of the crystal structure of the double lithium–yttrium borate LYBO, as well as the known double alkali–rare-earth borates, is the complex structure of the unit cell, which contains four formula units. This circumstance suggests a large number of different ways of formation of interatomic bonds. Yttrium atoms are located in eight-vertex polyhedra. Lithium atoms occupy six independent positions, four of which are surrounded by five oxygen atoms and two are coordinated by four oxygen atoms. Yttrium and lithium polyhedra are linked into a three-dimensional framework by three boron triangles occupying independent positions. Two thirds of B triangles are parallel to the $(10\bar{2})$ plane and one third are parallel to the $(\bar{3}01)$ plane.

The interatomic Y–O distances in eight-vertex polyhedra range from 2.306 to 2.527 \AA . The interatomic distances in Li tetrahedra and Li five-vertex polyhedra range within 1.865–2.133 \AA and 1.892–2.562 \AA , respectively. The average value of the B–O bond lengths in B triangles is 1.375 \AA .

Subjected to an impact, crystals were cleaved along the atomic layers parallel to the $(10\bar{2})$, (010) , and (121) planes. Observation of the cleavage surfaces with an optical microscope revealed portions with almost perfect cleavage for all three planes. As is known, the cleavage phenomenon is related to the specific features of the internal structure of crystals: the cleavage planes are parallel to the most weakly bound atomic layers. Analysis of the LYBO structure showed that neighboring atoms in the layers parallel to the cleavage planes

are bound by the longest Li–O bonds in five-vertex Li polyhedra: Li(3)–O (2.268 Å) and Li(4)–O (2.418 Å). In the case of each of the three cleavage planes, cleavage occurs along the atomic layers spaced from each other at anomalously large distances.

Each Y atom is surrounded by eight O atoms from five B triangles. The six coordination sites of yttrium are occupied by three B triangles, in each of which two O atoms are bound to the Y ion. The remaining two of eight positions are occupied by B triangles, in which the O atom serves as a bridge between the two nearest Y ions. These bonds between yttrium and bridge oxygen are perpendicular to the atomic layers parallel to the cleavage planes. Cleavage occurs specifically through these bridge bonds, being facilitated by the electrostatic repulsion of two similarly charged Y ions.

Isostructural $\text{Li}_6\text{GdB}_3\text{O}_9$ single crystals are characterized by a similar cleavage system. The nature of cleavage in these crystals was studied in detail in [7]; it is the same as in the crystal under study.

As in the case of cleavage, slip of separate regions of a crystal with respect to each other without its break also occurs in the planes of most weakly bound layers. Such atomic layers are generally most closely packed. It is known that the plastic deformation of a crystal can be investigated by observing the dislocation motion [15–17].

The dislocation structure of the crystals studied was revealed by etching them in a 10% HNO_3 solution for 1.5 min. After the etching, contrast etch pits, pointed at the bottom in the form of parallelograms were observed in the (010) plane. The geometry of the etch pits completely corresponded to the crystallographic characteristics of the monoclinic (010) plane. In the case of isostructural $\text{Li}_6\text{GdB}_3\text{O}_9$ crystals, etch pits in the monoclinic plane had the same morphology and their correspondence with dislocations was established by comparison of the etching patterns in paired cleaved faces [18]. Therefore, we can state that the etching figures obtained in the monoclinic plane of the LYBO single crystal corresponded to dislocations.

The figures in the etching patterns form polygonal boundaries in the form of dislocation pile-ups, extended along the [100], [001], and [103] directions (Fig. 1). The etch pits in the rows parallel to the [100] and [001] directions are symmetric, whereas the apexes of the etch pits located in the rows aligned along the [103] direction are off-centered. These irregular etch pit rows may result from the dislocation slip in the (001) and (100) planes, which are perpendicular to the face under consideration and in the $(\bar{3}31)$ plane, which is inclined to the monoclinic plane. The inclined face $(\bar{3}31)$ crosses the monoclinic plane in such a way as the face $(\bar{3}01)$ perpendicular to the (010) plane in the [103] direction.

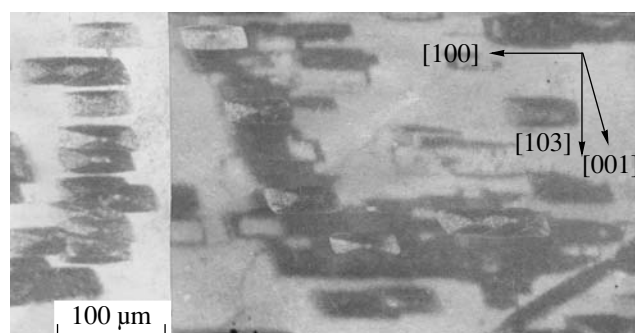


Fig. 1. Rows of etching figures in a $\text{Li}_6\text{YB}_3\text{O}_9$ crystal.

Etching figures can be used to trace the motion of dislocations in a plastically deformed region. It is known that selective etching near an indentation on a crystal face reveals a characteristic etching rosette, which corresponds to the traces of dislocations propagating in the slip planes to the crystal surface [15, 16]. After indentation of the LYBO crystal at room temperature and subsequent etching, characteristic dislocation rosettes were not observed and only the indenter impression was etched by the etchant. The dislocations formed under the action of a concentrated load, are localized only in a small volume near the indenter impression and are not revealed by etching. The absence of plastic deformation at room temperature seems to be a characteristic feature of double borates, whose structure includes the BO_3 group with covalent bonds. Indeed, it is known that in the crystal lattice of compounds with directed bonds, the Peierls force, which must be overcome to implement dislocation slip, is high and, hence, the dislocation mobility is low. To make it possible for dislocations to overcome high Peierls barriers, it is necessary to anneal the crystal to relax elastic stress near the indenter impression. At an annealing temperature of 700°C , dislocations begin to move in the slip planes. As a result, subsequent etching reveals dislocation regions in the form of rows of etching figures, forming rosette wings. The wings of the rosettes formed in the indentation are parallel to the [100], [001], and [103] directions and coincide with the orientation of polygonal boundaries. The above directions correspond to the intersections of the (001), (100), and $(\bar{3}31)$ planes with the monoclinic plane. Since the shape of the rosette (Fig. 2) is determined only by the symmetry of the slip planes in the crystal, we can say that the slip system in LYBO single crystals is as follows: $\{100\}\langle 001\rangle$, $\{001\}\langle 100\rangle$, and $\{\bar{3}31\}\langle 103\rangle$.

The etching-rosette wings have the same length; i.e., the mean free path of dislocations near the indentation is the same in all three directions. Therefore, the dislocation mobilities are the same in all slip planes. We can conclude that a preferred slip direction is absent in the crystal under study. The electrostatic attraction between the atomic layers parallel to the three cleavage planes is

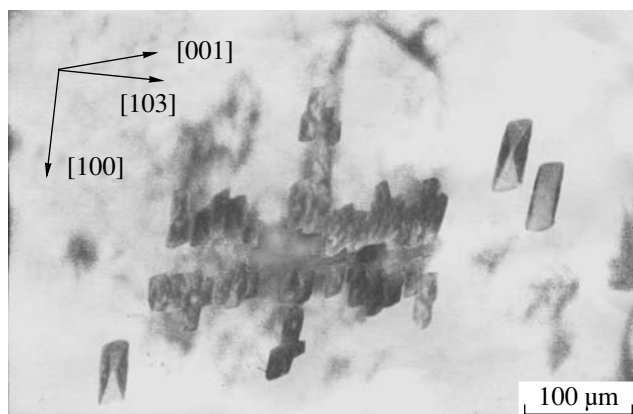


Fig. 2. Etching rosette at an indentation on the (010) face of a $\text{Li}_6\text{YB}_3\text{O}_9$ single crystal.

the same: at translation, similarly charged Li and Y atoms coincide with each other every second period. Therefore, the motion of one part of the crystal with respect to the other under the action of a concentrated load in the same in all slip directions.

The dislocations, whose motion leads to plastic deformation, move in strictly certain crystallographic planes and only in some crystallographic directions, depending on the internal structure of the crystal. The slip parameters are determined by the character of interatomic bonds and the positions of atoms in the crystal lattice. Since the largest ion in the LYBO structure is the oxygen ion, whose ionic radius is 1.36 \AA (for

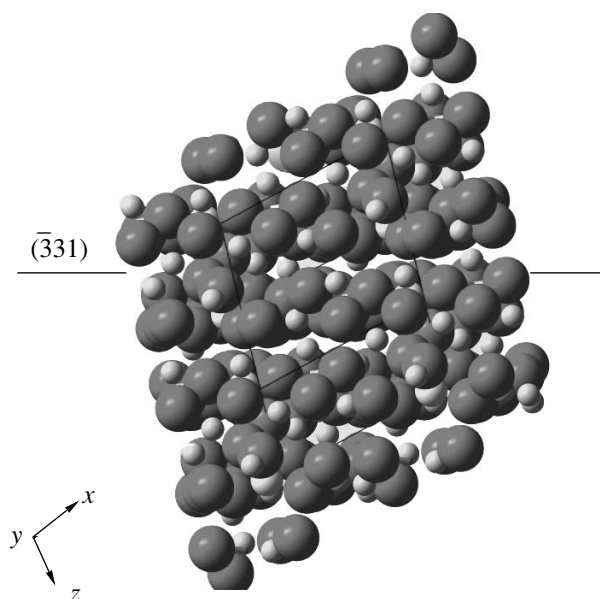


Fig. 3. Structure of $\text{Li}_6\text{YB}_3\text{O}_9$ along the $(\bar{3}31)$ plane: (●) Li, (●) Y, (●) B, and (●) O.

comparison, $R_{\text{Li}^+} = 0.68 \text{ \AA}$, $R_{\text{Y}^{3+}} = 0.97 \text{ \AA}$, and $R_{\text{B}^{3+}} = 0.20 \text{ \AA}$ [17], we can suggest that it is the translation of oxygen ions that determines the slip system in the crystal under consideration. Figure 3 shows that the (001), (100), and $(\bar{3}31)$ planes in LYBO are most close

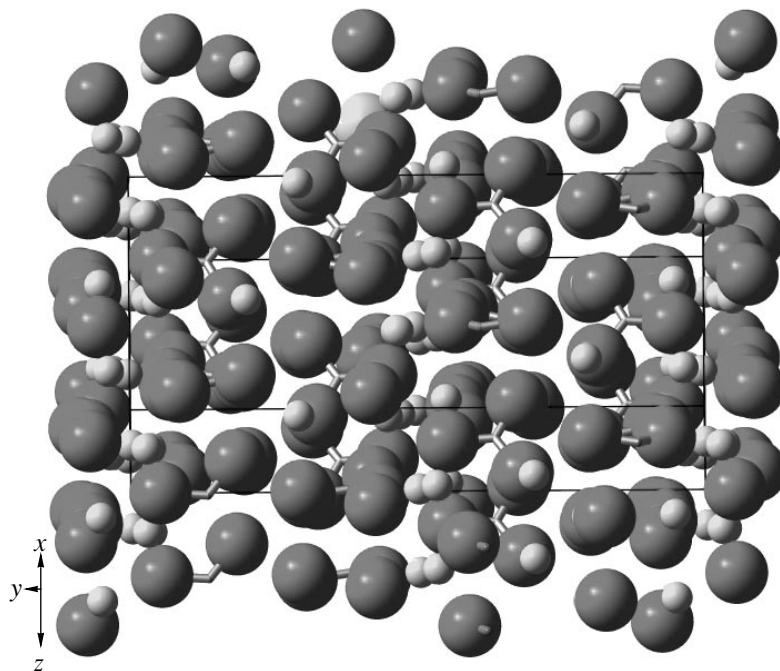


Fig. 4. Structure of $\text{Li}_6\text{YB}_3\text{O}_9$. The bonds between Li and Y atoms are not shown.

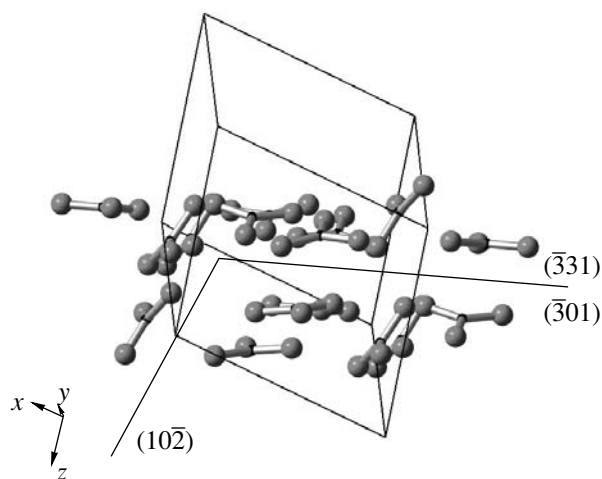


Fig. 5. Fragment of the crystal structure of $\text{Li}_6\text{YB}_3\text{O}_9$ showing the location of BO_3 groups in neighboring atomic layers parallel to the $(10\bar{2})$ and $(\bar{3}01)$ planes. Lithium and yttrium atoms are not shown. For clarity, the radii of O atoms are diminished.

packed with respect to oxygen ions, and the plastic deformation of this crystal is specifically the result of the displacement of atomic layers parallel to these planes with respect to each other. The highest reticular density of oxygen atoms is also observed in the $[100]$, $[001]$, and $[103]$ directions (Fig. 4).

The distinctive feature of LYBO crystals is that the plastic deformation occurs in them only during high-temperature annealing. At room temperature, the slip of atomic layers can be impeded by B triangles, whose rigid directed bonds allow for the motion of a B triangle only as an inseparable undistorted unit.

Figure 5 shows the location of B triangles in the atomic layers parallel to the $(\bar{3}31)$ slip plane. The oxygen atoms from the B triangles parallel to the $(10\bar{2})$ face of one of the layers are located in voids between the oxygen atoms belonging to the B triangles parallel to the $(\bar{3}01)$ face of the neighboring layer. Therefore, during the slip in the $(\bar{3}31)$ plane, the $(\bar{3}01)$ B triangles of one layer will impede the motion of the $(10\bar{2})$ B triangles of the neighboring layer and vice versa. Thus, the BO_3 groups from neighboring atomic layers, located in different crystallographic planes, i.e. $(\bar{3}01)$ and $(10\bar{2})$, impede each other's motion and, as a result, hinder slip in the crystal. A similar situation is observed

for the atomic layers parallel to the (100) and (001) planes. Thus, the slip of one part of an LYBO crystal with respect to another part cannot occur without significant distortion of B triangles, which is possible only at high temperatures.

REFERENCES

1. C. W. E. Van Eijk, in *Proceedings of the 4th International Conference on Inorganic Scintillators and Their Applications*, Ed. by Yin Zhiwen (Shanghai, 1997), p. 3.
2. J. P. Chaminade, O. Viraphong, F. Guillen, *et al.*, *IEEE Trans. Nucl. Sci.* **48** (4), Part 1, 1158 (2001).
3. C. W. E. Van Eijk, in *Proceedings of the 5th International Conference on Inorganic Scintillators and Their Applications*, Ed. by V. Mikhailin (Moscow, 2000), p. 22.
4. N. I. Leonyuk and L. I. Leonyuk, *Crystal Chemistry of Anhydrous Borates* (Mosk. Gos. Univ., Moscow, 1983) [in Russian].
5. G. K. Abdullaev and Kh. S. Mamedov, *Kristallografiya* **22** (2), 389 (1977) [*Sov. Phys. Crystallogr.* **22**, 220 (1977)].
6. G. K. Abdullaev, Kh. S. Mamedov, P. F. Rza-Zade, *et al.*, *Zh. Neorg. Khim.* **22** (12), 3239 (1977).
7. E. F. Dolzhenkova, V. N. Baumer, and S. I. Gordeev, *Kristallografiya* **48** (4), 628 (2003) [*Crystallogr. Rep.* **48**, 563 (2003)].
8. J. Rodriguez-Carvajal, in *Abstracts of the Satellite Meeting on Powder Diffraction of the 15th Congress of the IUCr, Toulouse, France, 1990*, p. 127.
9. J. Rodriguez-Carvajal and T. Roisnel, in *Commission for Powder Diffraction, International Union of Crystallography, Newsletter No. 20*, 1998.
10. J. Rodriguez-Carvajal, FULLPROF. Version May, 2003, LLB, private communication.
11. C. Y. Tu, A. D. Jiang, and Z. D. Luo, *J. Struct. Chem.* **8** (4), 215 (1989).
12. A. L. Spek, *PLATON. A Multipurpose Crystallographic Tool* (University of Utrecht, Netherlands, 1998).
13. J. K. Sung and O. C. Tadashi, private communication.
14. F. Izumi, private communication.
15. M. P. Shaskol'skaya, *Crystallography* (Vysshaya Shkola, Moscow, 1984) [in Russian].
16. K. Sangwal, *Etching of Crystals: Theory, Experiment, and Application* (North-Holland, Amsterdam, 1987; Mir, Moscow, 1990).
17. G. B. Bokiĭ, *Crystal Chemistry* (Nauka, Moscow, 1971) [in Russian].
18. E. F. Dolzhenkova, M. F. Dubovik, A. V. Tolmachev, and R. P. Yavetskiĭ, *Izv. Ross. Akad. Nauk, Neorg. Mater.* **40** (8), 764 (2004).

Translated by Yu. Sin'kov

PHYSICAL PROPERTIES
OF CRYSTALS

Theory and Computer Simulation of the Reflection
and Refraction of Bulk Acoustic Waves in Piezoelectrics
under the Action of an External Electric Field

S. I. Burkov*, B. P. Sorokin*, D. A. Glushkov*, and K. S. Aleksandrov**

* Krasnoyarsk State University, Svobodnyĭ pr. 79, Krasnoyarsk, 660041 Russia

e-mail: bsorokin@lan.krasu.ru

** Kirensky Institute of Physics, Siberian Division, Russian Academy of Sciences,
Akademgorodok, Krasnoyarsk, 660036 Russia

Received August 7, 2003; in final form, May 30, 2005

Abstract—The basic equations describing the conditions for reflection and refraction of bulk acoustic wave at the interface between acentric crystals subjected to the action of a uniform external electric field are reported. Numerical analysis of the effect of this field on the reflection and refraction anisotropy of bulk acoustic waves at the crystal/vacuum and piezoelectric/elastic-isotropic-medium interfaces is performed. © 2005 Pleiades Publishing, Inc.

INTRODUCTION

The theory of reflection and refraction of bulk acoustic waves (BAWs) at an interface between two nonpiezoelectric crystals was reported in [1, 2]. This theory was used, for example, to design polygonal ultrasonic delay lines. Further development of this theory is related to the consideration of the specific features of wave propagation in piezoelectrics [3]. The theory of propagation of bulk acoustic waves in piezoelectric crystals subjected to the action of an external electric field and stress was described in detail in [4, 5]. The effect of a uniform external electric field E on the propagation of surface acoustic waves (SAWs) in piezoelectric crystals was considered in [6]. In the first-order perturbation theory, the effect of \mathbf{E} is determined by changes in the conditions for BAW and SAW propagation, which are related to the nonlinearity of elastic, piezoelectric, and dielectric properties and the electrostriction. Therefore, the effect of \mathbf{E} can be calculated if the material constants of the nonlinear electromechanical properties are known. By date, complete sets of the coefficients of the nonlinear electromechanical properties have been investigated for some piezoelectric crystals (lithium niobate, crystals with sillenite structure, and langasite) [5, 7, 8].

REFLECTION AND REFRACTION OF ELASTIC
WAVES AT THE INTERFACE
BETWEEN PIEZOELECTRIC CRYSTALS
UNDER THE ACTION OF A DC ELECTRIC FIELD

Using the results of [5], we will derive necessary equations describing the effect of \mathbf{E} on the conditions

for the BAW reflection and refraction at an interface between two media. In the initial coordinate system, the wave equations for waves with small amplitudes in homogeneously deformed acentric media and the equation of electrostatics have the form [5]

$$\begin{aligned}\rho_0 \ddot{\tilde{\mathbf{U}}}_A &= \tilde{\boldsymbol{\tau}}_{AB,B}, \\ \tilde{\mathbf{D}}_{M,M} &= 0,\end{aligned}\quad (1)$$

where ρ_0 is the density of a unstrained crystal (initial state), $\tilde{\mathbf{U}}_A$ is the vector of dynamic elastic displacements (hereinafter, the sign \sim denotes the time-dependent quantities), $\boldsymbol{\tau}_{AB}$ is the tensor of thermodynamic stresses, and \mathbf{D}_M is the electric-displacement vector. A comma after an index denotes a spatial derivative and two periods above a variable denote the second derivative with respect to time. Latin coordinate indices run from 1 to 3. In what follows, summation over double indices is implied.

When the effect of \mathbf{E} is taken into account, the state equation for the dynamic components of thermodynamic stresses and the electric displacement have the form

$$\begin{aligned}\tilde{\boldsymbol{\tau}}_{AB} &= C_{ABCD}^* \tilde{\boldsymbol{\eta}}_{CD} - e_{NAB}^* \tilde{E}_N, \\ \tilde{D}_N &= e_{NAB}^* \tilde{\boldsymbol{\eta}}_{AB} + \boldsymbol{\varepsilon}_{NM}^* \tilde{E}_M,\end{aligned}\quad (2)$$

where $\boldsymbol{\eta}_{CD}$ is the strain tensor and the effective elastic, piezoelectric, and dielectric constants are determined

by the relations

$$\begin{aligned} C_{ABKL}^* &= C_{ABKL}^E + (C_{ABKLQR}^E d_{NQR} - e_{NABKL}) E \mathbf{M}_N, \\ e_{NAB}^* &= e_{NAB} + (e_{NABKL} d_{PKL} + H_{NPAB}) E \mathbf{M}_P, \\ \varepsilon_{NM}^* &= \varepsilon_{NM}^\eta + (H_{NMAB} d_{PAB} + \varepsilon_{NMP}^\eta) E \mathbf{M}_P. \end{aligned} \quad (3)$$

Here, d_{NQR} is the tensor of ‘‘linear’’ piezoelectric coefficients; C_{ABKLQR}^E , e_{NABKL} , ε_{NMP}^η , and H_{NPAB} are the nonlinear elastic, piezoelectric, dielectric, and electrostriction material tensors, respectively; \mathbf{M}_N is the unit vector of the external electric field, and E is the magnitude of the external electric field.

To consider the problem of the BAW reflection and refraction at an interface of two acentric media, let us choose the orthogonal coordinate system with the X_3' axis directed normally to the interface and the X_1' axis lying in the interface plane. It is assumed that an elastic wave is incident on the interface from the crystal occupying the half-space $X_3' < 0$. Solutions to the wave equation will be sought for in the form of plane waves. It is convenient to consider the conditions for the wave reflection and refraction using the expressions for a plane elastic harmonic wave and a wave of electrical potential, written in terms of the refraction vectors $\mathbf{m} = \mathbf{N}/v$ (\mathbf{N} is the unit vector of the wave normal, and v is the phase velocity of a BAW):

$$\begin{aligned} \tilde{U}_C &= \alpha_C \exp[i\omega(t - m_j x_j)], \\ \tilde{\varphi} &= \alpha_4 \exp[i\omega(t - m_j x_j)], \end{aligned} \quad (4)$$

where α_C and α_4 are the amplitudes of the elastic displacement and electrical potential, respectively.

Substituting expressions (4) into (1) and leaving only the terms linear in E , we obtain the system of four homogeneous equations [6]:

$$\begin{pmatrix} \Gamma_{11} - \rho_0 & \Gamma_{12} & \Gamma_{13} & \Gamma_{14} \\ \Gamma_{21} & \Gamma_{22} - \rho_0 & \Gamma_{23} & \Gamma_{24} \\ \Gamma_{31} & \Gamma_{32} & \Gamma_{33} - \rho_0 & \Gamma_{34} \\ \Gamma_{41} & \Gamma_{42} & \Gamma_{43} & \Gamma_{44} \end{pmatrix} \begin{pmatrix} \alpha_1 \\ \alpha_2 \\ \alpha_3 \\ \alpha_4 \end{pmatrix} = 0, \quad (5)$$

where the components of the modified Green–Christoffel tensor have the form

$$\begin{aligned} \Gamma_{BC} &= (C_{ABCD}^* + 2C_{ABFD}^E d_{JFC} M_J E) m_A m_D, \\ \Gamma_{B4} &= e_{IAB}^* m_I m_A, \\ \Gamma_{4B} &= \Gamma_{B4} + 2e_{PFD} d_{JDC} m_P m_F M_J E, \\ \Gamma_{44} &= -\varepsilon_{KLM}^\eta m_K m_L. \end{aligned} \quad (6)$$

The determinant of system (5) is a polynomial of power 8 with respect to the component m_3 of the refraction vectors of the reflected and refracted BAWs at a

given direction of an incident elastic wave. Generally, the values of m_3 may be complex due to the effect of total internal reflection [2]. In this case, the values of m_3 should have a negative imaginary part for the crystal occupying the lower half-space $X_3' < 0$ (reflected waves), and a positive imaginary part for the crystal in the upper half-space $X_3' > 0$ (refracted waves). As a result, the condition for the decay of reflected and refracted waves in the bulk of the corresponding crystals will be satisfied.

Determination of the refraction vectors \mathbf{m} makes it possible to obtain the values of the angles of reflection and refraction of BAWs and the corresponding phase velocities. However, the most important energy characteristics of reflection and refraction are the amplitude coefficients of the reflected and refracted waves, which characterize the distribution of the incident-wave energy between the reflected and refracted waves. To determine these coefficients, the boundary conditions should be formulated. In the case of a rigid acoustic contact between two crystals, the boundary conditions for the thermodynamic-stress tensor are reduced to the requirement for the continuity of the normal components of the stress tensors of reflected and refracted waves and the continuity of the elastic-displacement vectors [2]:

$$\begin{aligned} \tau_{IJ}^{(1)} n_J &= \tau_{IJ}^{(2)} n_J, \\ \mathbf{U}^{(1)} &= \mathbf{U}^{(2)}, \end{aligned} \quad (7)$$

where n_j is the normal unit vector on the interface. Taking into account the piezoelectric properties of the crystals, we have to formulate the boundary conditions for the electric-field characteristics. The conditions for the continuity of the tangential components of the electric field vector at the interface and the continuity of the normal components of the electric-displacement vector in the quasi-static limit can be written as

$$\begin{aligned} \varphi^{(1)} &= \varphi^{(2)}, \\ (\mathbf{D}^{(1)}, \mathbf{n}) &= (\mathbf{D}^{(2)}, \mathbf{n}). \end{aligned} \quad (8)$$

Substituting solutions (4) into Eqs. (7) and (8) and leaving only the terms linear in E , we obtain finally a system of linear equations with respect to the eight amplitude coefficients of the reflected and refracted waves:

$$\begin{aligned} \sum_{\mu=1}^4 (b_\mu G_{\mu B}^{(1)} - a_\mu G_{\mu B}^{(2)}) &= G_{0B}^{(2)}, \\ \sum_{\mu=1}^4 (\tilde{U}_B^{(\mu)} b_\mu - \tilde{U}_B^{(\mu)} a_\mu) &= \tilde{U}_B^0, \\ \sum_{\mu=1}^4 (b_\mu D_\mu^{(1)} - a_\mu D_\mu^{(2)}) &= D_0^{(2)}, \end{aligned} \quad (9)$$

where a_μ are the amplitude reflection coefficients and b_μ are the amplitudes of the refractive indices. In addition, the following designations are used:

$$G_{\mu B}^{(1,2)} = (C_{B3KL}^{(1,2)*} + 2d_{AKF}^{(1,2)} C_{3IFL}^{(1,2)E} M_A E) m_L^{(\mu)} \alpha_K^{(\mu)} + e_{P3B}^{(1,2)*} m_P^{(\mu)} \alpha_4^{(\mu)},$$

$$D_\mu^{(1,2)} = (e_{3KL}^{(1,2)*} + 2d_{JKP}^{(1,2)} e_{3PL}^{(1,2)} M_J E) m_L^{(\mu)} \alpha_K^{(\mu)} - \varepsilon_{3K}^{(1,2)*} m_K^{(\mu)} \alpha_4^{(\mu)}, \quad (10)$$

$$G_{0B}^{(2)} = (C_{B3KL}^{(2)*} + 2d_{AKF}^{(2)} C_{3IFL}^{(2)E} M_A E) m_L^0 \alpha_K^0 + e_{P3B}^{(2)*} m_P^0 \alpha_4^0,$$

$$D_0^{(2)} = (e_{3KL}^{(2)*} + 2d_{JKP}^{(2)} e_{3PL}^{(2)} M_J E) m_L^0 \alpha_K^0 - \varepsilon_{3K}^{(2)*} m_K^0 \alpha_4^0.$$

In (9) and (10), the superscript 1 corresponds to the crystal occupying the half-space $X_3' > 0$, the superscript 2 corresponds to the half-space $X_3' < 0$, the index 0 denotes the incident elastic wave, and the index μ denotes the types of the reflected and refracted elastic waves: a longitudinal (L) wave (1), a fast shear (FS) wave (2), and a slow shear (SS) wave (3).

When only the reflection of a wave from the crystal–vacuum interface is considered, it is necessary to change the boundary conditions. In this case, the stresses on the crystal surface should be absent; i.e.,

$$\sum_{J=1}^3 \tau_{3J} = 0|_{X_3=0}. \text{ The boundary conditions include}$$

also the requirement for continuity of the normal components of the electric displacement at the crystal–vacuum interface and the validity of the Laplace equation for the potential wave in a vacuum. The system of linear equations for the four amplitude coefficients can be written as

$$\sum_{\mu=1}^3 \{-a_\mu (C_{3KPI}^* \alpha_P^{(\mu)} + 2d_{AKF} C_{3KFI}^E M_A E) m_K^{(\mu)} - a_4 e_{K3I}^* m_K^{(\mu)} \alpha_4^{(\mu)}\} \quad (11)$$

$$= (C_{3KPI}^* \alpha_P^0 + 2d_{AKF} C_{3KFI}^E M_A E) m_K^0 - e_{K3I}^* m_K^0 \alpha_4^0,$$

$$\sum_{\mu=1}^3 \{-a_\mu (e_{3KL}^* + 2d_{JKP} e_{3PL} M_J E) m_L^{(\mu)} \alpha_K^{(\mu)} - a_4 (\varepsilon_{3K}^* m_K^{(\mu)} - i\varepsilon_0) \alpha_4^{(\mu)}\} \quad (12)$$

$$= (e_{3KL}^* + 2d_{JKP} e_{3PL} M_J E) m_L^0 \alpha_K^0 - \varepsilon_{K3}^* m_K^0 \alpha_4^0,$$

where ε_0 is the dielectric constant.

Note that these expressions for the boundary conditions are obtained for the case when a uniform external electric field is applied to the crystal and the edge

effects are neglected. The equations obtained take into account all changes in the configuration of the anisotropic continuous medium related to its static strain and, in particular, the changes in the crystal shape: extensions and rotations of elementary lines parallel to the sample edges [5].

CALCULATION OF THE EFFECT OF A DC ELECTRIC FIELD ON THE REFLECTION OF BAWs FROM THE FREE BOUNDARY OF A PIEZOELECTRIC CRYSTAL

As an example, we will consider the effect of a uniform external electric field on the reflection of BAWs from a free boundary of a cubic piezoelectric with symmetry 23. Let a wave be incident in the (010) plane (the sagittal plane). The normal to the interface coincides with the [001] direction. The dispersion equation for reflected BAWs (at $E = 0$) in the case of incidence of an L wave or an FS wave on the interface can be written as [3]

$$(C_{11}^E m_1^2 + C_{44}^E m_3^2 - \rho_0)(C_{44}^E m_1^2 + C_{11}^E m_3^2 - \rho_0) - (C_{12}^E + C_{44}^E)^2 m_1^2 m_3^2 = 0. \quad (13)$$

When a slow shear (SS) wave is incident on the interface, which is piezoelectrically active in the given sagittal plane and has a polarization directed along the [010] axis, i.e., orthogonally to the plane of incidence, the dispersion equation has the form

$$(C_{44}^E (m_1^2 + m_3^2) - \rho_0) \varepsilon_{11}^\eta (m_1^2 + m_3^2) - 4e_{14}^2 m_1^2 m_3^2 = 0. \quad (14)$$

Therefore, in the case of the incidence of an L wave of a FS wave (polarized in the plane of incidence), only L (quasi-longitudinal (QL)) and FS (fast quasi-shear (FQS)) waves will be reflected. In the case of incidence of a slow quasi-shear (SQS) wave, only an SQS wave is reflected, whose amplitude coefficient is very close to unity. However, owing to the piezoelectric activity of this wave, along with the elastic SQS wave, there is also a potential wave. Therefore, taking into account that the refraction vector of the reflected SQS wave is real, the amplitude coefficient for this wave is complex and its imaginary part characterizes the phase shift between the incident and reflected waves [3].

Application of an electric field to a crystal in the [001] direction, according to the Curie principle, decreases the crystal symmetry to the monoclinic class 2, in which the twofold symmetry axis is also directed along the [001] axis. As a result, new effective material constants (equal to zero in the absence of a field) are

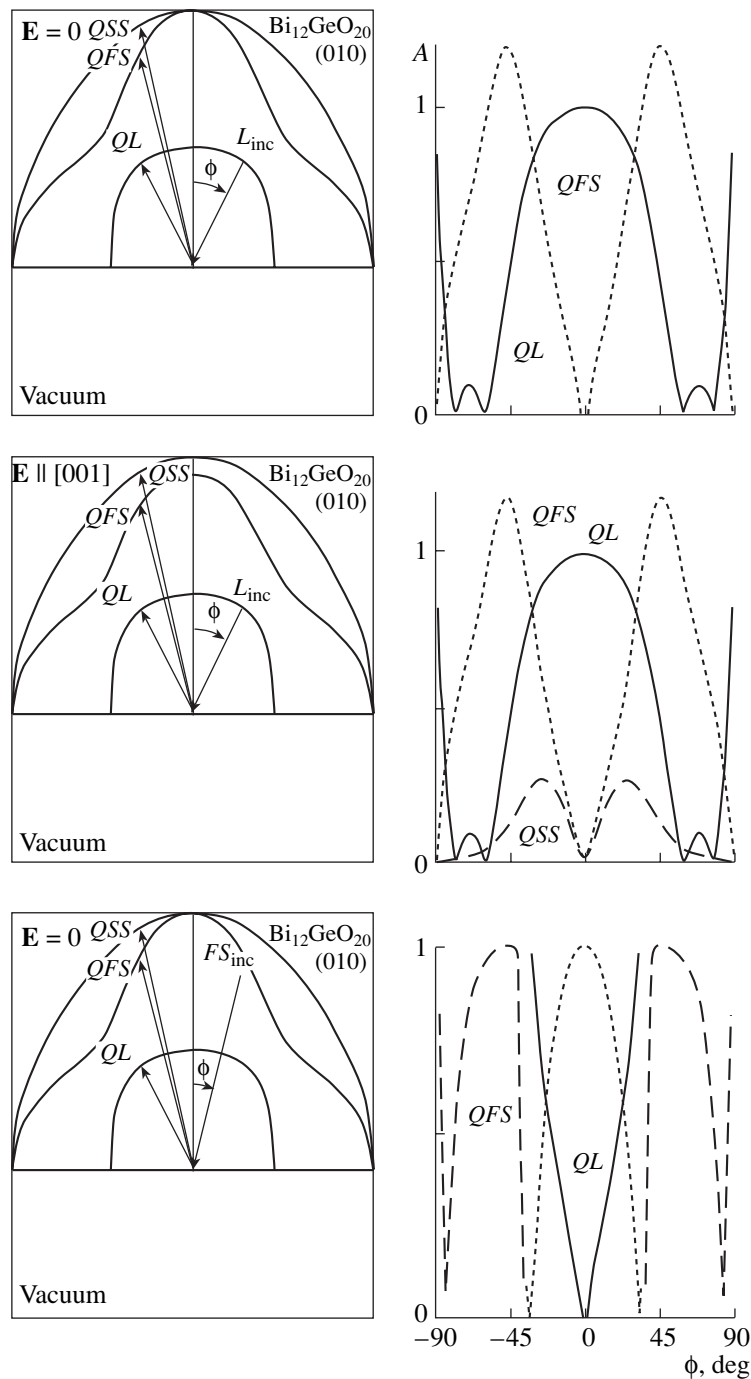


Fig. 1. Real parts of the amplitude reflection coefficients of BAWs reflecting from the germanosillenite-crystal/vacuum interface for the incidence in the plane (010).

induced:

$$\begin{aligned}\tilde{C}_{16} &= (C_{166}d_{14} - e_{124})E, & \tilde{C}_{36} &= (C_{144}d_{14} - e_{114})E, \\ \tilde{C}_{45} &= (C_{456}d_{14} - e_{154})E, & \tilde{e}_{15} &= (e_{156}d_{14} + H_{44})E, \\ \tilde{e}_{33} &= (e_{114}d_{14} + H_{11})E, & \tilde{e}_{31} &= (e_{124}d_{14} + H_{12})E.\end{aligned}\quad (15)$$

Thus, dispersion equations (13) and (14) become

polynomials of power 8 with respect to the components m_3 of the reflected waves. Figure 1 shows the real part of the amplitude reflection coefficients of BAWs in a $\text{Bi}_{12}\text{GeO}_{20}$ crystal at $\mathbf{E} \parallel [001]$ in the plane of incidence (010) for BAWs of the QL , FQS , and SQS types. When a QL wave is incident at an angle of 60° , transformation of reflected elastic waves occurs and only the FQS wave is reflected. In the case of incidence of an FQS

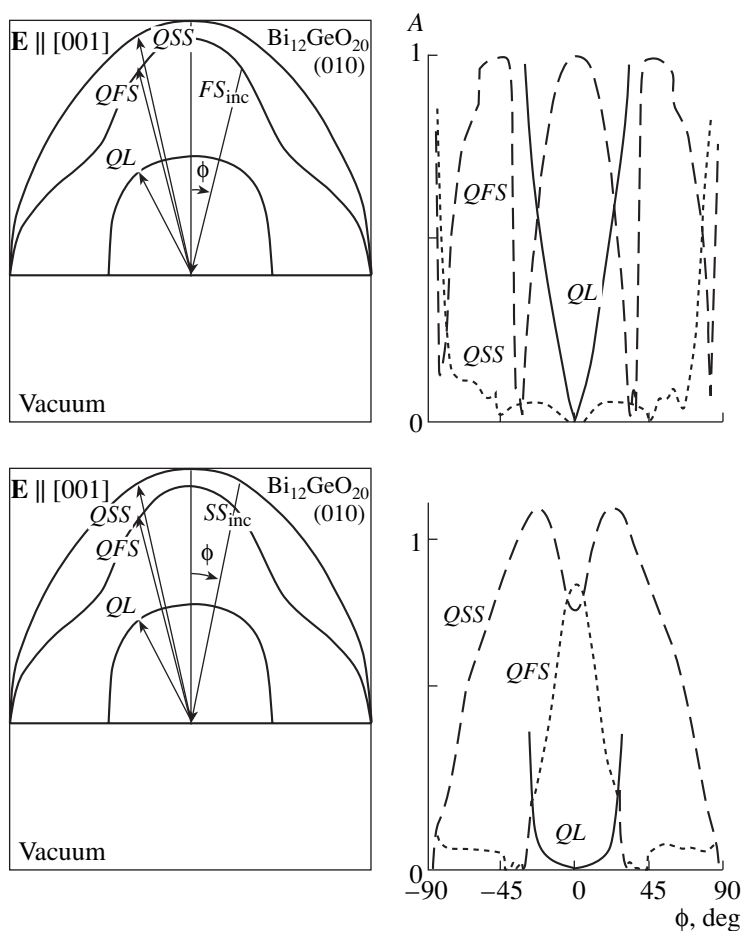


Fig. 1. (Contd.)

wave, for the reflected QL wave, beginning with an angle of incidence of 38° , the phenomenon of total internal reflection is observed. (The refraction vector of the elastic wave becomes complex.)

In the case of incidence of an SQS wave, application of an external electric field, which decreases the crystal symmetry, generates all three types of reflected waves. In the absence of a field directed along the normal to the free surface, there is an tangential acoustic axis [9]. Application of an electric field $\mathbf{E} \parallel [001]$, as discussed previously [10, 11], removes the degeneracy of shear waves in the $[001]$ direction. In this case, the initial acoustic axis is split into two conical axes lying in the (110) plane. Therefore, even normal incidence of an SQS wave leads to the generation of reflected shear waves of both types with real parts of the amplitude coefficients of 0.78 and 0.71 for the FS and SS waves, respectively. Note that, when an electric field is applied, the amplitude coefficients of reflected waves are always complex.

EFFECT OF A DC ELECTRIC FIELD ON THE REFLECTION AND REFRACTION OF BAWs AT THE INTERFACE BETWEEN AN ISOTROPIC ELASTIC MEDIUM AND A PIEZOELECTRIC CRYSTAL

Figure 2 shows the results of the calculation of the real parts of the amplitude reflection coefficients and amplitude refractive indices of BAWs in a system composed of fused quartz and germanosilicite $\text{Bi}_{12}\text{GeO}_{20}$ for the case when an external electric field is applied only to the $\text{Bi}_{12}\text{GeO}_{20}$ crystal along the twofold axis $[001]$, i.e., normally to the interface between these media. The cases of incidence of L and shear waves polarized either in the plane of incidence or normally to it are investigated. When $\mathbf{E} = 0$, for an incident L wave, there are only a reflected L wave and a shear wave (polarized in the plane of incidence) and a refracted L wave and an FS wave (polarized in the plane of incidence). A characteristic feature of this case is the transformation of the type of refracted waves since, at an angle of incidence of 58° , only the FS wave exists (from all refracted waves).

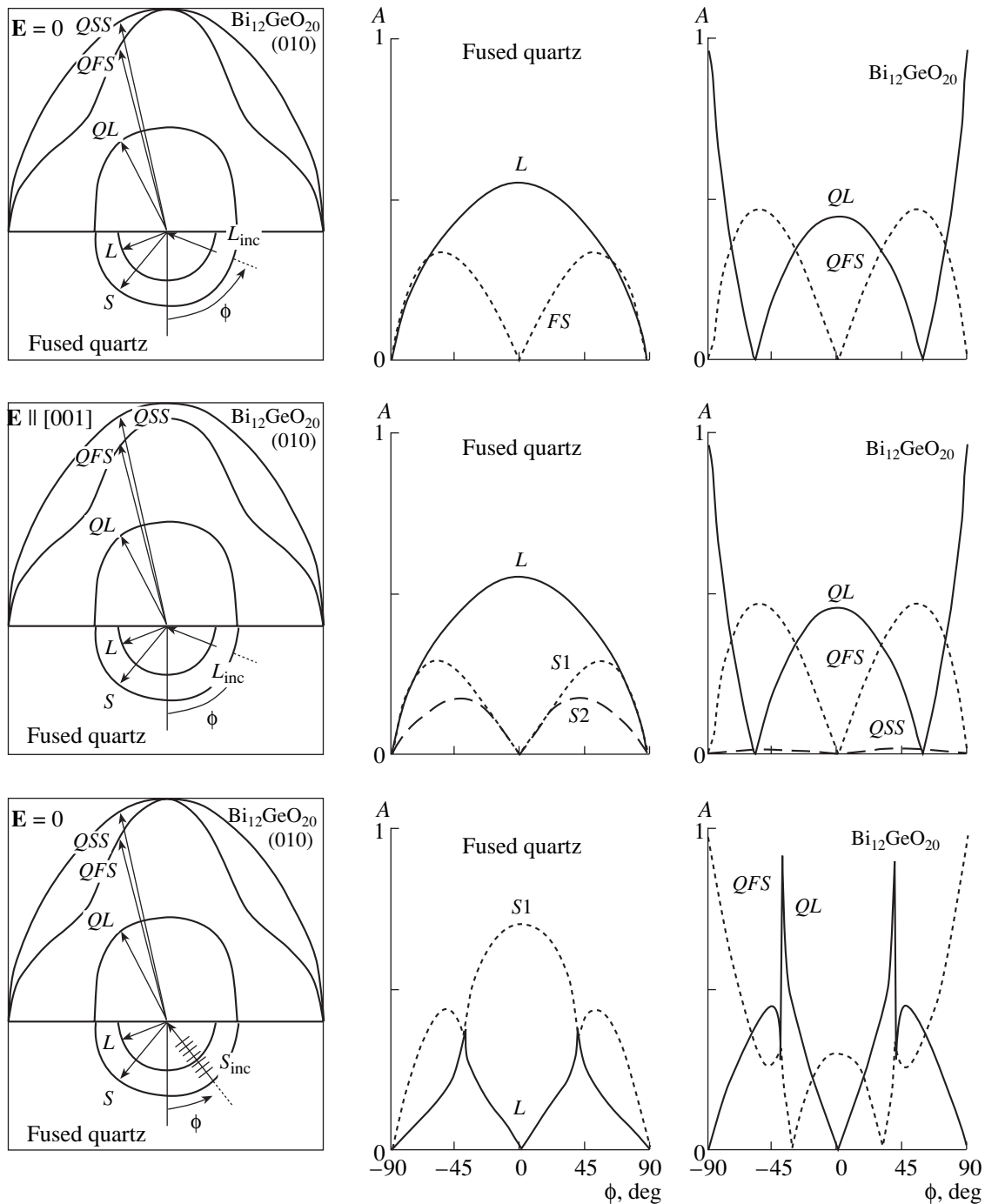


Fig. 2. Real parts of the amplitude reflection coefficients and amplitude refractive indices of BAWs incident on the fused-quartz/germanosillenite interface in the (010) plane. The case of incidence from the fused quartz.

A similar situation occurs when a shear wave polarized in the plane of incidence is incident on the interface. In this case, at an angle of incidence of 32° , there is only a refracted L wave. However, at an angle of incidence of 40° , the total internal reflection of this wave is observed.

When a shear wave polarized orthogonally to the plane of incidence is incident on the interface, the wave

of the same type is reflected. However, concerning refracted waves, there is only an SS wave in germanosillenite, which has a longitudinal piezoelectric activity. The piezoelectric activity of the SS wave leads to the generation of an electrostatic potential wave at the piezoelectric-crystal/isotropic-medium interface. This wave is not related to elastic vibrations in the isotropic medium and decays exponentially with an

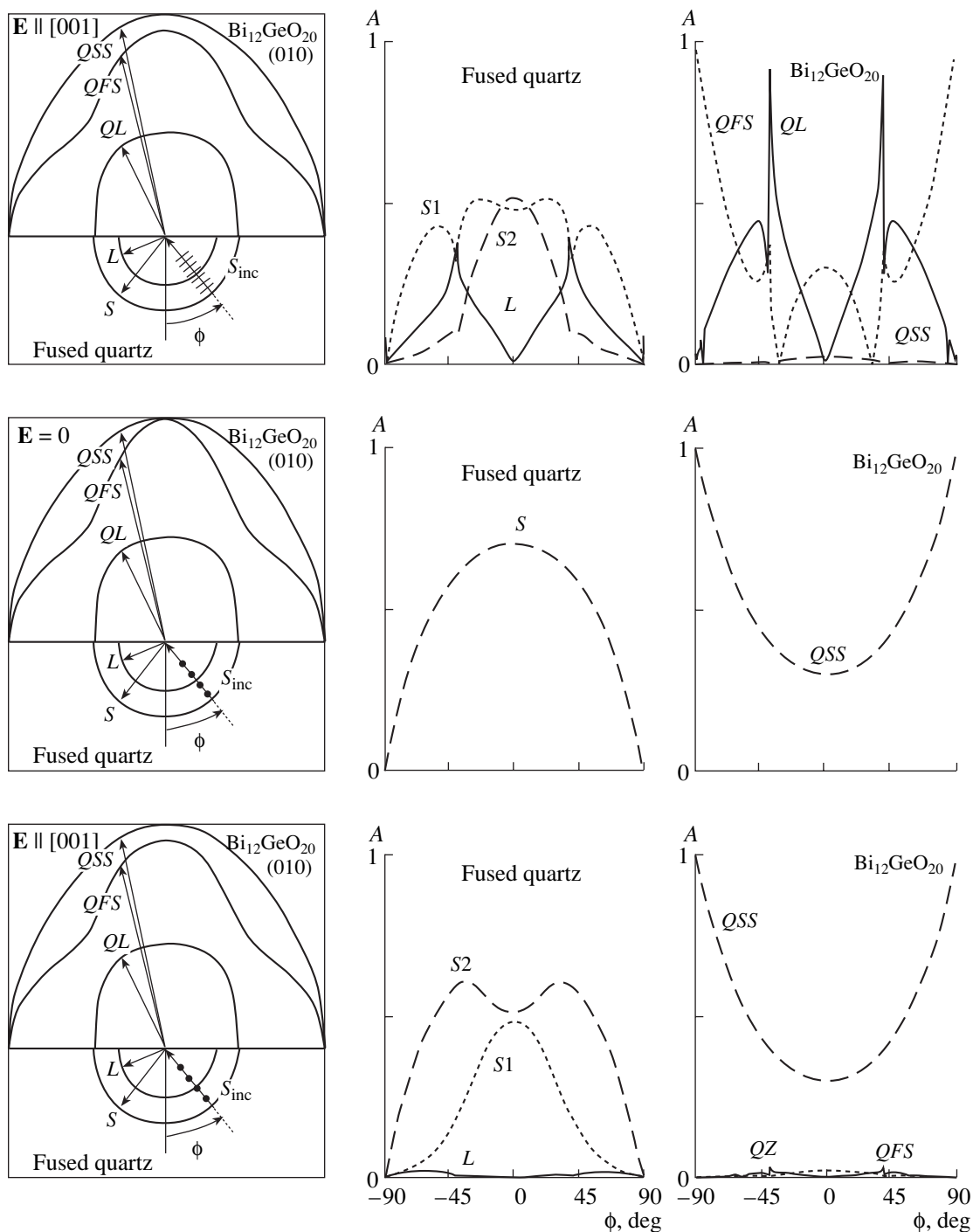


Fig. 2. (Contd.)

increase in the distance from the interface. As a result of the presence of a potential wave, the amplitude coefficient of the reflected elastic wave is a complex value and its refraction vector is real.

Application of an electric field $\mathbf{E} \parallel [001]$ to a $\text{Bi}_{12}\text{GeO}_{20}$ crystal, owing to the reduction in the crystal symmetry, leads to that the incidence of an elastic wave

of any type from an isotropic medium generates all three types of refracted and reflected waves. An interesting example is the incidence of a shear wave polarized normally to the plane of incidence. In this case, it appears as two reflected shear waves arise in the isotropic medium, one of which is polarized in the plane of incidence and the other is polarized normally to it. Naturally, shear waves of only one type can exist in an iso-

tropic medium. Nevertheless, the change in the boundary conditions caused by the application of an external electric field to a $\text{Bi}_{12}\text{GeO}_{20}$ crystal leads also to the change in the direction of the polarization vector of the incident SQS wave, which turns out to be directed at some angle to the plane of incidence. This circumstance allows for the existence of a reflected shear wave, also polarized at some angle to the plane of incidence.

CONCLUSIONS

The software package developed here makes it possible to investigate the processes of reflection and refraction of BAWs at interfaces between crystals of arbitrary symmetry and obtain results in the form of cross sections of refraction cavities. If the coefficients of the nonlinear electromechanical properties are known, this calculation can be supplemented by the consideration of the effect of an external electric field.

ACKNOWLEDGMENTS

This study was supported by the Federal Target Program "Integration," project no. 67, and the President of the Russian Federation (the program "Leading Scientific Schools," project no. NSh 939.2003.2).

REFERENCES

1. K. S. Aleksandrov, in *Problems of Modern Crystallography* (Nauka, Moscow, 1975), p. 327 [in Russian].
2. F. I. Fedorov, *Theory of Elastic Waves in Crystals* (Nauka, Moscow, 1965; Plenum Press, New York, 1968).
3. M. K. Balakirev and I. A. Gilinskiĭ, *Waves in Piezoelectric Crystals* (Nauka, Novosibirsk, 1982) [in Russian].
4. H. F. Tiersten, *J. Acoust. Soc. Am.* **57**, 660 (1975).
5. M. P. Zaitseva, Yu. I. Kokorin, Yu. M. Sandler, *et al.*, *Nonlinear Electromechanical Properties of Acentric Crystals* (Nauka, Novosibirsk, 1986) [in Russian].
6. K. S. Aleksandrov, B. P. Sorokin, and S. I. Burkov, *Fiz. Tverd. Tela (Leningrad)* **32**, 186 (1990) [*Sov. Phys. Solid State* **32**, 104 (1990)].
7. Y. Cho and K. Yamanouchi, *J. Appl. Phys.* **61**, 875 (1987).
8. B. P. Sorokin, P. P. Turchin, S. I. Burkov, *et al.*, *IEEE Proceedings of the International Symposium on Frequency Control, Honolulu, USA, 1996*, p. 161.
9. V. I. Alshits, A. V. Sarachev, and A. L. Shuvalov, *Zh. Eksp. Teor. Fiz.* **89**, 922 (1985) [*Sov. Phys. JETP* **62**, 531 (1985)].
10. V. I. Alshits and A. L. Shuvalov, in *Physical Crystallography*, Ed. by B. K. Vainshteĭn and L. A. Shuvalov (Nauka, Moscow, 1992) [in Russian].
11. B. P. Sorokin, Yu. I. Kokorin, S. I. Burkov, and K. S. Aleksandrov, *Kristallografiya* **31**, 706 (1986) [*Sov. Phys. Crystallogr.* **31**, 416 (1986)].

Translated by Yu. Sin'kov

PHYSICAL PROPERTIES
OF CRYSTALS

Electromagnetic Emission under Uniaxial Compression of Ice: I. Identification of Nonstationary Processes of Structural Relaxation by Electromagnetic Signals

A. A. Shibkov, M. A. Zheltov, V. V. Skvortsov,
R. Yu. Kol'tsov, and A. V. Shuklinov

Tambov State University, ul. Internatsional'naya 33, Tambov, Russia

e-mail: shibkov@tsu.tmb.ru

Received September 9, 2004

Abstract—Discrete electromagnetic emission caused by a jump of plastic deformation and fracture of single-crystal and polycrystalline ice is revealed and investigated. An album of electromagnetic signals is compiled, which makes it possible, on the basis of the electromagnetic-signal shape, to identify and study the kinetics of mesoscopic events of structural relaxation that are related to the dynamics of dislocation pile-ups and cracks.
© 2005 Pleiades Publishing, Inc.

INTRODUCTION

It was shown in [1–13] that the intrinsic electromagnetic emission in the frequency range $\sim 10^2$ – 10^6 Hz of a crystal with predominantly ionic bonds subjected to a mechanical and/or thermal load characterizes the deviation of the crystal from equilibrium under test conditions and is indicative of the processes of structural relaxation (plastic deformation and fracture) occurring in the crystal. It has been found that the dynamics of dislocation slip bands and cracks in A_1B_7 [3–10] and A_2B_6 [12] compounds is accompanied by characteristic electromagnetic-emission (EME) signals. This phenomenon makes it possible to identify in situ these events in more complex processes of structural relaxation (for example, during multiple slip [3], at indentation [9], under laser puncture of surface [10], etc.), establish correlation between them, perform statistical and multifractal analysis [11], estimate the growth rate of the leading group of dislocations, the area swept by a pile-up, and volume of the crack cavity [3, 4], etc. In ice, as well as in A_xB_{8-x} compounds, dislocations transfer electric charge, while the edges of a fast crack are electrically active. Therefore, the nonstationary motion of dislocation pile-ups and micro- and macrocracks should cause generation of not only acoustic [14] but also electromagnetic emission. Indeed, propagation of a single crack arising under bending [15], uniaxial compression [15–17], an impact of a point load [16], and freezing of water [18] is accompanied by a characteristic EME signal in the frequency range $\sim 10^3$ – 10^5 Hz. The EME caused by the motion of dislocations in ice has not been studied yet.

Investigation of the nature of electromagnetic phenomena accompanying dynamic processes in ice is of great applied importance, primarily, in view of the problems of navigation in northern latitudes. In addition, it is well known that, during the fall of glaciers and avalanches, propagation of cracks in frozen soils and ice covering water reservoirs, and even before these catastrophic events, bursts of electromagnetic emission arise in the middle radio-frequency range [19–21]. Therefore, along with the navigation problems, there is practical interest in continuous electromagnetic monitoring of the environment containing frozen soils and large masses of ice and snow, which are prone to catastrophic shifts. To analyze the problem of identification using electromagnetic signals, of different processes of structural relaxation (plastic deformation; fracture; friction; and regelation, i.e., melting under pressure with subsequent crystallization) and estimation of their contributions to the complex natural phenomenon, it is necessary to create experimental conditions under which one of the above-mentioned processes is dominant.

In this paper, we report the results of studying the characteristics of EME signals produced under the motion of single slip bands and cracks and under multiple slip and fracture. On the basis of the results obtained, an album of EME maps of nonstationary mesoscopic processes of structural relaxation in single-crystal and polycrystalline ice is compiled.

EXPERIMENTAL

In macroscopic experiments, plastic properties of ice are investigated generally by analyzing the defor-

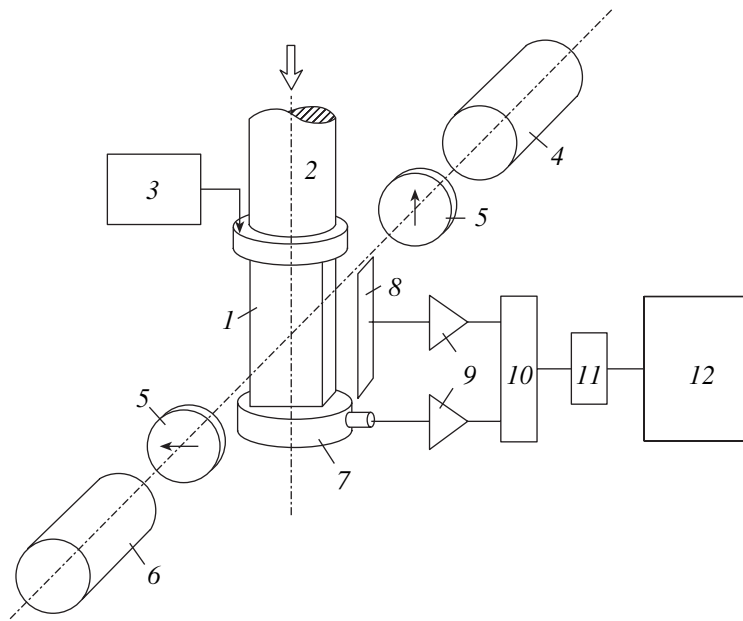


Fig. 1. Schematic of the experimental setup for studying the plastic deformation jump and fracture of ice by polarization optical, acoustic, and electromagnetic methods: (1) sample, (2) rod of the soft testing machine, (3) strain-measuring unit containing a mechanical indicator and a capacitance displacement sensor, (4) collimated light source, (5) polaroids, (6) digital video camera, (7) piezoelectric sensor, (8) capacitance probe, (9) high-resistivity preamplifier, (10) commutator, (11) ADC, and (12) computer.

mation curves obtained in a rigid testing machine [22, 23] or from creep curves [24]. It is preferable to study the plastic-flow instability under the conditions of active deformation of a crystal in a soft testing machine when the loading law is set in the form $\sigma = \sigma(t)$ and the measured response function is the strain $\varepsilon(t)$ itself. In this study, samples of single-crystal and polycrystalline ice $12 \times 18 \times 30 \text{ mm}^3$ in size were subjected to uniaxial compression in a soft testing machine with a constant stress rate $\dot{\sigma} = 5 \times 10^{-3} \text{ MPa/s}$ at the temperature $T = 250 \text{ K}$ in a soft testing machine. The samples were cut by a wire saw from blocks of freshwater (river) ice with an average grain size ranging from ~ 1 to $\sim 100 \text{ }\mu\text{m}$. Single-crystal samples were cut from large grains to be deformed in the basal slip system: the c axis made an angle of $\sim 40\text{--}50^\circ$ with the compression axis. To study the effect of grain boundaries on the formation and immobilization of dislocations and cracks, we prepared bicrystals: samples composed of two grains, i.e., having one grain boundary. The grain size in the polycrystalline samples ranged from 2 to 4.5 mm. To stabilize the ice structure, all samples were subjected to isothermal annealing at $T = 263 \text{ K}$ for $\sim 10^3 \text{ h}$.

During the sample deformation, we performed video recording in transmitted polarized light to detect the instants of formation of slip bands and cracks from the evolution of their photoelastic pattern. The deformation curve $\varepsilon = \varepsilon(t)$ was recorded using a mechanical motion sensor accurate to $1 \text{ }\mu\text{m}$. To measure small jumps of plastic deformation, we used a highly sensitive capacitance displacement sensor, which makes it

possible to fix deformation jumps in a sample with sensitivity to $\sim 10 \text{ nm}$ in the frequency range $\sim 1\text{--}300 \text{ Hz}$. The potential of the nonstationary electric field (EME signal) was measured using a plane capacitance sensor $20 \times 30 \text{ mm}^2$ in size, located at a distance of 5 mm from the sample surface. With allowance for the fact that the characteristic evolution times of cracks and dislocation slip bands in crystals are in the range $\Delta t \sim 10^{-6}\text{--}10^0 \text{ s}$, the bandwidth of the measurement channel was chosen to be in the range from 1 Hz to 3 MHz. The measurement channel included a high-resistivity broadband preamplifier ($R_{\text{in}} = 10^{12} \text{ }\Omega$, $C_{\text{in}} = 20 \text{ pF}$), an analog-to-digital converter (ADC) with a clock frequency up to 500 kHz, and a computer. In some experiments, an acoustic-emission (AE) signal from a piezoelectric sensor located in the bottom support of samples (Fig. 1) was recorded synchronously with measurement of an EME signal.

RESULTS AND DISCUSSION

Load Curves of Single-Crystal and Polycrystalline Ice

Figure 2a shows the typical load curves obtained with a constant stress rate for single-crystal ice (curve 1) and polycrystalline ice with the average grain size $\bar{d} \sim 3 \text{ mm}$ (curve 2). It can be seen that the hardening coefficient $\theta = d\sigma/d\varepsilon$ and the compression strength σ_{max} of single-crystal ice significantly exceed the corresponding values for polycrystalline ice. In addition, the defor-

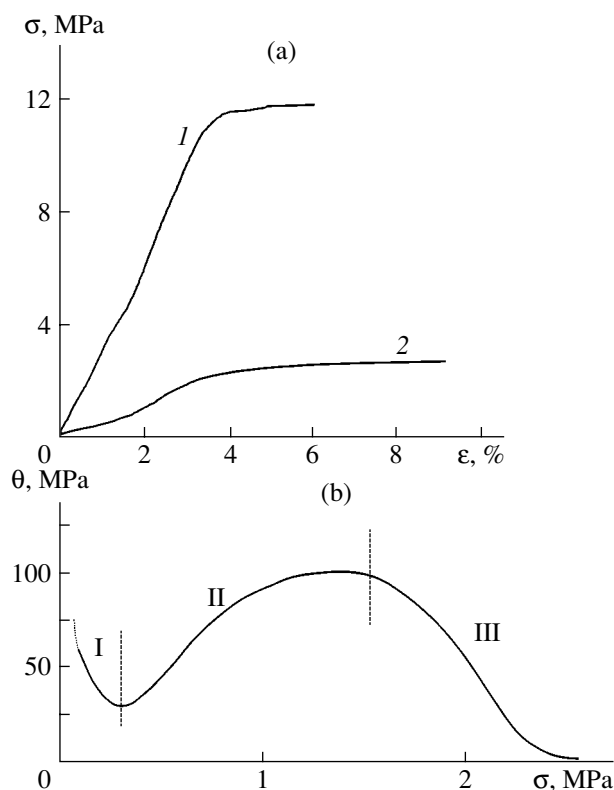


Fig. 2. (a) Load curves $\sigma(\epsilon)$ for (1) single-crystal and (2) polycrystalline ice deformed in a soft testing machine with a constant stress rate $\dot{\sigma} = 5$ kPa/s at $T = 250$ K. (b) Stress dependence of the hardening coefficient $\theta = d\sigma/d\epsilon$ of polycrystalline ice. Roman numerals I, II and III denote the stages of easy glide, strain hardening, and dynamic recovery, respectively.

mation curve of the latter is nonlinear in the entire range of applied stress and demonstrates at least three portions corresponding to the following main stages of the deformation process: the easy-glide stage I, which is not characteristic of polycrystals and is apparently due to the presence of large grains; the strain hardening stage II; and the dynamic recovery stage III, which is observed at $\sigma > 1.6$ MPa (Fig. 2b). It is reasonable to suggest that the higher nonlinearity of the deformation behavior of polycrystalline ice in comparison with single crystals is caused by the significant effect of grain boundaries on the multiplication and immobilization of dislocations.

Role of Grain Boundaries

The photoelasticity and optical activity of ice make it possible to investigate the distribution of internal elastic stress fields in situ; reveal grain boundaries; and estimate the role of the latter in the nucleation and deceleration of dislocation pile-ups with an excess of dislocations of the same mechanical sign (mechanical charges). These pile-ups are the main sources of long-range stress fields in plastically deformed crystals. As

an example of excellent photoelasticity of ice, Fig. 3a shows the classical stress-distribution pattern observed upon indentation of a small ball into the surface of a single-crystal sample. Such photoelastic rosettes, observed along the macroscopically planar grain boundary in a deformed bicrystal, decorate concentrators of internal stresses near microscopic irregularities of the boundary (Fig. 3b). Relaxation of these stresses may occur through different channels, depending on the stress level, strain rate, and temperature. Specifically, these channels are the formation of dislocation slip bands and microcracks; slip along the grain boundary, involving regelation processes; and migration of the grain boundary as a result of the ice recrystallization at high-temperature plastic deformation ($T = 0.94T_m$, where T_m is the melting temperature). Figure 3c shows the slip-band formation from a stress concentrator at the grain boundary.

In some experiments, stress concentrators were formed artificially by making scratches or notches with the use of a wire saw. Slip bands were formed generally by local sources near the intersection of a scratch or notch with a crystal edge, passed through the grain in the basal plane, and were locked by the grain boundary to form new stress concentrators in the head of the retarded pile-up (Fig. 3d). The new stress concentrators, in turn, serve as sources of slip bands and/or cracks (Figs. 3e, 3f) and set the stage for the relay-race transfer of shear or fracture to neighboring grains of the polycrystal. Figure 3g shows a crack growing along the grain boundary in a bicrystal. Video recording shows that this crack grows in steps and may suddenly, having changed the growth direction, pass into the grain volume (Fig. 3h). A deformed polycrystal is characterized by spontaneous formation (for ~ 1 s) of a random net of noncontacting mesocracks, whose size is of the same order of magnitude as the grain size. These mesocracks are located mainly along grain boundaries and, more rarely, intersect individual grains (Fig. 3i). The characteristic scale of this net, i.e., the distance between the most distant mesocracks, may be macroscopic (~ 1 cm), i.e., comparable with the sample size. Despite the large total fracture area, a sample is not fractured macroscopically and is not softened.

EME and AE Signals

It has been found that the process of plastic deformation of single-crystal and polycrystalline ice samples is accompanied by the generation of discrete EME and AE signals (Fig. 4). In all stages of deformation, AE signals have the form of damping harmonics with a shape, according to calibration, corresponding to the ballistic reaction of the machine-sample system. For this reason, the identification of dynamic processes of structural relaxation by the shape of AE signals meets significant difficulties, which limit the application of the AE method in physical investigations [25]. At the same time, EME signals are very diverse in shape. In

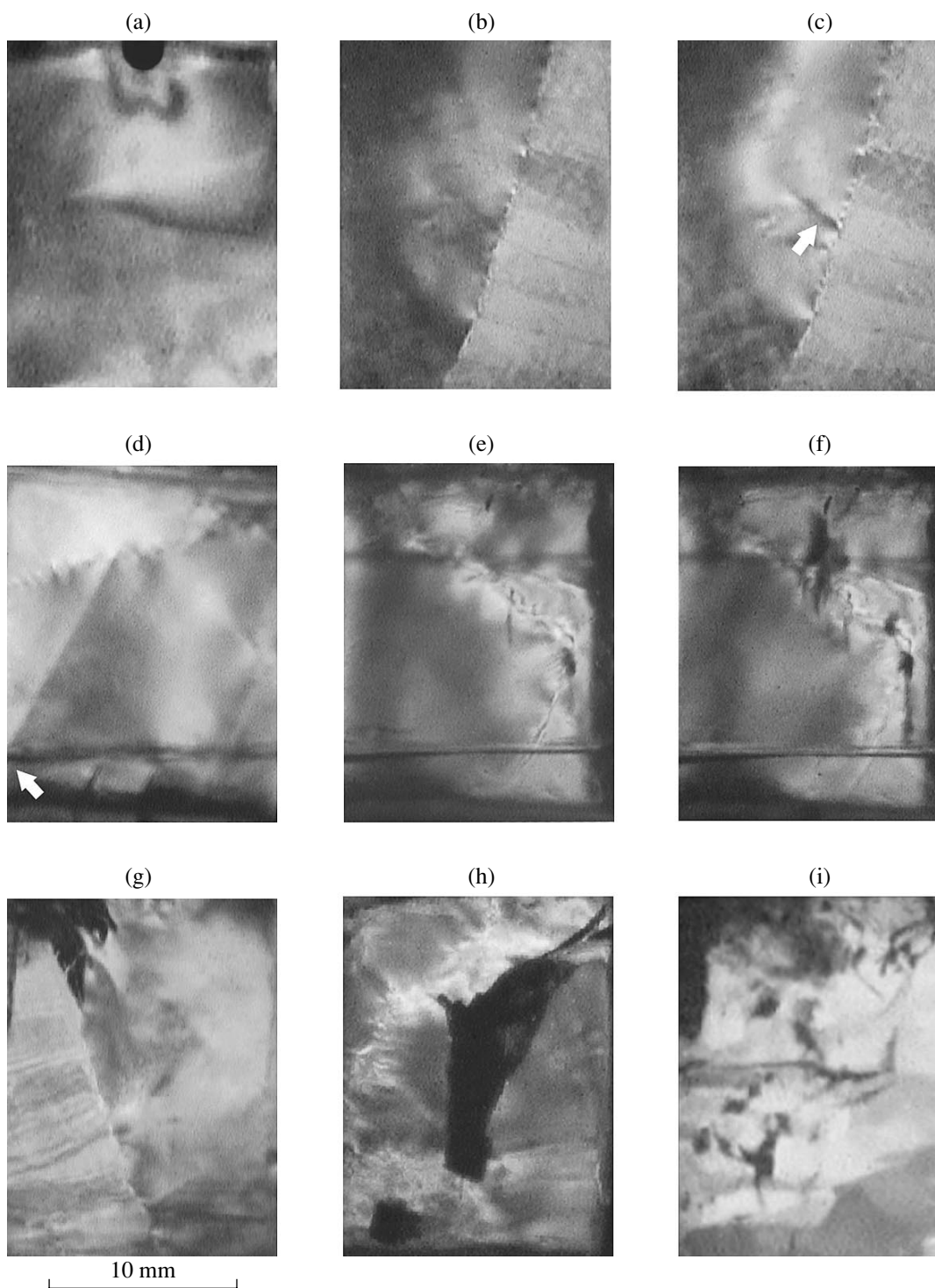


Fig. 3. Typical polarized-light images of deformed single-crystal and polycrystalline ice samples: (a) a photoelastic rosette obtained by indentation of a small ball into the surface of single-crystal ice (the ball was previously partially melted into the surface by regelation); (b) stress concentration near the grain boundary in a bicrystal subjected to uniaxial compression, $\sigma = 1.5$ MPa; (c) formation and propagation of a slip band (noted by an arrow) from the stress concentrator near the grain boundary, $\sigma = 2.3$ MPa; (d) a slip band blocked by the grain boundary in a bicrystal (the source of the band, noted by an arrow, is the region of intersection of a notch with the edge of the crystal), $\sigma = 2.5$ MPa; (e) formation and propagation of mesocracks in the grain volume from the concentrators located near the grain boundary, $\sigma = 9$ MPa; (f) the same at $\sigma = 9.7$ MPa; (g) propagation of a crack along the grain boundary in a bicrystal, $\sigma = 10.3$ MPa; (h) a macrocrack in a bicrystal, $\sigma = 11.2$ MPa; and (i) a fractal network of mesocracks propagating mainly along the grain boundaries in a polycrystalline sample (multiple subcritical fracture, $\sigma = 2.3$ MPa).

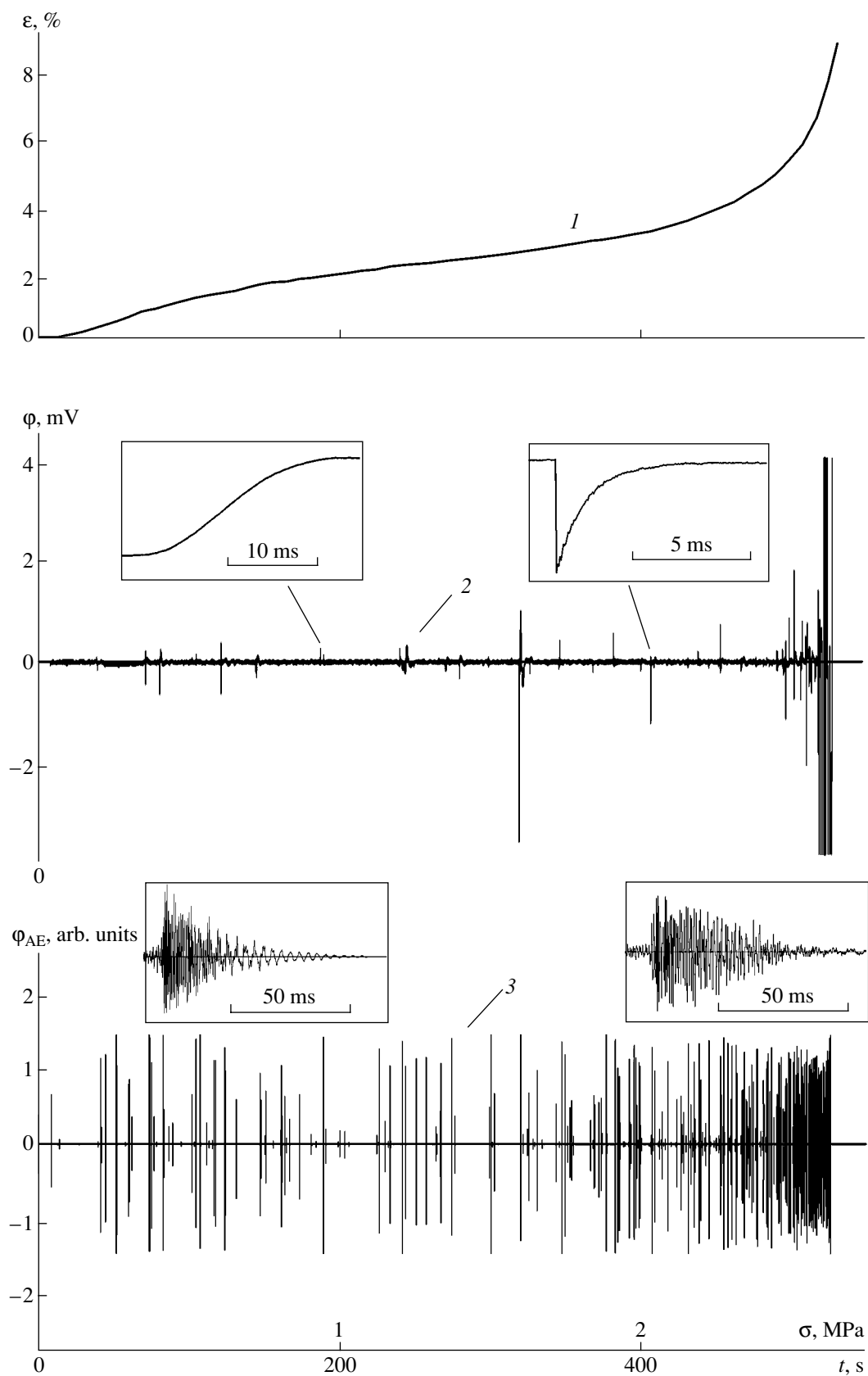


Fig. 4. Electromagnetic and acoustic emission during ice deformation: (1) the load curve recorded with a constant stress rate $\dot{\sigma} = 5$ kPa/s; (2) an EME signal; and (3) an AE signal. The insets show typical EME and AE signals in the initial and final stages of deformation.

Album of EME maps

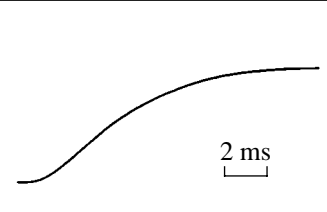
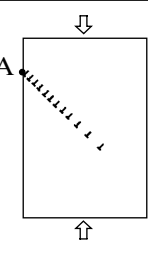
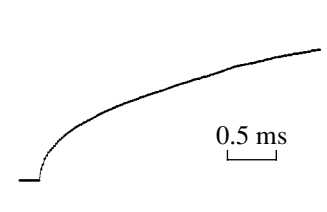
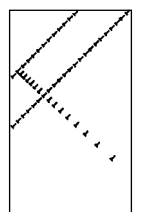
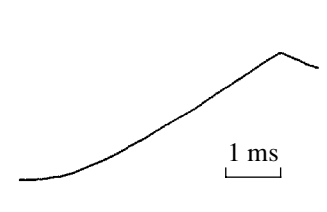
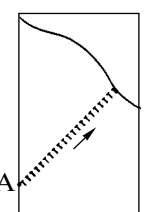
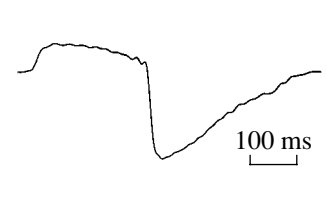
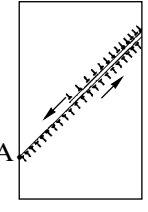
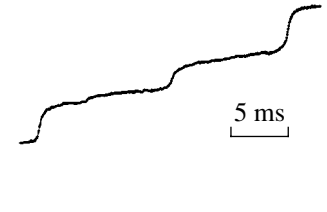
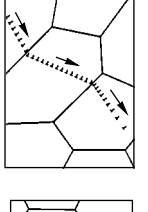
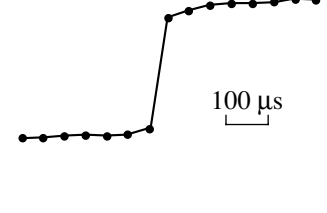
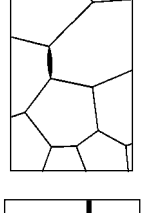
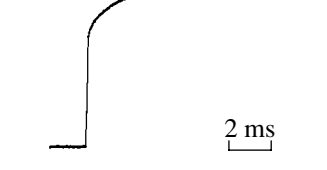
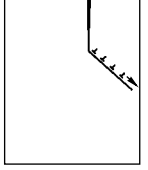
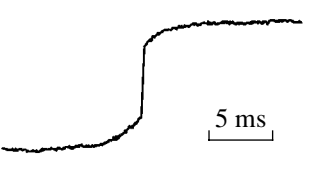
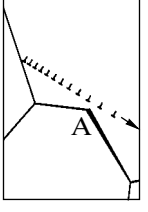
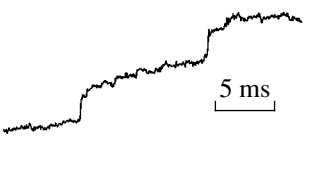
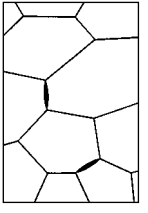
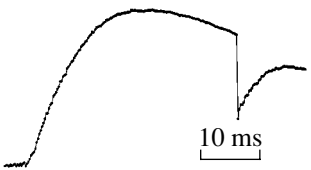
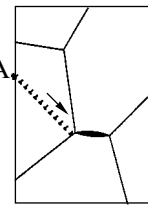
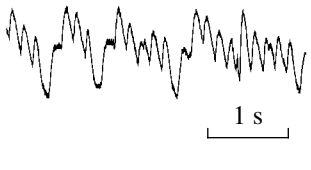
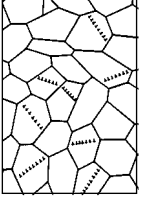
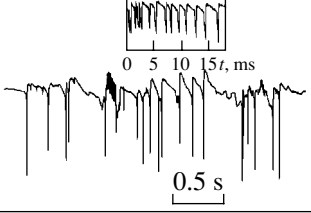
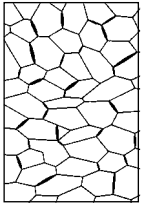
EME signal		Schematic of a process	Comment
no.	shape		
1			Formation and propagation of a slip band
2			Breakdown of a pile-up through a barrier (a low-angle boundary with an impurity atmosphere)
3			Generation, propagation, and blocking of a slip band
4			Secondary formation of a slip band by the crystal surface
5			Relay-race transfer of shear into neighboring grains
6			Development of a single microcrack
7			Development and stopping of a crack with plastic relaxation in the tip

Table. (Contd.)

EME signal		Schematic of a process	Comment
No.	Shape		
8			A propagating slip band initiates a microcrack source (of the type of stress concentrator A) by the elastic field of the pile-up head
9			Successive formation of two microcracks
10			A blocked band initiates a microcrack source
11			Relay-race (in time and space) transfer of shear involving many slip bands in different grains
12			Multiple subcritical fracture of a polycrystal

Note: The point A denotes the source of a mesoscopic defect (slip band or crack).

principle, synchronous video recording in polarized light and measurement of plastic deformation jumps by a highly sensitive displacement sensor makes it possible to identify jump processes of plastic deformation and fracture by EME signals.

In spite of the large variety of shapes of EME signals, they can be represented as a sequence of pulses of almost triangular shape, which are characterized by three main parameters: front width t_{fr} ; amplitude φ_m ; and the decay time τ_d (Fig. 5a), which is comparable with the Maxwellian relaxation time for ice τ_M in the range of mid and low frequencies [26, 27]. The quantity t_{fr} , which is determined by the characteristic time of the

crystal polarization caused by the evolution of an electrically active structural-kinetic element, turned out to be the most informative characteristic of EME signals. Depending on the value of t_{fr} , EME pulses can be divided into two groups: (i) pulses of type I with $t_{fr} \sim 3 \times 10^{-3} - 6 \times 10^{-1}$ s, which are accompanied by the generation of an AE signal but without appearance of visible microcracks, and (ii) pulses of type II with $t_{fr} \sim 10^{-5} - 3 \times 10^{-4}$ s, which are caused, according to the video recording data, by the formation and propagation of cracks with sizes greater than $\sim 100 \mu\text{m}$.

In a series of experiments, a signal of the highly sensitive sensor of the displacement of the machine's rod

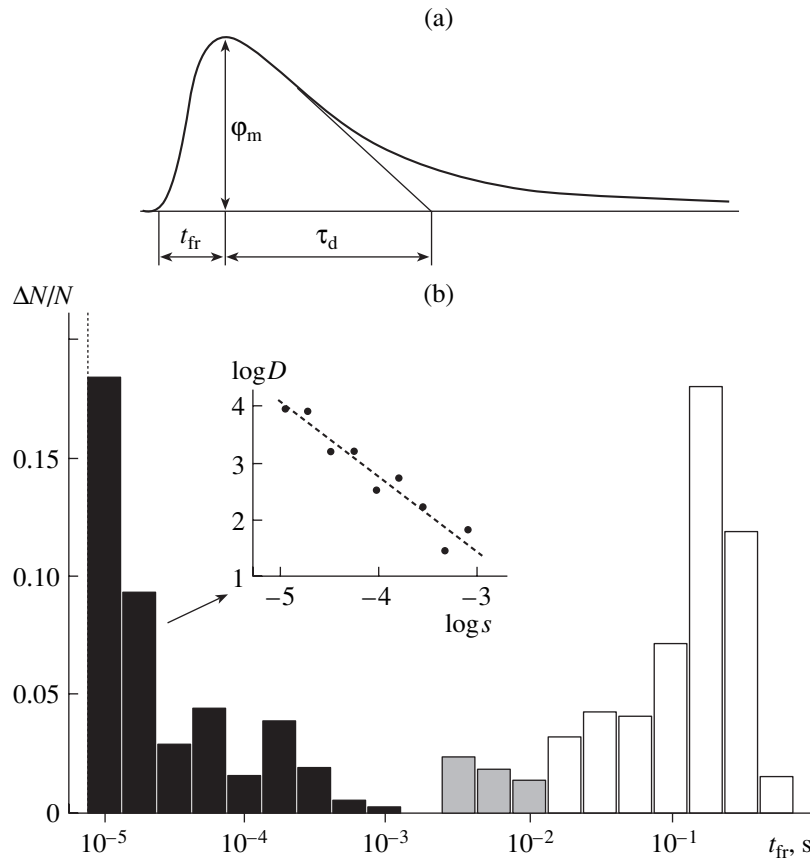


Fig. 5. (a) Schematic image of an EME pulse: ϕ_m is the amplitude, t_{fr} is the front width, and τ_d is the dielectric relaxation time. (b) Histogram of the front widths t_{fr} of EME pulses. EME pulses II, related to the development of micro- and macrocracks, are colored black; EME pulses I (described by the power function $\varphi(t) \sim t^{1/n}$), which are related to the dynamics of conservative dislocation pile-ups, are colored gray; and EME pulses I with a sigmoid front shape, related to the formation of slip bands (see table), are uncolored. The inset shows the distribution function $D(s)$ for EME pulses II (see text). The dashed line indicates the time resolution of the method ($8 \mu\text{s}$) corresponding to the maximum clock frequency of the ADC (500 kHz).

was recorded synchronously with the sample video recording in polarized light and the EME measurement. It was found that the development of a single slip band in a single-crystal sample in the initial stage of deformation ($\epsilon \sim 0.5\text{--}1\%$) is accompanied by a deformation jump $\Delta h \sim 0.1\text{--}1 \mu\text{m}$ and simultaneous generation of an EME pulse of type I (Fig. 6a). At the same time, the development of internal cracks with lengths $L_{cr} > 100 \mu\text{m}$ in the stage of developed deformation ($\epsilon > 3\%$) causes generation of EME signals of type II but does not lead to a significant (within the sensitivity limits) deformation jump (Fig. 6b).

Thus, two groups of EME signals (pulses I and II) account for two main nonstationary (in the frequency range $\sim 10^1\text{--}10^5$ Hz) processes in a deformed crystal: plastic-deformation jump and fracture. Owing to the significant difference between the instantaneous rates of plastic shear and propagation of microcracks and, therefore, the characteristic times of these processes, the histogram of the front widths t_{fr} of EME pulses is saddle-shaped (Fig. 5b). The range of forbidden values

of t_{fr} (the saddle region of the histogram) can be used for more exact separation of signals into pulses I and II and is important, for example, in carrying out statistical analysis of jumps of plastic deformation and fracture.

It can be seen from Fig. 5 that the histogram of the front widths of EME pulses I, related to plastic-deformation jumps, is bell-shaped, whereas the histogram of the front widths of EME pulses II, which are due to the formation and development of micro- and macrocracks in a sample, is described by power statistics: $D(s) \sim s^{-\alpha}$ (see inset in Fig. 5b), where $D(s) = N^{-1}\delta N(s)/\delta s$ is the normalized statistical distribution function of the quantity $s = t_{fr}$, $\delta N(s)$ is the number of events (EMe pulses) falling in the range from $s - \delta s$ to $s + \delta s$, and N is the statistical sampling size. For all single-crystal and polycrystalline ice samples under study, the exponent α is in the range from 1.2 to 1.6. Thus, EME pulses I and II are characterized by not only different front widths t_{fr} but also significantly different statistical distribution functions of this quantity.

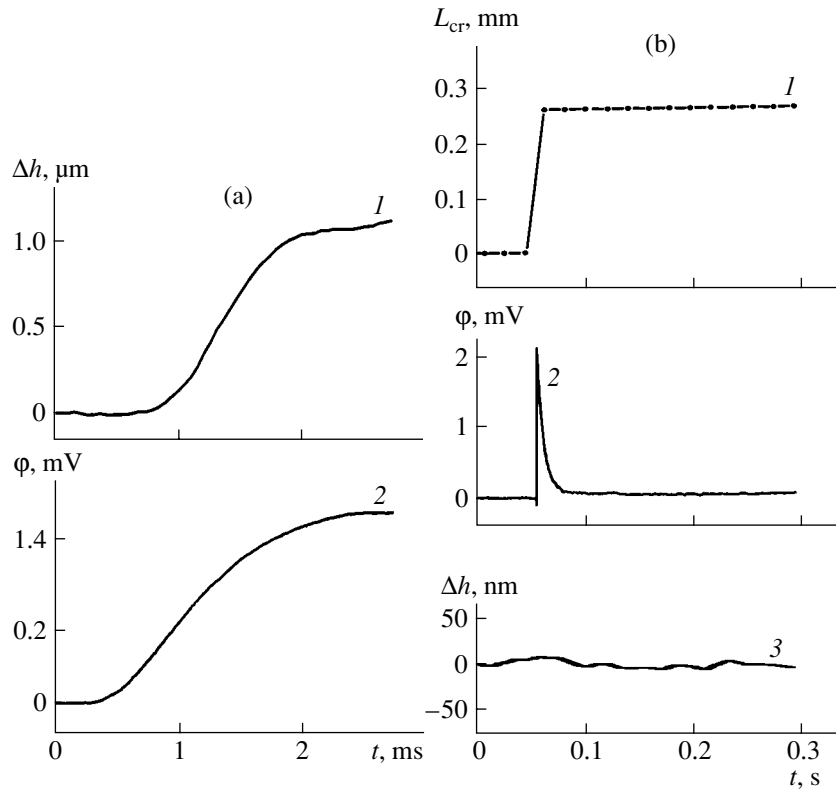


Fig. 6. Synchronous measurement data on the evolution of a slip band and a crack by the optical and electromagnetic methods: (a) synchronous recording of (1) the deformation jump Δh and (2) the EME signal ϕ of type I, which are caused by the development of a slip band (the time shift between the signal of the rod-displacement sensor and the EME signal is due to the inertia of the testing machine), and (b) synchronous video recording of (1) the jump in the length L_{cr} of a crack along the compression axis, (2) an EME signal II, and (3) a signal from the displacement sensor.

Another important characteristic of an EME signal is its front's shape, which reflects the kinetics of the corresponding processes of structural relaxation: jumps of plastic deformation and fracture. Concerning the shape, the observed single EME pulses I can be divided into at least two main groups: (i) sigmoid signals (table, signal 1), which were observed in all stages of plastic deformation, mainly in the range $0.5 < \varepsilon < 2\%$, and (ii) signals described by the power function $\phi(t) \sim t^{1/n}$, where $n = 2.1, \dots, 2.5$ (table, signal 2). The signals of the second group arise in the stage of developed deformation, when the applied stress σ is as high as ≈ 1 MPa in the polycrystalline ice samples and $\approx 3\text{--}4$ MPa in the single-crystal samples. These signals are characterized by the shortest front widths ($t_{fr} \approx 3\text{--}10$ ms) and, hence, are caused by the fastest plastic-deformation jumps. (The corresponding range of t_{fr} in the histogram in Fig. 5b is shaded gray.) As will be shown in our next paper, the signals of the first group, related to mesoscopic growth processes, are mainly due to the formation and propagation of slip bands, whereas the signals of the second group are related to sudden detachment of a large number of dislocations, for example, breakdown of a dislocation pile-up through a barrier.

Album of EME Maps

The table compiles the main types and combinations of EME signals, reflecting nonstationary mesoscopic events of plastic deformation and fracture of single-crystal and polycrystalline ice, which are related to the dynamics of dislocation pile-ups and cracks:

(i) Sigmoid signal I, according to the synchronous EME measurement and video recording of the photoelastic pattern, is caused by the formation and propagation of a single slip band.

(ii) The signal of type I in the form of a power function $t^{1/n}$ is caused, as will be shown in our next study, by the breakdown of a blocked dislocation pile-up or the drift of a pile-up to a cavity, or grain boundary, or outside the crystal surface.

(iii) The sigmoid signal with a sudden sharp decrease in the growth rate is the result of the development of a slip band with its subsequent blocking by the grain boundary (Fig. 3d).

(iv) The signal in the form of a sequence of sigmoid signals I of opposite signs accounts for the process of secondary formation of a slip band by the crystal surface. The surface source of the secondary band is initiated by the elastic field of the leading group of disloca-

tions in the primary pile-up. This process leads to the relaxation of the bending moment formed by the primary band with an excess of dislocations of the same mechanical sign and to a decrease in the total Burgers vector of the system of pile-ups.

(v) The signal in the form of a sequence of sigmoid signals I of the same sign is caused by the relay-race transfer of shear to neighboring grains.

(vi) EME signal II is caused by the development of a single microcrack.

(vii) The sequence of signals I and II reflects the development of a crack with plastic relaxation in the tip owing to the emergence of a dislocation pile-up from the tip of the crack that was stopped.

(viii) The superposition of signals I and II reflects the process in which the source of a microcrack is initiated in the stage of maximum growth rate of the slip band.

(ix) The sequence of two signals II is caused by the successive formation of two microcracks in neighboring grains of a polycrystal.

(x) The sequence of signals I and II accounts for the sequence of a mesoscopic event—slip—and subsequent formation of a microcrack. Specifically, propagation and blocking of a slip band initiate the formation of a microcrack along the grain boundary.

(xi) The sequence of a large number of signals I is, apparently, related to the relay-race transfer of slip bands into neighboring grains and similar to (v).

(xii) The fractal packet of signals of type II reflects the multiple cracking of polycrystalline ice, which is related to the spontaneous formation of a fractal network of cracks, mainly along the grain boundaries (Fig. 3i).

CONCLUSIONS

In this study, using a complex of in situ methods, including the methods of electromagnetic and acoustic emission in combination with the conventional technique of measuring deformation jumps and the polarization optical method, we investigated the plastic-deformation jump and the fracture of single-crystal and polycrystalline ice under uniaxial compression in a soft testing machine. It was found that the deformation of ice is accompanied by the generation of discrete pulses of the potential ϕ of the nonstationary electric field near the sample surface (EME signals). This phenomenon is indicative of thermodynamic deviation of a plastically deformed crystal from equilibrium and gives information about the kinetics of the structural relaxation of the crystal to a more equilibrium state (predominantly at the mesoscopic structural level). It was shown that measurement of EME signals makes it possible to map the complex process of formation of a structure of mesoscopic defects in a crystal to one degree of freedom—the time series $\phi(t)$. It was established that an EME signal is a superposition of elementary pulses I and II, which

reflect the dynamics of different processes of structural relaxation at the mesoscopic level—behavior of dislocation pile-ups and cracks, which play an important role in the general pattern of plastic deformation of a crystal. It is shown that analysis of the shape of the fronts of EME signals I makes it possible to distinguish the dynamics of slip bands (sigmoid signals, reflecting predominantly the processes of multiplication of dislocations in an ensemble) and conservative pile-ups (signals in the form $\phi \sim t^{1/n}$, which reflect the breakdown of a pile-up through the barrier). An album of EME maps was compiled, which allows one to identify in situ from the EME signal the most important events in a plastically deformed ice crystal, involving dislocation pile-ups and cracks (see table). This album, a sort of an “electromagnetic language” for the processes of structural relaxation, makes it possible to monitor the evolution of ensembles of defects of certain type (slip bands, conservative pile-ups, micro- and macrocracks) directly during the deformation; find correlation between them; perform statistical, multifractal, and dynamic analysis of the corresponding time series; and investigate, on the basis of EME analysis, the phenomena of self-organization, dynamic chaos, self-organizing criticality, and the evolution of a system toward a global catastrophe: macroscopic fracture.

ACKNOWLEDGMENTS

This study was supported by the Russian Foundation for Basic Research, project no. 04-02-16143, and the Ministry of Education of the Russian Federation, project no. E02-3.4-113.

REFERENCES

1. L. M. Belyaev, V. V. Nabatov, and Yu. P. Martyshev, *Kristallografiya* **7** (2), 576 (1962) [*Sov. Phys. Crystallogr.* **7**, 461 (1962)].
2. V. M. Finkel', Yu. I. Tyalin, Yu. I. Golovin, *et al.*, *Fiz. Tverd. Tela (Leningrad)* **21**, 1943 (1979) [*Sov. Phys. Solid State* **21**, 1116 (1979)].
3. Yu. I. Golovin and A. A. Shibkov, *Fiz. Tverd. Tela (Leningrad)* **28**, 3492 (1986) [*Sov. Phys. Solid State* **28**, 1964 (1986)].
4. Yu. I. Golovin and A. A. Shibkov, *Kristallografiya* **35** (2), 440 (1990) [*Sov. Phys. Crystallogr.* **35**, 254 (1990)].
5. Yu. I. Golovin, T. P. D'yachek, and V. M. Dolgova, *Fiz. Tverd. Tela (Leningrad)* **28**, 2502 (1986) [*Sov. Phys. Solid State* **28**, 1400 (1986)].
6. Yu. I. Golovin and A. A. Shibkov, *Kristallografiya* **32** (6), 1206 (1987) [*Sov. Phys. Crystallogr.* **32**, 710 (1987)].
7. Yu. I. Golovin and T. P. Dyachek, *Phys. Status Solidi A* **92**, 61 (1985).
8. Yu. I. Malyshev, V. F. Gordeev, V. P. Dmitriev, *et al.*, *Zh. Tekh. Fiz.* **54**, 336 (1984) [*Sov. Phys. Tech. Phys.* **29**, 197 (1984)].
9. Yu. I. Golovin, A. A. Shibkov, A. I. Tyurin, *et al.*, *Fiz. Tverd. Tela (Leningrad)* **30**, 3491 (1988) [*Sov. Phys. Solid State* **30**, 2005 (1988)].

10. Yu. I. Golovin, A. V. Gorbunov, and A. A. Shibkov, *Fiz. Tverd. Tela (Leningrad)* **30**, 1931 (1988) [*Sov. Phys. Solid State* **30**, 1116 (1988)].
11. Yu. I. Golovin, M. A. Lebyodkin, A. A. Shibkov, *et al.*, in *Proceedings of the Fourth International Conference on Single Crystal Growth and Heat and Mass Transfer ICSC-01, Obninsk, 2001*, Vol. 2, p. 543.
12. Yu. I. Golovin and A. A. Shibkov, *Kristallografiya* **32** (2), 413 (1987) [*Sov. Phys. Crystallogr.* **32**, 240 (1987)].
13. O. V. Charkina and K. A. Chishko, *Fiz. Tverd. Tela (St. Petersburg)* **43**, 1821 (2001) [*Phys. Solid State* **43**, 1898 (2001)].
14. J. Weiss and J. R. Grasso, *J. Phys. Chem. B* **101**, 6113 (1997).
15. V. F. Petrenko, in *Proceedings of the 11th International Symposium on Ice, IAHR 92, Banff, Alberta, Canada, June 15–19, 1992*, Vol. 2, p. 1140.
16. D. A. Fifolt, V. F. Petrenko, and E. M. Schulson, *Philos. Mag. B* **67**, 289 (1993).
17. V. F. Petrenko, *Philos. Mag. B* **67**, 301 (1993).
18. Yu. I. Golovin, A. A. Shibkov, M. A. Zheltov, *et al.*, *Izv. Akad. Nauk* **61**, 913 (1997).
19. L. G. Kachurin, I. O. Grigorov, Yu. I. Kuzin, *et al.*, *Dokl. Akad. Nauk SSSR* **248**, 41 (1979).
20. B. L. Berri, V. A. Gribov, I. O. Grigorov, *et al.*, *Edge Processes* (Mosk. Gos. Univ., Moscow, 1980), p. 18 [in Russian].
21. B. L. Berri and V. A. Gribov, *Vestn. Mosk. Univ., Ser. 5: Geogr.*, 15 (1982).
22. A. Higashi, S. Koinuma, and S. Mae, *Jpn. J. Appl. Phys.* **3**, 610 (1965).
23. S. J. Jones and J. W. Glen, *J. Glaciol.* **8**, 463 (1969a).
24. A. Higashi, S. Koinuma, and S. Mae, *Jpn. J. Appl. Phys.* **4**, 575 (1965).
25. O. V. Gusev, *Acoustic Emission in the Deformation of Single Crystals of Refractory Metals* (Nauka, Moscow, 1982) [in Russian].
26. V. F. Petrenko and R. W. Whitworth, *Physics of Ice* (Oxford Univ. Press, Oxford, 1999).
27. A. A. Shibkov, Yu. I. Golovin, M. A. Zheltov, and M. A. Tatarko, *Kristallografiya* **44** (6), 924 (1999) [*Crystallogr. Rep.* **44**, 863 (1999)].

Translated by Yu. Sin'kov